รายงานฉบับสมบูรณ์

โครงการ : Toward the Establishment of Design Guidelines for Earth Structures with Cement-Treated Soils

โดย รศ. ดร. พรเกษม จงประดิษฐ์

พฤษภาคม 2563

สัญญาเลขที่ BRG6080011

รายงานฉบับสมบูรณ์

โครงการ : Toward the Establishment of Design Guidelines for Earth Structures with Cement-Treated Soils

รศ. ดร. พรเกษม จงประดิษฐ์ มหาวิทยาลัยเทคโนโลยีพระจอมเกล้าธนบุรี

สนับสนุนโดย สำนักงานกองทุนสนับสนุนการวิจัย และมหาวิทยาลัยเทคโนโลยีพระจอมเกล้าธนบุรี

กิตติกรรมประกาศ

ผู้วิจัยขอขอบคุณสำนักงานกองทุนสนับสนุนการวิจัย และมหาวิทยาลัยเทคโนโลยีพระจอมเกล้าธนบุรีที่ได้สนับสนุนงบประมาณสำหรับงานวิจัยโครงการนี้ให้สามารถทำงานได้ผลสัมฤทธิ์โดยสะดวกตลอดระยะเวลาโครงการ นอกจากนั้นขอขอบคุณผู้ร่วมวิจัยทุกท่านที่ได้มีชื่อปรากฏเป็นผู้ร่วมเขียนในผลงานตีพิมพ์ที่ได้ช่วยกันทำให้งานสำเร็จอย่างมีคุณภาพ ขอขอบคุณบริษัท ปูนซีเมนต์ไทย จำกัด มหาชน บริษัท ซอยกรีตเทคโนโลยี จำกัด บริษัท อิตาเลียนไทย เดเวลลอปเมนท์ จำกัด มหาชน โรงพยาบาล ศูนย์การแพทย์ จักรี นฤบดินทร์ และกรมเจ้าท่า ที่ได้อำนวยความสะดวกในส่วนสถานที่ หรือ วัสดุวิจัย สุดท้ายขอขอบคุณนักศึกษา สาขาวิศวกรรมเทคนิคธรณี ภาควิชาวิศวกรรมโยธา มหาวิทยาลัยเทคโนโลยีพระจอมเกล้าธนบุรี ที่ได้ร่วมกันทำงานวิจัยอย่างมีความสุขและมีผลสำเร็จ

Abstract

Project Code : BRG6080011

Project Title : Toward the Establishment of Design Guidelines for Earth Structures with Cement-Treated Soils

Investigator : Dr. Pornkasem Jongpradist, KMUTT

Email Address : pornkasem.jon@kmutt.ac.th

Project Period 3 years (1 June 2017 to 31 May 2020)

This research utilize together three different tools including numerical analysis, field measurement and physical model test to assess both the failure and deformation behaviors of deep cement mixing piles used to support road embankments and deep excavations aiming to establish design guidelines and recommendations for future design. The combination and interplay among these three tools successfully tackled the interested problems and provided fruitful results. Preliminary investigation by numerical analysis accommodates understanding on key influencing parameters and responses. The physical model and/or field tests provides the verification and confidence of using the numerical analysis in further investigation. By series of parametric study analyses in conjunction with engineering decisions, guidelines and considerations for earth structures using cement-treated soils can be established. The guidelines developed in this study focuses on the selection of appropriate size or dimensions with the expected behaviors. This is very useful in the preliminary design. Furthermore, 9 international journal papers have been published from this project.

Keywords : Deep cement mixing, earth structure, design guidelines, numerical analysis, physical model, field test

บทคัดย่อ

รหัสโครงการ: BRG6080011

ชื่อโครงการ: งานวิจัยเพื่อจัดทำข้อแนะนำการออกแบบโครงสร้างดินที่ใช้เสาเข็มดินซีเมนต์ร่วมด้วย

ชื่อนักวิจัย : รศ. ดร. พรเกษม จงประดิษฐ์ มหาวิทยาลัยเทคโนโลยีพระจอมเกล้าธนบุรี

Email Address : pornkasem.jon@kmutt.ac.th

ระยะเวลาของโครงการ 3 ปี (1 มิถุนายน 2560 ถึง 31 พฤษภาคม 2563)

งานวิจัยนี้ใช้เครื่องมือที่แตกต่างกัน 3 วิธี ได้แก่ แบบจำลองทางกายภาพ การทดสอบในสนาม และการวิเคราะห์เชิงตัวเลข ร่วมกันสำหรับการเข้าใจพฤติกรรมของเสาเข็มดินซีเมนต์ ทั้งในแง่ของการวิบัติ/รับแรงสูงสุด และ การเสียรูป สำหรับในงานปรับปรุงดินคันทางถนน และการขุดลึก โดยมีเป้าหมายที่จะพัฒนาให้เกิดข้อแนะนำการออกแบบเสาเข็มดินซีเมนต์ในงานโครงสร้างดินในอนาคต ผลการศึกษาแสดงให้เห็นว่าการใช้เครื่องมือทั้งสามวิธีร่วมกันอย่างสมเหตุสมผล นำไปสู่การเข้าใจถึงปัญหาและให้ผลสัมฤทธิ์ที่น่าเชื่อถือ โดยใช้การวิเคราะห์เชิงตัวเลขในขั้นต้น ช่วยให้สามารถตรวจสอบตัวแปรอิทธิพล และพฤติกรรมตอบสนอง ที่น่าสนใจและเป็นสิ่งควบคุมพฤติกรรมหลักได้อย่างไม่สิ้นเปลือง การทดสอบด้วยแบบจำลองกายภาพ และ/หรือการทดสอบในสนามสามารถช่วยยืนยัน และปรับแก้วิธีการวิเคราะห์เชิงตัวเลขได้ ให้น่าเชื่อถือ และเหมาะสมสำหรับการวิเคราะห์เชิงตัวแปรต่อไป เพื่อให้สามารถวิเคราะห์กรณีที่หลากหลายได้มากขึ้น จากผลการวิเคราะห์ที่มากพอ และความเข้าใจถึงกลไกที่อยู่เบื้องหลัง ร่วมกับการตัดสินใจทางวิศวกรรม สามารถพัฒนาข้อแนะนำสำหรับการออกแบบเบื้องต้นได้ ซึ่งในการศึกษานี้สิ่งที่พัฒนาหลักๆอยู่ในรูปของผังภาพ ที่เป็นการแนะนำหรือเลือกขนาดที่เหมาะสม สำหรับออกแบบโดยที่สามารถคาดเดาพฤติกรรมที่จะเกิดขึ้นได้ ซึ่งจะเป็นประโยชน์อย่างมากสำหรับการออกแบบเบื้องต้น นอกจากนี้ผลการวิจัยได้เกิดผลผลิตเป็นบทความตีพิมพ์ในวารสารวิชาการนานาชาติ 9 ฉบับ

คำสำคัญ : การวิเคราะห์เชิงตัวเลข เสาเข็มดินซีเมนต์ โครงสร้างดิน แนวคิดการออกแบบ

Executive Summary

This research presents the development and implementation of the physical model tests, field tests and numerical analysis to investigate the behaviors of various deep cement mixing (DCM) column stabilized earth structures. These include stiffened deep cement (SDCM) and T-shaped deep cement mixing (TDM) columns aiming to improve the bearing performance of road embankment and deep excavation using DCM wall. These three different tools have been utilized together to assess both the failure and deformation behaviors of deep cement mixing piles which is used to support road embankments and deep excavations. The final aim of the study is to establish design guidelines and recommendations for future design. The combination and interplay among these three tools successfully tackled the interested problems and provided fruitful results.

Preliminary investigation by numerical analysis accommodates understanding on key influencing parameters and responses. The modeling concept and consideration are rationally discussed in detail. Advanced soil models are adopted as well as suitable parameter determination and calibration. The analysis method was verified with the filed measurement data of selected case studies before using in the preliminary investigation. The physical model and/or field tests provides the verification of using the numerical analysis. It is then confident to extend the analysis to investigate the behavior which cannot be observed by the available instrumentation. By series of parametric study analyses, understanding in complex behaviors and key influencing factors could be achieved. Based on the results obtained in parametric analysis, in conjunction with engineering decisions, guidelines and considerations for earth structures using cement-treated soils can be established. The guidelines developed in this study focuses on the selection of appropriate size or dimensions with the expected behaviors. This is very useful in the preliminary design. Besides, this provides the possibility to improve the design concept and introduce the new innovation in the future construction. Furthermore, 9 international journal papers have been published from this project.

เนื้อหางานวิจัย

Introduction

According to the soil condition of the Central Plain of Thailand, several ground improvement methods are essentially required to improve the strength and deformation characteristics of soft ground (such as, Cement Stabilization, Prefabricated Vertical Drains (PVD), Lightweight Geomaterials) before construction of any infrastructures, such as, highway, airport, drainage channel. Considering the versatility of cement stabilization, the method has gained wider acceptance especially in the Southeast Asia (Broms, 1984; Bergado et al., 1999; Uddin and Buensuceso, 2002; Petchgate et al., 2007). The deep soil stabilization so-called “Deep Cement Mixing (DCM)” has been widely applied to several types of construction such as foundation of road embankment, dike, small to medium size dam and taxiway for an airport, retaining structure for deep excavation of drainage channel and water reservoir and remediation of the failure of foundation (Petchgate et al., 2007).

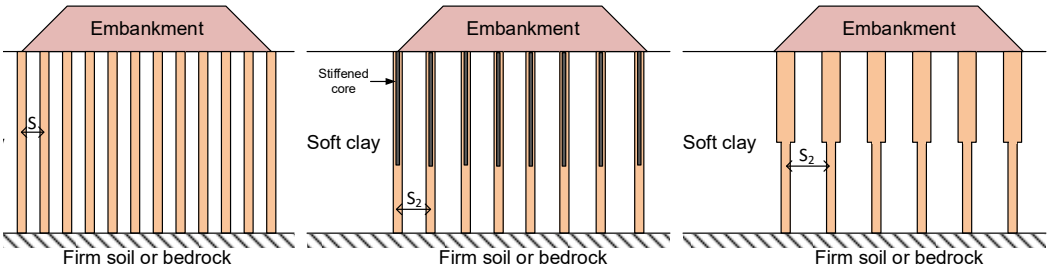

Fig. 1 Various types of DCM pile with recent innovation in road foundation works.

Among various current applications, the DCM piles have been used most often for foundations of road embankments (as shown in Fig. 1 (a)) to increase the stability of the native ground and to reduce settlement (Bergado et al., 1999; Lai et al., 2006). Under axial loading conditions, the stress along the pile length decreases with depth due to the load transfer to the surrounding soil, so that the maximum compressive stress occurs at the top of the pile (the pile head). In order to avoid pile failure (at the pile head), one possible solution is to increase the strength of the DCM pile by increasing the cement content. However, this method is uneconomical because only the top part of DCM piles is subjected to high compressive stress. Moreover, at higher cement contents, the strength of cement-treated clay does not linearly increase with the cement content, and the efficiency becomes inferior with increasing cement content (Uddin et al., 1997; Jongpradist et al., 2011b). Some innovative solutions have been proposed to solve this problem including stiffened deep cement mixing pile (see Fig. 2-middle) and T-shaped DCM pile (see Fig. 2-right).

The stiffened deep cement mixing (SDCM) pile was introduced in China; SDCM piles insert a small concrete pile or any reinforcement into the DCM pile immediately after finishing the DCM pile construction. The tests indicated that SDCM piles can resist higher loads compared to the conventional DCM piles of the same size and length. Series of researches focusing on the effect of core dimension on load carrying capacity and settlement of SDCM piles have been conducted (Dong et al., 2004; Jamsawang et al., 2010; Voottipruex et al., 2011; Wonglert and Jongpradist 2015; Wonglert et al., 2015). The establishment of a guideline for recommending an appropriate size of the core in SDCM

piles considering the failure modes with respect to the length of the core has been developed by recent researches (Wonglert and Jongpradist 2015).

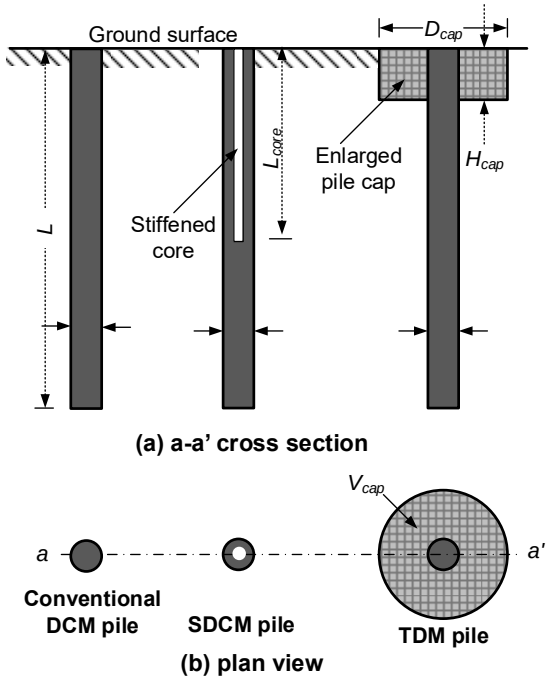

Fig. 2 Recent innovation in DCM pile

From the developed charts and given strength of DCM socket, the suitable core length and cross sectional dimension can be systematically chosen with known expected failure mode as schematically shown in Fig. 3. This provides the framework to construct design chart. The dimensions of the two units should be such that both work together effectively and use the full strength of the surrounding clay soil.

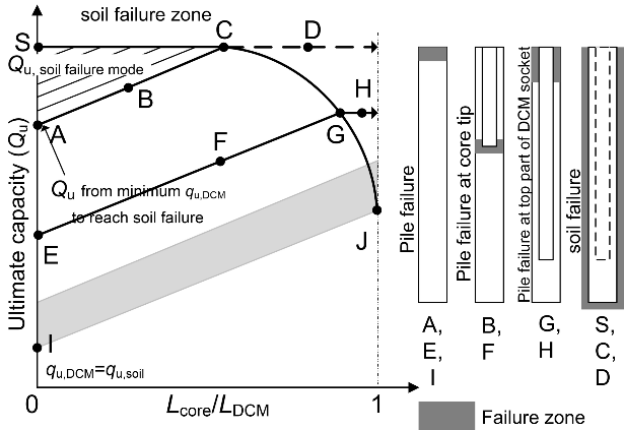

Fig. 3 Chart for suggesting the core length of SDCM (Wonglert and Jongpradist, 2015)

Although comprehensive understanding on mechanical behaviors of SDCM pile has been well established and some guidelines for designing have been developed. The studies so far have been focused on only individual pile, not the embankment pile system. Under the embankment circumstance, the interaction is not with only the surrounding soil, but also the embankment fill (see Fig. 1). The load transfer efficiency with respect to embankment fill weight and live load is also a key factor on utilizing

the highest capability of the designed piles under embankment. This depends on several factors, i.e. spacing between piles, thickness and stiffness of embankment. However, low quality fills as local available materials are preferable in engineering practice. Many past constructed road embankments exhibited differential settlement between DCM piles and surrounding soil as shown in Fig. 4. This is because the dimension and stiffness of between concrete pile and DCM (or SDCM) pile are much different. The concept and considerations used in designing the concrete pile-supported embankment cannot directly be applied to the DCM pile-supported embankment. The load transfer slab is thus introduced in this study as shown in Fig. 5. The full scaled embankment tests in the first phase of this research (RSA-grant) have been constructed and instrumented to verify this assumption. The results indicated that by introducing a stiff load transfer slab before filling, the differential settlement can be drastically reduced (Kriengtaweekij et al., 2014). This indicates the possibility to increase the pile spacing which consequently reduces the construction time.

Fig. 4 Photograph showing road serviceability problem due to excessive differential settlement

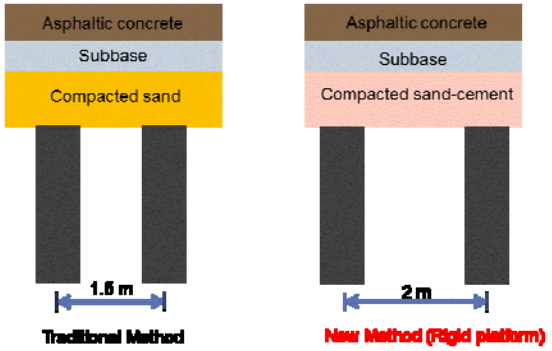

Fig. 5 Concept of rigid platform proposed in this study

However, due to the fact that the properties (particularly the stiffness) of both the DCM pile and load transfer slab can be varied depending on the materials used and limitation of budget, the required thickness of the load transfer slab is thus necessary to be defined under specific condition.

Based on an idea to combine the partial slab with the DCM pile, the “T-shaped, TDM,” which is larger in diameter at the top than the lower part (see Fig. 2-right), was introduced in China to support embankment. Full-scale test results indicated that TDM piles can reduce settlement of embankments as well as construction costs (Liu et al., 2012). This innovation has thus a potential to be economically competitive. However, up to date, only limited studies have been done and there are still insufficient understanding on this new system.

Besides the application to road foundation, recently the DCM piles are applied to deep excavation as a retaining structure. Some of congested urban areas require extra conditions of construction method such as very low noise and vibrating (Tanseng 2011). Deep Cement Mixing wall, as an alternative of retaining structure is introduced to meet the requirements. There were several reports of case history using Deep Cement Mixing wall to support the excavation in various forms of applications, e.g., DCM wall without bracing (Tanseng 2011), DCM wall with wall-strut (Tanseng 2012),

combination of DCM, sheet pile, and tie back supported excavation (Yang 2003), and DCM cross walls installation with diaphragm wall (Ou et al., 2003) and shown in Fig. 6. However, they are still highly empirical in terms of analysis and design with several assumptions due to unclear understandings on DCM wall behavior.

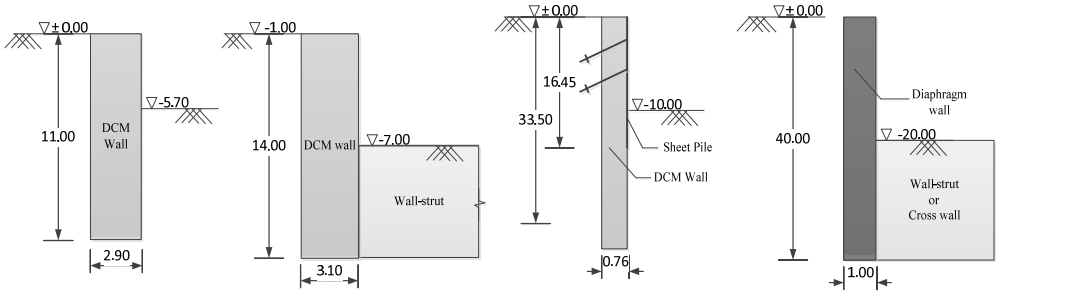

a) DCM wall without bracing [1] b) DCM wall with wall-strut [2] c) DCM with tie-back sheet pile wall [3] d) Diaphragm wall with DCM Cross wall [4]

Fig. 6 Various patterns of DCM wall used in case histories.

It is well known that to accomplish a good design, there are two main issues to be considered; the safety and the serviceability. The safety is defined to prevent the failure of structures, whereas, the serviceability for most major types of structure means to not allow excessive or differential deformations. With the recent urban development, another important aspect to be considered during design is the effect of any construction on adjacent structures. The current practice in the design of cement-stabilized ground is still mainly the safety evaluation based on results of unconfined compression tests. A number of calculation and analysis guidelines for safety assessment for many types of construction have been developed in the current design guidelines but very few of them consider the induced deformation. This is due to the lack of a design guidelines that consider this aspect. These are also because there is no link among each field of studies. The researches in laboratory have focused on understanding the behaviors as continuum media, whereas, the behaviors in full-scaled tests have been considered as structural members, such as, piles and retaining walls. The current design and guidelines are therefore based on the existing calculation methods of structural types considered. To achieve this, it requires better understanding of the mechanical behaviors the improved soil under field circumstance. To fulfill these, we have proposed an initial phase of research last 7 year under contract No. RSA5580007. The research focused on development of an analysis method which is capable of reflecting all dominant behaviors for estimating the deformation and potential failure consequence of earth structures with improved soils. Some preliminary guideline charts have been proposed. However, as the first phase of study, attentions have been mostly paid to individual members, not the entire system. The budget had been also partially paid on development of laboratory equipment for physical model testing and field embankment tests with instrumentation to verify our assumption and provide case study information. Base on the results and understandings obtained from the first phase, it is worth to continue the research in broader aspects as structural system to complete the final goal, the design guidelines. Together with the available equipment, knowhow, field testing results, relation with industrial for new plan of field test and current research team, the project was successfully completed.

The objective of this study is, thus, to perform the numerical analyses, physical model tests and field tests and integrate their results toward the establishment of a design guideline and recommendation for earth structure using cement-treated soil. The current research focuses on two types of problem; road embankment and deep excavation using DCM piles.

Problems to be considered

Three case studies i.e., stiffened deep cement mixing (SDCM) piles, T-shaped deep cement mixing (TDM) piles and deep cement mixing (DCM) wall as retaining structure in deep excavation were chosen in this study to investigate; 1) failure phenomena 2) influencing parameters and 3) potential to new innovation for solving the problem, respectively. The details of each case study are described in this section.

Physical model tests

SDCM piles

A series of scaled-down model tests under axial loading was performed to study the influence of the reinforced core length and DCM socket strength on load-carrying capacity, settlement and failure behaviors of SDCM columns. The main test program consisted of six experiments (settings A and B, see Table 1) by varying two influencing factors, the length of the reinforced core ($\mathbf{L_{core}}$) and the unconfined compressive strength of the DCM socket ($\mathbf{q_{u,DCM}}$). $\mathbf{L_{core}}$ and $\mathbf{q_{u,DCM}}$ values of 150, 350, and 500 mm and 35 and 135 kPa, respectively, were considered, as shown in Table 1 and Fig. 7. In addition to these six tests, additional tests were also conducted to better understand the mechanism behind the obtained results (settings C and D for DCM and SDCM columns, respectively, see Table 1).

Table 1 Testing program and details of SDCM and DCM piles in the physical model tests

	Type	No	$\mathbf{q_u}$ (kPa)		$\mathbf{q_{u,DCM}}$/ $\mathbf{q_{u,soil}}$	$\mathbf{L_{core}}$ (mm)	$\mathbf{Q_u}$ (N)		
							Testing result	Calculation	
			soil	DCM				Pile failure	Soil failure
Main Setting		A1	8	35	4.38	150	57	45	350
	SDCM	A2	8	35	4.38	350	97.7	45	350
		A3	8	35	4.38	500	131	45	350
		B1	8	135	16.88	150	210	170	350
	SDCM	B2	8	135	16.88	350	293	170	350
		B3	8	135	16.88	500	295	170	350
Supplement		C1	10	55	5.5	-	75	70	370
Setting	DCM	C2	10	275	27.5	-	350	350	370
		C3	10	280	28	-	364	360	370
		D1	10	280	28	150	375	350	370
	SDCM	D2	10	450	45	150	374	560	370

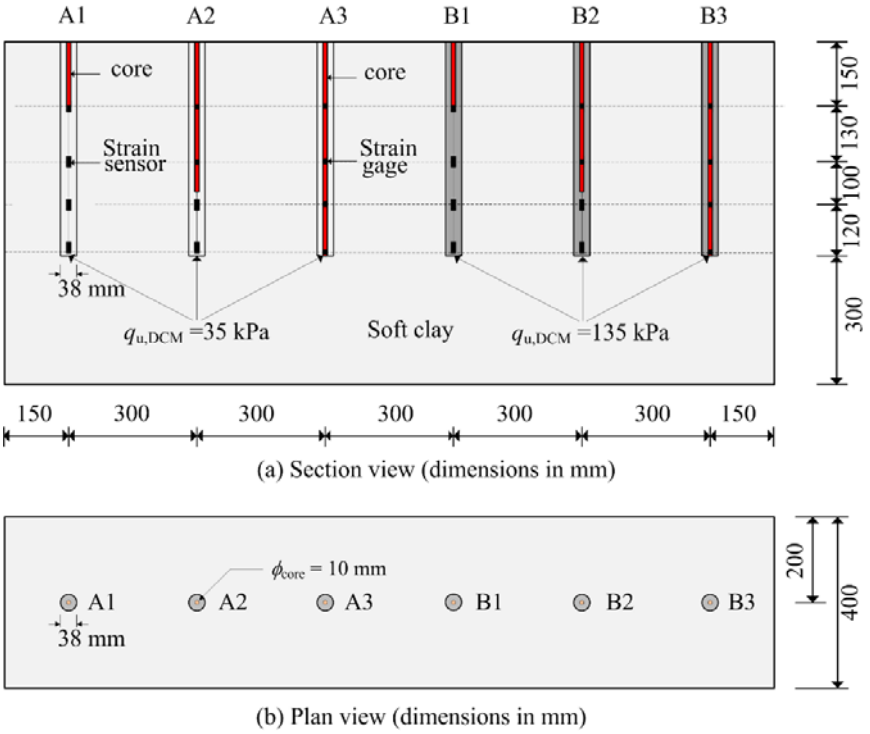

Fig. 7 Installation layout of SDCM piles in the main scaled down model tests.

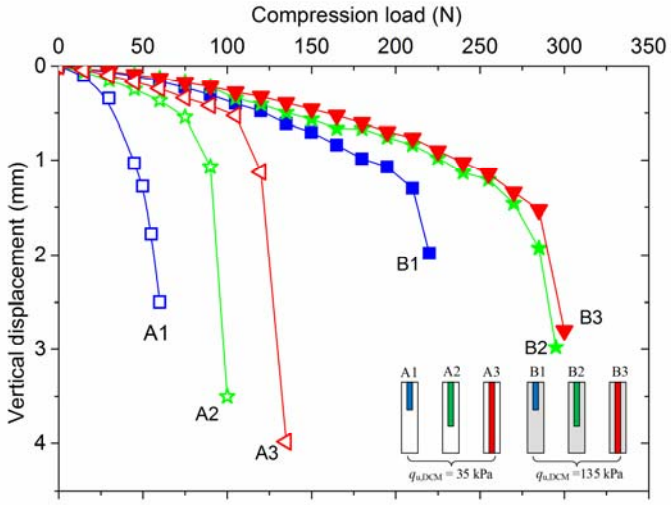

Fig. 8 Load-vertical displacement relation curves of SDCM piles with different strengths of socket pile and reinforced core lengths.

The load-vertical displacement relation curves of the floating SDCM columns in the main settings are illustrated in Fig. 8. Three SDCM columns, A1, A2, and A3, have the same $\mathbf{q}_{u,DCM}$ of 35 kPa with different core lengths of 0.15, 0.35, and 0.50 m, respectively. The results clearly indicate that increasing the core length leads to increases in the ultimate bearing capacity ($\mathbf{Q}_u$) and reductions in the vertical deformation of the columns. A similar behavior was observed for the SDCM columns with a $\mathbf{q}_{u,DCM}$ of 135 kPa (B1 and B2). However, insignificant improvements in both $\mathbf{Q}_u$ and vertical deformation of SDCM column were observed when the core length was increased from 0.35 (column

B2) to 0.50 m for column B3. This implies that when the $q_{u,DCM}$ increases to 135 kPa, the reinforced core need not be longer than 0.35 m. However, for the cases with a $q_{u,DCM}$ of 35 kPa, increasing the length of the core up to the entire length of the column can enhance the performances of the column. The effect of $q_{u,DCM}$ on the load-vertical displacement relation of SDCM columns can also be seen in this figure. A comparison between the two curves with the same L_{core} and different $q_{u,DCM}$ values (such as columns A2 and B2) reveals that SDCM columns with a higher $q_{u,DCM}$ (B2) are able to resist a larger applied load.

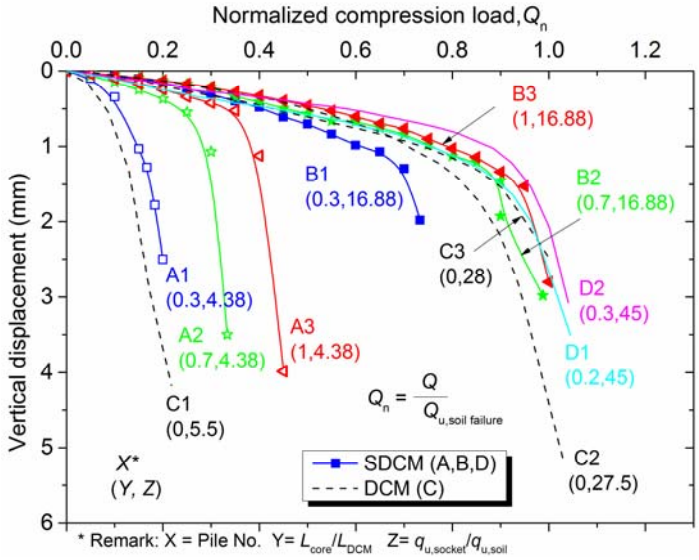

Fig. 9 Normalized load-vertical displacement relation curves of SDCM and DCM piles with different strengths of socket pile and soil and reinforced core lengths.

Figure 9 illustrates the normalized load, Q_n (normalized Q_u)-settlement curves of DCM and SDCM columns with different strengths of native soil and the DCM socket for the various test settings. All DCM and SDCM columns have the same dimensions (38 mm in diameter and 500 mm in length). In addition to the symbol of the test (such as A1), the numbers in parentheses indicate the core length ratio (L_{core}/L_{DCM}) and the column-to-soil strength ratio ($q_{u,DCM}/q_{u,soil}$). The relation curves show that if the column-soil strength ratio ($q_{u,DCM}/q_{u,\ soil}$) is larger than 27.5 (C2 (DCM), C3 (DCM), D1 (SDCM), and D2 (SDCM)), the columns should fail under the soil failure mode. For this case ($q_{u,DCM}$ is sufficiently high), inserting the core should not improve the behaviors of the column, as illustrated by the load-settlement curve of columns C3 and D1, because the ordinary DCM column is sufficiently strong and already failed with the soil failure mode. This conclusion is confirmed from the result for column D2. However, the core can assist in reducing the shortening of the column due to the higher stiffness compared to an ordinary DCM column, resulting in reduced settlement. In contrast, for SDCM columns A1, A2, and A3 and B1, B2, and B3, which have column-soil strength ratios of 4.38 and 16.88, respectively, increasing the core length results in an increase in Q_u and a decrease in the vertical deformation of the columns. DCM column C1, the column-soil strength ratio of which (5.5) is larger than that of SDCM column A1 (4.38) with a L_{core}/L_{DCM} value of 0.3, has inferior performance (in terms of the Q_u and settlement of the column) than column A1. This result implies that, at the lower strength

of the socket, insertion of stiffened core can improve the performance of DCM column. This suggests that to achieve the optimal design, the strength of the DCM socket should be selected such that the DCM column (without a stiffened core) will fail under column failure. Then, by inserting the core, the performance of the SDCM column will be improved up to the ultimate limit state at which the column will fail under the soil failure mode depending on the required capacity and cost considerations. Because the strength of the DCM socket can be reduced, the additional cost due to the insertion of the reinforced core will be compensated for by the reduction in the amount of cement.

In summary, the results obtained from the preliminary investigation by physical model test reveal that the strength of the DCM socket and the length of the core significantly affect the ultimate bearing capacity and settlement of the floating SDCM columns. The maximum load-carrying capacity appears to be limited at the ultimate bearing capacity under the soil failure mode. To achieve the maximum load-carrying capacity, the strength of the DCM socket can be reduced by inserting a sufficiently long reinforced core. There appears to be an optimum length of the stiffened core for a specific DCM socket strength, except when the socket is too weak.

TDM piles

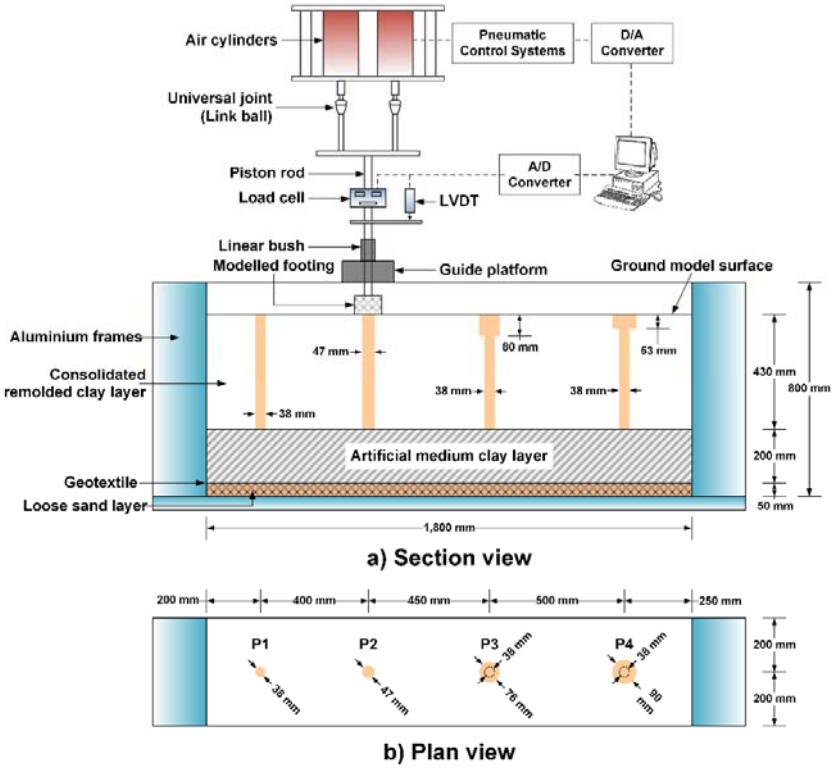

Fig. 10 Soil-cement piles and equipment configuration of the small-scale physical model tests

A series of small-scale physical model tests were conducted under equivalent pile volume. Three TDM shapes were selected to construct the model piles in the laboratory. These model piles were tested under vertical loading. A scaling factor of 13 was chosen for this small-scale physical model to reduce

the dimensions of the prototype piles. The tests included a ground model and four models of soil-cement piles, as shown in Fig. 10. Two conventional DCM piles with different sizes and volumes and two TDM piles with different pile cap sizes but the same volume were prepared under the same target pile strength. The models of the conventional DCM piles had $D_{DCM} = 38$ mm and L_{DCM} of 430 mm for the P1 pile (equivalent to the 0.5-m @5.6-m-long DCM pile of the prototype) and $D_{DCM} = 47$ mm for the P2 pile (equivalent to the 0.6-m @5.6-m-long DCM pile of the prototype). The models of the TDM piles had the same volume and length as the P2 pile. The dimensions of the enlarged pile cap for the P3 pile were as follows: surface pile diameter of 76 mm; thickness of the enlarged cap of 80 mm; pile body diameter of 38 mm. A larger surface pile diameter of 90 mm and a thinner enlarged cap of 53 mm were used for the P4 pile.

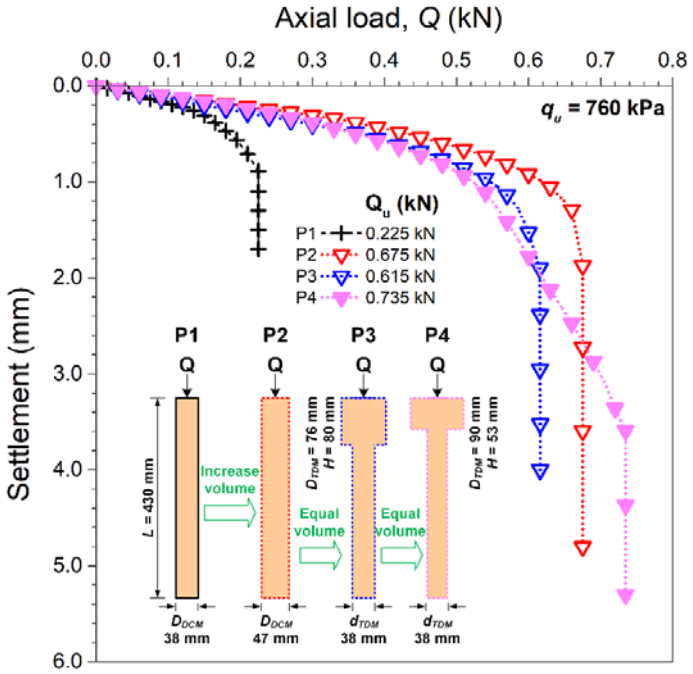

Fig. 11 Load-settlement curves of conventional DCM and TDM piles from the physical model tests

The load-settlement curves of the conventional DCM (P1-P2) and TDM (P3-P4) model piles from the laboratory loading tests are presented in Fig. 11. Q_{ult} of the P1 and P2 piles was 0.225 kN and 0.675 kN, respectively. Q_{ult} of the P2 pile was 3 times higher than that of the P1 pile because the P2 pile had a larger surface pile diameter, resulting in larger tip and side resistances. Additionally, the curve of the P2 pile shows smaller settlements than that of the P1 pile at the same load level. For the DCM and TDM piles with the same pile volume, the curves of the P2, P3 and P4 piles were nearly identical when the axial load was less than 0.3 kN. Once the axial load exceeded 0.3 kN, the curve of the P4 TDM pile indicated larger settlements than those of the other two piles. However, the P4 pile can sustain a larger maximum load, and the P3 TDM pile exhibited a smaller pile capacity than the P2 DCM pile. Enlarging the pile cap does not always guarantee an increase in the pile ultimate capacity. Q_{ult} is strongly influenced by the shape of the enlarged pile cap.

Field tests

SDCM piles

The full-scale tests were performed in the area of the Chakri Naruebodindra Medical Institute Hospital construction project in Samut Prakarn province. With the very thick soft clay layer in the site, the 10 m long DCM columns with diameter of 0.5 m have been designed and constructed to support the road embankment in the project. As part of the pile load tests in the project, the same size and length of DCM and SDCM columns were thus constructed. The DCM and SDCM columns were constructed to perform the column load test. The 0.5 m diameter and 10 m long columns were constructed by the high-pressure grouting method. To construct the SDCM column, immediately after the completion of the column installation process, eucalyptus wood with an average diameter of 0.15 m and length of 6.0 m was carefully inserted into the center of the DCM column to ensure that it was vertically aligned, as shown in Fig. 12a. Figure 12b illustrates the column cut-off before capping the column head with concrete. Two observed DCM columns were constructed adjacent to the test area to determine the strength of the column. The average value of the unconfined compressive strength is 1,200 kPa.

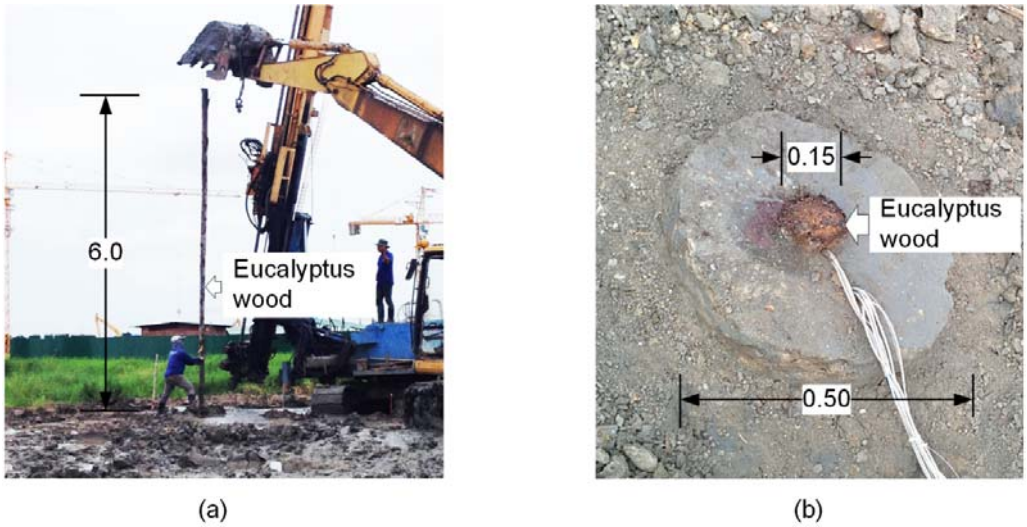

Fig. 12 Load-settlement curves of conventional DCM and TDM piles from the physical model tests

Figure 13 shows the load vertical displacement curves of the DCM and SDCM columns from the field column load tests. The settlements for both columns increase linearly with increasing applied load up to loads of approximately 150 and 200 kN for the DCM and SDCM columns, respectively. Then, the settlement increases rapidly until failure. The SDCM column can carry approximately 25% more load than the DCM column. At the same load, the SDCM column settles less than the DCM column. The results show that the performance of floating DCM column in terms of both the ultimate bearing capacity and settlement behavior can be improved by inserting eucalyptus wood as a core. These improvements in the SDCM column correspond well with the results from the physical model test in the previous section. The eucalyptus can potentially be utilized as a stiffened core. This provides an alternative of using less expensive and more sustainable material in the construction of SDCM columns.

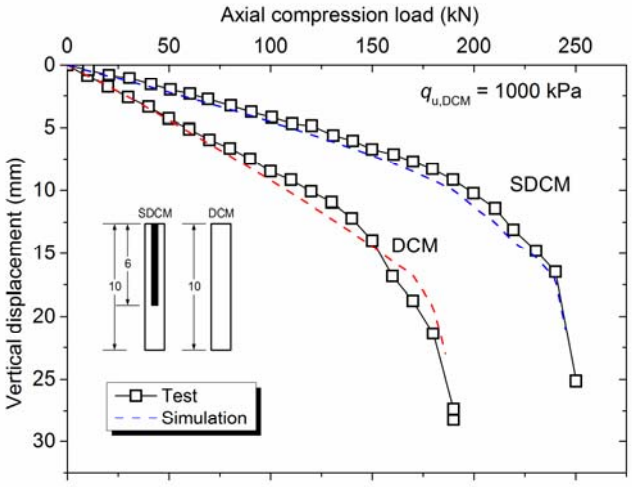

Fig. 13 Load-vertical displacement relations of DCM and SDCM piles from full-scale pile load tests and their simulation.

DCM walls

Downscaled unbraced-unreinforced DCM walls were fabricated in the soil conditions similar to the base case. The experiment was carried out in situ to investigate the excavation-induced wall displacement behavior. The experimental DCM walls were the t0.9 (t = 0.90 m, q_u = 600 kPa), t1.5 (t = 1.50 m, q_u = 600 kPa), and t0.9s (t = 0.90 m, q_u = 900 kPa) walls, with a constant wall length (H_w) of 7.5 m (Fig. 14).

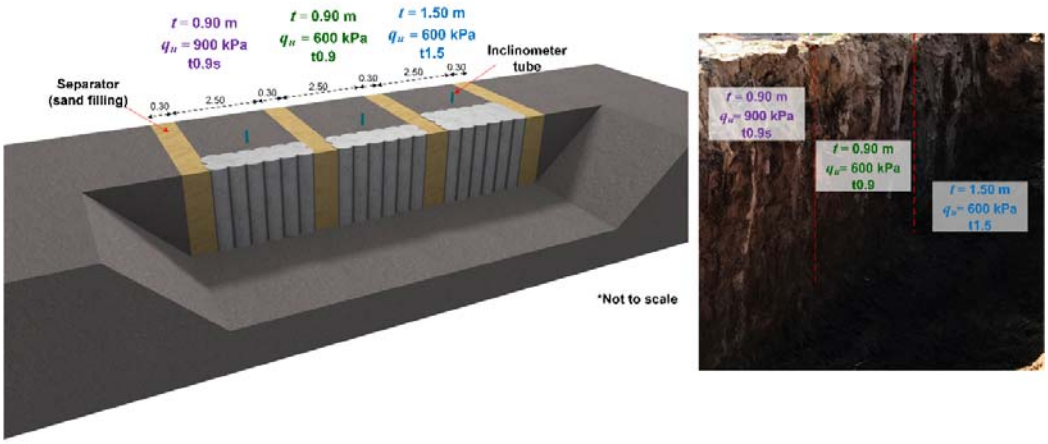

Fig. 14 Downscaled unbraced-unreinforced DCM walls with 7.5 m wall length and 2 and 4 m excavation depths

The excavation depth was varied between 2 and 4 m (i.e., 2 and 4 m) to assess the effect of excavation depth ratio (H_e / H_p) on the displacement behavior. To minimize the effect of interaction between the walls, the sand-filled separators were deployed. Three 12m-long inclinometer tubes were individually installed behind the DCM walls to monitor the excavation-induced displacement. Fig. 15 shows the horizontal displacement of the t0.9, t1.5, and t0.9s DCM walls at 2 and 4m excavation depths. All the experimental walls had mode A displacement behavior. The t0.9 and t1.5 walls exhibited

the largest and smallest displacement. At the excavation depth of 2 m (H_e / H_p = 0.36), the horizontal displacement of the strengthened wall (t0.9s) was considerably smaller than that of the t0.9 wall, indicating that the material improvement decreased the displacement. On the other hand, at 4 m (H_e / H_p = 1.14), the horizontal displacement of the t0.9s strengthened wall was comparably smaller than the t0.9 wall's, suggesting that the benefit of material improvement decreased as the excavation depth ratio increased. The findings validated the parametric study in that both the slenderness ratio (wall shape) and the excavation depth ratio played a crucial role in the displacement behavior of DCM walls.

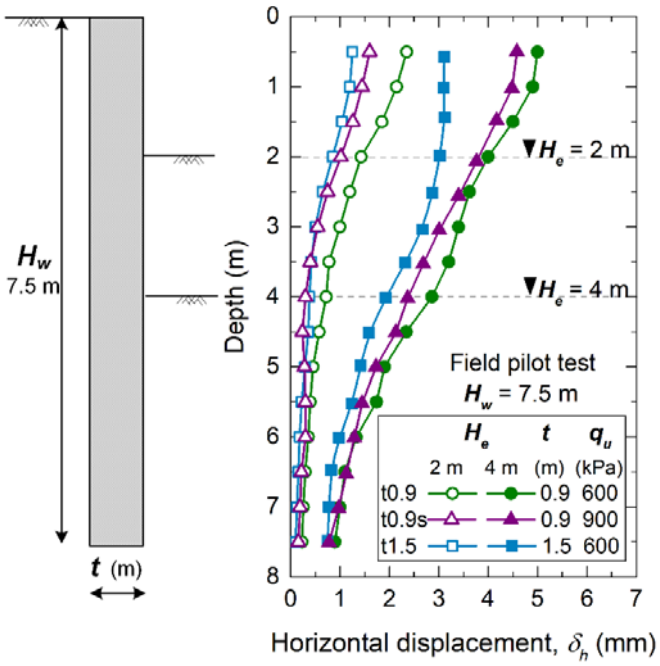

Fig. 15 Horizontal displacement of the downscaled DCM walls at 2 and 4m excavation depths

Numerical Analysis

SDCM and TDM piles

An extended study by finite element analysis (FEA) under the two-dimensional axisymmetric condition was conducted to further investigate the behavior of SDCM and TDM columns from physical model and full-scale tests. The conditions of the full-scale tests or referred field case were used as a reference case to perform the sensitivity analysis. A parametric study of the SDCM columns under axial loading by varying the strength and length of the DCM socket column and the length of the stiffened core was carried out, while the cap shape was varied for TDM piles. Before performing the numerical parametric study, verification was conducted by comparing with the results from the full-scale load tests. The finite element program PLAXIS 2D Version 8.2 (Brinkgreve, 2008) was used to analyze the DCM, SDCM and TDM columns during axial loading under the undrained condition in this study.

The load applied to the top of the wish-in-place DCM or SDCM or TDM columns in each analysis was gradually increased following ASTM D-1143, as performed in the field test after establishing the initial stress state. The column settlement at the column top and axial stress along the column length were

monitored for each applied interval load until the end of the analysis. The method by Marzukovic (1972) was used to determine the ultimate column capacity from the load-settlement curve of both the DCM and SDCM columns

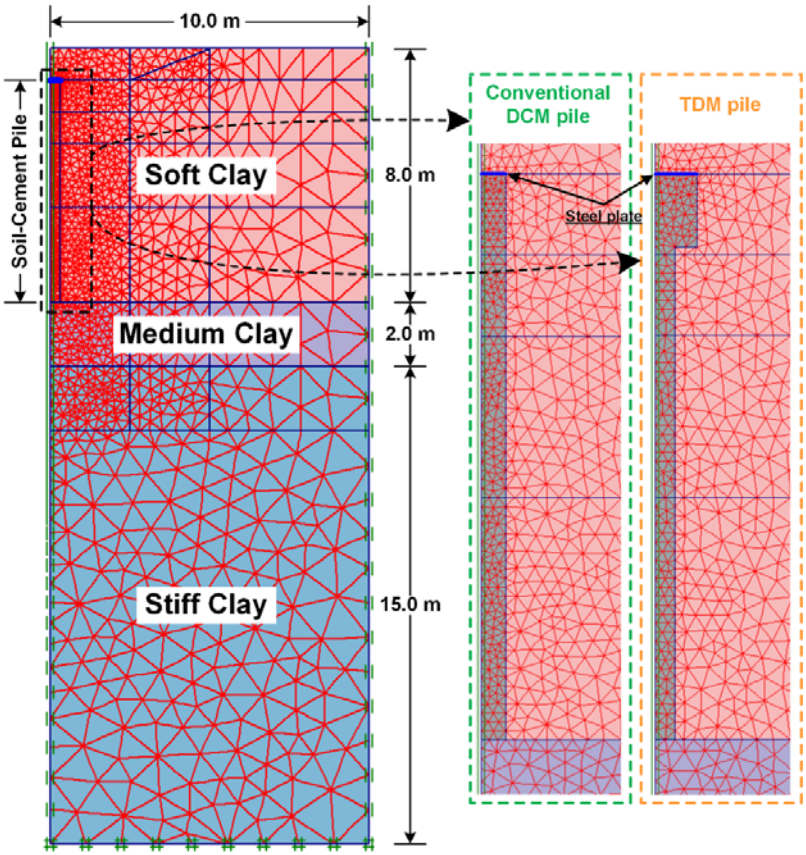

Fig. 16 Geometry, finite element mesh and boundary conditions of the considered problem

The clay was modeled using the hardening soil (HS) model considering the elasto-plastics with stress-dependent stiffness and shear dilatancy properties (Schanz et al., 1999). The model parameters were obtained from calibrating the oedometer test results. The cement-mixed soil is assumed to behave as an elastic–perfectly plastic material following the Mohr-Coulomb (MC) model. A linear elastic (LE) material model was used to model the core and concrete column cap. The soil parameters used in the analyses were mainly determined from calibration on triaxial testing results of soil specimens at AIT (Jongpradist et al., 2013). The values of the material parameters used in the numerical analysis are summarized in Table 2. The value of interface friction (Rinter) between the core and DCM socket was chosen to be 0.4 (Voottipruex et al., 2011) while the value of 1.0 (Brinkgreve 2008) is assigned for that between the DCM column and the surrounding soil.

Table 2 Material parameters used in finite element analyses

Material	Model	γ (kN/m^3)	c′ (kPa)	ϕ	Ψ	E (kPa)	E_{50} (kPa)	E_{ur} (kPa)	ν	m
Filled	HS (U)	15	1	27	0	10,000	10000	30000	0.3	1
Weathered	HS (U)	15	1	25	0	6,500	6500	25000	0.3	1
Soft clay	HS (U)	14	1	23	0	3,200	3200	20000	0.3	1

Medium clay	HS (U)	15	1	26	0	9,000	9000	30000	0.3	1
DCM pile										
q_u =125 kPa	MC(U)	14	60	30	0	16,800	-	-	0.3	-
q_u =250 kPa	MC(U)	14	120	30	0	33,500	-	-	0.3	-
q_u =500 kPa	MC(U)	14	240	30	0	67,000	-	-	0.3	-
q_u=1000 kPa	MC(U)	14	480	30	0	134,000	-	-	0.3	-
q_u=1500 kPa	MC(U)	14	700	30	0	200900	-	-	0.3	-
Wood	MC(U)	15	6500	30	-	$1.5x10^7$	-	-	0.25	-
Concrete	MC(U)	23	8000	40	-	$3x10^7$	-	-	0.2	-

Remark: HS = Hardening Soil Model, MC = Mohr-Coulomb Model, LE = Linear-Elastic Model,

p_{ref} for HS = 100 kPa, U = Undrained, * Parameter set of full scale test

DCM walls

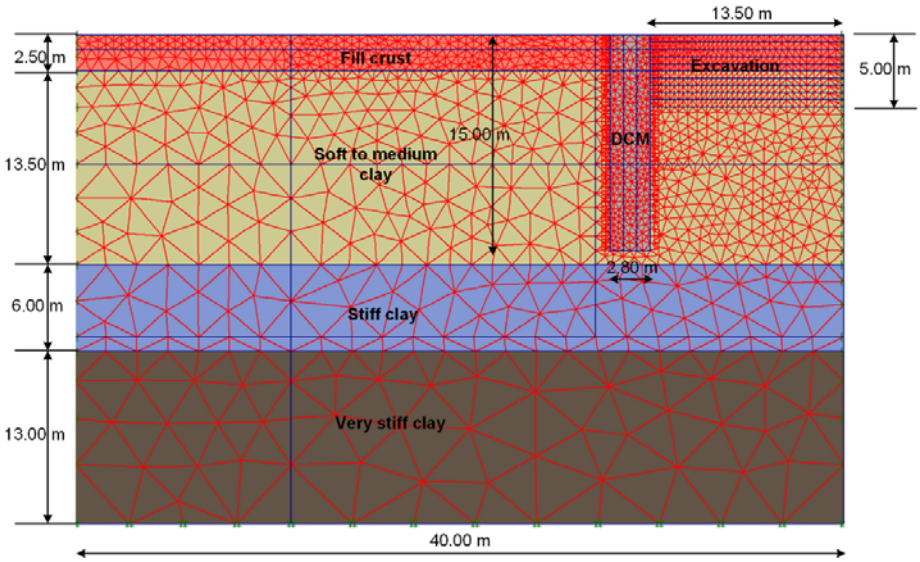

Fig. 17 Mesh model of the DCM-walled basement excavation and boundaries of the base case

Fig. 17 illustrates the mesh half-model of the DCM-walled basement excavation and boundaries of the base case using PLAXIS 2D. The mesh model was subsequently used to characterize the unbraced-unreinforced DCM wall behavior. Given the symmetry and sufficient length of the excavation, plane strain and half modeling were employed. The soil layers and the DCM wall were modeled as solid elements. Interface elements were also applied to both sides of the wall, simulating interaction between materials. The hard stratum of very stiff clay was assumed the bottom boundary of the model. Closed groundwater flow and displacement fixities were assumed for the side and bottom boundaries. In the figure, the half-modeling width of the excavation was 13.5 m. Besides, the project construction sequences were incorporated in the model generation and the mesh sensitivity analysis carried out.

The HSM parameters included the effective cohesion (c'), effective friction angle (ϕ'), reference secant, oedometer, and unloading-reloading moduli (E_{50}^{ref}, E_{oed}^{ref}, E_{ur}^{ref}), reference pressure (p^{ref} = 100 kPa), Poisson's ratio for unloading-reloading (ν_{ur} = 0.2), failure ratio (R_f = 0.9), and power factor (m). The DCM (wall material) parameters were: c'=242 kPa, ϕ'=35°, E_{50}^{ref} = E_{oed}^{ref} = 2.75×10^5

kPa, E_{ur}^{ref} = 8.25×10^5 kPa, and m = 1. The stiffness parameters obtained in this study are similar to those derived from Jamsawang et al. (2018) and Phutthananon et al. (2018).

Analysis results

SDCM piles

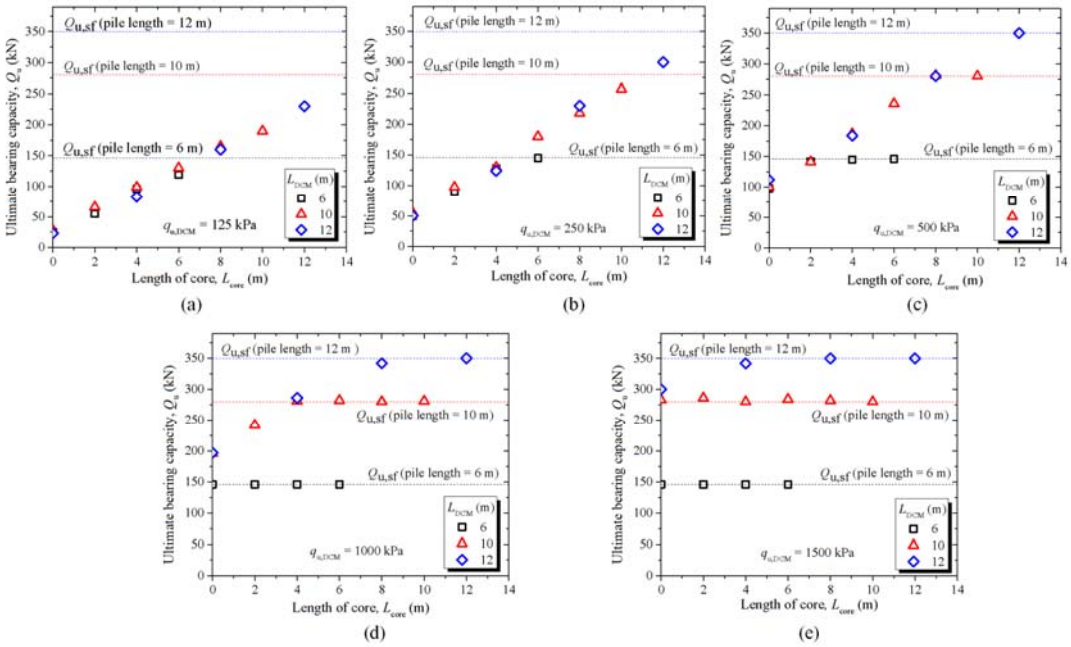

Fig. 18 Relation curves between Q_u and L_{core} of SDCM piles with (a) $q_{u,DCM}$= 125 kPa, (b) $q_{u,DCM}$ = 250 kPa, (c) $q_{u,DCM}$ = 500 kPa, (d) $q_{u,DCM}$ = 1000 kPa, and (e) $q_{u,DCM}$ = 1500 kPa

The influence of the length of the reinforced core on the ultimate bearing capacity of the SDCM column is presented. Figure 18 illustrates the plots of L_{core} versus Q_u of the SDCM columns with different values of L_{DCM} and $q_{u,DCM}$. The values of the ultimate capacity for the soil failure mode, $Q_{u,\ sf}$, for different column lengths are also included in the figure as horizontal dotted lines. In Fig. 18a, for low values of $q_{u,DCM}$ (125 kPa), the Q_u for all columns (L_{DCM} of 6, 10, and 12 m) increase linearly with increasing of L_{core} up to a L_{core}/L_{DCM} of 1. The Q_u values of all columns are still lower than their $Q_{u,sf}$. When the $q_{u,DCM}$ increases to 250 kPa, as illustrated in Fig. 18b, the SDCM columns with a L_{DCM} of 6 m reaches its $Q_{u,sf}$ (145 kN) with an L_{core} of approximately 4 m, whereas the other columns (lengths of 10 and 12 m) do not reach their $Q_{u,sf}$ (280 and 350 kN, respectively). The Q_u of these columns (10 and 12 m) increase proportionally with increases in L_{core}. With a $q_{u,DCM}$ of 500 kPa, as illustrated in Fig. 18c, the Q_u of all SDCM columns reaches their $Q_{u,sf}$ with different L_{core} values of 2, 8, and 12 m for L_{DCM} values of 6, 10, and 12 m, respectively. This indicates that increases in L_{core} leads to increases in Q_u until $Q_{u,sf}$ is reached. Once $Q_{u,sf}$ is reached, increasing L_{core} has no impact on Q_u. This conclusion is also confirmed from the results shown in Figs. 18d and 18e for $q_{u,DCM}$ values of 1,000 and 1,500 kPa, respectively. Furthermore, the L_{core} needed to reach the $Q_{u,sf}$ decreases with increasing $q_{u,DCM}$. For specific soil and DCM length, with sufficient $q_{u,DCM}$, inserting the core has no impact on the load-

carrying capacity of the columns. This implies that $\mathbf{q}_{u,DCM}$ can be decreased by inserting the core instead. Moreover, with the same $\mathbf{q}_{u,DCM}$, the longer columns (higher $\mathbf{L}_{DCM}$) require a longer core to reach $\mathbf{Q}_{u,sf}$.

TDM piles

The effects of the transformation to a TDM pile and of the enlarged pile cap dimension on the load-settlement curves are numerically investigated in this section. TDM piles with a volume equivalent to that of the conventional DCM pile with a diameter of 0.618 m and a length of 5.6 m was considered. The pile body diameter of 0.5 m was fixed while the enlarged cap size (surface diameter, D_{TDM}, and thickness, H) was varied within the same pile volume. Two values of q_u of the pile (525 and 655 kPa) are considered. D_{TDM} values of 0.73, 0.988, 1.17 and 1.32 m with corresponding H values of 2.62, 1.04, 0.65 and 0.50 m, respectively, are considered in the analyses. The simulated load-settlement curves are illustrated in Fig. 19. The values of calculated Q_{ult} are also reported in the figure. For piles with q_u of 525 kPa (Fig. 19a), the results clearly indicate that the change in the pile shape from conventional DCM to TDM leads to an increase in Q_{ult} and reduction of pile settlement at the same load level. Note that Q_{ult} decreases with increasing D_{TDM} from 0.73 to 0.988 m before increasing again when D_{TDM} is 1.17 m. However, Q_{ult} is still greater for $D_{TDM} = 0.988$ m than for $D_{DCM} = 0.618$ m.

A dissimilar result was observed for the piles with a q_u of 655 kPa, as shown in Fig.19b. The values of Q_{ult} slightly decreased as the pile shape changed from conventional DCM to TDM with $D_{TDM} = 0.730$ and 0.988 m. As D_{TDM} increased to 1.17 m, Q_{ult} increased. Additional insights can be obtained by comparing the results for a pair of select cases, as shown in Fig. 19c. Q_{ult} of the case for the TDM pile with D_{TDM} of 1.17 m and q_u of 655 kPa is nearly identical to that for the DCM pile of 0.618 m (same pile volume) and q_u of 900 kPa (upper subfigure). These results indicate the potential to reduce the pile strength (i.e., the cement content) while enlarging the pile cap to achieve the same pile capacity. In the lower subfigure, at the same pile strength (655 kPa in this case), Q_{ult} of the TDM pile with D_{TDM} of 1.32 m is almost identical to that of the 0.700-m-diameter DCM pile (larger pile volume). This result indicates the potential to reduce the pile volume while enlarging the pile cap to achieve the same pile capacity. These results confirm the benefits of using TDM piles to reduce construction costs.

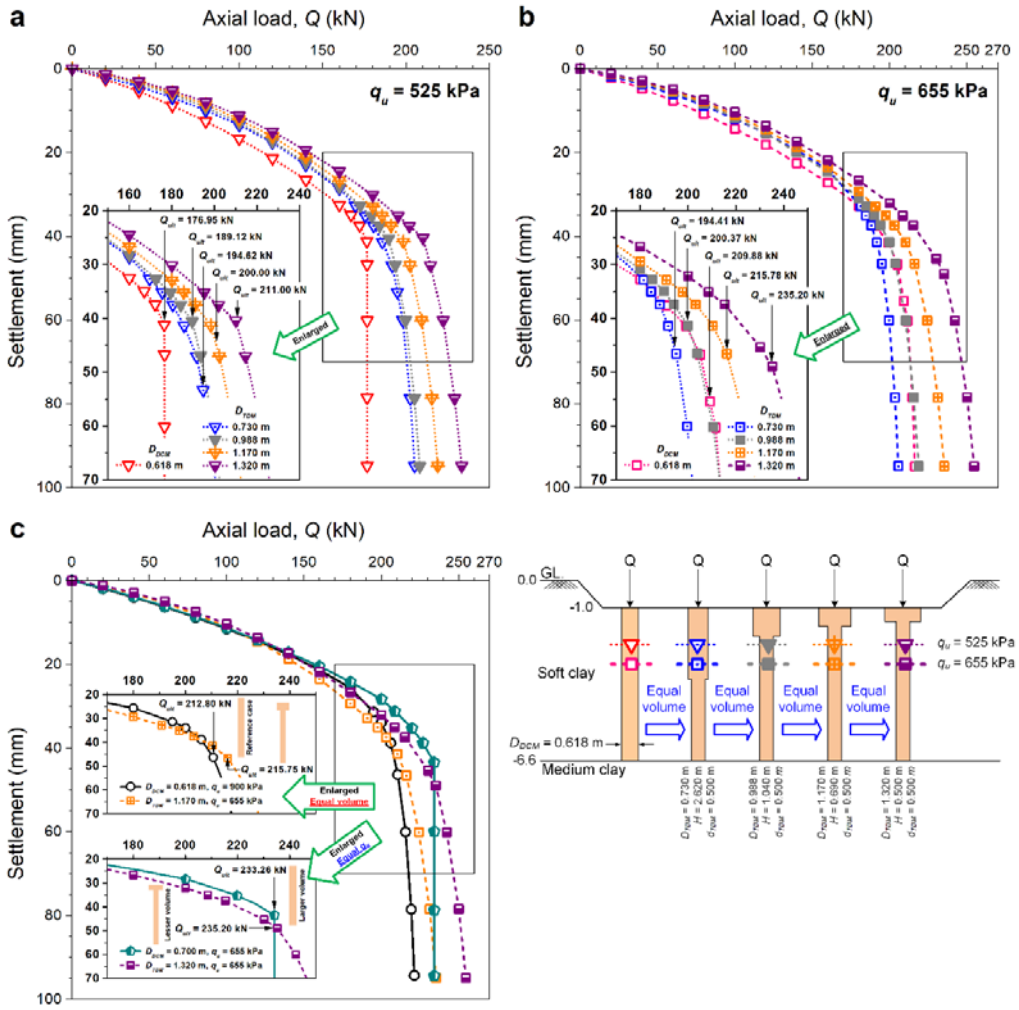

Fig. 19 Effect of an enlarged pile cap dimension of TDM piles with various strengths: (a) $q_u = 525$ kPa and (b) $q_u = 655$ kPa. (c) Comparisons of the effectiveness of conventional DCM and TDM piles with equivalent volume and strength

The above observations imply that the change from a conventional DCM pile to a TDM pile can offer benefits by reducing either the pile volume or strength for a target pile capacity. However, the effectiveness of the change from a conventional DCM pile to a TDM pile depends on the design of an appropriate shape. Both the shape of the pile cap and q_u play important roles in this load carrying behavior.

DCM walls

The effect of different wall shapes on the wall behavior was determined using four wall shapes of varying slenderness ratios (**S** = H_w / t), with an approximately constant DCM volume of 42 m^3/m and 5 m excavation. The constant volume is considered due to the fact that the construction cost of the DCM wall is primarily governed by the amount of cement used. Fig. 20 illustrates the simulated ground settlement and horizontal displacement profiles associated with the four DCM wall shapes (**S**

= 2.0, 2.4, 3.1, and 5.4, where S2.0 and S5.4 denote the bulkiest and most slender unbraced-unreinforced DCM walls, respectively.

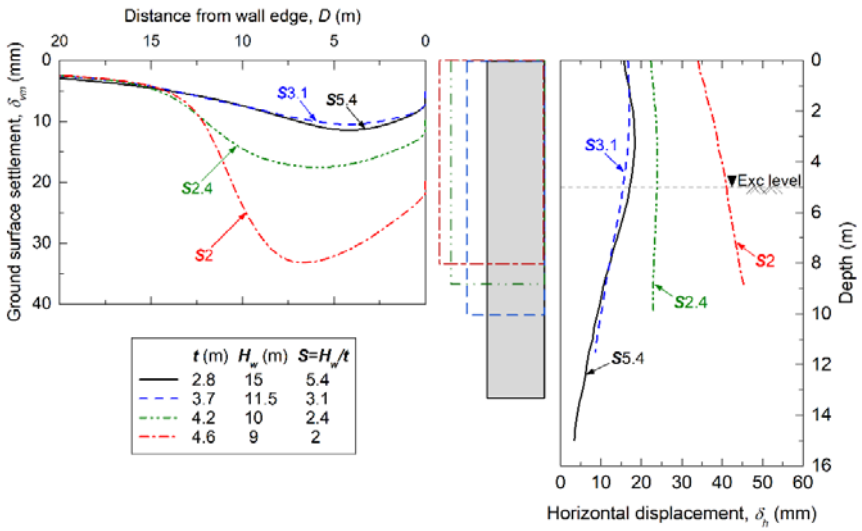

Fig. 20 Simulated ground settlement and horizontal displacement profiles of four DCM wall shapes

In the figure, three distinct movement (vertical and horizontal) patterns were observed, depending on the restraint condition and the wall tip level. The S5.4 DCM wall ($t = 2.8$ m, $H_w = 15$ m; most slender) exhibited a bulging-shape deformation with tip restraint (herein referred to as "mode A"). The S3.1 wall ($t = 3.7$ m, $H_w = 11.5$) displayed a combination of bulging and translation (mode B). The S2.4 and S2 walls demonstrated the toe-kicking phenomenon (mode C), where the displacement is critical near the wall tip level.

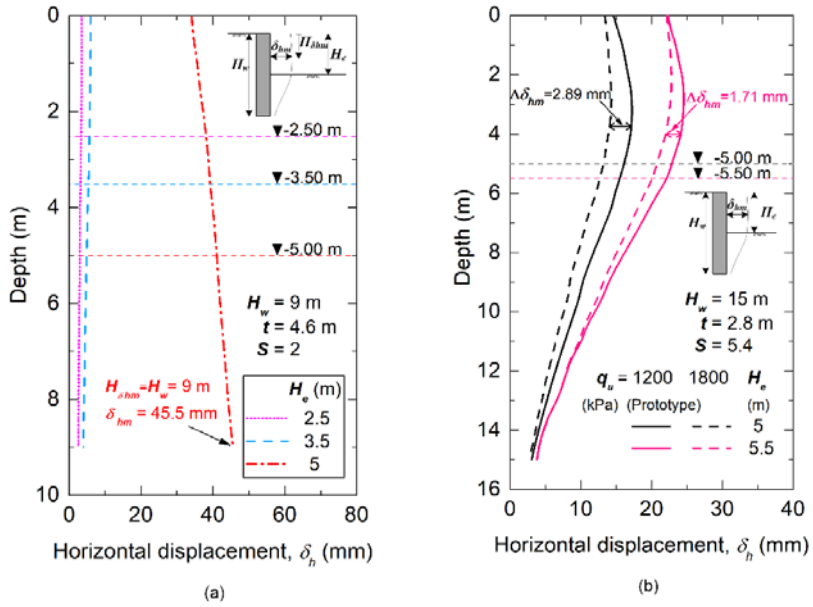

Fig. 21 Effect of excavation depths on: (a) the horizontal displacement, (b) the lower gain from wall strength improvement

Fig. 21(a) illustrates the effect of excavation depth ratio (H_e / H_p) on the horizontal displacement of a DCM wall (H_w = 9 m, t = 4.6 m). Under a certain wall length, this can be done by observation at various excavation depths (2.5, 3.5, and 5.0 m). The wall exhibited mode B displacement at the shallow excavation depths (2.5 and 3.5 m) and transformed to mode C at 5.0 m. Soil instability was observed beyond the 5.0 m depth. This phenomena which is similar to that of rigid walls (Ramadan et al., 2017), is attributed to the over-excavation that is a primary cause of excessive movements. By decreasing embedded depth, the behavior of wall deflection changes to toe-kicking. Fig. 21 (b) shows the effect of excavation depths (5.0 and 5.5 m) and the DCM strength (1200 and 1800 kPa) on the horizontal displacement of a more slender DCM wall (H_w = 15 m, t = 2.8 m). The results indicated that the reduction in displacement ($\Delta\delta_{hm}$), as a result of the material improvement (from 1200 to 1800 kPa), became smaller as the excavation depth ratio increased. The finding indicated that the excavation depth ratio impacted the wall displacement pattern and the displacement responsiveness to wall strength.

Development of charts as design guidelines

SDCM piles

From the results and understandings obtained from numerical sensitivity analyses, schematic diagram showing the relationship between $\mathbf{L_{core}/L_{DCM}}$ and $\mathbf{Q_u}$ of SDCM and the associated failure modes can be established as illustrated in Fig. 22. By inserting a core into the DCM which originally fails under pile failure mode ($\mathbf{Q_u} < \mathbf{Q_{u,sf}}$; along the green part of y-axis), the failure mode changes from failure at pile head to either pile failure at the core tip or soil failure depending on both the $\mathbf{L_{core}/L_{DCM}}$ and $\mathbf{q_{u,DCM}}$.

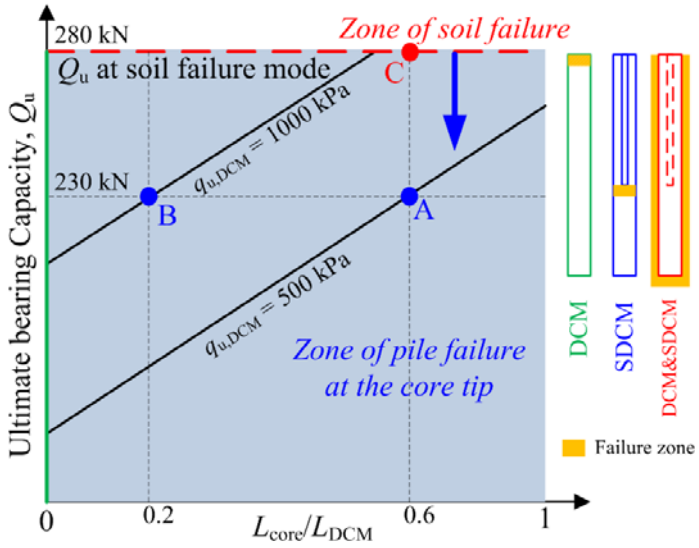

Fig. 22 Diagram demonstraing the L_{core}/L_{DCM} and Q_u relationship of floating SDCM and the associated failure modes

As an implementation example of the $\mathbf{Q}_u$ of floating SDCM column and its influencing factors in engineering practice, the characteristic chart of a floating SDCM column as a guideline for choosing the appropriate $\mathbf{L}_{core}$ can be obtained by plotting the value of $\mathbf{L}_{core}/\mathbf{L}_{DCM}$ that can reach $\mathbf{Q}_{u,sf}$ together with $\mathbf{q}_{u,DCM}$ and $\mathbf{L}_{DCM}$, as illustrated in Fig. 23. The effects of $\mathbf{L}_{core}/\mathbf{L}_{DCM}$, $\mathbf{L}_{DCM}$, and $\mathbf{q}_{u,DCM}$ are considered in this chart. The $\mathbf{L}_{DCM}$ is obtained by selecting the required $\mathbf{Q}_u$. Once $\mathbf{q}_{u,DCM}$ is selected, the $\mathbf{L}_{core}/\mathbf{L}_{DCM}$ needed to achieve the required $\mathbf{Q}_u$ is earned. This chart can be used to preliminarily design floating SDCM columns with lengths from 6 to 12 m with a diameter of 0.5 m, as considered in the analysis. It is also developed for the soil condition considered in this study (reference case in this study). However, the concept of the development of this chart can be applied to other areas and conditions. Note that the settlement criterion has not been considered in the development of this chart. Nonetheless, the results from this study suggested that for the same $\mathbf{Q}_u$, the settlement of the SDCM column is smaller than that of the DCM column.

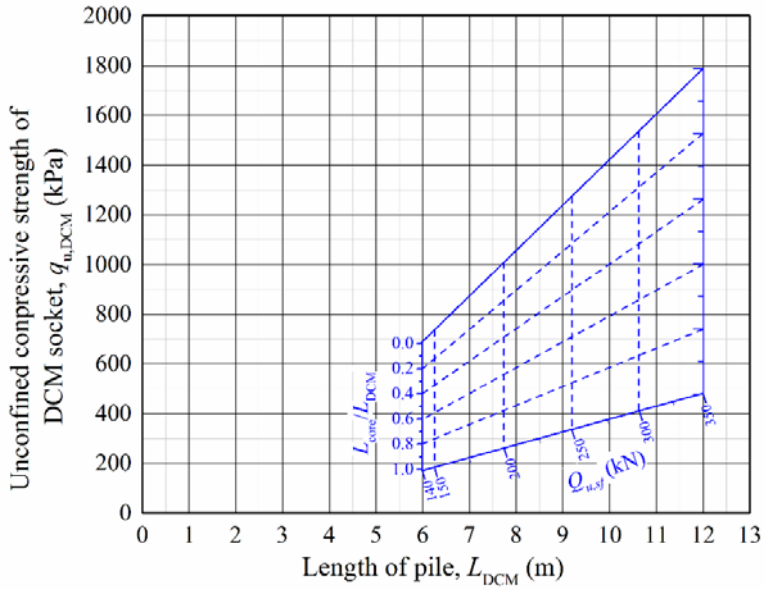

Fig. 23 Guideline chart for suggeting the Lcore for floating SDCM piles of this study area.

TDM piles

To accommodate the representation of the results regarding the enlargement of pile cap shape, the empirical "shape factor (α_s)" taking the geometry of the TDM pile into account, is hereafter used. Based on the fact that, with continually enlarging the pile cap, the surface diameter and skin area of the TDM piles become larger and smaller, respectively, compared to those of the DCM pile at the same volume. The ratio of bearing area of TDM pile to DCM pile over the ratio of shaft area of TDM pile to DCM pile as shown in Eq. 1 is thus appropriate.

$$\alpha_s = \frac{D_{TDM}^2 / D_{DCM}^2}{\left[\left(D_{TDM} - d_{TDM}\right)H + d_{TDM} L_{TDM}\right] / D_{DCM} L_{DCM}} \quad (1)$$

Under a controlled volume and constant pile body diameter, a larger value of α_s indicates a larger but thinner pile cap. The value of α_s for a conventional DCM pile is equal to 1.0. Note that the α_s in

the present form is for a controlled volume and constant pile body diameter, further development may be necessary if it will be applied for other conditions.

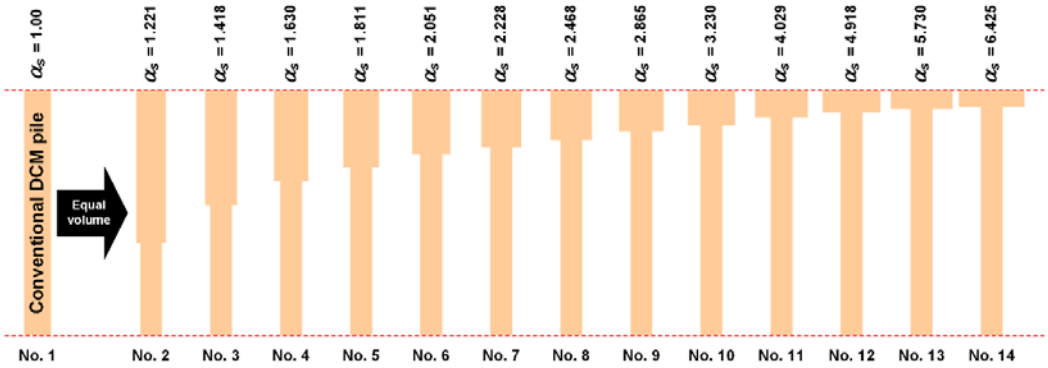

Fig. 24 Schematic of soil-cement piles with varying α

The preliminary investigation indicated that the behavior of TDM piles is strongly influenced by the interaction between (1) the shape of the enlarged pile cap, which can be represented by the shape factor (α_s), and (2) the strength of the soil-cement pile (q_u). Fig. 24 shows a schematic of the shapes of the DCM and TDM piles in this parametric study. q_u ranged from 320 to 700 kPa. The strength ratio (α_p) was used to denote the strength of the soil-cement pile in each case compared to the baseline case or optimum pile strength (700 kPa in this study) which provides the highest ultimate bearing capacity (depends on size of DCM pile). The α_p can be expressed in Eq. (2).

$$\alpha_p = \frac{q_u \text{ in each case}}{q_u \text{ of baseline case}} \tag{2}$$

The influence of α_s and α_p on the Q_{ult} of TDM piles is discussed in terms of the ultimate bearing capacity intensity ratio (α_Q), which is defined as

$$\alpha_Q = \frac{Q_{ult} \text{ of conventional DCM or TDM piles}}{Q_{ult} \text{ of baseline case}} \tag{3}$$

Fig. 25 shows the relationship between α_s and α_Q for the various analyzed cases of α_p. From the results, it is concluded that both cap shape and pile strength play important roles in both the TDM pile capacity and the failure pattern. Under constant volume, transforming the DCM pile to a TDM pile does not guarantee superior performance unless both factors are taken into consideration. To ensure that the transformation to a TDM pile will be effective regardless of pile strength, the shape corresponding to an α_s of greater than 3.0 is recommended. For a small enlarged pile cap (α_s less than 3.0), pile strength corresponding to a maximum α_Q of 0.85 is suggested. It is also possible to achieve pile capacity equivalent to the DCM pile at optimal strength by transformation to a TDM pile with lower strength. This finding is very interesting for the use of TDM piles to reduce construction costs.

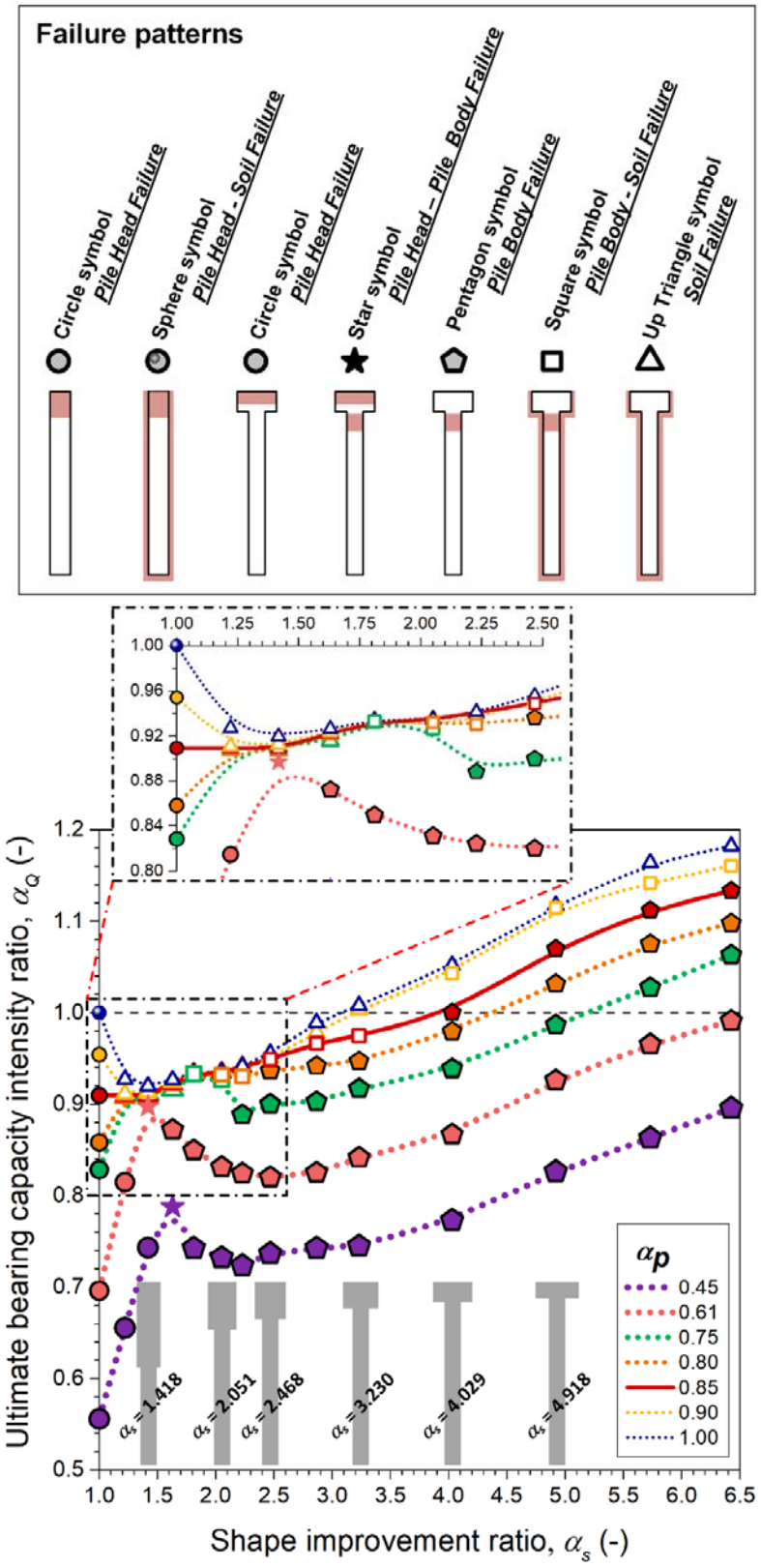

Fig. 25 α_s versus ultimate bearing capacity intensity of piles with various strengths and associated failure patterns

DCM walls

Fig. 26 illustrates the wall bottom displacement $(\delta_{h,bot})$ relative to the maximum horizontal displacement (δ_{hm}) under modes A, B, and C. Under mode A, the tip restraint $(\delta_{h,bot})$ was 20% of δ_{hm}, and almost half δ_{hm} under mode B. For mode C, $\delta_{h,bot}$ was identical to δ_{hm}. Mode A is normally found in a rigid slender retaining structure embedded in a hard stratum and fixed end, e.g., concrete diaphragm wall. As **S** is reduced, a bulging with slight translation developed in the wall, resulting in the mode B displacement. Further reduction in **S** contributed to fixity loss and considerable displacement near the wall tip (mode C). The finding suggested that the wall bottom displacement $(\delta_{h,bot})$ played a significant role in the mode difference. Thus, $\delta_{h,bot}$ should be accounted for in characterizing the movement behavior of DCM walls.

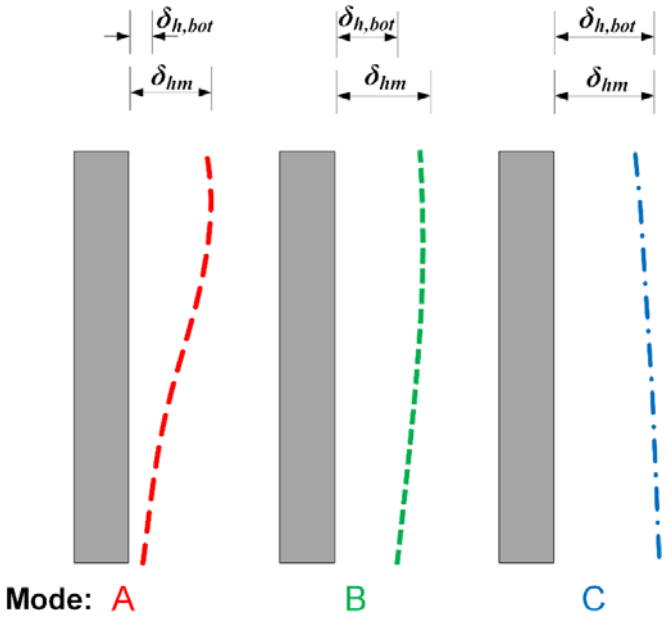

Fig. 26 Wall bottom displacement relative to the maximum horizontal displacement under modes A, B, and C displacement patterns

The wall-to-excavation shape factor was proposed to characterize the horizontal displacement behavior of DCM walls. The wall-to-excavation shape factor (β_w) is a function of the slenderness ratio (H_w / t) and embedment depth ratio (H_p / H_e), where H_p / H_e is the inversed excavation depth ratio (H_e / H_p).

$$\beta_w = \frac{H_w}{t} \times \frac{H_p}{H_e} \tag{4}$$

Comparing to the most commonly used parameter in current practice for conventional braced excavation, the system stiffness $(EI/\gamma_w h_{avg}^4)$ (Clough et al., 1989), the I/h_{avg}^4 ratio implicitly represents wall slenderness and excavation depth. Only the wall modulus (E) has not yet been

included in the proposed parameter. Further study is necessary to take into account the wall modulus for characterization of wall displacement, particularly for the mode A-type wall $(\beta_w > 5.5)$.

Fig. 27 illustrates the relationship between normalized maximum horizontal displacement (δ_{hm} / H_e) and β_w, based on the simulated data, downscaled field data, and the excavation databases of Bangkok and Shanghai. In the figure, δ_{hm} / H_e and β_w were inversely correlated. Specifically, the numerical analysis (simulated) data was more consistent with the field measurement data under the δ_{hm} / H_e and β_w relationship, compared to under the δ_{hm} / H_e and (H_p / H_e) relationship (Wang et al., 2010).

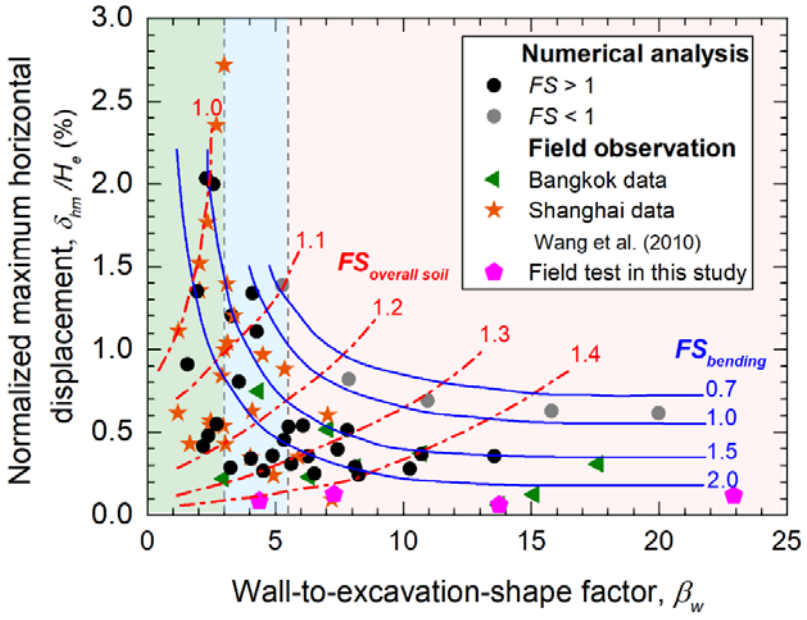

Fig. 27 Relationship between normalized maximum horizontal displacement and the wall-to-excavation shape factor

Fig. 27 also illustrates the contour lines of factor of safety (FS) of overall soil ($FS_{overall\ soil}$) based on $c'-\phi'$ reduction concept (Brinkgreve et al., 2002; Goh, 2017) and wall bending failures ($FS_{bending}$) (Jamsawang et al., 2016). The factors of safety ($FS_{overall\ soil}$ and $FS_{bending}$) were inversely correlated to δ_{hm} / H_e. Specifically, no bending failure materializes for the mode C-type wall $(\beta_w < 3)$, whereas the mode A-type wall $(\beta_w > 5.5)$ never encounters soil failure. Nevertheless, the mode B-type wall $(3 \le \beta_w \le 5.5)$ possibly suffers from both soil and bending failures. It is also noted that, for the mode A-type wall with $FS_{bending}$ greater than unity, the limit of δ_{hm} / H_e of approximately 1% is exhibited and approaches to 0.5% for greater β_w. These limits are consistent to those of slender cantilever wall reported by many works as summarized in Long (2001) and Pakbaz et al. (2013). More interestingly, for the mode C-type wall with $FS_{overall\ soil}$ greater than unity, the limit of δ_{hm} / H_e of approximately 1.5% is noticed. The results agree well with a common design criterion that limits the maximum wall deflection in the range of 0.5–1.5% of the excavation depth (H_e) (e.g., Moormann, 2004; Zhang et al., 2015).

In essence, the wall-to-excavation shape factor (β_w) could effectively characterize the horizontal displacement of DCM walls and determine the responsiveness of displacement behavior to wall strength (material improvement). The proposed factor is straightforward since it consists of four basic parameters: H_w , t , H_p, and H_e. In addition, the β_w shape factor could enhance the preliminary design process of DCM walls. The parameter provides a selection of suitable wall shape (thickness and length) to a given excavation depth depending on the preferable performance and behavior, including the deformation mode, potential failure mode and responsiveness to the wall strength increase.

Conclusions

Three different tools including physical model tests, field tests and numerical analyses were used together to get insight into the behaviors of deep cement mixing (DCM) piles in ground improvement for road embankment and deep excavation works. The conclusions that can be drawn from this study are as follows;

1. Not only the ultimate capacity of the DCM piles, the failure and deformation behaviors could be also understood by combination of these three methods.
2. Key influencing parameters can be preliminarily investigated and confirmed by numerical analyses and physical model/field tests, respectively.
3. Charts for suggestion the selection of appropriate size or dimensions are developed in the study.

References

Bergado DT, Ruenkrairergsa T, Taesiri Y, Balasubramaniam AS. 1999: Deep Soil Mixing Used to Reduce Embankment. Ground Improvement, 3: 141-162.

Brinkgreve RBJ, Broere W, Waterman D. PLAXIS 2D – materials model manual. The Netherlands; 2008.

Broms B. 1984: The Lime Column Method. Seminar on SoilImprovement and Construction Technique in Soft Ground, January, Singapore: 120-133.

Clough, G.W., Smith, E.M., Sweeney, B.P., 1989. Movement Control of Excavation Support Systems by Iterative Design, in: Foundation Engineering: Current Principles and Practices. American Society of Civil Engineers, New York.

Dong, P., Qin, R. and Chen, Z. 2004: Bearing capacity and settlement of concrete-cored DCM pile in soft ground. Geotechnical and geological engineering, 22 (1).

Goh, A.T.C., 2017. Basal heave stability of supported circular excavations in clay. Tunn. Undergr. Sp. Technol. 61, 145–149.

Jamsawang, P., Bergado, D.T. and Voottipruex, P. 2010: Field behaviour of stiffened deep cement mixing piles. Proceedings of the ICE - Ground Improvement, 164(1):33-49.

Jamsawang, P., Yoobanpot, N., Thanasisathit, N., Voottipruex, P., Jongpradist, P., 2016. Three-dimensional numerical analysis of a DCM column-supported highway embankment. Comput. Geotech. 72, 42–56.

Jamsawang, P., Voottipruex, P., Tanseng, P., Jongpradist, P., 2018. Effectiveness of deep cement mixing walls with top-down construction for deep excavations in soft clay : case study and 3D simulation. Acta Geotech.

Jongpradist, P., Kaewsri, T., Sawatparnich, A. Suwansawat, S., Youwai, S., Kongkitkul, W., and Sunitsakul, J. 2013: Development of tunneling influence zones for adjacent pile foundations by numerical analyses. Tunnelling and Underground Space Technology, 34: 96-109.

Kriengtaweekit, T., Wonglert, A., Petchmali, S., Jongpradist, P., Kongkitkul, W. and Submaneewong, C. 2014: Impact of Stiffness of Load Transfer Slab on Settlement Behavior of Cement-Column Supported Road Embankment, Proc. of the 19th National Convention on Civil Engineering, Khonkaen, Thailand, 14-16 May 2014, pp. 1739-1744.

Lai, Y.P., Bergado, D.T., Lorenzo, G.A., Duangchan, T. 2006; Full scale reinforcement embankment on deep jet mixing improved ground. Ground Improvement, 140(4):153-164.

Liu, S. Y., Du Y. J., Yi Y. L., and Puppala A. J., 2012; Field Investigations on Performance of T-Shaped Deep Mixed Soil Cement Column-Supported Embankments over Soft Ground, J. Geotech. Geoenviron. Eng, ASCE, 138(6), 718-727.

Long, M., 2001. DATABASE FOR RETAINING WALL AND GROUND MOVEMENTS DUE TODEEP EXCAVATIONS. J. Geotech. Geoenviron Eng. 127, 203–224.

Mazurkiewicz BK. 1972: Test loading of piles according to Polish Regulations. Preliminary Report No. 35. Commission on Pile Research. Stockholm: Royal Swedish Academy of Engineering Services.

Moormann, C., 2004. Analysis of wall and ground movements due to deep excavations in soft soil based on a new worldwide database. Soils Found. 44, 87–98.

Ou, C.U., Hsieh, P.G., and Lin, Y.L., 2003; A Parametric Study of Wall deflections in Deep Excavations with the installation of cross walls, Computers and Geotechnics, 50, 55-65.

Pakbaz, M.S., Imanzadeh, S., Bagherinia, K.H., 2013. Characteristics of diaphragm wall lateral deformations and ground surface settlements: Case study in Iran-Ahwaz metro. Tunn. Undergr. Sp. Technol. 35, 109–121.

Petchgate K, Jongpradist P, Youwai S. 2007: Field Investigations and Applications of Cement Columns in Thailand, A Country Report. Proc. of 40th Year Anniversary Symposium of The SEAGS, Kualalampur, Malaysia, 283-294.

Phutthananon, C., Jongpradist, P., Yensri, P., Jamsawang, P., 2018: Dependence of ultimate bearing capacity and failure behavior of T-shaped deep cement mixing piles on enlarged cap shape and pile strength, Comput. Geotech. 95, 27-41.

Ramadan, M.I., Ramadan, E.H., Khashila, M.M., 2017: Cantilever Contiguous Pile Wall for Supporting Excavation in Clay. Geotech. Geol. Eng. 1–14. doi:10.1007/s10706-017-0407-5

Schanz T, Vermeer PA, Bonnier PG. 1999: The hardening soil model: formulation and verification, Beyond 2000 in Computational Geotechnics. Rotterdam: Balkema.

Tanseng P. 2011; Soil-cement column wall without Bracing for Mat Foundation Construction in Bangkok Sub-Soils, in Proc. 14th Asian Regional Conference on Soil Mechanics and Geotechnical Engineering.

Tanseng P, 2012; Soil-cement column wall with wall-strut to minimize ground movement for a road tunnel construction in Bangkok subsoil, in Proc. 38th Int. Conf. At World Tunnel Congress.

Uddin, K. and Buensuceso, B.R. 2002: Lime Treated Clay: Salient Engineering Properties and Conceptual Model. Soils and Foundations, 42(5): 79-89.

Voottipruex P, Suksawat T, Bergado DT, Jamswang P. 2011: Numerical simulations and parametric study of SDCM and DCM piles under full scale axial and lateral loads. Computers and Geotechnics 38: 318-329.

Wang, J.H., Xu, Z.H., Wang, W.D., 2010. Wall and Ground Movements due to Deep Excavations in Shanghai Soft Soils. J. Geotech. Geoenviron Eng. 136, 985–994. Wonglert, A. and Jongpradist, P. 2015: Impact of reinforced core on performance and failure behavior of stiffened deep cement mixing piles, Computers and Geotechnics, 69, 93-104.

Wonglert, A., Jongpradist, P., Jamsawang, P. and Petchgate, W. 2015.: Efficiency of Using Eucalyptus Wood to Reinforce the Deep Cement Mixing Pile in Field: Pile Load and Embankment Tests , KMUTT research and development journal, 38 (3), 225-242 (In Thai)

Yang, D.S. 2003; Soil-Cement Walls for Excavation Support", in Proc. Int. Conf. On Earth Retention Systems.

Zhang, W.G., Goh, A.T.C., Xuan, F., 2015. A simple prediction model for wall deflection caused by braced excavation in clays. Comput. Geotech. 63, 67–72.

Output ที่ได้จากโครงการ

จากการศึกษา งานวิจัยเพื่อจัดทำข้อแนะนำการออกแบบโครงสร้างดินที่ใช้เสาเข็มดินซีเมนต์ร่วมด้วย ซึ่งสามารถแบ่งได้เป็นหลายส่วน รวมถึง งานที่ได้ปรับเปลี่ยน-เพิ่มเติม ดังที่ได้รายงานในรายงานความก้าวหน้าของโครงการแล้วนั้น output ที่ได้จากโครงการสามารถสรุปได้ ดังต่อไปนี้

1. บทความที่ได้รับการตีพิมพ์ในวารสารนานาชาติแล้ว 9 บทความ (กล่าวขอบคุณ สำนักงานคณะกรรมการการอุดมศึกษา และ สำนักงานกองทุนสนับสนุนการวิจัยในกิตติกรรมประกาศ) ดังนี้ (สำเนาต้นฉบับแสดงในภาคผนวก ก)
   1). Phutthananon, C., Jongpradist, P. and Jamsawang, P. (2020) Influence of cap size and strength on settlements of TDM-piled embankments over soft ground, Marine Georesources and Geotechnology (In Press). (ISI-IS2017 = 1.166, Q3)
   2). Waichita, S., Jongpradist, P. and Helmut F. Schweiger, H.F. (2020) Numerical and experimental investigation of failure of a DCM-wall considering softening behaviour, Computers and Geotechnics 119, 103380. (ISI-IF2018= 3.345, Q1)
   3). Jamsawang, P., Phongphinittana, E., Voottipruex, P., Bergado, D.T. and Jongpradist, P. (2019) Comparative performances of two- and three-dimensional analyses of soil-cement mixing columns under an embankment load, Marine Georesources and Geotechnology 37(7), 852-869. (ISI-IS2017 = 1.166, Q3)
   4). Jongpradist, P., Jamsawang, P. and Kongkitkul, W. (2019) Equivalent Void Ratio Controlling the Mechanical Properties of Cementitious Material-Clay Mixtures with High Water Content, Marine Georesources and Geotechnology 37(10), 1151-1162. (ISI-IS2017 = 1.166, Q3)
   5). Jamsawang, P., Voottipruex, P. Tanseng, P., Jongpradist, P. and Bergado, D.T. (2019) Effectiveness of deep cement mixing walls with top-down construction for deep excavations in soft clay: Case study and 3D simulation, Acta Geotechnica 14(1), 225–246. (ISI-IF2018= 3.247, Q1)
   6). Phutthananon, C., Jongpradist, P., Yensri, P. and Jamsawang, P. (2018) Dependence of ultimate bearing capacity and failure behavior of T-shaped deep cement mixing piles on enlarged cap shape and pile strength, Computers and Geotechnics 95, 27-41. (ISI-IF2018= 3.345, Q1)
   7). Jamsawang, P., Suansomjeen, T., Sukontasukkul, P., Jongpradist, P. and Bergado, D.T. (2018). Comparative flexural performance of compacted cement-fiber-sand, Geotextiles and Geomembranes 46(4), 414–425. (ISI-IF2018 = 3.972, Q1)
   8). Wonglert, A., Jongpradist, P., Jamsawang, P. and Larsson, S. (2018) Bearing Capacity and Failure Behaviors of Floating Stiffened Deep Cement Mixing Columns under Axial Load, Soils and Foundations 58, 446-461. (ISI-IF2018= 1.673, Q3)
   9). Jamsawang, P., Nuansrithong, N., Voottipruex, P., Songpiriyakij, S., Jongpradist, P. (2017) Laboratory investigations on the swelling behavior of composite expansive clays stabilized

with shallow and deep clay-cement mixing methods. Applied Clay Science 148, 83-94. (ISI-IS2018 = 3.890, Q1)

2. งบประมาณที่ได้จากทุนวิจัยบางส่วน ได้นำไปใช้ร่วมกับโครงการวิจัยจากทุนพัฒนานักวิจัยเพื่ออุตสาหกรรมเพื่อสร้างเครื่องมือ และ อุปกรณ์ รวมถึงค่าใช้จ่ายก่อสร้างในสนามจริง เพื่อการศึกษาหาวิธีที่จะติดตามพฤติกรรมการรับแรง การเสียรูปของกำแพงเสาเข็มดินซีเมนต์ในสนาม

การนำผลงานวิจัยไปใช้ประโยชน์

- เชิงพาณิชย์ (มีการนำไปผลิต/ขาย/ก่อให้เกิดรายได้ หรือมีการนำไปประยุกต์ใช้โดยภาคธุรกิจ/บุคคลทั่วไป)
- เชิงนโยบาย (มีการกำหนดนโยบายอิงงานวิจัย/เกิดมาตรการใหม่/เปลี่ยนแปลงระเบียบข้อบังคับหรือวิธีทำงาน)
- เชิงสาธารณะ (มีเครือข่ายความร่วมมือ/สร้างกระแสความสนใจในวงกว้าง)

มีการสร้างความร่วมมือเครือข่ายวิจัย แลกเปลี่ยนนักวิจัย และการเดินทางมาบรรยาย กับ 2 สถาบันจาก
3SR Laboratory, University of Grenoble Alps, France และ
Geotechnical laboratory, Graz University of Technology, Austria

- เชิงวิชาการ (มีการพัฒนาการเรียนการสอน/สร้างนักวิจัยใหม่)

งบประมาณที่ได้จากทุนวิจัยบางส่วน ได้นำไปใช้ร่วมกับโครงการโครงการทุนพัฒนานักวิจัยและงานวิจัยเพื่ออุตสาหกรรมเพื่อเป็นค่าใช้จ่ายทำการทดสอบในสนาม และทุนเพชรพระจอมเกล้าดุษฎีบัณฑิตเพื่อเป็นค่าใช้จ่ายทำการทดสอบในห้องปฏิบัติการ ทำให้สามารถผลิตนักวิจัยระดับสูงหน้าใหม่ได้ 2 คน
คือ ดร. ศิริวรรณ ไวยชิตา ที่เพิ่งสอบจบในเดือนกันยายน 2562 ขณะนี้ทำงานเป็นผู้เชี่ยวชาญงานขุดลึกกับภาคอุตสาหกรรม
และ ดร. ชนา พุทธานานนท์ ที่เพิ่งสอบจบในเดือนคุลาคม 2562 ขณะนี้ทำงานเป็นนักวิจัยหลังปริญญาเอก กับมหาวิทยาลัยเทคโนโลยีพระจอมเกล้าธนบุรี

ภาคผนวก ก

สำเนาบทความที่ได้รับการตีพิมพ์ในวารสารนานาชาติ 9 เรื่อง

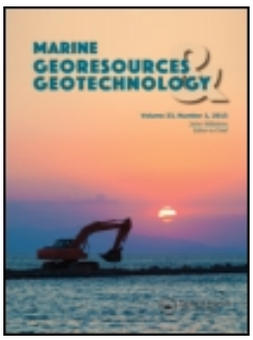

Marine Georesources & Geotechnology

ISSN: 1064-119X (Print) 1521-0618 (Online) Journal homepage: https://www.tandfonline.com/loi/umgt20

Influence of cap size and strength on settlements of TDM-piled embankments over soft ground

Chana Phutthananon, Pornkasem Jongpradist & Pitthaya Jamsawang

To cite this article: Chana Phutthananon, Pornkasem Jongpradist & Pitthaya Jamsawang (2019): Influence of cap size and strength on settlements of TDM-piled embankments over soft ground, Marine Georesources & Geotechnology, DOI: 10.1080/1064119X.2019.1613700

To link to this article: https://doi.org/10.1080/1064119X.2019.1613700

Published online: 21 May 2019.

MARINE GEORESOURCES & GEOTECHNOLOGY
https://doi.org/10.1080/1064119X.2019.1613700

Influence of cap size and strength on settlements of TDM-piled embankments over soft ground

Chana Phutthananon[a], Pornkasem Jongpradist[a] and Pitthaya Jamsawang[b]

[a]Department of Civil Engineering, Faculty of Engineering, King Mongkut's University of Technology Thonburi, Bangkok, Thailand; [b]Soil Engineering Research Center, Department of Civil Engineering, King Mongkut's University of Technology North Bangkok, Bangkok, Thailand

ABSTRACT

This study investigates the impact of pile cap size, soft layer thickness and pile strength on load transfer and settlement behaviors of embankments supported by floating and fixed T-shaped deep cement mixing piles and conventional DCM piles under volume control. Preliminary investigation is performed by a series of small-scale physical model tests. The results reveal that the differential settlement can be substantially reduced with an enlarging pile cap as a result of larger embankment load transferred to the piles. The extended numerical analysis results demonstrate that the pile efficacy is related to the individual pile bearing capacity, which, in turn, depends on the pile cap size. The soft layer thickness has an insignificant effect on differential settlement but a significant effect on average settlement, while the pile strength plays an important role in differential settlement only when the cap size is not very large. Shape factor of at least 3.0 is recommended to ensure the reduction in differential settlement and minimize the effect of the change in pile strength.

ARTICLE HISTORY
Received 4 January 2019
Accepted 25 April 2019

KEYWORDS
settlement; cement pile; embankment; soft ground; pile efficacy

1. Introduction

In the coming years, an increasing number of geotechnical structures will be constructed to support the growing in population, economic, and industrial development. For both of offshore and onshore, the most common geotechnical structures for supporting facilities are shallow and pile foundations and also the combination of shallow and pile foundation (e.g., Barari and Ibsen 2012; Barari et al. 2017; Pham et al. 2018; Pham et al. 2019; Pham and Dias 2019; Cho et al. 2012; Taghavi Ghalesari et al. 2013, 2015; Taghavi Ghalesari and Choobbasti 2018). The designing foundation systems over soft ground deposits for providing satisfactory performance and safety have attracted the attention of geotechnical engineers and researchers. Areas with soft ground deposits are universally encountered along coastal regions such as Bangkok Plain, Thailand (e.g., Horpibulsuk et al. 2007; Jamsawang et al. 2016), the eastern coast of China (e.g., Wu et al. 2015; Chen et al. 2016; Wang, Bian, and Wang 2017), Ariake Bay, Japan (e.g., Shen et al. 2003; Ma et al. 2011; Chai et al. 2015), and the eastern coast of Singapore (e.g., Bo et al. 2015; Ng and Tan 2015). These deposited layers, at a very high of water content, are typically classified as soft marine clay. When a geotechnical structure is constructed in this soft marine clay, the settlement is often relatively high due to the poor engineering properties, such as high sensitivity, high compressibility and low shear strength, of the clay (e.g., Ma et al. 2011; Wu et al. 2015; Abiodun and Nalbantoglu 2017; Wang, Bian, and Wang 2017). The settlements (total and differential settlements) must be carefully controlled to maintain the serviceability and to avoid damage to the earth structure. The soft ground stabilization technique of using deep cement mixing (DCM) piles is a popular technique for minimizing settlements, improving stability and increasing bearing capacity to bear the applied load of an on-ground structure, especially in the case of an embankment for transport infrastructures such as major highways and railways (e.g., Zheng et al. 2011; Liu et al. 2012; Chai et al. 2015; Jamsawang et al. 2016).

Most DCM piles under an embankment are fixed piles, for which the pile tips are positioned on a good bearing layer (commonly a medium clay layer) to guarantee that the bearing capacity and total settlement would be improved and reduced, respectively, as schematically shown in Figure 1(a) (e.g., Lai et al. 2006; Voottipruex et al. 2011; Liu et al. 2012; Jamsawang et al. 2016). Furthermore, based on the study by Jamsawang et al. (2016), the effectiveness in terms of reducing the bending moment and lateral movement can be further enhanced by extending the DCM pile length to a layer with higher bearing properties (i.e., the pile tip overlies a stiff clay layer). These piles are referred to as embedded piles (see Figure 1(a)). However, a previous case study of a fixed DCM pile-supported embankment (DPSE) over a soft clay layer indicated that the local differential settlement

CONTACT Pornkasem Jongpradist pornkasem.jon@kmutt.ac.th Department of Civil Engineering, Faculty of Engineering, King Mongkot's University of Technology Thonburi, 126 Pracha Uthit, Bang Mod, Thung Khru, Bangkok, Thailand
Color versions of one or more of the figures in the article can be found online at www.tandfonline.com/umgt.

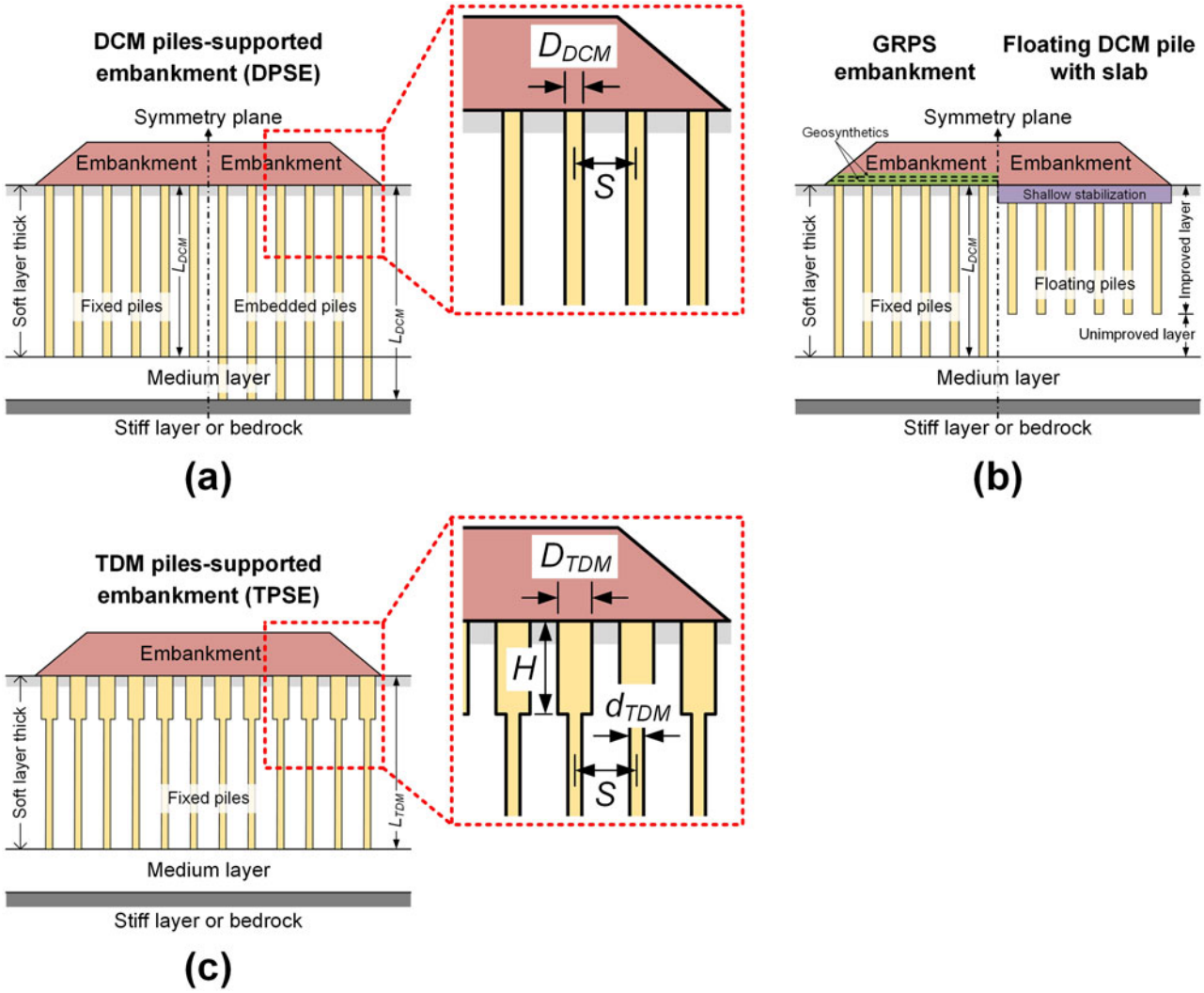

Figure 1. Schematic of soil-cement piles-supported embankment: (a) DPSE; (b) GRPS embankment and floating DCM pile with slab and (c) TPSE.

between the unimproved surrounding soil and DCM piles can reach 20% of the average settlement (Lai et al. 2006; Bergado et al. 2008). This local differential settlement often causes significant damage to the structure above the embankment, directly affecting the serviceability of the transport infrastructures (Han et al. 2007; Borges and Marques 2011). The allowable differential settlement is very strict in some circumstances, such as for high-speed train embankments or highway embankments (to control pavement cracking). An improvement technique to overcome this requirement is to use geosynthetic reinforcement (one or more layers) over the base of the DCM pile-supported embankment acting as a load transfer platform (LTP). This setup is schematically depicted in Figure 1(b) (a geosynthetic-reinforced and pile-supported (GRPS) embankment). Although this technique can effectively ensure a small differential settlement, it may lead to high construction costs owing to the augmentative cost of geosynthetic reinforcement and the increased volume improvement ratios used in the entire depth of the soft clay layer. Moreover, an unavoidable issue encountered in constructing a fixed DCM pile is the limitation depths of the required equipment, especially in some areas where the soft clay is quite thick (e.g., Igaya, Hino, and Chai 2011; Do and Nguyen 2013; Wonglert et al. 2018). Another technique is using shallow stabilization (slab) with floating DCM piles whose tips are not placed on the stronger clay layer, as also illustrated in Figure 1(b). This method has been extensively used for engineering practice in Japan (e.g., Chai and Pongsivasathit 2010; Ishikura, Yasufuku, and Brown 2016). Past studies revealed that floating DCM pile-slab-system-supported embankments gave the best performance in terms of reducing the differential settlement between the piles and surrounding soils.

A new technique called T-shaped DCM (TDM) pile-supported embankment (TPSE, see Figure 1(c)) was first used in China over ten years ago (Chen and Liu 2008; Yi et al. 2009). The cross-sectional view of this pile is similar to the letter "T" and results from the change in pile diameter between the pile head (larger than the DCM pile) and the pile body. Yi et al. (2017) conducted pile loading tests of single TDM and DCM piles (fixed pile type), and the results demonstrated that the ultimate bearing capacity (Q_{ult}) of the TDM pile was much greater than that of the DCM pile. However, the construction cost of the TDM pile exceeds that of the DCM pile owing to the larger pile volume. By

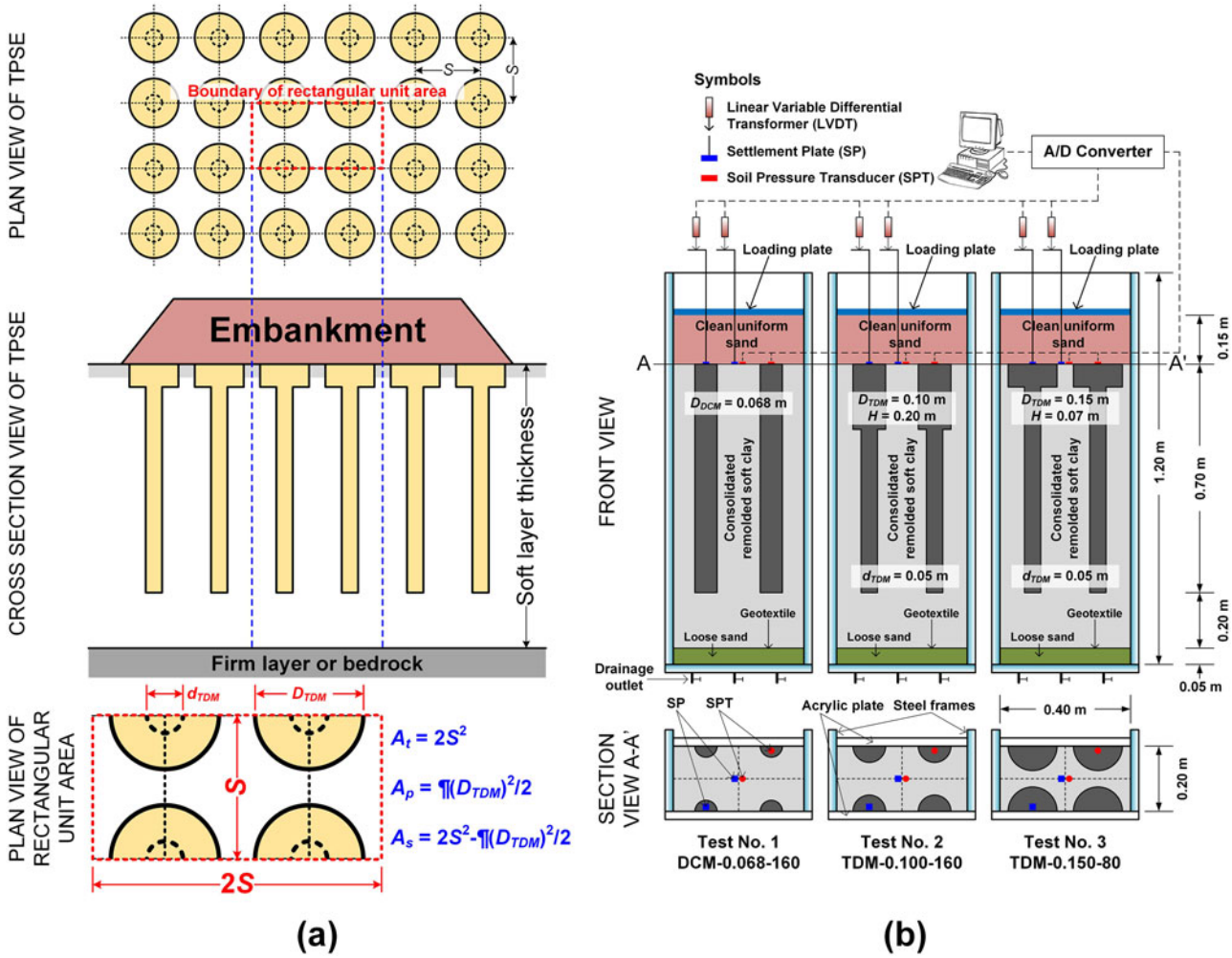

Figure 2. Three-dimensional rectangular unit area representation of the TDM piles improved ground in physical model tests: (a) actual condition and (b) experimental program and equipment configuration.

considering the effect of the pile cap enlargement on the basis of the controlled pile volume, Phutthananon et al. (2018) found that Q_{ult} predominantly depends on the pile shape and developed the shape factor $(\alpha)_s$ to represent the TDM pile shape. The minimum value of 3.0 for α_s is recommended to ensure the effectiveness of fixed TDM piles. Yi, Liu, and Puppala (2018) performed plate loading tests for composite foundations including fixed TDM piles and soft clay to examine Q_{ult}. The results demonstrated that Q_{ult} of a composite foundation significantly depends on pile cap size (thickness and diameter) and pile spacing. For the embankment loading test, Liu et al. (2012) performed a full-scale field test to compare the performance of both fixed TDM and DCM piles. Their research demonstrated that the use of TDM piles can provide cost-effective, rapid construction practices and reduction in the total settlement. Regarding the differential settlement, the closest relevant work is described in a publication by Yi, Liu, and Puppala (2016), who investigated the influence of an enlarged pile cap on the settlement behavior under embankments with fixed TDM and DCM piles through 1-g laboratory model tests. Their study reported that the TDM pile can suppress the differential settlement, unlike the DCM pile, and induce greater applied embankment loads (higher pile efficacy). Based on the past work, comprehensive studies investigating the bearing capacity and settlement behavior of fixed TDM piles have been continuously developed. However, no study on the floating TDM pile-supported embankment method has been conducted to date. This is very important when soft clay deposits are particularly thick, as in coastal environments. Moreover, the TDM pile volume to be used, as suggested in the literature of Yi, Liu, and Puppala (2016), is noticeably greater than that of the DCM pile, owing to the enlarged pile cap, while the TDM pile body diameter remained equal to the DCM pile diameter. Therefore, the comparison of the performance between TDM and DCM pile-supported embankment becomes imperative. In addition, our previous study (Phutthananon et al. 2018) reveals that the pile strength can be reduced to obtain the same or even a greater ultimate pile capacity by enlarging the pile cap with a suitable shape factor. The influence of the pile strength on settlement performance is also of interest.

In this article, comprehensive studies on the behavior of TPSE (fixed and floating pile types) are demonstrated and discussed in comparison with those of the traditional improvement (i.e., DPSE) on the basis of controlled pile volume. A series of small-scale physical model tests and 3D finite element (FE) analyses based on the selected full-scale

Table 1. Case investigated in the physical model test.

Test No.	Surface pile diameter (m) D_{DCM} or D_{TDM}	Thickness of enlarged pile cap (m) H	Pile body diameter (m) d_{TDM}	Length of pile (m) L_{DCM} or L_{TDM}	Area improvement ratio (-) a_r	Unconfined compressive strength (kPa) q_u	Note
1	0.068	–	–	0.700	0.091	160	DCM-0.068-160
2	0.100	0.200	0.050	0.700	0.196	160	TDM-0.100-160
3	0.150	0.070	0.050	0.700	0.442	80	TDM-0.150-80

Note: Depth improvement ratio (d_r)=0.78 for all cases (H_{sc}=0.9 m).

field test of DPSE (reference case, fixed pile type) have been performed. The tests are conducted to preliminarily examine the effect of the pile cap enlargement and pile strength of TDM piles (floating type) on the settlement and load transfer of the embankment over those of soil-cement piles. Subsequently, the 3D simulations based on the reference case were carried out by altering the soft layer thickness, pile cap shape and pile strength to extend the investigation.

2. Experimental investigations on floating TDM piles

Due to the exorbitant cost of full-scale field testing, a small-scale physical model test is chosen for preliminary investigation. Although a circular unit cell consisting of an individual pile encompassed by a cylindrical area of soil is the most popular setup for modeling the soil-cement pile composite foundation beneath an embankment (Yin and Fang 2006; Horpibulsuk et al. 2012; Yi, Liu, and Puppala 2016), this study proposed a rectangular unit area consisting of four half piles with soil between them, as shown in Figure 2(a). This technique is believed to be more suitable for capturing the maximum value of difference in settlement between the piles and surrounding soil due to the fact that the maximum soil settlement can directly be obtained. The model piles were arranged in a square pattern with equal pile spacing in both the transverse and longitudinal directions. The settlements of the models with floating TDM piles of different pile shapes are discussed by comparing their results with those of the model with DCM piles using the same pile volume and spacing. Furthermore, the measured vertical stress acting on the pile and surrounding soil is also taken into account for assessing the performance in terms of pile efficacy.

2.1. Experimental program

The tests were performed on three composite foundation models, including one model with floating DCM piles (Test No. 1) and two models with floating TDM piles (Test Nos. 2 and 3), as listed in Table 1. A scaling factor (Muir Wood 2004) of 1/10 was chosen to reduce the geometrical and mechanical parameters of the prototype. The pile lengths (L_{DCM} and L_{TDM}), pile body diameter (d_{TDM}) of the TDM pile, pile volume and pile spacing (S) were held constant at 0.70 m, 0.05 m, 2.542×10^{-3} m^3 and 0.20 m, respectively, for all the tests. The model of floating TDM piles of Test No. 2, hereafter referred to as the TDM pile with a smaller cap, had a surface pile diameter (D_{TDM}) of 0.10 m with an enlarged pile cap thickness (H) of 0.20 m. This composite foundation model was used to preliminarily investigate the influence of an enlarged pile cap on both the induced vertical stress and settlement in comparison with those of Test No. 1. The piles of Test No. 1 had a surface pile diameter (D_{DCM}) of 0.068 m. The unconfined compressive strength (q_u) of the pile models of Test Nos. 1 and 2 were determined to be the same value, 160 kPa. The detailed configurations of Test Nos. 1 and 2 are shown in Figure 2(b). Notably, for the same pile volume, the area improvement ratio, a_r (set as the ratio of the pile area to the rectangular unit area) of Test No. 1 (0.091), is less than that of Test No. 2 (0.196). In addition, the model of floating TDM piles of Test No. 3 was prepared with a smaller H but larger D_{TDM} and is hereafter called the TDM pile with a larger cap. The piles in Test No. 3 had D_{TDM} of 0.15 m and H of 0.07 m, with a corresponding a_r value of 0.442, as also shown in Figure 2(b). The q_u was reduced to 80 kPa for evaluating the potential of strength compensation with pile cap enlargement. The value of 80 kPa is determined from the numerical simulation of the single pile load test so that the pile capacity Q_{ult} of a single TDM pile in Test No. 3 is approximately the same as that of a single DCM pile in Test No. 1. This method of analysis refers to Phutthananon et al. (2018). Note that Q_{ult} of a single TDM pile is greater in Test No. 2 than in the other tests. For ease of illustration, the abbreviation system used to denote each case will be hereafter represented by the xxx-yyy-zzz system, where xxx represents the floating pile type (TDM pile or DCM pile), yyy represents the surface pile diameter in units of meters and zzz represents q_u of the piles in units of kPa. Note that all piles in this study are considered floating piles.

2.2. Preparation of experimental tests

A rigid test box was specifically designed for this study. This test box had plan dimensions of 0.20 m × 0.40 m and a height of 1.20 m, as depicted in Figure 2(b). The lateral sides and the bottom of the test box were made from steel plates and were braced with acrylic plates on the front and back sides. Three materials were utilized to perform the physical model: (i) soft clay; (ii) cement-admixed clay paste and (iii) sand. The details of the preparation of each material are as follows.

2.2.1. Preparation of the ground model

Initially, the inner surface of the test box was coated with grease to reduce the friction between the box wall and the ground model (Yin and Fang 2010; Dehghanbanadaki,

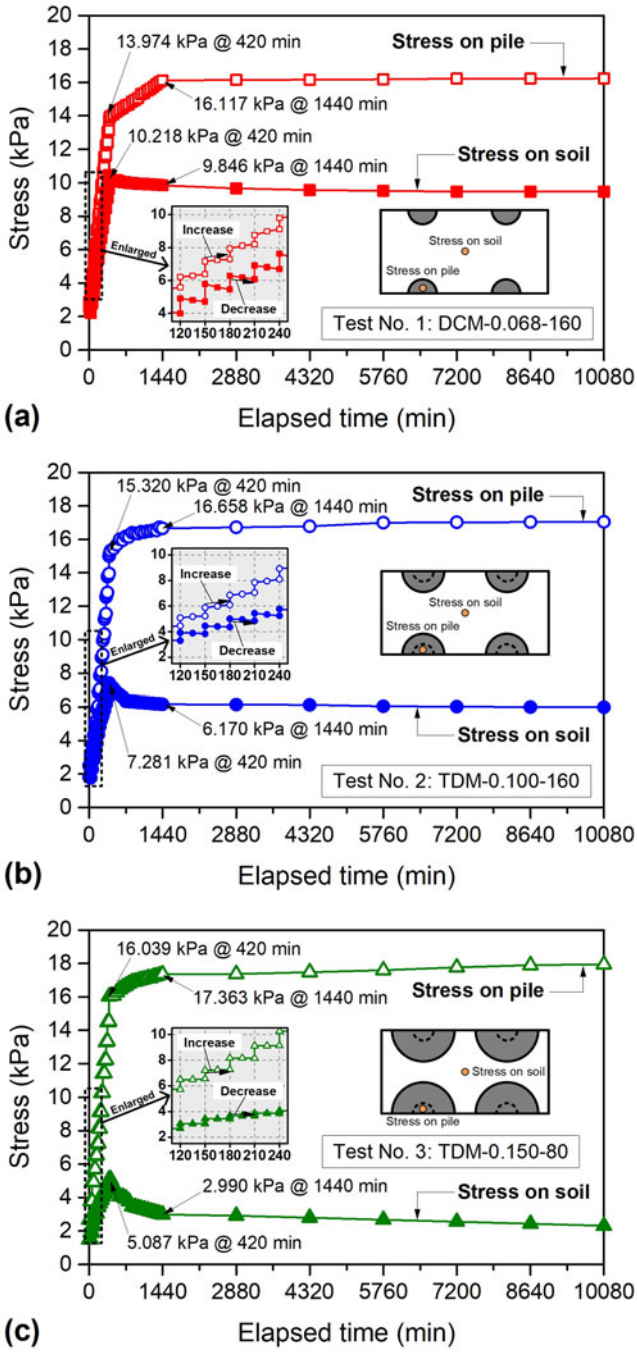

Figure 3. Measured stress on pile surface and soil surrounding at the center of rectangular unit area with elapsed time: (a) Test No. 1, (b) Test No. 2 and (c) Test No. 3.

Ahmad, and Ali 2016; Yi, Liu, and Puppala 2016). Then, a 0.15-m-thick uniform sand layer was placed across the bottom of the box, for drainage, and covered with geotextile, to separate the sand from the following layer. Remolded soft Bangkok clay at a water content of 120% was poured into the box, representing the ground model in which the piles were constructed. Then, the remolded clay was consolidated under a vertical pressure of 7.4 kPa to achieve the designed water content of 80% and target strength of 2 kPa. This process lasted approximately 30 days, and a degree of consolidation in the range of 90%–93% could be obtained. With the final applied stress of 14 kPa, the clay is in the normally consolidated state. The depth improvement ratio (d_r) for all the tests was approximately 0.78 (defined as the ratio of the floating pile length to the thickness of the ground model). At the end of the test, small vane shear test was performed at three locations each of which three depths was considered. Consequently, the average undrained shear strength value was approximately 2.4 kPa.

2.2.2. Preparation of the pile model

The model piles were made by pouring a mixture of Ordinary Portland Cement and remolded clay slurry into the prepared holes. A thin polyvinyl chloride (PVC) tube with an auger was used to create the holes by carefully pushing the tube into the ground model. To achieve the target q_u values of 80 and 160 kPa, cement contents of 5.4% and 15.8% by weight of dry soil were utilized, respectively. Samples of cement-admixed clay paste were collected during the installation process of the pile models and tested at the age of 30 days for confirmation of the target q_u.

2.2.3. Preparation of the embankment model

After the instruments were prepared (explained in the next section), a 0.15-m-thick clean uniform sand was added over the ground model to create the embankment model (flexible sand layer). This sand was air-pluviated, by using multiple sieving pluviation equipment, into the test box to guarantee a sand layer with a density of 1.5 g/cm^3 (Chantachot et al. 2016).

2.3. Testing instruments and procedure

For observing the settlements and vertical stress during the test, three kinds of instruments, namely, a settlement plate (SP), linear variable differential transformer (LVDT) and soil pressure transducer (SPT), were installed before preparation of the embankment model. Both the SP and SPT instruments were placed above the surface of the pile and ground models at the center of the box. The LVDT was connected to the SP after preparation of the embankment model to measure the settlement. The measured values of the settlements and vertical stress were automatically recorded by a computer via a data acquisition system. All the instruments were properly calibrated before testing. Figure 2(b) also presents the details of the instruments at the surface of the ground model. In all the tests, additional vertical pressure was applied incrementally using a surcharge load (deadweight) on a loading plate until the final stage of 14 kPa. The maximum applied pressure in this study is estimated from the vertical bearing capacity of the composite foundation presented by Yi, Liu, and Puppala (2018). An incremental vertical pressure of 1 kPa was applied instantaneously and maintained for 30 min in each stage.

Note that limited instrumentations can be installed to the modeled piles due to their small dimensions and limited measured data are thus reported and discussed in the part of physical model tests. Other information, such as load transfer along the piles and pile bearing mechanism, is investigated in the numerical part.

2.4. Experimental results and discussions

2.4.1. Vertical stress on the pile and surrounding soil

Figure 3 presents the relationship between the elapsed time and measured vertical stress for all the tests. With the increase in the applied vertical stress, both the stress on the pile (σ_p) and stress on the surrounding soil (σ_s) increase. Note that both values are measured from certain positions. As expected, σ_p is higher than σ_s owing to the larger modulus of the pile compared to that of the ground model. This result agrees with previous work on soil-DCM pile composite foundations (Horpibulsuk et al. 2012) and soil-TDM pile composite foundations (Yi, Liu, and Puppala 2016, 2018). When introducing the applied vertical pressure, both σ_p and σ_s increase rapidly. During the periods of constant pressure, an increase in σ_p and a reduction in σ_s were observed due to consolidation. After the final step of applying the vertical stress (t>420 min), σ_p increases with time; simultaneously, σ_s decreases to a certain magnitude at 1440 min (1 day after testing). Therefore, the stress concentration ratio, n (defined as σ_p/σ_s), increases with time. The increase in n means that the increasing proportion of the load conveyed from the surrounding soil to the pile (Yin and Fang 2006; Horpibulsuk et al. 2012; Yi, Liu, and Puppala 2016). This result is attributed to consolidation and consequent reduction in excess pore water pressure (Horpibulsuk et al. 2012; Yi, Liu, and Puppala 2016). A comparison of the results between Test No. 1 and Test No. 2 indicates that the induced σ_p on the TDM pile is higher than that on the DCM pile (see Figure 3(a,b)). In contrast, the opposite trend was observed for the induced σ_s. From 420 to 1440 min, σ_p on both piles continuously increases, whereas σ_s decreases, leading to a continuous increase in n over time. These figures clearly show that n of Test No. 2 is much greater than that of Test No. 1. This result is because the TDM pile has a larger cross-sectional surface area (high a_r). After 1440 min, the changes in both σ_p and σ_s are insignificant, or both values approximately remain constant. Converting σ_p (at the end of testing) to force (N) indicates that the TDM piles support a vertical load (261.7 N) greater than two times that supported by the DCM piles (111.7 N); hence, a TDM pile performs better in terms of sharing the loads from the embankment. Further investigation is performed by comparing the results between Test Nos. 2 and 3 (see Figure 3(b,c)). At the end of the applied loading stage (t=420 min), σ_p is 16.039 kPa in Test No. 3 (large cap TDM piles with small q_u), whereas σ_p measured in Test No. 2 is 15.320 kPa. The measured σ_s of Test Nos. 3 and 2 is 5.087 and 7.281 kPa, respectively. Therefore, the calculated n of the TDM pile with a large cap (3.152) is remarkably greater than that with a small cap (2.104), although the strength of the TDM pile with a large cap is lower. This emphasizes the influence of a_r on the load transfer from soil to pile. Furthermore, in the condition of controlled pile volume, the TDM pile with a larger cap and lower strength (i.e., 80 kPa) can induce larger loads (e.g., embankment load) than the DCM pile with a higher strength (i.e., 160 kPa). These results affirm the potential of using TDM piles to reduce the construction cost (i.e., the cement content). For example, to construct the TDM and DCM piles in actual field equivalent to the condition considered in the study, the amount of cement can be reduced by 50%. It is suggested that, for inducing embankment loads, the cap size of the TDM pile is a more significant influencing factor than pile strength.

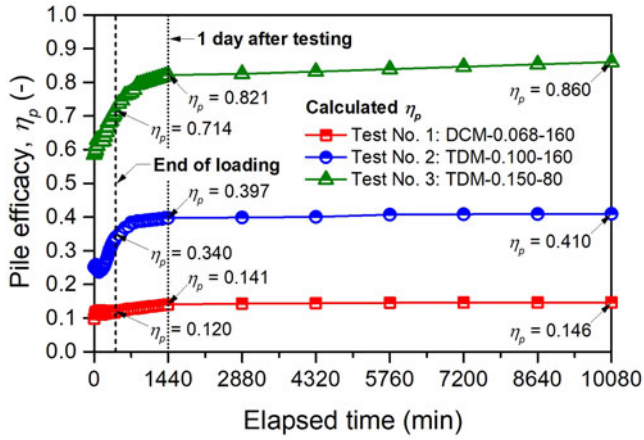

Figure 4. Change in calculated pile efficacy (η_p) with elapsed time.

2.4.2. Pile efficacy

The contribution of piles is generally quantified by the value of pile efficacy (η_p) to evaluate the proportion of the embankment load carried by the piles (Liu et al. 2012; Yi, Liu, and Puppala 2016; Zhang et al. 2016):

$$\eta_p = \frac{\sigma_p \cdot A_p}{\sigma_p \cdot A_p + \sigma_s \cdot A_s} \quad (1)$$

where σ_p and σ_s are the average stress on the pile surface and on the surface of the surrounding soil, respectively. A_p and A_s are the area of the pile surface and surrounding soil between the piles.

Figure 4 displays the evolution of η_p as a function of elapsed time, computed from the measured stresses from the above section using Equation (1). From the results of all the tests, the value of η_p increases significantly as the applied vertical stress continually increases (0<t<420 min) until 1440 min have elapsed. Then, η_p approaches a certain value when extending the time from 1440 to 10080 min (end of testing). The results reveal that η_p increases with the load and consolidation time. These results correspond to the findings of a previous study (Liu et al. 2012; Yi, Liu, and Puppala 2016). For comparison between Test Nos. 1 and 2, the η_p values throughout the TDM pile testing are greater than those of the DCM pile. Again, this result is attributed to the larger a_r of the enlarged pile cap of the TDM pile and is consistent with the observations of Liu et al. (2012) and Yi, Liu, and Puppala (2016). Figure 4 also illustrates the η_p value of Test No. 3; this value is notably larger than those of the other two cases. At the end of the test, the η_p values of the TDM piles with large caps are approximately 2.1 and 5.9 times than those of the TDM piles with small pile caps and DCM piles, respectively. Notably, η_p of a pile does not seem to be affected by the pile strength but considerably depends on a_r (or the cross-sectional surface pile area).

These findings deserve further examination, which is carried out in the numerical analyses.

2.4.3. Settlements of the pile and surrounding soil and the resulting differential settlement

Figure 5(a–c) illustrates the settlement-time behavior of the floating piles, surrounding soil and differential settlement from the three tests. All the test results show that the settlements increase substantially with an increase in the applied vertical stress ($0<t<420$ min) and then gradually increase with consolidation ($420<t<10080$ min) until the end of the test. The measured pile settlement (s_p) of the TDM piles is higher than that of the DCM piles. This is attributed to the large portion of the applied load delivered to the TDM piles (high η_p, see Figure 4). Considering the case with TDM piles, the result shows that the measured s_p of Test No. 3 is larger than that of Test No. 2. In addition to the larger portion of load that is delivered to the pile head (as seen in Section 2.4.2), this might also be due to the smaller pile modulus.

Regarding the soil settlement (s_s), as depicted in Figure 5(b), s_s of the model with DCM piles is clearly larger than that of the model with small cap TDM piles. This observation agrees with the results of Yi, Liu, and Puppala (2016). This fact supports the result shown in Figure 3(a) that a higher σ_s occurs in the case of the model with DCM piles. However, s_s of the model with large cap TDM piles (but lower modulus) is much larger than those of the other two cases. This pattern may be caused by the combination of the large pile surface diameter and small pile stiffness. As described above, the larger pile surface diameter can induce the large portion of load to the piles, resulting in a greater pile settlement. However, when pile modulus decreases, the settlements of the piles themselves are large and the piles cannot withhold the settlement of the surrounding soil. This tendency is in a reasonable agreement with the numerical results of embankment supported by rigid piles by Han and Gabr (2002) and embankment supported by DCM piles by Huang and Han (2010). They indicated that the decrease of pile modulus can lead to the larger soil settlements.

Figure 5(c) shows the differential settlement ($\Delta s = s_s - s_p$) between the surrounding soil and pile. The Δs values of all the tests increase drastically with an increase in applied vertical stress and slowly increase with consolidation. It was observed in the test that the model with DCM piles exhibits a greater Δs than that with TDM piles (for both small and large caps), following the results of previous research (Yi, Liu, and Puppala 2016). In summary, the results obtained from the preliminary examination by experimental testing imply that the differential settlement under a soil-cement pile-supported embankment can be decreased by enlarging the pile cap (transform DCM to TDM piles) without increasing the pile volume. Moreover, it is also possible to reduce the pile strength (cement content) if overall settlement is not a concern. The key mechanism is the transfer of load to the piles.

For qualitative observation of settlement and load transfer mechanism, the physical model tests of this study can

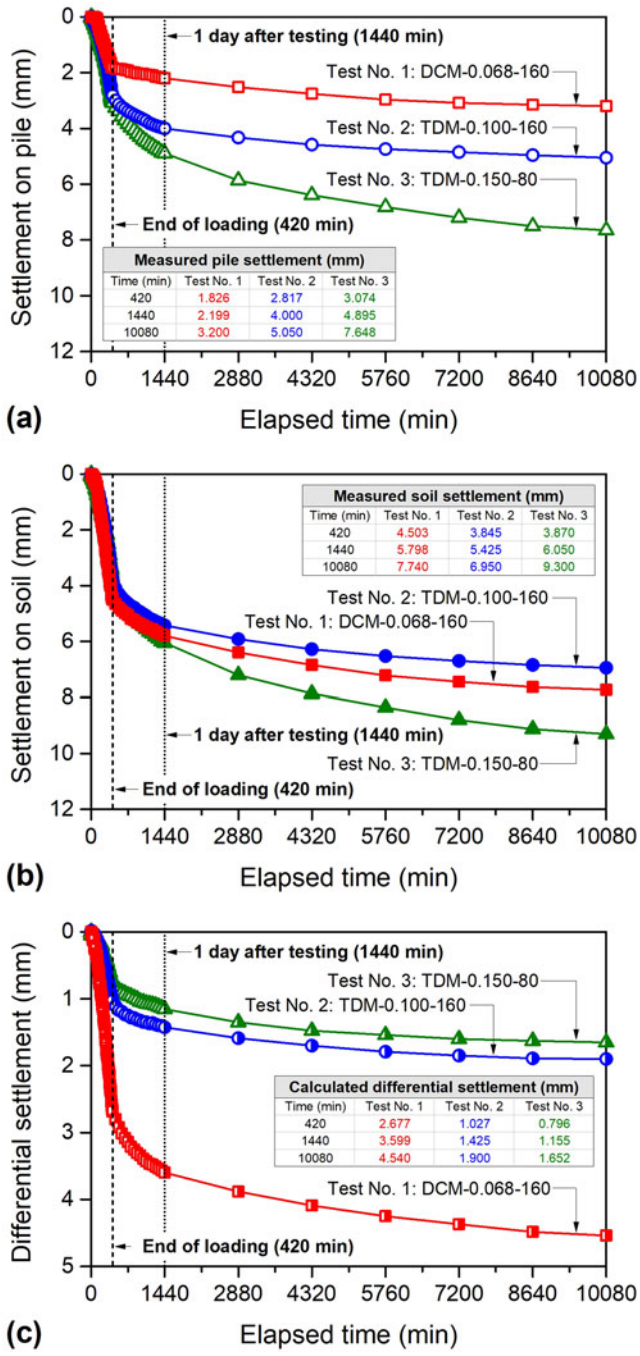

Figure 5. Measured settlement versus elapsed time on (a) pile surface and (b) surrounding soil surface and (c) calculated differential settlement.

suitably capture the significant behavior to assess the effectiveness of using TDM piles for supporting embankments. However, to better understand the behavior of TDM pile (floating and fixed types)-supported embankments, beyond the understanding provided by the tests, 3D FE analyses are favorable. Because the soil stress/strength profile in the rectangular model is low and almost uniform as a result of the small imposed self-weight increase over the depth of the model, the generation of soil settlement would be different to the actual field condition. Hence, 3D FE analyses on the basis of field conditions is preferred to consider a wide range of important factors (e.g., enlarged pile cap size, soft layer thickness and pile strength).

3. Numerical analysis of a full-scale DCM/TDM pile-supported embankment

3D full-scale numerical simulations were further carried out to obtain a better understanding of the performance of DCM/TDM piles beneath embankments. The finite element program Plaxis 3D 2013 (Brinkgreve, Engin, and Swolfs 2013), which are well-known commercial software programs based on a common finite element method, was utilized in the present study for conducting 3D simulations. The 3D finite element model consisted of the DCM/TDM piles, embankment and foundation soils. All of volumes were modeled using 10-node tetrahedral volume elements. The stresses and settlements on the piles and surrounding soil were observed to analyze the effect of influencing factors of pile cap size, soft layer thickness and pile strength on pile efficacy, differential settlement and average settlement. This work was conducted through a parametric study on the basis of a selected reference case.

3.1. Reference case

In the present study, a selected full-scale field case study of an embankment supported by fixed DCM piles was utilized as the reference case for performing the parametric analysis. With an embankment height of 5 m, the monitored settlements are impressively large. The embankment has a base of 21 m × 21 m and two side slopes (1 V:1.5H for the end slopes and 1 V:1.2H for the side slopes). Figure 6(a,b) presents the plan and cross-sectional views of the DCM pile-supported embankment (only half embankment), respectively. The embankment was constructed on a thick deposit of soft Bangkok clay in the Central Plain of Thailand and was located approximately 50 km northeast of the Gulf of Thailand. The foundation soil of this site included a 2-m-thick weathered crust above a 6-m-thick soft marine clay layer. A 2-m-thick medium clay layer was situated below the soft clay and underlain by a stiff clay layer with a thickness of 15 m. The groundwater level was 1.5 m beneath the original foundation surface. There are twelve DCM piles 0.6 m in diameter and 7 m in length beneath the embankment. The piles were arranged in a square grid pattern at a pile spacing of 2 m. Prior to pile installation, the weathered crust was excavated in a 21 m-by-21 m area to a depth of 1 m from the original foundation surface (base level of the embankment). After the DCM pile construction was finished, the trench area was backfilled with a layer of compacted silty sand 1 m thick. Subsequently, a 5-m-high embankment was constructed with weathered clay to obtain large loads and deformations of the foundation subsoil. Figure 6(a,b) also shows the positions of the instruments. Three surface settlement plates were set on the base of the embankment. The surface settlement plates were placed over the DCM pile (S11), surrounding clay between the DCM pile (S7) and unimproved clay at the center of the embankment (S4). A more detailed description of this site can be found in the literature (Voottipruex et al. 2011).

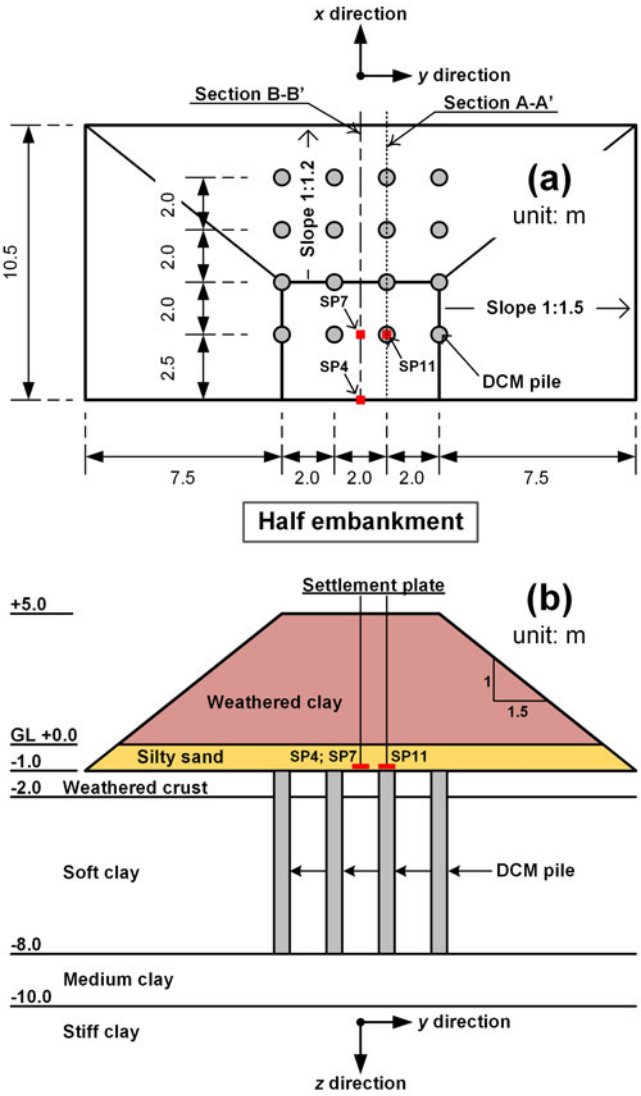

Figure 6. Plan (a) and cross-sectional (b) views of the DCM piles-supported embankment and locations of instrumentations (redrawn from Voottipruex et al. (2011)).

3.2. Soil models and parameters

The behavior of the weathered clay, silty sand and weathered crust was modeled as elastic-perfectly plastic using a Mohr-Coulomb (MC) yield criterion. The parameter sets of the MC model in this study were obtained from the previous work of Jamsawang, Bergado, and Voottipruex (2015), as listed in Table 2. The behavior of DCM and TDM piles was also simulated by MC model as commonly adopted by many scholars (Huang and Han 2010; Ignat et al. 2015; Jamsawang, Bergado, and Voottipruex 2015; Jamsawang et al. 2016; Wang, Zhang, and Deng 2018; Wonglert et al. 2018). Besides, it is common in current practice to utilize the MC model for simulating the soil-cement pile. Since effective shear strength parameters are not available for the reference case, the *Undrained (B)* function in Plaxis program was chosen for analysis by using the effective pile modulus (E') and undrained shear strength ($c_u = q_u/2$). Generally, unconfined compression (UC) tests were conducted to obtain the modulus (E_{SCP}) and strength (q_u) of the piles. The secant effective elastic modulus of the soil-cement pile

Table 2. Input soil parameters in MC model (Jamsawang, Bergado, and Voottipruex 2015).

Parameter	Symbol	Unit	Weathered clay	Silty sand	Weathered crust	DCM pile
Unit weight	γ	kN/m^3	16	17	17	15
Elastic modulus	E'	kPa	3,000	7,500	2,500	24,000
Poisson's ratio	ν'	–	0.25	0.30	0.25	0.33
Effective cohesion	c'	kPa	10	8	10	$c_u = 120$
Effective friction angle	ϕ'	degree	26	29	23	0
Permeability (vertical direction)	k_z	m/day	–	–	1×10^{-3}	0.012
Permeability (horizontal direction)	$k_x = k_y$	m/day	–	–	2×10^{-3}	0.024
Material behavior	–	–	Drained	Drained	Undrained type A	Undrained type B

(E'_{SCP}) was determined by correlation with the unconfined compressive strength ($q_u = 2c_u$) through the equation $E'_{SCP} = 100q_u$. Transforming this equation to the total stress parameter based on elasticity theory gives $E_{SCP} = 113q_u$, which is similar to that found in several previous studies (e.g., Jongpradist et al. 2010; Jongpradist et al. 2018; Jongpradist, Jamsawang, and Kongkitkul 2019; Voottipruex et al. 2011; Shen et al. 2013; Wonglert and Jongpradist 2015; Jamsawang, Bergado, and Voottipruex 2015; Jamsawang et al. 2016; Phutthananon et al. 2018). The input parameters for the DCM piles of the reference case are also tabulated in Table 2.

All foundation soil was modeled by the Hardening Soil (HS) model. This model is an advanced model for simulation of highly nonlinear soil behavior. The model has been adopted to analyze several geotechnical works in Bangkok subsoil (e.g., Jongpradist et al. 2013; Chheng and Likitlersuang 2018; Lueprasert et al. 2017; Jamsawang et al. 2017, 2018; Waichita, Jongpradist, and Jamsawang 2019). The input HS model parameters are tabulated in Table 3. All of the HS model parameters in the current study were considered in terms of the effective stress parameter. Calibration of the soil parameters was performed by comparing the HS model simulation results with the isotropically consolidated undrained triaxial (CIU) test results and the oedometer results obtained from the soil specimens at the test site. As an example, the calibration results of all the clay layers are shown in Figures 7(a,b), respectively, for the CIU and oedometer tests. Good agreement of the results was obtained, confirming the suitability of the material model and model parameters used in the current study to simulate the behavior of foundation soil. Note that the vertical permeability (k_z) values of the soft, medium and stiff clays in the present study were adopted from those reported in the previous work for the same site (Lai et al. 2006).

3.3. 3D FE analysis modeling

All the numerical analyses in this study were modeled using Plaxis 3D software (version 2013). Throughout the FE analyses, only half of the embankment was modeled, as depicted in Figure 8. To minimize the boundary effect, the side boundary of the model was extended horizontally by 29.5 m from the edge of the embankment base in both the x and y directions. Thus, the model had an area in the horizontal plane of 40 m (x direction)×80 m (y direction) and a depth of 25 m from the ground surface (see Figure 8). The bottom of the FE mesh was constrained in both the vertical and horizontal directions, and roller boundary conditions were used for four vertical sides. For drainage boundary conditions, the surface plane (z = 0 m) is a drainage boundary condition, while the bottom of the FE mesh (z = –25 m) and all the lateral boundaries were defined as impermeable. Figure 8 also shows an example of the FE mesh used in the simulations; this mesh consisted of approximately 330 thousand elements. This degree of mesh fineness (300–350 thousand elements) was chosen based on the mesh sensitivity analysis, as illustrated in Figure 9(a). Note that in this study, interface elements among the periphery between TDM/DCM piles and the foundation soils were not adopted to simulate the interfacial behavior because the interfacial shear strength between soil-cement pile and surrounding soil is higher than that of surrounding soft clay (Voottipruex et al. 2011; Jamsawang et al. 2015, 2016, 2018). Table 4 provides the details of the construction phases and sequences for the embankment test in the FE calculation, following the work of Voottipruex et al. (2011).

3.4. Validation of the numerical results

To validate the analysis method and sets of parameters before constructing the numerical parametric studies, the comparison was made between the results from the simulation and measurement. Figure 9(b) illustrates the prediction results from the FE analysis of the reference case (lines) in comparison with the measurement data (symbols). A good agreement is obtained, indicating that the sets of input parameters and the FE modeling procedure can efficiently predict the settlement behavior of the reference case. Thus, the proposed modeling approach can be reasonably utilized for modeling the piled embankment systems in future investigations.

4. Parametric analyses

This section was conducted to extend the study and elucidate the behavior of DCM/TDM pile-supported embankments beyond what can be earned from physical tests. The factors that are believed to influence the load transfer mechanism and settlement behavior are altered in the FE analysis. These factors consist of the shape of the TDM pile and the thickness of the soft layer. To that end, fourteen cases were carried out with TDM piles with a surface pile diameter (D_{TDM}) in the range of 0.65–1.30 m, which correspond to the thickness of the enlarged pile cap (H) in the range of 0.53–4.46 m (see Table 5). These piles represented the

Table 3. Input soil parameters in HS model.

Parameter	Symbol	Unit	Soft clay	Medium clay	Stiff clay
Unit weight	γ	kN/m^3	15	15	18
Secant stiffness	E_{50}^{ref}	kPa	2,400	5,000	9,000
Tangential stiffness	E_{oed}^{ref}	kPa	2,400	5,000	9,000
Unloading and reloading stiffness	E_{ur}^{ref}	kPa	7,200	25,000	27,000
Poisson's ratio for unloading-reloading	υ_{ur}	–	0.20	0.20	0.20
Power of the stress level dependency of the stiffness	m	–	1	1	1
Effective cohesion	c'	kPa	2	10	18
Effective friction angle	ϕ'	degree	22	22	22
Over consolidation ratio	OCR	–	1.1	2.0	2.5
Permeability (vertical direction)*	k_z	m/day	0.1×10^{-3}	0.05×10^{-3}	0.01×10^{-3}
Permeability (horizontal direction)*	$k_x = k_y$	m/day	0.2×10^{-3}	0.1×10^{-3}	0.02×10^{-3}
Material behavior	–	–	Undrained type A	Undrained type A	Undrained type A

Note: Angle of dilatancy, ψ=0°; Failure ratio, R_f=0.9; Reference stress, p^{ref}=100 kPa; *Lai et al. (2006).

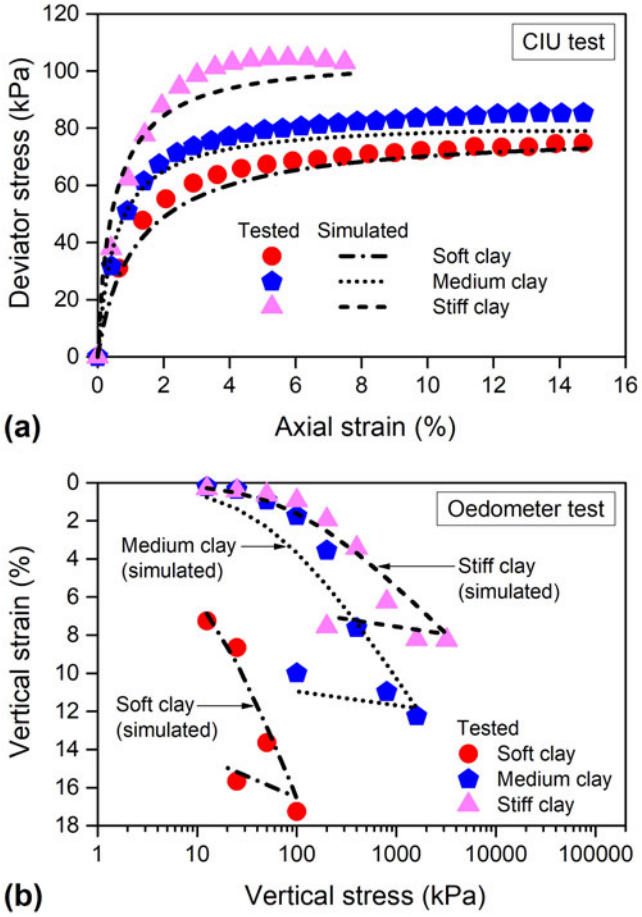

Figure 7. Soil parameter calibrations for soft, medium and stiff clays (a) isotropically consolidated undrained triaxial (CIU) test and (b) oedometer test.

improvement area ratios, a_r, of 8.3% to 33.2% for cases with pile spacing of 2.0 m. The range of a_r was carefully chosen from consideration on the available equipment in current engineering practice. The pile length (L_{TDM}) and pile body diameter (d_{TDM}) were 7 and 0.50 m, respectively. The pile volume for all cases remained equal to that of the DCM piles of the reference case to make a suitable comparison in terms of cost effectiveness. The shape factor (α_s) proposed by Phutthananon et al. (2018) was adopted to accommodate the assessment of the effect of pile shape. The α_s represents the ratio of bearing area of TDM pile to DCM pile over the ratio of shaft area of TDM pile to DCM pile under the same pile volume as shown in Equation (2).

$$\alpha_s = \frac{D_{TDM}^2 / D_{DCM}^2}{[(D_{TDM} - d_{TDM})H + d_{TDM}L_{TDM}]/D_{DCM}L_{DCM}} \quad (2)$$

Under a constant pile body diameter and controlled pile volume, a greater value of α_s indicates a larger pile diameter but thinner pile cap. The value of α_s for a traditional DCM pile is equal to 1.0.

To investigate the thickness of the soft clay layer, which commonly increases when approaching a coastal area, the thickness of the soft layer (H_{sc}) varies between 8.75 and 14 m in the analysis. A 14-m-thick soft layer is adopted based on the report by Horpibulsuk et al. (2007). The depth improvement ratios d_r (L_{pile}/H_{sc}) used in this work are thus 1.0, 0.8 and 0.5. The thickness of the medium clay layer was 2 m for all cases in this parametric study. Figure 10 shows a schematic of the DCM pile shape and some shapes of the TDM piles and the pattern of the foundation subsoil used in this parametric study. Notably, all the numerical results investigated in this and later sections were observed at 570 days after the completion of embankment filling (600 days of total time), corresponding to a consolidation degree of at least 85%. The obtained results are discussed with the results of the previous work on embankment tests; however, most of those studies are on embankments supported by DCM piles. Only some studies (i.e., Liu et al. 2012; Yi, Liu, and Puppala 2016, 2018) have considered TDM piles; however, pile volume control has not been taken into consideration in those studies.

4.1. Influence of shape factor and soft layer thickness on pile efficacy

Figure 11(a) shows the distribution of the η_p values for cases with various TDM shapes, α_s and different soft clay thicknesses, H_{sc}. The results confirm that η_p strongly depends on the TDM pile shape but insignificantly depends on the H_{sc}. This finding is consistent with the previous study of rigid pile-supported embankment by Bhasi and Rajagopal (2015), who demonstrated that the portion of embankment load transferred onto the floating piles is not related to d_r. This phenomenon is attributed to the embankment height (5 m in this study) being greater than the critical embankment height (H_{crit}), resulting in full soil arching (e.g., H>1.5$(s-a)$ (Jenck, Dias, and Kastner 2005), H>1.75$(s-a)$ (Rui et al. 2016) and H>0.8$(s-a)+3.0a$

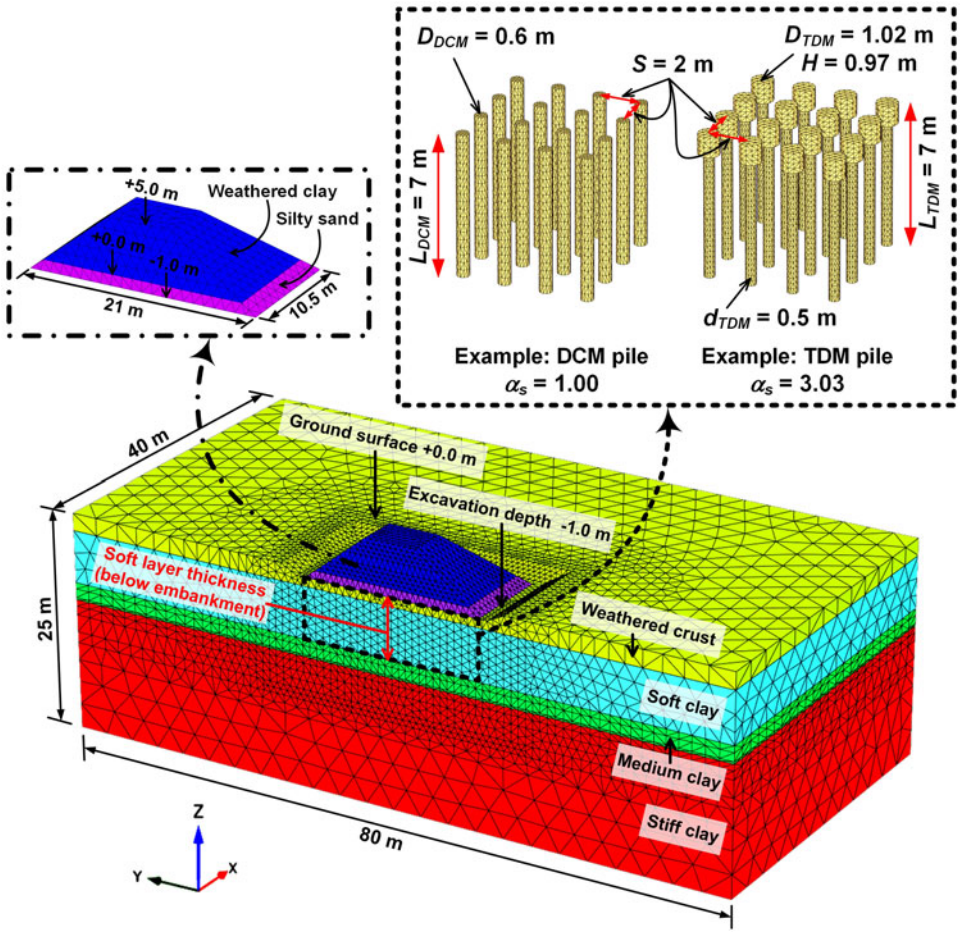

Figure 8. 3D finite element mesh of the DCM/TDM piles-supported embankment.

(Lai et al. 2018), where s is the pile spacing in meters and a is the pile cap or surface diameter in meters). Consequently, any vertical stress induced by the embankment weight or external surcharge load does not affect the load-carrying behavior of pile-supported embankments, even when the pile is short compared with the thickness of the soft layer.

The results clearly show that η_p increases nonlinearly with increasing α_s. This trend agrees with that obtained from the experiments in the previous section and the previously reported field tests of embankment with TDM piles (Liu et al. 2012). A similar trend is also observed from field tests of embankments with cement-fly ash-gravel piles (Zhang et al. 2016), experimental tests of piled embankments (Fagundes et al. 2015; Girout et al. 2016) and numerical analyses of rigid piles (Jenck, Dias, and Kastner 2007) and DCM piles (Jamsawang et al. 2016). All past work summarized that η_p increases with pile surface diameter (together with pile volume). Notably, in the present study, α_s increases under a constant pile volume. For all three soft clay thicknesses considered in the study, η_p increases considerably with increasing α_s from 1.00 to 2.07, before maintaining an approximately stable value of 0.30 as α_s reaches 3.03. Then, η_p increases again with α_s. Interestingly, α_s greater than 3.0 should be recommended to ensure a high η_p. A α_s value greater than 3.00 was also recommended in the previous study to guarantee the effectiveness of enlarging the pile cap to change the pile-bearing capacity (Phutthananon et al. 2018). The pile efficacy may be relevant to the individual pile bearing capacity. To clarify this, additional 2D axisymmetric analyses of pile load tests on individual piles with the same geometry of each case in the present study (same properties and subsoil profile) are performed, and the ultimate bearing capacity (Q_{ult}) is derived from the load-settlement curve by the De Beer method (De Beer 1967). As shown in Figure 11(b), the change in η_p with α_s is similar to that of Q_{ult} for a single pile. This result confirms that the pile efficacy is relevant to the individual pile-bearing capacity, which in turn depends on α_s. Moreover, the Q_{ult} of a single DCM and TDM piles can be estimated from simple equations recommended by Yi et al. (2017). The computed results of this study are in good agreement with the analytical results provided by Yi et al. (2017) as also shown in Figure 11(b).

4.2. Influence of shape factor and soft layer thickness on surface settlement

Changes in the surface settlements of both the pile and surrounding soil are observed. Figure 12(a–c) summarizes the surface settlements along the x direction in both the A-A' (dotted line) and B-B' (solid line) sections for the cases of α_s=1.00, 3.03 and 5.02, respectively. The distance x in these figures is defined as zero at the center of the embankment. For all simulation cases, it can be observed that the

settlements of both sections decrease toward zero when the distance x is approximately 11 m from the center of the embankment; the location is close to the edge of the embankment. The maximum surface settlement of each section was found at the transverse centerline of the embankment. At this centerline, the computed magnitude of the settlements of both sections for the same case of α_s and H_{sc} was found to be nearly the same. Moreover, when comparing the computed settlement of each section with various α_s at identical H_{sc}, an insignificant increase in the settlement was observed. This may be attributed to the long distance between the centerline of the embankment and the closest pile row (2.5 m); consequently, there was no significant influence of the piles observed. However, the results clearly indicate that the surface settlement at the embankment center mainly depends on H_{sc}. This is because of the thick layer of unimproved soft soil below the pile tip and large embankment load (5 m high). The results in the present study show a similar tendency to those of the previous work on embankments supported by rigid piles (Bhasi and Rajagopal 2015) and DCM piles (Jamsawang et al. 2016): The foundation surface settlement is mainly dependent upon d_r. The piles beneath the embankment can then move downward owing to high compressibility of the unimproved soft soil (Jamsawang et al. 2016). Figure 12(d) demonstrates the distribution of the axial forces along the pile. For the DCM pile, the maximum axial force occurs at the pile head and then gradually decreases with depth due to the friction between the pile and surrounding soil. Similarly, the highest axial force for the TDM pile was observed at the pile head. However, the axial force abruptly decreases under the bottom of the pile cap owing to the change in the cross-sectional area from the pile cap to the pile body and slightly increases again before gently decreasing to the pile tip. The sudden decrease of the axial force beneath the pile cap is mainly due to the enlarged size of the pile cap. Hence, the axial force can transfer to the soil under cap and the force in the pile appears to plummet. Additionally, some of the axial forces are conveyed to the surrounding soil around the pile and produces a negative relative displacement between pile and soil in the lower part of the enlarged pile cap. Negative skin friction behavior of pile-soil contact is developed leading to slight increment of the axial force at the upper part of pile body. This observation agrees with the results of a past study (Xi, Zhang, and Liu 2014). The axial force along the TDM pile body is smaller than that along the DCM pile due to the smaller cross-sectional area. Due to the large load from the embankment, the axial forces at the depth of the pile tip (–8 m) are still larger than 20 kN for all cases. For the cases of α_s>1.00 (TDM pile), the axial forces at the pile tip are almost identical except for the case of H_{sc}=7 m because the pile tip is situated on the medium clay. This observation confirms that with the 5-m-high embankment in this study, a large portion of the load can still transfer to the pile tips. Consequently, settlement occurs in the layer beneath the pile tip. Notably, the computed s_p is less than s_s for all the cases investigated.

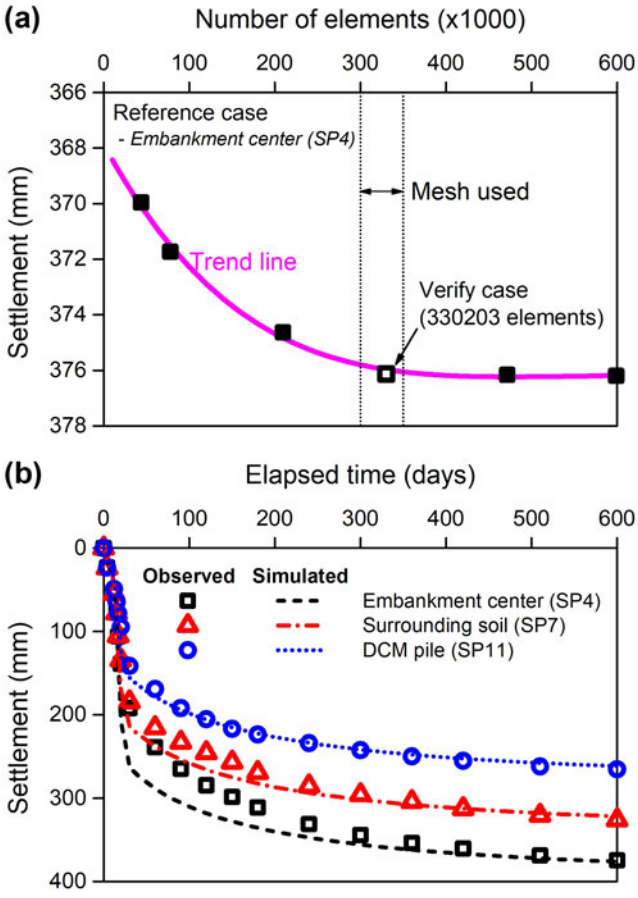

Figure 9. (a) Mesh sensitivity analyses and (b) validation of FE analysis with the measured settlement of reference case.

4.2.1. Differential settlement

Figure 13 presents the variation in the normalized differential settlement (λ_s) versus α_s for cases with different H_{sc}. The differential settlement in each condition, Δs ($s_s - s_p$), is

Table 4. Construction phases and sequences of the embankment test in FE simulation.

Phase	Construction sequences	Elapsed days (total days)
1	Generation of the initial stresses (K_o – condition)	–
2	Installation of the DCM or TDM piles	–
3	Excavation of the ground surface to the depth of –1.0 m	–
4	Construction of the base embankment (Silty sand) to the depth of 0.0 m	8 (8)
5	Construction of a 1.0-m-high base embankment (Weathered clay)	4 (12)
6	Construction of a 2.0-m-high base embankment (Weathered clay)	3 (15)
7	Construction of a 3.0-m-high base embankment (Weathered clay)	2 (17)
8	Construction of a 4.0-m-high base embankment (Weathered clay)	3 (20)
9	Construction of a 5.0-m-high base embankment (Weathered clay)	10 (30)
10	Consolidation after end of construction the embankment	570 (600)

Table 5. Case investigated in the parametric study.

No.	Surface pile diameter (m) D_{DCM} or D_{TDM}	Thickness of enlarged pile cap (m) H	Pile body diameter (m) d_{TDM}	Length of pile (m) L_{DCM} or L_{TDM}	Pile volume (m^3) –	Shape factor (–) α_s	Area improvement ratio (–) a_r	Thickness of soft layer (m) H_{sc}	Depth improvement ratio (–) d_r
1*	0.60	–	–	7.0	1.979	1.00	0.071		
2	0.65	4.46	0.50	7.0	1.979	1.18	0.083		
3	0.70	3.21	0.50	7.0	1.979	1.38	0.096		
4	0.75	2.46	0.50	7.0	1.979	1.59	0.110		
5	0.80	1.97	0.50	7.0	1.979	1.82	0.126		
6	0.85	1.63	0.50	7.0	1.979	2.07	0.142		
7	0.90	1.38	0.50	7.0	1.979	2.33	0.159		
8	0.95	1.18	0.50	7.0	1.979	2.61	0.177	7.00, 8.75, 14.00	1.00, 0.80, 0.50
9	1.02	0.97	0.50	7.0	1.979	3.03	0.204		
10	1.05	0.90	0.50	7.0	1.979	3.22	0.216		
11	1.10	0.80	0.50	7.0	1.979	3.55	0.238		
12	1.15	0.72	0.50	7.0	1.979	3.89	0.260		
13	1.20	0.65	0.50	7.0	1.979	4.25	0.283		
14	1.25	0.59	0.50	7.0	1.979	4.63	0.307		
15	1.30	0.53	0.50	7.0	1.979	5.02	0.332		

Note: *Reference case with E'_{SCP}=24,000 kPa and E^{ref}_{50}=2,400 kPa of soft clay; modulus ratio (E_p/E_s)=10; pile spacing (S)=2 m.

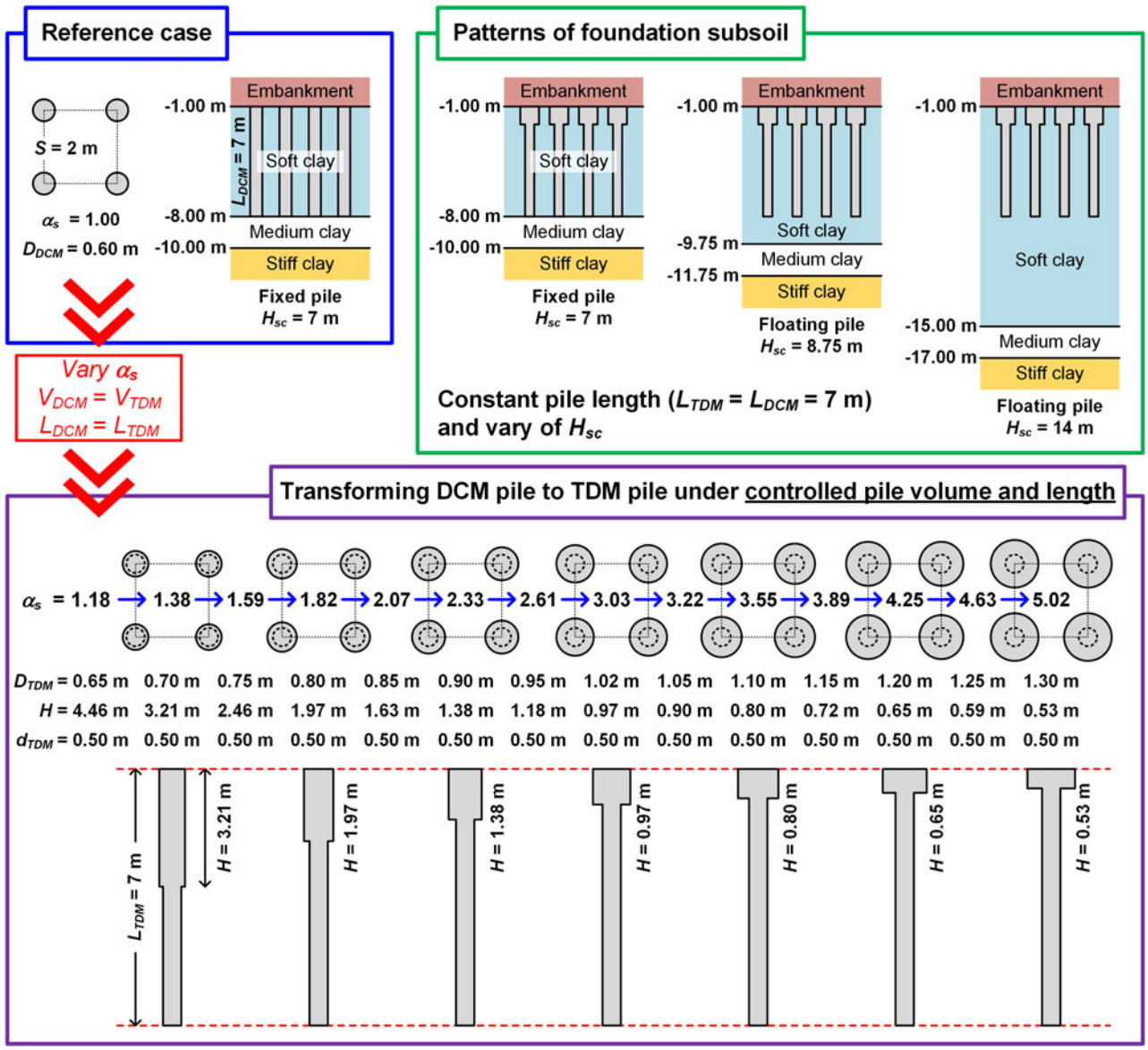

Figure 10. Schematic of soil-cement piles with varying shape factor (α_s) and patterns of foundation subsoil in the parametric analysis.

normalized by that of the reference case (DCM piles with H_{sc} of 7 m).

$$\lambda_s = \frac{\Delta s \text{ of each case}}{\Delta s \text{ of reference case}} \quad (3)$$

λ_s nonlinearly decreases with increasing α_s. Relative to the reference case, the λ_s values of cases with α_s of 3.03 and 5.02 at the same H_{sc}=7 m decrease by approximately 54% and 76%, respectively. In addition, as H_{sc} increases to 14 m (decreasing d_r), λ_s for the case with α_s of 1.00 is 0.96 (4% reduction from the reference case) and that for α_s of 3.03 and 5.02 decreased by 66% and 88%, respectively. These results confirm that the use of TDM piles, especially in the case of high α_s, can substantially reduce differential settlement, while the differential settlement is affected by the soft layer thickness to a significantly lower degree.

To gain insight into this main mechanism, the plots of s_p and s_s versus α_s and stress concentration ratio ($n = \sigma_p/\sigma_s$) versus α_s are depicted in Figure 14. As seen in Figure 14(a), s_p and s_s slightly decrease with transformation from the DCM piles to the TDM piles with a slightly larger pile head because a slightly larger portion of the pile head can induce a slightly larger load to the piles, as shown in Figure 14(b). When enlarging the pile head with α_s from 1.38 to 3.03, s_p and s_s increase substantially, but the rate of increase with respect to the change in cap shape (α_s) of s_p is more pronounced, resulting in a reduction in Δs with increasing α_s. In this range (α_s from 1.38 to 3.03), n drastically decreases with increasing α_s because the area of the pile head increases. This observation is similar to the findings from past studies of TDM and DCM piles by full-scale field test (Liu et al. 2012), physical model test (Yi, Liu, and Puppala 2016) and numerical analysis (Yi, Ni, and Puppala 2018) of which the load carried by the piles can be increased with the increase in surface pile diameter. When α_s exceeds 3, the Δs continues decreasing with a greater α_s but with a smaller rate (see Figure 13). Figure 14(a) shows that with increasing α_s, s_p gradually increases, whereas s_s shows a slightly decreasing trend. The tendency is also observed in the numerical results obtained by Yi, Ni, and Puppala (2018). For α_s greater than 3, n remains approximately constant with changing α_s, as illustrated in Figure 14(b). The greater cap area indicates that the load transferred to the pile might increase; however, this increase is only slight. Hence, n remains unchanged. Therefore, it can be concluded that the use of TDM pile can remarkably reduce the differential settlement between soil and pile under embankment loading compared to the conventional pile, especially in the case of high α_s (larger diameter but thinner cap). This summary is in close agreement with the numerical results obtained by Yi, Ni, and Puppala (2018) who discovered that the differential settlement is mainly controlled by the surface pile diameter while practically not influenced by the pile cap thickness. Meanwhile, the effect of H_{sc} on Δs is practically negligible when compared to its effect of α_s. Similar to the study of Ye, Cai, and Zhang (2017) on embankment with stiffened DCM piles, the depth improvement ratio (L_{pile}/H_{sc}) did not significantly affect the differential settlement. Thus, it can be summarized that the shape factor is more significant than the soft layer thickness (or depth improvement ratio) for reducing the differential settlement.

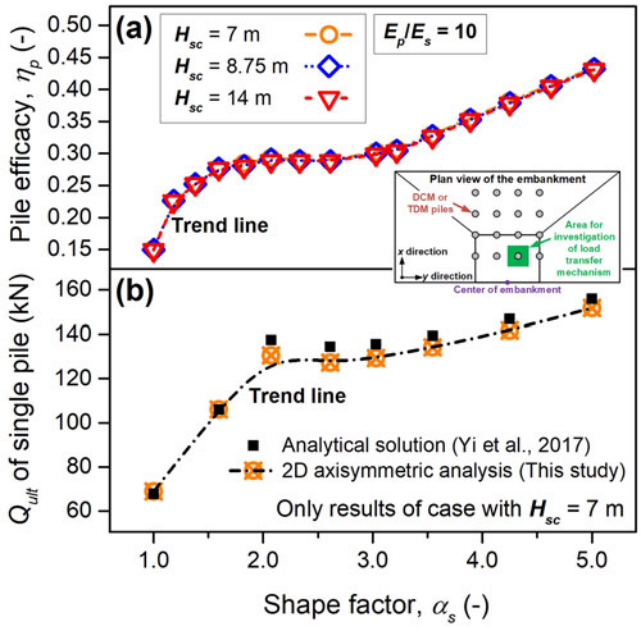

Figure 11. Influence of shape factor (α_s) on (a) pile efficacy (η_p) with different soft layer thickness (H_{sc}) and (b) ultimate bearing capacity (Q_{ult}) of single DCM/TDM piles.

4.2.2. Average settlement

The results of the foundation surface settlement of the embankment over TDM piles with α_s of 5.02 were used to demonstrate the difference in deformation characteristics between cases with H_{sc} of 7 and 14 m, as illustrated in Figure 15(a,b), respectively. The surface settlement in the case with H_{sc} of 14 m is larger than that with H_{sc} of 7 m at every observation point; however, the settlements vary spatially. To accommodate the comparison, the average settlement (s_{avg}) proposed by Watcharasawe, Kitiyodom, and Jongpradist (2015) was used to assess the effect of the influencing factors on the overall settlement. s_{avg} as shown in Equation (4) can be calculated through the relation between the settlement volume ($V_{settlement}$) and the area of the embankment base (A_{emb} = 21 m × 10.5 m).

$$s_{avg} = \frac{V_{settlement}}{A_{emb}} \quad (4)$$

The presentation is illustrated in terms of average settlement ratio β_s defined as

$$\beta_s = \frac{s_{avg} \text{ in each case}}{s_{avg} \text{ of reference case}} \quad (5)$$

Figure 16 presents the distribution of β_s versus α_s in association with H_{sc}. With increasing α_s, β_s increases linearly and maintains a relatively constant value at the α_s value of 3.03. In the studied range, the β_s values for cases with H_{sc} of 14, 8.75 and 7 m are approximately 1.439, 1.173 and 1.026 times larger than that of the reference case, respectively. However, for each H_{sc}, the changing value of α_s from 1.00 to 5.02 had a minimal influence on β_s. Consequently, when

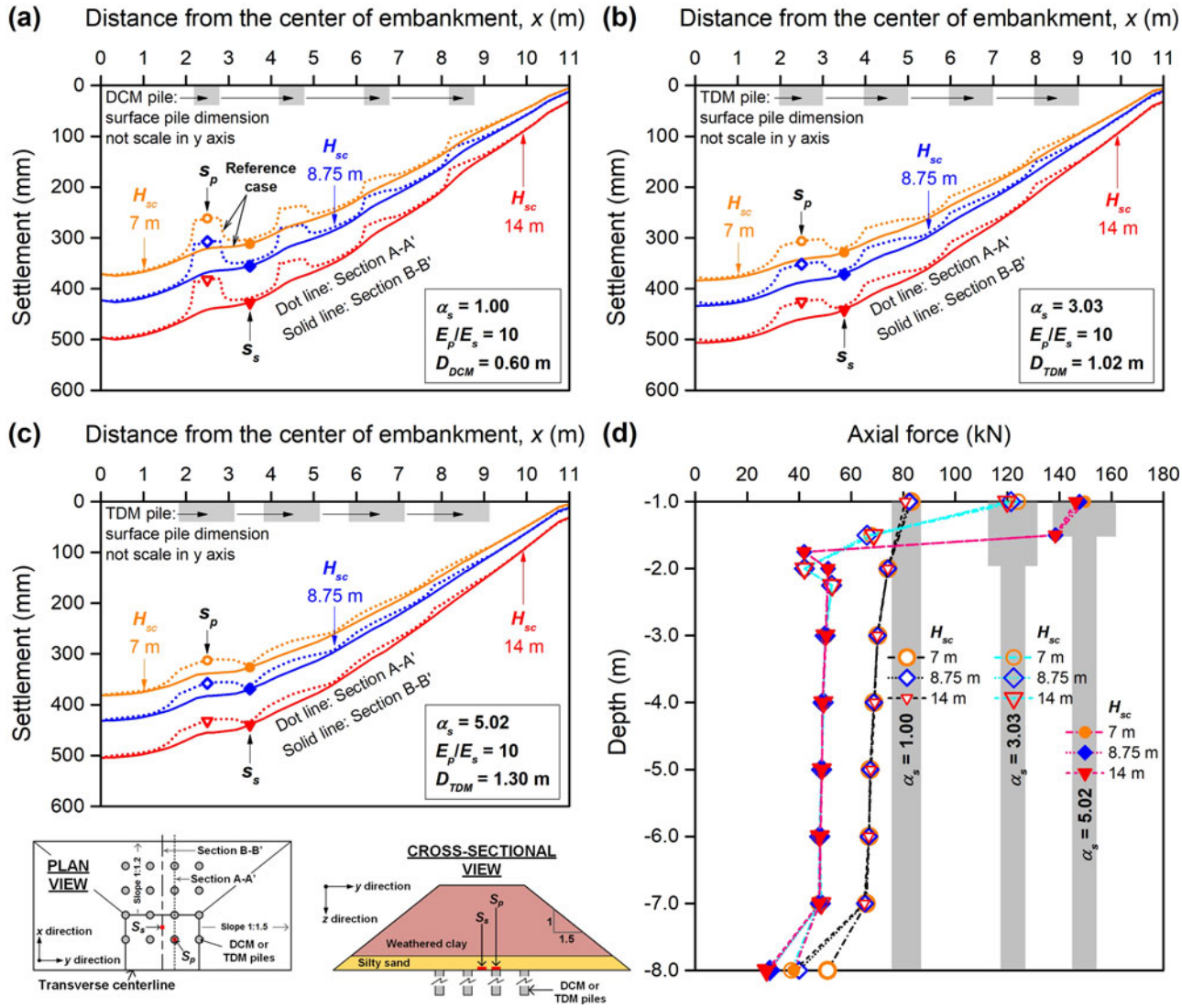

Figure 12. Settlements along the embankment width for sections A-A′ and B-B′ for cases with: (a) α_s=1.00, (b) α_s=3.03, (c) α_s=5.02 and (d) the computed axial force along DCM and TDM piles.

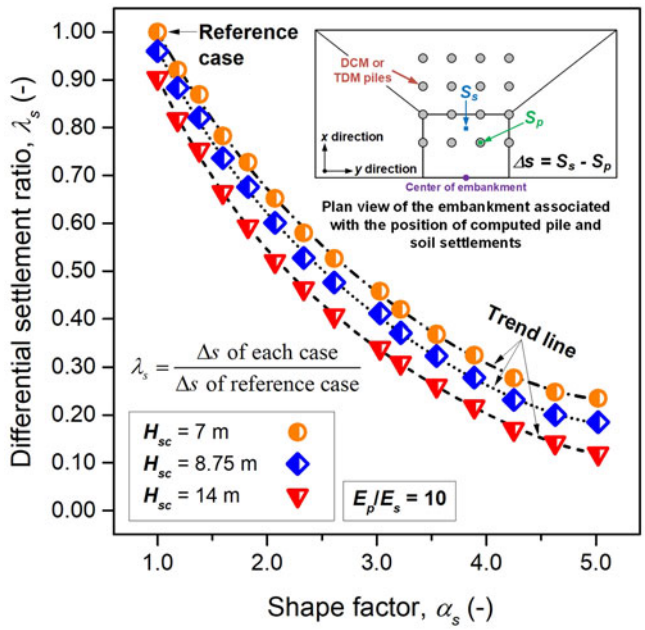

Figure 13. Influence of shape factor (α_s) in association with the thickness of soft layer (H_{sc}) on differential settlement ratio (λ_s).

replacing the DCM piles with the TDM piles to support the embankment, the average settlement is insignificantly affected by the pile shape change. Nevertheless, the soft layer thickness has an important effect on the average settlement for embankments with both DCM and TDM piles. Notably, the difference in s_{avg} is approximately consistent when H_{sc} changes from 7 m to 8.75 m (increasing s_{avg} of approximately 24 mm) and to 14 m (increasing s_{avg} of approximately 68 mm). This increase in s_{avg} is attributed to the effect of a thicker layer of highly compressible soft soil beneath the pile tip, as described in the previous section.

The abovementioned results indicate that the variation in settlement was governed by both the shape factor and the thickness of the soft layer. Δs of embankment with the TDM piles becomes significantly less than that of embankment with the DCM piles as the s_{avg} slightly increases. This indicates the effectiveness of utilizing the TDM piles to support the embankment. However, when the soft layer thickness exceeds the pile length (floating pile type, small d_r), a large s_{avg} can be induced if a large portion of the load can transfer to the pile tip. Hence, to evaluate the performance

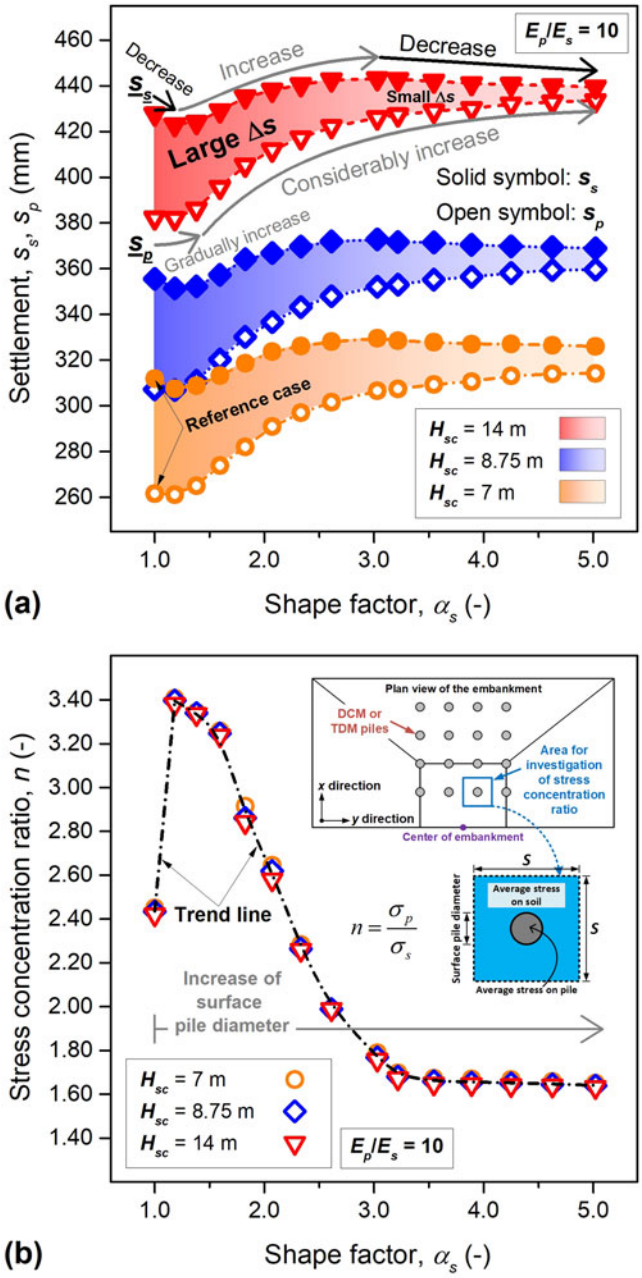

Figure 14. (a) s_p and s_s versus shape factor (α_s) with various soft layer thicknesses and (b) distribution of stress concentration ratio (n) against the shape factor (α_s).

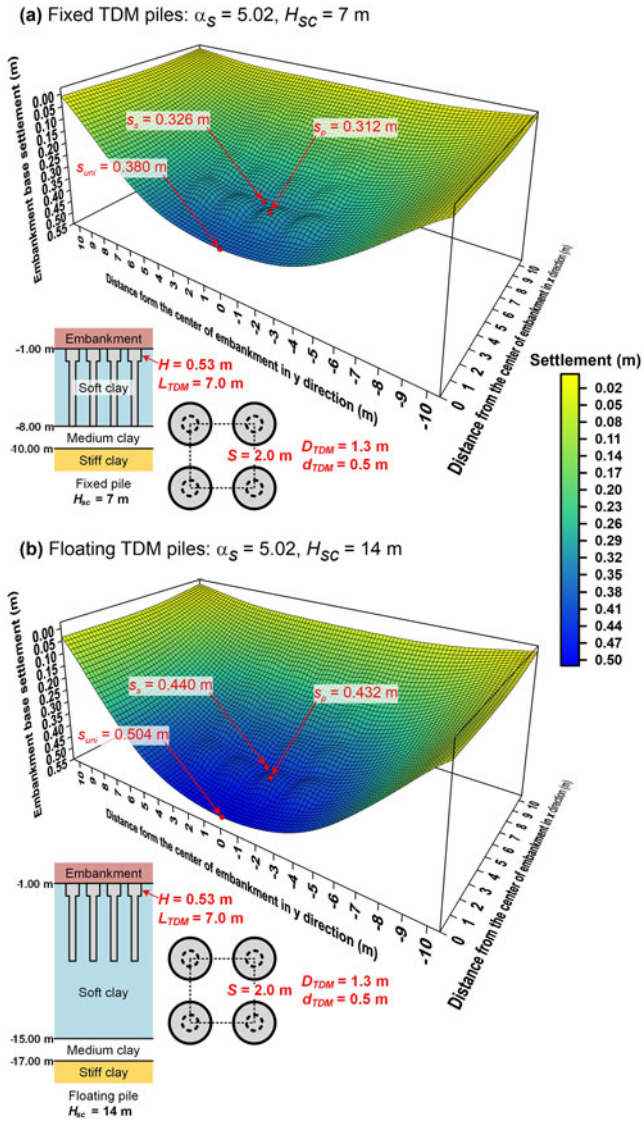

Figure 15. Example of foundation settlement of embankment supported by TDM pile with α_s of 5.02 with (a) H_{sc} of 7 m and (b) H_{sc} of 14 m.

of TDM pile-supported embankments in terms of settlement, these influencing factors should be considered simultaneously.

4.3. Influence of pile strength in terms of settlement behavior

To provide a better understanding of the effect of the pile strength on the settlement behavior for the TDM/DCM pile-supported embankment, all the investigated cases with H_{sc} of 8.75 m (d_r=0.8) were used, and the pile strength was varied (low strength: q_u=180 kPa; high strength: q_u=480 kPa). The obtained results involving λ_s and β_s are plotted against α_s in association with q_u, as depicted in Figures 17 and 18, respectively. The results of the reference case are also presented in these figures for comparison purposes.

The influence of pile strength, q_u on λ_s for cases with various α_s is presented in Figure 17. The change in q_u plays an important role in λ_s, especially in cases with α_s of less than 2. A decrease in q_u, in which E_p also decreases, can result in a severe reduction in λ_s. This "decrease" trend can be described by the modulus ratio between the pile and the soil materials (E_p/E_s). At the same α_s, the larger E_p/E_s promotes more Δs (or λ_s). In other words, there would be no Δs if the pile and the soil have the same modulus. This result is in agreement with the finding of previous studies based on the conventional piles (Han and Gabr 2002; Huang and Han 2009, 2010).

The variations in β_s with a change in q_u for several α_s are shown in Figure 18. Clearly, the use of high-strength piles can suppress s_{avg} due to the great pile modulus. These results are attributed to the difference in the pile modulus and the surrounding soil modulus, E_p/E_s (Jiang, Han, and Zheng 2014). In contrast, the average settlement increases

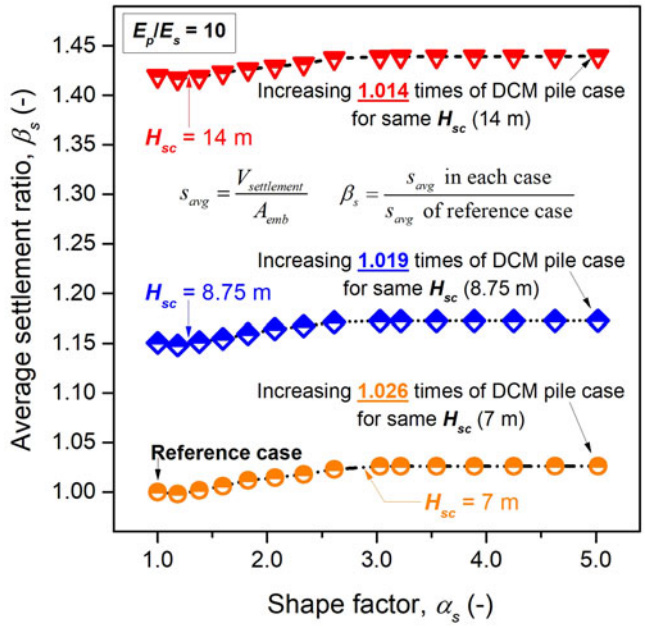

Figure 16. Influence of shape factor (α_s) in association with the thickness of soft layer (H_{sc}) on average settlement ratio (β_s).

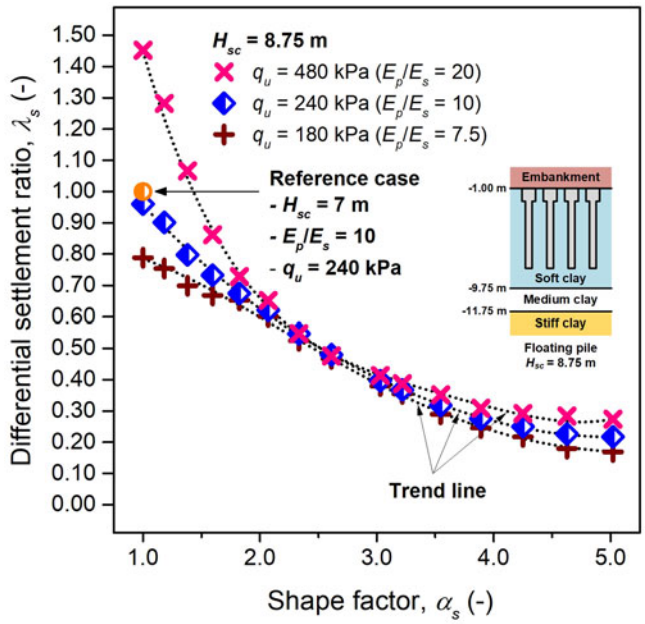

Figure 17. Distribution of differential settlement ratio (λ_s) against the shape factor (α_s) at H_{sc} of 8.75 m in consideration of pile strength (q_u).

with a decrease in the pile strength; however, the trend of the variation in β_s with α_s is insignificantly affected by q_u.

Based on these observations, it was summarized that q_u has a significant effect on Δs for α_s of less than 2 and a certain effect on the average settlement. Thus, in the design of an embankment supported by TDM piles, a low-strength pile can be carefully considered with the criterion of s_{avg}.

5. Conclusion

In this study, small-scale physical model tests were performed to preliminarily investigate the effectiveness of enlarging the cap of embankment support piles on the

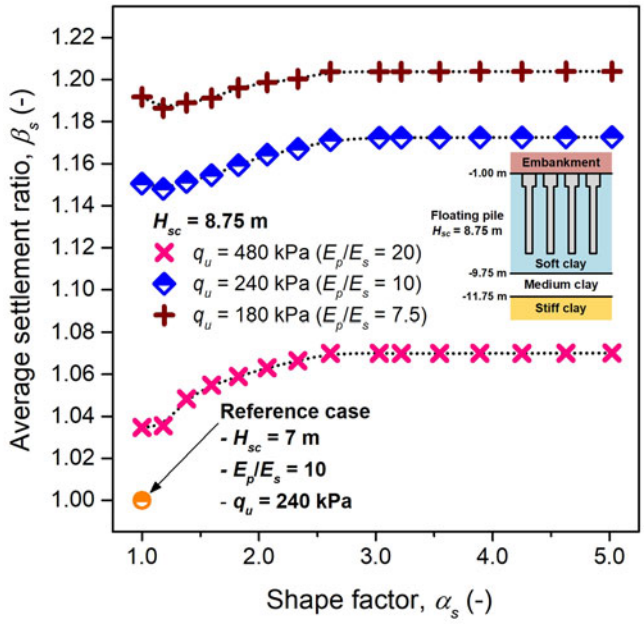

Figure 18. Distribution of average settlement ratio (β_s) against the shape factor (α_s) at H_{sc} of 8.75 m in consideration of pile strength (q_u).

reduction in differential settlement. Three physical model tests with different shapes of floating DCM/TDM piles were conducted under a controlled pile volume. A 3D FE parametric study on pile-supported embankment was carried out to study the key influencing factors, including pile shape factor, soft layer thickness and pile strength. The discussions on the pile efficacy, settlement surface along the width of the embankment, differential settlement and average settlement are provided in terms of the reference case and under a controlled pile volume. The main conclusions are as follows:

1. The physical model test results indicate that under the same pile volume, the cap shape of the TDM pile plays an important role in the load ratio shared by the piles (or pile efficacy, η_p). Consequently, the settlements of the surrounding soil (s_s) and pile (s_p) decrease and increase, respectively, leading to a reduction in differential settlement (Δs). Furthermore, by enlarging the pile cap, a Δs less than that for DCM piles can be obtained despite reducing the pile strength.
2. The numerical analyses confirm that η_p increases significantly with increasing pile shape factor (α_s) or pile cap size. This pile efficacy is relevant to the individual pile-bearing capacity, which in turn depends on α_s.
3. The effectiveness of using TDM piles to reduce the Δs of embankment on soft soil is indicated. The reduction in Δs is primarily due to the larger pile settlement as a result of the larger induced load on the pile; this is true for all pile tip conditions (floating and fixed types) and any soft clay thicknesses (H_{sc}) considered in this study.
4. The H_{sc} has a small impact on Δs because both s_p and s_s increase with H_{sc}. However, with increasing H_{sc}, the effectiveness of increasing α_s (enlarging cap size) on the reduction in Δs becomes more prominent.

5. Under the level of embankment loading considered here, the average settlement (s_{avg}) is significantly governed by H_{sc} because the load can be transferred to the pile tip. While the impact of α_s is relatively low.
6. It is possible to reduce the TDM pile strength to achieve a small differential settlement. However, the increase in average settlement must be taken into consideration.
7. The α_s values of at least 3.0 are recommended to ensure a substantial reduction in differential settlement and minimize the effect of the change in pile strength.

Funding

The authors gratefully acknowledge the financial supports from King Mongkut's University of Technology Thonburi (KMUTT) and the Thailand Research Fund (TRF) under The Petchra Pra Jom Klao scholarship contact No. 32/2558 and TRF Basic Research Grant No. BRG6080011. The authors also would like to express the sincerest gratitude for King Mongkut's University of Technology North Bangkok (KMUTNB) under contract No. KMUTNB-61-GOV-D-61.

References

Abiodun, A. A., and Z. Nalbantoglu. 2017. A Laboratory Model Study on the Performance of Lime Pile Application for Marine Soils. *Marine Georesources & Geotechnology* 35 (3): 397–405. doi:10.1080/1064119X.2016.1190429.

Barari, A., and L. B. Ibsen. 2012. Undrained Response of Bucket Foundations to Moment Loading. *Applied Ocean Research* 36: 12–21. doi:10.1016/j.apor.2012.01.003.

Barari, A., L. B. Ibsen, A. Taghavi Ghalesari, and K. A. Larsen. 2017. Embedment Effects on Vertical Bearing Capacity of Offshore Bucket Foundations on Cohesionless Soil. *International Journal of Geomechanics* 17 (4): 04016110. doi:10.1061/(ASCE)GM.1943-5622.0000782.

Bergado, D. T., P. Jamsawang, T. Tanchaisawat, Y. P. Lai, and G. A. Lorenzo. 2008. Performance of Reinforced Load Transfer Platforms for Embankments supported by Deep Cement Mixing Piles. In *GeoCongress 2008: Geosustainability and Geohazard Mitigation*, eds. K. R. Reddy, M. V. Khire, and A. N. Alshawabkeh, 620–27. Virginia, USA: ASCE. doi:10.1061/40971(310)77.

Bhasi, A., and K. Rajagopal. 2015. Numerical Study of Basal Reinforced Embankments Supported on Floating/End Bearing Piles considering Pile-Soil Interaction. *Geotextiles and Geomembranes* 43 (6): 524–536. doi:10.1016/j.geotexmem.2015.05.003.

Bo, M. W., A. Arulrajah, P. Sukmak, and S. Horpibulsuk. 2015. Mineralogy and Geotechnical Properties of Singapore Marine Clay at Changi. *Soils and Foundations* 55 (3): 600–613. doi:10.1016/j.sandf.2015.04.011.

Borges, J. L., and D. O. Marques. 2011. Geosynthetic-Reinforced and Jet Grout Column-Supported Embankments on Soft Soils: Numerical Analysis and Parametric Study. *Computers and Geotechnics* 38 (7): 883–896. doi:10.1016/j.compgeo.2011.06.003.

Brinkgreve, R. B. J., E. Engin, and W. M. Swolfs. 2013. *Plaxis 3D 2013 Manual*. The Netherlands: Plaxis bv.

Chai, J. C., and S. Pongsivasathit. 2010. A Method for Predicting Consolidation Settlements of Floating Column Improved Clayey Subsoil. *Frontiers of Architecture and Civil Engineering in China* 4 (2): 241–251. doi:10.1007/s11709-010-0024-3.

Chai, J. C., S. Shrestha, T. Hino, W. Q. Ding, Y. Kamo, and J. Carter. 2015. 2D and 3D Analyses of an Embankment on Clay Improved by Soil-Cement Columns. *Computers and Geotechnics* 68: 28–37. doi:10.1016/j.compgeo.2015.03.014.

Chantachot, T., W. Kongkitkul, S. Youwai, and P. Jongpradist. 2016. Behaviours of Geosynthetic-Reinforced Asphalt Pavements Investigated by Laboratory Physical Model Tests on a Pavement Structure. *Transportation Geotechnics* 8: 103–118. doi:10.1016/j.trgeo.2016.03.004.

Chen, L., and S. Y. Liu. 2008. Consolidation Calculation of Soft Ground improved by T-shape Deep Mixing Columns. In *GeoCongress 2008: Geosustainability and Geohazard Mitigation*, eds. K. R. Reddy, M. V. Khire, and A. N. Alshawabkeh, 620–27. Virginia, USA: ASCE. doi:10.1061/40971(310)77620–627.

Chen, J., S. L. Shen, Z. Y. Yin, Y. S. Xu, and S. Horpibulsuk. 2016. Evaluation of Effective Depth of PVD Improvement in Soft Clay Deposit: A Field Case Study. *Marine Georesources & Geotechnology* 34 (5): 420–430. doi:10.1080/1064119X.2015.1016638.

Chheng, C., and S. Likitlersuang. 2018. Underground Excavation Behaviour in Bangkok Using Three-Dimensional Finite Element Method. *Computers and Geotechnics* 95: 68–81. doi:10.1016/j.compgeo.2017.09.016.

Cho, J., J. H. Lee, S. Jeong, and J. Lee. 2012. The Settlement Behavior of Piled Raft in Clay Soils. *Ocean Engineering* 53: 153–163. doi:10.1016/j.oceaneng.2012.06.003.

De Beer, E. E. 1967. Proefondervindlijke Bijdrage Tot de Studie Van Het Grensdraag Vermogen Van Zand Onder Funderingen op Staal. *Tijdshift Der Openbar Verken Van Belgie* 6.

Dehghanbanadaki, A., K. Ahmad, and N. Ali. 2016. Experimental Investigations on Ultimate Bearing Capacity of Peat Stabilized by a Group of Soil–Cement Column: A Comparative Study. *Acta Geotechnica* 11 (2): 295–307. doi:10.1007/s11440-014-0328-x.

Do, D. H., and M. H. Nguyen. 2013. High-Rise Building Foundation on Floating Soil-Cement Columns. In *Proceedings of the 5th International Young Geotechnical Engineers' Conference*, 81–84. doi:10.3233/978-1-61499-297-4-81.

Fagundes, D. F., M. S. S. Almeida, R. Girout, M. Blanc, and L. Thorel. 2015. Behaviour of Piled Embankment without Reinforcement. *Proceedings of the Institution of Civil Engineers - Geotechnical Engineering* 168 (6): 514–525. doi:10.1680/jgeen.14.00155.

Girout, R., M. Blanc, L. Thorel, D. F. Fagundes, and M. S. S. Almeida. 2016. Arching and Deformation in a Piled Embankment: Centrifuge Tests Compared to Analytical Calculations. *Journal of Geotechnical and Geoenvironmental Engineering* 142 (12): 04016069. doi:10.1061/(ASCE)GT.1943-5606.0001557.

Han, J., and M. A. Gabr. 2002. Numerical Analysis of Geosynthetic-Reinforced and Pile-Supported Earth Platforms over Soft Soil. *Journal of Geotechnical and Geoenvironmental Engineering* 128 (1): 44–53. doi:10.1061/(ASCE)1090-0241(2002)128:1(44).

Han, J., S. Oztoprak, R. L. Parsons, and J. Huang. 2007. Numerical Analysis of Foundation Columns to Support Widening of Embankments. *Computers and Geotechnics* 34 (6): 435–448. doi:10.1016/j.compgeo.2007.01.006.

Horpibulsuk, S., A. Chinkulkijniwat, A. Cholphatsorn, J. Suebsuk, and M. D. Liu. 2012. Consolidation Behavior of Soil-Cement Column Improved Ground. *Computers and Geotechnics* 43: 37–50. doi:10.1016/j.compgeo.2012.02.003.

Horpibulsuk, S., S. Shibuya, K. Fuenkajorn, and W. Katkan. 2007. Assessment of Engineering Properties of Bangkok Clay. *Canadian Geotechnical Journal* 44 (2): 173–187. doi:10.1139/t06-101.

Huang, J., and J. Han. 2009. 3D Coupled Mechanical and Hydraulic Modeling of a Geosynthetic-Reinforced Deep Mixed Column-Supported Embankment. *Geotextiles and Geomembranes* 27 (4): 272–280. doi:10.1016/j.geotexmem.2009.01.001.

Huang, J., and J. Han. 2010. Two-Dimensional Parametric Study of Geosynthetic-Reinforced Column-Supported Embankments by Coupled Hydraulic and Mechanical Modeling. *Computers and Geotechnics* 37 (5): 638–648. doi:10.1016/j.compgeo.2010.04.002.

Igaya, Y., T. Hino, and J. C. Chai. 2011. Measured Behavior of a Trial Embankment on Floating Column Improved Soft Ariake Clay Deposit. *Lowland Technology International* 13 (1): 41–46.

Ignat, R., S. Baker, S. Larsson, and S. Liedberg. 2015. Two- and Three-Dimensional Analyses of Excavation Support with Rows of Dry Deep Mixing Columns. *Computers and Geotechnics* 66: 16–30. doi:10.1016/j.compgeo.2015.01.011.

Ishikura, R., N. Yasufuku, and M. J. Brown. 2016. An Estimation Method for Predicting Final Consolidation Settlement of Ground Improved by Floating Soil Cement Columns. *Soils and Foundations* 56 (2): 213–227. doi:10.1016/j.sandf.2016.02.005.

Jamsawang, P., D. T. Bergado, and P. Voottipruex. 2015. Full-Scale Tests on Stiffened Deep Cement Mixing Piles including Three-Dimensional Finite Element Simulation. In *Ground Improvement Case Histories: Chemical, Electrokinetic, Thermal and Bioengineering Methods*, eds. Buddhima Indraratna, Jian Chu, and Cholachat Rujikiatkamjorn, 31–77. Oxford, UK: Butterworth-Heinemann. doi:10.1016/B978-0-08-100191-2.00002-2.

Jamsawang, P., P. Voottipruex, P. Jongpradist, and D. T. Bergado. 2015. Parameters Affecting the Lateral Movements of Compound Deep Cement Mixing Walls by Numerical Simulations and Parametric Analyses. *Acta Geotechnica* 10 (6): 797–812. doi:10.1007/s11440-015-0417-5.

Jamsawang, P., N. Yoobanpot, N. Thanasisathit, P. Voottipruex, and P. Jongpradist. 2016. Three-Dimensional Numerical Analysis of a DCM Column-Supported Highway Embankment. *Computers and Geotechnics* 72: 42–56. doi:10.1016/j.compgeo.2015.11.006.

Jamsawang, P., S. Jamnam, P. Jongpradist, P. Tanseng, and S. Horpibulsuk. 2017. Numerical Analysis of Lateral Movements and Strut Forces in Deep Cement Mixing Walls with Top-down Construction in Soft Clay. *Computers and Geotechnics* 88: 174–181. doi:10.1016/j.compgeo.2017.03.018.

Jamsawang, P., E. Phongphinnittana, P. Voottipruex, D. T. Bergado, and P. Jongpradist. 2018. Comparative Performances of Two- and Three-Dimensional Analyses of Soil-Cement Mixing Columns under an Embankment Load. *Marine Georesources & Geotechnology* 1–18. doi:10.1080/1064119X.2018.1504261.

Jenck, O., D. Dias, and R. Kastner. 2005. Soft Ground Improvement by Vertical Rigid Piles Two-Dimensional Physical Modelling and Comparison with Current Design Methods. *Soils and Foundations* 45 (6): 15–30. doi:10.3208/sandf.45.15.

Jenck, O., D. Dias, and R. Kastner. 2007. Two-Dimensional Physical and Numerical Modeling of a Pile-Supported Earth Platform over Soft Soil. *Journal of Geotechnical and Geoenvironmental Engineering* 133 (3): 295–305. doi:10.1061/(ASCE)1090-0241(2007)133.

Jiang, Y., J. Han, and G. Zheng. 2014. Influence of Column Yielding on Degree of Consolidation of Soft Foundations Improved by Deep Mixed Columns. *Geomechanics and Engineering* 6 (2): 173–194. doi:10.12989/gae.2014.6.2.173.

Jongpradist, P., W. Homtragoon, R. Sukkarak, W. Kongkitkul, and P. Jamsawang. 2018. Efficiency of Rice Husk Ash as Cementitious Material in High-Strength Cement-Admixed Clay. *Advances in Civil Engineering* 2018 (Article ID 8346319): 1–11. doi:10.1155/2018/8346319.

Jongpradist, P., P. Jamsawang, and W. Kongkitkul. 2019. Equivalent Void Ratio Controlling the Mechanical Properties of Cementitious Material-Clay Mixtures with High Water Content. *Marine Georesources & Geotechnology* 1–12. doi:10.1080/1064119X.2018.1539534.

Jongpradist, P., N. Jumlongrach, S. Youwai, and S. Chucheepsakul. 2010. Influence of Fly Ash on Unconfined Compressive Strength of Cement-Admixed Clay at High Water Content. *Journal of Materials in Civil Engineering* 22 (1): 49–58. doi:10.1061/(ASCE)0899-1561(2010)22:1(49).

Jongpradist, P., T. Kaewsri, A. Sawatparnich, S. Suwansawat, S. Youwai, W. Kongkitkul, and J. Sunitsakul. 2013. Development of Tunneling Influence Zones for Adjacent Pile Foundations by Numerical Analyses. *Tunnelling and Underground Space Technology* 34: 96–109. doi:10.1016/j.tust.2012.11.005.

Lai, Y. P., D. T. Bergado, G. A. Lorenzo, and T. Duangchan. 2006. Full-Scale Reinforced Embankment on Deep Jet Mixing Improved Ground. *Proceedings of the Institution of Civil Engineers - Ground Improvement* 10 (4): 153–164. doi:10.1680/grim.2006.10.4.153.

Lai, H., J. Zheng, R. Zhang, and M. Cui. 2018. Classification and Characteristics of Soil Arching Structures in Pile-Supported Embankments. *Computers and Geotechnics* 98: 153–171. doi:10.1016/j.compgeo.2018.02.007.

Liu, S. Y., Y. J. Du, Y. L. Yi, and A. J. Puppala. 2012. Field Investigations on Performance of T-Shaped Deep Mixed Soil Cement Column-Supported Embankments over Soft Ground. *Journal of Geotechnical and Geoenvironmental Engineering* 138 (6): 718–727. doi:10.1061/(ASCE)GT.1943-5606.0000625.

Lueprasert, P., P. Jongpradist, P. Jongpradist, and S. Suwansawat. 2017. Numerical Investigation of Tunnel Deformation Due to Adjacent Loaded Pile and Pile-Soil-Tunnel Interaction. *Tunnelling and Underground Space Technology* 70: 166–181. doi:10.1016/j.tust.2017.08.006.

Ma, L., S. L. Shen, C. Y. Luo, and Y. S. Xu. 2011. Field Evaluation on the Strength Increase of Marine Clay under Staged Construction of Embankment. *Marine Georesources & Geotechnology* 29 (4): 317–332. doi:10.1080/1064119X.2011.554965.

Muir Wood, D. 2004. *Geotechnical Modelling*. London: E&F Spon.

Ng, K. S., and S. A. Tan. 2015. Nonlinear Behaviour of an Embankment on Floating Stone Columns. *Geomechanics and Geoengineering* 10 (1): 30–44. doi:10.1080/17486025.2014.902118.

Pham, H. V., L. Briançon, D. Dias, and J. Racinais. 2019. Footings over Rigid Inclusion-Reinforced Soft Soil. Experimental and Numerical Approaches. *Canadian Geotechnical Journal*. doi:10.1139/cgj-2018-0495.

Pham, H. V., and D. Dias. 2019. 3D Numerical Modeling of a Piled Embankment under Cyclic Loading. *International Journal of Geomechanics* 19 (4): 04019010. doi:10.1061/(ASCE)GM.1943-5622.0001354.

Pham, H. V., D. Dias, T. Miranda, N. Cristelo, and N. Araújo. 2018. 3D Numerical Modeling of Foundation Solutions for Wind Turbines. *International Journal of Geomechanics* 18 (12): 04018164. doi:10.1061/(ASCE)GM.1943-5622.0001318.

Phutthananon, C., P. Jongpradist, P. Yensri, and P. Jamsawang. 2018. Dependence of Ultimate Bearing Capacity and Failure Behavior of T-Shaped Deep Cement Mixing Piles on Enlarged Cap Shape and Pile Strength. *Computers and Geotechnics* 97: 27–41. doi:10.1016/j.compgeo.2017.12.013.

Rui, R.,. A. F. van Tol, Y. Y. Xia, S. J. M. van Eekelen, and G. Hu. 2016. Investigation of Soil-Arching Development in Dense Sand by 2D Model Tests Available Arching Models for Piled Embankments. *Geotechnical Testing Journal* 39 (3): 415–430. doi:10.1520/GTJ20150130.

Shen, S. L., X. C. Huang, S. J. Du, and J. Han. 2003. Laboratory Studies on Property Changes in Surrounding Clays Due to Installation of Deep Mixing Columns. *Marine Georesources & Geotechnology* 21 (1): 15–35. doi:10.1080/10641190306711.

Shen, S. L., Z. F. Wang, S. Horpibulsuk, and Y. H. Kim. 2013. Jet Grouting with a Newly Developed Technology: The Twin-Jet Method. *Engineering Geology* 152 (1): 87–95. doi:10.1016/j.enggeo.2012.10.018.

Taghavi Ghalesari, A., A. Barari, P. Fardad Amini, and L. B. Ibsen. 2013. The Settlement Behavior of Piled Raft Interaction in Undrained Soil. *IACGE 2013: Challenges and Recent Advances in Geotechnical and Seismic Research and Practices, GSP 232*, 605–612. doi:10.1061/9780784413128.071.

Taghavi Ghalesari, A., A. Barari, P. Fardad Amini, and L. B. Ibsen. 2015. Development of Optimum Design from Static Response of Pile-Raft Interaction. *Journal of Marine Science and Technology* 20 (2): 331–343. doi:10.1007/s00773-014-0286-x.

Taghavi Ghalesari, A., and A. J. Choobbasti. 2018. Numerical Analysis of Settlement and Bearing Behaviour of Piled Raft in Babol Clay. *European Journal of Environmental and Civil Engineering* 22 (8): 978–1003. doi:10.1080/19648189.2016.1229230.

Voottipruex, P., D. T. Bergado, T. Suksawat, P. Jamsawang, and W. Cheang. 2011. Behavior and Simulation of Deep Cement Mixing (DCM) and Stiffened Deep Cement Mixing (SDCM) Piles under Full Scale Loading. *Soils and Foundations* 51 (2): 307–320. doi:10.3208/sandf.51.307.

Waichita, S., P. Jongpradist, and P. Jamsawang. 2019. Characterization of Deep Cement Mixing Wall Behavior Using Wall-to-Excavation Shape Factor. *Tunnelling and Underground Space Technology* 83: 243–253. doi:10.1016/j.tust.2018.09.033.

Wang, Z. F., X. Bian, and Y. Q. Wang. 2017. Numerical Approach to Predict Ground Displacement Caused by Installing a Horizontal Jet Grout Column. *Marine Georesources & Geotechnology* 35 (7): 970–977. doi:10.1080/1064119X.2016.1273288.

Wang, A., D. Zhang, and Y. Deng. 2018. Lateral Response of Single Piles in Cement-Improved Soil: numerical and Theoretical Investigation. *Computers and Geotechnics* 102: 164–178. doi:10.1016/j.compgeo.2018.06.014.

Watcharasawe, K., P. Kitiyodom, and P. Jongpradist. 2015. Numerical Analyses of Piled Raft Foundation in Soft Soil Using 3D-FEM. *Geotechnical Engineering Journal of the SEAGS & AGSSEA* 46 (1): 109–116.

Wonglert, A., and P. Jongpradist. 2015. Impact of Reinforced Core on Performance and Failure Behavior of Stiffened Deep Cement Mixing Piles. *Computers and Geotechnics* 69: 93–104. doi:10.1016/j.compgeo.2015.05.003.

Wonglert, A., P. Jongpradist, P. Jamsawang, and S. Larsson. 2018. Bearing Capacity and Failure Behaviors of Floating Stiffened Deep Cement Mixing Columns under Axial Load. *Soils and Foundations* 58 (2): 446–461. doi:10.1016/j.sandf.2018.02.012.

Wu, H. N., S. L. Shen, L. Ma, Z. Y. Yin, and S. Horpibulsuk. 2015. Evaluation of the Strength Increase of Marine Clay under Staged Embankment Loading: A Case Study. *Marine Georesources & Geotechnology* 33 (6): 532–541. doi:10.1080/1064119X.2014.954180.

Xi, P. S., X. T. Zhang, and B. Liu. 2014. Numerical Simulation of Load Transfer Mechanism of T-Shaped Soil-Cement Deep Mixing Column. *Applied Mechanics and Materials* 580–583: 118–122. doi:10.4028/www.scientific.net/AMM.580-583.118.

Ye, G., Y. Cai, and Z. Zhang. 2017. Numerical Study on Load Transfer Effect of Stiffened Deep Mixed Column-Supported Embankment over Soft Soil. *KSCE Journal of Civil Engineering* 21 (3): 703–714. doi:10.1007/s12205-016-0637-8.

Yi, Y. L., S. Y. Liu, and A. J. Puppala. 2016. Laboratory Modelling of T-Shaped Soil–Cement Column for Soft Ground Treatment under Embankment. *Géotechnique* 66 (1): 85–89. doi:10.1680/jgeot.15.P.019.

Yi, Y. L., S. Y. Liu, and A. J. Puppala. 2018. Bearing Capacity of Composite Foundation Consisting of T-Shaped Soil-Cement Column and Soft Clay. *Transportation Geotechnics* 15: 47–56. doi:10.1016/j.trgeo.2018.04.003.

Yi, Y. L., S. Y. Liu, A. J. Puppala, and P. S. Xi. 2017. Vertical Bearing Capacity Behaviour of Single T-Shaped Soil–Cement Column in Soft Ground: laboratory Modelling, Field Test, and Calculation. *Acta Geotechnica* 12 (5): 1077–1088. doi:10.1007/s11440-017-0555-z.

Yi, Y. L., S. Y. Liu, D. W. Zhang, and Z. D. Zhu. 2009. Experimental Study on T-shaped Soil-cement Deep Mixing Column Composite Foundation. *GeoHunan International Conference 2009: Slope Stability, Retaining Walls, and Foundations*, 1–7. doi:10.1061/41049(356)1.

Yin, J. H., and Z. Fang. 2006. Physical Modelling of Consolidation Behaviour of a Composite Foundation Consisting of a Cement-Mixed Soil Column and Untreated Soft Marine Clay. *Géotechnique* 56 (1): 63–68. doi:10.1186/1471-2148-6-63.

Yin, J. H., and Z. Fang. 2010. Physical Modeling of a Footing on Soft Soil Ground with Deep Cement Mixed Soil Columns under Vertical Loading. *Marine Georesources & Geotechnology* 28 (2): 173–188. doi:10.1080/10641191003780872.

Zhang, C., G. Jiang, X. Liu, and O. Buzzi. 2016. Arching in Geogrid-Reinforced Pile-Supported Embankments over Silty Clay of Medium Compressibility: Field Data and Analytical Solution. *Computers and Geotechnics* 77: 11–25. doi:10.1016/j.compgeo.2016.03.007.

Zheng, G., Y. Jiang, J. Han, and Y. F. Liu. 2011. Performance of Cement-Fly Ash-Gravel Pile-Supported High-Speed Railway Embankments over Soft Marine Clay. *Marine Georesources & Geotechnology* 29 (2): 145–161. doi:10.1080/1064119X.2010.532700.

Computers and Geotechnics 119 (2020) 103380

Contents lists available at ScienceDirect

Computers and Geotechnics

journal homepage: www.elsevier.com/locate/compgeo

Research Paper

Numerical and experimental investigation of failure of a DCM-wall considering softening behaviour

Siriwan Waichita[a], Pornkasem Jongpradist[a,*], Helmut F. Schweiger[b]

[a] Civil Engineering Department, Faculty of Engineering, King Mongkut's University of Technology Thonburi, Bangkok, Thailand
[b] Institute of Soil Mechanics, Foundation Engineering and Computational Geotechnics, Graz University of Technology, Graz, Austria

ARTICLE INFO

Keywords:
Failure
Deep cement mixing
Excavation
Softening
Ground spring

ABSTRACT

The failure behaviour of a deep cement mixing (DCM) wall due to excavation on one side of the wall was studied by means of finite element analysis and a simplified small-scale test. The DCM-wall was simulated using two constitutive models: an elastic perfectly plastic (Mohr-Coulomb) model and a concrete model, which considers tension and compression softening. Measured and simulated wall displacements were compared for different excavation stages. Structural failure of the wall with progressing excavation could be captured in the analysis using the concrete model. Furthermore, a reliable evaluation of the stress distribution and crack pattern in the wall could be obtained, which provides a step forward in the understanding of ultimate state conditions of DCM-walls. Overall the agreements between numerical simulation and laboratory experiment/field test can be considered very reasonable.

1. Introduction

Deep mixing techniques have been successfully employed in several applications of ground improvement during within the last decades. Deep cement mixing (DCM) is well-known since cement binder is frequently utilised. Most recent applications of DCM include its use for excavation support structures [e.g.,1–9], particularly in the urban environment. For intermediate excavation depths, an unbraced DCM-wall has been proven to be an attractive alternative to more conventional retaining structures such as sheet pile or diaphragm walls due to the low construction cost and short construction time. Attempts to understand the behaviour of DCM wall by numerical investigations based on case histories and monitoring data have been presented [2,5–7]. However, limited studies have considered the ultimate limit state of DCM walls, especially for unreinforced DCM walls. By means of a numerical parametric study Waichita et al. [2] has shown that the displacement pattern and the potential failure mode of these walls are primarily governed by the wall shape and the excavation depth. With the constraint of limited space in an urban environment, the wall becomes longer and slender with deeper embedment. Under these circumstances, the wall becomes prone to structural failure which can cause an immediate collapse and may constitute a significant risk for surrounding structures. Although failure mechanisms of rows and groups of laterally loaded DCM columns have been investigated and described in previous studies [10–12], very limited investigations for DCM wall have been reported up to date, particularly for unreinforced DCM-walls. This is mainly because a field test excavating in front of the wall up to failure of the DCM wall is risky. Although, a few test sections have been performed in previous studies, such as overlapped wall and columns [4] and grid type DCM walls [13], the excavation up to failure was done only in the latter case. Moreover, both are rather gravity-type walls, not the modern DCM walls whose geometry is more slender. For the latter case, a series of numerical analyses was performed in an attempt to observe on crack patterns, but no discussion on the failure mechanism is reported.

Numerical analyses studying the behaviour of DCM improved soils have been published, however, most of DCM modelling in the past employed a simple constitutive model, namely an elastic perfectly plastic Mohr–Coulomb failure criterion to describe the material behaviour of the DCM improved soils [5–9]. In order to study the DCM wall behaviour close to or at failure, the Mohr–Coulomb model becomes unreliable because most likely the development of cracks will have significant influence on the failure mechanism and therefore a constitutive model which is capable to allow for cracking and softening is important [13–15].

For cement treated soils, advanced constitutive models have been developed on the basis of critical state soil mechanics. Horpibulsuk et al. [16] and Suebsuk et al. [17] utilised the bonded soil concept first

* Corresponding author at: Civil Engineering Department, Faculty of Engineering, King Mongkut's University of Technology Thonburi, 126 Pracha Uthit, Bang Mod, Thung Khru, Bangkok 10140, Thailand.
E-mail address: pornkasem.jon@kmutt.ac.th (P. Jongpradist).

https://doi.org/10.1016/j.compgeo.2019.103380
Received 29 April 2019; Received in revised form 15 October 2019; Accepted 1 December 2019

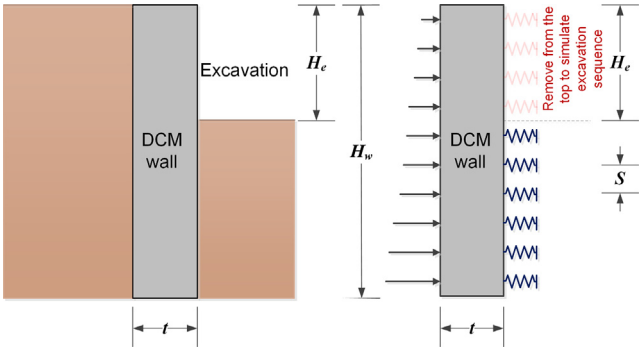

Fig. 1. Schematic diagrams of (a) an excavation and (b) ground spring concept in an excavation.

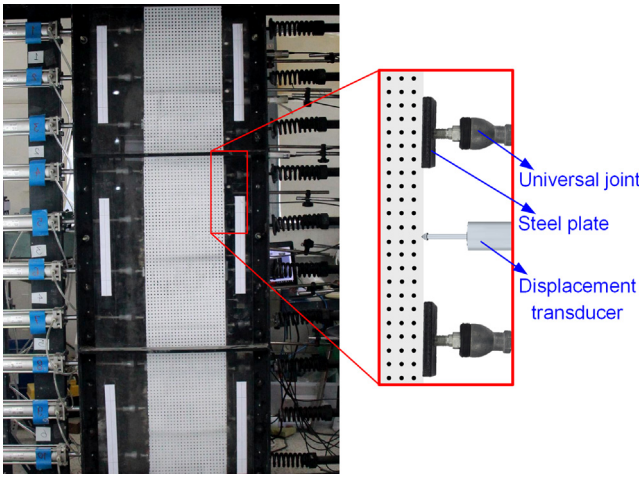

Fig. 2. Small-scale test of an excavation with ground spring concept.

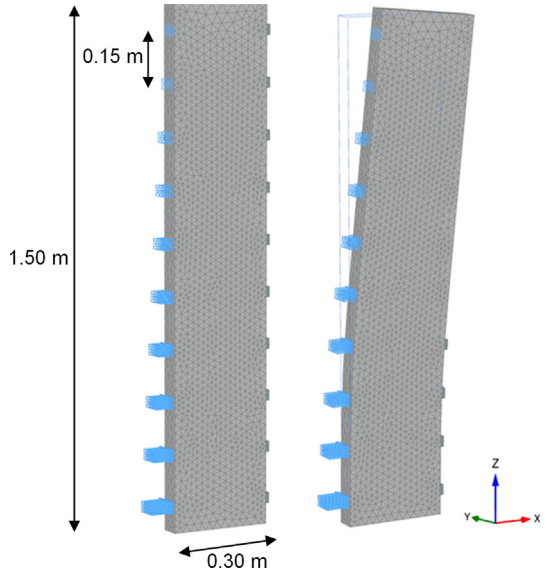

Fig. 3. Model geometry of DCM wall excavation with ground spring concept and deformed mesh.

published in [18] in a constitutive model for cemented clay by means of extension and modification of the Structured Cam Clay theoretical framework presented in [19]. The Clay and Sand Model (CASM) developed by Yu [20] was also employed in the development of a bonded CASM, proposed by Arroyo et al. [21]. Post-yield strain-softening feature was later introduced in the constitutive model of cement treated

Table 1
The variation of pressure applied on wall active side.

No.	Depth from the wall top (m)	Applied pressure (kPa)
1	0.075	5.376
2	0.225	16.127
3	0.375	26.877
4	0.525	37.626
5	0.675	48.376
6	0.825	59.125
7	0.975	69.875
8	1.125	80.624
9	1.275	91.373
10	1.425	102.123

Table 2
The Mohr-Coulomb model parameters for DCM wall in small-scale test.

Description	Parameter	unit	value
Young's modulus	E_{28}	kPa	50,000
Poisson's ratio	ν	–	0.25
Effective cohesion	c'	kPa	108.8
Friction angle	ϕ	°	30
Dilatancy angle	ψ	°	0

Table 3
The concrete model parameters for DCM wall in small-scale test.

Description	Parameter	unit	value
Young's modulus	E_{28}	kPa	50,000
Poisson's ratio	ν	–	0.25
Uniaxial compressive strength	$f_{c,28}$	kPa	377
Uniaxial tensile strength	$f_{t,28}$	kPa	40
Maximum friction angle	ϕ_{max}	°	30
Normalised initially mobilised strength	f_{c0n}	–	0.7
Normalised failure strength (compression)	f_{cfn}	–	0.75
Normalised residual strength (compression)	f_{cun}	–	0.35
Uniaxial plastic failure strain	ε_{cp}^{p}	–	−0.003
Compressive fracture energy	$G_{c,28}$	kN/m	0.075
Ratio of residual to peak tensile strength	f_{tun}	–	0
Tensile fracture energy	$G_{t,28}$	kN/m	0.01
Safety factor for compressive strength	γ_{fc}	–	1
Safety factor for tensile strength	γ_{ft}	–	1

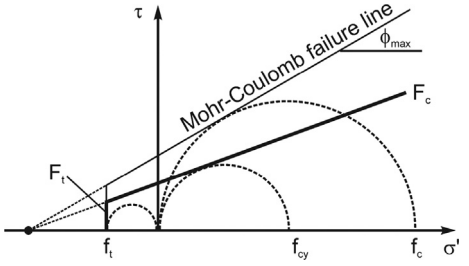

Fig. 4. Yield surfaces and failure envelope for Concrete model [24].

soil by Wijerathna and Liyanapathirana [14]. In [22] a tension cut-off criterion together with a Mohr–Coulomb failure criterion including viscous effects has been presented for cemented materials.

On the other hand, the fracture energy concept may be utilised when developing constitutive models for concrete-like materials such as shotcrete, and deep mixing [11,13,15,23,24]. The concrete model proposed by Schädlich and Schweiger [24] was originally developed for applications in tunnelling where the time dependent behaviour of shotcrete has to be taken into account. However, the model has also been used for modelling the behaviour of jet grout slabs [15,23]. One of

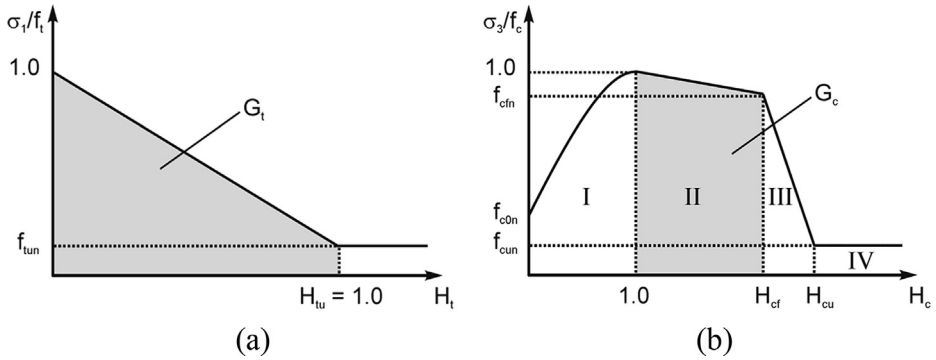

Fig. 5. Normalised stress-strain curve in (a) tension and (b) compression [24].

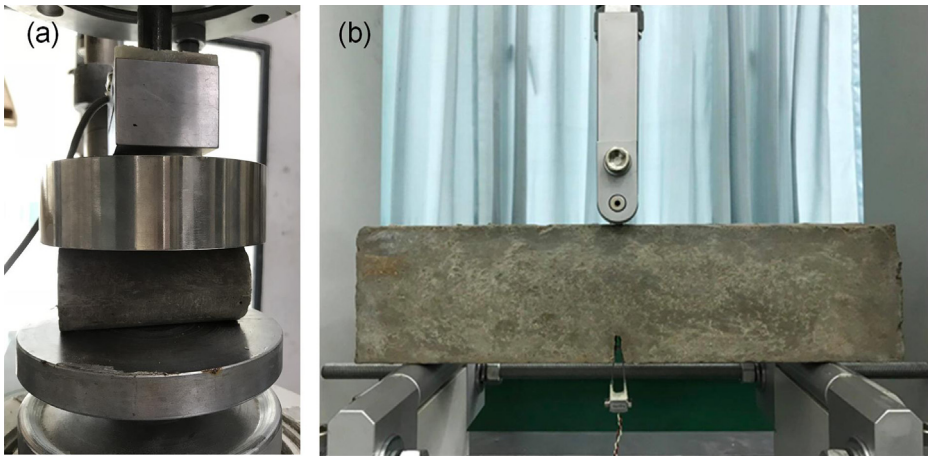

Fig. 6. (a) Split tensile test and (b) Three-point flexural test on notched beam.

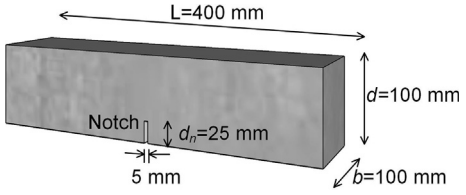

Fig. 7. Notched beam dimensions.

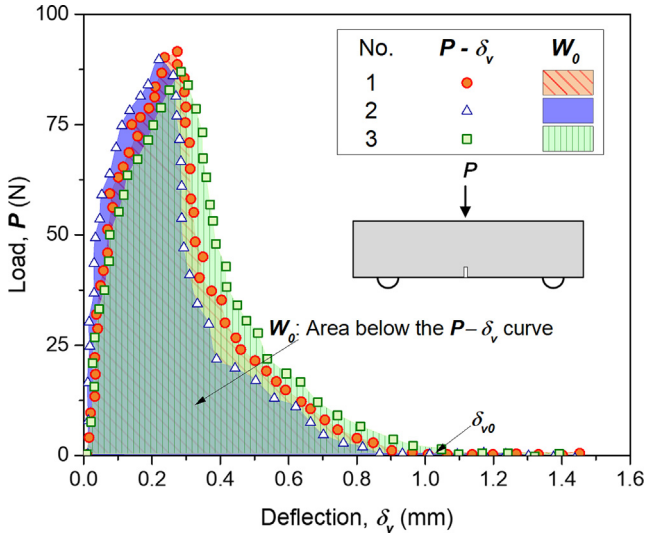

Fig. 8. Load-deflection curves of three-point flexural test on notched beams.

the key features of the model is the capability of accounting for strain softening in tension which is an important feature for the problem discussed in the following. It is noted that a similar concept has been used in developing the concrete damaged plasticity (CDP) model originally developed by Lubliner et al. [25] and modified by Lee and Fenves [26]. The CDP model has been used to investigate the failure mechanism of a cemented soil pile group and row under controlled lateral load in a large shear box. The main differences between the two models are the yield surface and the ability to take into account creep and shrinkage effects.

In this paper, results from a small-scale test of a DCM-wall are presented, where failure is initiated by excavation on one side of the wall. The wall response during the excavation process is monitored. Numerical modelling of the test is also performed employing two different constitutive models for the wall, namely the well-known elastic perfectly plastic Mohr-coulomb failure criterion (considering a tension cut-off) and the concrete model described in [24]. The study aims to gain a better insight into the pre-failure behaviour and the failure mechanism of the DCM-wall. The differences in results for the two constitutive models are highlighted and it is shown that only the more advanced concrete model is capable of capturing the crack development and failure mechanism in a DCM wall as observed in the small-scale test.

2. Small-scale test of DCM-wall

In order to investigate the mechanical behaviour and failure mechanism of a DCM-wall due to excavation, a 1-g physical model of an DCM-wall has been prepared. Since soil with low strength and stiffness cannot be adequately represented by a scaling law in 1-g conditions [27], a novel testing procedure has been designed. On the passive side

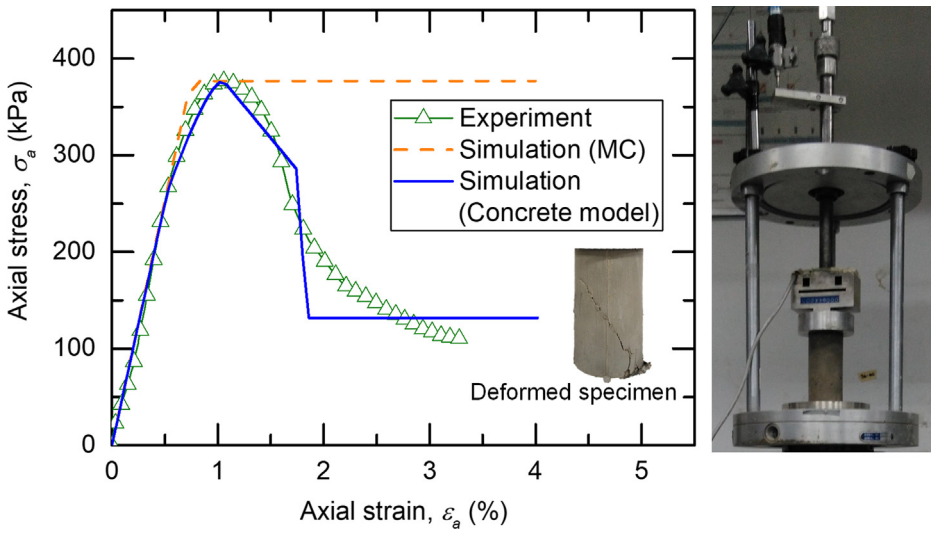

Fig. 9. Axial stress–strain result of uniaxial compression test on collected sample together with the simulation results of the models used in the numerical analyses.

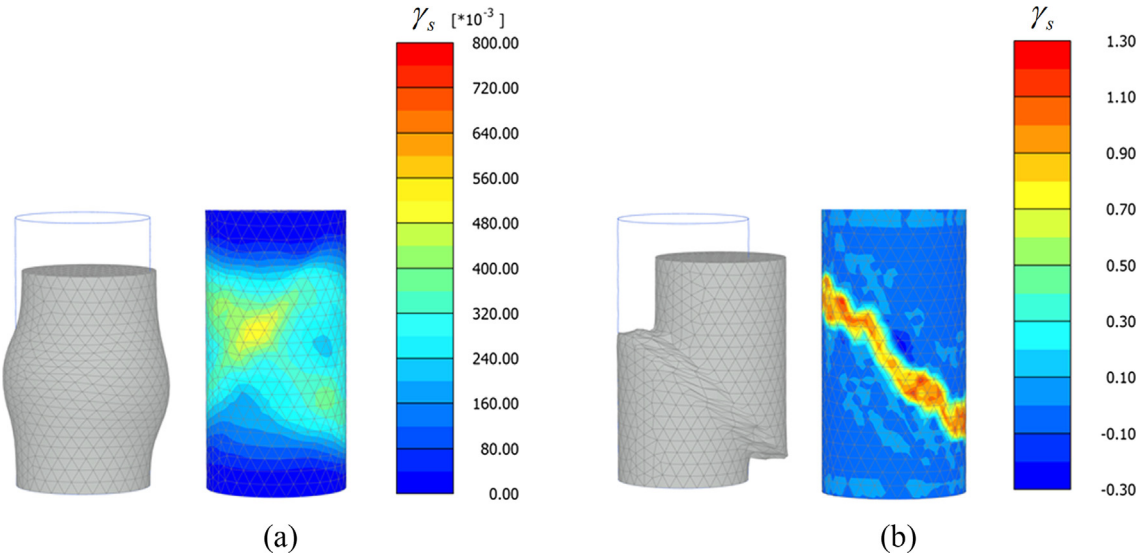

Fig. 10. Deformed mesh and deviatoric shear strain distribution of uniaxial compression test simulation using (a) Mohr-Coulomb model and (b) concrete model.

the wall is supported by a row of springs whereas on the active side the earth pressure is applied mechanically via loading plates, as indicated in Fig. 1. The step-by-step excavation is simulated by the removal of individual springs starting from the top level. Both the loading plates and springs are arranged with a certain spacing, S (15 cm in this study), along the wall depth H_w of 150 cm. The equipment consists of a steel spring set, air cylinders equipped with a pneumatic loading system, an acrylic mould, roller-based support and a steel testing frame as shown in Fig. 2. In the experiment, a DCM-wall with a rectangular cross section ($H_w \times t$ of 150 cm × 30 cm) and a width of 6 cm is casted in the mould and tested. To ensure that the wall structural failure will occur, a wall thickness of 30 cm is chosen. The out-of-plane deformation is constrained by acrylic plates. More detailed information on the test setup will be presented in a companion paper.

2.1. Specimen preparation

The DCM-wall with the dimension of 30 × 150 × 6 cm was made up from a clay-cement mixture with high workability. Clay collected from a site was remoulded with water and mixed with Portland cement following the pre-determined mix design. In this study, the unconfined compressive strength of the DCM-wall was about 380 kPa, which could be achieved from the mixing ratio of 200% water content and 40% cement content by weight of dry soil. The mould was assembled in the testing frame and lubricated with grease. The clay-cement mixture was poured into the mould, and the top of specimen with melt paraffin covered during the curing period of 28 days. Although it is acknowledged that curing stress has an influence on the strength and stiffness properties of the cemented clay [28,29] it has not been taken into account in this study.

2.2. Experimental procedures

At the end of curing, paraffin on the top layer was removed. Consequently, the loading plates used to transfer the load of both springs and air cylinders were adjusted and attached to the side surfaces of the specimen. At the initial stage of the experiment, lateral earth pressure is applied via air cylinders on the loading plates attached to the active side. The pressures from the air cylinders vary with wall depth. Throughout the experiment the maximum mobilised earth pressure did not exceed the maximum pressure the springs could carry in the elastic range. Displacement transducers were installed along the

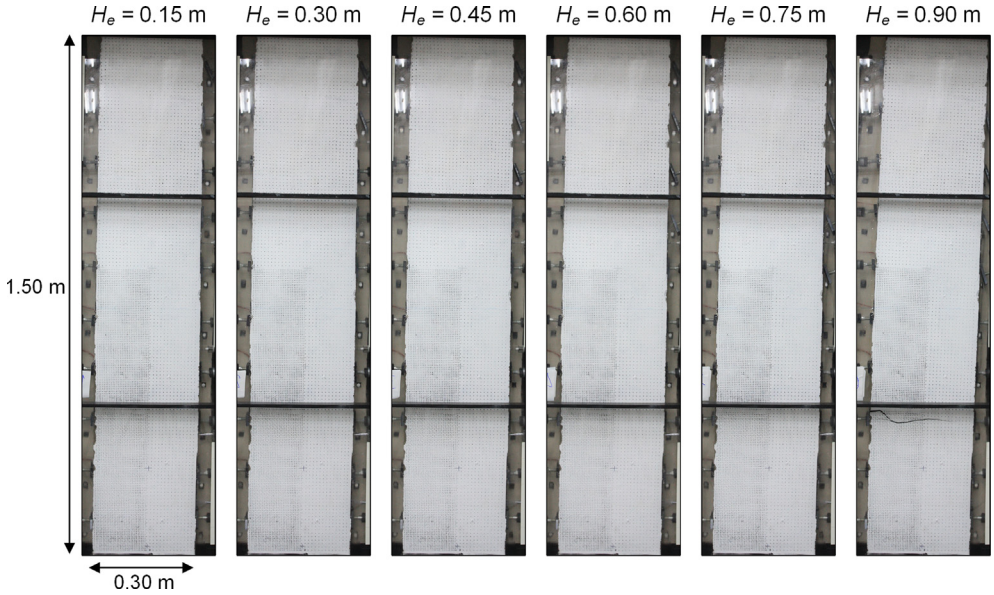

Fig. 11. Evolution of DCM wall excavations with ground spring concept (in experiment).

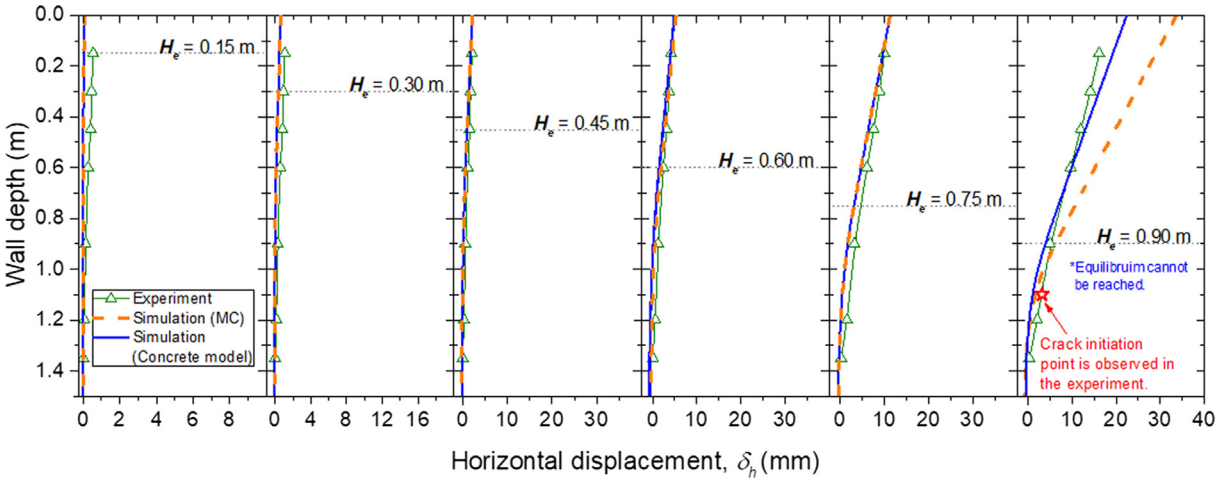

Fig. 12. Evolution of horizontal displacement in DCM wall excavation: experiment and simulation results.

wall depth and logged automatically during the experiment. An excavation process was simulated by removing supporting springs one by one, keeping the load on the wall constant. Simulation of the excavation was started from the top spring and continued until significant cracking has been observed in the DCM-wall specimen. It is noted that the test program was designed to apply constant loads, since the precision of the regulator is not sufficient to adjust load changes during the test. For safety concerns the test was terminated after the crack appeared. Photographs of the experiment are taken in each stage of excavation.

3. Numerical analysis

3.1. Model geometry and sequence

Fig. 3 shows the geometry of the problem and the finite element mesh. The finite element code Plaxis3D was used for this study. The springs at the excavation side were simulated by so-called anchor elements (line elements) which were attached to load transfer plates (solid elements). The springs have constant stiffness of 73 kN/m, calculated from horizontal modulus subgrade reaction [30]. The load is applied via surface pressure according to the test setup (Table 1). The boundary conditions are as follows: the bottom boundary is fully restrained in x,y,z-directions and the out-of-loading-plane is restrained horizontally.

3.2. Constitutive models

Two constitutive models are employed to describe the mechanical behaviour of the cement mixed material in order to investigate the wall response and failure mechanism during excavation. The first model used is the elastic perfectly plastic Mohr-coulomb failure criterion considering a tension cut-off (MC model) and the parameters are listed in the Table 2. The effective cohesion (c') was calculated from the Mohr-Coulomb failure envelope, assuming a friction angle of 30° [31,32] and a uniaxial compressive strength of 377 kPa. The Poisson's ratio for deep cement mixing is in the range of 0.15–0.33 [8,11,32–34] and a value of 0.25 was used in this study. A tensile strength of 40 kPa was assigned as tension cut off in the MC model. The second constitutive model is a concrete model, developed by Schädlich and Schweiger [24], which is implemented in the finite element code Plaxis [35]. Although this model can account for time dependent strength and stiffness, creep and shrinkage, these features were not utilised in this study due to the fact that loading is applied only after curing of the DCM-wall for 28 days. Table 3 shows the complete list of the model input parameters with its descriptions. Although the maximum friction

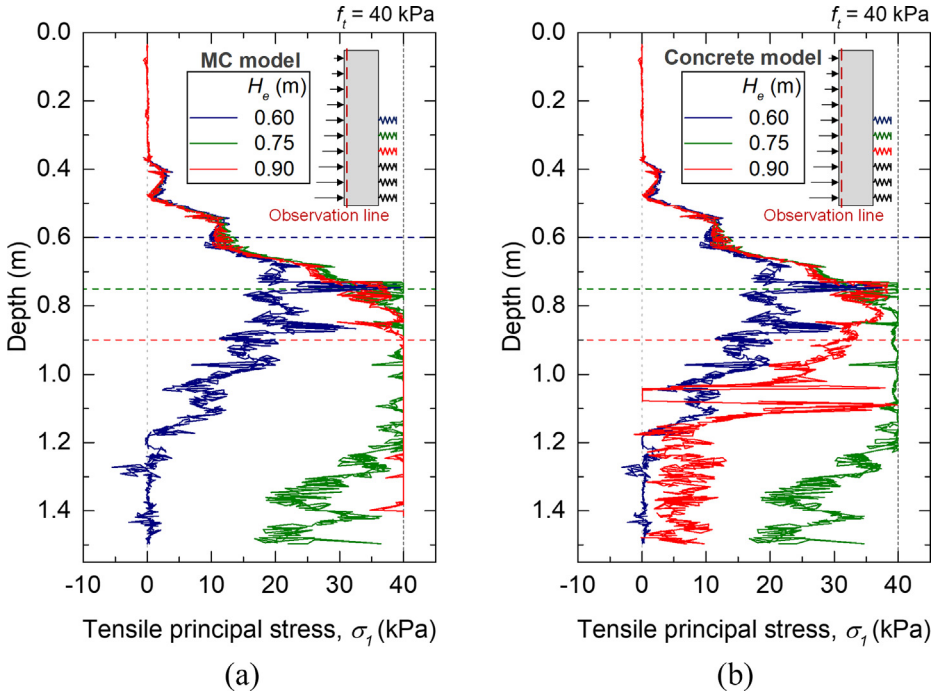

Fig. 13. Tensile principal stress in retained side at 0.60, 0.75, and 0.90 m excavation depths, simulated with (a) Elastic perfectly plastic model with Mohr-Coulomb failure criteria and (b) concrete model.

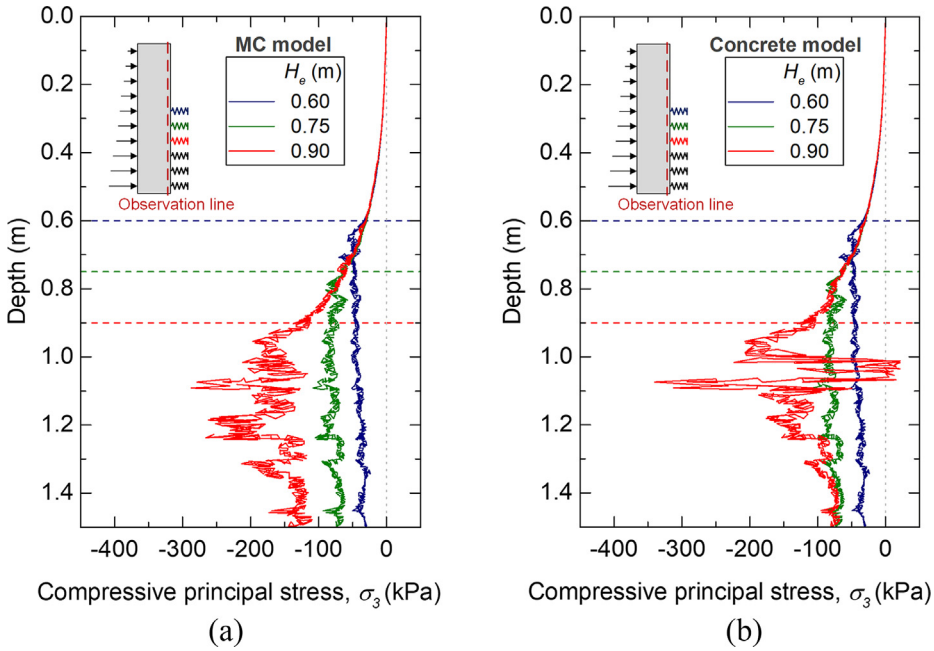

Fig. 14. Compressive principal stress in excavation side at 0.60, 0.75, and 0.90 m excavation depths, simulated with (a) Elastic perfectly plastic model with Mohr-Coulomb failure criteria and (b) concrete model.

angle and the Poisson's ratio were adopted from literature (same as for the MC model), the remaining input parameters were calibrated using the unconfined compression test results of the collected specimens. The main features of the concrete model are briefly explained as follows.

The Mohr-coulomb yield surface (F_c) and Rankine yield surface (F_t) are employed for deviatoric and tensile loading respectively as shown in Fig. 4. Irreversible plastic strains are calculated based on strain hardening and softening elasto-plasticity. Compression hardening and softening behaviour as proposed by Schütz et al. [36] is adopted in this model. Fig. 5a illustrates a normalised stress-strain curve in tension. The material behaves as linear elastic when tensile stresses are below the tensile strength (f_t). Once the f_t is reached, then linear strain softening starts (Eq. (1)), indicated by a normalised hardening and softening parameter in tension ($H_t = \varepsilon_1^p/\varepsilon_{tu}^p$) is larger than zero, where ε_1^p is major (tensile) principal plastic strain and ε_{tu}^p is plastic ultimate strain in uniaxial tension derived from tensile fracture energy (G_t). Consequently, there is no further softening, when the residual tensile strength is reached ($f_{tu} = f_{tun} \cdot f_t$) indicated by H_t-values larger than 1.

$$f_{ty} = f_t \cdot (1 + (f_{tun} - 1) \cdot H_t) \quad (1)$$

The normalised stress-strain curve in compression is shown in

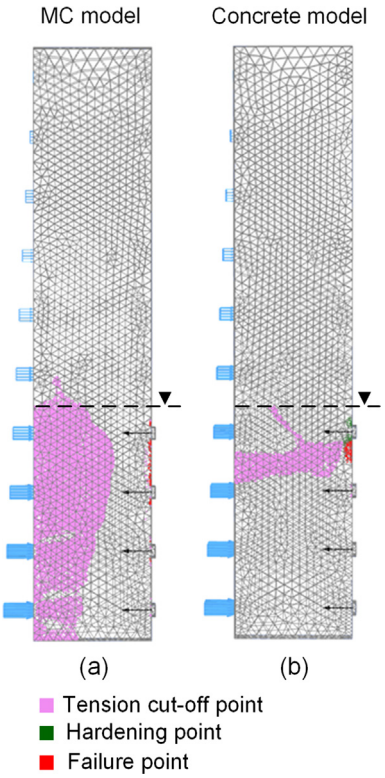

Fig. 15. Plastic points at 0.90 m excavation depths, simulated with (a) Elastic perfectly plastic model with Mohr-Coulomb failure criteria and (b) concrete model.

Fig. 5b, which is composed of four parts. Compression strain hardening follows a quadratic function (Eq. (2)) up to peak strength (f_c) in part I followed by a bi-linear softening in part II and III (Eqs. (3) and (4)). A normalised hardening and softening parameter in compression ($H_c = \varepsilon_3^p/\varepsilon_{cp}^p$) is utilised, while ε_3^p is the minor (compressive) principal strain and ε_{cp}^p is plastic peak strain in uniaxial compression. For additional information regarding the concrete model the reader is referred to Schädlich and Schweiger [24].

$$f_{cy,I} = f_c \cdot (f_{c0n} + (1 - f_{c0n}) \cdot (2H_c - H_c^2)) \tag{2}$$

$$f_{cy,II} = f_c \cdot \left(1 + (f_{cn} - 1) \cdot \left(\frac{H_c - 1}{H_{cf} - 1}\right)\right) \tag{3}$$

$$f_{cy,III} = f_c \cdot \left(f_{cfn} + (f_{cun} - f_{cfn}) \cdot \left(\frac{H_c - H_{cf}}{H_{cu} - H_{cf}}\right)\right) \tag{4}$$

4. Tensile and compressive parameters determination and calibration

Cylindrical specimens of cement mixed clay were collected, cured for 28 days and subjected to split tensile tests (Fig. 6a). Tensile strengths were in the range of 38–42 kPa with an average of 40 kPa. The tensile strength obtained from split tensile tests can be correlated with an unconfined compressive strength as $f_{t,28} = 0.11 f_{c,28}$, which has also been found in the study of cement-treated clay in Singapore [13].

The tensile strength obtained from the split tensile test was used instead of that of a uniaxial tension test in the simulation. Notched beams of cement mixed clay with dimension of 100 × 100 × 400 mm ($b \times d \times L$) had been prepared (Fig. 7). The notch is 5 mm wide with a depth of 25 mm created by plywood inserting when the beams were casted. The size of the beam and notch were not varied in this study since no significant difference of tensile fracture energy was found in the variation of sample size and notch width in three-point flexural test on cement-treated Singapore marine clay [13].

Three-point flexural tests had been performed on the notched beams of cement mixed clay (Fig. 6b) and load-deflection curves are shown in Fig. 8. The maximum load carried by the beam is approximately 90 N.

The area below the load-deflection curve (W_0) and deflection at $P = 0$, (δ_{v0}) are used to calculate the tensile fracture energy according to the RILEM method [37] as follows

$$G_f = \frac{W_0 + mg\delta_{v0}}{A_{lig}} \tag{5}$$

where the area of ligament (A_{lig}) or fracture area is defined as the projection of the fracture zone on beam perpendicular plane, $A_{lig} = b(d - d_n)$. The tensile fracture energy is in the range of 9.6–10.7 N/m and an average value of 10 N/m (0.01 kN/m) has been in this study.

A uniaxial compression test had been conducted on the cylindrical specimens.

End-plates are not fully lubricated, i.e. there is some friction which triggers the formation of rupture bands when using the concrete model

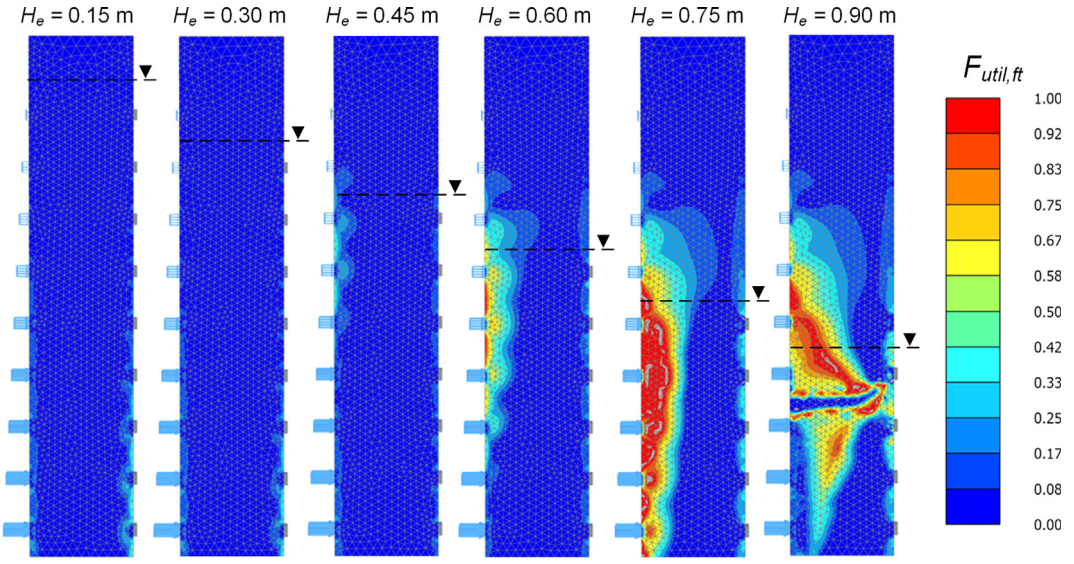

Fig. 16. Evolution of concrete utilisation factor in tension.

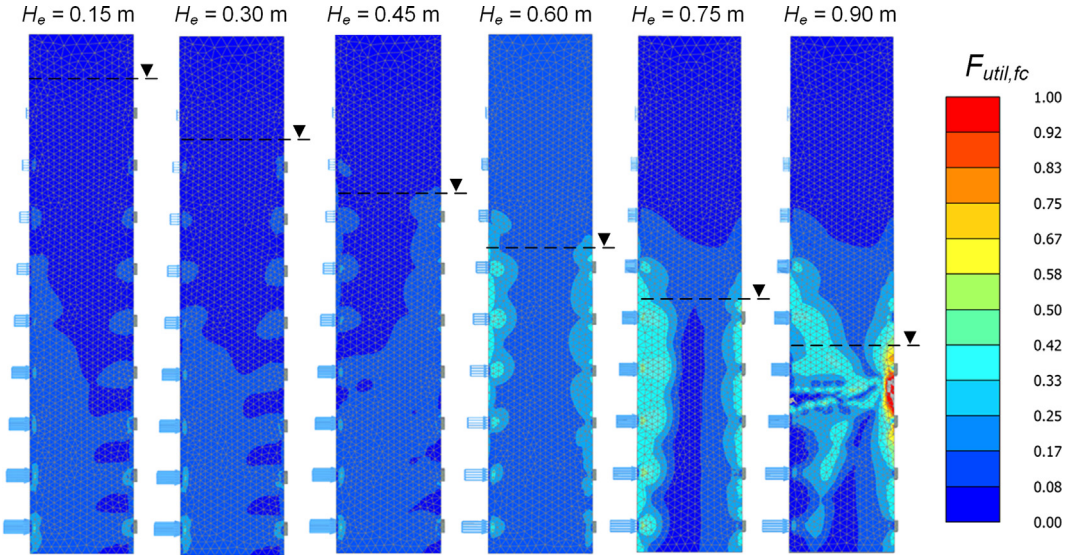

Fig. 17. Evolution of concrete utilisation factor in compression.

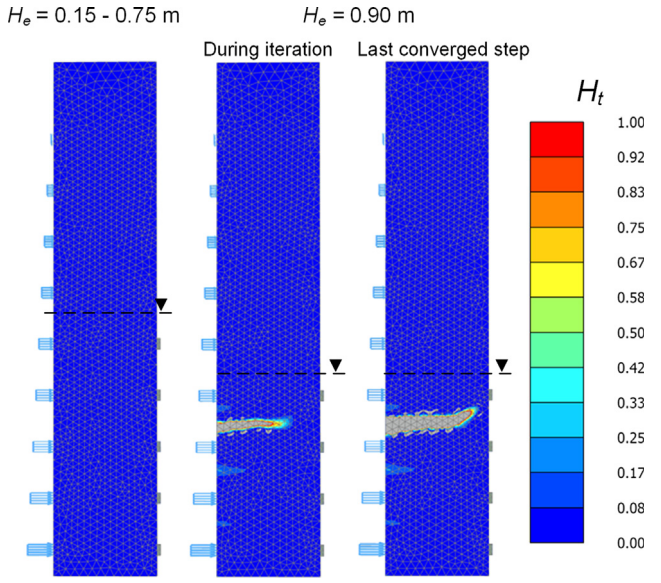

Fig. 18. Normalised tensile softening parameter development.

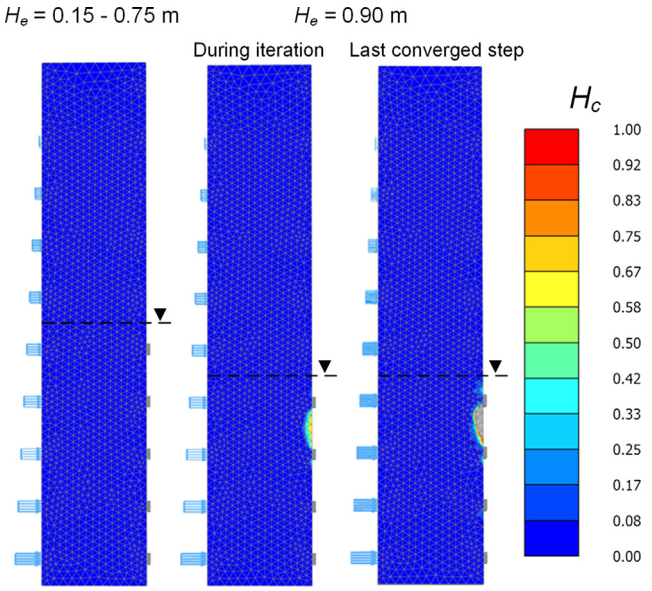

Fig. 19. Normalised compressive hardening and softening parameter development.

(see Fig. 10). The compressive strength ($f_{c,28}$) ranged between 372 and 383 kPa and a representative value of 377 kPa has been used in this study. To calibrate the parameters used in the analysis, the uniaxial compression test is simulated numerically with both constitutive models (MC and concrete model). Fig. 9 illustrates the axial stress-strain relationship from the test and simulation. It should be mentioned that the experiment had to be modelled as a boundary value problem because post-peak behaviour involving softening cannot be modelled by a so-called single element test due to the inhomogeneity of stresses across the sample. It also important to note the real dimensions of the test have to be used in the finite element model because there is a scale effect in these problems. Of course the MC-model cannot model this behaviour which follows from Fig. 6. However it is clearly shown that the concrete model is capable of reproducing post-peak behaviour with a high degree of accuracy.

Looking at the results of 2% axial strain the differences between the two models are obvious and are illustrated in Fig. 10a and b where the deformed mesh and deviatoric shear strain distributions are compared. A barrel like deformed shape is obtained for the MC model, whereas a clear strain localisation is evident for the concrete model, reflecting well the observed behaviour in the test (see insert in Fig. 9).

5. Results and discussion

During the experiment photographs were taken to capture the evolution of wall displacement and failure as shown in Fig. 11. The experimental and numerical analysis results are discussed in the following in order to highlight the differences in results obtained for the Mohr-Coulomb model and the concrete model. The numerical analysis provides additional insight into stresses in the wall, crack initiation and failure mechanism.

5.1. Evolution of wall displacement

The measured horizontal wall displacements along the wall depth are presented in Fig. 12 for progressing excavation stages, simulated by withdrawal of corresponding springs. In the figure, the calculated wall displacements obtained from numerical analyses using the MC and concrete models are also shown. It is seen that, from H_e = 0.15–0.75 m

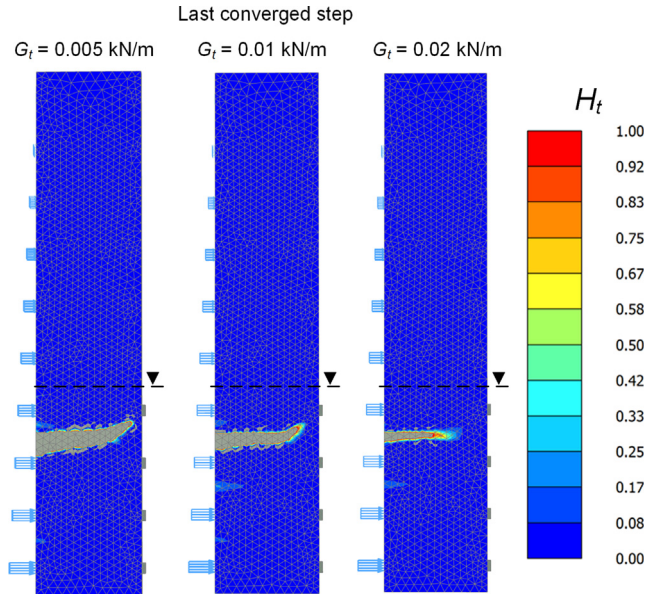

Fig. 20. Influence of tensile fracture energy on localisation of normalised tensile softening parameter.

Table 4
The hardening soil model parameters for soil layers in field test.

Parameter	unit	Weathered crust	Soft to medium stiff clay	Stiff clay	Very stiff clay
c'	kPa	12	5	25	40
ϕ	°	27	22	23	28
E_{50}^{ref}	kPa	17,000	12,000	25,000	40,000
E_{oed}^{ref}	kPa	17,000	12,000	25,000	40,000
E_{ur}^{ref}	kPa	60,000	40,000	75,000	120,000
p_{ref}	kPa	100	100	100	100

Remarks: $m = 1$, $R_f = 0.9$ and $\nu_{ur} = 0.2$ [30].

of excavation, the calculated displacements from both models show a good agreement with measurements although a slight underestimation can be observed. At the final level ($H_e = 0.90$ m) in which the wall failed, significantly larger displacements were observed from the MC model, whereas the concrete model yielded a much better agreement with measured wall displacements.

Thus, the results of numerical analyses using the concrete model generally showed good agreement with the measured wall displacements from the beginning of the test up to failure. For the final excavation level equilibrium could not be established in the numerical model which is consistent with the failure exhibited at this stage in the experiment. On contrary, the analysis employing MC model can still be continued although the strength of the material is reached in some parts of the wall (see next section). In terms of safety, it can be concluded that the utilisation of MC model in the numerical analysis may lead to an overestimation of the DCM-wall structural stability.

5.2. Stress distribution

The distribution of tensile and compressive principal stresses along the wall depth of both retained and excavation sides are illustrated in Figs. 13 and 14, respectively. As expected, stresses increase as the excavation progresses. Since the main interest in this study is the mechanical behaviour of the wall at the failure state, only the results from the $H_e = 0.60$ m to the final excavation ($H_e = 0.90$ m) are shown in these figures. Fig. 13a and b depicts the distribution of the tensile principal stress (σ_1) along the retained side obtained from the analyses with the MC and concrete models. For H_e of 0.60–0.75 m, similar distributions of σ_1 from both models can be seen. At a wall height of 0.80–1.20 m σ_1 reaches the tensile strength of the wall material ($f_y = 40$ kPa). At H_e of 0.90 m, the stresses obtained from the analysis with the MC model still keep increasing with excavation depth, resulting that σ_1 reaches the tensile strength for the wider range of the wall height (0.80–1.40 m). In contrast, from H_e of 0.75–0.90 m, a drastic decrease of σ_1 at the wall height below 0.80 m was revealed from the analysis with the concrete model. Specifically, at the wall depth of 1.05–1.10 m, zero tensile principal stress is observed and this indicates that the wall is fully cracked in this zone. Significantly different stress distributions obtained from the concrete and MC model were also found in analyses of anchored jet grout slabs constructed below the base of an excavation as uplift resistance [23].

In a similar manner, the compressive principal stress (σ_3) is shown along the excavation side in Fig. 14a and b for the MC and concrete models, respectively. The σ_3 distribution of both models are similar for the H_e of 0.60–0.75 m. With further excavation, the σ_3 distribution was more oscillatory than those in previous excavation levels. The maximum σ_3 was found at the depth of 1.10 m for both models. For the MC model (Fig. 14a) it is seen that σ_3 at H_e of 0.90 m is generally larger than those of H_e of 0.60–0.75 m, particularly below the excavation level. On the other hand, σ_3 obtained from the concrete model (Fig. 14b) decreased to zero in wall depth of 1.00–1.10 m. Below the depth of 1.10 m, the σ_3 distribution pattern of both models are resembled, however, the magnitude of σ_3 from the analysis with the concrete model is smaller.

5.3. Plastic points

According to failure and tension cut-off criteria assigned in the models, states of stress with respect to each criterion can be shown using plastic points. The plastic points denote either a tension cut-off point, a failure point, or a hardening point. The emphasis of this section is placed on the tension cut-off point, which indicates the tensile strength is reached. In Fig. 15a and b, plastic points generated from the analyses with the two models at final excavation level are presented and compared.

In Fig. 15a for analysis with the MC model, the widespread tension cut-off points can be seen in the wall on the excavation side below the final excavation level. This corresponds to the zone where the tensile strength is reached as shown in Fig. 13a. Some failure points were also observed below the excavation level, at the excavation side of the wall.

In contrast, the tension cut-off points developed as a "crack indicator" at the depth of approximately 1.05 m for the analysis with the concrete model as depicted in Fig. 15b. The band of tension cut-off points propagated from the retained side to the excavation side. In addition, some failure and hardening points also occurred at the excavation side just below the excavation level.

Significant difference in development of tension cut-off points from the numerical analyses with MC and concrete models are clearly seen. Comparing the crack pattern observed after the completion of the test as shown in Fig. 11, it is clear that more reasonable results can be obtained from the analysis employing the concrete model.

5.4. Utilisation factor in compression and tension

The concrete model also provides the feature of plotting tension and compression utilisation (Eqs. (6) and (7)), which can trace the current stress of the element in a ratio of the strength or current yield stress.

$$F_{util,ft} = \frac{\sigma_1}{f_t/\gamma_{ft}} \tag{6}$$

$$F_{util,fc} = \frac{1}{f_c/\gamma_{fc}} \cdot \left[\sigma_1 \cdot \frac{1 + \sin\phi_{max}}{1 - \sin\phi_{max}} - \sigma_3 \right] \tag{7}$$

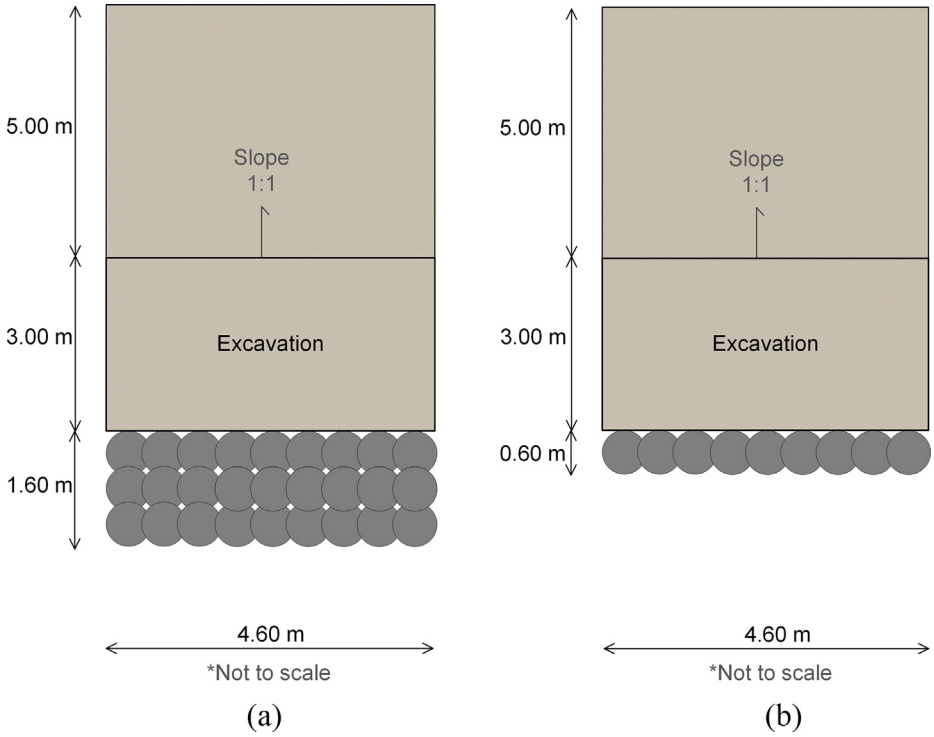

Fig. 21. Top view of DCM wall excavations: (a) 1.6 m thick, (b) 0.6 m thick.

Table 5
The concrete model parameters for DCM wall in field test.

Description	Parameter	unit	value
Young's modulus	E_{28}	kPa	147,000
Poisson's ratio	ν	–	0.25
Uniaxial compressive strength	$f_{c,28}$	kPa	1500
Uniaxial tensile strength	$f_{t,28}$	kPa	150
Maximum friction angle	$\phi_{\max}$	°	30
Normalised initially mobilised strength	f_{c0n}	–	0.25
Normalised failure strength (compression)	f_{cfn}	–	0.75
Normalised residual strength (compression)	f_{cun}	–	0.35
Uniaxial plastic failure strain	ε_{cp}^{p}	–	−0.002
Compressive fracture energy	$G_{c,28}$	kN/m	0.15
Ratio of residual to peak tensile strength	f_{tun}	–	0
Tensile fracture energy	$G_{t,28}$	kN/m	0.012
Safety factor for compressive strength	γ_{fc}	–	1
Safety factor for tensile strength	γ_{ft}	–	1

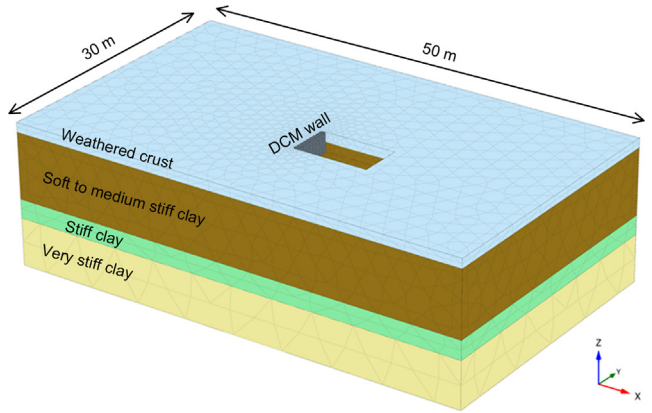

Fig. 22. Example of mesh model of DCM wall excavation.

Fig. 16 shows shadings of the utilisation factor in tension ($F_{util,ft}$) developed in each excavation stage. The concentration of $F_{util,ft}$ at the retained side started from H_e of 0.45 m but the magnitude is still lower than 1. Some elements in the wall at the retained side also started reaching the tensile strength ($F_{util,ft} = 1$) at H_e of 0.60 m. Then, a full mobilisation of tensile strength rapidly expanded downward at H_e of 0.75 m. Finally, the $F_{util,ft}$ propagated toward to the excavation side and zero $F_{util,ft}$ is found in the localised band at the wall depth where the tensile principal stress is zero due to cracking.

The evolution of the utilisation factor in compression ($F_{util,fc}$) is shown in Fig. 17. The concentrations of $F_{util,fc}$ were found on both the retained and excavation sides since the stage of $H_e = 0.60$ m. The $F_{util,fc}$ distribution expanded in the similar way as that of the $F_{util,ft}$ up to H_e of 0.75 m. Note that the magnitudes of $F_{util,fc}$ were in range from 0.30 to 0.60 m implying that the compressive strength was not fully mobilised in these stages. At the final excavation depth, the maximum $F_{util,fc}$ localised at the depth of approximately 1.05 m on the excavation side. The full mobilisation of $F_{util,fc}$ was also found in this depth but on the excavation side.

5.5. Crack initiation

The occurrence of tension and compression softening can also be visualized by normalised state variables denoted as (H_t) for tension and (H_c) for compression.

Fig. 18 shows the development of the normalised tensile softening parameter (H_t). No tensile softening takes placed until $H_e = 0.75$ m, which is in accordance with the development of $F_{util,ft}$ in the previous section. Finally, an initiation and rapid propagation of H_t were found during the final excavation level ($H_e = 0.90$ m). A value of H_t between 0 and 1 indicates strain softening behaviour whereas a value larger 1 means that the crack is fully developed and tensile stresses are reduced to zero. This corresponds to the zero tensile principal stress found at the depth of 1.10 m as presented in Section 5.2. In addition, the position of the crack, illustrated by the H_t, in the final excavation level also agrees well with the crack pattern observed in the experiment (Fig. 11). The somewhat inclined crack pattern was also observed in the simulation

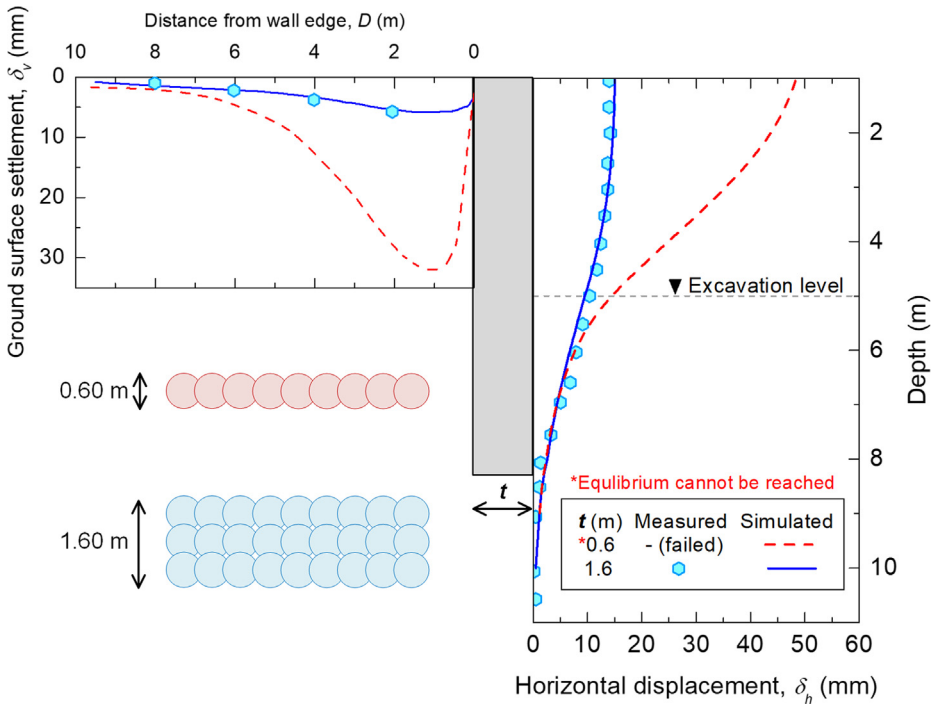

Fig. 23. Simulated and measured ground surface settlement and horizontal displacement profiles of DCM walls.

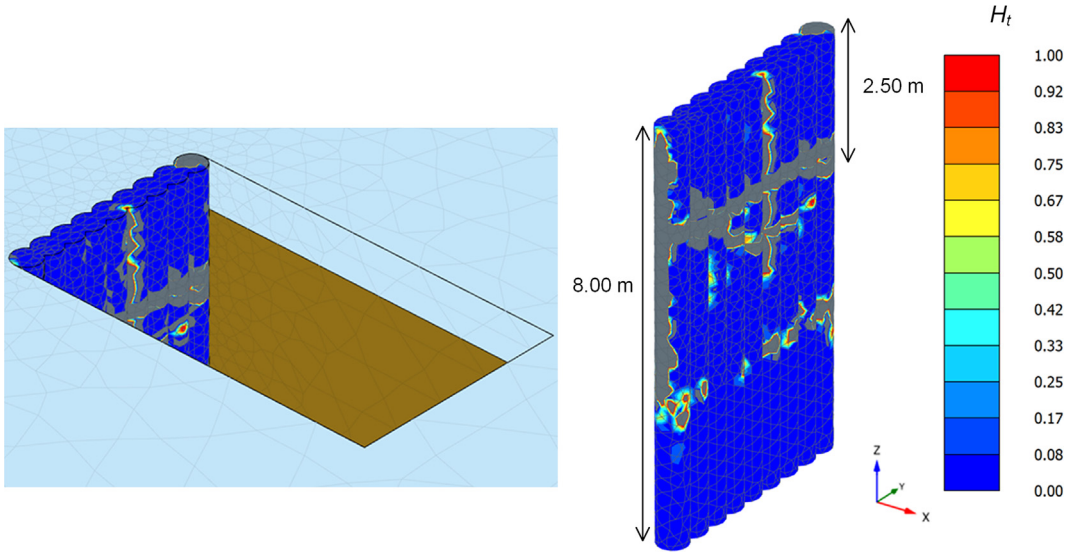

Fig. 24. Normalised tensile softening parameter of the 0.6 m thick DCM wall at 5 m-excavation.

and experimental result of laterally loaded lime-cement columns [11]. Stress states in compression, were also investigated. First compression hardening ($0 < H_c < 1$) is observed at the excavation side at the depth where tension softening starts at the opposite side eventually compression softening is initiated but this zone is of very limited extent (Fig. 19).

The development of H_t and H_c can be evaluated during the iteration steps resolving the last excavation level. At first tension softening reaches residual level, then compression hardening takes place followed by compression softening. Thus the normalised hardening and softening parameters can be employed to investigate the development of the failure mechanisms in more detail.

6. Sensitivity analysis on tensile parameters

The tensile fracture energy (G_t) is found in the range of 0.005–0.02 kN/m for cemented soil which is adopted in the parameter variation [11,13,23,38]. The variation of G_t keeping the tensile strength constant (as the base case, $f_{t,28}$ = 40 kPa) shows that the wall also failed at the final excavation, which means that the influence is not significant and could be captured only by a refinement of the excavation steps.

In addition, the effect of tensile strength on the excavation capability has been investigated. The tensile strength of DCM ($f_{t,28}$) is varied between 8 and 15 % of the unconfined compressive strength ($f_{c,28}$) [11,23,39,40]. This $f_{t,28}$ variation is performed with reference to $f_{c,28}$ of 377 kPa. Again, within the scope of this study no major deviations from the base case can be observed. It can be concluded that the overall failure mechanism is not significantly influenced by these two parameters, given the relatively small range of plausible values.

Fig. 25. Photographs of failure of the 0.6 m thick DCM wall at 5 m-excavation; (a) Side view, (b) Front view.

However, the crack pattern changes to some extent with the tensile fracture energy (Fig. 20).

7. Case study of failure in DCM wall

To illustrate the practical usage of the concrete model, simulation of DCM wall supported excavation was examined by means of a field test [41] located in an area which mainly consists of clayey soils. A 1 m thick weathered crust was present above 7 m soft to medium clay layer and stiff and hard clay layers were found at −10 and −13 m, respectively. The Hardening Soil model was employed for the soil layers and parameters are summarized in Table 4. DCM columns with diameter of 0.60 m were overlapped by 0.10 m to form 4.60 m wide DCM walls. Perpendicular to the excavation, one and three rows (0.60 and 1.60 m thick) of DCM walls were separately constructed as shown in the plan view in Fig. 21. Inclinometer tubes and settlement plates were provided for monitoring of wall displacement and ground settlement. The DCM length of 8 m and mixing proportion were carefully controlled in this field test. As mentioned, the concrete model was employed for the DCM walls and the parameters are listed in Table 5. The finite element mesh and problem geometry for this simulation are displayed in Fig. 22.

After completion of 5 m excavation, horizontal wall displacements and ground settlements were measured. At this excavation depth, the 0.60 m thick wall collapsed whereas the excavation supported by the 1.60 m thick wall remained stable and therefore measurements are available only for the 1.60 m thick wall as shown in Fig. 23. The calculated results of the 1.60 m-wall showed excellent agreement with the measured data. In the numerical analysis the 0.60 m-wall was still stable but showed large horizontal displacements and ground settlements indicating that it is close to failure. As already shown in the numerical analysis of the small-scale test in the previous sections, crack initiation and propagation can be illustrated by evaluating the normalised tensile softening parameter (H_t). The H_t at 5 m excavation (failure state) of the 0.60 m thick wall is shown in Fig. 24. The first transverse crack band fully developed at 2.50 m below ground surface and the second is initiated at −5.50 m. Besides, longitudinal cracks were also observed at wall edges and the middle of the wall (in y-axis) which are caused from the restraints between DCM wall and surrounding soil.

From the field test, pictures of the 0.60 m thick wall collapse are shown in Fig. 25. It follows that the failure depth of the wall is approximately at 2.50 m below surface which corresponds well to the localisation of the normalised tensile softening parameter (H_t) fully developed in the numerical analysis result (Fig. 24).

8. Conclusions

In this paper, a novel testing equipment has been developed to run a 1-g small-scale test of a model DCM-wall subjected to an excavation procedure up to the failure. The wall response during the test was monitored and the failure pattern was captured. Numerical simulations were also conducted and results were compared with the experimental result. A recently developed concrete model was employed and its capabilities were presented and compared with a Mohr-Coulomb failure criterion with tension cut-off. A uniaxial compression test was also simulated for calibration of the model parameters. Both models were able to match the test result in the pre-peak range, but only the concrete model could capture the post-peak behaviour. At the final excavation stage where significant cracking occurred in the experiment the analysis with the Mohr-Coulomb model resulted in too large displacements. Furthermore, wall failure which occurred in the experiment could be captured only in the analysis with the concrete model, whereas the Mohr-Coulomb model still indicated stable behaviour. This result indicated that numerical analyses with the Mohr-Coulomb model, as is current practice, may lead an overestimation of stability for this type of structures.

After reaching the tensile strength of the material, more reasonable results with respect to the stress distribution and plastic points in the wall were obtained with the concrete model as compared to the simple Mohr-Coulomb failure criterion with tension cut-off. Stress utilisation in tension and compression illustrated the wall failure mechanism by means of its evolution with excavation depth.

The wall failure mechanisms are also illustrated using normalised hardening and softening parameters. Tension softening started at the beginning of final excavation and continually developed. Compression hardening and softening were the consequences after tension softening had taken placed. The predicted tensile crack illustrated by plotting the tension softening parameter agreed well with the crack occurring in the experiment. In addition, the localisation of tension softening parameter also exhibited in the same location where failure was observed in the field test of DCM wall. Thus, it has been demonstrated that the concrete model captures the wall failure mechanisms reasonably well.

A sensitivity analysis on tensile parameters had been performed. Even though tensile parameters in the possible range referred to base case properties are adjusted, the analysis fails at the same excavation level as the base case. The capability of excavation is fully controlled by tensile fracture energy. The predicted cracks are located at almost the same depth of the base case; however, the crack opening size is conversely related with the tensile fracture energy. The crack also propagated upward when the tensile fracture energy decreased.

Besides investigating the failure mechanism of the DCM walls during excavation using small-scale test and numerical analysis as

presented in this work, the failure mechanisms of the DCM walls with different geometry and material properties are also of interest. A series of small-scale tests on walls with different configurations is currently being performed by the authors. We expect to report the results in the near future.

Declaration of Competing Interest

The authors declare that they have no known competing financial interests or personal relationships that could have appeared to influence the work reported in this paper.

Acknowledgements

The authors gratefully acknowledge support from the Thailand Research Fund (TRF), 1D2 Group Co., Ltd., and King Mongkut's University of Technology Thonburi (KMUTT) under Research and Researchers for Industries (RRi) scholar contract PHD57I0076, and Basic Research Grant No. BRG6080011, respectively. The authors would like to extend the appreciation to the OeAD for initiating this research collaboration through the Ernst Mach scholarship. Our appreciation is also extended to Dr. Ittipon Meepon, Prof. Panich Voottipruex and Assoc. Prof. Pitthaya Jamsawang for data sharing.

References

[1] Shao Y, Macari EJ, Cai W. Compound deep soil mixing columns for retaining structures in excavations. J Geotech Geoenvironmental Eng 2005;131:1370–7. https://doi.org/10.1061/(ASCE)1090-0241(2005) 131:11(1370).
[2] Waichita S, Jongpradist P, Jamsawang P. Characterization of deep cement mixing wall behavior using wall-to-excavation shape factor. Tunn Undergr Sp Technol 2019;83:243–53. https://doi.org/10.1016/j.tust.2018.09.033.
[3] Ignat R, Baker S, Liedberg S, Larsson S. Behavior of braced excavation supported by panels of deep mixing columns. Can Geotech J 2016;53:1671–87. https://doi.org/10.1139/cgj-2016-0137.
[4] Briaud J-L, Nicholson P, Lee J. Behavior of full-scale VERT wall in sand. J Geotech Geoenvironmental Eng 2000;126:808–18. https://doi.org/10.1061/(ASCE)1090-0241(2000) 126:9(808).
[5] Ignat R, Baker S, Larsson S, Liedberg S. Two- and three-dimensional analyses of excavation support with rows of dry deep mixing columns. Comput Geotech 2015;66:16–30. https://doi.org/10.1016/j.compgeo.2015.01.011.
[6] Mun B, Kim T, Moon T, Oh J. SCM wall in sand: Numerical simulation and design implications. Eng Geol 2012;151:15–23. https://doi.org/10.1016/j.enggeo.2012.09.003.
[7] Jamsawang P, Jamnam S, Jongpradist P, Tanseng P, Horpibulsuk S. Numerical analysis of lateral movements and strut forces in deep cement mixing walls with top-down construction in soft clay. Comput Geotech 2017;88:174–81. https://doi.org/10.1016/j.compgeo.2017.03.018.
[8] Jamsawang P, Voottipruex P, Tanseng P, Jongpradist P. Effectiveness of deep cement mixing walls with top-down construction for deep excavations in soft clay: case study and 3D simulation. Acta Geotech 2018. https://doi.org/10.1007/s11440-018-0660-7.
[9] Waichita S, Jongpradist P. Submaneewong C. Application of ground spring model in excavation supported by deep cement mixing. Int J Geomate 2017;12. https://doi.org/10.21660/2017.31.6522.
[10] Charbit B. Numerical analysis of laterally loaded lime/cement columns MSc Thesis KTH Royal Institute of Technology; 2009
[11] Larsson S, Malm R, Charbit B, Ansell A. Finite element modelling of laterally loaded lime-cement columns using a damage plasticity model. Comput Geotech 2012;44:48–57. https://doi.org/10.1016/j.compgeo.2012.03.004.
[12] Larsson S, Broms BB. Shear box model tests with lime/cement columns – some observations of failure mechanisms. ISRM Int. Symp. Melbourne, Australia: International Society for Rock Mechanics and Rock Engineering; 2000. https://doi.org/10.1007/s11213-010-9182-4.
[13] Lee SA. Characterization and modeling of cement-treated soil column used as cantilever earth retaining structure PhD thesis National University of Singapore; 2014
[14] Wijerathna M, Liyanapathirana DS. Numerical issues in modelling DCM column-supported embankments featuring post-yield strain-softening: 2D simplified vs 3D models. Int J Geotech Eng 2019;00:1–10. https://doi.org/10.1080/19386362.2019.1586109.
[15] Schädlich B, Schweiger HF. Application of a novel constitutive shotcrete model to tunnelling. Rock Eng. Rock Mech. Struct. Rock Masses - Proc. EUROCK 2014, ISRM Eur. Reg. Symp. 2014. p. 799–804. https://doi.org/10.1201/b16955-137.
[16] Horpibulsuk S, Liu MD, Liyanapathirana DS, Suebsuk J. Behaviour of cemented clay simulated via the theoretical framework of the Structured Cam Clay model. Comput Geotech 2010;37:1–9. https://doi.org/10.1016/j.compgeo.2009.06.007.
[17] Suebsuk J, Horpibulsuk S, Liu MD. Modified Structured Cam Clay: A generalised critical state model for destructured, naturally structured and artificially structured clays. Comput Geotech 2010;37:956–68. https://doi.org/10.1016/j.compgeo.2010.08.002.
[18] Gens A, Nova R. Conceptual base for a constitutive model for bonded soils and weak rocks. Int. Symp. Geotech. Eng. ofhard soils-soft rocks, Athens. 1993. p. 485–94.
[19] Liu MD, Carter JP. A structured Cam Clay model. Can Geotech J 2002;39:1313–32. https://doi.org/10.1139/t02-069.
[20] Yu HS. CASM: a unified state parameter model for clay and sand. Int J Numer Anal Methods Geomech 1998;22:621–53. https://doi.org/10.1002/(SICI)1096-9853(199808)22:8<621::AID-NAG937>3.0.CO;2-8.
[21] Arroyo M, Ciantia M, Castellanza R, Gens A, Nova R. Simulation of cement-improved clay structures with a bonded elasto-plastic model: a practical approach. Comput Geotech 2012;45:140–50. https://doi.org/10.1016/j.compgeo.2012.05.008.
[22] Kudella P, Mayer P, Ag EZ. Testing and modelling the ductility of buried jetgrout structures. In: Natau O, Fecke E, Pimentel E, editors. Int. Symp. Geotech. Meas. Model. Karlsruhe, Rotterdam: Balkema; 2003.
[23] Schweiger H, Sedighi P, Henke S, Borchert K. Numerical modelling of ground improvement techniques considering tension softening. 8th Int. Symp. Geotech. Asp. Undergr. Constr. Soft Gr., Seoul 2014. p. 209–14. https://doi.org/10.1201/b17240-39.
[24] Schädlich B, Schweiger H. A new constitutive model for shotcrete. 8th Eur. Conf. Num. Meth. Geot. Eng., Delft, The Netherlands 2014. p. 103–8. https://doi.org/10.1201/b17017-20.
[25] Lubliner J, Oliver J, Oller S, Onate E. a Plastic-damage model. Int J Solids Struct 1989;25:299–326. https://doi.org/10.1016/0020-7683(89)90050-4.
[26] Lee J, Fenves GL. Plastic-damage model for cyclic loading of concrete structures. J Eng Mech 1998;124:892–900. https://doi.org/10.1061/(ASCE)0733-9399(1998)124:8(892).
[27] Wood DM. Geotechnical modelling. CRC Press; 2004. doi:10.4324/9780203477977.
[28] Jongpradist P, Youwai S, Manorat P, Kongkitkul W, Chucheepsakul S. Influence of curing stress on one-dimensional yielding of cement-admixed Bangkok clay at high water content. Soils Found 2011;51:351–7. https://doi.org/10.3208/sandf.51.351.
[29] Zhang R, Zheng J, Bian X. Experimental investigation on effect of curing stress on the strength of cement-stabilized clay at high water content. Acta Geotech 2017;12:921–36. https://doi.org/10.1007/s11440-016-0511-3.
[30] Bowles JE. Foundation analysis and design. 5th ed. The McGraw-Hill Companies Inc.; 1996. doi: 10.1016/0013-7952(84)90010-3.
[31] Voottipruex P, Suksawat T, Bergado DT, Jamsawang P. Numerical simulations and parametric study of SDCM and DCM piles under full scale axial and lateral loads. Comput Geotech 2011;38:318–29. https://doi.org/10.1016/j.compgeo.2010.11.006.
[32] Yapage NNS, Liyanapathirana DS, Poulos HG, Kelly RB, Leo CJ. Numerical modeling of geotextile-reinforced embankments over deep cement mixed columns incorporating strain-softening behavior of columns. Int J Geomech 2015;15:04014047. https://doi.org/10.1061/(asce)gm.1943-5622.0000341.
[33] Phutthananon C, Jongpradist P, Yensri P, Jamsawang P. Dependence of ultimate bearing capacity and failure behavior of T-shaped deep cement mixing piles on enlarged cap shape and pile strength. Comput Geotech 2018;97:27–41. https://doi.org/10.1016/j.compgeo.2017.12.013.
[34] Phutthananon C, Jongpradist P, Jamsawang P. Influence of cap size and strength on settlements of TDM-piled embankments over soft ground. Mar Georesources Geotechnol 2019:1–20. https://doi.org/10.1080/1064119X.2019.1613700.
[35] Brinkgreve RBJ, Eingin E, Swolfs WM. Finite element code for soil and rock analyses. Users Manual. The Netherlands: Plaxis bv; 2018.
[36] Schütz R, Potts DM, Zdravkovic L. Advanced constitutive modelling of shotcrete: model formulation and calibration. Comput Geotech 2011;38:834–45. https://doi.org/10.1016/j.compgeo.2011.05.006.
[37] RILEM TC 50-FMC. Determination of the fracture energy of mortar and concrete by means of three-point bend tests on notched beams. Mater Struct 1985:287–90.
[38] Tariq KA, Maki T. Mechanical behaviour of cement-treated sand. Constr Build Mater 2014;58:54–63. https://doi.org/10.1016/j.conbuildmat.2014.02.017.
[39] Jamsawang P, Yoobanpot N, Thanasisathit N, Voottipruex P, Jongpradist P. Three-dimensional numerical analysis of a DCM column-supported highway embankment. Comput Geotech 2016;72:42–56. https://doi.org/10.1016/j.compgeo.2015.11.006.
[40] Chai JC, Shrestha S, Hino T, Uchikoshi T. Predicting bending failure of CDM columns under embankment loading. Comput Geotech 2017;91:169–78. https://doi.org/10.1016/j.compgeo.2017.07.015.
[41] Meepon I. Application of soil cement column in shallow excavation PhD dissertation North Bangkok: King Mongkut's University of Technology; 2016

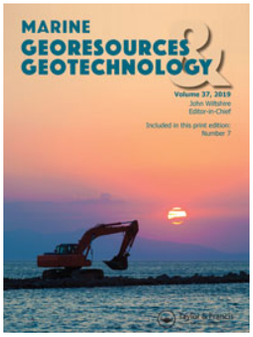

Marine Georesources & Geotechnology

ISSN: 1064-119X (Print) 1521-0618 (Online) Journal homepage: https://www.tandfonline.com/loi/umgt20

Comparative performances of two- and three-dimensional analyses of soil-cement mixing columns under an embankment load

Pitthaya Jamsawang, Ekkarin Phongphinittana, Panich Voottipruex, Dennes T. Bergado & Pornkasem Jongpradist

To cite this article: Pitthaya Jamsawang, Ekkarin Phongphinittana, Panich Voottipruex, Dennes T. Bergado & Pornkasem Jongpradist (2019) Comparative performances of two- and three-dimensional analyses of soil-cement mixing columns under an embankment load, Marine Georesources & Geotechnology, 37:7, 852-869, DOI: 10.1080/1064119X.2018.1504261

To link to this article: https://doi.org/10.1080/1064119X.2018.1504261

MARINE GEORESOURCES & GEOTECHNOLOGY
2019, VOL. 37, NO. 7, 852–869
https://doi.org/10.1080/1064119X.2018.1504261

Taylor & Francis
Taylor & Francis Group

Comparative performances of two- and three-dimensional analyses of soil-cement mixing columns under an embankment load

Pitthaya Jamsawang[a], Ekkarin Phongphinittana[b], Panich Voottipruex[c], Dennes T. Bergado[d] and Pornkasem Jongpradist[e]

[a]Soil Engineering Research Center, Department of Civil Engineering, King Mongkut's University of Technology North Bangkok, Bangkok, Thailand; [b]Department of Mechanical and Aerospace Engineering, King Mongkut's University of Technology North Bangkok, Bangkok, Thailand; [c]Department of Teacher Training in Civil Engineering, King Mongkut's University of Technology North Bangkok, Bangkok, Thailand; [d]School of Engineering and Technology, Asian Institute of Technology, Bangkok, Thailand; [e]Department of Civil Engineering, Faculty of Engineering, King Mongkut's University of Technology Thonburi, Bangkok, Thailand

ABSTRACT

This research presents measurements and simulations of the full-scale behavior of a test embankment built on a soft marine clay deposit improved using soil–cement mixing (SCM) columns in Bangkok, Thailand, using both two-dimensional (2D) and 3D finite element analyses (FEAs). Fixed SCM columns with two different installation patterns, that is, column groups and column rows, were constructed in the soft clay foundation prior to the construction of the embankment. Three column wall methods, namely, equivalent width, equivalent axial rigidity, and equivalent flexural rigidity approaches, were used to convert the 3D individual columns into 2D plane strain column walls. A comparison of the results obtained through the 3D and 2D FEAs revealed that the 2D analyses provide inaccurate results in terms of the column lateral movements, bending moments, and axial loads induced in the SCM columns in addition to the factors of safety against slope failure. This outcome occurred because the actual columns in the 2D FEA were modeled using extended walls, which essentially prevent the movements of soil between two columns or column rows. Correction factors used to convert the 2D analysis results into 3D analysis results were also proposed in this study.

ARTICLE HISTORY
Received 2 April 2018
Accepted 19 July 2018

KEYWORDS
Deep mixing; embankment; ground improvement; simulation; soft marine clay

1. Introduction

Soft marine clays, which are widely known as highly problematic soils, are generally encountered in the form of deposited layers in coastal areas (Wu et al. 2015) and are universally distributed throughout coastal regions such as Ariake Bay, Japan (Ma et al. 2011), the eastern coast of China (Xu et al. 2013), the eastern coast of Singapore (Arulrajah and Bo 2008; Bo et al. 2015), and the Bangkok Plain (Horpibulsuk, Rachan, and Suddeepong 2012a; Horpibulsuk et al. 2007; Lorenzo and Bergado 2004). The majority of these soft marine clays were deposited during the Quaternary period (Hong et al. 2007; 2012); these Quaternary deposits are generally characterized by a high natural water content in addition to a high compressibility, high sensitivity, high viscosity, and low shear strength (Yin, Yin, and Huang 2015). Consequently, the construction of embankments overlying these soft marine clays often leads to large movements and excessive settlement, resulting in slope and bearing failures that usually result in long construction delays and costly remedial work (Abusharar, Zheng, and Chen 2009).

The soil–cement mixing (SCM) method is a well-known technique that has been widely used to support embankments on soft marine clay deposits in Asia, Europe, North America, and other parts of the world (Jamsawang et al. 2015b). In this technique, a cement admixture in either powder or slurry form is inserted into the soft marine clay and is blended with the native soil using high-pressure grouting or mixing blades, thereby creating a hard, stabilized soft marine clay column known as an SCM column (Horpibulsuk, Rachan, and Suddeepong 2012b; Horpibulsuk et al. 2011; Liu et al. 2012; Shen et al. 2013a, 2013b; Wang, Shen, and Cheng 2018). The SCM columns beneath the embankment are generally installed straight through relatively soft subsurface deposits to transfer the embankment loads into deeper, harder beds (Han et al. 2007; Horpibulsuk, Rachan, and Suddeepong 2012a; Liu et al. 2012; Okyay and Dias 2010). Individual SCM columns arranged in square or rectangular grid patterns (column groups) are commonly used to reduce the amount of surface settlement with typical improvement area ratios (a_r) between 0.1 and 0.5 (Topolnicki 2013), whereas single row patterns (column rows) are applied to reduce lateral movements and increase the slope stability of the embankment (Filz et al. 2012). The improvement depth can be classified as having one of the two patterns, namely, a floating column type or a fixed column type, depending on whether the SCM column

CONTACT Pitthaya Jamsawang pitthaya_kmutnb@hotmail.com Soil Engineering Research Center, Department of Civil Engineering, King Mongkut's University of Technology North Bangkok, Bangkok 10800, Thailand

tips are installed atop the harder soil layer. Fixed columns are generally used to limit the surface settlement and lateral displacement and to increase the slope stability, whereas floating columns are typically chosen in the presence of a thick soft marine clay layer (Kitazume and Terashi 2013).

A two-dimensional finite element analysis (2D FEA) is often used to study the behaviors of overlying soft clays improved using SCM columns under embankment loads (Borges and Marques 2011; Huang and Han 2010; Jiang, Han, and Zheng 2014; Oliveira, Pinheiro, and Correia 2011; Yapage et al. 2014; Zhang et al. 2013). However, a 3D FEA was recently employed to investigate the performance of an embankment over soft clay improved using SCM columns to simulate the actual column conditions (Huang and Han 2009; Jamsawang et al. 2015a; 2016a, 2016b; Voottipruex et al. 2011). Because the 3D modeling of multiple problems is complex and time consuming, geotechnical engineers often attempt to analyze 3D columns as a 2D continuous wall under plane strain known as a column wall (Chai et al. 2014; Oliveira, Pinheiro, and Correia 2011) that has either equivalent dimensions or equivalent properties. For the equivalent dimension approach, the wall width is assumed to be similar to that of the 3D column, and the properties of the wall are reduced from those of the 3D columns based on the improvement area ratio. In contrast, for the equivalent property approach, the properties of the wall are identical to those of the 3D columns, but the width of the wall is reduced from that of the 3D column based on either the equivalent bending rigidity or the equivalent axial rigidity (Abusharar and Han 2011; Tan, Tjahyono, and Oo 2008).

Tan, Tjahyono, and Oo (2008) found that the long-term surface settlement of an embankment constructed on ground improved using stone columns computed using the column wall model based on the equivalent property approach was more accurate than that obtained using the column wall method based on the equivalent dimension approach. Furthermore, Abusharar and Han 2011 conducted a 2D numerical study on the deep-seated stability of embankments over soft clay improved using stone columns, and Zhang, Han, and Ye (2014) performed a 3D numerical analysis of the same work. The results of these analyses showed that the values of the factor of safety (*FS*) analyzed using the equivalent dimension approach were greater than those obtained using 2D numerical analysis with the column wall method. In addition, Chai et al. (2015) concluded that 2D FEA provides inappropriate results in terms of the bending moments and the lateral displacements of the floating columns beneath an embankment toe compared with 3D FEA, but they did not propose a correction factor to convert the 2D FEA results into 3D FEA results. However, most of the aforementioned studies modeled only the column group; unfortunately, few studies have compared the results obtained using both 3D and 2D models for fixed SCM column groups and column rows.

This paper focuses on a numerical analysis of the full-scale behavior of a 5-m-high embankment built on soft Bangkok clay, improved using an SCM column group and an SCM column row. The surface settlements of the columns and surrounding soils and the lateral movements during the construction of an embankment were measured during a field study over a period of ~61 days. Plaxis 2D Version 2015 and Plaxis 3D Version 2013 were used for the 2D FEA and 3D FEA, respectively. The FEAs were employed to simulate the consolidation behavior of the improved soft clay under an embankment load using a coupled mechanical and hydraulic model. Three column wall methods, namely, the equivalent width, equivalent bending rigidity, and equivalent axial rigidity approaches, were used to convert the 3D individual columns into 2D column walls under plane strain. The bending moment and axial load of the columns and the *FS* against slope failure obtained from the 3D FEA were also compared with those obtained from the 2D FEA. Finally, a correction factor was proposed to convert the D FEA results to 3D FEA results for fixed SCM column groups and SCM column rows under an embankment load.

2. Test site and soil profile

The test site of this study was located at the geotechnical engineering research area of the Asian Institute of Technology campus in Klong Luang District, Pathumthani Province, Thailand. A field vane test was performed at the study site, and a borehole was drilled. The soil profile, which is presented in Figure 1(a), consisted of four layers: 2 m of weathered crust, 6 m of soft clay, 2 m of medium stiff clay, and 2 m of stiff clay. Figure 1(b–k) presents the soil properties, including the undrained shear strength, field vane shear strength, natural moisture content, Atterberg limits, wet unit weight, specific gravity, initial void ratio (e_o), compression index (c_c), recompression index (c_r), coefficient of permeability, and overconsolidation ratio. The permeability coefficients of the foundation soils were calculated from the experimental results of oedometer tests, as were the compression and recompression indices and overconsolidation ratios. The overconsolidation ratio profile adopted for both the 2D FEA and the 3D FEA was estimated based on the average values of the overconsolidation ratio data for the same foundation soil layers. The undrained shear strengths of the clayey soils were determined through uniaxial compression tests on undisturbed samples. The groundwater level was located 2.0 m below the original ground surface. The undrained shear strengths of the clayey soils tended to increase with increasing depth, as illustrated in Figure 1(b). The soft, medium stiff and stiff clays at this study site were classified as high-plasticity clays based on the Unified Soil Classification System.

3. Test embankment on soft clay improved using SCM columns

3.1. Construction of SCM columns

Prior to initiating the construction of the test embankment, the foundation subsoil was improved using SCM columns

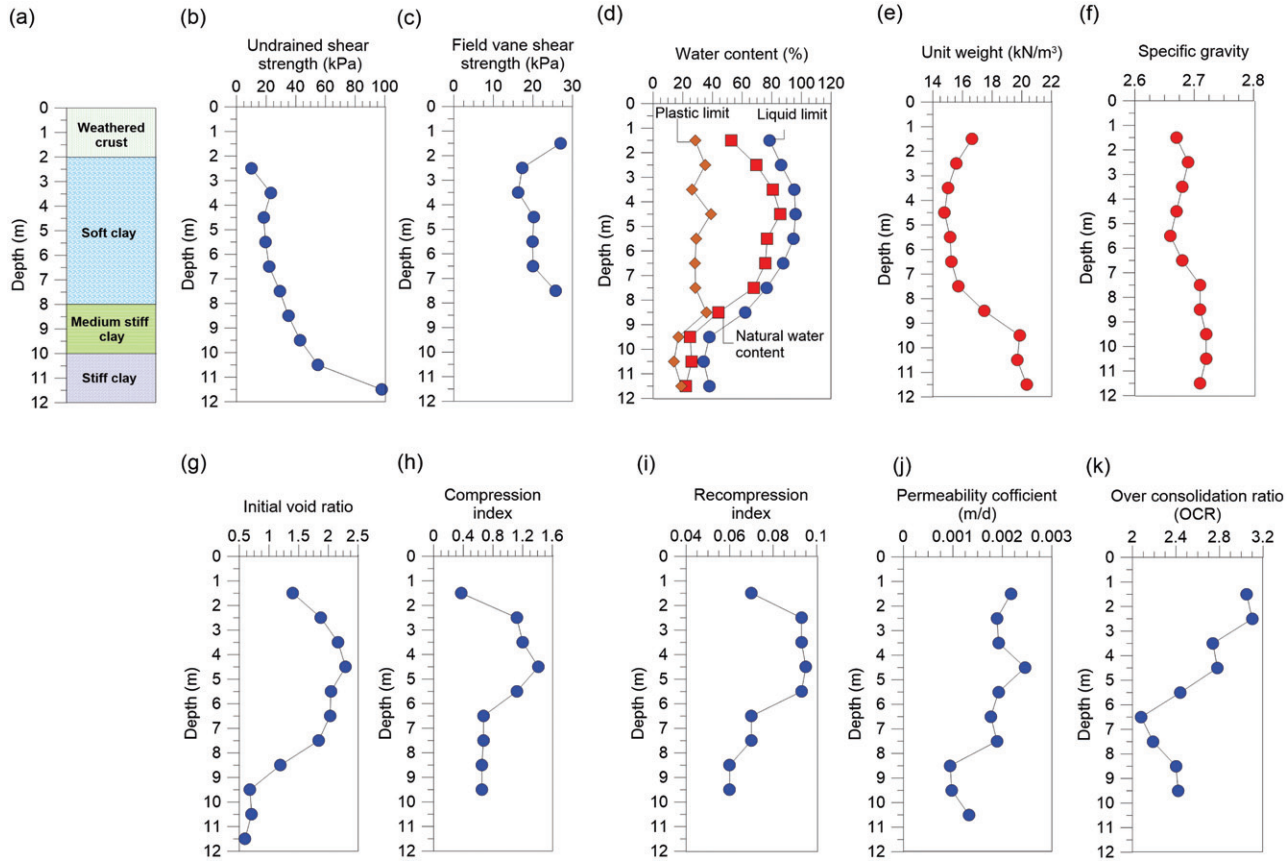

Figure 1. Soil profile and soil properties.

with two different patterns, that is, a column group and a column row, to observe the deformation characteristics. Twenty-four SCM columns were constructed *in situ* through a blade mixing method with a wet process. Twelve columns were used for the column row pattern, and the remaining 12 columns were used for the column group pattern. Three column rows were constructed by installing four individual SCM columns with a row spacing of 4.2 m. The column group was constructed in a rectangular pattern with a spacing of 2.0 m × 2.80 m (Figure 2(a)). Each SCM column had a diameter and length of 1.0 m and 7.0 m, respectively, and each column was embedded in both a weathered crust layer and a soft clay layer; fixed SCM column types were employed with the column tip located atop the medium stiff clay layer, as shown in Figure 2(b). The water–cement ratio of the cement paste and the amount of cement used for the installation of the SCM columns were 0.8 and 150 kg/m^{-3} of the moist clay volume, respectively. After the construction of the SCM columns was completed, core specimens were collected from both the SCM column group and the SCM column row at depths of 2.5, 5.0, and 7.0 m to determine the field unconfined compressive strength (q_u) and the secant modulus of elasticity at 50% of the unconfined compressive strength (E_{50}). The unconfined compression tests were performed on core specimens with a diameter of 50 mm and a height of 100 mm. The values of q_u and E_{50} were 600 kPa and 40,000 kPa, respectively, indicating an empirical relationship of $E_{50} = 67q_u$ corresponding to the findings of previous research (Jamsawang et al. 2015a, 2016a, 2016b).

3.2. Construction of the test embankment

A weathered crust layer with a depth of 1 m was excavated prior to constructing the test embankment. Accordingly, a trench excavation was performed, and a 15-m-wide, 36-m-long, and 1-m-deep section of weathered crust (Figure 2(b)) was removed. Then, the excavated area was backfilled with compacted silty sand to a depth of 1 m; the 1-m-thick silty sand layer was compacted to obtain a required total unit weight of 17.7 kN/m^3. Then, a 5-m-high embankment with 1:1 end slopes and 1:2 side slopes was constructed. The top and base dimensions of the test embankment were 8 × 5 m and 18 × 28 m, respectively, as shown in Figure 2(b). Weathered clay taken from areas adjacent to the test embankment were utilized as backfill material for the construction of the embankment. A lift thickness of 0.3 m was required for the compaction of the weathered clay backfill to achieve a wet unit weight of 16.1 kN/m^3. Finally, the embankment toes were excavated to a depth of 2 m to obtain large lateral movements of the foundation subsoil for 20 days after the embankment construction had been completed. A plan view of the excavation of the embankment toe is presented in Figure 2(c). Real photos of the equipment and construction stages of the test embankment are also shown in Figure 3.

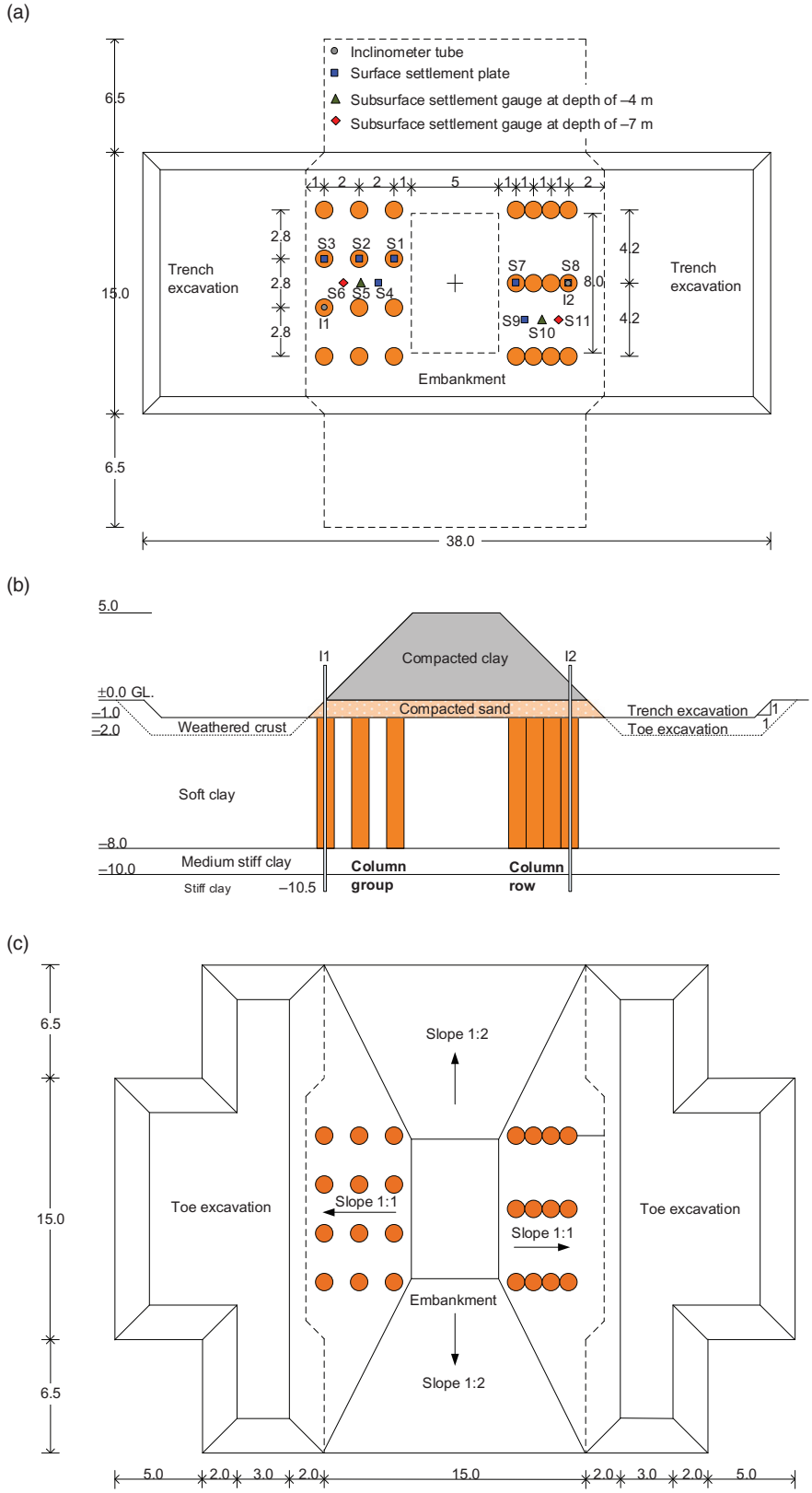

Figure 2. Cross-sectional and plan views of the embankment over soft clay improved by SCM piles and the locations of instruments: (a) cross-sectional view; (b) plan view of the instrumented embankment; (c) plan view of the embankment after toe excavation.

3.3. Field instruments

Figure 2(a,b) show plan and cross-sectional views, respectively, of the locations of the field instruments. A surface settlement plate was used to measure the settlement of the SCM column head and the surrounding clay near the ground surface, whereas a subsurface settlement gauge was employed to observe the settlement of the surrounding clay at depths below the ground surface. The surface settlement

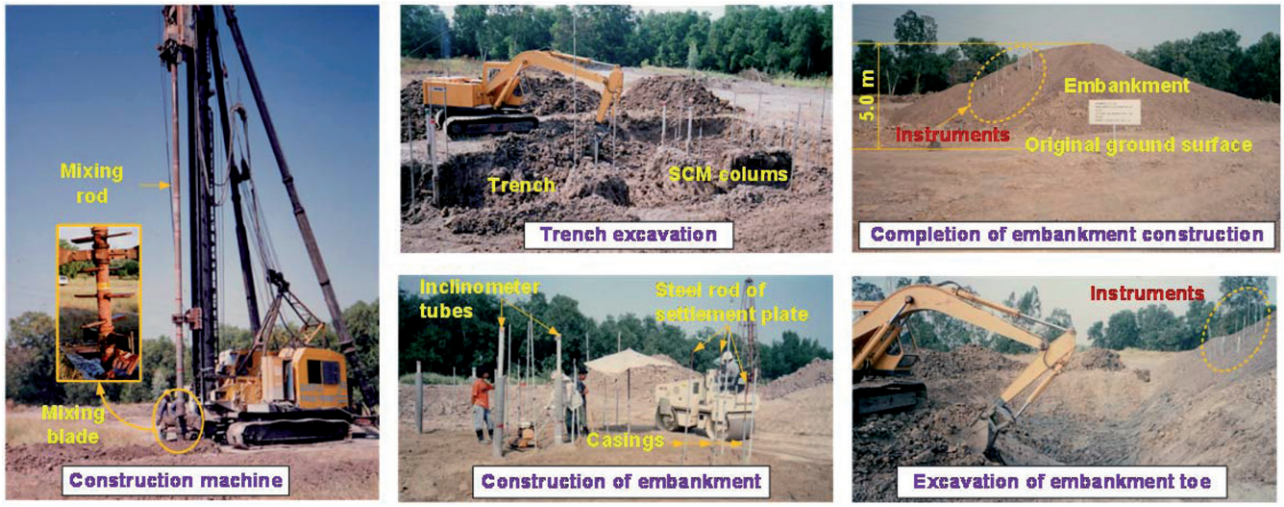

Figure 3. Photos of the equipment and construction stages of the test embankment.

plate was composed of a 16-mm-diameter steel rod welded to a square steel plate base with dimensions of 0.4 × 0.4 m and a thickness of 3 mm, and it was covered by a 19-mm-diameter steel casing. The subsurface settlement gauge was installed at the desired depth in the surrounding clay.

The instruments were installed after the excavation of the 1-m-deep trench. Surface settlement plates were placed at the tops of the column group (S1, S2, and S3) and column wall (S8 and S7) and were buried at a depth of -0.15 m relative to the original ground level in the clay surrounding the column group (S4) and column row (S9). Four subsurface settlement gauges were also installed at depths of −4.0 m and −7.0 m relative to the original ground level in the clay surrounding the column group (S5 and S6) and column row (S10 and S11). Inclinometers were employed to measure the lateral movements along the depths of the SCM columns; two inclinometer tubes were embedded (one each) in the SCM column group (I1) and column row (I2) at the embankment toes ranging from a depth of −1 m to a depth of −10.5 m.

4. Finite element method used for the simulations

Plaxis 2D Version 2015 and Plaxis 3D Version 2013, which are well-known commercial software programs based on a common finite element method, were used to conduct the 2D and 3D simulations, respectively, in this study. These user-friendly software programs contain various features such as static elastic-plastic deformation, advanced soil models, and consolidation and safety analyses. Thus, these software programs were selected because of their availability in addition to their ease and convenience of use. The governing equations for consolidation settlement in PLAXIS 2D and PLAXIS 3D follow Biot's theory for coupled consolidation (Biot 1956) with a finite element formulation, and Darcy's law for fluid flow through the soil skeleton is also assumed. This formulation is based on small strain theory according to Terzaghi's principle. Furthermore, advanced soil models were applied for consolidation analysis under elastoplastic consolidation.

4.1. 3D FEM modeling

The embankment shown in Figure 2(a–c) is truly three-dimensional, as each SCM column is not continuous in the out-of-plane direction. In the case labeled 3D-True, only half of the embankment was modeled to avoid the effects of interactions resulting from different patterns of SCM columns on the modeling. Solid elements were used to model the SCM columns. Octagonal cylindrical elements were used instead of actual circular cylinders to model the SCM columns due to the convenience associated with the mesh generation. The cross-sectional area of the modeled octagonal cylinder was kept equivalent to that of the 1-m-diameter SCM column. The modeled volume was 60 m × 80 m in the *xy*-plane, and the depth of the column was 30 m below the ground level to minimize the boundary effect. Ultrafine meshes were generated in the model; the total number of nodes was approximately 150,000, and the total number of elements was approximately 110,000. Figure 4(a,b) shows an overview of the model and an enlargement of the solid elements used to model both the column group and the column row. An alternative 3D method utilizing planes of symmetry (i.e., symmetric boundaries) makes it possible to analyze a 3D slice only. In the 3D-Symmetry case designed in Figure 4(c,d), only plane strain strips containing two rows of half-columns and one row of whole columns are modeled for the column group and column row patterns, respectively, and the thicknesses of the strips were 2.8 and 4.2 m, respectively. The numbers of nodes and elements were approximately 20,000 and 13,000, respectively. Figure 4(c,d) shows plan and cross-sectional views of the 3D-Symmetry model for the column group and column row, respectively.

4.2. 2D FEM modeling

The individual SCM columns were converted into column walls under continuous plane strain, as shown in Figure 5, for 2D analysis. For this conversion, two approaches are commonly used: matching the geometries of the columns or

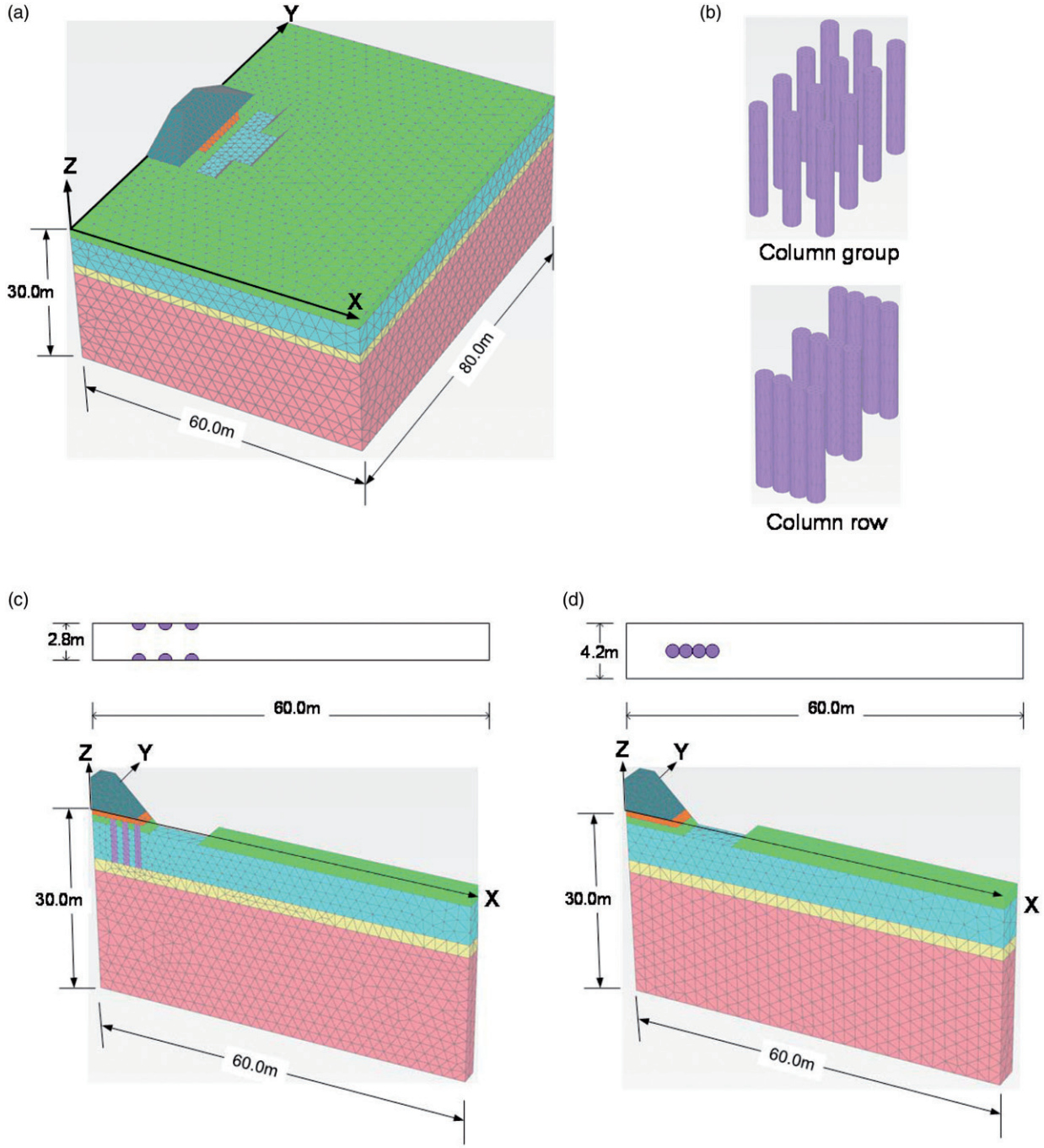

Figure 4. 3D-FE mesh: (a) 3D-True case; (b) enlargement of solid elements used for modeling the column group and column row; (c) 3D-Symmetry case for a column group; (d) 3D-Symmetry case for a column row.

matching the properties of the columns (Tan, Tjahyono, and Oo 2008). The approach of matching the geometries of the columns is referred to as 2D-Equal B in this paper. In this method, the effective width of the column wall is assumed to be the same as the diameter of an individual column (i.e., $B_{\text{wall}} = D_{\text{column}}$, where B_{wall} is the width of the column wall and D_{column} is the diameter of an individual column). The equivalent properties of the column walls, such as the elastic modulus of the column wall E_{wall} and the cohesion of the column wall c_{wall}, are determined based on the area-weighted average of the properties of the SCM columns and the surrounding soft clay within each row of columns:

$$E_{\text{wall}} = E_{\text{column}} a_{\text{r}} + E_{\text{soil}}(1 - a_{\text{r}}) \tag{1}$$

$$c_{\text{wall}} = c_{\text{column}} a_{\text{r}} + c_{\text{soil}}(1 - a_{\text{r}}) \tag{2}$$

where E_{column} and E_{soil} are the elastic moduli of the individual SCM columns and soft clays, respectively; c_{column} and c_{soil} are the cohesion of the individual SCM columns and soft clays, respectively; and a_{r} is the improvement area ratio resulting from the SCM columns within a row of columns. In this study, E_{soil} and c_{soil} are sufficiently smaller than E_{column} and c_{soil}, respectively, such that they can be ignored

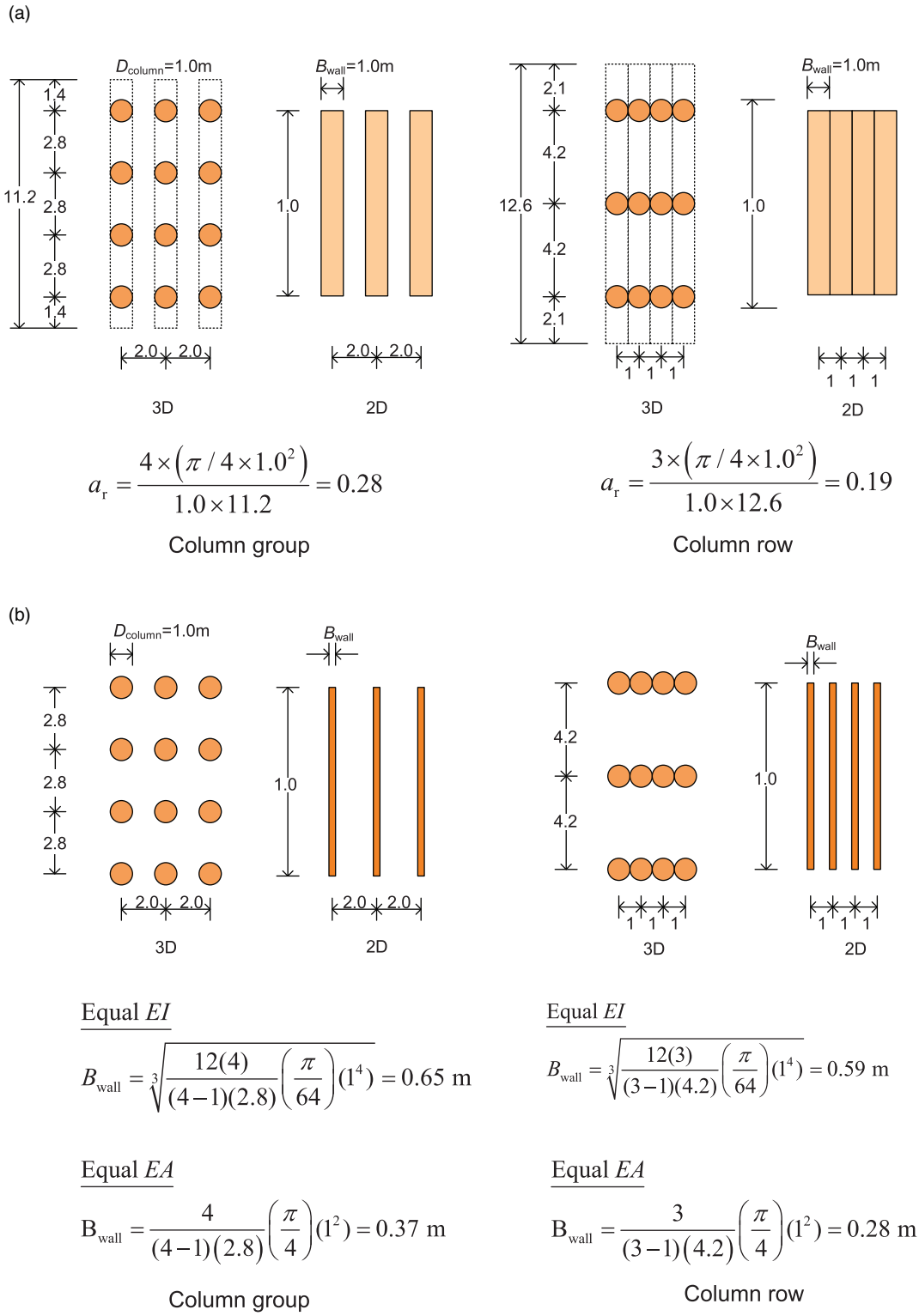

Figure 5. Conversion from a 3D column to an equivalent 2D column wall: (a) equal *B* method; (b) equal *EA* or *EI* method.

when calculating Equations (1) and (2), respectively. An alternative 2D equivalency method, which is referred to as 2D-Equal *EA* or simply 2D-Equal *EI*, assumes that the properties of the column walls are equal to those of the individual SCM columns; therefore, the effective width of the column wall is different from the diameter of an individual column. The SCM columns were modeled as continuous walls under plane strain conditions considering either equal values of the axial rigidity (*EA*) or equal values of the flexural rigidity (*EI*) (2D-Equal *EA* and 2D-Equal *EI*, respectively) (Table 1), where *E* is modulus of elasticity, *I* is the second moment of the area, and *A* is the cross-sectional area of the column. In this analysis, the center-to-center distance between two contiguous walls was kept identical to

the spacing of two contiguous 3D columns. The formulations used to obtain a 2D equivalent wall for a group of columns in the plane strain direction are as follows.

The equal flexural rigidity relationship can be expressed as follows:

$$E_{\text{wall}}I_{\text{wall}}(n-1)s = n(E_{\text{column}}I_{\text{column}}) \tag{3}$$

In this study, E_{wall} and E_{column} are equal because the same materials are employed. Thus, Equation (3) becomes the following:

$$\left(\frac{1}{12}\right)(1)B_{\text{wall}}^{3}(n-1)s = n\left(\frac{\pi}{64}\right)D_{\text{column}}^{4} \tag{3.1}$$

$$B_{\text{wall}} = \sqrt{\frac{12n}{(n-1)s}\left(\frac{\pi}{64}\right)D_{\text{column}}^{4}3} \tag{3.2}$$

The equal axial rigidity relationship can be expressed as follows:

$$E_{\text{wall}}A_{\text{wall}} = \frac{n(E_{\text{column}}A_{\text{column}})}{(n-1)s} \tag{4}$$

$$(1)B_{wall}(n-1)s = n\left(\frac{\pi}{4}\right)D_{\text{column}}^{2} \tag{4.1}$$

$$B_{wall} = \frac{n}{(n-1)s}\left(\frac{\pi}{4}\right)D_{\text{column}}^{2} \tag{4.2}$$

where n is the number of columns in the plane strain direction and s is the center-to-center column spacing between two columns in the plane strain direction. The adopted boundary conditions and FE mesh are presented in Figure 6.

Table 1. Analyzed cases.

Case		Remark
3D	3D-True	True 3D
	3D-Symmetry	Macro: plane strain with 3D column
2D	2D-Equal *B*	Plane strain
	2D-Equal *EA*	Plane strain
	2D-Equal *EI*	Plane strain

Only half of the embankment was modeled due to symmetry; a horizontal length of 60.0 m and a vertical depth of 30 m from the original ground level were used for the modeled area. For the region of interest, in which the development of large plastic strains is expected, especially in the zone between the SCM columns and surrounding soil in the soft clay layer, a finer discretization mesh with an appropriate aspect ratio was used to accommodate the precision of the solutions. For both the 2D and the 3D models, interface elements were not applied to simulate the interfacial behavior between the peripheries of the SCM columns and the surrounding clayey soils, because the interfacial shear strength between the SCM column and the surrounding clay is greater than the shear strength of the surrounding clay (Voottipruex et al. 2011a, 2011b). At the left and right sides of the 3D model boundaries, the lateral displacement in the x-direction was fixed, while vertical movement in the z-direction was permitted. In other words, both rigid and smooth boundaries were considered in this study. The horizontal and vertical displacements were both fixed at the bottom boundary. In addition, the left, right, and bottom boundaries were considered impermeable, whereas the ground surface was considered completely permeable. The movements in the y-direction were prohibited for the back and front boundaries in the 3D models (Figure 6). The foundation soil and embankment in the 2D and 3D models were modeled using elements (with and without degrees of freedom, respectively) with an excess pore water pressure at all nodes. The construction stages for the 2D FEA and 3D FEA were similar to those for the field conditions, as shown in Table 2. Although the meshes were prepared with great care, the analyses in this study were performed using a certain degree of mesh discretization, which could marginally influence the computational results. However, the conclusions derived from the study were not affected by this discretization.

4.3. Installation of the SCM columns in the FE models

To install the SCM columns in the 2D and 3D models, the foundation soil properties of the relevant elements were

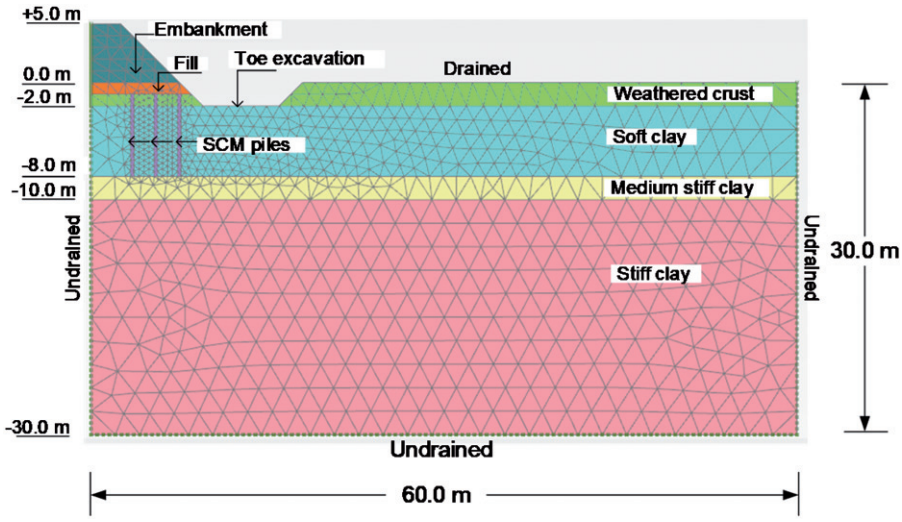

Figure 6. 2D-FE mesh example for the column group case with the conversion using the 2D-Equal *EA* case.

Table 2. Stages of construction in the 2D FEA and 3D FEA.

Stage	Description	Elapsed time (day)
0	Generation of initial stresses (K_o - condition)	None
1	SCM column installation	None
2	1-m-depth trench excavation	None
3	1-m-high backfill construction	0
4	1-m-high embankment construction	2
5	2-m-high embankment construction	4
6	3-m-high embankment construction	6
7	4-m-high embankment construction	8
8	5-m-high embankment construction (end of construction)	10
9	Consolidation of full height embankment	28
10	Toe excavation	34
11	Consolidation of full height embankment (end of monitoring)	61
12	Factor of safety analysis	61

Table 3. Parameters used in the Mohr-Coulomb model.

	Embankment	Backfill	SCM column
Unit weight, γ (kN/m^3)	16	17	16
Modulus of elasticity, E (kPa)	10,000	15,000	40,000
Poisson's ratio, ν	0.33	0.33	0.33
Cohesion, c (kPa)	10	10	$c_u = 150$
Angle of internal friction, ϕ (degree)	30	35	0
Coefficient of permeability, k (m/d)	–	–	5×10^{-4}
Drainage behavior of material	Drained		Undrained type B

replaced with SCM column properties without simulating the SCM column construction process. Thus, any effects resulting from disturbances of the surrounding clayey foundation soils due to the installation of SCM columns were specifically ignored (Chai et al. 2014; Jamsawang et al. 2015a, 2015b, 2016a, 2016b).

4.4. Constitutive models and soil parameters

The behaviors of the embankment, fill material layer, and SCM columns were simulated using the Mohr–Coulomb (i.e., from linearly elastic to perfectly plastic) model (Huang and Han 2009; Jamsawang et al. 2015a, 2015b, 2016a, 2016b; Voottipruex et al. 2011a, 2011b). The tensile strength of the SCM columns, which was approximately $0.16q_u$ (Jamsawang, Bergado, and Voottipruex 2011), was considered the tension cutoff for the Mohr–Coulomb model. This model requires five parameters: the modulus of elasticity (E), Poisson ratio (ν), cohesion (c), friction angle (ϕ), and dilatancy angle (ψ). The undrained type B was used to simulate the undrained response of the SCM column. The soft soil model was applied to describe the responses of the weathered crust, soft clay, and medium stiff clay layers. In addition to the shear strength parameters, the stiffnesses of the soils in terms of the modified compression index (λ^*) and modified swelling index (κ^*), which were obtained from the oedometer test results according to $\lambda^* = c_c/2.3(1+e_o)$ and $\kappa^* = 2c_r/2.3(1+e_o)$, were also required. The permeability coefficients for the SCM columns were set equal to those for the surrounding clays corresponding to the test results of Horpibulsuk, Rachan, and Suddeepong 2012a. The soil response of the stiff clay layer was simulated using the hardening soil model (Surarak et al. 2012), which contains several key features that consider soil behaviors, for example, plasticity, two yielding surfaces with hardening functions, stress-dependent soil stiffnesses, and loading/unloading responses. The hardening soil model requires five parameters of the soil deformation behaviors: the secant modulus from a standard drained triaxial compression test (E_{50}^{ref}), the tangential modulus from a consolidation test (E_{oed}^{ref}), the unloading/reloading modulus (E_{ur}^{ref}), the unloading/reloading Poisson ratio (ν_{ur}), and the power of the stress-level dependency of the stiffness (m). The permeability coefficients for all foundation soils were set equal in all directions. The input soil parameters for the Mohr–Coulomb, soft soil and hardening soil models are listed in Tables 3–5, respectively.

5. Measured and simulated results

5.1. Settlements

The settlements at the measurement points (see Figure 2(a) for their locations) are compared in Figures 7(a–f) and 8(a–e) for the column group and column row, respectively. The 2D analyses resulted in fair simulations except for the 2D-Equal B case regarding the settlement of the column row (Figure 11(a)), and the 3D analyses (3D-True and 3D-Symmetry) resulted in good modelling simulations of the field settlement curves for the column group and column row as well as the surrounding clays at depths of −1, −4, and −7 m. The 2D-Equal EA case gave settlement results that are the closest to the measured data among the other 2D cases, implying that the approach of matching the column properties by considering a similar axial stiffness is the most appropriate for predicting vertical deformations under compression loads. In addition, the 2D-Equal EI case provided smaller simulated settlements than the 2D-Equal EA case because the value of B_{wall} obtained from the former was greater than that obtained from the latter, resulting in a larger axial stiffness (Figure 5(b)). However, the 2D-Equal B case provided the largest settlements among the 2D analysis cases because the 2D-Equal B case possesses the largest improvement area ratio, resulting in a larger stress concentration in the column but a lower stiffness. The maximum differences between the settlements obtained from the 2D-Equal B and 2D-Equal EI cases were 55 and 65% in the column group and column row cases, respectively. The problem associated with modeling the column row in the 2D-Equal B case is that the value of a_r is considerably lower than that used to model the column group due to the larger

Table 4. Parameters used in the soft soil model.

	Weathered crust	Soft clay	Medium stiff clay
Unit weight, γ (kN/m^3)	17	14	16
Modified compression index, λ^*	0.22	0.19	0.09
Modified swelling index, κ^*	0.04	0.03	0.04
Poisson's ratio, ν	0.15	0.15	0.15
Cohesion, c (kPa)	10	2	10
Angle of internal friction, ϕ (degree)	25	23	25
Overconsolidation ratio (OCR)	2.5	2.2	2.5
Coefficient of permeability, k (m/d)	5×10^{-2}	5×10^{-4}	2.5×10^{-4}
Drainage behavior of material	Undrained		

Table 5. Parameters used in the hardening soil model.

	Stiff clay
Unit weight, γ (kN/m^3)	20
Secant modulus, E_{50}^{ref} (MPa)	50
Tangential modulus, E_{oed}^{ref} (MPa)	50
Unloading/reloading modulus, E_{ur}^{ref} (MPa)	150
Power of the stress-level dependency of the stiffness, m	1
Unloading/reloading Poisson's ratio, ν_{ur}	0.2
Cohesion, c (kPa)	18
Angle of internal friction, ϕ (degree)	25
Overconsolidation ratio (OCR)	2.5
Coefficient of permeability, k (m/d)	2.5×10^{-4}
Drainage behavior of material	Undrained

spacing, resulting in a larger reduction in both the strength and the stiffness of the wall.

5.2. Lateral movements

The lateral movement profiles of the SCM columns under the toe of the embankment for the column group and column row cases shown in Figure 2(a,b) are compared in Figures 9(a,b) and 10(a,b) for the column group and column row cases, respectively, at the end of the embankment construction and at 61 days after the beginning of embankment construction. All analysis results overestimated the lateral movements upon completion of the embankment construction for both the column group and the column row cases (Figures 9(a) and 10(a)), and the 3D-True analysis provided the smallest result, which was very similar to the observed data. After 61 days of elapsed time for the column group, the 3D-True case yielded simulated results similar to the field measured data, whereas the 3D-Symmetry and all 2D analyzed cases overestimated the lateral movements (Figures 9(b) and 10(b)), because true 3D effects can spread soil movements in all directions, particularly lateral movements, due to the consolidation process. However, the 2D-Equal *EA* and 2D-Equal *EI* analyses were better at capturing the shapes of the column group lateral movement profiles than they were at capturing those of the column row lateral movement profiles because the column row slenderness was increased and the interactions between columns in the column rows were decreased. Thus, the deformation modes changed from translation to flexural. The 2D-Equal *B* case provided the largest lateral movement for modeling the column rows due to the larger reductions in the strength and stiffness of the wall. A large lateral movement at the head of the column row can also be seen in the 2D-Equal *B* case. The 2D-Equal *EI* case provided better agreement results in terms of the lateral movements than the 2D-Equal *EA* case, indicating that matching the properties of the columns using an equivalent flexural stiffness is the most suitable approach for calculating the lateral displacements of SCM columns subjected to an embankment load at the toe of the embankment.

5.3. Bending moments

The 3D FEA results were effectively verified using the measured field data corresponding to the settlements and lateral movements of the SCM columns. However, in addition to the settlement and lateral movement of the test embankment, the bending moments and axial loads induced in the SCM columns are required for design purposes in terms of the ultimate limit state, for example, safety against SCM column failure. However, no measured data of the bending moments and axial loads induced in the SCM columns were available in this study due to the lack of field instruments. Consequently, the computed bending moments and axial loads induced in the SCM columns obtained through the 3D-True analysis were considered more reliable and reasonable than those obtained through the 2D analysis (see the corresponding verification in Appendix A), that is, the results of the 3D-True analysis were correct, whereas those of the 2D analysis had to be verified using the results of the 3D-True analysis.

The bending moments induced in the individual SCM columns below the embankment toe (Figure 2(I1,I2)) were computed using the following equations:

$$\sigma_{\max} = \sigma_a + \frac{M(D_{\text{column}}/2)}{I_{\text{column}}} \tag{5}$$

$$\sigma_{\min} = \sigma_a - \frac{M(D_{\text{column}}/2)}{I_{\text{column}}} \tag{6}$$

where $\sigma_{\max}$ and $\sigma_{\min}$ are the maximum and minimum normal vertical effective stresses, respectively, in the SCM column, derived using the 3D and 2D FEA results. $\sigma_{\max}$ and $\sigma_{\min}$ occur at the points on the cross-sectional area that are farthest from a neutral axis. The variation in the normal vertical effective stresses between the integration points is assumed to be linear and can be determined using extrapolation (Chai et al. 2014, 2015). σ_a is the normal vertical effective stress, which is assumed to be distributed equally across the cross-sectional area. M is the bending moment induced in an SCM column determined by solving Equations (5) and (6). From Figure 5, a bending moment in the equivalent column wall is converted into that of an

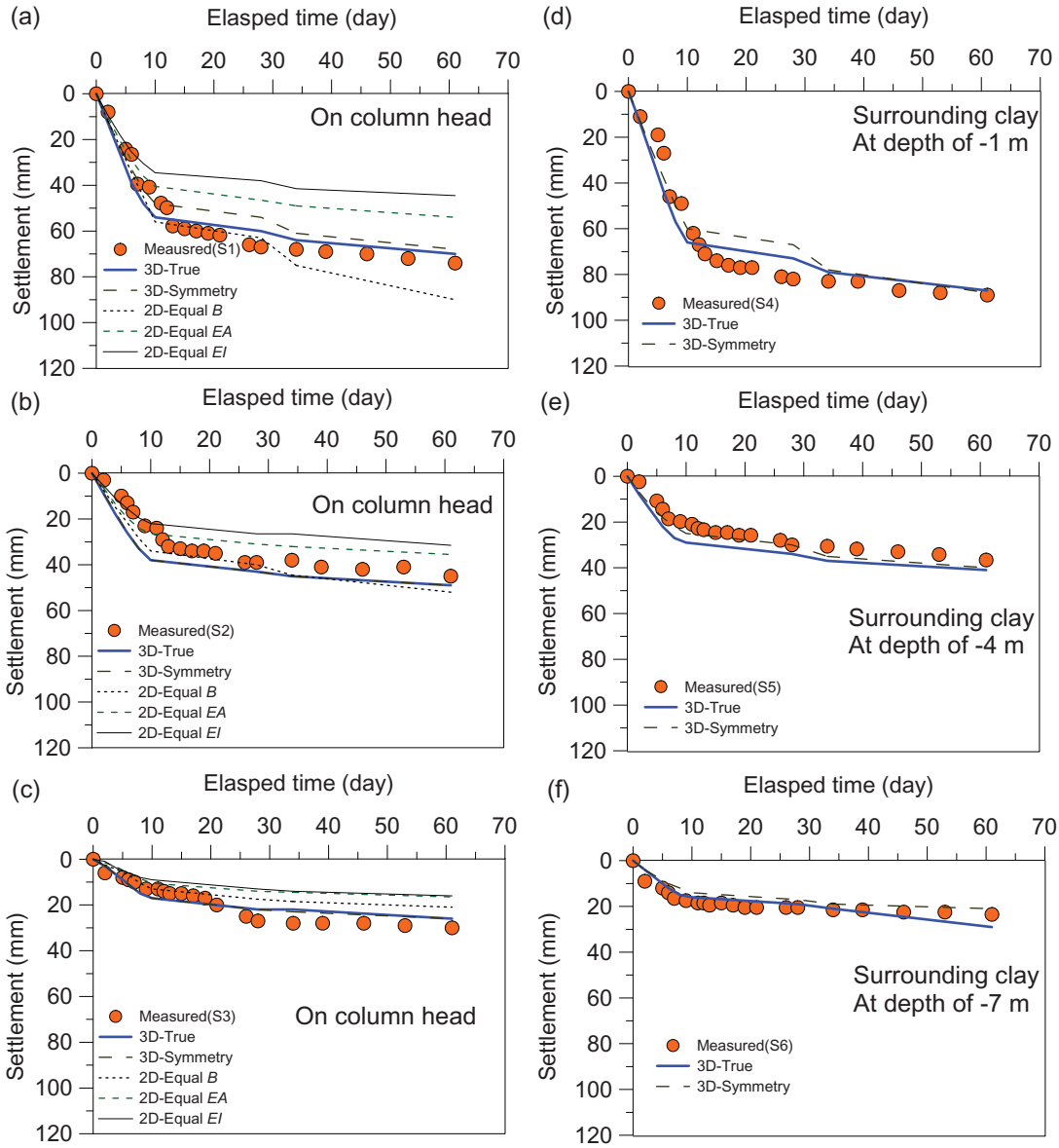

Figure 7. Settlement-time curves for the column group case.

individual SCM column for the column group case as follows:

$$M_{\text{column}} n = M_{\text{wall}}[(n-1)s] \tag{7}$$

where M_{column} is the bending moment of an individual column and M_{wall} is the bending moment of the column wall. The calculated bending moment profiles of each SCM column located at the embankment toe after 61 days of elapsed time for the column group and column row cases are compared in Figure 11(a,b), respectively. These figures show that the overall shapes of the bending moment profiles and the locations of the maximum bending moments obtained from the 3D and 2D analyses are similar, although the magnitudes of the bending moments are different. Insignificant differences in the bending moment profiles exist between the 3D-True and 3D-Symmetry cases.

The maximum bending moment (M_{max}) is located at the interface between the weathered crust and soft clay layers, that is, at a depth of 2 m from the original ground level. The bending moments induced in the SCM column group computed in the 3D-True case are larger than those in the SCM column row due to the influence of the moment of inertia, as expected. The 2D-Equal *EA* and 2D-Equal *EI* cases provide underestimated and overestimated bending moments, respectively, compared with the 3D-True case. However, the 2D-Equal *EA* and 2D-Equal *EI* analyses were better at capturing the shapes of the column group lateral movement profiles than they were at capturing those of the column row lateral movement profiles because the column row slenderness was increased and the interactions among the columns in the column rows were decreased. Thus, the deformation modes changed from translation to flexural. The 2D-Equal *B* case provided the largest bending moments when modeling the column rows due to the larger reductions in both the strength and the stiffness of the column wall.

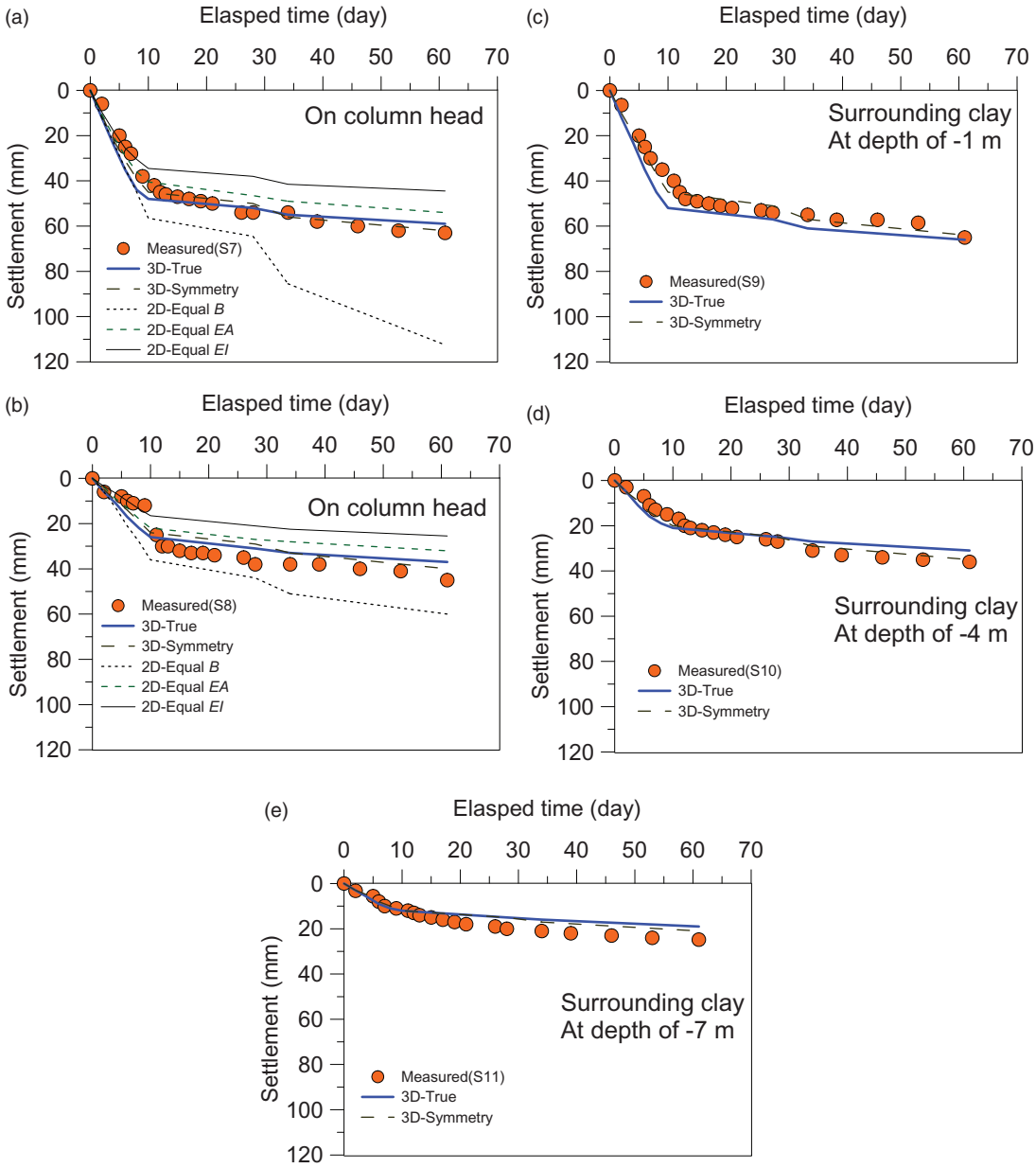

Figure 8. Settlement-time curves for the column row case.

The yield bending moment of an SCM column (M_{yield}) can be determined using the following equation (Jamsawang, Bergado, and Voottipruex 2011, 2016):

$$M_{yield} = \frac{\sigma_f I_{column}}{(D_{column}/2)} \tag{8}$$

where σ_f is the tensile strength of an SCM column, that is, 96 kPa, which is equivalent to 0.16 times q_u (600 kPa), in accordance with Jamsawang, Bergado, and Voottipruex (2011). The value of M_{yield} for a column having a diameter of 1.0 m based on Equation (11) is 9.4 kN-m. The computed M_{max} values for the column group and column row are 7.9 and 3.2 kN-m, respectively, and the corresponding *FSs* against bending moment failure are approximately 1.19 and 2.94. The M_{max} values computed from the 2D-Equal *B* case are 10.4 and 16.5 kN-m for the column group and column row, respectively, which are correspondingly overestimated by 1.32 and 5.16 times compared with the 3D-True case.

5.4. Axial loads induced in the columns

Kitazume and Terashi (2013) suggested that the ultimate carrying load (Q_{ult}) of a single SCM column can be computed depending on the failure mode as follows:

$$Q_{ult}(\text{column failure}) = q_{u(\text{column})}\frac{\pi}{4}D_{column}^2 \tag{9}$$

$$Q_{ult}(\text{soil failure}) = \pi D_{column}\sum(c_{ui}H_i) + (9c_{u(end)})\frac{\pi}{4}D_{column}^2 \tag{10}$$

where $q_{u(column)}$ is the unconfined compressive strength of an SCM column; D_{column} is the diameter of an SCM

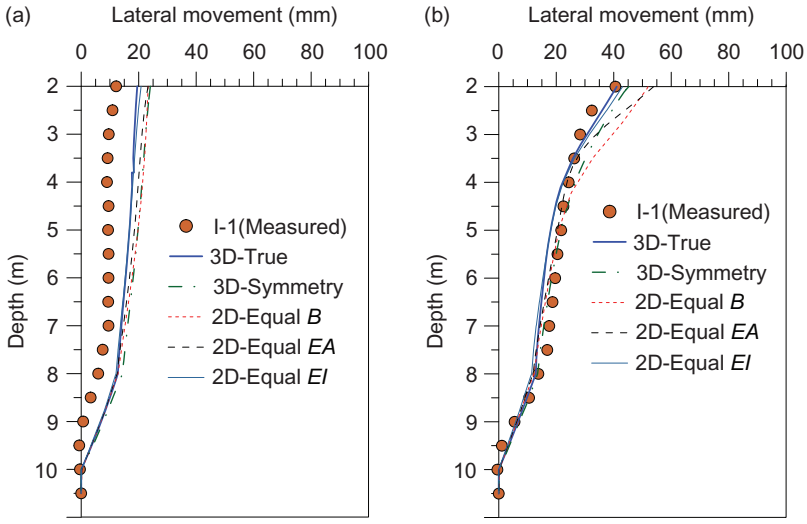

Figure 9. Lateral movement profiles for the column group: (a) end of embankment construction; (b) 61 days of time elapsed after the initiation of embankment construction.

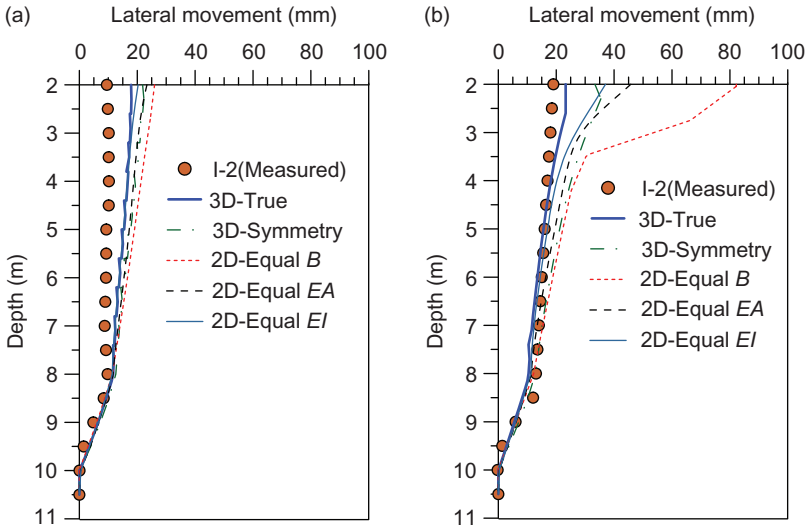

Figure 10. Lateral movement profiles for the column row: (a) end of embankment construction; (b) 61 days of time elapsed after the initiation of embankment construction.

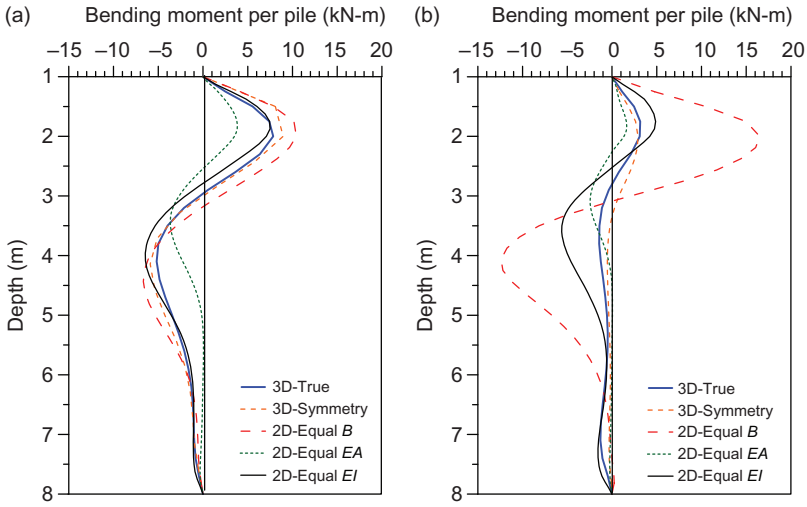

Figure 11. Bending moment profiles at 61 days of elapsed time for the (a) column group and (b) column row.

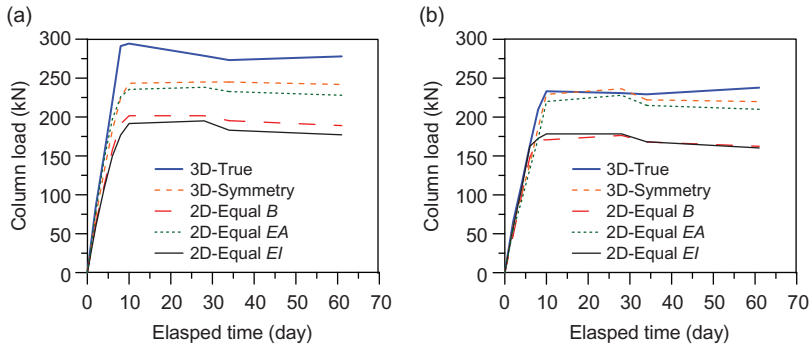

Figure 12. Axial load transfer in the (a) column group and (b) column row.

column; $\sum(c_{ui}H_i)$ is the summation of the product of the undrained shear strength (c_{ui}) of all clay layers and the corresponding thickness of the clay layer (H_i) along the SCM column length; and $c_{u(end)}$ is the undrained shear strength of the clayey soil at the tip of the column. The values of Q_{ult} in the cases of soil failure and column failure were calculated to be 714 and 471 kN, respectively. Thus, the Q_{ult} value of a 1-m-diameter SCM column should be 471 kN. The method for converting the axial load of an equivalent column wall into that of an individual SCM column for the column group case (Figure 5) is as follows:

$$Q_{column}n = Q_{wall}[(n-1)s] \tag{11}$$

where Q_{column} is the axial load of an individual column and Q_{wall} is the axial load of the column wall. Evidently, Q_{column} mainly depends on s; the greater the value of s is, the larger the value of Q_{column}, resulting in a decrease in the SCM column capacity in terms of the *FS* against SCM column failure.

The axial loads in the SCM columns below the embankment crest were computed based on the normal vertical effective stress multiplied by the cross-sectional area of the columns. Figure 12(a,b) shows the computed axial loads acting on the tops of the column group and the column row, respectively, versus the elapsed time. When the embankment height increased to 5.0 m, the maximum column loads in the 3D-True case were 295 and 230 kN for the column group and column row, respectively. Therefore, the *FSs* against SCM column failure of a single column were 1.60 and 2.04 for the column row and column group, respectively. The 3D-Symmetry case provided results consistent with those of the 3D-True case for both the magnitudes and the shapes of the curves, whereas all 2D results showed underestimated column loads compared with those of the 3D-True case, implying that a risk of column failure exists.

5.5. Slope stability analysis

The functions of the SCM column group and the SCM column row in this study are to improve the stability of an embankment insomuch that a slope stability analysis can be performed to determine the induced *FS* against the slope failure of the improved ground. A method involving a reduction in the shear strength (i.e., in *phi-c*) was employed to compute the *FS* against slope failure. In the approach consisting of a reduction in *phi-c*, the shear strength parameters of the soil tan ϕ and c are decreased until soil structure failure occurs. A total multiplier ($\sum M_{sf}$) is used to characterize the shear strength values of the soil for a given stage of the slope stability analysis:

$$\sum M_{sf} = \frac{\tan\phi_{input}}{\tan\phi_{reduced}} = \frac{c_{input}}{c_{reduced}} \tag{12}$$

where $\tan\phi_{input}$ and c_{input} denote the shear strength parameters inputted for sets of the soil materials and $\tan\phi_{reduced}$ and $c_{reduced}$ denote the decreased values of the shear strength parameters in the slope stability analysis. At the beginning of the computation, $\sum M_{sf}$ is set to 1.0 to provide the unreduced values for all material strengths. An increase in *Msf* is used to define an increase in the shear strength in the initial computation step. The last step provides a full development of the failure mechanism. Therefore, the *FS* against slope failure can be computed as follows:

$$\text{FS} = \text{Value of}\sum M_{sf}\ \text{at failure} = \frac{\text{Input strength}}{\text{Reduced strength at failure}} \tag{13}$$

Table 6 shows the *FSs* against slope failure computed in the 2D and 3D analysis cases. The results of all 2D analysis cases and the 3D-Symmetry case underestimated the *FSs* compared with the 3D-True case, but the 3D-Symmetry case provided an *FS* similar to that of the 3D-True case. Because true 3D effects can spread soil movements in all directions, the embankment weight is reduced, but the strengths of the foundation soils remain the same, resulting in the maximum *FS*.

Table 6. Factor of safety for each case.

	Factor of safety against slope failure	
Case	Column group	Column row
3D-True	1.55	1.55
3D-Symmetry	1.36	1.39
2D-Equal *B*	1.20	1.23
2D-Equal *EA*	1.17	1.17
2D-Equal *EI*	1.21	1.20

6. Discussion

A comparison of the data obtained through either analyses or measurements (as described in Sections 5.1–5.5)

Table 7. Summary of correction factors used to convert the 2D results into 3D results.

Case	S_{max} (mm)	Correction factor	δ_{max} (mm)	Correction factor	Q_{max} (kN)	Correction factor	M_{max} (kN)	Correction factor	*FS*	Correction factor
Column group										
3D-True	70	1.00	41	1.00	294	1.00	7.9	1.00	1.55	1.00
3D-Symmetry	68	1.03	45	0.91	245	1.20	9.0	0.88	1.36	1.14
2D-Equal *B*	90	0.78	52	0.79	202	1.46	10.4	0.76	1.20	1.29
2D-Equal *EA*	54	1.30	54	0.76	195	1.51	3.8	2.08	1.17	1.32
2D-Equal *EI*	45	1.56	43	0.95	238	1.24	7.5	1.05	1.21	1.28
Column row										
3D-True	59	1.00	23	1.00	238	1.00	3.2	1.00	1.55	1.00
3D-Symmetry	62	0.95	33	0.70	236	1.01	2.9	1.07	1.39	1.12
2D-Equal *B*	113	0.52	82	0.28	176	1.35	16.5	0.19	1.23	1.33
2D-Equal *EA*	54	1.09	46	0.50	178	1.34	2.5	1.28	1.17	1.32
2D-Equal *EI*	39	1.51	37	0.60	228	1.04	5.6	0.57	1.20	1.29

illustrates that, when simulating the performance of an embankment over soft clay that has been improved using fixed SCM columns, a 2D analysis under designated plane strain conditions through 2D-Equal *B*, 2D-Equal *EA* or 2D-Equal *EI* can provide acceptable results for predictions of the settlements of a column group and column row; the exception is the 2D-Equal *B* case when modeling a column row. However, these 2D analyses may yield incorrect simulation results regarding the lateral movements, the axial loads induced in the SCM columns, the bending moments in the SCM columns under the embankment toe and the *FSs* against slope failure. These inaccuracies occur because the SCM columns are modeled as continuous walls in the 2D analysis; consequently, the soil movements between the surrounding clays and columns are unrealistic, resulting in incorrect predictions of the lateral movements, axial loads induced in the SCM columns, bending moments induced in the SCM columns and *FSs* against slope failure.

The 2D-Equal *EA* and 2D-Equal *EI* analyses more accurately predicted the lateral movement profiles. However, the 2D-Equal *EA* analysis underpredicted and overpredicted the bending moments induced in the SCM columns because of the basic constraints of the 2D analysis. Generally, an SCM column has a compressive strength that is greater than its flexural and/or tensile strength. Thus, the SCM columns located below the embankment toe might undergo tensile failure. Moreover, all of the 2D analyses underestimated the axial loads induced in the columns. Therefore, the *FSs* against bearing capacity failure were higher than the required values, leading to unexpected failures of the columns located below the embankment crest. Finally, the 2D analyses underestimated the *FSs* against slope failure. The analysis results show that the 3D model rather than the 2D plane strain model with an extended column wall is more suitable for precisely analyzing and designing an embankment over a soft clay layer improved using SCM columns, especially when the bending moments, axial loads induced in the columns, and *FSs* against slope failure must be captured accurately. Finally, the correction factors for the maximum settlement (S_{max}) and lateral movement (δ_{max}) of an SCM column, the maximum axial load (Q_{max}) and bending moment (M_{max}) in an SCM column, and the *FS* against slope failure that are needed to convert the 2D analysis results into 3D analysis results are presented in Table 7. Note that the field test results of only one case study were used in this research, thereby limiting any possible future use of the proposed correction factors summarized in Table 7. Thus, various types of installation patterns from different case studies will be investigated to obtain additional correction factors in future studies.

7. Conclusions

The behavior of a test embankment over a soft clay layer stabilized through the construction of a fixed SCM column group and fixed SCM column row was studied using both 3D FEA and 2D FEA. Based on data measured in the field and numerical simulation results, the following conclusions were drawn:

1. The 3D-Symmetry case can accurately simulate the performances of the SCM column group and column row under embankment loads compared with the observed data and simulated results of the 3D-True case, implying that the 3D-Symmetry analysis, which requires a relatively short calculation time due to the lower total number of elements than 3D-True (approximately 10 times fewer), is sufficient to capture the overall performances.
2. A comparison of the results of the 3D-True case and all 2D FEA cases indicated that, in terms of the SCM column settlement, 2D analysis is able to provide acceptable simulation results with the exception of the 2D-Equal *B* case for column rows. However, 2D analysis yields incorrect results for the lateral movements under the embankment toe, the bending moments and the axial loads induced in the columns in addition to the *FS* against slope failure because the interactions between the clay layers and between the walls and the surrounding clays are prevented by the continuous column walls, which are modeled in the 2D analyses instead of using actual columns.
3. 3D analysis is recommended when accurate values of the bending moments and axial loads induced in the columns as well as the *FSs* against slope failure are required. Accordingly, correction factors for converting the 2D analysis results into 3D analysis results were proposed in this study.
4. A comparison of the 2D-Equal *B*, 2D-Equal *EA*, and 2D-Equal *EI* results indicated the following: (a) in terms

of the settlements and lateral movements of the columns, the 2D-Equal *B* case provided the largest settlements because its largest improvement area ratio and lowest stiffness resulted in a larger stress concentration in the column and a lower stiffness; (b) the 2D-Equal *B* case provided the largest bending moment induced in a column, indicating that 2D-Equal *B* is the most conservative case with regard to design; (c) regarding the *FS* against slope failure, all 2D analysis methods provided underestimated values and are thus conservative regarding design purposes.

5. The column wall pattern is more beneficial than the column group pattern in terms of settlements, lateral movements, bending movements in the columns, axial loads induced in the columns and *FSs* against slope failure. Fixed SCM columns can reduce the settlement of the soft clay layer under the embankment weight and accelerate the settlement rate because of the considerably high stiffness of the column materials.

Disclosure statement

No potential conflict of interest was reported by the authors.

Funding

The research was funded by the Faculty of Engineering, King Mongkut's University of Technology, North Bangkok, under Grant [No. ENG-59-07]. The authors also extend their appreciation to the Thailand Research Fund (TRF) and King Mongkut's University of Technology Thonburi (KMUTT) for granting financial support through the TRF Basic Research Contract [No. BRG 6080011].

References

Abusharar, S. W., and J. Han. 2011. Two-Dimensional Deep-Seated Slope Stability Analysis of Embankments over Stone Column-Improved Soft Clay. *Engineering Geology* 120 (1–4): 103–110. doi:10.1016/j.enggeo.2011.04.002.

Abusharar, S. W., J. J. Zheng, and B. G. Chen. 2009. Finite Element Modeling of the Consolidation Behavior of Multi-Column Supported Road Embankment. *Computers and Geotechnics* 36 (4): 676–685. doi:10.1016/j.compgeo.2008.09.006.

Arulrajah, A., and M. W. Bo. 2008. Characteristics of Singapore Marine Clay at Changi. *Geotechnical and Geological Engineering* 26 (4): 431–441. doi:10.1007/s10706-008-9179-2.

Biot, M. 1956. General Solutions of the Equation of Elasticity and Consolidation for a Porous Material. *Journal of Applied Mechanics* 78: 91–96.

Bo, M. W., A. Arulrajah, P. Sukmak, and S. Horpibulsuk. 2015. Mineralogy and Geotechnical Properties of Singapore Marine Clay at Changi. *Soils and Foundations* 55 (3): 600–613. doi:10.1016/j.sandf.2015.04.011.

Borges, J. L., and D. O. Marques. 2011. Geosynthetic-Reinforced and Jet Grout Column-Supported Embankments on Soft Soils: Numerical Analysis and Parametric Study. *Computers and Geotechnics* 38 (7): 883–896. doi:10.1016/j.compgeo.2011.06.003.

Chai, J., S. Shen, W. Ding, H. Zhu, and J. Carter. 2014. Numerical Investigation of the Failure of a Building in Shanghai, China. *Computers and Geotechnics* 55 (7): 482–493. doi:10.1016/j.compgeo.2013.10.001.

Chai, J. C., S. Shrestha, T. Hino, W. Q. Ding, Y. Kamo, and J. Carter. 2015. 2D and 3D Analyses of an Embankment on Clay Improved by Soil-Cement Columns. *Computers and Geotechnics* 68: 28–37. doi:10.1016/j.compgeo.2015.03.014.

Filz, G., T. Adams, M. Navin, and A. E. Templeton. 2012. Design of Deep Mixing for Support of Levees and Floodwalls. In *Grouting and Deep Mixing 2012*, ed. L. F. Johnsen, D. A. Bruce, and M. J. Byle. Reston, VA: ASCE.

Han, J., S. Oztoprak, R. L. Parsons, and J. Huang. 2007. Numerical Analysis of Foundation Columns to Support Widening of Embankments. *Computers and Geotechnics* 34 (6): 435–448. doi:10.1016/j.compgeo.2007.01.006.

Hong, Z. S., S. L. Shen, Y. Deng, and T. Negami. 2007. Loss of Soil Structure for Natural Sedimentary Clays. *Geotechnical Engineering, Proceedings of ICE* 160 (3): 153–159. doi:10.1680/geng.2007.160.3.153.

Hong, Z. S., L. L. Zeng, Y. J. Cui, Y. Q. Cai, and C. Lin. 2012. Compression Behaviour of Natural and Reconstituted Clays. *Géotechnique* 62 (4): 291–301. doi:10.1680/geot.10.P.046.

Horpibulsuk, S., A. Chinkulkijniwat, A. Cholphatsorn, J. Suebsuk, and M. D. Liu. 2012. Consolidation Behavior of Soil-Cement Column Improved Ground. *Computers and Geotechnics* 43: 37–50. doi:10.1016/j.compgeo.2012.02.003.

Horpibulsuk, S., R. Rachan, and A. Suddeepong. 2012. State of the Art in Strength Development of Soil–Cement Columns. *Ground Improvement* 165 (4): 201–215. doi:10.1680/grim.11.00006.

Horpibulsuk, S., R. Rachan, A. Suddeepong, and A. Chinkulkijniwat. 2011. Strength Development in Cement Admixed Bangkok Clay: Laboratory and Field Investigations. *Soils and Foundations* 51 (2): 239–251. doi:10.3208/sandf.51.239.

Horpibulsuk, S., S. Shibuya, K. Fuenkajorn, and W. Katkan. 2007. Assessment of Engineering Properties of Bangkok Clay. *Canadian Geotechnical Journal* 44 (2): 173–187. doi:10.1139/t06-101.

Huang, J., and J. Han. 2009. 3D Coupled Mechanical and Hydraulic Modeling of a Geosynthetic-Reinforced Deep Mixed Column-Supported Embankment. *Geotextiles and Geomembranes* 27 (4): 272–280. doi:10.1016/j.geotexmem.2009.01.001.

Huang, J., and J. Han. 2010. Two-Dimensional Parametric Study of Geosynthetic-Reinforced Column-Supported Embankments by Coupled Hydraulic and Mechanical Modeling. *Computers and Geotechnics* 37 (5): 638–648. doi:10.1016/j.compgeo.2010.04.002.

Jamsawang, P., D. T. Bergado, and P. Voottipruex. 2011. Field Behaviour of Stiffened Deep Cement Mixing Piles. *Proceedings of the Institution of Civil Engineers - Ground Improvement* 164 (1): 33–49. doi:10.1680/grim.900027.

Jamsawang, P., P. Boathong, W. Mairaing, and P. Jongpradist. 2016. Undrained Creep Failure of a Drainage Canal Slope Stabilized with Deep Cement Mixing Columns. *Landslides* 13 (5): 939–955. doi:10.1007/s10346-015-0651-9.

Jamsawang, P., P. Voottipruex, P. Boathong, W. Mairaing, and S. Horpibulsuk. 2015. Three-Dimensional Numerical Investigation on Lateral Movement and Factor of Safety of Slopes Stabilized with Deep Cement Mixing Column Rows. *Engineering Geology* 188: 159–167. doi:10.1016/j.enggeo.2015.01.017.

Jamsawang, P., P. Voottipruex, P. Jongpradist, and D. T. Bergado. 2015. Parameters Affecting the Lateral Movements of Compound Deep Cement Mixing Walls by Numerical Simulations and Parametric Analyses. *Acta Geotechnica* 10 (6): 797–812. doi:10.1007/s11440-015-0417-5.

Jamsawang, P., N. Yoobanpot, N. Thanasisathit, P. Voottipruex, and P. Jongpradist. 2016. Three-Dimensional Numerical Analysis of a DCM Column-Supported Highway Embankment. *Computers and Geotechnics* 72: 42–56. doi:10.1016/j.compgeo.2015.11.006.

Jiang, Y., J. Han, and G. Zheng. 2014. Numerical Analysis of a Pile-Slab-Supported Railway Embankment. *Acta Geotechnica* 9 (3): 499–511. doi:10.1007/s11440-013-0285-9.

Kitazume, M., and M. Terashi. 2013. *The deep mixing method*, 297–298. London: Taylor and Francis Group.

Liu, S. Y., Y. J. Du, Y. L. Yi, and A. J. Puppala. 2012. Field Investigations on Performance of T-Shaped Deep Mixed Soil Cement Column – Supported Embankments over Soft Ground.

Journal of Geotechnical and Geoenvironmental Engineering 138 (6): 718–727. doi:10.1061/(ASCE)GT.1943-5606.0000625.
Lorenzo, G. A., and D. T. Bergado. 2004. Fundamental Parameters of Cement-Admixed Clay — New Approach. *Journal of Geotechnical and Geoenvironmental Engineering* 130 (10): 1042–1050. doi:10.1061/(ASCE)1090-0241(2004)130:10(1042).
Ma, L., S. L. Shen, C. Y. Luo, and Y. S. Xu. 2011. Field Evaluation on the Strength Increase of Marine Clay under Staged Construction of Embankment. *Marine. Georesources and Geotechnology* 29 (4): 317–332. doi:10.1080/1064119X.2011.554965.
Okyay, U. S., and D. Dias. 2010. Use of Lime and Cement Treated Soils as Pile Supported Load Transfer Platform. *Engineering Geology* 114 (1–2): 34–44. doi:10.1016/j.enggeo.2010.03.008.
Oliveira, P. J. V., J. L. P. Pinheiro, and A. A. S. Correia. 2011. Numerical Analysis of an Embankment Built on Soft Soil Reinforced with Deep Mixing Columns: Parametric Study. *Computers and Geotechnics* 38 (4): 566–576. doi:10.1016/j.compgeo.2011.03.005.
Shen, S. L., Z. F. Wang, S. Horpibulsuk, and Y. H. Kim. 2013a. Jet Grouting With a Newly Developed Technology: the Twin-Jet method. *Engineering Geology* 152 (1): 87–95. doi:10.1016/j.enggeo.2012.10.018.
Shen, S. L., Z. F. Wang, J. Yang, and C. E. Ho. 2013b. Generalized Approach for Prediction of Jet Grout Column Diameter. *Journal of Geotechnical and Geoenvironmental Engineering* 139 (12): 2060–2069. doi:10.1061/(ASCE)GT.1943-5606.0000932.
Smethurst, J. A., and W. Powrie. 2007. Monitoring and Analysis of the Bending Behaviour of Discrete Piles Used to Stabilise a Railway Embankment. *Géotechnique* 57 (8): 663–677. doi:10.1680/geot.2007.57.8.663.
Surarak, C., S. Likitlersuang, D. Wanatowski, A. Balasubramaniam, E. Oh, and H. Guan. 2012. Stiffness and Strength Parameters for Hardening Soil Model of Soft and Stiff Bangkok Clays. *Soils and Foundations* 52 (4): 682–697. doi:10.1016/j.sandf.2012.07.009.
Tan, S. A., S. Tjahyono, and K. K. Oo. 2008. Simplified Plane-Strain Modeling of Stone-Column Reinforced Ground. *Journal of Geotechnical and Geoenvironmental Engineering* 134 (2): 185–194. doi:10.1061/(ASCE)1090-0241(2008)134:2(185).
Topolnicki, M. 2013. In Situ Soil Mixing. In *Ground Improvement*, eds. K Kirsch, and A Bell. 3rd edn. London: CRC Press Taylor and Francis Group.
Voottipruex, P., D. T. Bergado, T. Suksawat, P. Jamsawang, and W. Cheang. 2011. Behavior and Simulation of Deep Cement Mixing (Dcm) and Stiffened Deep Cement Mixing (Sdcm) Piles under Full Scale Loading. *Soils and Foundations* 51 (2): 307–320. doi:10.3208/sandf.51.307.
Voottipruex, P., T. Suksawat, D. T. Bergado, and P. Jamsawang. 2011. Numerical Simulations and Parametric Study of Sdcm and Dcm Piles Under Full Scale Axial and Lateral Loads. *Computers and Geotechnics* 38 (3): 318–329. doi:10.1016/j.compgeo.2010.11.006.
Wang, Z. F., J. S. Shen, and W. C. Cheng. 2018. Simple Method to Predict Ground Displacements Caused by Installing Horizontal Jet-Grouting Columns. *Mathematical Problems in Engineering* 2018: 1–11. doi:10.1155/2018/1897394.
Wu, H. N., S. L. Shen, L. Ma, Z. Y. Yin, and S. Horpibulsuk. 2015. Evaluation of the Strength Increase of Marine Clay under Staged Embankment Loading: A Case Study. *Marine. Georesources and Geotechnology* 33(6): 532–541. doi:10.1080/1064119X.2014.954180.
Xu, Y. S., S. L. Shen, Y. J. Du, J. C. Chai, and S. Horpibulsuk. 2013. Modelling the Cutoff Behavior of Underground Structure in Multi-Aquifer-Aquitard Groundwater System. *Natural Hazards* 66 (2): 731–748. doi:10.1007/s11069-012-0512-y.
Yapage, N. N. S., D. S. Liyanapathirana, R. B. Kelly, H. G. Poulos, and C. J. Leo. 2014. Numerical Modeling of an Embankment over Soft Ground Improved with Deep Cement Mixed Columns: Case History. *Journal of Geotechnical and Geoenvironmental Engineering* 140 (11): 04014062. doi:10.1061/(ASCE)GT.1943-5606.0001165.
Yin, Z. Y., J. H. Yin, and H. W. Huang. 2015. Rate-dependent and long-term yield stress and strength of soft Wenzhou marine clay: Experiments and modeling. *Marine Georesources and Geotechnology* 33 (1): 79–91.
Zhang, Z., J. Han, and G. Ye. 2014. Numerical Investigation on Factors for Deep-Seated Slope Stability of Stone Column-Supported Embankments Over Soft Clay. *Engineering Geology* 168: 104–113. doi:10.1016/j.enggeo.2013.11.004.
Zhang, J., J. J. Zheng, B. G. Chen, and J. H. Yin. 2013. Coupled Mechanical and Hydraulic Modeling of a Geosynthetic-Reinforced and Pile-Supported Embankment. *Computers and Geotechnics* 52: 28–37. doi:10.1016/j.compgeo.2013.03.003.

Appendix A

Verification of the 3D FEA results

As mentioned in Sections 5.3 and 5.4, no measured data regarding the axial loads and bending moments induced in the SCM columns were acquired for this study. This section provides a verification of the 3D FEA in terms of both the axial loads and the bending moments induced in the SCM columns through a comparison with actual measurements from similar previous case studies.

Case study 1: SCM column-supported highway embankment

Jamsawang et al. (2016) reported measured field data and 3D simulated data of an SCM column-supported highway embankment over soft Bangkok clay. All SCM columns were installed in a square grid pattern with a spacing of 1.5 m, and the columns had a diameter of 0.6 m and a depth of 14.00 m. A total earth pressure cell was installed at the top of the SCM column to measure the axial loads transferred to the SCM columns.

Case study 2: Concrete pile-reinforced railway embankment

Because no instruments can be applied to measure the bending moment induced in an SCM column, the available measured data of the bending moment profiles of other materials, such as concrete piles, were more appropriate for consideration. Smethurst and Powrie (2007) presented a measured bending moment profile of reinforced bored concrete columns employed to reinforce a railway embankment over Weald clay in the UK. Two hundred piles with a diameter of 0.6 m and a length of 10 m were installed along the embankment length with a spacing of 2.4 m. Strain gauges were installed in the concrete piles to measure the bending moments induced by embankment toe movements.

The results of comparisons between the measured and 3D or 2D FEA data in terms of the axial load versus the time for an SCM column and the distribution of the bending moment with depth for a concrete column from case study 1 and case study 2 are presented in Figures A1 and A2, respectively. It can be verified that the 3D results provide the best agreement with the measured data, whereas the 2D results included both underestimated and overestimated field-measured data.

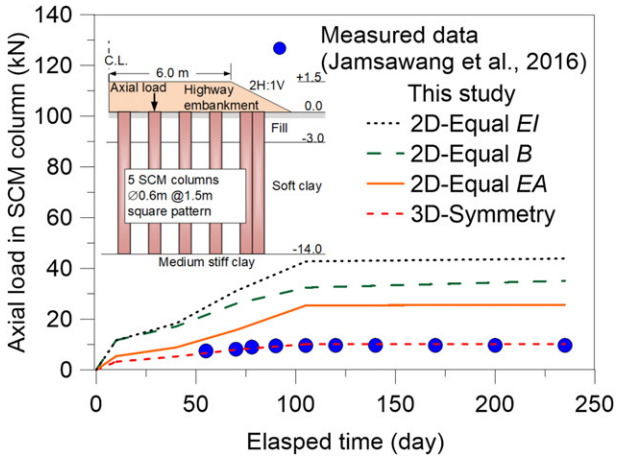

Figure A1. Verification of the axial load induced in an SCM column.

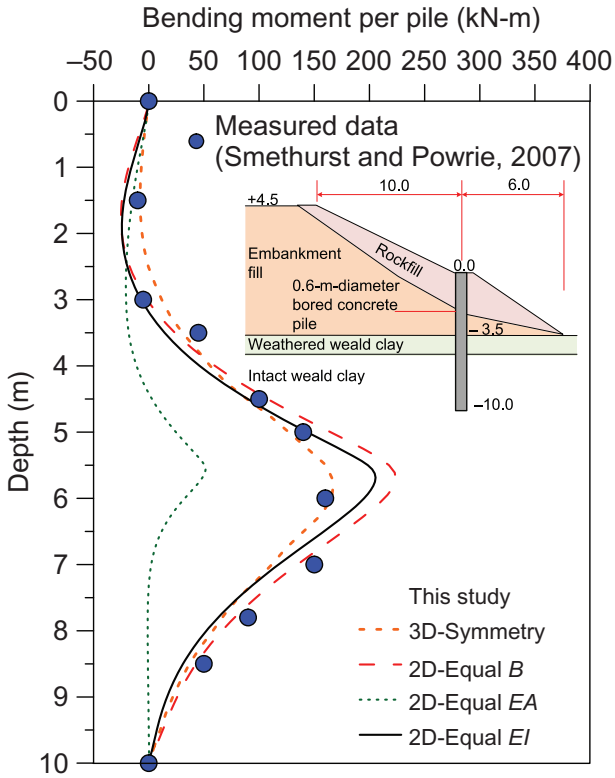

Figure A2. Verification of the bending moment in a concrete pile.

Abbreviations

a_r	improvement area ratio
A	cross-sectional area
B_{wall}	width of the column wall
c	cohesion
c_c	compression index
c_{column}	cohesion of an individual column
c_{input}	input cohesion
c_r	recompression index
$c_{reduced}$	decreased value of cohesion
c_{soil}	cohesion of an individual column
c_u	undrained cohesion
$c_{u(end)}$	undrained cohesion of the clay layer at the tip of the column
c_{ui}	undrained cohesion of the clay layers denoted by the subscript i
D_{column}	diameter of an individual column
e_o	initial void ratio
E	modulus of elasticity
E_{column}	modulus of elasticity of an individual column
E_{soil}	modulus of elasticity of the soil
E_{wall}	modulus of elasticity of the column wall
E_{50}	secant modulus of elasticity at 50% of the unconfined compressive strength, E_{50}^{ref}: secant modulus from a standard drained triaxial compression test, E_{oed}^{ref}: tangential modulus from a consolidation test, E_{ur}^{ref}: unloading/reloading modulus
FS	factor of safety
H_i	thickness of the clay layers denoted by the subscript i
I	second moment of the area
I_{column}	second moment of the area of an individual column
I_{wall}	second moment of the area of the column wall
k	coefficient of permeability
m	power of the stress-level dependency of the stiffness
M	bending moment induced in the column
M_{column}	bending moment of an individual column
M_{max}	maximum bending moment
M_{sf}	multiplier
M_{yield}	yield bending moment
n	number of columns in the plane strain direction
q_u	unconfined compressive strength
$q_{u(column)}$	unconfined compressive strength of an SCM column
Q_{column}	axial load of an individual column
Q_{ult}	ultimate carrying load of a single column
Q_{wall}	axial load of the column wall
s	center-to-center column spacing between two columns in the plane strain direction
S_{max}	maximum settlement
σ_a	normal vertical effective stress
σ_{max}	maximum normal vertical effective stress
σ_{min}	minimum normal vertical effective stress
σ_f	tensile strength
ϕ_{input}	input friction angle
$\phi_{reduced}$	decreased value of the friction angle
ν	Poisson's ratio
ϕ	friction angle
ψ	dilatancy angle
λ^*	modified compression index
κ^*	modified swelling index, ν_{ur}: unloading/reloading Poisson's ratio
γ	unit weight
δ_{max}	maximum lateral movement

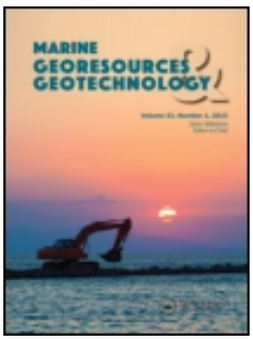

Taylor & Francis
Taylor & Francis Group

Marine Georesources & Geotechnology

ISSN: 1064-119X (Print) 1521-0618 (Online) Journal homepage: http://www.tandfonline.com/loi/umgt20

Equivalent void ratio controlling the mechanical properties of cementitious material-clay mixtures with high water content

Pornkasem Jongpradist, Pitthaya Jamsawang & Warat Kongkitkul

To cite this article: Pornkasem Jongpradist, Pitthaya Jamsawang & Warat Kongkitkul (2019): Equivalent void ratio controlling the mechanical properties of cementitious material-clay mixtures with high water content, Marine Georesources & Geotechnology, DOI: 10.1080/1064119X.2018.1539534

To link to this article: https://doi.org/10.1080/1064119X.2018.1539534

Published online: 12 Jan 2019.

MARINE GEORESOURCES & GEOTECHNOLOGY
https://doi.org/10.1080/1064119X.2018.1539534

Equivalent void ratio controlling the mechanical properties of cementitious material-clay mixtures with high water content

Pornkasem Jongpradist[a], Pitthaya Jamsawang[b] and Warat Kongkitkul[c]

[a]Civil Engineering Department Faculty of Engineering, King Mongkut's University of Technology Thonburi, Bangkok, Thailand; [b]Soil Engineering Research Center, Department of Civil Engineering, King Mongkut's University of Technology North Bangkok, Bangkok, Thailand; [c]Civil Engineering Department Faculty of Engineering, King Mongkut's University of Technology Thonburi, Bangkok, Thailand

ABSTRACT

This research develops a parameter defined as the equivalent void ratio, e'_{st}, which is able to accurately describe the dependence of the mechanical properties of cementitious material-clay mixtures on the influencing parameters, i.e., the mixing proportion, curing time, and initial state of the mixture, for different types of cementitious materials based on the results of unconfined compression, oedometer, and triaxial tests. Besides Portland cement, cementitious materials, such as fly ash and rice husk ash, are considered supplementary cement with different levels of efficiency. This equivalent cementitious material concept is then adapted for parameter development in conjunction with the effective void ratio proposed from our previous study. The developed single parameter, e'_{st}, can assess the mechanical properties of cementitious material-clay mixtures with different types of cementitious materials and under different test conditions.

ARTICLE HISTORY
Received 30 May 2018
Accepted 15 October 2018

KEYWORDS
Ashes; cementitious material-Clay; equivalent cement; efficiency factor; mechanical properties; void ratio

1. Introduction

Soil stabilization techniques have been extensively implemented to enhance the engineering properties of the marine clays for applications of both using dredged clays as backfill for land reclamation (e.g., Kang, Tsuchida, and Athapaththu 2016; Liu et al. 2017) in offshore and ground improvement for foundations of structures as well as excavation supported structures (e.g., Jamsawang et al. 2016; Wonglert et al. 2018; Jamsawang et al. 2018) in onshore. The technique uses chemical additives, generally ordinary Portland cement (OPC) in the form of either slurry or powder, to mix with the soft marine clays. The dredged clays and clay deposit typically have high initial water content. Yet, the mixing method for construction of soil cement column (SCC) using cement slurry by jet mixing involves breaking up the soil matrix by a high pressure water jet following with the cement grout. The method yields high water content in the cement-clay mixture. Since the strength of the SCC is governed by the water-to-cement ratio (Miura, Horpibulsuk, and Nagaraj 2001), a significant amount of OPC has to be consumed in cement-treated clay at high water content, resulting in a substantially higher cost when a large volume of backfill materials or large area replacement ratio (closely spaced SCCs) is needed in the construction. To decrease the cost for construction of SCCs, which is principally dominated by the cost of the cement, it is necessary to either widen the space between the SCCs or to replace the cement with lower cost materials. For the first case, the problem of differential settlement between treated and untreated soils is often encountered. The solutions in current use include load transfer platforms (incurring additional cost) and recently, T-shaped cement columns (e.g., S. Y. Liu et al. 2012; Phutthananon et al. 2018) and stiffened deep cement columns (e.g., Voottipruex et al. 2011; Wonglert and Jongpradist 2015; Wonglert et al. 2018), which were proven to be effective with respect to both performance and cost. Some research has also been conducted on partially replacing OPC with industrial ashes, such as fly ash (FA) (e.g., Horpibulsuk, Rachan, and Raksachon 2009; Jongpradist et al. 2010), combination of FA and cement kiln dust (Yoobanpot, Jamsawang, and Horpibulsuk 2017), rice husk ash (RHA) (Jongpradist et al. 2018) and bagasse ash (Jamsawang, Poorahong, et al. 2017). These studies confirmed the potential of utilizing industrial ashes. In terms of the strength (q_u) and stiffness (E_{50}), industrial ashes could be employed as a pozzolanic material for the partial replacement of cement or as an additive to the mixture. This study is concerned with the latter cost reduction method discussed: replacing cement with pozzolanic materials, which can also be attractive for application to land reclamation with dredged clays.

Many researchers have investigated and attempted to assess the mechanical properties of cement-clay mixtures to develop parameters that control those properties. It was revealed that the strength development of cured cement-clay mixture is governed by the total amount of water in the

CONTACT Pornkasem Jongpradist pornkasem.jon@kmutt.ac.th Civil Engineering Department, Faculty of Engineering, King Mongkut's University of Technology Thonburi, 126 Pracha Uthit, Bang Mod, Thung Khru, Bangkok, Thailand 10140
Submitted to: Marine Georesources & Geotechnology

Table 1. Relationships between the unconfined compressive strength and the other mechanical properties of cement-clay mixtures (E_{50} or K or P'_y or $P'_{py} = C \times q_u$).

Property	C	Curing time (day)	R^2	Clay	Location	
E_{50} (sample prepared in laboratory)	114	28	–	Bangkok		Win (1997)
	147	28	0.986	Bangkok	AIT	Lorenzo and Bergado (2006)
	93	7	0.931	Bangkok	KMUTT	Jongpradist et al. (2010)
	88	28	0.786	Bangkok	KMUTT	Jongpradist et al. (2010)
E_{50} (sample taken from construction site)	150–500	28	–	Japan		Futaki et al. (1996)
	100–700	28	–	Tokyo	Port areas	Saitoh et al. (1996)
	50–150	28	–	Boston		Porbaha (1998)
	120–150	28	–	Bangkok		Petchgate et al. (2003)
	100 (avg.)	7	–	Singapore-Marine	River # 3 project	Lee at al. (2005)
	88–200	28	-			
*K	25.17	28	0.987	Singapore-Marine		Xiao (2017)
P'_y Oedometer	1.7	–	–	Tokyo		Terashi et al. (1979)
	1.27	–	–	Ariake		Kamon and Bergado (1992)
	2.2	28	0.990	Ariake		Horpibulsuk et al. (2004)
	1.4	28	0.985	Bangkok	AIT	Lorenzo and Bergado (2006)
	1.58	28	0.904	Bangkok	KMUTT	Jongpradist et al. (2011a)
**P'_{py}	0.598	28	0.981	Singapore-Marine		Cheng et al. (2018)

*Stress-free modulus.
**Primary isotropic compression yield stress.

cement-clay paste (C_w) (Miura, Horpibulsuk, and Nagaraj 2001). The ratio between the water content and cement content (C_w/A_w), was thus suggested as a key parameter controlling the mechanical properties of cement-clay mixture (Horpibulsuk, Miura, and Nagaraj 2005). In the same period of time, Lorenzo and Bergado (2004) developed a new approach for characterizing the compressibility and strength properties of cement-clay mixture by taking the effect of the cement content, curing time, and total clay water content into consideration. It was shown that the ratio between the after-curing void and the cement content (e_{ot}/A_w) is appropriate to assess the compressibility and strength properties of cement-clay mixture at high water contents. A similar concept, which considers the ratio between the void and cement but uses volume fraction, was proposed by Consoli et al. (2007, 2012, 2017) for compacted soil-cement mixtures. However, the investigation by Jongpradist, Youwai, and Jaturapitakkul (2011) revealed that the role played by the water content and void ratio is different in situations where the voids are not fully occupied by water, as is the case for lightweight geomaterials such as air-cement-treated clays. Thus, a new parameter, defined as the effective void ratio (e_{st}), which accounts for the effect of both the water content and void ratio, was developed to assess the mechanical properties of clay-cement mixtures with high water contents in both unsaturated and saturated conditions, including air-cement-treated clays (AC) and deep cement mixing clays.

To assist engineering decisions on the curing time and the mixing proportions for specific target properties of various types of cementitious material-clay mixtures, a single parameter that is capable of describing their mechanical properties is needed. This paper begins with a preliminary investigation on the available data of unconfined compressive strengths, q_u and moduli of cement-FA-clay mixtures from the literature to clarify the role played by the FA on the mixture properties, followed by the conceptual development of a parameter. The changes of the structure of the mixtures are observed using scanning electron microscopy (SEM). Together with the additional testing results presented in this study, the assessment of the mechanical properties of mixtures with various types of cementitious materials under different test conditions using the new parameter is presented. Furthermore, the development of strength and other mechanical properties in the mixtures with different types of cementitious materials is investigated relative to curing time.

2. Preliminary investigation

2.1. Relationships among the mechanical properties of cementitious material-clay mixtures

The investigations to evaluate and understand the behavior of cementitious material-clay mixtures commonly begin with the strength and deformation characteristics, which are based on unconfined compression (UC) tests (e.g., Futaki, Nakano, and Hagino 1996; Saitoh et al. 1996; Win 1997; Porbaha 1998; Miura, Horpibulsuk, and Nagaraj 2001; Petchgate, Jongpradist, and Panmanajareonphol 2003; Lee et al. 2005; Lorenzo and Bergado 2006 (for cement-clay mixture); Jongpradist et al. 2010 (for cement-FA-clay mixture)). Because the most popular application of SCCs is in the construction of foundations for structures, roads, and taxiways for airports, the current design method uses 50% of the strength. Therefore, the q_u and the modulus of elasticity in terms of the secant (50% of q_u) modulus, E_{50}, are commonly investigated from the tested results. For cement-clay mixtures, the investigations have been extended to the compressibility characteristics by oedometer, K_o consolidation and isotropic compression tests (e.g., Terashi et al. 1979; Kamon and Bergado 1992; Horpibulsuk, Miura, and Bergado 2004; Lorenzo and Bergado 2004; Jongpradist, Youwai, and Jaturapitakkul 2011; Ouhadi et al. 2014; Xiao 2017; Cheng et al. 2018) and undrained shear behavior by consolidated undrained triaxial compression (TC) tests (e.g., Horpibulsuk, Miura, and Bergado 2004; Lorenzo and Bergado 2006; Jongpradist, Youwai, and Jaturapitakkul 2011; Subramaniam, Sreenadh, and Banerjee 2016). The yield stress, P'_y, and maximum deviatoric stress, q_{max}, are also often considered under those testing conditions. As a result, plenty of data of q_u and E_{50} and some data of P'_y are available. For cement-clay mixtures, the role played by the amount of cement in the mixture is the degree of

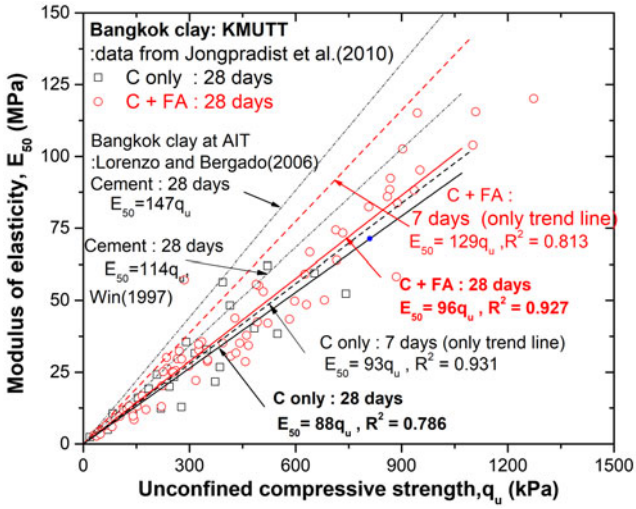

Figure 1. Relationship between the modulus of elasticity (E_{50}) and the unconfined compressive strength of cement- and cement-FA-treated clay.

cementitious bonding and the increasing amount of cementitious products (which in turn makes the void reduced). The increasing cement content results in higher mechanical properties, such as q_u, P'_y, q_{max} and E_{50}. Moreover, it appears that there are relationships among these mechanical properties, particularly q_u, as quantified by many past reports, the results of which are summarized in Table 1. Therefore, it is logical that a parameter that is capable of characterizing q_u should be able to assess the other mechanical properties.

In this section, the relationships between q_u and the other mechanical properties are considered. Because the investigation of the mechanical properties of cement-clay mixtures with added pozzolanic materials is still a relatively new area of research, only data from the UC tests are available. The relationship between q_u and E_{50} of cement-clay mixtures with added FA from a previous study (Jongpradist et al. 2010) on Bangkok clay is plotted in Figure 1, together with the trend lines of some cement-clay mixtures from previous studies. The data covers cement contents from 10 to 30%, water contents of 130, 160, and 200% and FA contents from 10 to 30% with curing times of 7 and 28 d. The figure indicates a good correlation between q_u and E_{50} for cement-FA-clay mixtures. Moreover, the q_u and E_{50} of cement-clay mixtures both with and without FA can be fitted with a fair coefficient of determination. This result shows that the mechanical properties of cement-FA-clay mixtures are similar to those of mixtures without FA. The idea that the parameter capable of characterizing q_u should be able to characterize other mechanical properties can be logically applied to cement-clay mixtures with added FA and most likely to other cementitious materials. The added FA is considered to act as a complementary cementing agent with a level of efficiency.

2.2. Changes in microstructures of treated clay with different cementitious materials by SEM investigation

The microstructure of the treated clay by cementitious materials can be investigated by SEM. The SEM is considered to be sufficient since the purpose is to qualitatively support our hypothesis that the cementitious materials act as complementary cement. The samples investigated in this study include the cement-clay mixture (C-only), cement-FA-clay mixture, and cement- RHA-clay mixture. Details of mixture materials and sample preparation are described in section 4.

The observation of C-only, as shown in Figure 2a, illustrates that the major hydration reaction product was CSH covering clay surface in the early stage of 7 days. The CSH products in the fabric forms distribute on clay clusters and some voids between clay particles were found. The ettringite crystals, which are needle–like crystals formed between clay and CSH fabric, can also be observed. At 28 days, an additional amount of CSH fabrics and ettringite crystals were continuously formed over a period of curing to cover the clay surface. This makes clay structure stiffer, resulting in an increase in inter-cluster bonding and therefore higher strength of cement-treated clay. No significant amount of voids was observed. This implies that the amount of voids decreased with increasing curing time because the amount of water in the cement decreased following the OPC hydration and pozzolanic reactions (Jamsawang, Poorahong, et al. 2017; Jamsawang, Nuansrithong, et al. 2017), resulting in strength increasing with time.

Significant changes in the clay structures of cement-FA-clay mixture and cement-RHA-clay mixture are illustrated in Figure 2b and c, respectively. At 7 days, CSH fabric was formed to cover the clay surface similar to those found in the C-only sample. Furthermore, it was observed that the FA and RHA particles were distributed together with the CSH fabric and filled in the void space between clay particles. Thus, the amount of void in clay structure was reduced. At 28 days, more amounts of CSH fabric and ettringite crystals were formed affecting the denser clay structures. The CSH fabric covered both the clay surface and the FA and RHA particles. The abundant CSH fabric along with the FA and RHA particles embedded in the clay structure became a clay matrix. The FA and RHA particles filled the void space in the clay structure which provided reduction in void ratio and increase in strength with the curing time. Therefore, reduction in void ratio of cement-FA-clay mixture and cement-RHA-clay mixture was caused by not only the OPC hydration and pozzolanic reactions but also filling effect of existence of FA and RHA particles.

The advantage of FA and RHA used as cementitious materials was suggested as found by previous studies that the FA and RHA are beneficial to reduce void space of clay particle and enhance clay strength in long term curing (Shaheen, Hooda, and Tsadilas 2014; Wang et al. 2018). Based on the SEM observation, it can be concluded that the formation and the progressive growth of the primary reaction products make the stabilized clay structure become stiffer and denser than untreated clay and result in the increase in strength after curing. The results support our idea that the added ashes act as a complementary cementing agent.

3. Development of the equivalent void ratio

From the above investigation and ideas, our newly developed parameter should be able to assess the mechanical

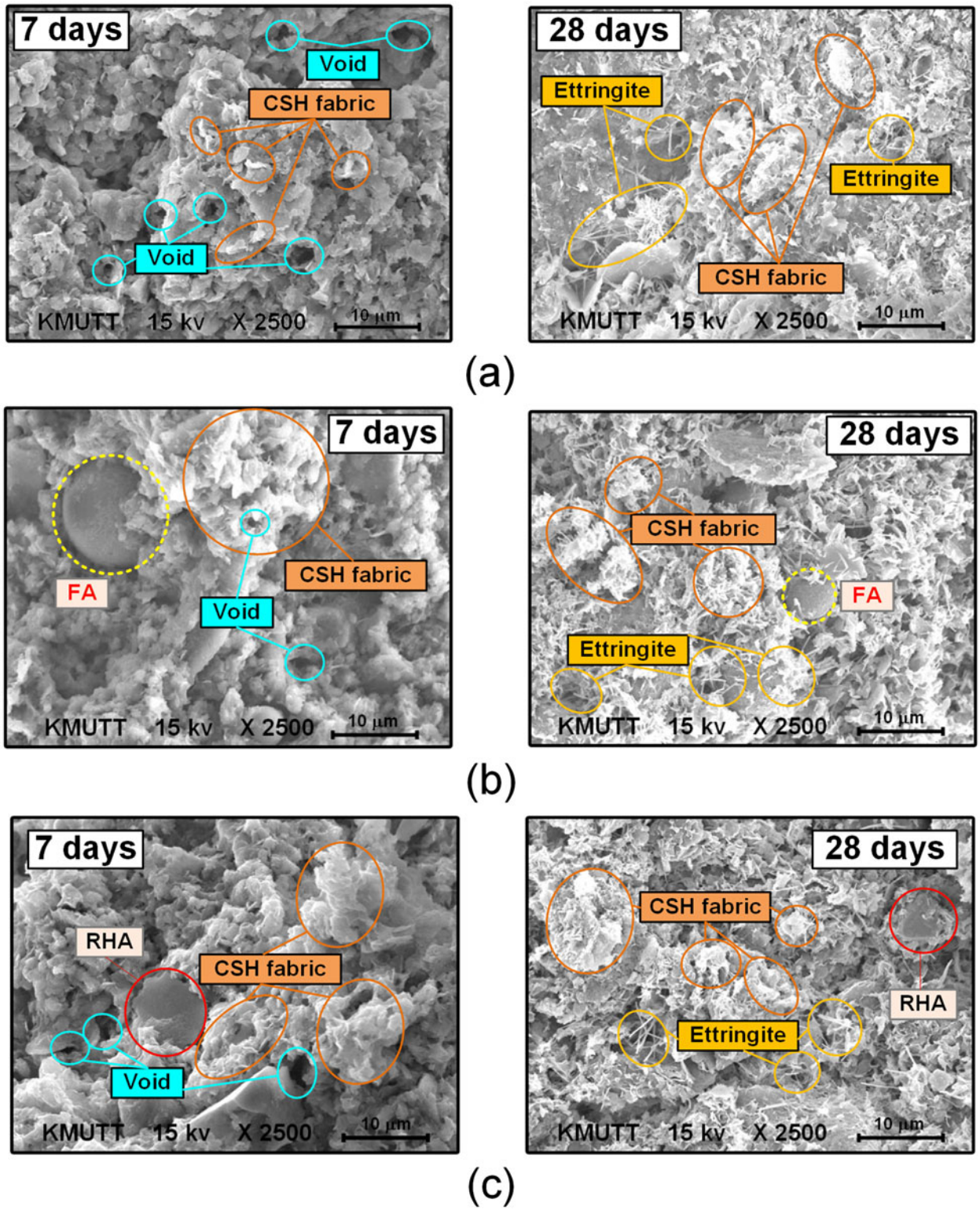

Figure 2. SEM micrographs for treated clay specimens at curing times of 7 and 28 days: (a) Cement-treated clay, (b) cement-FA-clay mixture, and (c) cement-RHA-clay mixture.

properties of cementitious material-clay mixtures that use cement both with and without an additive. The added ashes can be considered as complementary cement which results to cementing bonding and reduction on void ratio of the mixtures. The influencing factors on the mechanical properties of both mixtures are first reviewed to recognize the differences and similarities. Past research on of cement-clay mixtures indicated that their mechanical properties are mainly influenced by the physicochemical properties of the clay, the water content, the cement content, and the curing time and stress (Miura, Horpibulsuk, and Nagaraj 2001; Lorenzo and Bergado 2004; Lee et al. 2005; Horpibulsuk, Miura, and Nagaraj 2005; Jongpradist, Youwai, and Jaturapitakkul 2011; Zhang, Zheng, and Bian 2017), while

those of cement-FA-clay mixture for a specific type of FA and clay are influenced by the amounts of cement and FA, the water content and the curing time (Horpibulsuk, Rachan, and Raksachon 2009; Jongpradist et al. 2010). The physicochemical properties of the clay and cementitious materials are dependent on their composition and mineralogy (Maubec, Deneele, and Ouvrard 2017). Therefore, it is difficult to include the clay and cementitious material types in the parameter. The curing stress is also difficult to be included in the parameter, but it can be separately introduced in an empirical equation for strength characterization (Zhang, Zheng, and Bian 2017). This research thus aims to develop a parameter from the cement and additional cementitious material contents, the curing time and the water content. With this new parameter, the mechanical properties, for instance strength, modulus of elasticity and yield stress, of cement-clay mixtures with and without additional cementitious materials having the same clay and cement type should be accurately assessed.

In principle, the parameter should be developed on the basis of its capability to capture the engineering properties of the mixtures under various initial and loading conditions. Therefore, the effective void ratio, e_{st}, developed by Jongpradist, Youwai, and Jaturapitakkul (2011), is adopted for further development as it includes the influence of clay water content, initial void ratio, cement content, and curing time on the mechanical properties of both saturated and unsaturated cement-clay mixtures under various testing conditions. The e_{st} can be computed by the following relationship:

$$e_{st} = C_w \times \ln(e_{ot}/A_w) \tag{1}$$

where A_w is the cement content reflecting the degree of cementitious bonding while e_{ot} reflects the void amount and can be computed by using the following relationship:

$$e_{ot} = \frac{(1+w_t)G_{st}\gamma_w}{\gamma_t - 1} \tag{2}$$

The G_{st} is the after-curing specific gravity, γ_w is the unit weight of water, w_t is the after-curing water content, and γ_t is the after-curing unit weight. To accommodate our purposes, the after curing parameters can be calculated by the method of normalizing parameters proposed by Lorenzo and Bergado (2004) as empirical equations. The derivation is described in detail in Appendix A. The effect of cement content on void reduction can be noted.

This parameter is able to reflect the final conditions of the cured, treated clay. However, under TC conditions, the subsequent state before being subjected to loading has not yet been considered. Therefore, the pre-shear after-curing void ratio, $e_{ot,ps}$, should be taken into account and can be obtained from following equation:

$$e_{ot,ps} = e_{ot} - (1+e_{ot})\frac{\Delta V}{V} \tag{3}$$

Where e_{ot} is the after-curing void ratio prior to process of consolidation, V is the initial volume, and ΔV is the volume change during the consolidation stage.

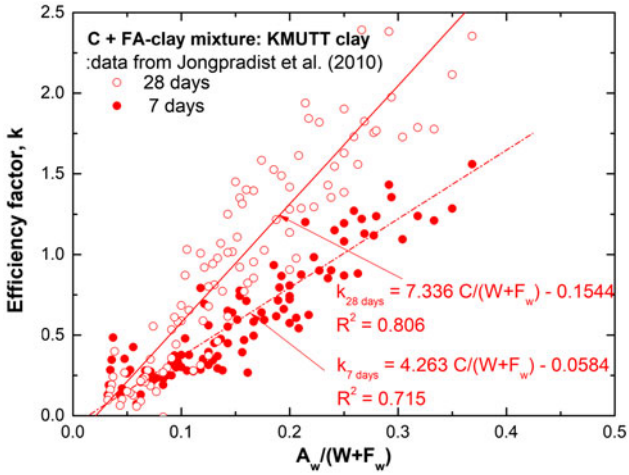

Figure 3. Relationship between the efficiency factor k of FA and $A_w/(W+F_w)$.

As mentioned earlier, the role played by additional ashes is the same as cement, which is to enhance the cementitious bonds and reduce the void between clay clusters, but with different degree of efficiency. This enhancement results in increased mechanical properties, including q_u and E_{50}. Therefore, it is logical to factor in the role of additional cementitious materials by considering them as equivalent to cement. The concept of equivalent cementitious material in concrete technology is thus employed in developing the desired parameter. This concept was proven to be effective in empirical equations to predict the strength of cement-FA-clay mixtures (Horpibulsuk, Rachan, and Raksachon 2009; Jongpradist et al. 2010). In the equivalent cementitious material concept, the effect of the cementitious material is regarded as if it is an equivalent amount of cement, the total cement content thus comes from the cement content and the equivalent content from cementitious material as;

$$\mathrm{A_w^*} = \mathrm{A_w} + \mathrm{kF_w} \tag{4}$$

Where k represents the efficiency factor of the cementitious material, which depends on its grain size distribution and chemical composition, and F_w is the cementitious material content (%).

The value of k can be computed after the strength evaluation with the modified Feret's equation (Papadakis, Antiohos and Tsimas 2002) as described in Eq. (5).

$$q_u = K\left(\frac{1}{W/(A_w + kF_w)} - a\right) \tag{5}$$

K and a are constants that depend on the physicochemical properties of the base clay and cement used, and W is the total water content subtracted by a constant. A previous study (Jongpradist et al. 2010) showed that the constant is equal to 80, and the k values are a linear function of the mixture components, $Aw/(Fw+W)$, in the studied ranges shown in Figure 3, which can be represented by Eq. (6).

$$\mathrm{k} = \mathrm{C_1}\left[\mathrm{A_w}/(\mathrm{W}+\mathrm{F_w})\right] + \mathrm{C_2} \tag{6}$$

The constants C_1 and C_2 depend on the curing time, the type of cementitious material and, most likely, its gradation.

Table 2. Parameters in the modified Feret's equation for cement-clay mixture with added FA or RHA.

		C1	C2	K	a
28 days	FA	7.336	−0.1544	1703	0.0374
	RHA	11.353	−0.0792		
7 days	FA	4.263	−0.0584	1050	0.0529
	RHA	4.319	0.1143		

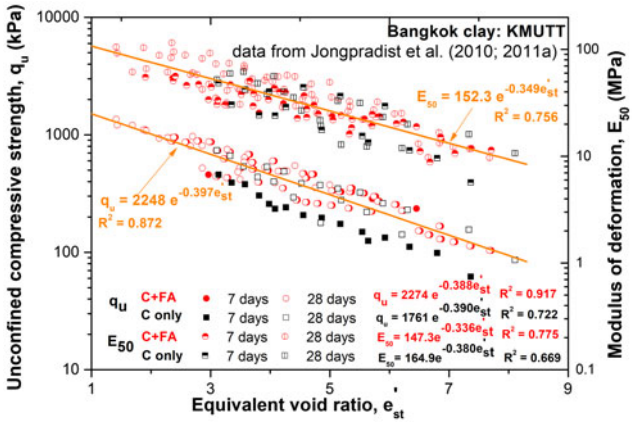

Figure 4. Relationships between the parameter e'_{st} and the unconfined compressive strength and modulus of deformation of cement-treated Bangkok clay with and without FA.

The values of C_1 and C_2 for cement-clay mixtures with added FA are given in Table 2.

Using the above concepts, a new parameter, the equivalent void ratio, e'_{st}, is proposed, which can be calculated using Eq. 7.

$$e'_{st} = C_w \times \ln\left(e_{ot}/A^*_w\right) \tag{7}$$

The derivation by the method of normalizing the parameters yields an empirical relation for parameter e_{ot}, as shown in Eq. (8).

$$e_{ot} = \left[\left(\frac{1+\frac{C_w}{100}G_{so}}{\frac{100}{C_w}+1}\right) \times \left(\frac{\left(\frac{100}{C_w} - 0.012A^*_w - 0.012\log(t) + 0.99\right)\left(1-\frac{A^*_w}{100}\right)^{-0.06072}}{0.0025A^*_w + 0.01\log(t) + 1.008}\right)\right]^{-1} \tag{8}$$

The above equations consider the additional cementitious materials (apart from cement) as additional cement with different enhancement efficiencies of the mechanical properties. Therefore, the equivalent void ratio, e'_{st}, can describe the mechanical properties of not only the cement-FA clay but also the cement clay without the added ash. Moreover, not only the strength but also the other mechanical properties can be assessed by the parameter e'_{st}. The q_u and E_{50} values of cement-FA-clay mixtures are plotted according to the parameter e'_{st} in Figure 4, together with those of cement-clay mixtures without added FA. The e'_{st} values are calculated using Eqs. (7), (8), (4) and (6). It is noted that the values of k are determined based solely on the values of q_u. From the figure, it is evident that e'_{st}, which is capable of characterizing q_u, is also able to characterize E_{50}. The mechanical properties (q_u and E_{50}) of cement-clay mixtures with and without FA can be accurately predicted. Although some scattering can be seen, a satisfactory correlation can be obtained. The result indicates that the use of the equivalent cementitious content concept is appropriate in developing this new parameter. The effectiveness of the developed parameter, e'_{st}, for assessing the other engineering properties of cement-clay mixtures with other cementitious materials is demonstrated in the next section.

4. Experimental investigation

To verify the effectiveness of the developed parameter on characterizing the engineering properties of cement-clay mixtures with added cementitious materials, two sets of testing programs are conducted in this study. The first is the UC tests on cement-clay mixtures with added RHA using the same cement and clay types as the previous study (Jongpradist et al. 2010). This part aims to reveal the effectiveness of this new parameter for different types of cementitious materials. Rice husk ash is chosen because of its potential as an effective cementitious material in concrete technology (e.g., Chindaprasirt et al. 2014; Prasittisopin and Trejo 2018) and recently in soil stabilization (e.g., Hossain 2011; Ashango and Patra 2016). Moreover, it is renewable and available in significant amounts, suggesting its economic potential. The other testing program considers diverse loading conditions of cement-clay mixtures with added FA using the same types of clay, cement and FA that have been considered so far. The data from these experiments include those from the oedometer and consolidated-undrained TC tests. This part aims to demonstrate that the new parameter, which is developed from the q_u, is also applicable to other mechanical properties under various loading conditions.

4.1. Materials

The materials used in this study are soft clay, cement, and industrial ashes (FA and RHA). The soft clay utilized in the research was sampled from a depth of 4–5 m in the soft Bangkok clay layer from a site in King Mongkut's University of Technology Thonburi (KMUTT), Bangkok, Thailand. Table 3 shows the properties of the Bangkok clay used together with those of other clays referred in the study. The q_u of the KMUTT clay ranged from 32 to 34 kPa. The cement utilized in this research was OPC whose chemical composition is given in Table 4.

The FA used in this study was from the same batch as that used by Jongpradist et al. (2010). It was waste FA from Mae Moh Power Plant, Thailand, at a disposal time of 6 months, prepared by grinding such that at least 95% by weight of the powder passing through a No. 325 sieve. The RHA used was a processed waste material incinerated at a controlled temperature (400–800 °C) and atmosphere. The chemical composition of the RHA is given in Table 4. It is black in color, and chemical analysis indicated that the material was principally composed of SiO_2 (93%) and can be used as a pozzolanic material, according to ASTM C618–12a (2012). The silica content of the RHA is much higher than that of the FA. From previous studies on the use of

Table 3. Index and physical properties of clays.

Properties	Bangkok Clay-KMUTT (This study and Jongpradist et al. 2010)	Bangkok Clay-AIT (Lorenzo and Bergado 2004)	Tokyo Clay-Ota/Chuo (HGS Research Consortium 2005)	Singapore Marine Clay*
Liquid limit, LL (%)	117	103	55/104	63–120
Plastic limit, PL (%)	39	43	33/51	39–80
Water content, w (%)	84	76–84	59/96	60–110
Specific gravity, G_S	2.65	2.61	2.70/2.64	–
Total unit weight,γ_t (kN/m^3)	14.6	14.3	16.2/14.4	14–17.5
Dry unit weight, γ_d (kN/m^3)	7.92	7.73	10.21/7.32	–
Initial void ratio, e_i	2.28	2.31	1.59/2.53	1.4–2.5
Soil Classification (USCS)	CH	CH	MH/MH	NA

*Summarized from a few sources and listed in Lee et al. (2005).

Table 4. Chemical compositions of the cement and ashes used in this study.

Chemical Composition	Cement Type I (This study and Jongpradist et al. 2010, 2011a)	Fly Ash (This study and Jongpradist et al. 2010)	Rice Husk Ash
Sio_2 (%)	20.20	48	92.99
Al_2O_3 (%)	5.40	26	0.17
Fe_2O_3 (%)	2.90	10	0.35
$Sio_2 + Al_2O_3 + Fe_2O_3$ (%)	28.50	84	93.51
SO_3 (%)	2.30	0.7	0.11
CaO (%)	63.80	5	0.91
MgO (%)	1.50	2	0.42
Na_2O (%)	2.72	0–2	0.63
K_2O (%)	0.30	0–5	2.82
LOI.	2	3	4.7

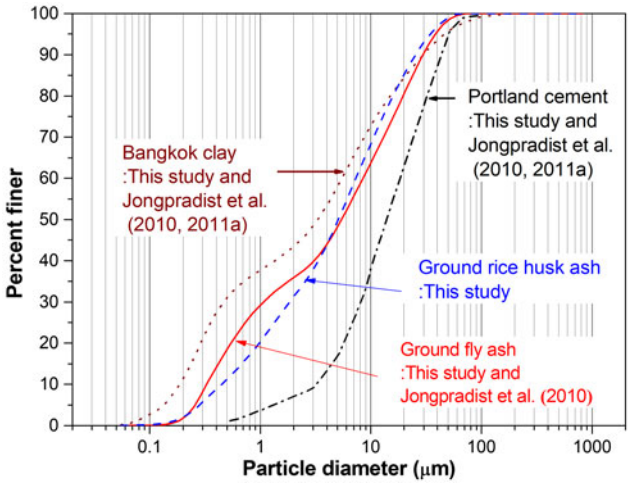

Figure 5. Grain size distributions of ground ashes, Portland cement, and Bangkok soft clay.

agrowaste ashes as constituents in concrete, RHA can be used as a pozzolanic material when it has a fine particle size (Mehta 1977). Moreover, by grinding, the porous structure of the RHA particles collapses, and the negative effect on the water absorption is dramatically reduced (Bui, Hu, and Stroeven 2005). Before being used in the experiments, the RHA was sieved through sieve No. 16 and then ground by a grinding machine to achieve a similar grain size distribution as that of the FA used in previous research (Jongpradist et al. 2010) for the sake of comparison. The grain size distribution is depicted in Figure 5, together with those of the cement, FA and clay used in this study.

4.2. Preparation of the specimens

The Bangkok clay was remolded with water to achieve water contents of 130, 160, and 200% before the cement and ash were admixed, as previously done by Jongpradist et al. (2010), Jongpradist, Youwai, and Jaturapitakkul (2011), and Jongpradist et al. (2011). This amount of water is defined as the remolding clay water content (w^*). The purpose of this intentional increase in the water content is to simulate the water content increase that occurs during the wet jet grouting method of dispensing cement admixtures in deep mixing. The remolded clay with the water content corresponding to the above levels was thoroughly mixed with the cementing slurry (cement-FA or cement-RHA with a water:cement ratio, w/c, of 1:1) by a laboratory mixing machine. Therefore, the C_w of the cement-clay mixture can be computed as follow;

$$C_w = w^* + (w/c)A_w \tag{9}$$

For the UC and TC tests, the uniform paste was tamped into cylindrical molds 35 mm in diameter and 70 mm in height, taking care to prevent any air entrapment before capping. The samples were cured in a humidity room at a maintained humidity of 97% and ambient temperature of 25 °C. After curing for 2–3 days, the molds were dismantled and the samples were wrapped in plastic film before further curing in the humidity room for 7 or 28 d. For the oedometer tests, the paste was directly tamped into the oedometer rings. The friction that may be encountered between the sample and the ring is minimized by smearing silicone grease onto the inner side of the ring before putting a vinyl sheet on the smeared grease layer (Fang et al. 2004). The samples were cured in the humidity room for 28 d.

4.3. Testing program

Unconfined compression tests were conducted on the RHA-added samples after 7 and 28 d of curing. The A_w varies from 10 to 30%. This range is commonly used for SCC in

Table 5. Summary of the testing programs for the one-dimensional and TC tests.

Name of test	Cement content, A_w(%)	Remolding FA, F_w(%)	Curing time water content,w*(%)	(Days)
1	5*,15	10,20*	130,160,200	28
2	10	10*,15**,20*,30*	130,160,200	28

*Only for one-dimensional compression tests.
**Only for TC tests.

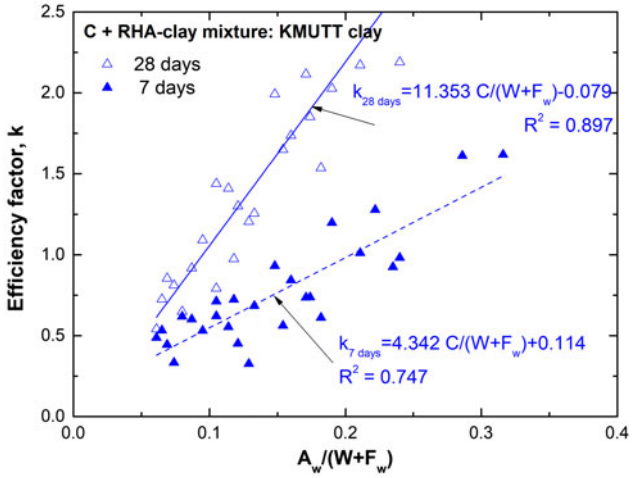

Figure 6. Relationships between the parameter e'_{st} and the unconfined compressive strength and modulus of deformation of cement-treated Bangkok clay with and without ashes.

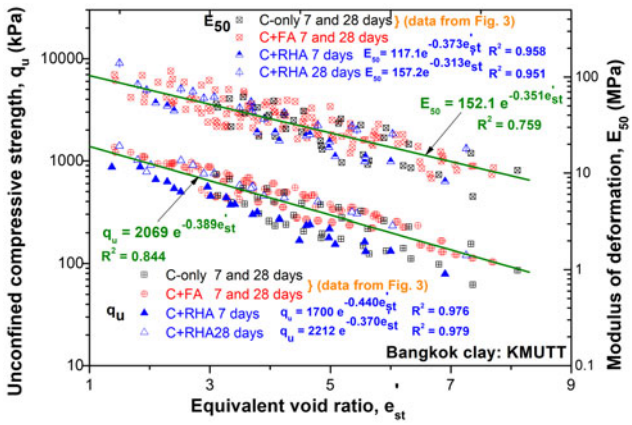

Figure 7. Relationship between the efficiency factor k of RHA and $A_w/(W+F_w)$.

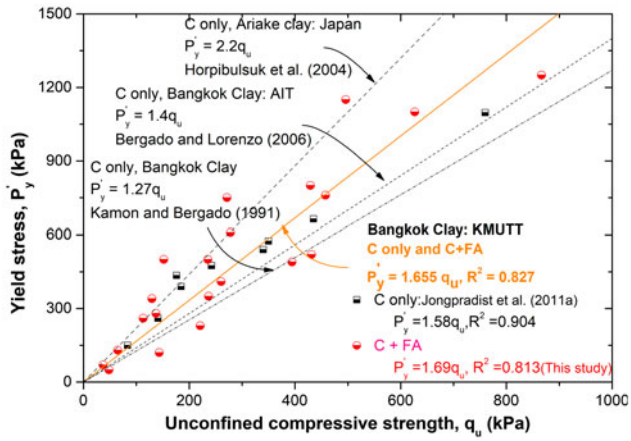

Figure 8. Relationships between the unconfined compressive strength and yield stress of cementitious material-treated Bangkok-KMUTT clay.

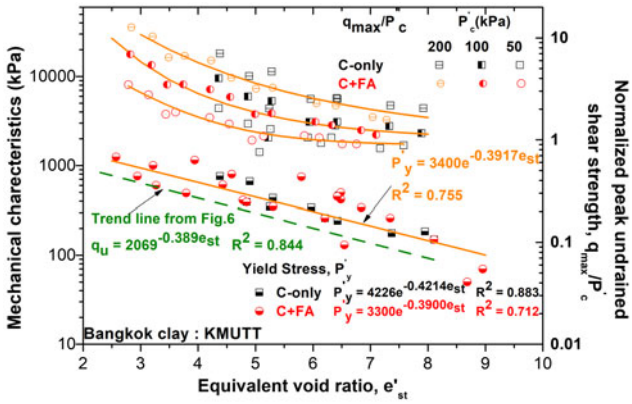

Figure 9. Relationships between the parameter e'_{st} and the mechanical properties of cementitious material-treated Bangkok-KMUTT clay.

soft Bangkok clay. The RHA content varies from 5 to 25% of the dry soil by weight. Prior to testing, the unit weight of the sample was measured. The shearing rate of 1.14% per minute, as used by Jongpradist et al. (2010), and Jongpradist, Youwai, and Jaturapitakkul (2011), is maintained for the UC tests.

One-dimensional compression tests were conducted on the prepared samples (with added FA) that were cured for 28 d. A compression pressure from 40 to 2560 kPa with an incremental loading ratio $\Delta p/p$ of 1.0 was applied, followed by unloading to 40 kPa. The final values of void ratio and water content were measured after the tests. Table 5 shows the testing program in this study.

Consolidated undrained TC tests were conducted on FA-added samples after a 28 d curing following the procedure recommended by Head (1998). The effective confining pressures (pre-shear consolidation pressure, P'_c) were 50, 100, and 200 kPa, with a backup pressure maintained at 200 kPa to ensure a high saturation degree at all levels of testing. The rate of compression was fixed at 1.14% per minute.

5. Results and discussion

5.1. Assessment of the q_u and E_{50} of cement-clay mixtures with different added ashes using e'_{st}

The efficiency factors, k, for each mixing ratio and curing time of RHA in the mixtures are computed by substituting the values of q_u and the mixture proportions into Eq. (5) using the predetermined K and a for each curing time (see Appendix B) listed in Table 2. The k values of RHA have a linear relationship with the mixture component, $A_w/(F_w+W)$, with satisfactory correlations, as shown in Figure 6. Therefore, Eq. (6) can also be used for RHA-cement-clay mixtures. With equal curing times and mixing ratios, the k values of the RHA

Table 6. Summary of the constants A and B for different clays and different mechanical properties.

Clay	Cementitious materials	Type of mixture	Mechanical Property	A	B
Bangkok Clay (KMUTT)	cement, cement + FA,*cement + RHA	SCC	q_u/p_a	20.4	−0.389
			E/p_a	1501	−0.351
			P'_y/p_a	33.6	−0.390
**Bangkok Clay (AIT)	cement	SCC, AC	q_u/p_a	22.3	−0.406
			E/p_a	5339	−0.540
			P'_y/p_a	73.4	0.501
**Tokyo Clay Ota : Chuo	cement	AC	q_u/p_a	25.4 : 12.4	−0.490 : −0.165

*Only for q_u and E.
**From Jongpradist et al. (2011a).

are higher than those of the FA. The constants C_1 and C_2 for the RHA- and FA-added cement-clay are different because of the different cement replacement efficiencies of RHA and FA. This difference in efficiency is due to the difference in the chemical composition as shown in Table 4.

The q_u and E_{50} values of the RHA-added cement-clay mixtures are plotted versus the parameter e'_{st} in Figure 7, together with those of the cement-clay and FA-added cement-clay mixtures (previously illustrated in Figure 4). The testing results of all the treated clays are from similar mixtures made from the same clay (KMUTT site in Bangkok) and the same type of cement. All the mixtures are comprised of clay, water and cement with or without the addition of ashes (FA or RHA). The values of both q_u and E_{50} for the three different mixtures can be appropriately assessed using the parameter e'_{st}. Relations were established for the three types of mixtures, with R^2 values of 0.847 and 0.762 for the fitted data for q_u and E_{50}, respectively. The validity of employing the parameter e'_{st} to assess the mechanical properties of cement-clay mixtures with different types and combinations of cementitious materials is indicated.

5.2. Assessment of the mechanical properties of FA-blended cement-clay mixtures under various testing conditions using e'_{st}

The yield stresses, P'_y of cement-FA-treated clay are correlated to their corresponding q_u at 28 d curing as obtained previously, and the results are shown in Figure 8 (shown as circles). The P'_y demonstrates a linear relationship with the q_u. This result reveals that the yield stresses of the cement-FA-treated clay mixtures are also related to the strength properties and implies that one of them can be predicted from a known value of the other. By correlating the P'_y values of all the samples (mixtures with and without FA) with the q_u values, as illustrated in Figure 8, linear relations are found for cement-clay mixtures with and without FA. In the figure, similar correlations for other cement-clay mixtures from the literature are also shown.

The mechanical properties of cement-clay mixtures with and without FA under various testing conditions are assessed by the parameter e'_{st} in Figure 9. These data include the P'_y from the one-dimensional compression test and the undrained shear strength, q_{max}, from the TC test. In the figure, the q_{max} are normalized to the confining pressure (P'_c). Note that the parameter e'_{st} for the TC conditions must be calculated the e_{ot} shown in Eq. (3). The figure reveals that the parameter e'_{st} is appropriate to assess the P'_y of cement-clay mixtures both with and without added FA for various mixing components. The trend line of q_u from Figure 7 is also shown in Figure 9. The parameter e'_{st} is also proven to be able to assess the normalized q_{max} under each P'_c for both different mixing proportions and different cementitious materials. Not only the q_u and E_{50} values but also the P'_y and q_{max}/P'_c of both types of mixtures could be assessed by this parameter with a fairly high R^2. However, the linear correlation between the parameter e'_{st} and the q_{max}/P'_c cannot be obtained in the semi-log space. Based on the limited data from a few experiments on Bangkok clay with specific types of cementitious materials, the relationship derived by Jongpradist, Youwai, and Jaturapitakkul (2011) to describe the mechanical properties of cement-clay mixture, as shown in Eq. (10), is used for cementitious material-treated clay as follows:

$$q' = Ae^{Be'_{st}} \tag{10}$$

Where q' is any normalized engineering property, i.e., q_u/p_a, P'_y/p_a, and E/p_a, p_a is the atmospheric pressure, and A and B are non-dimensional constants. From the results obtained, the constants A and B for different properties, different types of mixtures and different clays are given in Table 6. The values for different cement-clay mixtures derived from a previous study (Jongpradist, Youwai, and Jaturapitakkul 2011) are also listed in the table. These values depend on the clay composition and mineralogy. For the stress level-dependent properties, such as q_{max}/P'_c, further development by taking the stress level into account is needed.

6. Conclusions

A review of the relationships between the unconfined compressive strength, q_u, and the other mechanical properties of cement-clay mixtures, as well as those of FA-cement-clay mixtures, indicated that these other mechanical properties are related to q_u. This result implies that a parameter with the capability to characterize q_u should also be able to assess these other mechanical properties. From the view point of q_u, the added FA can be regarded as supplementary cement with a certain level of efficiency. The equivalent void ratio, e'_{st}, is developed from the effective void ratio, e_{st}, in conjunction with the equivalent cementitious material concept using the efficiency factors computed from the values of q_u. It is proven that the new parameter can accurately assess the E_{50} values. Additional laboratory tests on cement-treated clays with added cementitious materials under different loading conditions were conducted to validate the effectiveness of this parameter on the assessment of the mechanical

properties. The results indicate that the equivalent cementitious material concept is applicable towards added cementitious material-cement-clay mixtures. The equivalent void ratio is an effective parameter to assess the mechanical properties of cementitious material-clay mixtures. However, limited data from specific soils and certain types of cementitious material has been utilized in development of the parameter, a broader set of experiments is needed to enhance the reliability of this parameter.

Acknowledgments

The authors gratefully acknowledge the financial support from the Thailand Research fund (TRF) under TRF Basic Research Contract No. BRG6080011 and the Faculty of Engineering, King Mongkut's University of Technology, North Bangkok under Contract No. ENG-60-19. The authors would also like to thank Mr. Apiwat Treeleg and Mr. Watee Homtragoon for their assistance with the laboratory experiments.

Disclosure statement

No potential conflict of interest was reported by the authors.

References

Ashango, A. A., and N. R. Patra. 2016. Behavior of Expansive Soil Treated with Steel Slag, Rice Husk Ash, and Lime. *Journal of Materials in Civil Engineering* 28 (7): 06016008. 10.1061/(ASCE)MT.1943-5533.0001547

ASTM C618-12a. 2012. *Standard Specification for Coal Fly Ash and Raw or Calcined Natural Pozzolan for use in Concrete*. West Conshohocken, PA: ASTM International. 10.1520/C0618

Bui, D. D., J. Hu, and P. Stroeven. 2005. Particle Size Effect on the Strength of Rice Husk Ash Blended Gap-Graded Portland Cement Concrete. *Cement and Concrete Composites* 27 (3): 357–66. 10.1016/j.cemconcomp.2004.05.002

Cheng, Q., H. Xiao, Y. Liu, W. Wang, and L. Jia. 2018. Primary Yielding Locus of Cement-Stabilized Marine Clay and its Applications. *Marine Georesources & Geotechnology*. 10.1080/1064119X.2017.1422162

Chindaprasirt, P., T. Sinsiri, W. Kroehong, and C. Jaturapitakkul. 2014. Role of Filler Effect and Pozzolanic Reaction of Biomass Ashes on Hydrated Phase and Pore Size Distribution of Blended Cement Paste. *Journal of Materials in Civil Engineering* 26 (9): 04014057. 10.1061/(ASCE)MT.1943-5533.0000921

Consoli, N. C., A. V. da Fonseca, S. R. Silva, R. C. Cruz, and A. Fonini. 2012. Parameters Controlling Stiffness and Strength of Artificially Cemented Soils. *Géotechnique* 62 (2): 177–83. 10.1680/geot.8.P.084

Consoli, N. C., D. Foppa, L. Festugato, and K. S. Heineck. 2007. Key Parameters for Strength Control of Artificially Cemented Soils. *Journal of Geotechnical and Geoenvironmental Engineering* 133 (2): 197–205. 10.1061/(ASCE)1090-0241(2007)133:2(197)

Consoli, N. C., R. A. Quiñonez, L. E. González, and R. A. López. 2017. Influence of Molding Moisture Content and Porosity/Cement Index on Stiffness, Strength, and Failure Envelopes of Artificially Cemented Fine-Grained Soils. *Journal of Materials in Civil Engineering* 29 (5): 04016277. doi:10.1061/(ASCE)MT.1943-5533.0001819

Fang, Y. S., T. J. Chen, R. D. Holtz, and W. F. Lee. 2004. Reduction of Boundary Friction in Model Tests. *Geotechnical Testing Journal* 27 (1): 3–12. doi:10.1520/GTJ10812

Futaki, M., K. Nakano, and Y. Hagino. 1996. Design Strength of Soil-Cement Columns as Foundation Ground for Structures. In *Proceedings of IS-Tokyo'96, 2nd International Conference on Ground Improvement Geosystems, Grouting and Deep Mixing*. Tokyo, 481–84

Head, K. H. 1998. *Manual of Soil Laboratory Testing: Effective Stress Tests*. New York, NY: John Wiley & Sons

Horpibulsuk, S., N. Miura, and D. T. Bergado. 2004. Undrained Shear Behavior of Cement Admixed Clay at High Water Content. *Journal of Geotechnical and Geoenvironmental Engineering* 130 (10): 1096–105. doi:10.1061/(ASCE)1090-0241(2004)130:10(1096)

Horpibulsuk, S., N. Miura, and T. S. Nagaraj. 2005. Clay-Water/Cement Ratio Identity for Cement Admixed Soft Clays. *Journal of Geotechnical and Geoenvironmental Engineering* 131 (2): 187–92. doi:10.1061/(ASCE)1090-0241(2005)131:2(187)

Horpibulsuk, S., R. Rachan, and Y. Raksachon. 2009. Role of Fly Ash on Strength and Microstructure Development in Blended Cement Stabilized Silty Clay. *Soils and Foundations* 49 (1): 85–98. doi:10.3208/sandf.49.85

Hossain, K. M. A. 2011. Stabilized Soils Incorporating Combinations of Rice Husk Ash and Cement Kiln Dust. *Journal of Materials in Civil Engineering* 23 (9): 1320–7. doi:10.1061/(ASCE)MT.1943-5533.0000310

Jamsawang, P., P. Boathong, W. Mairaing, and P. Jongpradist. 2016. Undrained Creep Failure of a Drainage Canal Slope Stabilized with Deep Cement Mixing Columns. *Landslides* 13 (5): 939–55. doi:10.1007/s10346-015-0651-9

Jamsawang, P., N. Nuansrithong, P. Voottipruex, S. Songpiriyakij, and P. Jongpradist. 2017. Laboratory Investigations on the Swelling Behavior of Composite Expansive Clays Stabilized with Shallow and Deep Clay-Cement Mixing Methods. *Applied Clay Science* 148: 83–94. doi:10.1016/j.clay.2017.08.013

Jamsawang, P., E. Phongphinittana, P. Voottipruex, D. T. Bergado, and P. Jongpradist. 2018. Comparative Performances of Two- and Three-Dimensional Analyses of Soil-Cement Mixing Columns Under an Embankment Load. *Marine Georesources & Geotechnology*. doi:10.1080/1064119X.2018.1504261

Jamsawang, P., H. Poorahong, N. Yoobanpot, S. Songpiriyakij, and P. Jongpradist. 2017. Improvement of Soft Clay with Cement and Bagasse Ash Waste. *Construction and Building Materials* 154: 61–71. doi:10.1016/j.conbuildmat.2017.07.188

Jongpradist, P., W. Homtragoon, R. Sukkarak, W. Kongkitkul, and P. Jamsawang. 2018. Efficiency of Rice Husk Ash as Cementitious Material in High-Strength Cement-Admixed Clay. *Advances in Civil Engineering* 2018: 1. doi:10.1155/2018/8346319

Jongpradist, P., N. Jumlongrach, S. Youwai, and S. Chucheepsakul. 2010. Influence of Fly Ash on Unconfined Compressive Strength of Cement-Admixed Clay at High Water Content. *Journal of Materials in Civil Engineering* 22 (1): 49–58. doi:10.1061/(ASCE)0899-1561(2010)22:1(49)

Jongpradist, P., S. Youwai, and C. Jaturapitakkul. 2011. Effective Void Ratio for Assessing the Mechanical Properties of Cement-Clay Admixtures at High Water Content. *Journal of Geotechnical and Geoenvironmental Engineering* 137 (6): 621–7. doi:10.1061/(ASCE)GT.1943-5606.0000462

Jongpradist, P., S. Youwai, P. Manorat, W. Kongkitkul, and S. Chucheepsakul. 2011. Influence of Curing Stress on One-Dimensional Yielding of Cement-Admixed Bangkok Clay at High Water Content. *Soils and Foundations* 51 (2): 351–7. doi:10.3208/sandf.51.351

Kamon, M., and D. T. Bergado. 1992. Ground Improvement Techniques. In *Proceeding of the 9th Asian Regional Conference on Soil Mechanics and Foundation Engineering*, Bangkok, Thailand, Vol. 2, 526–46

Kang, G., T. Tsuchida, and A. M. R. G. Athapaththu. 2016. Engineering Behavior of Cement-Treated Marine Dredged Clay During Early and Later Stages of Curing. *Engineering Geology* 209: 163–74. doi:10.1016/j.enggeo.2016.05.008

Lee, F. H., Y. Lee, S. H. Chew, and K. Y. Yong. 2005. Strength and Modulus of Marine Clay-Cement Mixes. *Journal of Geotechnical and Geoenvironmental Engineering* 131 (2): 178–86. doi:10.1061/(ASCE)1090-0241(2005)131:2(178)

Liu, S. Y., Y. J. Du, Y. L. Yi, and A. J. Puppala. 2012. Field Investigations on Performance of T-shaped Deep Mixed Soil Cement Column-Supported Embankments Over Soft Ground. *Journal of Geotechnical and Geoenvironmental Engineering* 138 (6): 718–27. doi:10.1061/(ASCE)GT.1943-5606.0000625

Liu, W., Q. Chen, G. Chiaro, and H. Jiang. 2017. Effect of a Cement-Lignin Agent on the Shear Behavior of Shanghai Dredged Marine Soils. *Marine Georesources & Geotechnology* 35 (1): 17–25. doi:10.1080/1064119X.2015.1024903

Lorenzo, G. A., and D. T. Bergado. 2004. Fundamental Parameters of Cement-Admixed Clay—New Approach. *Journal of Geotechnical and Geoenvironmental Engineering* 130 (10): 1042–50. doi:10.1061/(ASCE)1090-0241(2004)130

Lorenzo, G. A., and D. T. Bergado. 2006. Fundamental Characteristics of Cement-Admixed Clay in Deep Mixing. *Journal of Materials in Civil Engineering* 18 (2): 161–74. doi:10.1061/(ASCE)0899-1561(2006)18:2(161)

Maubec, N., D. Deneele, and G. Ouvrard. 2017. Influence of the Clay Type on the Strength Evolution of Lime Treated Material. *Applied Clay Science* 137: 107–14. doi:10.1016/j.clay.2016.11.033

Mehta, P. K. 1977. Properties of Blended Cements Made from Rice-Husk Ash. *ACI Materials Journal* 74 (9): 440–2

Miura, N., S. Horpibulsuk, and T. S. Nagaraj. 2001. Engineering Behavior of Cement Stabilized Clay at High Water Content. *Soils and Foundations* 41 (5): 33–45. doi:10.3208/sandf.41.5_33

Ouhadi, V. R., R. N. Yong, M. Amiri, and M. H. Ouhadi. 2014. Pozzolanic Consolidation of Stabilized Soft Clays. *Applied Clay Science* 95: 111–8. doi:10.1016/j.clay.2014.03.020

Papadakis, V. G., S. Antiohos, and S. Tsimas. 2002. Supplementary Cementing Materials in Concrete Part I: Efficiency and Design. *Cement and Concrete Research* 32 (10): 1533–8. doi:10.1016/S0008-8846(02)00829-3

Petchgate, K., P. Jongpradist, and S. Panmanajareonphol. 2003. Field Pile Load Test of Soil-Cement Column in Soft Clay. In *Proceedings of the International Symposium 2003 on Soil/Ground Improvement and Geosynthetics in Waste Containment and Erosion Control Applications*, AIT, Thailand, 175–84

Phutthananon, C., P. Jongpradist, P. Yensri, and P. Jamsawang. 2018. Dependence of Ultimate Bearing Capacity and Failure Behavior of T-shaped Deep Cement Mixing Piles on Enlarged Cap Shape and Pile Strength. *Computers and Geotechnics* 97: 27–41. doi:10.1016/j.compgeo.2017.12.013

Porbaha, A. 1998. State of the Art in Deep Mixing Technology. Part I: Basic Concepts and Overview. *Ground Improvement* 2 (2): 81–92. doi:10.1680/grim.2000.4.3.91

Prasittisopin, L., and D. Trejo. 2018. Effects of Mixing Time and Revolution Count on Characteristics of Blended Cement Containing Rice Husk Ash. *Journal of Materials in Civil Engineering* 30 (1): 04017262. doi:10.1061/(ASCE)MT.1943-5533.0002133

Saitoh, S., Y. Suzuki, S. Nishioka, and R. Okumura. 1996. Required Strength of Improved Ground. In *Proceedings of IS-Tokyo'96, 2nd International Conference on Ground Improvement Geosystems, Grouting and Deep Mixing*. Tokyo, 557–62

Shaheen, S. M., P. S. Hooda, and C. D. Tsadilas. 2014. Opportunities and Challenges in the Use of Coal Fly Ash for Soil Improvements - A Review. *Journal of Environmental Management* 145: 249–67. doi:10.1016/j.jenvman.2014.07.005

Subramaniam, P., M. M. Sreenadh, and S. Banerjee. 2016. Critical State Parameters of Dredged Chennai Marine Clay Treated with Low Cement Content. *Marine Georesources & Geotechnology* 34 (7): 603–16. doi:10.1080/1064119X.2015.1053641

Terashi, M., H. Tanaka, T. Mitsumoto, Y. Niidome, and S. Honma. 1979. Fundamental Properties of Lime and Cement Treated Soils (2nd Report). *Report of Port and Harbour Research Institute* 19 (1): 33–62. (in Japanese).

Voottipruex, P., T. Suksawat, D. T. Bergado, and P. Jamsawang. 2011. Numerical Simulations and Parametric Study of SDCM and DCM Piles Under Full Scale Axial and Lateral Loads. *Computers and Geotechnics* 38 (3): 318–29. doi:10.1016/j.compgeo.2010.11.006

Wang, D., R. Zentar, N. E. Abriak, and S. Di. 2018. Long-Term Mechanical Performance of Marine Sediments Solidified with Cement, Lime, and Fly Ash. *Marine Georesources & Geotechnology* 36 (1): 123–30. doi:10.1080/1064119X.2017.1320600

Win, S. M. K. 1997. Curing time dependent properties of cement treated Bangkok clay. Master of Engineering Thesis NO. GE-96-31, Asian Institute of Technology, Bangkok, Thailand.

Wonglert, A., and P. Jongpradist. 2015. Impact of Reinforced Core on Performance and Failure Behavior of Stiffened Deep Cement Mixing Piles. *Computers and Geotechnics* 69: 93–104. doi:10.1016/j.compgeo.2015.05.003

Wonglert, A., P. Jongpradist, P. Jamsawang, and S. Larsson. 2018. Bearing Capacity and Failure Behaviors of Floating Stiffened Deep Cement Mixing Columns Under Axial Load. *Soils and Foundations* 58 (2): 446–61. doi:10.1016/j.sandf.2018.02.012

Xiao, H. 2017. Evaluating the Stiffness of Chemically Stabilized Marine Clay. *Marine Georesources & Geotechnology* 35 (5): 698–709. doi:10.1080/1064119X.2016.1219891

Yoobanpot, N., P. Jamsawang, and S. Horpibulsuk. 2017. Strength Behavior and Microstructural Characteristics of Soft Clay Stabilized with Cement Kiln Dust and Fly Ash Residue. *Applied Clay Science* 141: 146–56. doi:10.1016/j.clay.2017.02.028

Zhang, R., J. Zheng, and X. Bian. 2017. Experimental Investigation on Effect of Curing Stress on the Strength of Cement-Stabilized Clay at High Water Content. *Acta Geotechnica* 12 (4): 921–36. doi:10.1007/s11440-016-0511-3

Appendix A

Eq. (2) can be used only if the values of the after-curing parameters are measured. In the cases where the prediction of q_u is desired, e_{ot} must be estimated. The empirical relations of each after-curing parameter must be derived. The normalizing approach proposed by Lorenzo and Bergado (2004) is then adapted to derive the empirical relations for the estimation of w_t, γ_t, and G_{st} from the measured data. It is noted that the data were obtained from the samples with the mixing ratio listed in the one-dimensional compression test program. The normalized plots of each after-curing parameter to obtain the empirical relations can be fitted with the measured data with a high correlation. By substituting the empirical expressions of each after-curing parameter into the fundamental relationship in Eq. (2), the empirical equation to calculate e_{ot} from the basic properties, mixing ratio, and curing time can be expressed as Eq. (8). Figure 10 shows the comparison between the predicted and measured values of e_{ot}. The figure demonstrates that the calculated e_{ot} values using Eq. (8) were in reasonable agreement with the measured values.

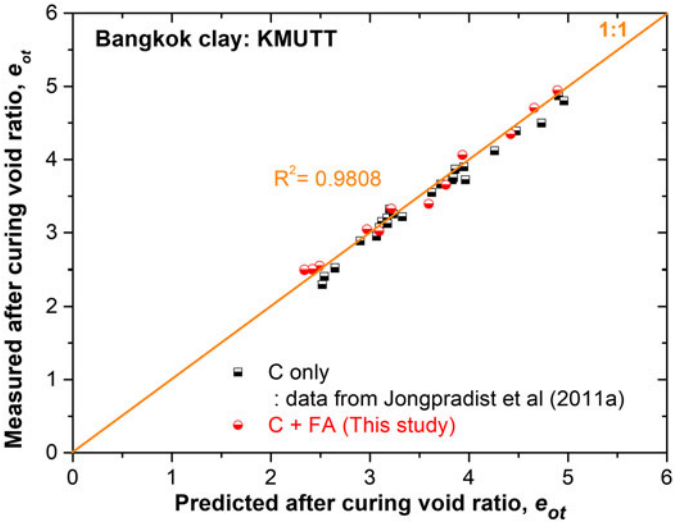

Figure 10 Predicted versus measured after-curing void ratios of cement-treated clay with and without FA.

Appendix B

Prior to attaining k, the values of K and a in Eq. (5) must be determined. This can be done by plotting the relationship between the q_u and A_w/W of the mixtures without ashes. As illustrated in Figure 11, the K values for each curing time can then be calculated from the slopes of the lines, whereas the a values are the y-intercepts divided by the K values. The values for each curing time are listed in Table 2.

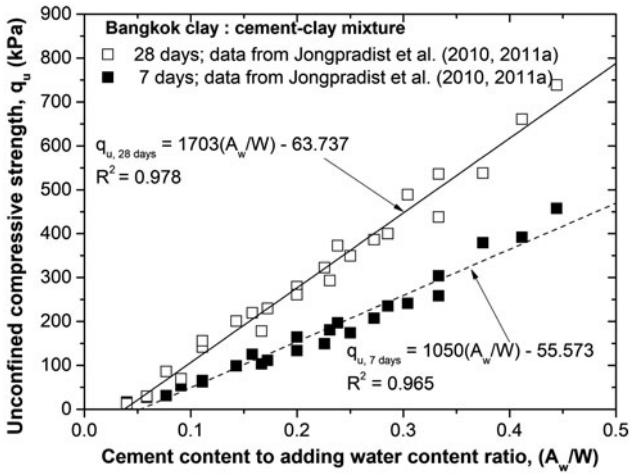

Figure 11 q_u versus A_w/W after curing for 7 and 28 d (modified from Jongpradist et al.2010).

Acta Geotechnica (2019) 14:225–246
https://doi.org/10.1007/s11440-018-0660-7

RESEARCH PAPER

Effectiveness of deep cement mixing walls with top-down construction for deep excavations in soft clay: case study and 3D simulation

Pitthaya Jamsawang[1] · Panich Voottipruex[2] · Pornpot Tanseng[3] · Pornkasem Jongpradist[4] · Dennes T. Bergado[5]

Received: 6 October 2017 / Accepted: 17 April 2018 / Published online: 25 April 2018

Abstract
This paper presents the observed and simulated effectiveness of deep cement mixing walls created using top-down (DCM-TD) construction techniques for a deep excavation in soft Bangkok clay. The wall system consisted of four rows of 0.7-m-diameter DCM columns, and the bracing system consisted of two 0.25-m-thick basement slabs and seven temporary struts. The effectiveness of the wall system compared to that of other wall systems was evaluated using the measured results of previous case studies. A 3D numerical analysis was performed to calculate forces in the basement slabs and bending moments in the DCM wall. Finally, series of parametric analyses of both DCM-TD and deep cement mixing walls created using bottom-up (DCM-BU) construction techniques were carried out, and their results were compared to highlight the effectiveness of DCM-TD and its applicability to excavations at greater depths. The field and numerical results show that DCM-TD is more effective than DCM-BU in terms of the limitations of lateral wall movement, the bending moment in a DCM wall and the thickness of a DCM wall for various depths because of a larger system stiffness. Therefore, DCM-TD is very effective and suitable for use in potential future deep excavations in urban areas.

Keywords Deep excavation · Deep mixing · Finite element · Simulation · Top-down construction in three dimensions · Wall

1 Introduction

Numerous deep excavation projects involving the development of basements for high-rise buildings have been carried out in Bangkok, Thailand, over the past 10 years because of the rapid increase in the economy and size of the city. Deep excavations in soft clays are frequently performed near other buildings and infrastructure [42]. To protect adjacent properties, proper retention systems and construction techniques are required. In the bottom-up (BU) construction technique, sheet pile walls (SPWs), contiguous pile walls (CPWs), and diaphragm walls (DWs) are commonly used as retention systems. SPWs are among the most commonly used to support deep excavations because of their low operational costs, but serious problems may occur, such as larger displacements due to low structural stiffnesses and/or ground movement due to pile driving and extraction. The use of CPWs and DWs comprising thick cast-in-place reinforced concrete walls in the ground can avert the problems of SPWs, but the costs of

✉ Pitthaya Jamsawang
pitthaya.j@eng.kmutnb.ac.th

[1] Department of Civil Engineering, Soil Engineering Research Center, King Mongkut's University of Technology North Bangkok, Bangkok, Thailand

[2] Department of Teacher Training in Civil Engineering, King Mongkut's University of Technology North Bangkok, Bangkok, Thailand

[3] Department of Civil Engineering, Suranaree University of Technology, Nakhon Ratchasima, Thailand

[4] Department of Civil Engineering, Faculty of Engineering, King Mongkut's University of Technology Thonburi, Bangkok, Thailand

[5] School of Engineering and Technology, Asian Institute of Technology, Khlong Nueng, Thailand

such concrete walls are relatively high [38]. Deep cement mixing (DCM) and stiffened DCM (SDCM) walls, which are alternative retaining structures used in BU construction, have been introduced to support deep excavations in soft clays over the past 20 years in Scandinavia, Japan, Germany, the USA and Asia [16]. In a DCM wall, the columns are formed by mixing in situ soil with cement. A DCM wall will typically have a thick cross section due to its low tensile strength and is typically excavated without struts. SDCM walls, which are constructed by inserting steel H-beams into DCM columns to increase the bending moment capacity, are an improvement over DCM walls [15]. Thus, the thickness of a DCM wall can be reduced [42].

The top-down (TD) construction method is used for deep excavations in urban areas when there are extremely strict environmental protections, insufficient working space and extremely short construction times. One advantage of this method is that a basement excavation and a support from the critical path of the project can be removed after the walls and pile foundations are constructed and the first slab is cast. The slabs act as permanent lateral braces for the wall, which are considerably stiffer than cross-lot braces and should minimize adjacent ground movements typically encountered in BU construction [2]. Long [27] summarized the performances of 300 case histories of deep excavations and found no discernible differences in the magnitudes of ground movements associated with both methods. Moormann [29] presented a database of 530 case histories of deep excavations, most of which were through soft soils. The influence of the type of excavation method on performance suggested that the TD systems tended to result in smaller movements than the BU methods. Wang et al. [42] presented a database of 300 case histories of deep excavations through soft soils in Shanghai. The walls that were constructed using the TD method included DWs, CPWs, and SDCM walls, whereas SPWs and DCM walls were constructed using the BU method. They concluded that the TD methods generally resulted in smaller lateral wall displacements. Much research has been conducted using three-dimensional (3D) finite element analysis to investigate the performances of excavations involving DWs, CPWs and SDCM walls with the TD and BU methods in terms of lateral wall movement and settlement behind the walls [10–12, 14, 17, 23, 24, 32, 45]. However, few studies on the performance of DCM walls for deep excavations with TD (DCM-TD) construction in soft clays have been conducted using field observations and numerical investigations.

This paper focuses on evaluations of the effectiveness of a DCM-TD when applied to a deep excavation in soft clay based on a field case study in Bangkok, Thailand. In the field case study, lateral movement profiles around the perimeters of the excavation area and strut forces were observed during the final stage of excavation. The effectiveness of DCM-TD in comparison with other support systems is assessed quantitatively based on field observation data. 3D finite element analysis is used for further investigation. The numerical analysis simulates the lateral wall movement and axial forces in the struts and calculates the force in the concrete slab and the bending moments in the DCM wall induced during excavation. Finally, an investigation of the effect of DCM wall thickness on the lateral movement and bending moment of a DCM wall for excavations at depths greater than that of the case study is numerically carried out to assess the effectiveness and applicability of DCM-TD compared to deep cement mixing walls using the bottom-up (DCM-BU) method.

2 Subsoil conditions

The project construction site was located along Sukhumvit road in central Bangkok, Thailand. The soil profile at this site was a 2-m-thick weathered crust underlain by an 11-m-thick soft clay, a 3-m-thick medium stiff clay, a 14-m-thick stiff clay, and a thick dense sand layer, as shown in Fig. 1a. Detailed laboratory tests were conducted prior to construction to evaluate the geotechnical engineering properties of the foundation soils. The basic physical properties of the tested soils, including natural water content (w_n), liquid limits (LL), plastic limits (PL), wet unit weight (γ), soil specific gravity (G_s) and initial void ratio (e_o), were also characterized. Undrained shear strengths (s_u) obtained from unconfined compression tests were used to characterize the clay types based on strength. These basic properties of the foundation soils are tabulated in Table 1. Conventional oedometer tests and conventional triaxial tests based on consolidated undrained tests were performed on foundation soil specimens taken from the project site at depths of − 1.5, − 7, − 14 and − 18 m for the weathered crust, soft clay, medium stiff clay and stiff clay, respectively, to determine the soil parameters for the numerical simulations. The geotechnical engineering properties of the soils are summarized in the soil profile presented in Fig. 1b–f. The results of the triaxial tests indicate that the effective friction (ϕ') varied from 23° to 28°, whereas the effective cohesion (c') varied from 2 to 30 kPa. These shear strength parameters are consistent with the values for the numerical modeling of Bangkok clays presented in Jamwawang et al. [17]. The ratio of the swelling index (c_s) to the compression index (c_c) obtained from the oedometer tests ranged from 0.13 to 0.25 for stiff and soft clays, which falls within the range of c_s/c_c for the Bangkok subsoils reported by Bergado et al. [3]. The OCR profiles determined based on the oedometer tests show that the weathered crust, medium

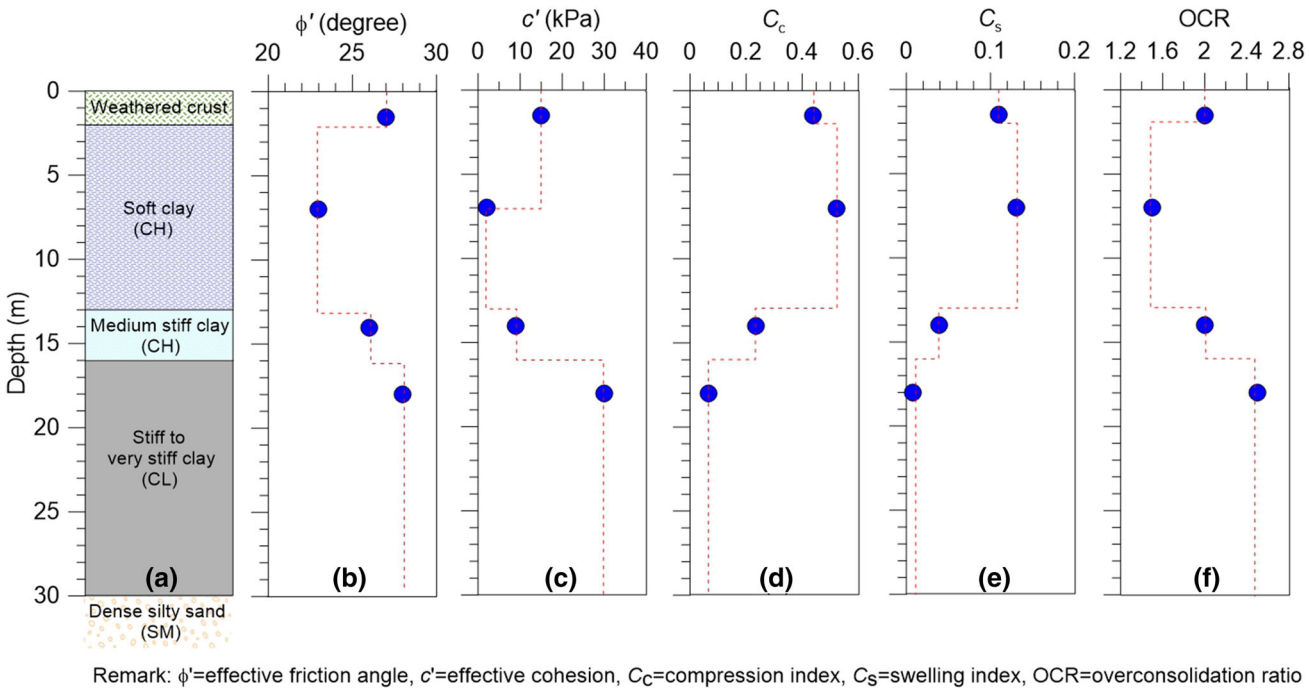

Fig. 1 Soil profiles and soil properties

Table 1 Basic properties of the foundation soils

Depth (m)	Foundation soils	w_n (%)	LL (%)	PL (%)	γ (kN/m^3)	G_s	e_o	s_u (kPa)
0–2	Weather crust	40	58	27	15.5	2.65	1.1	25
2–13	Soft clay	55–72	63–76	27–32	14.5–16.2	2.62–2.68	1.4–1.9	15–20
13–16	Medium stiff clay	48–55	60–73	29–32	16.6–18.1	2.66–2.68	1.2–1.4	25–50
16–30	Stiff to very stiff clay	22–36	40–70	27–32	18.1–18.8	2.65–2.70	0.6–1.0	75–200

stiff clay and stiff clay were heavily overconsolidated and that the soft clay was slightly overconsolidated.

3 Project details

The project involved an 18-story condominium with two underground parking garages, with a maximum excavation depth of 7.90 m. The excavation area involved only the soft clay layer. With insufficient space to construct a thick gravity DCM wall, a DCM wall with temporary bracing systems was designed to reduce the wall thickness. The TD construction technique was used to minimize the construction time, with a permanent basement slab serving as the lateral support. Figure 2a shows the layout of the DCM wall and pile foundation and the locations of the temporary struts. Figure 2b presents the cross section of the DCM wall. The maximum and minimum excavation depths were 7.9 and 6.3 m on the western and eastern sides, respectively, of the excavation area, which were close to a public road and a 2-story building. In addition, an 8-story building and a public road were adjacent to the southern and northern sides of the excavation area, respectively. Within this limited space surrounded by adjacent structures, a performance-based design was adopted. A performance-based design is one that is mainly based on the serviceability of an excavation support system with consideration of the fact that the induced deformation and stress must satisfy the design requirement of a project. Based on past experience related to the design of deep excavation works in the urban Bangkok area, the maximum allowable lateral movement is 65 mm. Within the range bounded by this value, no damage to the ground near the excavation area induced by the slab was found. Another requirement for temporary structural members is a minimum safety factor of 1.50.

The project involved two basements: B1 and B2. The levels of the two basement slabs were different; the B1-A

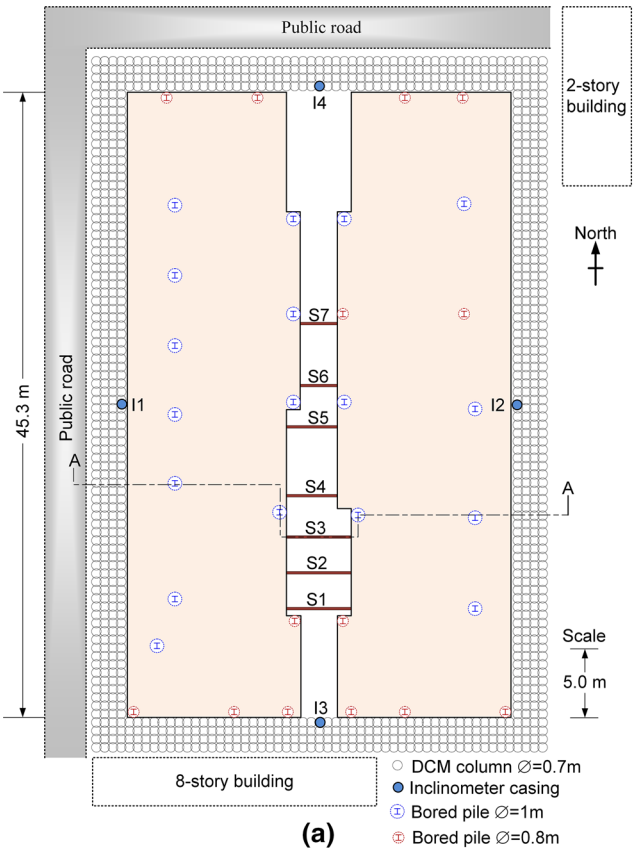

(a)

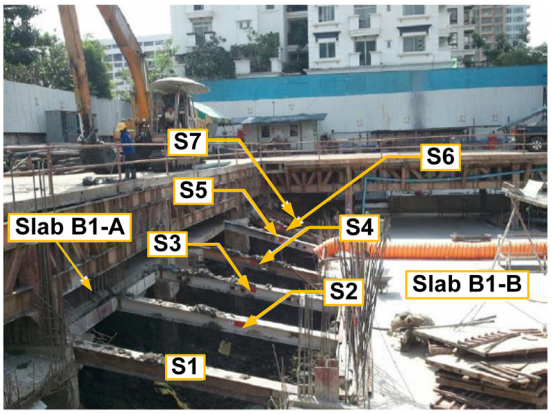

(c)

Strut No.	Strut length, L (m)	Angle, θ (degree)
S1	5.0	19
S2	5.0	19
S3	5.0	19
S4	4.0	24
S5	4.0	24
S6	3.2	30
S7	3.2	30

(d)

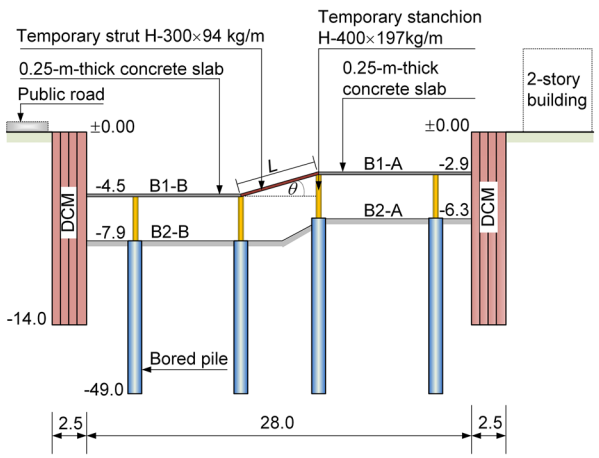

(b)

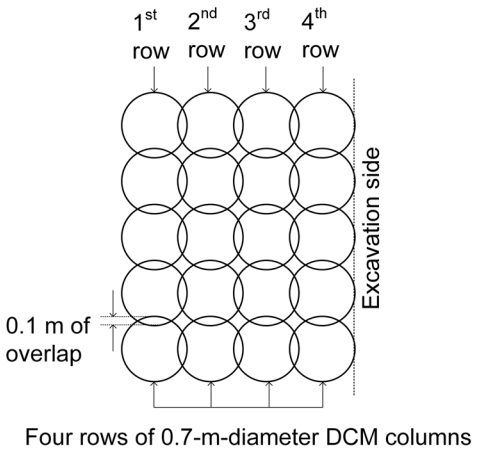

(e)

Fig. 2 **a** Plane view of the excavation area, **b** cross-sectional view A–A of the excavation, **c** DCM wall during TD construction, **d** details of struts and **e** enlargement of the DCM wall

slab was at a level of − 2.9 m, while the B1-B slab was at a level of − 4.5 m. The excavation for B2 was unequal; for the B2-A side, the excavation level was at − 6.3 m, whereas the excavation level for the B2-B side was − 7.9 m. Because the construction employed the TD method, the B1-A and B1-B basement slabs were used as lateral supports between the southern and northern sides of the DCM wall, and they were installed before the construction of the mat foundation. The basement slabs were posttensioned concrete slabs with a thickness and an ultimate compressive strength of 0.25 m and 35 MPa, respectively. In addition, seven temporary struts were connected between the two slabs B1-A and B1-B to act as bracings for transferring the lateral forces induced on the

western and eastern sides of the wall. Notably, the struts used in this project had different lengths and were installed with different inclinations to the horizontal level, as shown in Fig. 2c and d. Finally, temporary stanchions, which were embedded into the bored piles prior to the excavation work, were required to support the basement slabs. The DCM wall used at this site comprised four rows of 0.7-m-diameter DCM columns with 0.1 m of overlap, an enlarged view of which is shown in Fig. 2e. The entire thickness of the DCM walls was 2.5 m, and the tip was − 14.0 m from the ground surface. The DCM wall tip was embedded 1 m into the medium stiff clay layer. The DCM walls were installed using a low-pressure mechanical mixing method. The cement content was 250 kg/m^3 of wet soil, and the water/cement ratio was 1.1. Figure 2e also shows the construction sequences of the DCM walls. The first row, which is farthest from the excavation side, was first constructed to prevent lateral movement induced by the installation of subsequent rows of the DCM columns. Then, the second, third and fourth rows were installed.

After the DCM wall construction was completed, core samples were extracted from the DCM columns at various depths in three locations, C-1, C-2 and C-3, for the laboratory tests. Figure 3 presents the test results of the core samples. The bulk unit weights ranged from 15 to 16.5 kN/m^3, and the moisture content varied from 35 to 70%. The unconfined compressive tests were performed on samples 50 mm in diameter and 100 mm in height. The unconfined compressive strengths of the DCM columns, $q_{u(DCM)}$, ranged from 1.4 to 2.1 MPa, with an average value of 2.0 MPa, whereas the moduli of elasticity (E_{DCM}) ranged from 120 to 290 MPa, with an average value of 200 MPa, indicating an empirical relationship $E_{DCM} = 100\ q_{u(DCM)}$, corresponding to the test results of Huang and Han [13], Jongpradist et al. [20] and Jamsawang et al. [15–19].

The excavation stages versus construction periods are listed in Table 2. A waiting period of 3 days was required for the strength of the concrete slabs to reach 60% of the ultimate design strength (35 MPa) before the next stage of excavation was performed. The strength and stiffness of the concrete slabs at 60% of the ultimate design strength are sufficient for them to function as wall bracings [2]. After the floor zone B2-B was completely installed, a lean concrete was immediately poured to create permanent lateral bracings. In addition, permanent reinforced concrete walls and columns covering the stanchion were constructed. All stages of the excavation work are illustrated in Fig. 4. With a good design construction sequence for a moderate excavation depth of approximately 7.9 m with two basement levels, the excavation could be successfully accomplished in 88 days, with an average construction period of 7 days for each excavation stage. Arboleda-Monsalve and Finno [2] recorded the lateral movement of walls during a 15-m-depth deep excavation via TD construction in clayey soils. The entire excavation construction period was 480 days, with an average construction period of 45 days for each excavation stage. Field measurement data showed that creep effects represented approximately 30% of the maximum measured lateral wall movement, whereas the remaining 70% arose from stress relief. Due to the short average construction period, the creep effect, which may play an important role in long-term deep excavations, was thus minimal in this project and can be disregarded. Figure 23 illustrates that the creep effect provided only 7% of the maximum observed lateral wall movement, with the remaining 93% caused by stress relief.

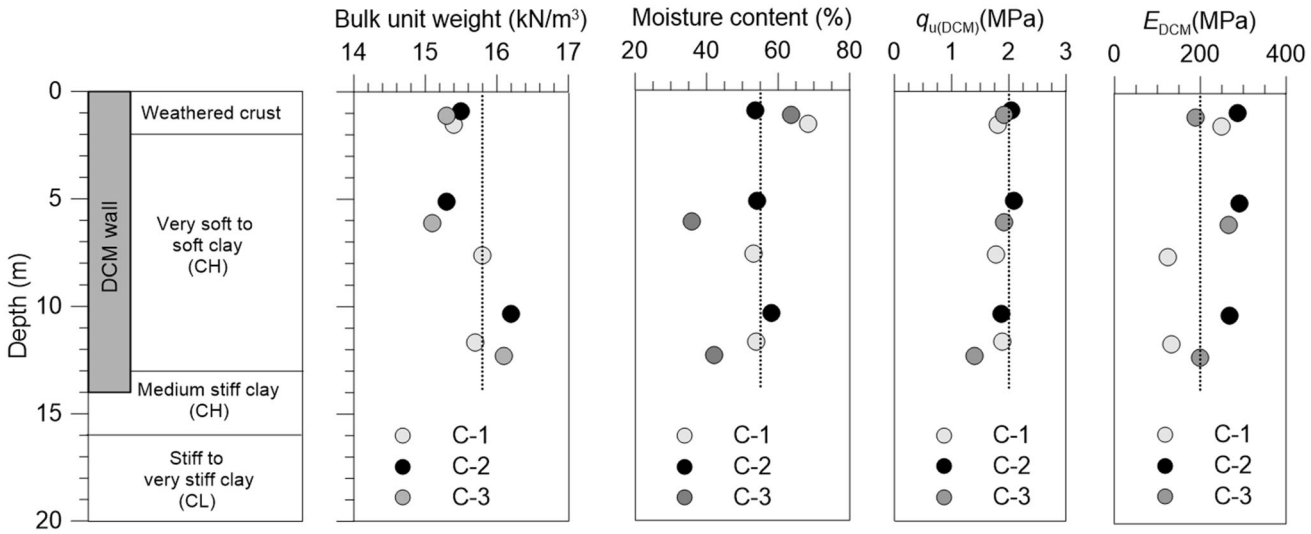

Fig. 3 Properties of the cored DCM columns

Table 2 Excavation stages versus construction period

Stage	Detail	Duration (days)
1	Construct 0.7- and 0.8-m-diameter bored piles to support the structural load	–
2	Install a temporary column (stanchion) using H-400 × 197 kg/m steel embedded into the bored piles to transfer the weight from the basement floor during construction to the bored piles	–
3	Install DCM column walls by deep wet mixing around the excavated area to be used as a temporary retaining structure for the construction of the basement	–
4	Excavate to − 3.20 m for floor zone B1-A	5
5	Install concrete slab zone B1-A	2
6	Wait for strength development of concrete slab zone B1-A	3
7	Excavate to − 4.80 m for floor zone B1-B	15
8	Install concrete slab zone B1-B	2
9	Wait for strength development of concrete zone B1-B	3
10	Install temporary struts between slab zones B1-A and B1-B using H 300 × 94 kg/m steel to transfer the lateral load due to the excavation	2
11	Excavate to − 6.30 m for space between floor zones B1-B and B1-A	5
12	Excavate to − 6.30 m for floor zone B2-A	28
13	Excavate to − 7.90 m for floor zone B2-B	23
	Total	88

Four inclinometer casings were installed up to the stiff clay layer at a depth of 19.0 m, which is approximately 2.5 times the excavation depth (H_e) and is sufficient to obtain a zero reading at this depth based on the practical work related to deep excavation projects in soft Bangkok clay reported by Likitlersuang et al. [23]. Inclinometer casings were installed in the middle of the walls on four sides of the excavation boundary to monitor the lateral wall movement, as shown in Fig. 2a. To measure the forces in the temporary struts installed between B1-A and B1-B and to avoid the bending stress component, electrical strain gauges were attached to the neutral axes of the struts. A dummy strain gauge was used to eliminate any effect of temperature. No prestressed loading of the struts was performed for this project.

4 Numerical analysis of the field case study

4.1 Finite element mesh and boundary condition

A finite element simulation using the PLAXIS 3D version 2013 software was conducted to describe the performance of the DCM wall. The 3D finite element model comprised the DCM columns, bored piles and foundation soils. The soil volume was modeled using ten-node tetrahedral volume elements. The circular columns (bored piles) were modeled as prismatic columns with square cross-sectional areas and diameters of 0.8 and 1.0 m. The stanchions and struts (Fig. 2a and b) were modeled using beam elements, whereas the basement slabs (Fig. 2a and b) were modeled using plate elements. Figure 5a and b illustrates the 430,000-element 3D finite element mesh used in the analysis, which corresponds to the DCM wall configuration in Fig. 2a and b. At the bottom of the finite element mesh, the displacements were set to zero in the *x*-, *y*- and *z*-directions. The vertical model boundaries were fixed in the *x*- and *y*-directions and free in the *z*-direction. To avoid boundary effects, the length and width of the model were chosen to be 160 and 140 m, respectively, and its depth was 30 m.

4.2 Constitutive model and model parameters

The hardening soil model is an advanced model for simulating the behavior of different types of soft and stiff soils [16–19, 33, 37, 39, 43, 44, 46] and was used to simulate the behavior of the weathered crust, soft clay, medium stiff clay, stiff clay and DCM column in this study. Schanz et al. [36] explained in detail that the most significant features of the present hardening soil model are the use of a hyperbolic stress–strain curve and the control of the stress-level dependency because the stiffness of real soils depends on the stress level. The theory of plasticity [4], soil dilatancy and a yield cap are also applied in the model. Thus, the yield surface is able to expand due to plastic strain. Hardening processes can be divided into two main types: compression and shear. The former is used for modeling

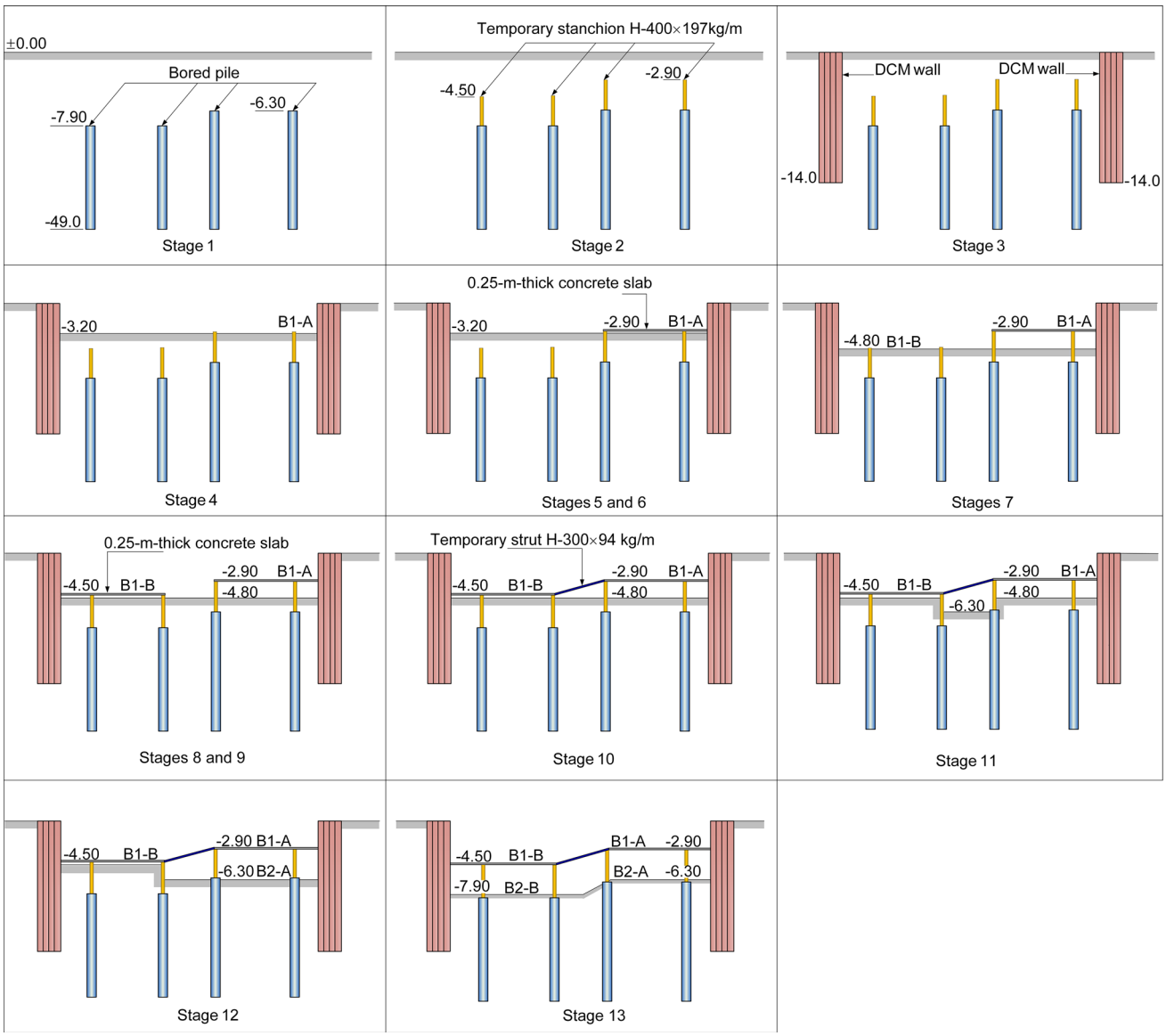

Fig. 4 Stages of the excavation construction

the irreversible plastic strains caused by primary compression in oedometer and isotropic loadings, whereas the latter is employed for modeling irreversible strains due to primary deviatoric loading. A soil that is subjected to primary deviatoric loading exhibits a decrease in stiffness, and irreversible plastic strains concurrently develop.

The stress–strain relationship due to the primary loading is assumed to be a hyperbolic curve in the hardening soil model. The hyperbolic function for the drained triaxial test can be formulated as

$$-\varepsilon_1 = \frac{1}{E_i}\frac{q}{1-q/q_a} \quad \text{for } q < q_f \tag{1}$$

where q_a is the asymptotic value of the shear strength, and E_i the initial stiffness. E_i is related to E_{50} by

$$E_i = \frac{2E_{50}}{2-R_f} \tag{2}$$

This relationship is plotted in Fig. 6. The parameter E_{50} is the confining stress-dependent stiffness modulus for primary loading, which is 50% of the secant stiffness modulus and is given by the equation

$$E_{50} = E_{50}^{\text{ref}}\left(\frac{c'\cos\phi' - \sigma_3'\sin\phi'}{c'\cos\phi' + p^{\text{ref}}\sin\phi'}\right)^m \tag{3}$$

where E_{50}^{ref} is a reference stiffness modulus corresponding to the reference confining pressure, p^{ref}, of 100 kPa. The actual stiffness depends on the minor principal stress, σ_3', which is the confining pressure in a triaxial test. The amount of stress dependency is given by the power

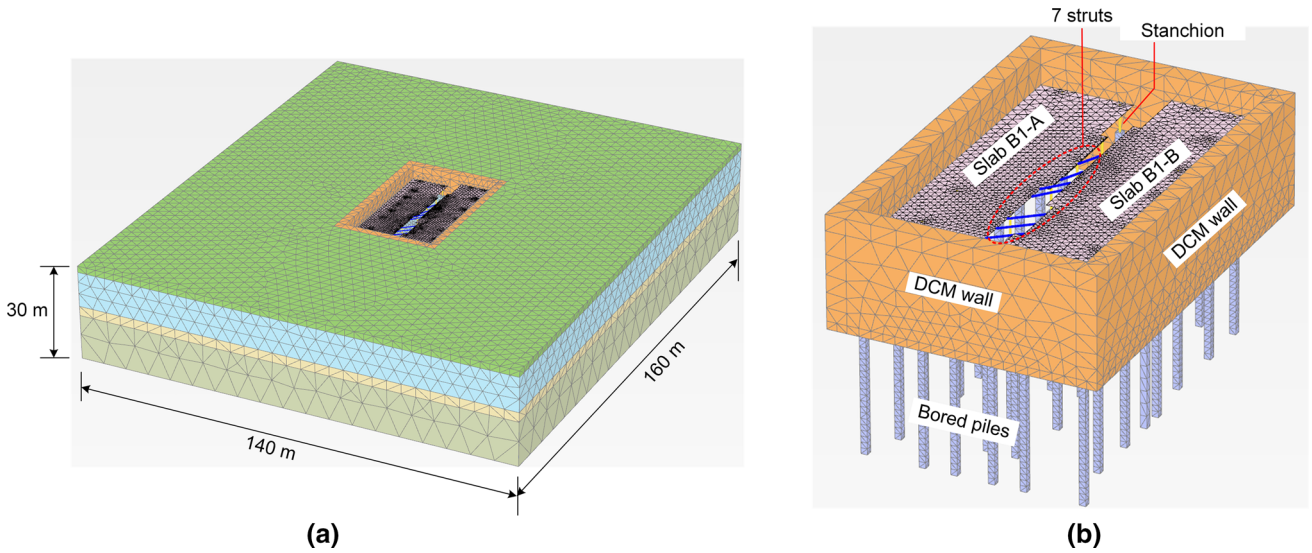

Fig. 5 **a** 3D finite element mesh of the wall and **b** enlargement of the modeling excavation area

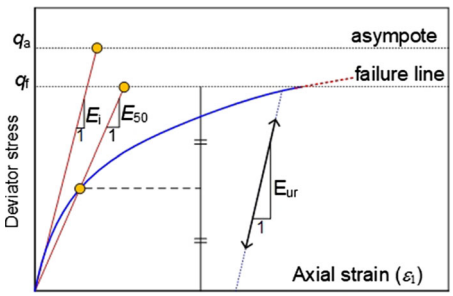

Fig. 6 Hyperbolic stress–strain relation in primary loading for a standard drained triaxial test (Schanz et al. [36])

m. Surarak et al. [39] reported a range of m values from 0.5 to 1 for different soil types, with values of 0.9–1 for clayey soils. The ultimate deviatoric stress, q_f, and the quantity q_a in Eq. (1) are defined as

$$q_f = (c' \cot \phi' - \sigma_3') \frac{2 \sin \phi'}{1 - \sin \phi'} \tag{4}$$

$$q_a = \frac{q_f}{R_f} \tag{5}$$

The above relationship for q_f is derived from the Mohr–Coulomb failure criterion, which involves the strength parameters c′ and ϕ'. The ratio between q_f and q_a is given by the failure ratio R_f, which should clearly be smaller than 1. An R_f of 0.9 is chosen as a suitable value for various soil types [16–19, 33, 37, 39, 43, 44, 46]. For the unloading and reloading stress paths, another stress-dependent stiffness modulus is used:

$$E_{ur} = E_{ur}^{ref} \left(\frac{c' \cos \phi' - \sigma_3' \sin \phi'}{c' \cos \phi' + p^{ref} \sin \phi'} \right)^m \tag{6}$$

where E_{ur}^{ref} is the reference Young's modulus for unloading and reloading, corresponding to the reference pressure p^{ref} of 100 kPa. The shear hardening yield function, f, in the hardening soil model is given as

$$f = \bar{f} - \gamma^p \tag{7}$$

where $\bar{f}$ is a function of the stress and γ^p is a function of the plastic strain:

$$\bar{f} = \frac{2}{E_i} \frac{q}{1 - q/q_a} - \frac{2q}{E_{ur}} \tag{8}$$

$$\gamma^p = -\left(2\varepsilon_1^p - \varepsilon_v^p\right) \approx -2\varepsilon_1^p \tag{9}$$

$$\varepsilon_1^p \approx \frac{1}{2}\bar{f} = \frac{1}{E_i} \frac{q}{1 - q/q_a} - \frac{q}{E_{ur}} \tag{10}$$

where ε_1^p and ε_v^p are the plastic vertical strain and the plastic volumetric strain, respectively.

In addition to plastic strains, the model also accounts for elastic strains. Plastic strains develop in primary loading alone, but elastic strains develop both in primary loading and in unloading/reloading. For drained triaxial test stress paths with $\sigma_2' = \sigma_3'$ = constant, the elastic Young's modulus E_{ur} remains constant, and the elastic strains are given by

$$-\varepsilon_1^e = \frac{q}{E_{ur}} \tag{11}$$

$$-\varepsilon_2^e = -\varepsilon_3^e = -\nu_{ur} \frac{q}{E_{ur}} \tag{12}$$

where ν_{ur} is the unloading/reloading Poisson's ratio and ε_2^e and ε_3^e are the elastic radial strains. A value of ν_{ur} of 0.2 is typically used in this model [21, 36, 46]. For the deviatoric loading stage of the triaxial test, the axial strain is the sum

Table 3 Parameters used in hardening soil model

	Weathered crust	Soft clay	Medium stiff clay	Stiff clay	DCM column
Unit weight, γ (kN/m^3)	16	15	17	19	16
Secant stiffness, E_{50}^{ref} (kPa)	10,000	1200	10,000	20,000	200,000
Tangential stiffness, $E_{\text{oed}}^{\text{ref}}$ (kPa)	12,000	960	12,000	25,000	150,000
Unloading and reloading stiffness, $E_{\text{ur}}^{\text{ref}}$ (kPa)	35,000	4000	45,000	95,000	600,000
Power of the stress-level dependency of the stiffness, m	1.0	1.0	0.9	0.9	0.9
Poisson's ratio for unloading–reloading, ν_{ur}	0.2	0.2	0.2	0.2	0.2
Effective cohesion, c' (kPa)	15	2	9	30	510
Effective friction angle, ϕ' (degrees)	27	23	26	28	36
Angle of dilatancy, ψ (degrees)	0	0	0	0	0
Over-consolidation ratio, OCR	2.0	1.5	2.0	2.4	–
Material behavior	Undrained	Undrained	Undrained	Undrained	Undrained

of an elastic component given by Eq. (11) and a plastic component obtained from Eq. (10). Hence, it follows that

$$-\varepsilon_1 = \varepsilon_1^{\text{e}} - \varepsilon_1^{\text{p}} \approx \frac{1}{E_{\text{i}}} \frac{q}{1 - q/q_{\text{a}}} \tag{13}$$

Another input parameter, the reference oedometer modulus ($E_{\text{oed}}^{\text{ref}}$), is used to control the magnitude of the plastic strains that originate from the yield cap. In a similar manner to the triaxial moduli, the oedometer modulus (E_{oed}) obeys the stress dependency law

$$E_{\text{oed}} = E_{\text{oed}}^{\text{ref}} \left(\frac{c' \cos\phi' - \frac{\sigma_3'}{K_{\text{o}}^{\text{nc}}} \sin\phi'}{c' \cos\phi' + p^{\text{ref}} \sin\phi'} \right)^m \tag{14}$$

where E_{oed} is a tangent stiffness modulus and K_{o}^{nc} is K_{o} for normal consolidation, which is $1 - \sin\phi'$. The tensile strength of the DCM columns, which were considered using the tension cutoff in the model, was 15% of $q_{\text{u(DCM)}}$ [19]. The linear elastic model was employed to model the behaviors of the concrete slabs, stanchions, struts and bored piles [17]. The parameters of the linear elastic model are listed in Table 3.

4.3 Soil parameter calibration for the foundation soils and DCM columns

The laboratory test results and hardening soil model were calibrated by modeling the triaxial and oedometer tests using a 2D finite element method using axisymmetric geometries of 50 × 25 mm and 10 × 30 mm, as shown in Fig. 7a and b, respectively, to obtain reasonable soil parameters for simulating the field behaviors of the foundation soils. The results of the triaxial tests are presented in the form of the deviator stress versus axial strain, whereas those of the oedometer tests are shown as plots of the

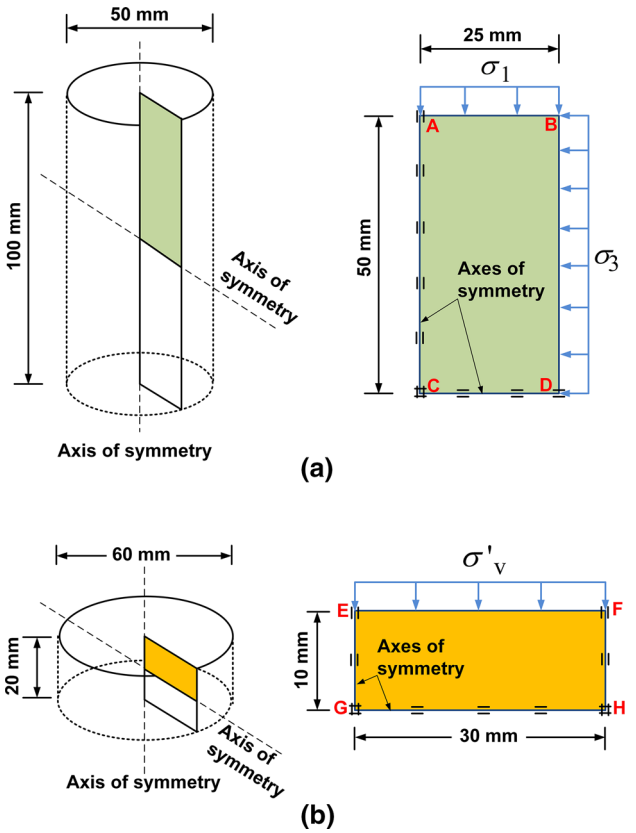

Fig. 7 Simplified geometries of: **a** triaxial test and **b** oedometer test in 2D finite element models

logarithm of the vertical effective stress versus the vertical strain curves, as shown in Fig. 8a–e. These tests included loading and unloading, from which the loading stiffness, the unloading stiffness and the power of the stress-level dependency of the stiffness could be determined [17].

The simplified geometries in the triaxial and oedometer models represent one-quarter of the soil specimens. The

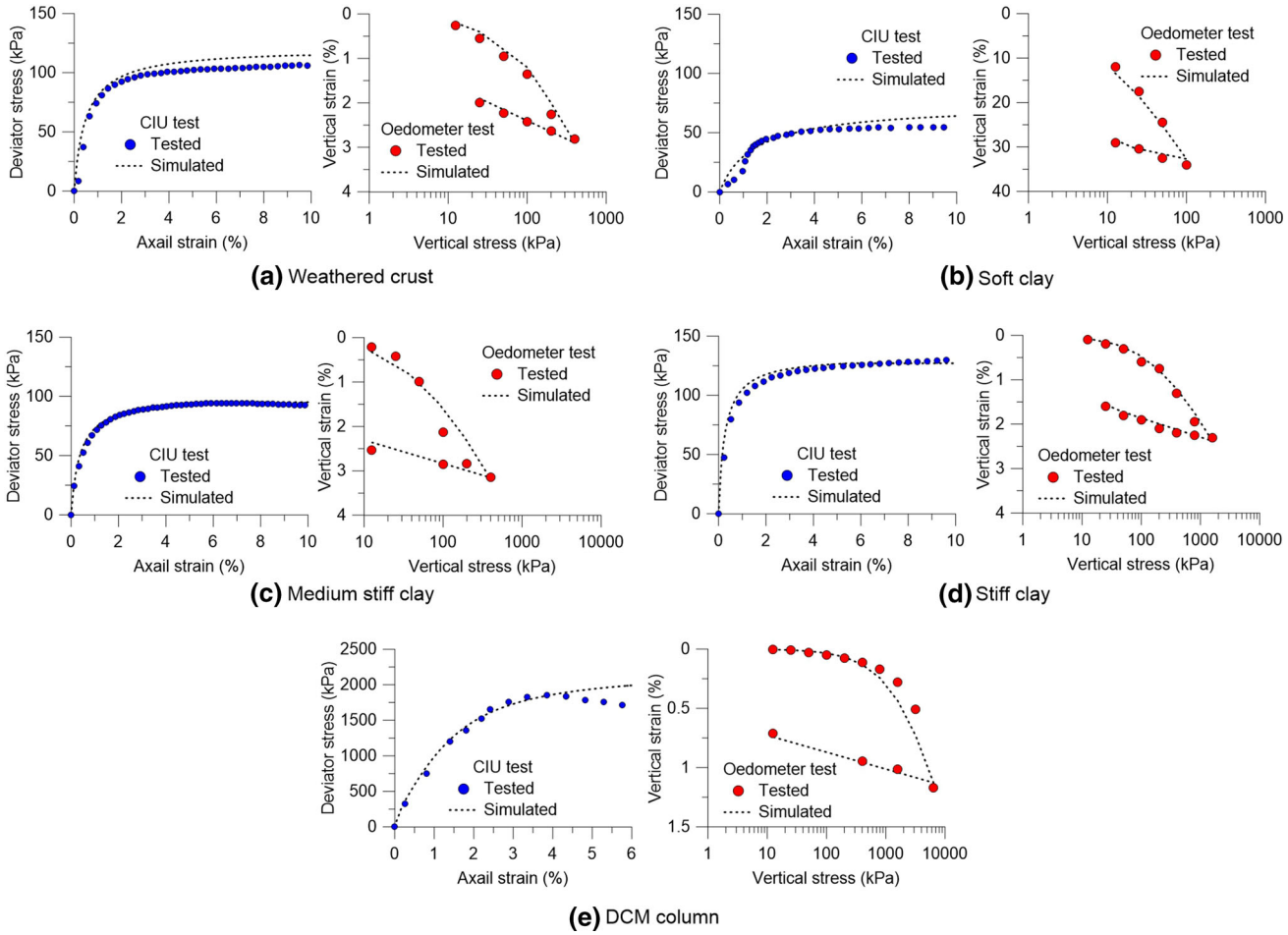

Fig. 8 Soil parameter calibrations

deformations along the boundaries for the triaxial model (lines AC and CD) and for the oedometer model (lines EG, GH and FH) were kept free to allow smooth movement along the axes of symmetry, whereas the deformations perpendicular to the boundaries were fixed. The boundaries AB, BD and EF were free to move. The applied vertical and confining stresses were simulated as distributed load systems σ_1 and σ_3 for the triaxial model, while the applied normal effective stress was simulated as a distributed load system σ'_v for the oedometer model. A 15-node triangular element was selected for this analysis. The clusters, representing a quarter of the soil specimens in both tests, were divided into soil elements during the mesh generation process.

The input shear strength parameters c' and ϕ' for the foundation soils and DCM column were obtained from the triaxial test results. The values of the parameters E_{50}^{ref}, $E_{\text{oed}}^{\text{ref}}$, $E_{\text{ur}}^{\text{ref}}$ and m are independent inputs in the hardening soil model. These parameters were adjusted to obtain suitable values to provide the best-fit results of the stress–strain curves. The results shown in Fig. 8a–e reveal good agreement with the stress–strain curves for the weathered crust, soft clay, medium stiff clay, stiff clay and DCM column, respectively. Therefore, suitable soil parameters of the hardening soil model for the 3D finite element analysis for this study are presented in Table 4. The stiffness parameters used in this study are similar to those derived by Surarak et al. [39] for Bangkok clay.

5 Numerical results and comparisons with measurement data

Because of the limited space of the construction site, only some instruments, i.e., inclinometers and strain gauges, which were used to measure the lateral movements and strut loads, respectively, were installed. A 3D finite element analysis was thus performed with careful consideration of both the material parameters and analysis procedures to generate the responses of the soil and wall, which could not be directly obtained from the field. In this section, the simulated results are compared with the

Table 4 Parameters used in linear elastic model

	Concrete slab	Bored pile	Temporary strut	Stanchion
Unit weight, γ (kN/m^3)	24	24	78	78
Moment of inertia, I (m^4)	1.3×10^{-3} m^4/m	0.012–0.020	2.0×10^{-4}	7.1×10^{-4}
Cross-sectional area, A (m^2)	0.25 m^2/m	0.38–0.50	0.012	0.025
Elastic modulus, E (kPa)	2.8×10^7	2.0×10^7	2.1×10^8	2.1×10^8
Poisson's ratio, v	0.15	0.15	–	–
Material behavior	Plate element	Non-porous	Beam element	Beam element

measurement data to verify the computed values, which will be discussed later.

5.1 Lateral movement profile

The observed lateral movement profiles of the DCM wall in the middle of each side of the excavation area were obtained from the four inclinometers (shown in Fig. 2a), I1, I2, I3 and I4, at the western, eastern, southern and northern parts of the excavation, respectively. The lateral wall movement profiles of the final stage of the excavation (stage 13) are shown in Fig. 9a–d. In the figures, the computed lateral movement profiles from the 3D finite element analysis are also included for comparison. The trends of the lateral movement profiles were reasonably well captured, and the computed magnitudes were generally in good agreement with the observed data for I1, I2, I3 and I4. The 20% maximum overestimation of the computed δ_{hm} at a depth of 8 m (20 mm) for I4 was 5 mm, whereas the 20% maximum underestimation of the calculated δ_{hm} at a depth of 9 m (15 mm) for I3 was 5 mm.

For the I1 side, the wall movement showed a small curvature, which means that the wall was tilted like a block. The wall was permitted to deflect as a cantilever beam. The maximum lateral wall movement (δ_{hm}) located at the top of the wall (near the ground surface) was 58 mm, and the movement at the tip of the wall (at a depth of 14 m) was 15 mm, which implies that the movement pattern was a combination of slight overturning and sliding. For inclinometer I2, the amount of wall movement was less than that detected by I1 because the excavation depth was smaller. δ_{hm} was 32 mm at the top of the wall, and the movement at the tip of the wall was 10 mm. The lateral movement profiles for the I3 and I4 sides are presented in Fig. 9c and d, respectively. The magnitudes of the lateral movements were considerably smaller than those of the I1 and I2 sides because of the smaller wall length and sufficient lateral support from the concrete slab bracings B1-B and B1-A. Because the final excavation depths (H_e) were the same, there were no significantly different lateral wall deflections on the two sides of I3 and I4. The lateral movement profiles developed into a bulged profile pointed

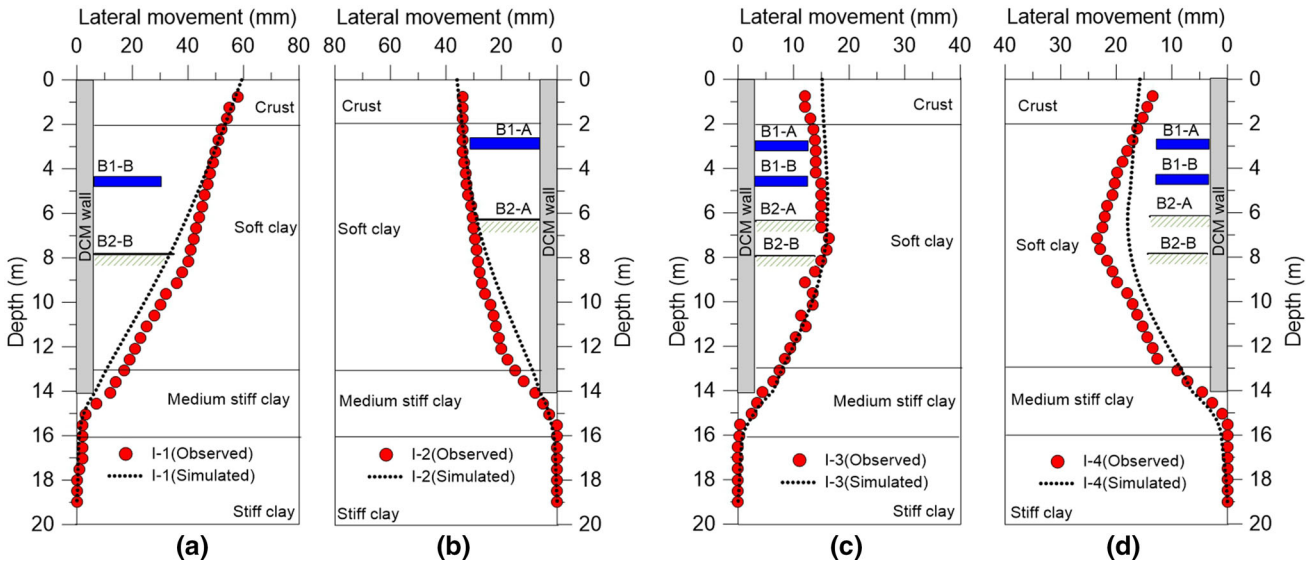

Fig. 9 Comparison of measured and computed lateral wall movements

inward toward the excavation area, indicating that the walls of the two sides were well propped near the surface. Thus, the maximum lateral movement (H_{hm}) occurred at a deeper depth. δ_{hm} was 22 and 26 mm at distances 4.5 and 7 m below the ground surface for the walls associated with I3 and I4, respectively. The tip movements of the retaining wall were only 5 mm for I3 and I4.

H_{hm} was at the ground surface for I1 and I2, whereas it was 0.63 and 1.0 H_e below the ground surface for I3 and I4, respectively. Ou et al. [30] found that the H_{hm} of eight case histories in Taipei soft soil were often observed near the excavation surface. The analysis of Moormann [29] showed that the δ_{hm} for most deep excavations in a soft soil were observed at depths from 0.5 to 1.5 H_e under the ground surface. Wang et al. [42] reported that H_{hm} was observed at depths from 0.5 to 1.0 H_e under the ground surface in 53% of the case histories. For 43% of the case histories, H_{hm} was observed at depths from 1.0 to 1.4 H_e under the ground surface. H_{hm} was observed at the top of the wall for only approximately 4% of the case histories. δ_{hm} for the DCM walls without internal struts occurred at the tops of the walls. Deep-seated wall displacements were observed when internal struts were used to support the DCM walls. The results of Ou et al. [30], Moormann [29] and Wang et al. [42] were broadly confirmed by this study.

The tip movement of the retaining wall was found to occur at I1 and I2. Wang et al. [41] reported that the embedded depth ratio of the wall (D/H_e) may contribute to the toe movement, where D is the embedded length of the wall. D/H_e is an important index that reflects the economy of the retaining wall. It also has some impact on the factor of safety against basal heave. Here, the embedment ratio was $0.77D/H_e$ for the DCM wall and mainly varied between 0.8 and 1.4, being 1.08 on average [41]. Thus, D/H_e was the smallest in this study. A larger D/H_e ratio could help in suppressing the toe movement because more soils under the excavation surface would be strengthened.

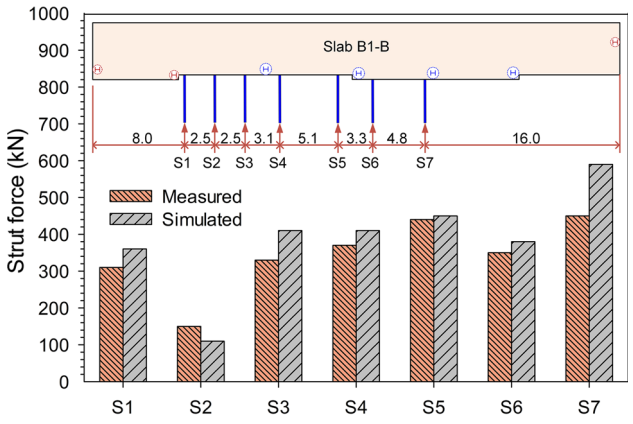

Fig. 10 Comparison of measured and calculated strut forces

5.2 Strut force

Figure 10 shows comparisons of the measured and computed strut forces induced by the 7.9-m-deep excavation for all struts, as shown in Fig. 2a–c. The measured values of the strut forces were 310, 150, 330, 370, 440, 350 and 450 kN, whereas the computed values were 360, 110, 410, 410, 450, 380 and 590 kN for struts S1 to S7, respectively. Strut S7 was farthest from the edge of the slab and experienced a larger axial force than the other struts. The yield strength of the steel used in the struts was 250 MPa, resulting in a yield axial force of 3000 kN. Thus, minimum factors of safety against structural failure of 6.7 and 5.1 were obtained for this project, which were based on measured and simulated values of the strut forces, respectively.

A comparison of the observed and computed data indicated a maximum underestimation of 36% and overestimation of 24% for struts I2 and I7, respectively. However, the average error in the comparison was only 16%. Therefore, the computed magnitudes of the strut forces were generally in good agreement with the observed data. The calculated force in strut S7 was approximately twice the measured and calculated forces in strut S1 because the spacing of S7 was twice the spacing of S1. This shows that the computed strut forces provide reliable results. These comparisons give us confidence in the values computed using the 3D finite element analysis, which will be used later in the discussion.

A strut is generally a compressive structural member (Fig. 11a), but all the struts used in this study were installed with inclinations due to the different levels of the

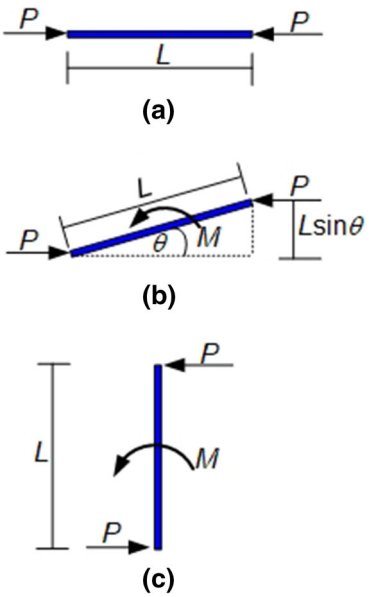

Fig. 11 Orientation of strut with respect to the applied force direction and the induced structural force for: **a** $\theta = 0^o$, **b** $0^o < \theta < 90^o$ and **c** $\theta = 90^o$

two basement slabs. Thus, the excess bending moment induced produces a combination of compressive and tensile stresses in a cross section of the struts instead of pure compression. The excess bending moment can be approximately calculated as the product of the lateral force transferred from the basement slabs, P, and the moment arm, $L\sin\theta$; where L is the strut length and θ is the inclination angle, as shown in Fig. 11b. It can be seen that the strut length and inclination angle have influences on the normal force on the strut section; the greater the value of $L\sin\theta$, the larger the excess bending moment. Considering only the term θ, an increase in θ changes the function of a strut from a compressive to a flexural structural member (Fig. 11c). The numerical results show that the excess couple bending moments induced are 61, 43, 45, 62, 53, 54 and 60 kN-m for struts S1–S7, respectively. However, the excess bending moments were compensated by the high value of the factor of safety against structural failure of 5.1.

5.3 Sensitivity analysis of input soil parameters on the maximum lateral movement

This section presents the results of a sensitivity analysis of the soil parameters used in the model regarding the magnitude of the computed maximum lateral movement obtained from wall I1 to investigate which parameters have the most significant influence on the results. The parameters studied are (1) E_{50}^{ref}, (2) $E_{\text{oed}}^{\text{ref}}$, (3) $E_{\text{ur}}^{\text{ref}}$, (4) m, (5) v_{ur}, (6) c', (7) ϕ' and (8) R_{f}. As mentioned previously, one parameter was varied with respect to the case study in each analysis to determine the influence of that specific parameter. The values of each parameter had error variations from − 50% to 50% of the input values in the case study, as tabulated in Table 3. The computed maximum lateral movement was 60 mm based on the parameters in Table 4. Figure 12 shows the influence of these soil parameters; $E_{\text{ur}}^{\text{ref}}$ has the most influence, providing values of 111 and 44 mm or 185% overestimation and 73% underestimation for percent errors of − 50 and 50, respectively, because of the maximum lateral movement induced by the unloading of the soil weight from the excavation. Thus, $E_{\text{ur}}^{\text{ref}}$ is a main parameter that quickly responds to unloading soil behavior, whereas E_{50}^{ref}, $E_{\text{oed}}^{\text{ref}}$ and c' can be considered insignificant and the rest of the parameters slightly affect the maximum lateral movement. However, all the values of $E_{\text{ur}}^{\text{ref}}$ used in this study are in the range of the test results reported by Surarak et al. [39] for Bangkok clay.

5.4 Discussion of the effectiveness of DCM-TD compared to that of other support systems

The relationship between δ_{hm} and H_{e} in this deep excavation is shown in Fig. 13. The results indicate that the values

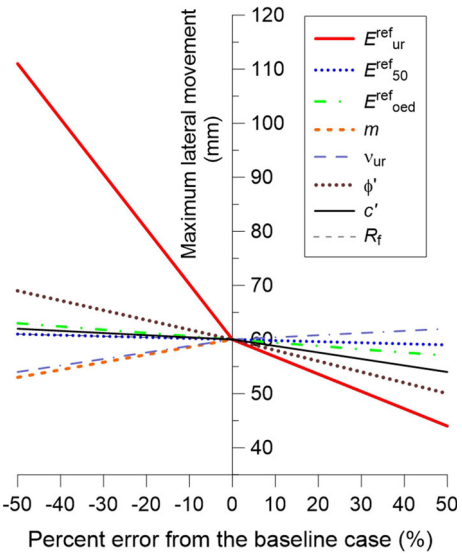

Fig. 12 Sensitivity analysis of input soil parameters on the maximum lateral movement

of δ_{hm} were 0.73, 0.51, 0.23 and 0.33%H_{e} for the walls associated with I1, I2, I3 and I4, respectively. The measured results for all types of supporting systems obtained for the metro excavations in Bangkok and Shanghai soft clays are also shown for comparison because properties of the foundation soils are similar. All types of supporting systems were used, including DWs constructed using the TD method (DW-TD) and using the BU method (DW-BU), DCM walls constructed using the BU method (DCM-BU), and SPWs constructed using the BU method. The results of Wang et al. [42] indicated that the mean values of δ_{hm} for DW-TD, DW-BU, DCM-BU and the SPWs were 0.27, 0.4, 0.91 and 1.5%H_{e}, respectively, whereas the database in the Bangkok area shows that those for DW-TD, DW-BU, DCM-BU and the SPWs were 0.25, 0.31, 1.37 and

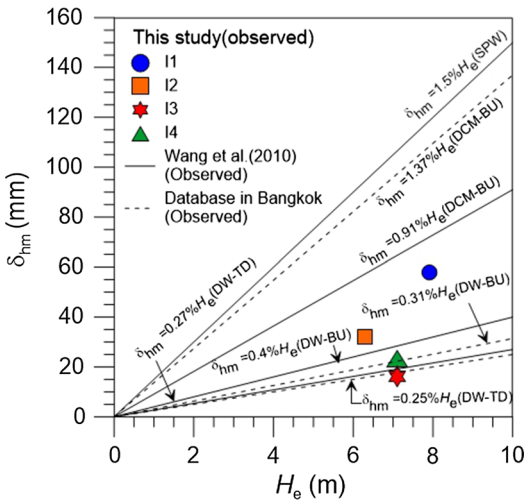

Fig. 13 Observed lateral movement versus excavation depth

1.45%H_e, respectively. Thus, the values of the ratio δ_{hm}/H_e for each type of supporting system used in Bangkok and Shanghai soft clays are similar, except that of DCM-BU, which is different because the quality control of a DCM construction might be different for each country. For the DCM-TD method in this study, the larger values of δ_{hm}/H_e (based on I1 and I2) were between those of DCM-BU and DW-BU, whereas the smaller values of δ_{hm}/H_e (based on I3 and I4) were between those of DW-BU and DW-TD. The type of wall and construction technique used have a significant influence on δ_{hm}, as expected. The values of δ_{hm} for the DCM-BU method were considerably larger than those for any other type of wall, except the SPWs, because the DCM walls were largely excavated in the manner of a cantilever. The δ_{hm} trend was significantly smaller for relatively stiff walls, including the DW-BU and DW-TD. The mean value of δ_{hm} for this study was 0.45%H_e, which is approximately 2 and 3 (or 2.5 (average)) times smaller than the observed values of δ_{hm} for the DCM-BU in Shanghai and Bangkok soft clays, respectively. In addition, the mean value of δ_{hm} for DCM-TD was 0.8 and 0.5 times larger than the average observed values of δ_{hm} for DW-BU and DW-TD, respectively. The observed effectiveness of DCM-TD in comparison with that of DCM-BU was assessed quantitatively in terms of the reduction ratio for the lateral wall movement, which was defined as the ratio of the difference in δ_{hm} between DCM-BU and DCM-TD to the value of δ_{hm} of DCM-BU. Thus, reduction ratios of 50 and 67% were obtained for DCM-BU in Shanghai and Bangkok soft clays, respectively.

5.5 Distribution of lateral wall movements around the excavation area

The lateral wall movements observed and computed around the sides of the excavation area provided an opportunity to study whether corner effects existed in such a deep and long excavation. Figure 14 shows the relationship between δ_{hm}/H_e and the distance ratio along the west and east long sides and south and north short sides. The distance ratio was measured from the south corner to the north corner and from the west corner to the east corner. The maximum values of δ_{hm}/H_e were 0.8 and 0.6% for the west and east sides of the excavation area, respectively, which were located at the mid-span of each excavation side. The minimum values of δ_{hm}/H_e were 0.05 and 0.1% for the west and east sides of the excavation area, respectively, which were located at the corners of the mid-span of each excavation side. The results observed for the 38-m-deep multistrutted excavation in Shanghai soft clay reported by Lui et al. [26] were also plotted for comparison. There was no significant difference in the values of δ_{hm}/H_e

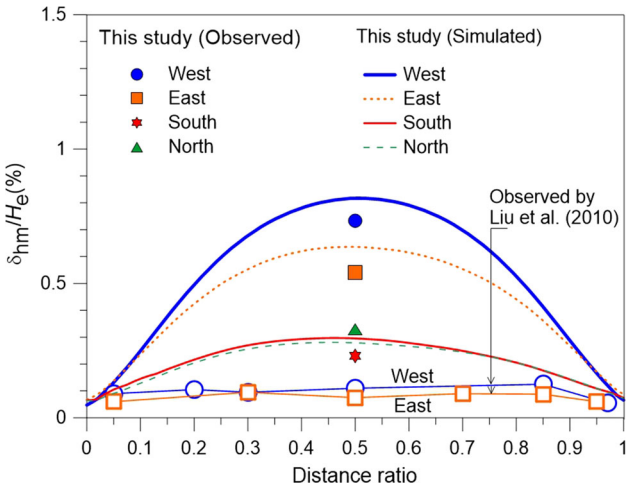

Fig. 14 Relationship between normalized maximum lateral wall movement and distance

for the mid-span and the corner of the excavation area, which were 0.05 to 0.1%H_e, respectively.

A three-dimensional distribution of the lateral wall movements can also be observed in Fig. 14. The support system, stiffness of the strutting system, and length-to-depth and length-to-width ratios should be considered when studying the corner effect of the excavation. The length, width and depth represent the dimensions of the longer side, shorter side and excavation depth of the excavation works, which are 45.3, 28.0 and 7.9 m, respectively, in this study. Studies on corner effects in Singapore and Taiwan clays [8, 22, 25, 31] suggested that a low length-to-depth ratio and smaller length-to-width ratio give rise to more significant corner effects. Lui et al. [26] showed that the length-to-depth ratio and length-to-width ratio were 4.6 and 7.6, respectively, for a deep multistrutted excavation, and no corner effect was found because of the high length-to-width ratio and the sufficient stiffness of the heavy strutting system. However, in this study, the length-to-depth and length-to-width ratios were 5.7 and 1.6, respectively. The low length-to-width ratio compared to that for the excavation system presented by Lui et al. [26] and the insufficient stiffness of the strut system may have contributed to the corner effect in this project.

5.6 Maximum lateral movements versus factor of safety against basal heave (FOS_{base})

Mana and Clough [28] investigated the relationship between δ_{hm} and FOS_{base} using a statistical collection based on several excavations in clay areas around the world (Boston, San Francisco, Chicago, California, Oslo, and others). Some excavations using DW-TD and DW-BU in Shanghai collected by Wang et al. [42], and some databases of excavations using SPWs, DCM-BU and DW-TD

in Bangkok are also cited here. Mana and Clough [28] proposed the limit lines for this relationship. The values of δ_{hm}/H_e for the case in this study are plotted against FOS_{base} in Fig. 15a. The method proposed by Terzaghi [40] was adopted to calculate FOS_{base}. Figure 15a shows that δ_{hm}/H_e tended to decrease with the increasing FOS_{base}. The measured δ_{hm}/H_e in this study falls between the two limit lines, with FOS_{base} values ranging from 1.4 to 1.5. The results indicate that the limits provided by Mana and Clough [28] can also be applicable to DCM-TD in this study. The majority of the data points collected by Wang et al. [42] are within the two limit lines (being nearer to the lower one).

5.7 Influence of system stiffness

Previous studies executed by many researchers, including Rowe [35], Goldberg et al. [9], Clough et al. [7], Potts and Day [34], and Addenbrooke [1], showed that the stiffness of the supporting system is an important factor governing the performance of an excavation. The stiffness of the supporting system relates to many factors, including the bending stiffness of the retaining wall, the axial stiffnesses of the struts, the locations of the struts, and the vertical spacings between the struts. Figure 15b shows the relationship between δ_{hm}/H_e and the system stiffness $EI/\gamma_w h^4$, as defined by Clough et al. [7], for the walls in this study. The design curves, in terms of FOS_{base}, proposed by Clough and O'Rourke [6] are also shown in the figure to illustrate the trends. The stiffness of the wall EI was calculated using a Young's modulus value $E = 20$ MPa for the DCM wall and the second moment of inertia of the wall section, calculated using $I = t^3/12$, where t is the wall thickness, h is the average vertical strut spacing and γ_w is the unit weight of water. Figure 15b shows the value of the system stiffness for DW-TD and DW-BU from the work of Wang et al. [42] for comparison. The system stiffness values for this project were bounded by two curves, $FOS_{base} = 1.2$ and $FOS_{base} = 1.5$, with $FOS_{base} = 1.35$ being an approximate average curve. The DW-TD data points obtained by Wang et al. [42] were between an FOS_{base} of 1.4 and an FOS_{base} of 3.0, with an average FOS_{base} of 2.2. The data points for DW-TD were broadly bounded by the curves $FOS_{base} = 1.1$ and $FOS_{base} = 3.0$. The curve $FOS_{base} = 2.0$ represents an approximate average of this data set. Figure 15b shows that there is a relatively wide scatter of the values of δ_{hm}/H_e for a given system stiffness. However, there is slight evidence of a decreasing trend of δ_{hm}/H_e with increasing system stiffness. This trend is consistent with the findings of Long [27] for case histories in soft soils of significant thicknesses. Moreover, DCM-TD (this study), DW-BU and DW-TD provided the smallest, medium and largest average FOS_{base} values, respectively, which correspond to the average values of δ_{hm}/H_e for various support systems, as shown in Fig. 13.

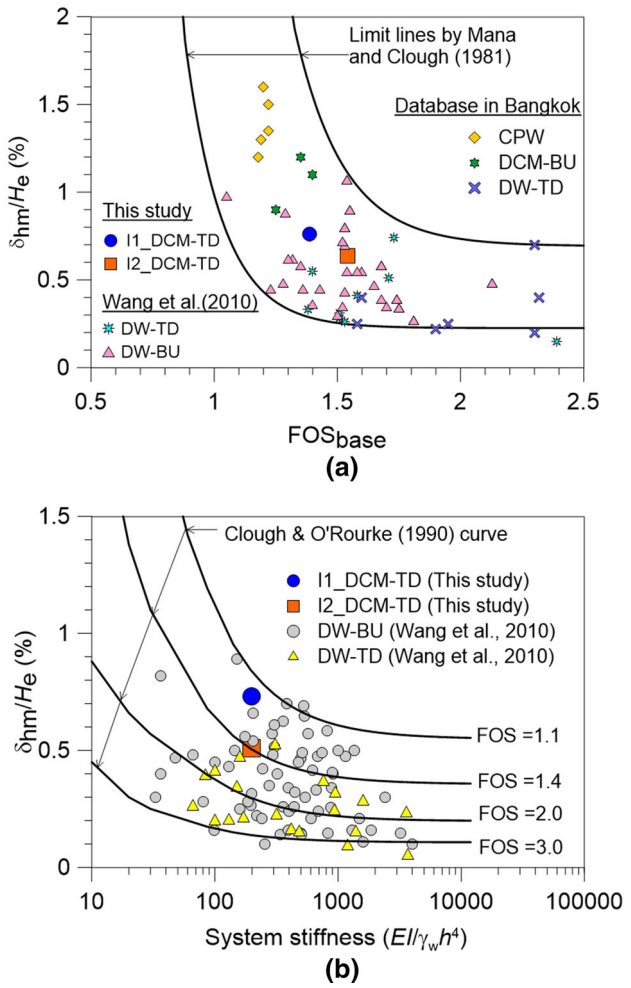

Fig. 15 Normalized maximum lateral wall movement versus: **a** factor of safety against basal heave; **b** system stiffness

5.8 Computed normal forces in the slabs

The distributions of the normal forces per unit length perpendicular to the length of the wall induced in slabs B1-A and B1-B due to the − 7.9-m excavation are presented in Fig. 16. The maximum normal forces in slabs B1-A and B1-B, 130 and 120 kN/m, were located near the centers of the slabs lengthwise. The resultant normal forces in slabs B1-A and B1-B, in units of kN, are summations of the areas under the curves of normal force per unit length versus distance, as shown in Fig. 16. The resultant normal forces in slabs B1-A and B1-B were 4380 and 4370 kN, respectively. Thus, the average resultant normal force was 4375 kN. The summation of the forces in struts S1 to S7 was 2710 kN. Therefore, the difference force was 1665 kN. This force may have been borne by the corners of the walls

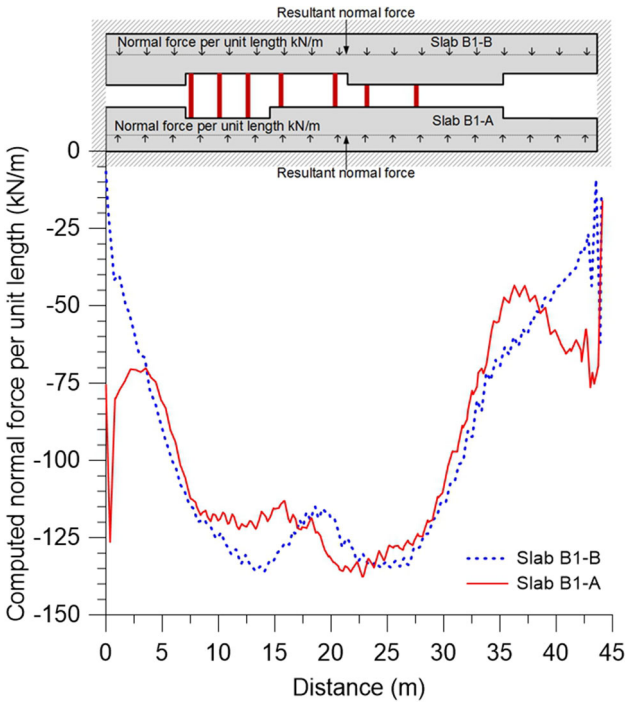

Fig. 16 Distribution of computed normal forces in concrete slabs

in the excavation and the side friction between the slabs and DCM walls. This means that the struts may have borne 62%, with the remaining 38% being borne by the corners and side friction.

5.9 Computed bending moments in the DCM wall

The maximum bending moment (M_{max}) induced in a DCM wall must be known to prevent local failure due to exceeding the moment capacity (M_{yield}) of the DCM wall section. DCM columns typically have higher compressive strengths than tensile and flexural strengths (σ_f). σ_f can be assumed to be $0.15q_{u(DCM)}$ [19] for the design in this study, which corresponds to a σ_f value of 300 kPa. Therefore, a DCM wall can fail when M_{max} reaches M_{yield} [5, 19]. The M_{yield} of a DCM wall in units of kN-m/m can be calculated using the following relationship [15, 19]:

$$M_{yield} = \sigma_f \frac{I}{t/2} \quad (15)$$

Thus, according to Eq. 15, M_{yield} for a DCM wall with a thickness of 2.5 m was 310 kN-m/m. The computed bending moment profiles of the DCM wall located in the middle of each wall side around the excavation area are presented in Fig. 17. The bending moments M_{1-1} and M_{2-2} are the bending moments due to bending around the length and the height of the wall, respectively. The shape is similar to that of a single pile under a lateral load. Between

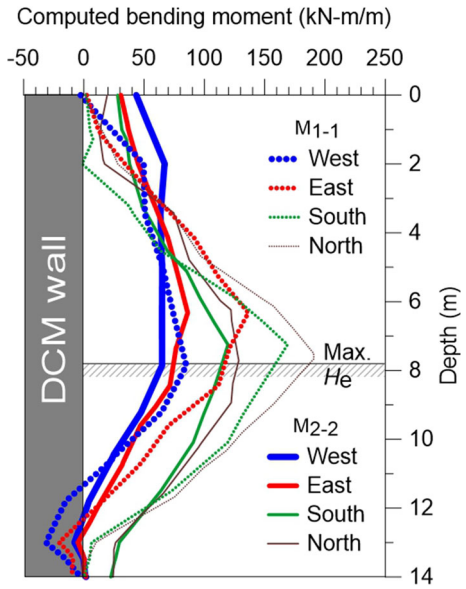

Fig. 17 Computed bending moment profiles for DCM walls

the two long sides of the excavation area, the maximum bending moments M_{1-1} and M_{2-2} were induced on the east side, with magnitudes of 135 and 120 kN-m/m located at depths of 6.1 and 7.1 m, respectively, below the ground surface. In the same way, the wall located at the north side of the excavation provided maximum M_{1-1} and M_{2-2} of 200 and 130 kN-m/m, respectively, at a depth of 7.1 m or 1.0 H_e. Thus, a minimum factor of safety against bending failure ($FS_{bending}$) of 1.55 was obtained for the DCM-TD of this case study. Clearly, the short side provided a maximum M_{1-1} greater than that of the long side by approximately 1.5 times the corresponding length-to-width ratio or 1.6 in this case study.

6 Numerical analysis results of DCM-TD in comparison with those of DCM-BU for the case study

To investigate the effectiveness of the DCM-TD method for deep excavation work, the lateral movement and bending moment profiles of a DCM wall without a permanent concrete slab bracing or a DCM wall using the BU construction method (DCM-BU) were numerically investigated. The DCM-BU method was simulated by omitting the concrete slabs and the temporary struts from the excavation area. The lateral movement profile obtained via 3D finite element analysis, as shown in Fig. 9, was the so-called case study for the analysis presented in the following sections.

Figure 18a shows a comparison of the computed lateral wall movements for the cases with and without concrete

slabs for the walls associated with I1, I2, I3 and I4. The DCM-BU method resulted in considerably larger lateral movements. The shapes of the computed lateral movement profiles for the walls associated with I3 and I4 in Fig. 18a tended to move further toward the excavation, unlike those in the case study. This result confirms that the existence of a slab affected the type of lateral wall movement profiles for the walls associated with I3 and I4, as noted in Sect. 5.1. For the DCM-BU case, the values of δ_{hm} at the top of the wall were approximately 101, 88, 59 and 60 mm for the walls associated with I1, I2, I3 and I4, respectively. Note that the δ_{hm} value for walls associated with I1 and I2 for DCM-BU is larger than the maximum allowable lateral movement of 65 mm for this project. The computed δ_{hm}/H_e ratios for the DCM-BU method were close to the ranges of the observed values for DCM walls in Bangkok and Shanghai shown in Fig. 13. However, when the concrete slabs were installed using the DCM-TD method, the ratio could be reduced to approximately 38, 48, 39 and 39 mm. Therefore, the reduction ratios were 38, 55, 67 and 65% for the walls associated with I1, I2, I3 and I4, respectively. The high reduction ratios reflect the high impact of the existence of a concrete slab bracing. Thus, the DCM-TD method can reduce lateral movement, with an average reduction ratio of 56% for this project.

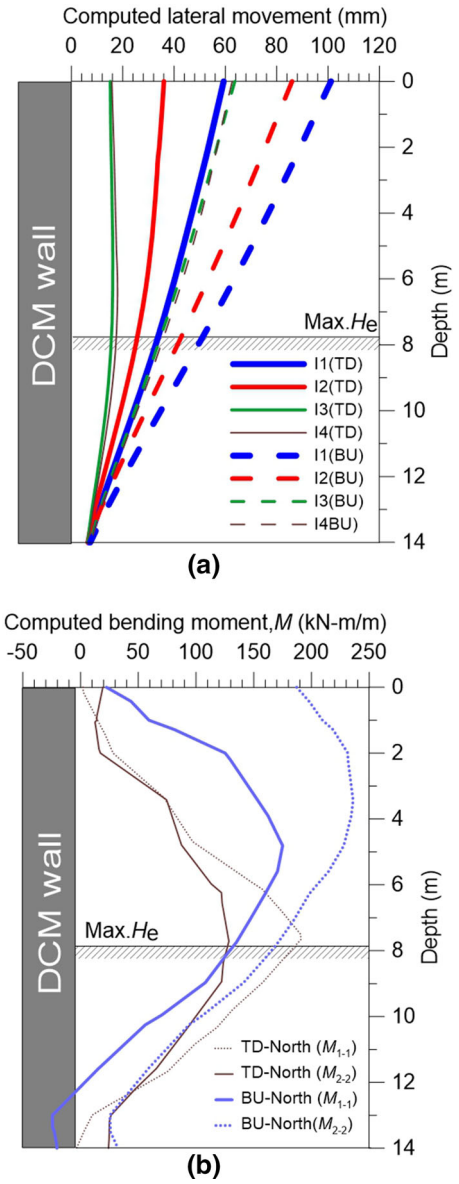

Fig. 18 Comparison of **a** computed lateral wall movement profiles and **b** bending moment profiles for DCM-TD and DCM-BU

The bending moment profiles of the DCM-TD and DCM-BU methods for the northern side of the excavation area are presented in Fig. 18b. The bending moment M_{2-2} of the DCM walls with and without the concrete slab was significantly different in both magnitude and shape, especially at depths above the excavation depth. The location of maximum moment M_{2-2} changed from a depth of 8 m to a depth of 3 m for DCM-TD and DCM-BU, respectively. The magnitude of the maximum moment M_{2-2} changed from 130 to 240 kN-m/m for DCM-TD and DCM-BU, respectively. However, there was an insignificant change in bending moment M_{1-1}. The magnitude of the maximum moment M_{1-1} changed from 200 to 180 kN-m/m for DCM-TD and DCM-BU, respectively. Note that the construction method can change the magnitude of M_{max} from M_{1-1} to M_{2-2}, namely M_{1-1} is minimum for DCM-BU, whereas M_{2-2} is minimum for DCM-TD because of the existence of a concrete slab. A minimum $FS_{bending}$ of 1.29 was obtained for DCM-BU, which is smaller than that for DCM-TD and is lower than the $FS_{bending}$ value of 1.50 required for this project. Thus, DCM-BU with four rows of DCM walls is unsuitable for this project based on the performance-based design.

As mentioned above, both the lateral wall movement and the bending moments (particularly M_{2-2}) in a DCM wall above the excavation level drastically decrease when the concrete slab is introduced. This result reveals that the lateral earth pressure applied to the wall has been substantially transferred to the concrete slabs. It also implies the potential of implementing the DCM-TD method for excavations at greater depths when the wall thickness is kept constant.

7 Numerical investigation on applicability and future potential of DCM-TD compared to DCM-BU for greater excavation depths

This section presents the applicability of the DCM-TD method to investigate its future potential for greater excavation depths. Thus, the excavation depths used in additional analyses increase from 7.9 to 10.9 and 13.9 m, which

correspond to three and four levels of slabs, respectively. The thickness of the slabs and number of struts at each level were assumed to be the same as in the case study, as shown in Fig. 19. In addition, the design of a deep excavation work in an urban area is limited to an insufficient space close to a property line. Thus, the thickness of the DCM wall is an important factor for designing using the DCM-TD and DCM-BU methods. The wall thickness for this project was limited to 2.5 m, or four rows of a DCM wall, because of the insufficient space. M_{max} in the DCM wall is an important design parameter because it establishes the wall thickness required to maintain a performance-based design. Based on Eq. 1, M_{yield} depends on the wall thickness, whereas σ_f is a property of the soil–cement material. Assuming that all DCM walls in this study comprise a homogeneous and isotropic material, the value of M_{yield} for various wall thicknesses can be determined using Eq. 1 and, as shown in Fig. 20, using the same σ_f value of 300 kPa. These values are used for comparison with the M_{max} value computed for the DCM wall based on 3D-FEM.

First, an appropriate wall thickness must be determined based on the minimum $FS_{bending}$ of 1.50 to prevent bending failure of the wall. Then, δ_{hm} must be calculated to verify that the induced δ_{hm} is smaller than 65 mm based on the performance-based design. Figure 21a shows the effects of the DCM wall thickness on the minimum $FS_{bending}$ at various excavation depths for DCM-BU and DCM-TD.

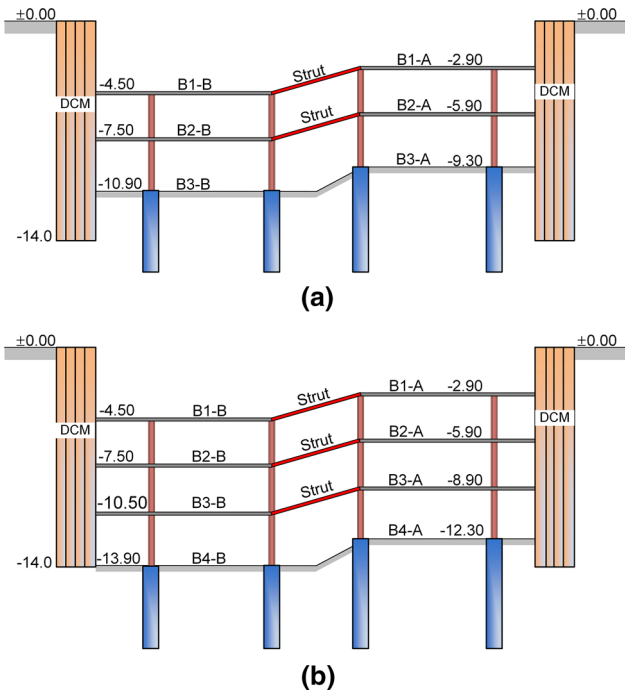

Fig. 19 Cross-sectional view of DCM-TD for **a** H_e = 10.9 m and H_e = 13.9 m

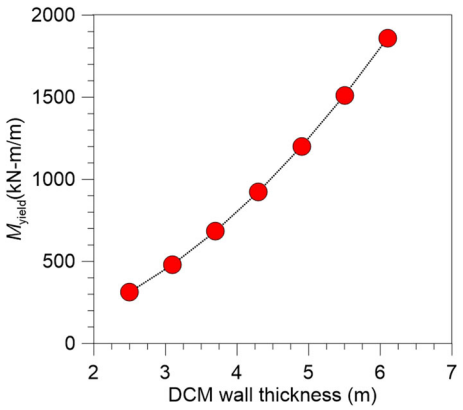

Fig. 20 M_{yield} versus DCM wall thickness

The numerical results show that the $FS_{bending}$ of the DCM wall increases with increasing wall thickness because of the increase in M_{yield} for both DCM-TD and DCM-BU and that the incremental rates for DCM-BU were higher than those for DCM-TD. This result implies that DCM-TD has an advantage in distributing induced bending moments and lateral loads from a deep excavation. Figure 21b presents only the corresponding δ_{hm} for a DCM wall providing a minimum $FS_{bending}$ value greater than 1.50, and the value of δ_{hm} decreases with the increasing wall thickness because of the increase in wall rigidity [42] for both DCM-TD and DCM-BU. Because of the existence of concrete slabs, the values of δ_{hm} for the same wall thickness at different H_e are insignificantly different. The values of δ_{hm} for the wall are almost unchanged with increasing excavation depths, unlike the DCM-BU method, because of the very high stiff lateral support of the concrete slab. This system is more suitable for deep excavations in urban environments, particularly under conditions of limited perimeter space and adjacent existing structures. In addition, the DCM-TD method for the field case study (H_e = 7.9 m) requires almost half the wall thickness of the DCM-BU method to obtain the required δ_{hm} value of 65 mm. In the same manner, a wall thickness of 3.1 m is sufficient for DCM-TD for H_e values greater than 7.9 m, while wall thicknesses of 4.9 and 6.1 m are required for DCM-BD for H_e values of 10.9 and 13.9 m, respectively.

To evaluate the effectiveness of DCM-TD considering the effect of the wall thickness and H_e, the reduction ratio versus the wall thickness for various H_e values is presented in Fig. 21c. The reduction ratio values decrease with increasing wall thickness for all H_e, which implies that DCM-TD is appropriate for thin DCM walls. The reduction ratios increase with increasing H_e for the same wall thickness, and the average values of the reduction ratios are 33, 44 and 57% for H_e of 7.9, 10.9 and 13.9 m, respectively, which reflects the fact that DCM-TD is more effective for deeper excavations.

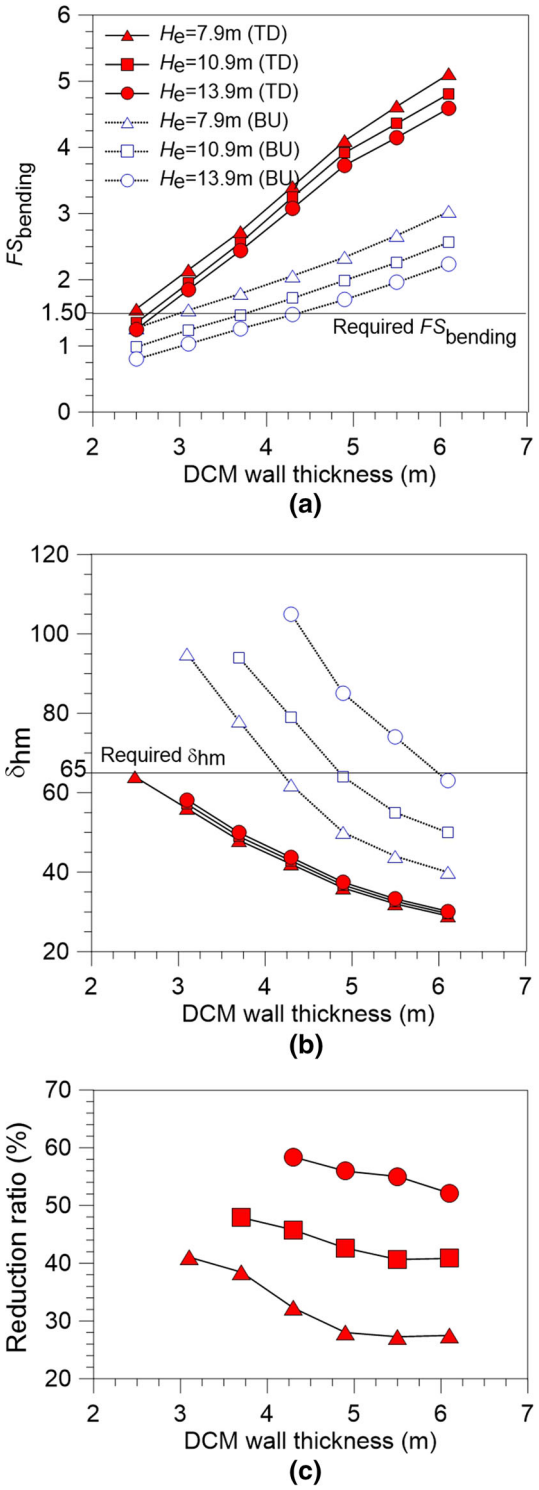

Fig. 21 Effect of DCM wall thickness and excavation depth on **a** $FS_{bending}$, **b** δ_{hm} and **c** reduction ratio

Figure 22 shows the effect of wall thickness on the average normal forces in the struts and the slabs for various H_e for DCM-TD, which are defined as the total normal forces in the struts divided by the total numbers of struts

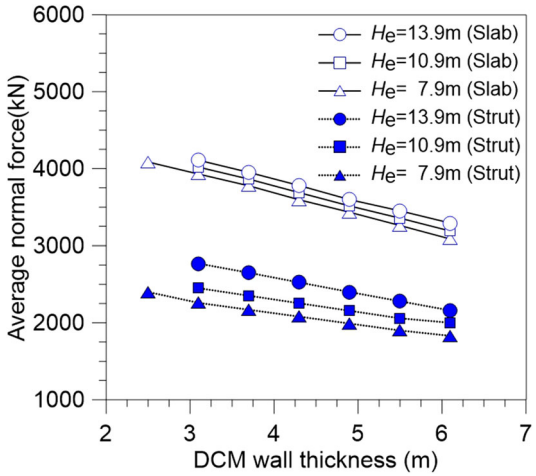

Fig. 22 Effect of DCM wall thickness and excavation depth on average normal force in strut and slab

and the total normal forces in the slabs divided by the total numbers of slabs, respectively. The figure shows that the wall thickness has a substantial effect on the forces in struts and slabs. As expected, the results show that the overall tendency is the reduction in forces in struts and slabs with increasing wall rigidity for various H_e. In addition, the forces in the struts and slabs increase with the increasing H_e for the same wall thickness, which confirms that a concrete slab requires a greater lateral load to maintain similar values of δ_{hm} for different H_e, as shown in Fig. 21b. The differences between the forces in the slabs and struts or the remaining forces borne by the corners and side friction were approximately 38, 33 and 29% for H_e of 7.9, 10.9 and 13.9 m, respectively.

8 Summary and conclusions

A case study of a DCM wall applied using a top-down construction method (DCM-TD) for a deep excavation in soft Bangkok clay has been reported. The lateral movements of the wall system and the strut forces at the proposed excavation depth were observed. A calibration of laboratory test results using a hardening soil model was performed to obtain the best parameters for simulating the behavior of the foundation soils and DCM column. The magnitude of the maximum lateral movement of the wall (δ_{hm}) was compared with the results for various types of supports used in previous studies. An analysis of the results of the case study was then conducted to assist in understanding the wall behavior in terms of the lateral movements and the forces in structural members using the three-dimensional finite element analysis. Finally, a numerical investigation of the applicability and future potential of DCM-TD at greater depths in comparison with the DCM

wall using the bottom-up construction method (DCM-BU) was carried out. The following conclusions were drawn based on the observed and simulated results:

1. The DCM-TD in this study provided a measured maximum δ_{hm} of 58 mm and a minimum $FS_{bending}$ of 1.55 by assuming that $\sigma_f = 0.15q_{u(DCM)}$, which meets the criteria for performance-based designs for deep excavation works in the urban Bangkok area, namely δ_{hm} and $FS_{bending}$ values equal to 65 mm and 1.50, respectively. Based on a design with the mentioned criteria, no damage to the ground near the excavation area was observed for the DCM-TD used for this study.
2. The upper bound of the observed δ_{hm}, $0.73\%H_e$, for a DCM-TD was within the average values of the observed δ_{hm} for DW-BU and DCM-BU obtained in previous studies. The mean value of δ_{hm} for this study, $0.45\%H_e$, reflects that the observed effectiveness of DCM-TD was superior to that of DCM-BU by as much as three times but close to that of DW-BU, with a difference of as much as 0.8 times.
3. The δ_{hm}/H_e value measured in this study falls between the two limit lines presented by Mana and Clough [28], with an average FOS_{base} value of 1.45, whereas the average FOS_{base} value obtained from the relationship between δ_{hm}/H_e and the system stiffness is 1.35, implying that this wall system provides a high potential resistance against basal heave. The DCM with the TD method (this study), DW-BU and DW-TD provided the smallest, medium and largest average FOS_{base} values, respectively.
4. Based on the strut forces observed in this study, a minimum factor of safety against structural failure of 6.7 was obtained, which was confirmed by a performance-based design. The excess bending moments were induced in the strut due to the effect of installation with an inclination, which produced maximum excess bending moments of 62 kN-m. However, the excess bending moments were compensated by a high value of the factor of safety against structural failure.
5. Sixty-two percent of the total normal forces perpendicular to the length of the slabs were shared by the struts, and the remaining 38% of the forces were shared by the corners and side friction.
6. The computed maximum bending moment induced in the DCM-TD wall is the bending moment due to bending around the length of the wall. The short side provided a maximum M_{1-1} greater than the long side by approximately 1.5 times corresponding to the length-to-width ratio or 1.6 in this case study.
7. The numerical results of the case study show that the concrete slab used in the TD construction had a large effect on the lateral wall movements and bending moment in the DCM walls. With the concrete slab, the lateral movements were reduced, with an approximate average reduction ratio of 62% based on four locations of δ_{hm} around the excavation area. The existence of the slab also changed the magnitude of M_{max} from M_{1-1} to M_{2-2} and reduced the magnitude of M_{2-2} by as much as 1.85 times.
8. For the specific case study of the DCM-TD wall in soft Bangkok clay, a series of parametric studies of excavation at depths greater than that of the case study indicate that DCM-TD provides insignificant changes in δ_{hm}, as the system stiffness is large enough such that any further increase in H_e in the range of this study will not increase the value of δ_{hm} further. The induced lateral forces and bending moments are thus mainly absorbed by the slabs and struts, which is confirmed by higher loads in the concrete slabs and struts for larger values of H_e.
9. The DCM-TD method for the field case study (H_e = 7.9 m) requires almost half the wall thickness of the DCM-BU method to obtain the required δ_{hm} value of 65 mm. In the same manner, a wall thickness of 3.1 m is sufficient for DCM-TD for H_e values greater than 7.9 m, while wall thicknesses of 4.9 and 6.1 m are required for DCM-BD for H_e values of 10.9 and 13.9 m, respectively.
10. An evaluation of the effectiveness of DCM-TD compared to that of DCM-BU without the creep time effect showed that the reduction ratios for lateral wall movement are 33, 44 and 56% for H_e of 7.9, 10.9 and 13.9 m, respectively, based on the computed maximum δ_{hm}. This reveals the future potential of implementing DCM-TD for deep excavation works in urban environments.

Acknowledgements This research was funded by King Mongkut's University of Technology North Bangkok under Contract No. KMUTNB-GOV-59-03. The authors also extend their appreciation to the Thailand Research Fund (TRF) under Basic Research Grant No. BRG6080011.

Appendix: Creep effect on lateral wall movements

Figure 23 shows the creep effect on the lateral movements of the walls associated with I1 and I2 for excavation stages 7 and 9 and stages 4 and 6, respectively. As shown, the creep effect is insignificant for this project.

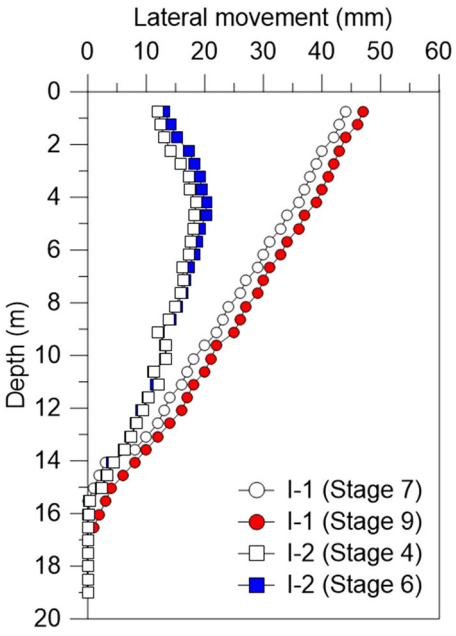

Fig. 23 Creep effect on the lateral movements of the walls

References

1. Addenbrooke TI (1994) A flexibility number for the displacement controlled design of multi propped retaining walls. Gr Eng 27:41–45
2. Arboleda-Monsalve LG, Finno RJ (2015) Influence of concrete time-dependent effects on the performance of top-down construction. J Geotech Geoenviron Eng 141:985–994. https://doi.org/10.1061/(ASCE)GT.1943-5606.0001260
3. Bergado DT, Teerawattanasuk C, Youwai S, Voottipruex P (2000) Finite element modeling of hexagonal wire reinforced embankment on soft clay. Can Geotech J 37:1209–1226. https://doi.org/10.1139/t00-065
4. Borja RI (2013) Plasticity modeling and computation. Springer, Berlin-Heidelberg
5. Chai J, Shrestha S, Hino T, Ding W, Kamo Y, Carter J (2015) 2D and 3D analyses of an embankment on clay improved by soil–cement columns. Comput Geotech 68:28–37. https://doi.org/10.1016/j.compgeo.2015.03.014
6. Clough GW, O'Rourke TD (1990) Construction induced movements of in situ walls. In: Proceedings of the ASCE conference on design and performance of earth retaining structures. American Society of Civil Engineers, New York, pp 439–470
7. Clough GW, Smith EM, Sweeney BP (1989) Movement control of excavation support systems by iterative design. In: Proceedings of the ASCE foundation engineering: current principles and practice, vol 2. American Society of Civil Engineers, New York, pp 869–884
8. Finno RJ, Blackburn JT, Roboski JF (2007) Three-dimensional effects for supported excavations in clay. J Geotech Geoenviron Eng 133:30–36. https://doi.org/10.1061/(ASCE)1090-0241(2007)133:1(30)
9. Goldberg DT, Jaworski WE, Gordon MD (1976) Lateral support systems and underpinning. Rep No. FHWA-RD-75-129. Federal Highway Administration, Washington
10. Hou YM, Wang JH, Zhang LL (2009) Finite-element modeling of a complex deep excavation in Shanghai. Acta Geotech 4:7–16. https://doi.org/10.1007/s11440-008-0062-3
11. Hsieh P, Ou C, Lin Y (2013) Three-dimensional numerical analysis of deep excavations with cross walls. Acta Geotech 8:33–48. https://doi.org/10.1007/s11440-012-0181-8
12. Hsiung BB, Yang K, Aila W, Hung C (2016) Three-dimensional effects of a deep excavation on wall deflections in loose to medium dense sands. Comput Geotech 80:138–151. https://doi.org/10.1016/j.compgeo.2016.07.001
13. Huang J, Han J (2009) 3D coupled mechanical and hydraulic modeling of a geosynthetic-reinforced deep mixed column-supported embankment. Geotext Geomembr 27:272–280. https://doi.org/10.1016/j.geotexmem.2009.01.001
14. Ignat R, Baker S, Larsson S, Liedberg S (2015) Two- and three-dimensional analyses of excavation support with rows of dry deep mixing columns. Comput Geotech 66:16–30. https://doi.org/10.1016/j.compgeo.2015.01.011
15. Jamsawang P, Bergado DT, Voottipruex P (2011) Field behaviour of stiffened deep cement mixing piles. Proc Inst Civ Eng Ground Improv 164:33–49. https://doi.org/10.1680/grim.900027
16. Jamsawang P, Voottipruex P, Boathong P, Mairaing W, Horpibulsuk S (2015) Three-dimensional numerical investigation on lateral movement and factor of safety of slopes stabilized with deep cement mixing column rows. Eng Geol 188:159–167. https://doi.org/10.1016/j.enggeo.2015.01.017
17. Jamsawang P, Voottipruex P, Jongpradist P, Bergado DT (2015) Parameters affecting the lateral movements of compound deep cement mixing walls by numerical simulations and parametric analyses. Acta Geotech 10:797–812. https://doi.org/10.1007/s11440-015-0417-5
18. Jamsawang P, Boathong P, Mairaing W, Jongpradist P (2016) Undrained creep failure of a drainage canal slope stabilized with deep cement mixing columns. Landslides 13:939–955. https://doi.org/10.1007/s10346-015-0651-9
19. Jamsawang P, Yoobanpot N, Thanasisathit N, Voottipruex P, Jongpradist P (2016) Three-dimensional numerical analysis of a DCM column-supported highway embankment. Comput Geotech 72:42–56. https://doi.org/10.1016/j.compgeo.2015.11.006
20. Jongpradist P, Jumlongrach N, Youwai S, Chucheepsakul S (2010) Influence of fly ash on unconfined compressive strength of cement-admixed clay at high water content. J Mater Civ Eng 22:49–58. https://doi.org/10.1061/(ASCE)0899-1561(2010)22:1(49)
21. Jongpradist P, Kaewsri T, Sawatparnich A, Suwansawat S, Youwai S, Kongkitkul W, Sunitsakul J (2013) Development of tunneling influence zones for adjacent pile foundations by numerical analyses. Tunn Undergr Space Technol 34:96–109. https://doi.org/10.1016/j.tust.2012.11.005
22. Lee F, Yong K, Quan KCN, Chee K (1998) Effect of corners in strutted excavations: field monitoring and case histories. J Geotech Geoenviron Eng 124:339–349. https://doi.org/10.1061/(ASCE)1090-0241(1998)124:4(339)
23. Likitlersuang S, Surarak C, Wanatowski D, Oh E, Balasubramaniam A (2013) Finite element analysis of a deep excavation: a case study from the Bangkok MRT. Soils Found 53:756–773. https://doi.org/10.1016/j.sandf.2013.08.013
24. Lim A, Hsieh P, Ou C (2016) Evaluation of buttress wall shapes to limit movements induced by deep excavation. Comput Geotech 78:155–170. https://doi.org/10.1016/j.compgeo.2016.05.012
25. Liu KX (1995) Three dimensional analysis of deep excavation in soft clay. Masters, National University of Singapore
26. Liu GB, Jiang RJ, Ng CWW, Hong Y (2011) Deformation characteristics of a 38 m deep excavation in soft clay. Can Geotech J 48:1817–1828. https://doi.org/10.1139/t11-075
27. Long M (2001) Database for retaining wall and ground movements due to deep excavations. J Geotech Geoenvironmental Eng 127:203–224. https://doi.org/10.1061/(ASCE)1090-0241(2001)127:3(203)

28. Mana AI, Clough GW (1981) Prediction of movements for braced cuts in clay. J Geotech Eng (Div) 6:759–777
29. Moormann C (2004) Analysis of wall and ground movements due to deep excavations in soft soil based on a new worldwide database. Soils Found 44:87–98. https://doi.org/10.3208/sandf.44.87
30. Ou C, Hsieh P, Chiou D (1993) Characteristics of ground surface settlement during excavation. Can Geotech J 30:758–767. https://doi.org/10.1139/t93-068
31. Ou C, Liao J, Lin H (1998) Performance of diaphragm wall constructed using top-down method. J Geotech Geoenviron Eng 124:798–808. https://doi.org/10.1061/(ASCE)1090-0241(1998)124:9(798)
32. Ou CY, Hsieh PG, Lin YL (2013) A parametric study of wall deflections in deep excavations with the installation of cross walls. Comput Geotech 50:55–65. https://doi.org/10.1016/j.compgeo.2012.12.009
33. Phutthananon C, Jongpradist P, Yensri P, Jamsawang P (2018) Dependence of ultimate bearing capacity and failure behavior of T-shaped deep cement mixing piles on enlarged cap shape and pile strength. Comput Geotech 97:27–41. https://doi.org/10.1016/j.compgeo.2017.12.013
34. Potts DM, Day RA (1991) The effect of wall stiffness on bending moments. In: The 4th international conference on piling and deep foundations, pp 435–444
35. Rowe PW (1952) Anchored sheet-pile walls. Proc Inst Civ Eng 1:27–70. https://doi.org/10.1680/iicep.1952.10942
36. Schanz T, Vermeer PA, Bonnier PG (1999) The hardening-soil model: formulation and verification. In: Brinkgreve RBJ (ed) Beyond 2000 in computational geotechnics. Balkema, Rotterdam, pp 281–290
37. Sexton BG, McCabe BA (2013) Numerical modelling of the improvements to primary and creep settlements offered by granular columns. Acta Geotech 8:447–464. https://doi.org/10.1007/s11440-012-0205-4
38. Shao Y, Macari EJ, Cai W (2005) Compound deep soil mixing columns for retaining structures in excavations. J Geotech Geoenviron Eng 131:1370–1377. https://doi.org/10.1061/(ASCE)1090-0241(2005)131:11(1370)
39. Surarak C, Likitlersuang S, Wanatowski D, Balasubramaniam A, Oh E, Guan H (2012) Stiffness and strength parameters for hardening soil model of soft and stiff Bangkok clays. Soils Found 52:682–697. https://doi.org/10.1016/j.sandf.2012.07.009
40. Terzaghi K (1943) Theoretical soil mechanics. Wiley, New York
41. Wang ZW, Ng CW, Liu GB (2005) Characteristics of wall deflections and ground surface settlements in Shanghai. Can Geotech J 42:1243–1254. https://doi.org/10.1139/t05-056
42. Wang JH, Xu ZH, Wang WD (2010) Wall and ground movements due to deep excavations in Shanghai soft soils. J Geotech Geoenviron Eng 136:985–994. https://doi.org/10.1061/(ASCE)GT.1943-5606.0000299
43. Wonglert A, Jongpradist P (2015) Impact of reinforced core on performance and failure behavior of stiffened deep cement mixing piles. Comput Geotech 69:93–104. https://doi.org/10.1016/j.compgeo.2015.05.003
44. Wonglert A, Jongpradist P, Jamsawang P, Larsson S (2018) Bearing capacity and failure behaviors of floating stiffened deep cement mixing columns under axial load. Soils Found. https://doi.org/10.1016/j.sandf.2018.02.012
45. Zhang W, Goh ATC, Xuan F (2015) A simple prediction model for wall deflection caused by braced excavation in clays. Comput Geotech 63:67–72. https://doi.org/10.1016/j.compgeo.2014.09.001
46. Zhao C, Lavasan AA, Barciaga T, Zarev V, Datcheva M, Schanz T (2015) Model validation and calibration via back analysis for mechanized tunnel simulations—the western Scheldt tunnel case. Comput Geotech 69:601–614. https://doi.org/10.1016/j.compgeo.2015.07.003

Available online at www.sciencedirect.com

ScienceDirect

Soils and Foundations 58 (2018) 446–461

www.elsevier.com/locate/sandf

Bearing capacity and failure behaviors of floating stiffened deep cement mixing columns under axial load

Anucha Wonglert [a], Pornkasem Jongpradist [a,*], Pitthaya Jamsawang [b], Stefan Larsson [c]

[a] *Department of Civil Engineering, King Mongkut's University of Technology Thonburi, Thailand*
[b] *Department of Civil Engineering, King Mongkut's University of Technology North Bangkok, Thailand*
[c] *Division of Soil and Rock Mechanics, Department of Civil and Architectural Engineering, KTH Royal Institute of Technology, Sweden*

Received 18 April 2017; received in revised form 16 November 2017; accepted 26 December 2017
Available online 21 February 2018

Abstract

This research aims to clarify and gain an insight into the impact of the length of the stiffened core and the strength of the deep cement mixing (DCM) socket on the behaviors of floating stiffened deep cement mixing (SDCM) columns. The observed behaviors include the axial ultimate bearing capacity, settlement and failure mode. The study begins by conducting a series of physical model tests as a preliminary investigation. The results reveal that the strength of the DCM socket can be reduced to a certain value by inserting a sufficiently long reinforced core to achieve the highest possible load-carrying capacity, indicating an optimum length of the stiffened core for a specific DCM socket strength. For a parametric study on the actual scale condition, full-scale load tests on a floating DCM and an SDCM column with eucalyptus wood as a core in the thick soft clay layer area were carried out to provide a reference case. The extended numerical analysis results suggest that the modes of failure depend on the length of the stiffened core and the strength of the DCM socket. The results from the numerical parametric study were used to establish a guideline chart for suggesting the appropriate length of the core in accordance with the strength of the DCM socket of the floating SDCM columns. The field pile load test results also confirm that core materials with a lower strength and stiffness, such as eucalyptus wood, could potentially be used as a reinforced core.

Keywords: DCM; SDCM; Bearing capacity; Failure; Numerical analysis; Physical model

1. Introduction

The deep mixing method is widely used to improve the engineering properties of soft ground by injecting cement powder or slurry to bond the soil particles and form a column. Deep cement mixing (DCM) columns are widely used to support the vertical load and to reduce the settlement of earth structures acting as foundations for road embankments. For the majority of projects in the past and in current practice in many countries, designers often specify the tip of a DCM column at the depth of the firm layer (often medium clay) as the fixed column type to ensure that the settlement will be minimal. However, in areas where the soft clay layer is particularly thick, such as the southern part of Bangkok, fixed column-type DCM columns (hereafter called end bearing DCM columns) can lead to high construction costs. To reduce construction costs, DCM columns with a certain length (not the depth of the firm layer) or floating DCM columns are applied in engineering practice (e.g., Teeracharti, 1998). This floating DCM column type has also been implemented in many countries

Peer review under responsibility of The Japanese Geotechnical Society.
* Corresponding author at: Civil Engineering Department, Faculty of Engineering, King Mongkut's University of Technology Thonburi, 126 Pracha Uthit, Bang Mod, Thung Khru, Bangkok 10140, Thailand.
E-mail address: pornkasem.jon@kmutt.ac.th (P. Jongpradist).

https://doi.org/10.1016/j.sandf.2018.02.012
0038-0806/

that have thick soft deposit clay layers, such as Japan (e.g., FNHO, 2003; Tsutsumi, 2008), Sweden (e.g., Holm, 1999; Alén et al., 2005) and Vietnam (e.g., Do and Nguyen, 2013).

Because the strength of soil-cement is controlled by the water-cement ratio (Miura et al., 2001), a large amount of cement is required to construct DCM columns in soft ground areas where the water content is high, particularly if the wet process with the jet grouting method is used. In current practice, the cement content is often increased as a strategy to achieve the target strength of DCM columns. However, it has been found in a number of studies (e.g., Uddin et al., 1997; Jongpradist et al., 2011a, 2011b) that when the cement content is increased to a certain amount, the strength of cement-admixed clay does not increase linearly with the cement content. In other words, the cost efficiency in increasing the cement content to increase the strength is rather low. One possible alternative is to partially replace the cement with lower-cost binders, such as fly ash (e.g., Horpibulsuk et al., 2009; Jongpradist et al., 2010).

The vertical load distribution along a column decreases with depth. Thus, the highest compressive stress occurs at the top part of the column, and thus, high strength is only required at the top of the column. Considering this, Dong et al. (2004) introduced the stiffened deep cement mixing (SDCM) column in China. They inserted a small reinforced concrete pile in the center of an ordinary DCM column after finishing the DCM column construction. The results of field load tests on the ordinary DCM and SDCM columns revealed that the stiffened core improved both the load-carrying capacity and settlement of the DCM columns under axial compression loading. Full-scale load tests of SDCM columns in the northern part of Bangkok with various core sizes and lengths performed by Jamsawang et al. (2010) and the subsequent numerical investigation by Voottipruex et al. (2011a) and (2011b) indicated that the ratio of the length of the core and DCM and the core size has a significant effect on the load-carrying capacity and settlement of the DCM columns. However, increasing either the length or size of the reinforced core would increase the construction cost due to the additional core material, which is often more expensive than the DCM itself. By considering the impact of the core on load-carrying capacity based on the controlled core volume, Wonglert and Jongpradist (2015) found that for a constant reinforced core volume, SDCM columns with a more slender core provide a higher ultimate load and less settlement. These researchers also found that the effectiveness of a reinforced core in increasing the ultimate load of the SDCM columns and the associated failure mode mainly depend on the core dimensions, core volume and strength of the DCM socket. There are three possible failure modes for SDCM columns under axial loading: soil failure, column failure at the core tip and column failure in the DCM socket at the top of the column. The SDCM columns considered in most previous studies (Jamsawang et al., 2010; Raongjant and Meng, 2013; Wang et al., 2014; Wonglert and Jongpradist, 2015; Ye et al., 2017) are the end bearing piles (fixed column type), as schematically shown in Fig. 1, whereas the only comprehensive study on the floating SDCM columns was reported by Dong et al. (2004). The effectiveness of inserting the concrete core was confirmed and an understanding on load transfer was obtained. However, the effect of the core dimensions in relation to the DCM socket strength on mechanical behavior of floating SDCM columns has yet to be demonstrated. Moreover, most previous studies considered only a high-strength and stiff core, such as concrete and steel with a much higher stiffness (approximately 100–1000 times) than those of the DCM column. Only the study by Wonglert and Jongpradist (2015) numerically investigated the possibility of using a less stiff material as a core. No full-scale tests have been performed to confirm that a less stiff material, such as wood, can be used as a stiffened core for SDCM columns. Besides the lower price, by using wood instead of concrete or steel, the CO_2 emission from their production can be reduced. Since eucalyptus wood is widely used in the construction industry in many countries and can be produced in substantial quantities, it is the focus in this study.

In this study, a series of physical model tests on scaled-down floating SDCM columns under axial loading conditions was performed to preliminarily investigate the influence of the core length and DCM socket strength on the load-carrying capacity of floating SDCM columns. With the evidence confirmed by the physical model tests, a numerical parametric study considering the full-scale problem was performed to extend the investigation. In order to achieve this, full-scale loading tests on floating DCM and SDCM columns with a eucalyptus wood core were conducted as a reference case, and to confirm the effectiveness of using wood as a stiffened core for SDCM columns. Based on the numerical parametric study, understanding the relationship between the core length, the DCM socket strength and associate failure mode for specific soil, and the DCM length can be obtained. An example chart illustrating the relationship between the DCM socket strength, the stiffened core length and the DCM column length at the optimum performance is also presented as a guideline for suggesting a suitable core length.

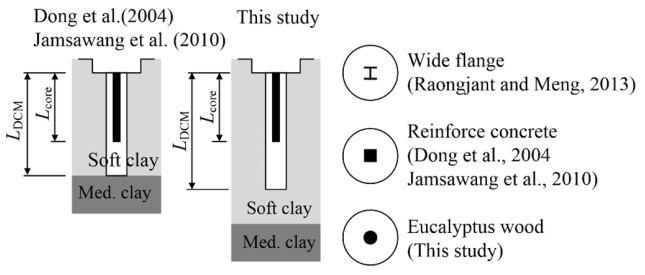

Fig. 1. Schematic of SDCM piles considered in this study (floating type) compared to previous Studies.

2. Physical model tests on scaled-down floating SDCM columns

A series of scaled-down model tests under axial loading was performed to study the influence of the reinforced core length and DCM socket strength on load-carrying capacity, settlement and failure behaviors of SDCM columns. The main test program consisted of six experiments (settings A and B, see Table 1) by varying two influencing factors, the length of the reinforced core (L_{core}) and the unconfined compressive strength of the DCM socket ($q_{u,DCM}$). L_{core} and $q_{u,DCM}$ values of 150, 350, and 500 mm and 35 and 135 kPa, respectively, were considered, as shown in Table 1 and Fig. 2. In addition to these six tests, additional tests were also conducted to better understand the mechanism behind the obtained results (settings C and D for DCM and SDCM columns, respectively, see Table 1).

2.1. Materials and preparation

2.1.1. Soft clay layer

The soft clay layer in the model tests was made from remolded Bangkok soft clay taken from the Mahai Sawan Intersection located in southwestern part of Bangkok. The layer was remolded at a water content of 120% before being poured into a cuboid container and then consolidated under a surcharge load of 60 N/m^2 until the degree of pre-consolidation reached 95% or greater. Samplings of the remolded soft clay were taken at various depths and locations in the model soil for testing to ensure that the strength and corresponding water content of the prepared soft clay layer satisfied the target values of 8 kPa and 75%, respectively. The physical properties of the soft clay layer after preparation are listed in Table 2.

2.1.2. Deep cement mixing columns

After completing the consolidation process of the soft clay layer, a thin steel tube was carefully pushed into the soil as a casing before gradually bringing the soil in the casing out. Prepared clay-cement slurry was poured into drilled holes in the soft clay layer to construct the 38 mm diameter and 500 mm long DCM columns. This method of model DCM column installation may not fully reflect the field installation approach, particularly in terms of field interface interaction. A more rigorous method can be followed by using specially designed devices for laboratory mixing (such as Larsson, 1999; Chen et al., 2014). A length of 500 mm was chosen for further investigation with the end bearing SDCM columns performed in the previous study (Wonglert and Jongpradist, 2015). Our assumption is that the required strength of the DCM socket to achieve the optimum performance can be reduced by inserting the core. The DCM socket strengths were thus designed to obtain the column failure mode (for DCM column) by two different mixing ratios. Cement contents of 63 kg/m^3 and 190 kg/m^3 of wet soil were used in the mixing process to obtain the $q_{u,DCM}$ of 35 kPa and 135 kPa, respectively. During the installation of the DCM columns, samples of the clay-cement mixtures were collected and tested at a curing age of 30 days to reconfirm the target strengths.

2.1.3. Reinforced core

In the case of SDCM columns, Polyaramid or Nylon cores 10 mm in diameter were installed in the center of the DCM columns immediately after the DCM column installation. Polyaramid was chosen because of its ability to maintain its stiffness ratio during the test ($E_{Polyaramid}/E_{DCM}$) to be equivalent to that in the field (E_{wood}/E_{DCM}). The elastic modulus of 600 MPa was obtained from the unconfined compression test. The cores were attached with 1–4 strain gauges at different levels to measure the strain distribution along the column depth during performing the column load test as shown in Fig. 3a.

2.1.4. Strain sensor

For SDCM columns with cores shorter than the columns (A1, A2, B1, and B2), the strain sensors were embedded at the center of DCM column (only in the part under the core tip) in order to observe the load transfer mechanism between the columns and the surrounding clay. As a strain sensor, two strain gauges were installed on the polyurethane (PU) cylindrical bar with a modulus in the range of the modulus in the DCM socket in the study. The dimensions of the PU bars, at10 mm in diameter and 25 mm in length, are illustrated in Fig. 3b. The elastic modulus of the PU is 20 MPa, as obtained from the unconfined compression test. Fig. 3c shows the strain sensors after preparation and before waterproofing with the silicone. The strain gauges were formulated as half bridge circuits to measure the strain in the DCM columns during the test. The strain sensors were installed vertically into the center of DCM column immediately after finishing the DCM column construction and before inserting the core. The positions of installation of the sensors are shown in Fig. 2.

2.2. Testing equipment

The loading module composes of two main parts; the pressure generator and modelled footing, as illustrated in Fig. 4a. All loads from air cylinders were transferred to the modelled footing through universal joints. In order to reduce the friction force, a linear bush was installed between the modelled footing and the loading rod. An axial load cell was set up with electro-pneumatic transducers connecting to the computer controlled load system. Fig. 4b shows a soil container used to model the soil layer in the small-scale model test in this study. The container is 1800 mm long, 800 mm high, and 400 mm wide (the out-of-plane direction). Excess pore water pressure transducers were embedded at 2 different depths (300 and 600 mm from top) at the edge of container (400 mm wide side) during the test. No excess water pressure could be observed during the pile load tests, which indicates that the boundary of

Table 1
Testing program and details of SDCM and DCM piles in the physical model tests.

	Type	No	q_u (kPa)		$q_{u,DCM}/q_{u,soil}$	L_{core} (mm)	Q_u (N)		
			soil	DCM			Testing result	Calculation	
								Pile failure	Soil failure
Main setting	SDCM	A1	8	35	4.38	150	57	45	350
		A2	8	35	4.38	350	97.7	45	350
		A3	8	35	4.38	500	131	45	350
	SDCM	B1	8	135	16.88	150	210	170	350
		B2	8	135	16.88	350	293	170	350
		B3	8	135	16.88	500	295	170	350
Supplement setting	DCM	C1	10	55	5.5	–	75	70	370
		C2	10	275	27.5	–	350	350	370
		C3	10	280	28	–	364	360	370
	SDCM	D1	10	280	28	150	375	350	370
		D2	10	450	45	150	374	560	370

150 mm is sufficient and therefore, the horizontal spacing of 300 mm between two tested columns is also sufficient to eliminate the interaction effect of the columns. The geo-textile was overlaid over the 50 mm thick uniform-size clean sand at the bottom of the container as the drainage area in the consolidation step of soil layer preparation. The soil container can be moved in the longitudinal direction with the rollers for multiple loading tests in the preparation of each of the soils.

2.3. Testing procedure

Fig. 5 shows the configuration of the physical model test and the test set up of the six main SDCM columns (Settings A and B). An axial compression load test following ASTM-D1143 was conducted 30 days after the columns were installed. An incremental axial compression load of 15 N was applied at the column top every 5 min until failure. The axial applied load and vertical deformation data of the DCM or SDCM columns were measured by a load cell and displacement transducers and logged automatically. During the test, water was sprayed on the soil surface to prevent cracking due to the surface of the soft clay layer drying.

2.4. Results and discussion

The load-vertical displacement relation curves of the floating SDCM columns in the main settings are illustrated in Fig. 6. Three SDCM columns, A1, A2, and A3, have the same $q_{u,DCM}$ of 35 kPa with different core lengths of 0.15, 0.35, and 0.50 m, respectively. The results clearly indicate that increasing the core length leads to increases in the ultimate bearing capacity (Q_u) and reductions in the vertical deformation of the columns. A similar behavior was observed for the SDCM columns with a $q_{u,DCM}$ of 135 kPa (B1 and B2). However, insignificant improvements in both Q_u and vertical deformation of SDCM column were observed when the core length was increased from 0.35 (column B2) to 0.50 m for column B3. This implies that when the $q_{u,DCM}$ increases to 135 kPa, the reinforced core does not need to be longer than 0.35 m. However, for the cases with a $q_{u,DCM}$ of 35 kPa, increasing the length of the core up to the entire length of the column can enhance the performance of the columns. The effect of $q_{u,DCM}$ on the load-vertical displacement relation of SDCM columns can also be seen in this figure. A comparison between the two curves with the same L_{core} and different $q_{u,DCM}$ values (such as columns A2 and B2) reveals that SDCM columns with a higher $q_{u,DCM}$ (B2) are able to resist a larger applied load.

A previous study on field load tests of DCM columns (Petchgate et al., 2003a) and its back calculation indicated that the Q_u of a column can be determined based on the consideration of two modes of failure, the column and soil failure modes. The possible maximum Q_u of the column in each soil condition is then governed by the soil failure mode, which mainly depends on the strength of the native soil surrounding the column. Therefore, the Q_u with the soil failure mode is appropriate as a normalized parameter to compare the load-vertical displacement curves of the testing results with different strengths of native soil. Fig. 7 illustrates the normalized load, Q_n (normalized Q_u)-settlement curves of DCM and SDCM columns with different strengths of native soil and the DCM socket for the various test settings in Table 1. All DCM and SDCM columns have the same dimensions (38 mm in diameter and 500 mm in length). In addition to the symbol of the test (such as A1), the numbers in parentheses indicate the core length ratio (L_{core}/L_{DCM}) and the column-to-soil strength ratio ($q_{u,DCM}/q_{u,soil}$). The relation curves show that if the column-soil strength ratio ($q_{u,DCM}/q_{u,\ soil}$) is larger than 27.5 (C2 (DCM), C3 (DCM), D1 (SDCM), and D2 (SDCM)), the columns should fail under the soil failure mode. In this case ($q_{u,DCM}$ is sufficiently high), inserting the core should not improve the behaviors of the column, as illustrated by the load-settlement curve of columns C3 and D1, because the ordinary DCM column is sufficiently strong and already failed with the soil failure mode. This conclusion is confirmed by the results for column D2.

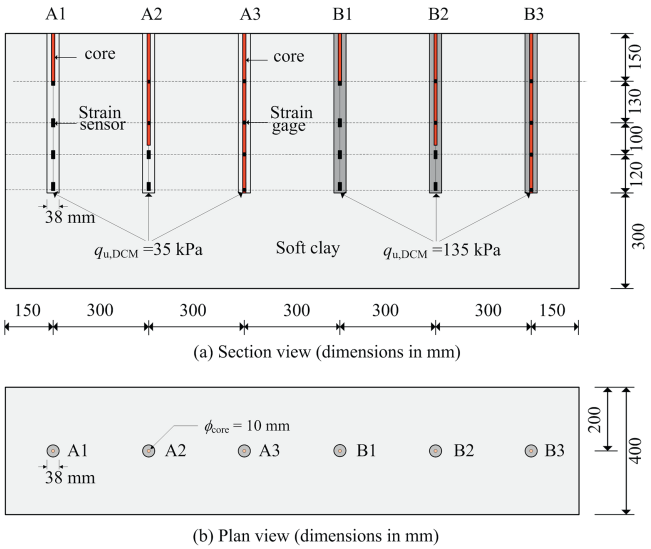

Fig. 2. Installation layout of SDCM piles in the main scaled down model tests.

Table 2
Physical properties of soft clay layer.

Properties	Value
Liquid limit, LL (%)	103
Plastic limit, PL (%)	43
Plastic index, PI (%)	60
Natural water content, w_n (%)	72
Undrained shear strength, s_u (kPa)	8
Elastic modulus, E_u (kPa)	300
Total unit weight (kN/m^3)	14
Specific gravity	2.68

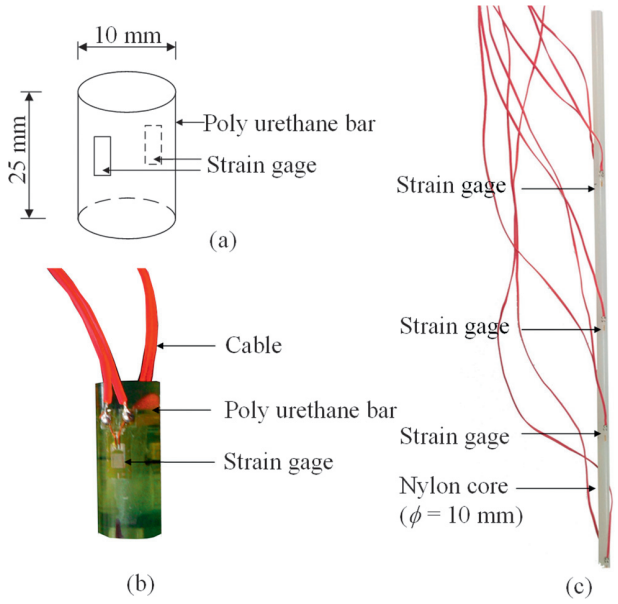

Fig. 3. Setting of strain sensors: (a) schematic of strain sensor, (b) photo of strain sensor, and (c) photo of strain gage installation on stiffened core.

However, the core can assist in reducing the shortening of the column due to the higher stiffness compared to an ordinary DCM column, resulting in reduced settlement. In contrast, for the SDCM columns A1, A2, and A3 and B1, B2, and B3, which have column-soil strength ratios of 4.38 and 16.88, respectively, increasing the core length results in an increase in Q_u and a decrease in the vertical deformation of the columns. DCM column C1, the column-soil strength ratio of which (5.5) is larger than that of SDCM column A1 (4.38) with a L_{core}/L_{DCM} value of 0.3, has inferior performance (in terms of the Q_u and settlement of the column) than column A1. This implies that, at the lower strength of the socket, the insertion of a stiffened core can improve the performance of a DCM column. This suggests that to achieve the optimal design, the strength of the DCM socket should be selected such that the DCM column (without a stiffened core) will fail under column failure. Then, by inserting the core, the performance of the SDCM column will be improved to the ultimate limit state at which the column will fail under the soil failure mode depending on the required capacity and cost considerations. Because the strength of the DCM socket can be reduced, the additional cost due to the insertion of the reinforced core will be compensated for by the reduction in the amount of cement.

The axial strains along the column length that were measured from embedded strain sensors are used to calculate the axial internal force according Eq. (1), as shown in Fig. 8.

$$F = \epsilon \cdot (EA)_{socket} \quad (1)$$

where

F = Internal force in the column
ε = Axial strain measured from the strain sensor
A = Cross-sectional area of the DCM socket column
E = Elastic modulus of the DCM socket column

Fig. 8a illustrates the load transfer along the column depth at applied forces of 15, 30 and 60 kN for columns A1, A2 and A3, respectively. A comparison of the results indicates that the SDCM column with a longer core can transfer the applied load to a greater depth than the SDCM column with a shorter core. The difference in the load transfer along the column between the shorter and longer cores can be clearly observed with increases in the applied load. As a result, the load shared by the surrounding soil of the SDCM column with a longer core are expected be smaller. Thus, for the same applied load, the vertical displacement of the SDCM column with a longer core is smaller than that with a shorter core, as shown in Fig. 6. For SDCM columns with different DCM socket strengths, only a slight difference in the load distribution along the SDCM column for the same applied load and core length can be observed, as shown in Fig. 8b for columns A1 and B1. The effect of the core length is dominant.

Fig. 9 presents the relationship between the core length ratio (L_{core}/L_{DCM}) and Q_u of all of the SDCM columns tested in the main settings. The values of Q_u at a

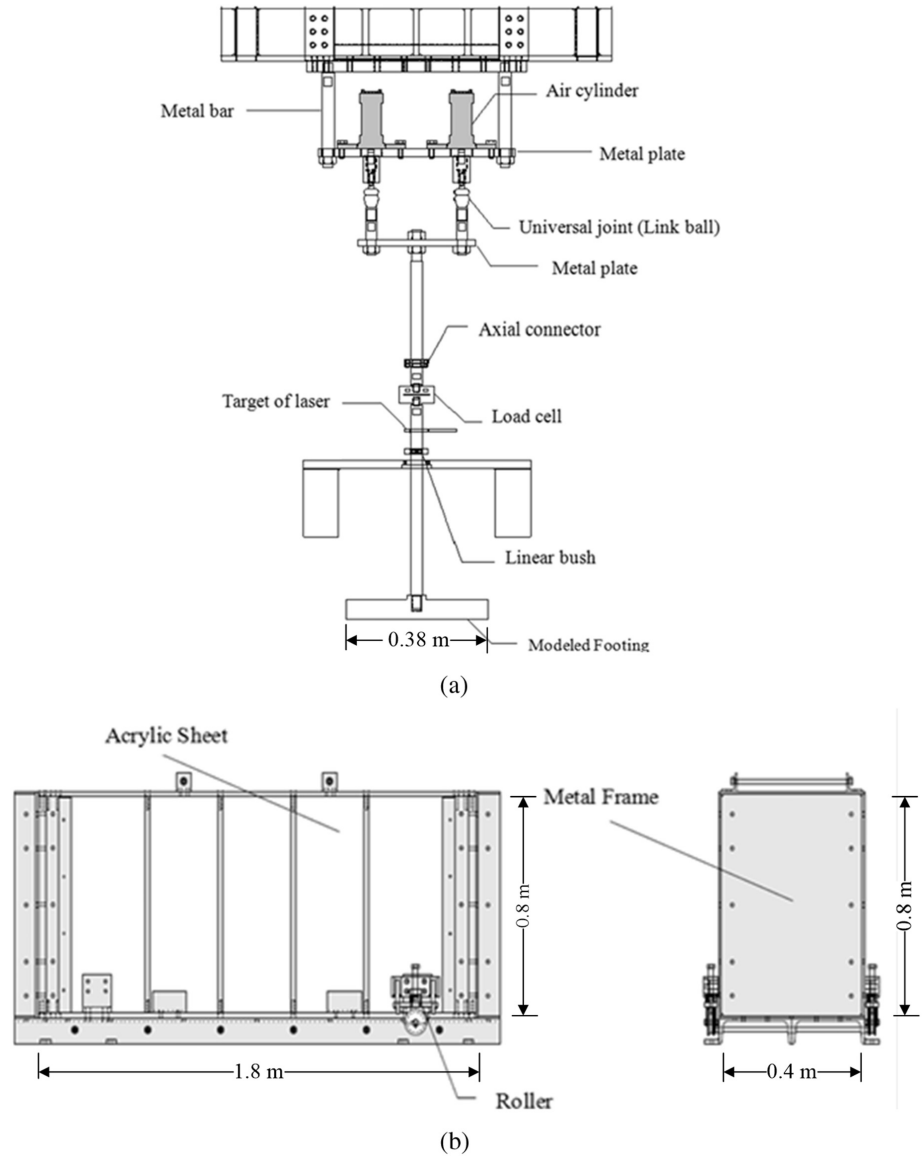

Fig. 4. Details of the testing apparatuses in this study: (a) loading module and (b) soil container.

L_{core}/L_{DCM} of zero for both $q_{u,DCM}$ values are also included in the figure. The values were calculated from the unconfined compressive strengths (q_u) of the cured cement-soil mixtures sampled during the column installation step. The relation curves clearly show that at a given L_{core}/L_{DCM}, the SDCM column with a higher $q_{u,DCM}$ can carry a higher applied load than that with a lower $q_{u,DCM}$. In the figure, Q_u increases linearly with increases in L_{core}/L_{DCM} up to unity for the SDCM columns with a $q_{u,DCM}$ of 35 kPa. In contrast, the relation curves with a $q_{u,DCM}$ of 135 kPa, exhibits as a bi-linear relation. Q_u increases with increases in L_{core}/L_{DCM} until reaching a certain value at a L_{core}/L_{DCM} of approximately 0.7, after which it remains constant. Further investigation indicated that the obtained maximum Q_u can be approximately calculated from the Q_u in the case of soil failure using the soil strength and the dimensions of the DCM column by method. The results confirm that to maintain Q_u, the cement content in the DCM socket can be decreased by inserting a sufficiently long core. This also implies that the failure mode may change from column failure to soil failure.

In summary, the results obtained from the preliminary investigation by physical model test reveal that the strength of the DCM socket and the length of the core significantly affect the ultimate bearing capacity and settlement of the floating SDCM columns. The maximum load-carrying capacity appears to be limited at the ultimate bearing capacity under the soil failure mode. To achieve the maximum load-carrying capacity, the strength of the DCM socket can be reduced by inserting a sufficiently long reinforced core. There appears to be an optimum length of the stiffened core for a specific DCM socket strength, except when the socket is too weak.

Note that the soil vertical stress/strength profile in the physical model test tank is low and almost uniform owing

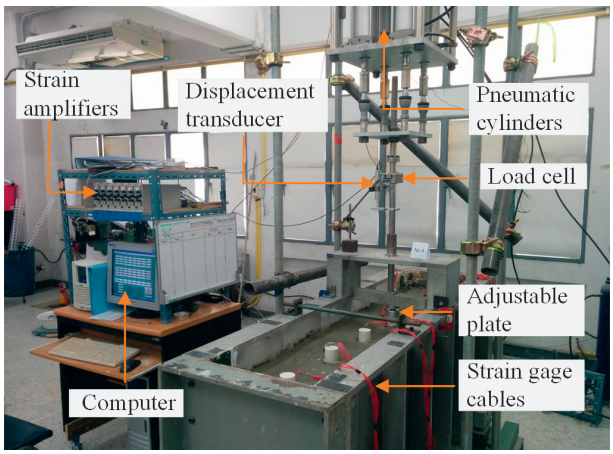

Fig. 5. Test setup during performing pile load test.

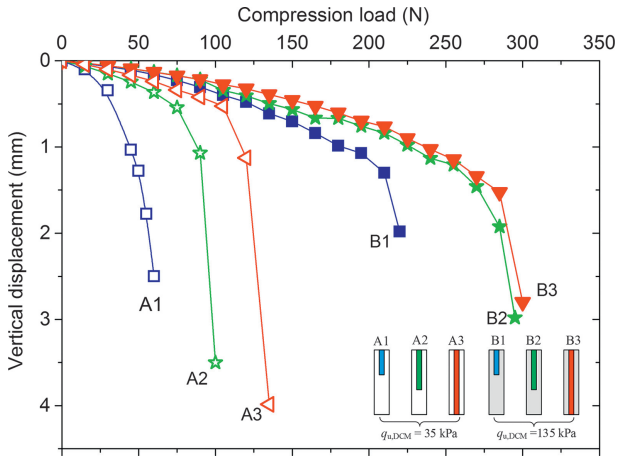

Fig. 6. Load-vertical displacement relation curves of SDCM piles with different strengths of socket pile and reinforced core lengths.

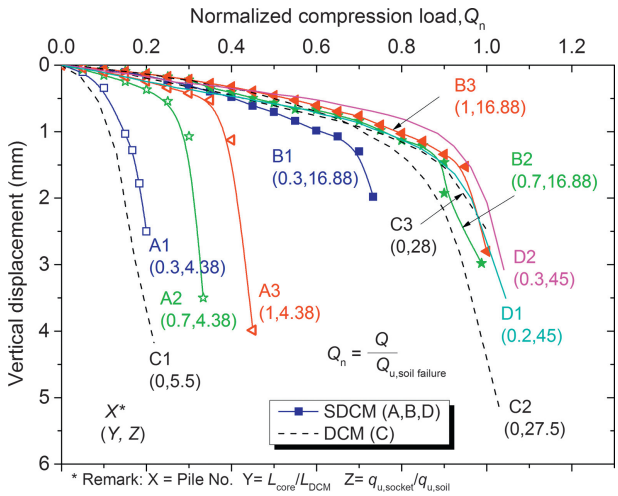

Fig. 7. Normalized load-vertical displacement relation curves of SDCM and DCM piles with different strengths of socket pile and soil and reinforced core lengths.

to the small imposed self-weight stress increase over the depth of the model. Hence, the generation of pile resistance would be different with the actual field condition. To parametrically study the impact of reinforce core and strength of DCM socket on lthe oad carrying capacity and failure behavior of the SDCM column, a numerical sensitivity analysis on the basis of field conditions is thus preferred.

3. Full-scale column load test on floating DCM and SDCM columns

Due to the lack of a field case for a floating SDCM column, full-scale column load tests have been conducted to be used as a reference case for the numerical parametric study presented in the next section. Other objectives are to confirm the effectiveness of inserting a reinforced core on the mechanical behaviors of a floating DCM column and to confirm that the reinforced core can be made of wood.

3.1. Test location

The full-scale tests were performed in the area of the Chakri Naruebodindra Medical Institute Hospital construction project in Samut Prakarn province. The soil profile at the site consists of 0.5 m thick filled over a 1.5 m thick weathered crust layer. The soft clay and medium clay layers were found at levels of −2 and −13 m, respectively. Below the level of −30 m, the sand layer alternates with a stiff clay layer until the end of the boring. The ground water table was found at the level of −0.5 m. With the very thick soft clay layer in the site, 10 m long DCM columns with a diameter of 0.5 m were designed and constructed to support the road embankment in the project. As part of the pile load tests in the project, the same size and length of DCM and SDCM columns were thus constructed. It is noted that the slenderness ratio of the DCM and SDCM columns between the physical model tests in the previous section and in the field are different. However, this difference might not affect the qualitative conclusion observed between the physical model tests and the subsequent numerical analyses. The physical properties and soil profile at the test site are shown in Fig. 10a.

3.2. Deep cement mixing column

The DCM and SDCM columns were constructed to perform the column load test, as shown in Fig. 10b. The 0.5 m diameter and 10 m long columns were constructed by the high-pressure grouting method using a jet pressure of 250 bars by a jet grouting machine. Cement slurry with a water-cement ratio of 1.1 was injected into the soil by automatically controlling the flow rate to maintain a cement powder weight of 250 kg/m^3 of wet soil. To construct the SDCM column, immediately after the completion of the column installation process, eucalyptus wood with an average diameter of 0.15 m and length of 6.0 m was carefully inserted into the center of the DCM column to ensure that

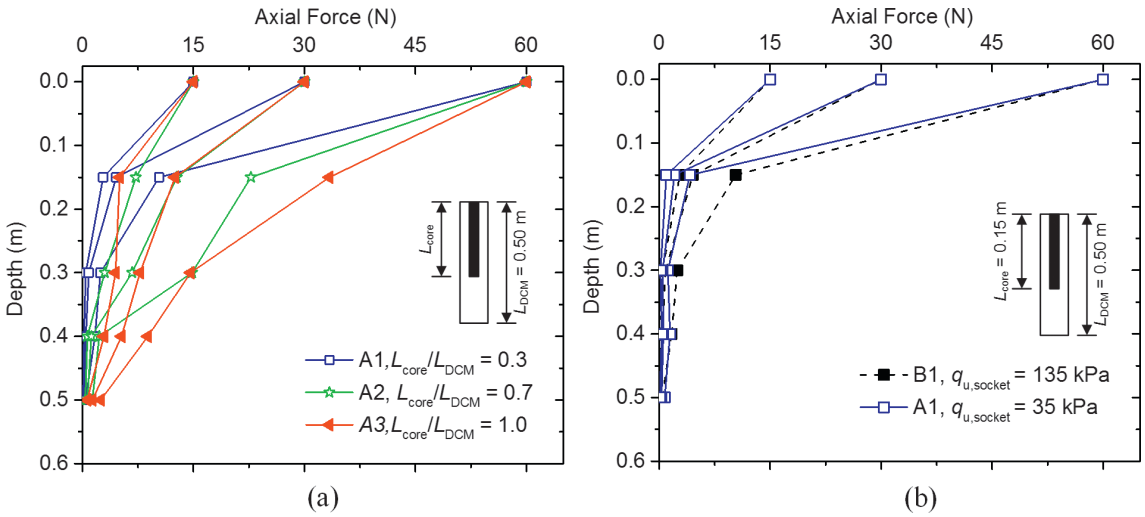

Fig. 8. Internal axial load transfer along SDCM piles: (a) different core lengths with $q_{u,DCM}$ of 35 kPa, (b) different $q_{u,DCM}$ for core length of 0.15 m.

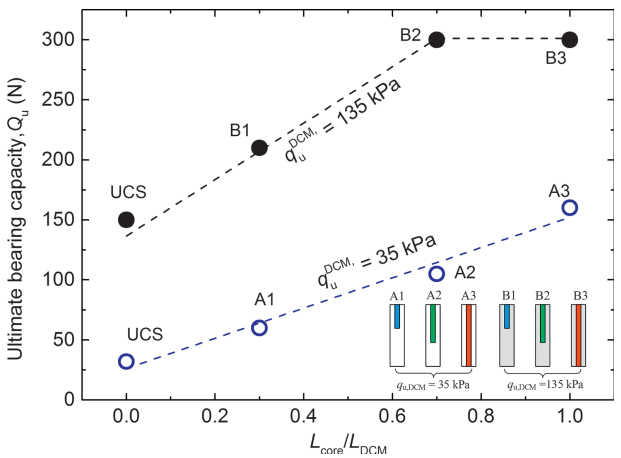

Fig. 9. Relation between ultimate bearing capacity (Q_u) and L_{core}/L_{DCM} obtained from the physical model tests.

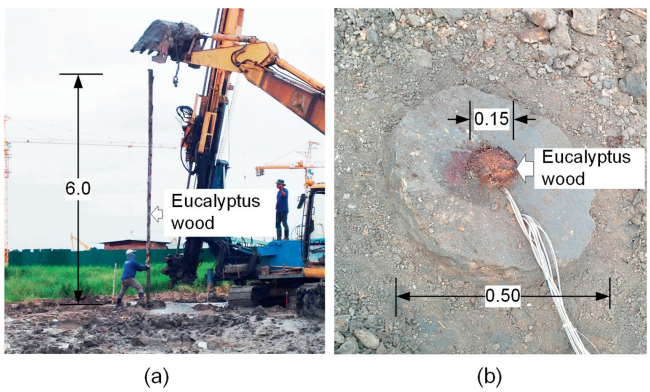

Fig. 11. (a) Stiffened core installation; (b) photo of SDCM pile before testing.

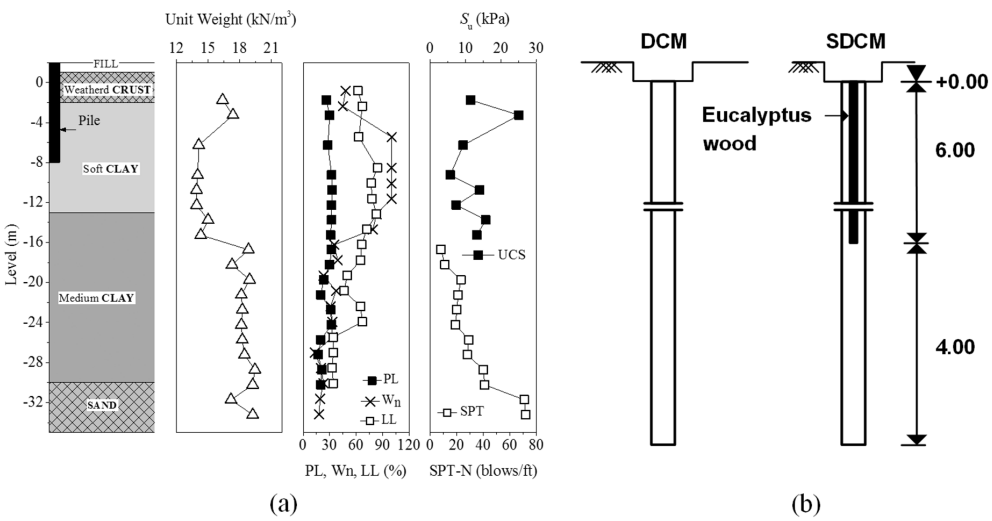

Fig. 10. (a) Soil profile and physical properties of soil at test location; (b) Schematic of DCM and SDCM piles for pile load tests in this study.

Table 3
Unconfined compression test results of the samples taken from the observed piles in the field test.

Pile no.	Depth (m)	q_u (kPa)	E_{50} (kPa)
1	0.0–5.0	1410	215,000
	6.0–10.0	1330	221,000
2	0.0–5.0	961	140,000
	6.0–10.0	1136	170,000

it was vertically aligned, as shown in Fig. 11a. Fig. 11b illustrates the column cut-off before capping the column head with concrete. Two observed DCM columns were constructed adjacent to the test area to determine the strength of the column. The unconfined compressive strengths of the four cored samples from the observed columns are shown in Table 3. The average value of the unconfined compressive strength is 1200 kPa.

3.3. Test procedure

The column load tests on the DCM and SDCM columns were performed following ASTM-D1143 standard by the quick loading method. An incremental axial compression load of 10 kN was applied at the top of the column head through a concrete column cap with a 0.7 m diameter every 10 min until failure. During the tests, the axial applied load and settlement data of the DCM or SDCM columns were measured by a load cell and displacement transducer, respectively, and recorded by an automatic data logger.

3.4. Test results

Fig. 12 shows the load vertical displacement curves of the DCM and SDCM columns from the field column load tests. The settlements for both columns increase linearly with increasing applied load up to loads of approximately 150 and 200 kN for the DCM and SDCM columns, respectively. Then, the settlement increases rapidly until failure. The SDCM column can carry approximately 25% more load than the DCM column. At the same load, the SDCM column settles less than the DCM column. The results show that the performance of floating DCM column in terms of both the ultimate bearing capacity and settlement behavior can be improved by inserting eucalyptus wood as a core. These improvements in the SDCM column correspond well with the results from the physical model test in the previous section. The eucalyptus can potentially be utilized as a stiffened core. This provides an alternative of using less expensive and more sustainable material in the construction of SDCM columns.

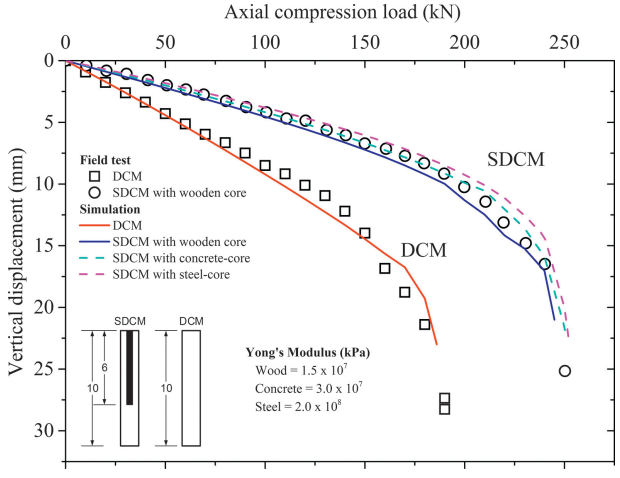

Fig. 12. Load-vertical displacement relations of DCM and SDCM piles from full-scale pile load tests and their simulation.

4. Finite element analysis

An extended study by finite element analysis (FEA) under the two-dimensional axisymmetric condition was conducted to further investigate the behavior of SDCM columns from physical model and full-scale tests. The conditions of the full-scale tests from the previous section were used as a reference case to perform the sensitivity analysis. A parametric study of the SDCM columns under axial loading by varying the strength and length of the DCM socket column and the length of the stiffened core was carried out. Before performing the numerical parametric study, verification was conducted by comparing with the results from the full-scale load tests. The finite element program PLAXIS 2D Version 8.2 (Brinkgreve et al., 2008) was used to analyze the DCM and SDCM columns during axial loading under the undrained condition in this study.

4.1. Analysis and initial conditions

A fifteen-node triangle element was used to model the DCM columns, stiffened core and soil. Fig. 13 shows the 2D-axis symmetry finite element mesh used for all cases in this study. All vertical sides were supported by a roller, which restricted the displacement in the horizontal direction. A pin support was applied to the base of the model. The in-situ stress is generated by the given unit weight of soil and the coefficient of earth pressure at rest, K_o, for all soil layers. The hydrostatic pore water pressure is in equilibrium with the water table at 1.5 m below the ground surface.

The load applied to the top of the wish-in-place DCM or SDCM columns in each analysis was gradually increased following ASTM-D1143, as performed in the field test after establishing the initial stress state. The column settlement at the column top and axial stress along

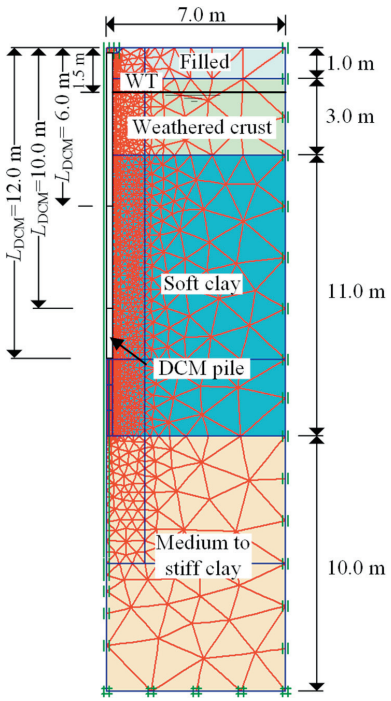

Fig. 13. Finite element mesh and geometry of the problem considered in the analyses.

the column length of the DCM and SDCM columns were monitored for each applied interval load until the end of the analysis. The method by Mazurkiewicz (1972) was used to determine the ultimate column capacity from the load-settlement curve of both the DCM and SDCM columns.

4.2. Material models and model parameters

The clay was modelled using the hardening soil model (HS) considering the elasto-plastics with stress-dependent stiffness and shear dilatancy properties (Schanz et al., 1999). The HS model has been using to simulate the behaviors of various types of both soft and stiff soils (e.g., Jamsawang et al., 2015; Surarak et al., 2012). The model parameters were obtained from calibrating the oedometer test results. The cement-mixed soil and the concrete and wood core are assumed to behave as an elastic–perfectly plastic material following the Mohr-Coulomb (MC) model. A linear elastic (LE) material model was used to model the steel core and concrete column cap. The soil parameters used in the analyses were mainly determined from calibration on triaxial testing results of soil specimens at AIT (Jongpradist et al., 2013). The values of the material parameters used in the numerical analysis are summarized in Table 4. The value of interface friction (R_{inter}) between the core and DCM socket was chosen to be 0.4 (Voottipruex et al., 2011a, 2011b) while the value of 1.0 (Brinkgreve et al., 2008) is assigned for that between the DCM column and the surrounding soil.

4.3. Sensitivity analysis

To obtain a better understanding of the behavior of SDCM columns beyond what can be obtained from the physical model tests, a numerical sensitivity analysis was used to analyze their behavior in this section. The factors that are believed to affect the ultimate bearing capacity of the SDCM columns are varied in the numerical sensitivity analysis. These factors include the length (L_{DCM}) and strength ($q_{u,DCM}$) of the DCM socket and the length of the stiffened core (L_{core}). Eucalyptus wood is used as the core material in all sensitivity analysis cases. The following ranges of factors are considered in the numerical sensitivity: $q_{u,DCM}$ values of 125, 250, 500, 1000, or 1500 kPa; L_{core} values of 2, 4, 6, 8, 10, or 12 m; and L_{DCM} values of 6, 10, or 12 m. The relation $E_{50} = 150q_{u,DCM}$ obtained from the average testing results of the field specimens, which corresponds to previous studies (Petchgate et al., 2003b; Lorenzo and Bergado, 2006), was used to assume the elastic modulus of the DCM column in the analyses, as shown in Table 4. To confirm the analysis conditions and material parameters before performing the numerical sensitivity

Table 4
Material parameters used in finite element analyses.

Material	Model	γ (KN/m^3)	c' (kPa)	ϕ' (°)	ψ' (°)	E_{50}^{ref}, E' (kPa)	E_{oed}^{ref} (kPa)	E_{ur}^{ref} (kPa)	ν	m	R_{inter}	OCR
Filled	HS (U)	15	1	27	0	10,000	10,000	30,000	0.3	1	1	3
Weathered crust	HS (U)	15	1	25	0	6500	6500	25,000	0.3	1	1	2
Soft clay	HS (U)	14	1	23	0	3200	3200	20,000	0.3	1	1	1.5
Medium clay	HS (U)	15	1	26	0	9000	9000	30,000	0.3	1	1	1
DCM pile												
q_u = 125 kPa	MC (U)	14	60	30	0	16,800	–	–	0.3	–	0.4	–
q_u = 250 kPa	MC (U)	14	120	30	0	33,500	–	–	0.3	–	0.4	–
q_u = 500 kPa	MC (U)	14	240	30	0	67,000	–	–	0.3	–	0.4	–
q_u = 1000 kPa[a]	MC (U)	14	480	30	0	134,000	–	–	0.3	–	0.4	–
q_u = 1500 kPa	MC (U)	14	700	30	0	200,900	–	–	0.3	–	0.4	–
Wood	MC (U)	15	6500	30	–	1.5×10^7	–	–	0.25	–	1	–
Concrete	MC (U)	23	8000	40	–	3×10^7	–	–	0.2	–	1	–

Remark: HS = Hardening Soil Model, MC = Mohr-Coulomb Model, LE = Linear-Elastic Model, p_{ref} for HS = 100 kPa, U = Undrained.
[a] Parameter set of full scale test.

analysis, the analysis method was validated. In Fig. 12, the relation curves between the load and settlement of both the DCM and SDCM columns from the FEM simulation are also included. The comparison with the field test results indicates that the analysis method employed can be used in further investigations with confidence. Moreover, the simulated load-settlement curves of SDCM columns with concrete and steel as the core are also included in the figure. The results agree well with those of Wonglert and Jongpradist (2015) for the end bearing SDCM columns that, due to the shortening of the core caused by lower stiffness, the wood SDCM column exhibits larger settlements at the same applied load. However, similar column capacities among wood, concrete and steel SDCM piles can be obtained. Further investigation on load transfer along the column depth revealed that majority of the applied load is carried by the core. This results are in good agreement with the observation by Dong et al. (2004). The comparison among SDCM columns with different core materials in this study reveals that the load induced in the stiffer core (steel in this study) becomes larger.

4.4. Influence of L_{core} on Q_u

In this section, the influence of the length of the reinforced core on the ultimate bearing capacity of the SDCM column is presented. Fig. 14 illustrates the plots of L_{core} versus Q_u of the SDCM columns with different values of L_{DCM} and $q_{u,DCM}$. The values of the ultimate capacity for the soil failure mode, $Q_{u,\,sf}$, for different column lengths are also included in the figure as horizontal dotted lines. In Fig. 14a, for low values of $q_{u,DCM}$ (125 kPa), the Q_u for all columns (L_{DCM} of 6, 10, and 12 m) increase linearly with increasing of L_{core} up to a L_{core}/L_{DCM} of 1. The Q_u values of all columns are still lower than their $Q_{u,sf}$. When the $q_{u,DCM}$ increases to 250 kPa, as illustrated in Fig. 14b, the SDCM columns with a L_{DCM} of 6 m reaches its $Q_{u,sf}$ (145 kN) with an L_{core} of approximately 4 m, whereas the other columns (lengths of 10 and 12 m) do not reach their $Q_{u,sf}$ (280 and 350 kN, respectively). The Q_u of these columns (10 and 12 m) increase proportionally with increases in L_{core}. With a $q_{u,DCM}$ of 500 kPa, as illustrated in Fig. 14c, the Q_u of all SDCM columns reaches their $Q_{u,sf}$ with different L_{core} values of 2, 8, and 12 m for L_{DCM} values of 6, 10, and 12 m, respectively. This indicates that increases in L_{core} leads to increases in Q_u until $Q_{u,sf}$ is reached. Once $Q_{u,sf}$ is reached, increasing L_{core} has no impact on Q_u. This conclusion is also confirmed from the results shown in Fig. 14d and 14e for $q_{u,DCM}$ values of 1000 and 1500 kPa, respectively. Furthermore, the L_{core} needed to reach the $Q_{u,sf}$ decreases with increasing $q_{u,DCM}$. For specific soil and DCM length, with sufficient $q_{u,DCM}$, inserting the core has no impact on the load-carrying capacity of the columns. This implies that q_u,

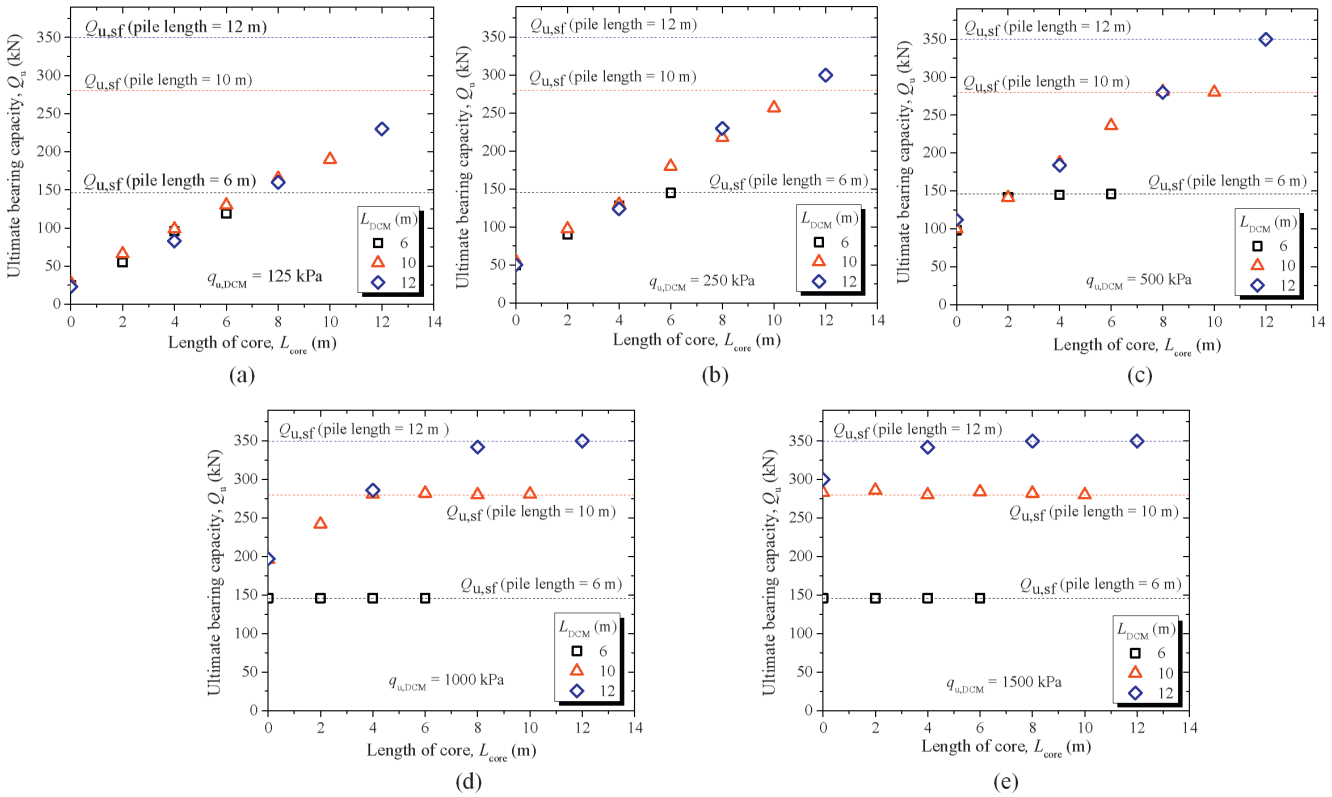

Fig. 14. Relation curves between Q_u and L_{core} of SDCM piles with (a) $q_{u,DCM} = 125$ kPa, (b) $q_{u,DCM} = 250$ kPa, (c) $q_{u,DCM} = 500$ kPa, (d) $q_{u,DCM} = 1000$ kPa, and (e) $q_{u,DCM} = 1500$ kPa.

$_{DCM}$ can be decreased by inserting the core instead. Moreover, with the same $q_{u,DCM}$, the longer columns (higher L_{DCM}) require a longer core to reach $Q_{u,sf}$.

4.5. Influence of $q_{u,DCM}$ on Q_u

To further illustrate the influence of $q_{u,DCM}$ on Q_u, the Q_u of the SDCM columns vs. the core length ratio (L_{core}/L_{DCM}) is plotted for various $q_{u,DCM}$ values using the same data set as in Fig. 14. Each sub-figure illustrates the results for different values of L_{DCM}. In the same manner as previously described, with a sufficient DCM socket strength, the Q_u increases linearly with increasing L_{core}/L_{DCM} before remaining constant after achieving $Q_{u,sf}$ at the optimum L_{core}. For example, the optimum core lengths of the 6 m-long column are approximately 2.1($L_{core}/L_{DCM} = 0.35$) and 4.9 ($L_{core}/L_{DCM} = 0.82$) m for $q_{u,DCM}$ values of 500 and 250 kPa, respectively, as shown in Fig. 15a. This can also be seen for the column lengths of 10 and 12 m in Fig. 15b and 15c. This implies that the optimum L_{core} depends on $q_{u,DCM}$ and L_{DCM}. In contrast to the high-strength DCM socket, there is no optimum L_{core} for the SDCM column with the low-strength DCM socket ($q_{u,DCM} = 125$ kPa). When $q_{u,DCM}$ is insufficient, for example, $q_{u,DCM} = 125$ kPa, inserting the stiffened core can improve Q_u from $L_{core}/L_{DCM} = 0$ up to 1.0. With this DCM socket strength, the Q_u cannot reach $Q_{u,sf}$. To maintain the highest possible Q_u of the SDCM, the minimum required $q_{u,DCM}$ can be obtained at the optimum L_{core}/L_{DCM} of 1. From the analysis data available in this work, the minimum $q_{u,DCM}$ for the 6, 10, and 12 m-long DCM columns are in the ranges of 125–250, 250–500, and approximately 500 kPa, respectively. The minimum $q_{u,DCM}$ increases with increasing L_{DCM}. The minimum $q_{u,DCM}$ should also depend on the strength of the untreated soil, column dimension (length, diameter), and diameter of the reinforced core.

4.6. Failure modes of the SDCM columns

Because the core material is considerably stiffer than the DCM socket, it is difficult for the SDCM column to fail under the core failure mode. Then, the failure mode of the SDCM column can be either soil or column failure. Using the elasto-plastic soil model, the failure zone can be traced according to the Mohr-Coulomb failure criteria. Fig. 16 presents the evolution of the failure zones through the Mohr-Coulomb plastic points (MCP) at 25%, 50%, 75% and 100% of Q_u. For the column failure mode (Fig. 16a and b), when the load is first applied (0.25Q_u), the MCPs develop in the DCM socket at the core tip. As the load increases to 0.5Q_u, the soil surrounding the top part of the column mobilizes a new failure zone together with the progression of the failure zone at the core tip. The column eventually fails when the failure zone at the core tip increases in size over the cross-section of the column at 100% Q_u (230 kN). These two SDCM columns

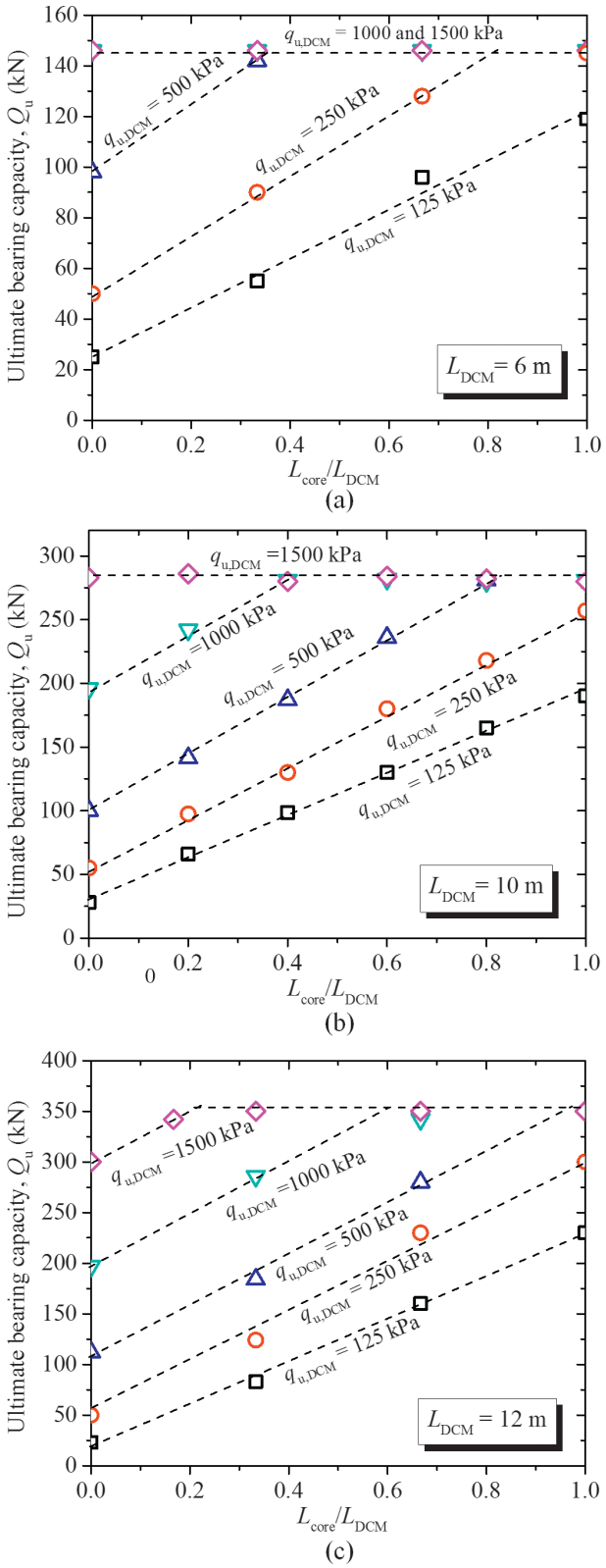

Fig. 15. Relation curves between Qu and L_{core}/L_{DCM} of SDCM piles with (a) $L_{DCM} = 6$ m, (b) $L_{DCM} = 10$ m, and (c) $L_{DCM} = 12$ m.

have the same failure mechanism even though they have different L_{core} and $q_{u,DCM}$. When L_{core} increases from 2 to 6 m ($q_{u,DCM} = 1000$ kPa), as shown in Fig. 16b and c,

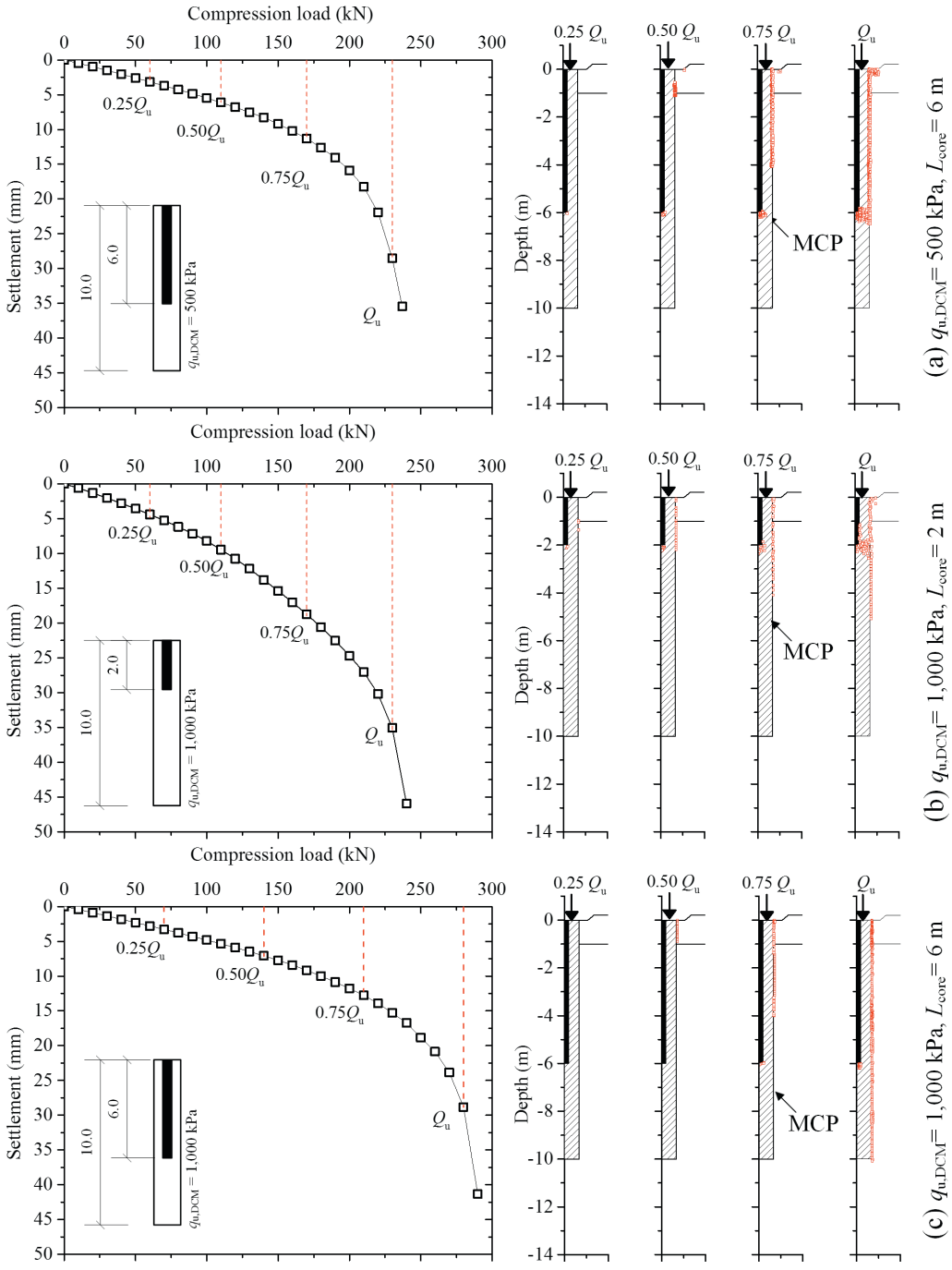

Fig. 16. Development of Mohr-Coulomb points of SDCM piles having different $q_{u,DCM}$ and L_{core} during increase of applied load.

the failure mode changes from column to soil failure. There are only a few MCPs at the core tip at the beginning until the ultimate load is reached. The MCPs in the surrounding soil gradually increase from the top to the tip of the column with increases in the applied load until the ultimate load (280 kN). The results indicate that L_{core}/L_{DCM} and $q_{u,DCM}$ have a significant impact on the failure mechanism of the floating SDCM columns. From the results (Figs. 14–16) and understandings obtained from numerical sensitivity analyses, a schematic diagram showing the relationship between L_{core}/L_{DCM} and Q_u of SDCM and the associated failure modes can be established, as illustrated in Fig. 17. Three sample cases in Fig. 16 are also mapped in the figure. By inserting a core into the DCM column which originally fails under pile failure mode ($Q_u < Q_{u,sf}$; along the green part of y-axis), the failure mode changes from failure at the pile head to either pile failure at the core tip (Point A; case in Fig. 16a and B; case in Fig. 16b) or soil failure (Point C; case in Fig. 16c) depending on both the L_{core}/L_{DCM} and $q_{u,DCM}$.

Unlike end-bearing SDCM columns, for which three failure modes are possible (Wonglert and Jongpradist, 2015), this study reveals that only two possible failure modes can occur for floating SDCM columns with very stiff

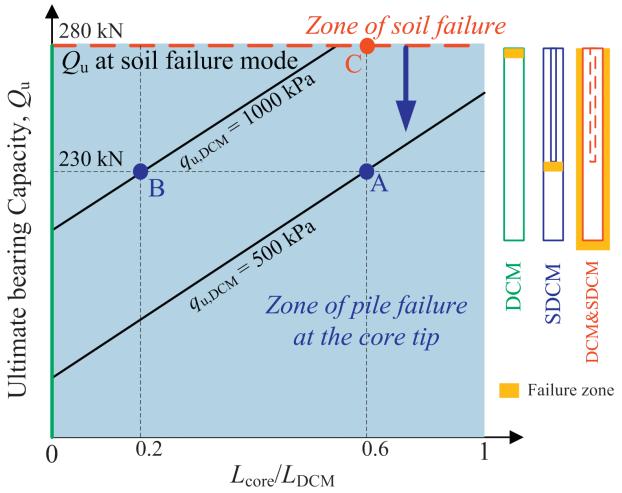

Fig. 17. Diagram demonstraing the L_{core}/L_{DCM} and Q_u relationship of floating SDCM and the associated failure modes.

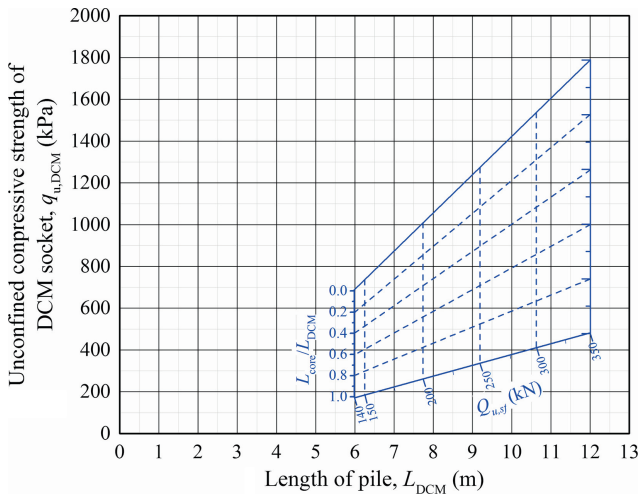

Fig. 18. Guideline chart for suggeting the L_{core} for floating SDCM piles of this study area.

core, namely, column failure at the core tip and soil failure. However, the observation from the study by Dong et al. (2004) reveals other failure mode; the pile body failure by upper part of concrete core. This may be due to the much lower soil and DCM socket strengths in this study than those in their study.

4.7. Development of the guideline chart for floating SDCM columns

As an implementation example of the Q_u of floating SDCM column and its influencing factors in engineering practice, the characteristic chart of a floating SDCM column as a guideline for choosing the appropriate L_{core} can be obtained by plotting the value of L_{core}/L_{DCM} that can reach $Q_{u,sf}$ together with $q_{u,DCM}$ and L_{DCM}, as illustrated in Fig. 18. The effects of L_{core}/L_{DCM}, L_{DCM}, and $q_{u,DCM}$ are considered in this chart. The L_{DCM} is obtained by selecting the required Q_u. Once $q_{u,DCM}$ is selected, the L_{core}/L_{DCM} needed to achieve the required Q_u is earned. This chart can be used to preliminarily design floating SDCM columns with lengths from 6 to 12 m with a diameter of 0.5 m, as considered in the analysis. It is also developed for the soil condition considered in this study (reference case in this study). However, the concept of the development of this chart can be applied to other areas and conditions. Note that the settlement criterion has not been considered in the development of this chart. Nonetheless, the results from this study suggested that for the same Q_u, the settlement of the SDCM column is smaller than that of the DCM column.

5. Conclusion

A series of physical model tests was performed on scaled-down floating SDCM columns under axial loading to preliminarily investigate the influence of the stiffened core length and DCM socket strength on the column bearing capacity. Full-scale column load tests were carried out to be a reference cases for subsequent numerical parametric studies. The tests were also designed to determine the effectiveness of the stiffened core on the behaviors of the floating columns and the potential of using wood as a core. Finally, the numerical analyses were employed to further investigate the parameters influencing the behaviors of floating SDCM columns. The effect of the stiffened core length, DCM socket strength, and DCM socket length were considered in the analyses. The ultimate bearing capacity and column settlement were used to indicate the column performance. The conclusions of this study can be summarized as follows:

(1) The preliminary results from small-scale tests under a normal gravity load suggest that the DCM socket strength and stiffened core length significantly influence the ultimate bearing capacity and settlement behaviors of the SDCM columns. Increasing the strength of the DCM socket and core length has potential to increase the ultimate bearing capacity and reduce the column settlement.
(2) The field test results demonstrate the potential of eucalyptus wood (and probably other materials whose stiffness is less than concrete) for use as a stiffened core. For the reference case in this study, the ultimate bearing capacity of the SDCM column with a eucalyptus wood core is approximately 25% higher than that of the original DCM column.
(3) Numerical parametric analyses considering the full-scale condition clarify that there is a minimum $q_{u,DCM}$ for each dimension of the SDCM column to achieve the highest ultimate bearing capacity. At this DCM socket strength, the insertion of a core along the column length ($L_{core}/L_{DCM} = 1$) can cause the soil failure mode to occur. Beyond this minimum $q_{u,DCM}$, the required length of the stiffened core decreases with increasing $q_{u,DCM}$ to achieve the soil

failure mode. In contrast, when the $q_{u,DCM}$ is lower than the minimum $q_{u,DCM}$, increasing L_{core} up to the column length ($L_{core}/L_{DCM} = 1$) does not cause the soil failure mode to occur. The minimum $q_{u,DCM}$ increases with increases in the column length.

(4) There are two possible failure modes for floating SDCM columns (unlike the end-bearing SDCM columns, for which three failure modes are possible) in soft ground, soil failure and column failure in the DCM socket at the core tip. For the low strength DCM which fails under pile failure mode at the column head, inserting a stiff core results change of failure position to the core tip. If the DCM socket strength is sufficient, increasing the core length up to a certain value will change the failure mode to soil failure. In this range, the Q_u also increases. Beyond this core length, the Q_u remains constant.

(5) By inserting a core into a floating DCM column, less settlement can be expected regardless of the $q_{u,DCM}$ and whether the Q_u increases.

(6) Under the soil conditions and column lengths considered in this study, a guideline chart is developed to recommend the appropriate L_{core} of an SDCM column to achieve the highest performance under the soil failure mode. The chart was developed based on the numerical data in this study. It considers the influence of pile length, core length, and DCM socket strength. The chart was created for the specific area, and the settlement criterion is not considered. However, the concept of the chart development can be applied to other areas.

Acknowledgements

This research was financial supported by Thailand Research Fund (TRF) and King Mongkut's University of Technology Thonburi (KMUTT) through the Royal Golden Jubilee Ph.D. program, under contact grant PHD/0001/2554 and TRF Basic Research Grant Contract No. BRG6080011. The support from the Faculty of Engineering, King Mongkut's University of Technology, North Bangkok under Contract No. ENG-60-18 is also acknowledged.

References

Alén, C., Baker, S., Bengtsson, P.E. and Sällfors, G., 2005. Lime/cement column stabilised soil – a new model for settlement calculation. In: Proc. of the Int. Conf. on Deep Mixing, Stockholm, vol. 1, pp. 205–212.

Brinkgreve, R.B.J., Broere, W., Waterman, D., 2008. PLAXIS 2D – Materials Model Manual, The Netherlands.

Chen, E.J., Lee, F.H., Ma, X.F., 2014. A dual-shaft deep cement mixing apparatus for centrifuge modeling. In: Geo-Congress 2014-GSP 234, Atlanta, USA, pp. 2481–2490.

Do, H.D., Nguyen, M.H., 2013. High-rise building foundation on floating soil-cement columns. In: Proc. of 5th Int. Young Geot. Eng. Conf, pp. 81–84. http://doi.org/10.3233/978-1-61499-297-4-81.

Dong, P., Qin, R., Chen, Z., 2004. Bearing capacity and settlement of concrete-cored DCM pile in soft ground. Geotech. Geol. Eng. 22 (1), 105–119. https://doi.org/10.1023/B:GEGE.0000013994.73567.cc.

Fukuoka National Highway Office (FNHO), 2003. Report on the field monitoring of test embankments at Shaowa-Biraki. Road No. 208, Fukuoka, Part-1, Kyushu Regional Development Bureau, Minister of Land, Infrastructure, Transport and Tourism. (in Japanese).

Holm, G., 1999. Keynote lecture: applications of dry deep mixing methods for deep soil stabilization. Proc. Int. Conf. on Dry Mix Methods for Deep Soil Stabilization, Stockholm, pp. 3–13.

Horpibulsuk, S., Rachan, R., Raksachon, Y., 2009. Role of fly ash on strength and microstructure development in blended cement stabilized silty clay. Soils Found. 49 (1), 85–98. https://doi.org/10.3208/sandf.49.85.

Jamsawang, P., Bergado, D.T., Voottipruex, P., 2010. Field behaviour of stiffened deep cement mixing piles. In: Proceedings of ICE – Ground Improvement, vol. 164(1), pp. 33–49.

Jamsawang, P., Voottipruex, P., Jongpradist, P., Bergado, D.T., 2015. Parameters affecting the lateral movements of compound deep cement mixing walls by numerical simulations and parametric analyses. Acta Geotech. 10, 797–812.

Jongpradist, P., Jumlongrach, N., Youwai, S., Chucheepsakul, S., 2010. Influence of fly ash on unconfined compressive strength of cement-admixed clay at high water content. J. Mater. Civ. Eng. 22 (1), 49–58. https://doi.org/10.1061/(ASCE)0899-1561(2010) 22:1(49).

Jongpradist, P., Youwai, S., Jaturapitukkul, C., 2011a. Effective void ratio for assessing the mechanical properties of cement-clay admixtures at high water content. J. Geotech. Geoenviron. Eng., ASCE 137 (6), 621–627. https://doi.org/10.1061/(ASCE)GT.1943-5606.0000462.

Jongpradist, P., Youwai, S., Manorat, P., Chucheepsakul, S., 2011b. Influence of curing stress on one-dimensional yielding of cement admixed Bangkok clay at high water content. Soils Found. 51 (2), 351–357. https://doi.org/10.3208/sandf.51.351.

Jongpradist, P., Kaewsri, T., Sawatparnich, A., Suwansawat, S., Youwai, S., Kongkitkul, W., Sunitsakul, J., 2013. Development of tunneling influence zones for adjacent pile foundations by numerical analyses. Tunn. Undergr. Space Technol. 34, 96–109. https://doi.org/10.1016/j.tust.2012.11.005.

Larsson, S., 1999. Shear box apparatus for modeling chemical stabilized soil – introductory tests. In: Dry Mix Methods for Deep Soil Stabilization, Linkoping, Sweden, pp. 115–121.

Mazurkiewicz, B.K., 1972. Test loading of piles according to Polish Regulations. Preliminary Report No. 35, Commission on Pile Research, Royal Swedish Academy of Engineering Services, Stockholm.

Miura, N., Horpibulsuk, S., Nagaraj, T.S., 2001. Engineering behavior of cement stabilized clay at high water content. Soils Found. 41 (5), 33–45. https://doi.org/10.3208/sandf.41.5_33.

Petchgate, K., Jongpradist, P. and Samanrattanasatien, P., 2003a. Lateral movement behavior of cement column retaining wall during construction of a reservoir. In: Proc., Int. Symp. on Soil/Ground Improvement and Geosynthetics in Waste Containment and Erosion Control Applications, Asian Center for Soil Improvement and Geosynthetics, Prathumtani, pp. 195–205.

Petchgate, K., Jongpradist, P. and Panmanajareonphol, S., 2003b. Field pile load test of soil-cement column in soft clay. In: Proc. Int. Symp. 2003 on Soil/Ground Improvement and Geosynthetics in Waste Containment and Erosion Control Applications, AIT, Thailand, pp. 175–184.

Raongjant, W., Meng, J., 2013. Field testing of stiffened deep cement mixing piles under lateral cyclic loading. Earthq. Eng. Eng. Vibr. 12 (2), 261–265. https://doi.org/10.1007/s11803-013-0169-x.

Schanz, T., Vermeer, P.A., Bonnire, P.G., 1999. The hardening soil model: formulation and verification. Beyond 2000 in Computational Geotechnics. Balkema, Rotterdam.

Lorenzo, G.A., Bergado, D.T., 2006. Fundamental characteristics of cement-admixed clay in deep mixing. J. Mater. Civ. Eng. 18 (2), 161–174. https://doi.org/10.1061/(ASCE)0899-1561(2006) 18:2(161).

Surarak, C., Likitlersuang, S., Wanatowski, D., Balasubramaniam, A., Oh, E., Guan, H., 2012. Stiffness and strength parameters for hardening soil model of soft and stiff Bangkok clays. Soils Found. 52 (4), 682–697.

Tsutsumi, T., 2008. Consolidation behavior of floating column improved soft clayey ground, Dissertation for Master Degree, Department of Civil Engineering, Saga University, Saga, Japan. (in Japanese).

Teeracharti, R., 1998. Design and construction of cement column embankment on the Bang Na-Bang Pakong High way. In: 2nd Seminar of Japan-Thailand Joint Study Project of Soft Clay Foundation, Bangkok.

Voottipruex, P., Bergado, D.T., Suksawat, T., Jamsawang, P., 2011a. Behavior and simulation of Deep Cement Mixing (DCM) and Stiffened Deep Cement Mixing (SDCM) piles under full scale loading. Soils Found. 51 (2), 307–320. https://doi.org/10.3208/sandf.51.307.

Voottipruex, P., Suksawat, T., Bergado, D.T., Jamsawang, P., 2011b. Numerical simulations and parametric study of SDCM and DCM piles under full scale axial and lateral loads. Comput. Geotech. 38, 318–329. https://doi.org/10.1016/j.compgeo.2010.11.006.

Uddin, K., Balasubramianiam, A.S., Bergado, D.T., 1997. Engineering behavior of cement-treated Bangkok soft clay. Geotech. Eng. 28 (1), 89–119.

Wonglert, A., Jongpradist, P., 2015. Impact of reinforced core on performance and failure behavior of stiffened deep cement mixing piles. Comput. Geotech. 69, 93–104. https://doi.org/10.1016/j.compgeo.2015.05.003.

Wang, C., Xu, Y.F., Dong, P., 2014. Working characteristics of concrete-cored deep cement mixing piles under embankments. J. Zhejiang Univ.-Sci. A (Appl. Phys. Eng.) 15(6), 419–431. http://doi.org/10.1631/jzus.A1400009.

Ye, G., Cai, Y., Zhang, Z., 2017. Numerical study on load transfer effect of stiffened deep mixed column-supported embankment over soft soil. KSCE J. Civ. Eng. 21 (3), 703–714. https://doi.org/10.1007/s12205-016-0637-8.

Geotextiles and Geomembranes 46 (2018) 414–425

Contents lists available at ScienceDirect

Geotextiles and Geomembranes

journal homepage: www.elsevier.com/locate/geotexmem

Comparative flexural performance of compacted cement-fiber-sand

Pitthaya Jamsawang[a,*], Thanawan Suansomjeen[b], Piti Sukontasukkul[c], Pornkasem Jongpradist[d], Dennes T. Bergado[e]

[a] Soil Engineering Research Center, Department of Civil Engineering, King Mongkut's University of Technology North Bangkok, Bangkok, Thailand
[b] Vigor Merger Company Limited, Thailand
[c] Construction and Building Materials Research Center, Department of Civil Engineering, King Mongkut's University of Technology North Bangkok, Thailand
[d] Department of Civil Engineering, Faculty of Engineering, King Mongkut's University of Technology Thonburi, Bangkok, Thailand
[e] School of Engineering and Technology, Asian Institute of Technology, Thailand

ARTICLE INFO

Keywords:
Fiber-reinforced soil
Flexural performance
Geosynthetics
Pavement materials
Soil stabilization
Toughness

ABSTRACT

This research investigates the influence of seven different fiber types on the flexural performance of compacted cement-fiber-sand (CCFS) with four fiber fractions (0.5, 1, 1.5 and 2% by volume). The seven types of fibers are 12 mm polypropylene, 19 mm polypropylene, 40 mm polypropylene, 55 mm polypropylene, 33 mm steel, 50 mm steel and 58 mm polyolefin fibers. The overall CCFS performance was divided into seven sub design performance indicators: (1) peak strength; (2) peak strength ratio; (3) residual strength ratio; (4) ductility index; (5) toughness; (6) equivalent flexural strength ratio; and (7) maximum crack width. The interaction mechanism of the fiber/cement-sand interface was investigated by scanning electron microscopy. Finally, the effectiveness of each fiber type was compared and rated in terms of the overall performance. The results show that the 50 mm steel fiber provided the best overall sub performance, resulting in an excellent overall flexural performance; in comparison, the 12 mm polypropylene fiber exhibited very poor performance. However, the 19 mm polypropylene and 33 mm steel fiber specimens provided very good and good overall performances, respectively. The nature of the fiber surface and the fiber length affects the overall performance of CCFS. The surface of the steel fibers, compared to the other synthetic fiber types, is more hydrophilic and is more compacted in a cemented-sand matrix without separation of the interfacial zone, providing the best overall flexural performance.

1. Introduction

Cement-treated soils are extensively utilized worldwide as a pavement base and in subbase applications (Consoli et al., 2011a; Horpibulsuk et al., 2013; Ma et al., 2014; Mohammadinia et al., 2015; Yi et al., 2015; Güllü and Fedakar, 2016; Jiang et al., 2016; Phummiphan et al., 2016) due to their high compressive strength and stiffness. In reality, the structural layers in pavement are subjected to tensile and flexural stresses rather than compressive stresses, whereas cement-treated soils have very low tensile and flexural strengths compared to their compressive strengths. Moreover, cement-treated soils exhibit brittle behavior under flexural loading (Plé et al., 2012; Sukontasukkul and Jamsawang, 2012; Onyejekwe and Ghataora, 2014; Jamsawang et al., 2015a; Disfani et al., 2014), while ductile behavior is required for pavement materials to prevent immediate failure due to excessive traffic loads and to save cost in terms of increasing the performance life of the pavement and reducing the frequency of maintenance operations (Disfani et al., 2014). The inclusion of randomly oriented discrete synthetic fibers in cement-treated soils led to substantive improvements in their tensile and flexural performances (Estabragh et al., 2012; Hejazi et al., 2012; Olgun, 2013; Chen et al., 2015; Correia et al., 2015; Jamsawang et al., 2015a; Ates, 2016; Kumar and Gupta, 2016; Anggraini et al., 2016, 2017; Oliveira et al., 2016; Ayeldeen and Kitazume, 2017; Festugato et al., 2017; Kim and Kim, 2017) because fibers capture and redistribute loads through their tensile strength, mobilizing a wider mass of cement-treated soil (Festugato et al., 2017).

Compacted cement-sand (CCS) is mostly used as a base or subbase of pavement structures (Al-Aghbari et al., 2009; Consoli et al., 2011a; Jamsawang et al., 2015a; Ates, 2016). Most previous researchers concentrated on the effect of fiber inclusions on the splitting tensile strength of compacted cement-fiber-sand (CCFS) due to the availability of test apparatuses, the convenience of specimen preparation and their familiarity with the splitting test rather than the flexural test, even though flexural strength tests have the potential of more accurately simulating field conditions than those in splitting tensile strength tests,

* Corresponding author.
E-mail address: pitthaya.j@eng.kmutnb.ac.th (P. Jamsawang).

https://doi.org/10.1016/j.geotexmem.2018.03.008
Received 25 November 2017; Received in revised form 13 March 2018; Accepted 16 March 2018

for a better prediction of the actual performance of pavement structures (Viswanadham et al., 2010; Onyejekwe and Ghataora, 2014), and often concluded that the splitting tensile strength of CCFS increases with the volume fraction, aspect ratio (length/diameter) and orientation of the fibers, cement content, and soil type and properties (Consoli et al., 2011b; Consoli et al., 2012, 2013; Festugato et al., 2017, 2018). Moreover, flexural strength is significant in pavement design and is used to determine slab thickness (ASTM D1635-00, 2000).

However, limited research on flexural strength performance of CCFSs was reported until Onyejekwe and Ghataora (2014) studied the influence of fiber inclusions on the flexural performances of CCS according to ASTM D1635-00 (2000) and found that the inclusion of the fibers led to significant improvements in the flexural load-carrying capacity of the CCSs, increasing the toughness of the specimens and degree of residual load after the first crack over those of unreinforced specimens and their brittle, catastrophic failure. The residual load of the CCFSs was as much as 75% of the maximum load at 10 times the deflections of the CCSs at first crack.

In fact, standard ASTM D1635-00 (2000) can only determine the flexural strength of CCS without fiber inclusion, which is unusual for CCFS, whereas standard ASTM C1609/C1609M-10 (2010) is commonly used to investigate the flexural performances of concrete and concrete-type materials, or so-called fiber-reinforced cementitious composite (FRCC) (Sukontasukkul and Pomchiengpin, 2010; Kim et al., 2011; Nematollahi et al., 2014). The flexural performance of CCFS can be considered similar to that of FRCC; therefore, Jamsawang et al. (2015a) presented the effect of fiber and cement contents on the flexural response of CCFS according to ASTM C1609/C1609M-10 (2010) using one type of polypropylene fiber. The fiber contents of 0.5–2% and cement contents of 3–7% were employed in the study. CCFSs can exhibit a higher strength, residual strength, ductility and toughness and a smaller crack width than CCSs, which fail in tension immediately after the formation of a single crack. The performance of a CCFS can be improved to exhibit a deflection-hardening response in bending accompanied by multiple cracks after initial cracking, depending on the fiber content. In such a case, the CCFS is known as a deflection-hardening CCFS; thus, a much smaller amount of fiber is required to obtain a deflection-hardening response than to induce deflection-softening behavior. The minimum polypropylene fiber content of 1% was required to obtain a deflection-hardening response for the CCFS, and a higher cement content provided better flexural performance due to the increase in interfacial bond between the polypropylene fiber and cement-sand matrix.

The flexural performances of FRCC depends on various factors, such as the fiber material properties (strength and stiffness), fiber geometry (smooth, hooked end, crimped, or twisted), fiber volume content, strength of the matrix properties, and interface properties (adhesion, friction, and mechanical bond) (Cho et al., 2006; Tang et al., 2010; Kim et al., 2011; Nematollahi et al., 2014; Hannawi et al., 2016; Sarir et al., 2016; Simoes et al., 2017). Clearly, for a given matrix, the type and quantity of fiber are key parameters that influence the performance of FRCC, as well as the material cost. All else being equal, matrixes in which a low fiber-volume fraction can be used while still attaining a strain-hardening or deflection-hardening response are attractive in terms of cost (Kim et al., 2011; Nematollahi et al., 2014). The summary of suitable fiber types was often present in term of individual sub performance, whereas the overall performance is required to specify the best fiber type for FRCC.

The influence of fiber types on the flexural performance of cement-admixed soft clay was investigated by Sukontasukkul and Jamsawang (2012) sing short steel, long steel and polypropylene fibers at three different volume fractions of 0.5, 0.75 and 1.0% under test standard ASTM C1609/C1609M-10 (2010). The high cement content of 20% was used to attain the required compressive strength of 700 kPa. With fiber inclusions, the flexural performance of the cement-admixed soft clay was improved in terms of its toughness, equivalent flexural strength ratio and residual strength but not its peak flexural strength. The degree of improvement increased with the fiber volume fraction. The polypropylene fiber is found to perform better than the steel fibers without using a comparative evaluation method to determine the ability of each fiber type and without microstructural analysis on the nature of the interfacial bonds between the fiber surface and surrounding cement-admixed clay matrix, which is significant for investigating the influence of fiber types (Tang et al., 2010; Hejazi et al., 2012; Hannawi et al., 2016; Simoes et al., 2017) on the flexural performances.

Previous studies of the flexural response of CCFS used unusual test standards and addressed different matrix composition and fiber volume fractions with only one fiber type in each experiment. In addition, the comparative flexural performance of CCFS with various fiber types has not yet been comprehensively studied at the macro-scale and micro-scale. Moreover, no reasonable comparative guideline has been proposed to determine how to select the most suitable fiber type for a pavement structure. Therefore, the current status of CCFS research in the literature and the need to isolate the effects of fiber type on the flexural performance of CCFS, including the hardening or softening responses, have motivated the experimental study reported in this paper. Specifically, this study focuses on the sub flexural performance indicators of peak strength, peak strength ratio, residual strength ratio, ductility index, toughness, equivalent flexural strength ratio and maximum crack width. The interactions between the fiber surface and the stabilized soil were analyzed by means of scanning electron microscopy (SEM). Finally, the effect of the fiber type on the overall performance of CCFS was evaluated and rated in this study to determine a suitable fiber type for use in pavement materials.

2. Experimental program

The experimental program was carried out in three parts. First, the geotechnical properties of the studied sand and physical and engineering properties of all fiber types were characterized. Second, a series of flexural strength tests were carried out for both the CCS and CCFS specimens. Finally, a series of SEM analyses was conducted on the CCFS samples to observe the interaction mechanism of a fiber/cement-sand interface and to describe the effect of fiber type on the flexural performances of the CCFS test beam.

2.1. Materials

The sand used in the present experimental tests was obtained from Ayutthaya province, Thailand, and is commonly used as a construction material for embankment, fill and pavement applications. The grain size distribution curve and physical properties of Ayutthaya sand are shown in Fig. 1 and Table 1, respectively. This sand is classified as poorly graded sand (SP) according to the Unified Soil Classification System (USCS). Fig. 1 also shows an enlargement of the sand particles obtained from the SEM analysis, which illustrates angular and sub-angular shapes with a rough surface. The results of X-ray diffraction (XRD) analysis show that the mineral composition of the sand used was 60% feldspar and 40% quartz. The cement used in the test was ordinary Portland cement type I with a specific gravity of 3.15. Table 2 is a summary of the chemical composition of the cement used. Fibers used in this study were divided into two major types, depending on the size of the fibers: micro-fibers and macro-fibers. The size of the macro-fiber can be simply specified by ordinary mechanical measuring instruments, whereas the microscopic size of the micro-fiber is unspecified. A total of seven fiber types were used in the current study, which consisted of two macro-fiber and five micro-fiber types, respectively. Fig. 2a–g shows the shape and feather of the seven fiber types, namely, the micro 12 mm polypropylene, micro 19 mm polypropylene, macro 40 mm polypropylene, macro 55 mm polypropylene, 33 mm steel fiber, 50 mm steel and macro 58 mm polyolefin fibers. These fibers were distinguished mainly by their materials (steel or synthetic), dimensions (macroscopic

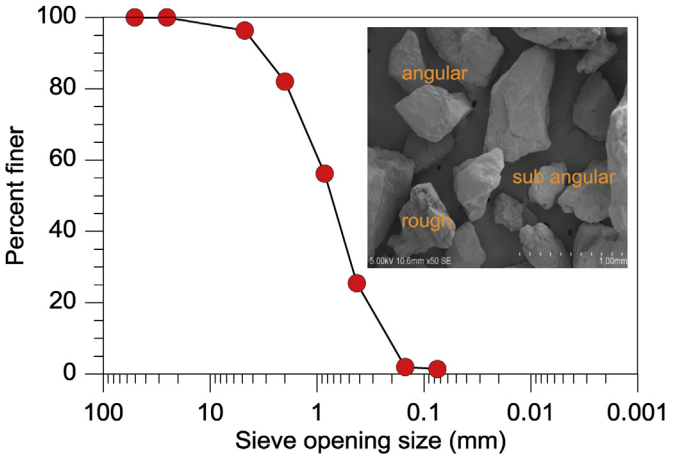

Fig. 1. Grain size distribution curve and shape of the sand used in this study.

Table 1
Physical properties of the sand used in this study.

Property	Value
Specific gravity	2.67
Gravel content (%)	3.7
Sand content (%)	94.9
Fine content (%)	1.4
D_{60} (mm)	0.95
D_{30} (mm)	0.49
D_{10} (mm)	0.22
Coefficient of uniformity	4.32
Coefficient of gradation	1.14
Soil classification (USCS)	SP
Maximum, minimum void ratios	0.68,0.45
Maximum dry unit weight (kN/m^3)	17.8
Optimum moisture content (%)	13.2

Table 2
Chemical composition of the cement used in this study.

Oxide	Common name	Content (%)
SiO_2	Silica	21.20
Al_2O_3	Alumina	4.95
Fe_2O_3	Iron	2.82
SO_3	Sulfuric anhydrite	2.63
CaO	Lime	62.81
MgO	Magnesia	4.00
Na_2O and K_2O	Alkali	0.30

or microscopic) and mechanical properties, as summarized in Table 3; all of this information is provided by the manufacturers.

2.2. Specimen preparation

For the preparation of all CCS and CCFS specimens, dry sand was mixed in a concrete mixer with Portland cement for 3 min, and then, fibers at specific contents were randomly included and mixed for an additional 3 min. The water was added to the cement-fiber-sand mixture to attain the optimum water content (obtained from the standard Proctor test) followed by mixing thoroughly for 5 min. The specimens were then prepared in the form of a beam with dimensions of 100 mm in width, 100 mm in height and 350 mm in length. The uniform mixture was compacted by a wooden hammer until the maximum dry unit weight was reached. The fiber contents were varied among 0.5, 1, 1.5, and 2% of the sand volume, whereas the cement content was fixed at 5% by weight of the dry sand. The optimum water content and maximum dry unit weight were essentially the same for all fiber contents, as shown in Table 1. The specimens were demolded after 24 h and wrapped with a plastic sheet for a 28-day curing period prior to the test date.

2.3. Experiments

After curing for 28 days, the specimens were subjected to a flexural performance test according to ASTM C1609/C1609M-10 (2010). To minimize the influence of casting direction, the beams were rotated through 90° from their casting position before testing. Fig. 3 shows the test equipment and test setup. A 20-kN load cell was used to measure the applied loads. Two linear variable differential transducers were attached to a reference beam for measuring the net deflections at the middle of the tested beam. The deflection rate of 0.05 mm/min was controlled by an electric motor and the test was stopped at a net deflection of 4 mm. The data logger obtained a sufficient number of data points to generate very sensitive load–deflection curves, which were then used to estimate the reliable flexural performance of each CCFS and to interpret the test results effectively.

2.4. Parameters describing flexural behavior of CCFS

The flexural responses of CCFS can generally be classified as either deflection-softening or deflection-hardening (Kim et al., 2011; Nematollahi et al., 2014; Jamsawang et al., 2015a), as shown by curves (a) and (b), respectively, in Fig. 4. A CCFS sample showing deflection-hardening behavior generates a higher load carrying capacity after first cracking, in comparison with CCS and deflection-softening CCFS. In this research, along the load–deflection curve, the point that clearly shows nonlinearity is defined as the first cracking point (Kim et al., 2011; Nematollahi et al., 2014; Jamsawang et al., 2015a). This point is appropriate for defining the first peak point for CCFSs exhibiting either deflection-hardening and softening responses according to the ASTM standard C 1018-97 (1997) and ASTM C1609/C1609M-10 (2010). The load value at this point is termed P_1, and the corresponding deflection value is δ_1. The peak load (P_P) is defined as the point at which softening first occurs after point P_1. Thus, $P_1 = P_P$ is noted in the case of deflection-softening CCFS. The corresponding deflection value at P_P is termed δ_P. In addition to the P_1 and P_P points, a deflection point of $L/150$ corresponding to 2 mm for a 300-mm-span length specimen is recommended according to ASTM C1609/C1609M-10 (2010). The flexural strength (f) at any deflection is obtained from

$$f = \frac{PL}{bd^2} \tag{1}$$

where P is the load (kN) corresponding to the required f (kPa), L is the span length (m), b is the width of the specimen (m) and d is the depth of specimen (m). The flexural strengths corresponding to the P_1 and P_P are defined as the first peak strength (f_1) and peak strength (f_P), respectively. The load carried by CCFS after P_1 at the deflection of $L/150$ is termed the residual load P_{150}, which corresponds to the residual strength at a deflection of $L/150$ (f_{150}). The energy equivalent to the area under the load–deflection curve up to a given deflection is defined as toughness. T_{150} is specified as the toughness value at the deflection of $L/150$.

According to Nematollahi et al. (2014), the ductility of a composite material is considered to be the ratio of the deflection at the peak strength to the first-crack deflection (δ_P/δ_1). That is, the higher the ratio of δ_P/δ_1, the more ductile the CCFS is. Hence, the ductility index (DI) can be defined as follows:

$$\mathrm{DI} = \delta_P/\delta_1 \tag{2}$$

where δ_P and δ_1 are the net deflections of the specimen at the peak strength and first peak strength, respectively, in units of mm. The flexural performance of CCFS is commonly evaluated using the equivalent flexural strength ratio ($R_{T,150}$), which is determined from the energy absorption capacity up to the deflection of $L/150$ of the beam

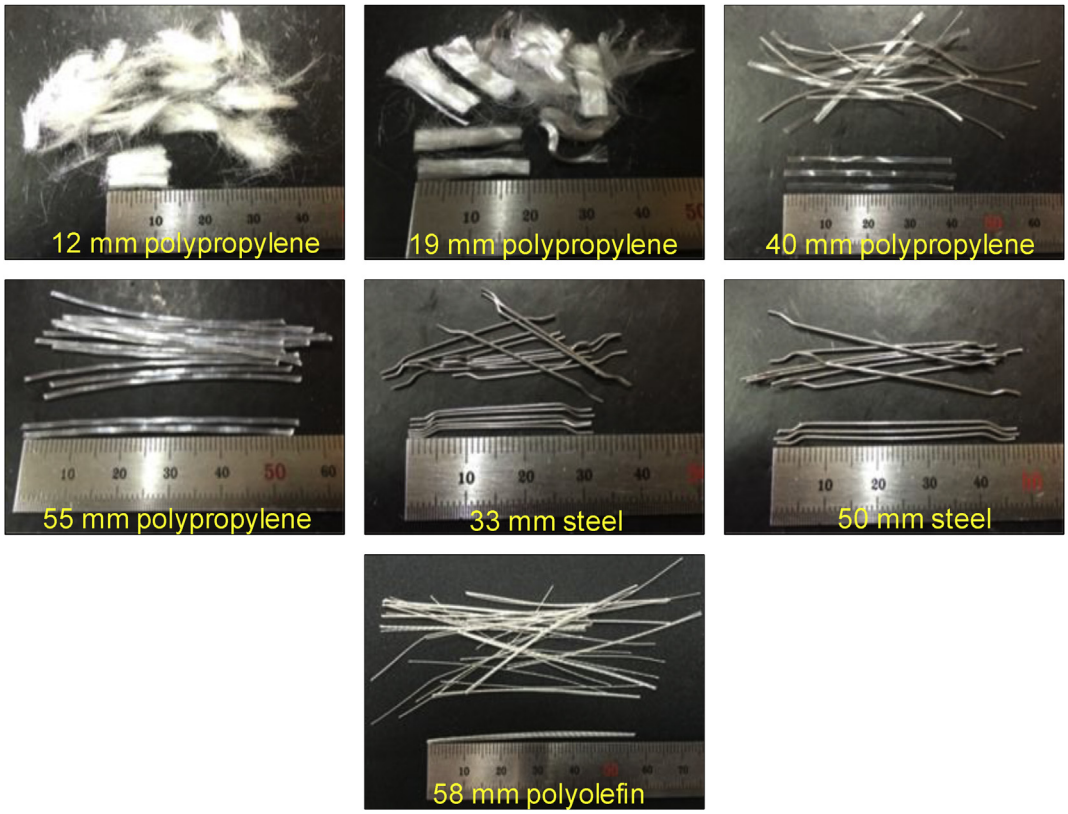

Fig. 2. Different fiber types used in this study.

Table 3
Properties of the fibers (from the manufacturer).

Type	Micro Polypropylene	Micro Polypropylene	Macro Polypropylene	Macro Polypropylene	Macro Steel	Macro Steel	Macro Polyolefin
Length (mm)	12	19	40	55	33	50	58
Designation	CCFS12	CCFS19	CCFS40	CCFS50	CCFS33	CCFS50	CCFS58
Shape	Straight	Straight	Flat-wide	Crimped	Hooked	Hooked	Twisted
Section	Circular	Circular	Rectangular	Circular	Circular	Circular	Circular
Diameter or width (mm)	–	–	1.55	0.85	0.60	0.75	0.25
Specific weight	0.91	0.91	0.92	0.91	7.8	7.8	0.9–0.92
Tensile strength (MPa)	320–400	320–400	620	250	> 1200	> 1100	620
Young's modulus (GPa)	3.5–3.9	3.5–3.9	3.0	3.0	210	210	> 7
Color	White	White	Shiny	White	Gray	Gray	Gray

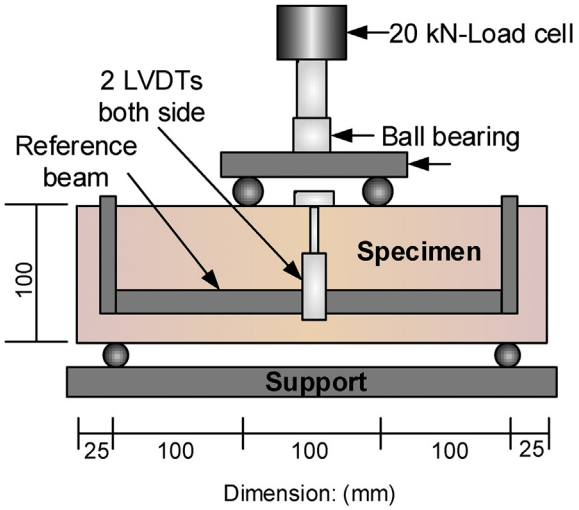

Fig. 3. Test specimen and setup.

span and the first peak load. Therefore, from the load-deflection curves obtained from the measurements, the value of $R_{T,150}$ can be calculated using the following Eq. (3).

$$R_{T,150} = \frac{T_{150}}{P_1 \frac{L}{150}} \times 100\% \tag{3}$$

An $R_{T,150}$ value higher than 100% is associated with $P_P > P_1$ and indicates a high-toughness material. In contrast, $R_{T,150}$ values are smaller and greater than 100% for deflection-softening ($P_P = P_1$) and deflection-hardening ($P_P > P_1$) behaviors, respectively.

3. Analysis and discussion on flexural test results

3.1. Behavior of load–deflection curves

Fig. 5a–d presents the load–deflection curves for CCS and CCFS beams with different fiber types and fiber contents. The Figs. clearly show that the fiber type affects the load–deflection response at the same fiber content, which indicates different flexural performances in terms

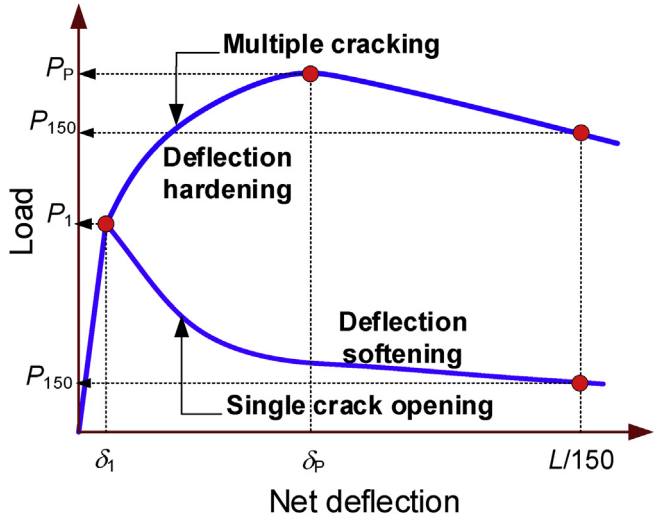

Fig. 4. Parameter calculations obtained from load–deflection curves (adapted from ASTM C1609/C1609M-10, 2010).

of load carrying ability, ductility and toughness. For the CCS, the specimen shows deflection-softening and brittle behavior; that is, the load increases in proportion to the net deflection until it reaches P_1, and then a sudden decrease in load is clearly observed. Therefore, P_1 and P_P are the same values, and no residual load after the first crack is carried. Unlike the CCFS beams with 0.5, 1, 1.5 and 2% fiber contents, the CCS beam shows either deflection-softening or deflection-hardening responses depending on the fiber types and fiber contents. The fully developed deflection-softening response, e.g., no influence of fiber contents on the load–deflection response, is found in CCFS12, which gives a $P_P = P_1$ similar to CCS.

In contrast, the CCFS33 and CCFS50 samples show a fully developed deflection-hardening response, in which $P_P > P_1$. At the beginning, there is a linear increase of the load with deflection, which is very similar to that of the CCS; this trend continues until the point of failure of the latter. However, the load carrying capacity of the CCFS33 and CCFS50 continues to increase beyond the limit of proportionality, exhibiting a deflection-hardening behavior without initial deflection-softening behavior, which is characteristic of the ductile response. This behavior continues until reaching a deflection value significantly larger than the maximum deflection value of the CCS and deflection-hardening CCFS. Furthermore, the CCFSs with the other fiber types exhibit either deflection-softening or deflection-hardening behaviors, depending on the fiber contents. CCFS19 and CCFS55 required a minimum fiber content of 1% to obtain deflection-hardening behavior, whereas CCFS40 and CCFS58 required a minimum content of 2%. However, due to the existence of fiber reinforcement, all deflection-softening CCFSs can carry more residual load than CCS.

3.2. First peak strength (f_1) and peak strength (f_P)

The f_1 refers to the stress caused by bending along the bottom face of the beam when the first crack formed. Fig. 6a and b shows the effect of fiber type and fiber content on the values of f_1 and f_P, respectively. The f_1 value for CCS is 0.45 MPa, whereas the values for the CCFSs range from 0.35 to 0.70 MPa. The increase in fiber content has a negligible impact because f_1 for CCFS depends mainly on the strength of the cement-sand matrix rather than the fiber bridging capacity (Sukontasukkul and Pomchiengpin, 2010), such that the f_1 values are insignificantly different for all CCFSs except CCFS33 with a 2% fiber content and CCFS55 with fiber contents from 0.5 to 2%. However, the overall f_P increases according to increasing fiber contents of all CCFS samples. The CCFSs with steel fiber (CCFS33 and CCFS50) provide higher f_P than the CCFSs with other fibers due to their fully developed hardening response, in which CCFS50 contributed the highest values of 0.65–1.05 MPa for 0.5–2% fiber content; as a result, the peak strengths of CCS were improved by factors of 1.44–2.33. The rate of increase in f_P of CCFS33 and CCFS50 is highest in comparison with other fiber types, which implies that they are able to react with the load faster at the same fiber contents. Moreover, the f_P of CCFS with shorter fibers dropped below that of CCFS with longer steel fibers and polypropylene fibers (CCFS33 < CCFS50, CCFS12 < CCFS19 and CCFS40 < CCFS55).

3.3. Peak strength ratio

In this study, the comparative degree of hardening of each CCFS is evaluated in terms of a peak strength ratio (PSR), which is defined as f_P divided by f_1. This ratio indicates the ability of the fiber to gain strength after the first crack has occurred. More specifically, values of PSR = 1 and PSR > 1 also indicate softening and hardening responses, respectively, and the higher the PSR, the higher the degree of hardening. Fig. 7 shows that CCFS19 and CCFS55 provided an increase in PSR with increasing fiber content and that they give the highest PSRs of 2.0 and 1.7, respectively, at 2% fiber content, whereas CCFS33 and CCFS50 show an optimum fiber content of 1.5% with maximum PSRs of approximately 1.6. Thus, CCFS19 has a higher degree of hardening by as much as 1.25 times those of CCFS33 and CCFS 50. CFS40 and CCFS58 provided PSRs greater than 1.0 for specific fiber contents (as much as 2.0%) with recorded values of 1.6 and 1.3, respectively. However, the fiber content had no effect on the PSR for fully developed softening in CCFS12 because PSR was recorded as 1 for all fiber contents.

3.4. Residual strength ratio at a deflection of L/150

In addition to PSR, a residual strength ratio at a deflection of $L/150$ (RSR_{150}) is also introduced in this study to measure the ability of each fiber type to carry the residual load from the first crack point to the deflection of $L/150$. Thus, RSR_{150} can be defined as f_{150} divided by f_1. This ratio also implies the effectiveness of each fiber type in maintaining the hardening of CCFS at a large deflection, e.g., $RSR_{150} < 1$ and $RSR_{150} > 1$ also indicate softening and hardening responses at a deflection of $L/150$, respectively.

Fig. 8 shows that all strain-softening CCFSs provided $RSR_{150} < 1$. CCFS12 give values of RSR_{150} varying between 0.2 and 0.5, which indicates that CCFS12 can carry P_{150} by as much as half the P_1. The results for CCFS33 and CCFS50 show that the fiber content of 1.5% is optimum to obtain the maximum RSR_{150} values of approximately 1.55 and 1.45, respectively. However, RSR_{150} increased with increasing fiber contents for CCFS19, CCFS55, CCFS 40 and CCFS58 yielding the highest values for each of 1.9, 1.75, 1.1 and 1.5 respectively, at 2% fiber content. It seems that CCFS19 was the most effective in terms of RSR_{150} among the other fiber types. Considering the 2% fiber content, CCFS19, CCFS55 and CCFS 40 provided better performance than the CCFSs with steel fibers by factors of approximately 1.7, 1.6 and 1.3, respectively. The steel fiber is limited in its ability to carry a residual load to a large deflection.

3.5. Ductility index

There are several trends in the ductility index (DI) values for all CCFSs, as presented in Fig. 9. The values of DI are equal to 1 and greater than 1 for fully developed softening CCFSs (CCFS12) and fully developed hardening CCFSs (CCFS33 and CCFS50), respectively. CCFS19 and CCFS33 show optimum fiber contents of 1.5 and 1% with maximum DI values of approximately 88 and 28, respectively. The DI values tend to decrease and increase with increasing fiber contents for CCFS50 and CCFS55, respectively, which yield values of 54 to 6 and 1 to 64 at 0.5–2% fiber contents for CCFS50 for CCFS55, respectively. For hardening CCFS40 and CCFS58 at 2% fiber contents, DI values of 72 and 16

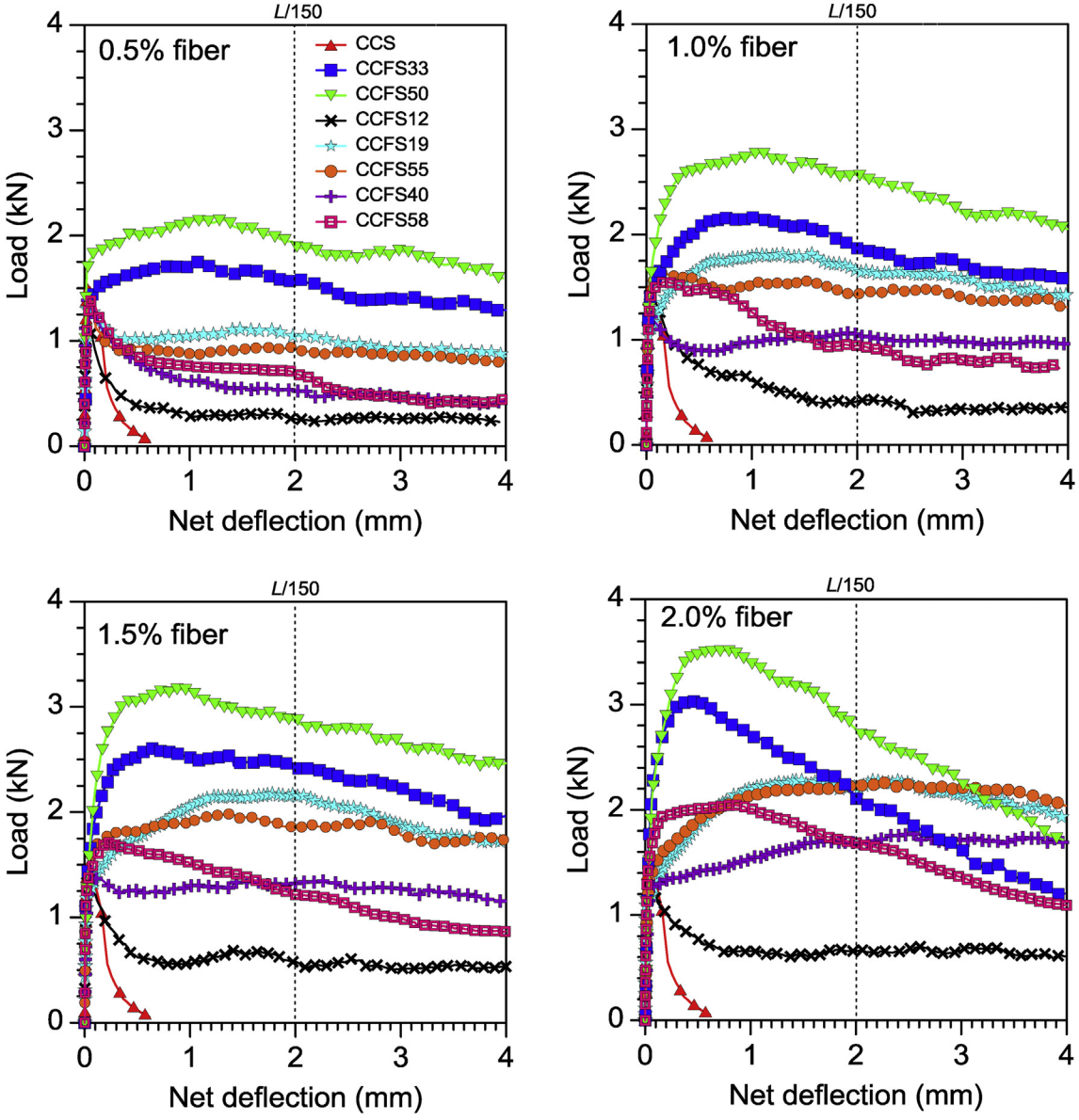

Fig. 5. Load-deflection curves for CCFS with different fiber types and different fiber contents.

are given, respectively. It seems that the steel fiber has a low DI due to its high stiffness, which allows it to be quite effective in terms of carrying the peak load at a small deflection. In contrast, CCFS19, CCFS40 and CCFS55 react to the load slower than the steel fibers because, according to the data, the deflection must be sufficiently large before the polypropylene fibers will take on a fraction of the load. Thus, the CCFS19 at 1% fiber content and the CCFS40 and CCFS55 at a 2% fiber content are appropriate when designing CCFS with extremely high ductility.

3.6. Toughness at a deflection of L/150

The toughness at a deflection point of 2 mm corresponding to $L/150$ (T_{150}) was considered in this study. The results show that the T_{150} of CCFS is found to be dependent upon the fiber content and fiber type, as shown in Fig. 10. Higher fiber contents exhibited a greater T_{150} for all fiber types, owing to the improvement of the fiber bridging capacity at the crack surfaces. CCFS beams that exhibited deflection-hardening behavior performed better in toughness than those exhibiting deflection-softening behavior because they absorbed more energy after cracking [21]. Therefore, steel fiber-reinforced CCFS33 and CCFS50 are able to absorb the largest amount of T_{150} when compared to the CCFS with other fiber types, whereas CCFS12 produced the lowest T_{150}. CCFS50 and CCFS33 yielded values of T_{150} between 4 and 6.3 and between 3.2 and 5.2 N-m, respectively. CCFS19, CCFS55 and CCFS58 gave similar values for T_{150} (approximately 2–4 N-m). CCFS40 and CCFS12 provided values in the range from 1.3 to 3 and 0.7 to 1.5 N-m, respectively. The value of T_{150} for CCS was 0.42 N-m. Thus, for the 2% fiber content, the CCFS50 and CCFS 12 improved the T_{150} of CCS by as much as 15 and 3.6 times, respectively. The values of T_{150} are in the following order: CCFS50 > CCFS33 > CCFS19 > CCFS55 > CCFS58 > CCFS40 > CCFS12. Note that the trend of $R_{T,150}$ is similar to that of RSR_{150}, as mentioned in Section 3.2.

3.7. Equivalent flexural strength ratio

Fig. 11 clearly shows that all softening and hardening CCFSs provided $R_{T,150} < 100\%$ and $R_{T,150} > 100\%$, respectively. According to the data for CCFS33 and CCFS50, a 1.5% fiber content was optimum for yielding the maximum $R_{T,150}$ values of approximately 160 and 150%,

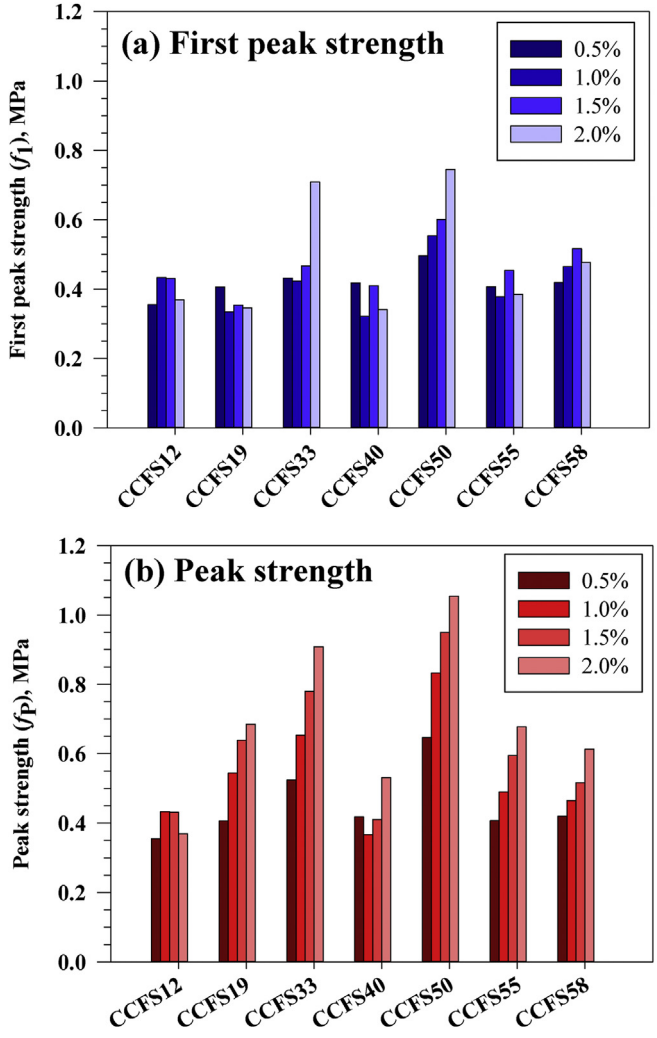

Fig. 6. Effect of fiber type on first peak strength and peak strength at different fiber contents.

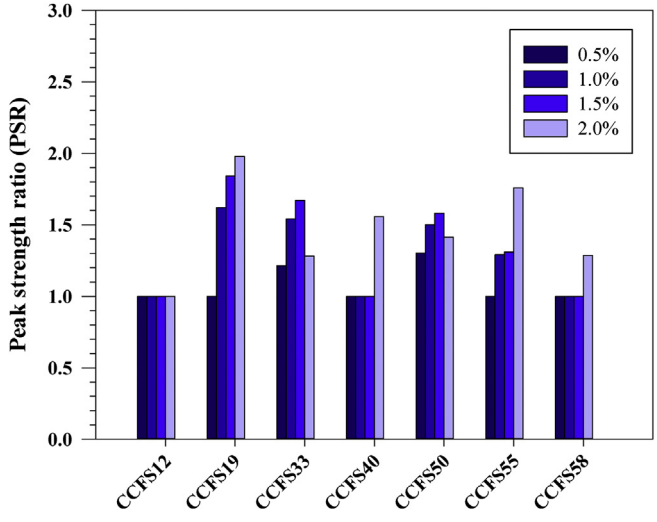

Fig. 7. Effect of fiber type on peak-to-strength ratio (PSR) at different fiber contents.

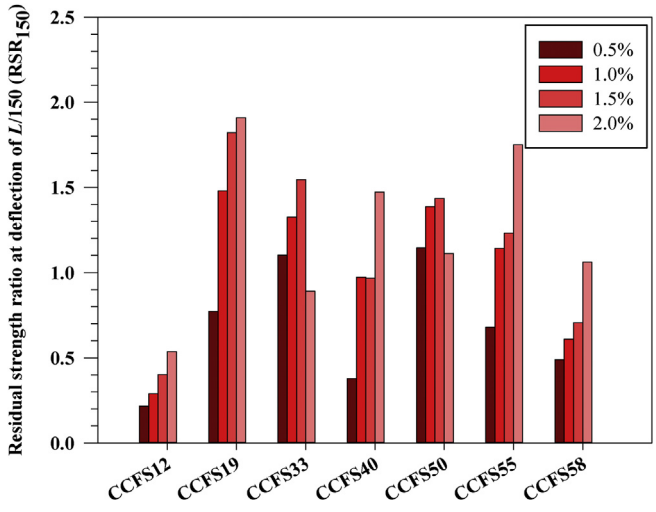

Fig. 8. Effect of fiber type on the residual strength ratio at a deflection of L/150 (RSR_{150}) at different fiber contents.

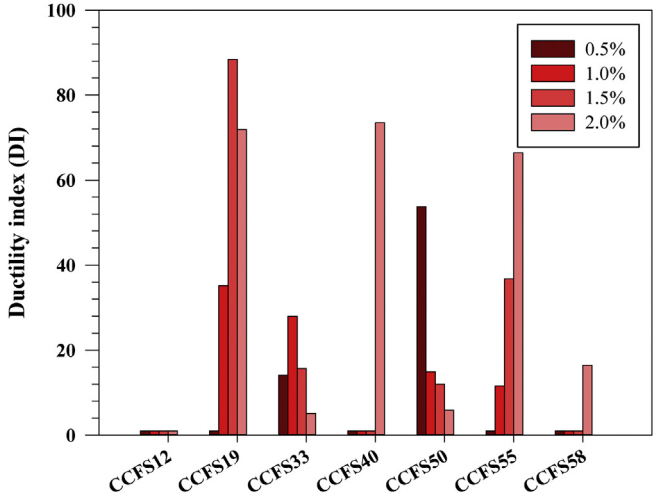

Fig. 9. Effect of fiber type on the ductility index (DI) at different fiber contents.

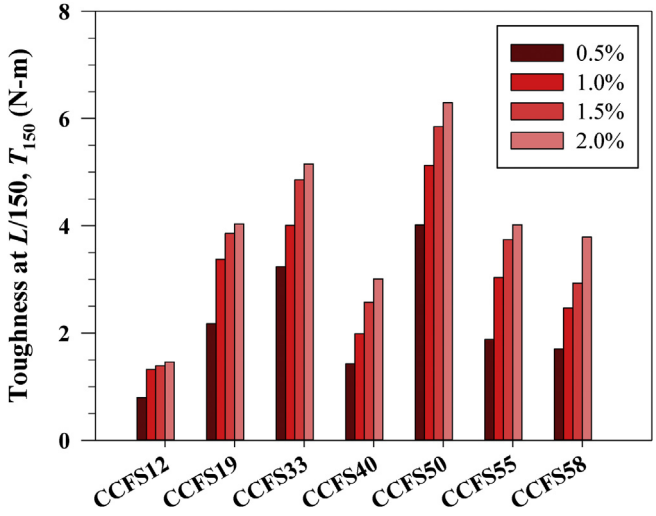

Fig. 10. Effect of fiber type on the toughness at a deflection of L/150 (T_{150}) at different fiber contents.

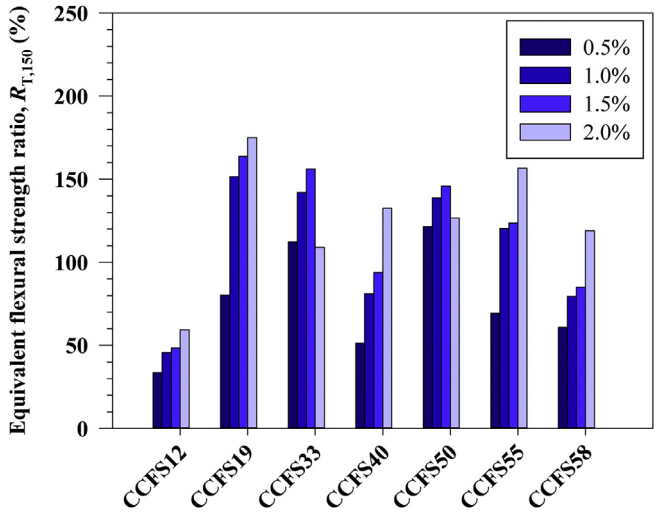

Fig. 11. Effect of fiber type on the equivalent flexural ratio ($R_{T,150}$) at different fiber contents.

respectively. In contrast, $R_{T,150}$ increased with increasing fiber content for CCFS19, CCFS55, CCFS 40 and CCFS58 and had the highest values of 175, 130, 155 and 120%, respectively, at a 2% fiber content. Thus, CCFS19 provided the best performance in terms of $R_{T,150}$. Considering the 2% fiber content, CCFS19, CCFS55 and CCFS 40 provided better performance than the CCFSs with steel fibers by factors of approximately 1.5, 1.4 and 1.1, respectively. Due to the fully developed softening response, the $R_{T,150}$ values of CCFS12 varied only from 30 to 60%.

3.8. Crack patterns of CCFS

The crack patterns, including the shape and maximum crack width (MCW), of the CCFS specimens were investigated because the crack patters are typically one of the main parameters for characterizing the performance of a fiber type (Sukontasukkul and Pomchiengpin, 2010; Kim et al., 2011; Nematollahi et al., 2014). The crack patterns of CCFS can be divided into two types, a single crack and multiple cracks, depending on the fiber type and fiber content. All specimens fail due to tension at the bottom of the tested beam; therefore, the cracks propagate from bottom to the top. As expected, the CCS beam fractured suddenly into two pieces, as shown in Fig. 12a, and exhibited a typical brittle failure mode by a readily visible single crack with the MCW of 30 mm due to the concentration of tensile stress at approximately mid span, which resulted in the inability of the CCS to carry any residual load.

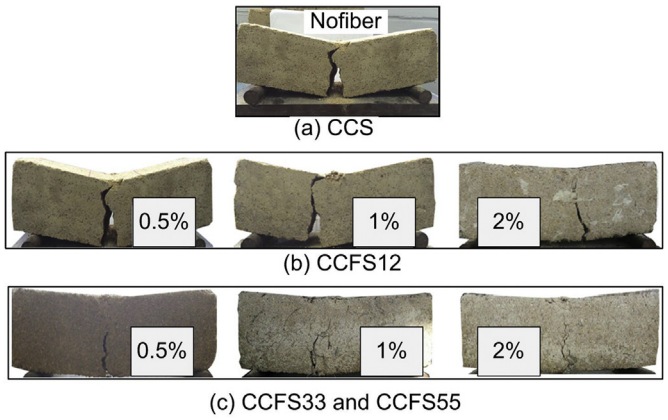

Fig. 12. Crack pattern of CCS and CCFS at different fiber contents.

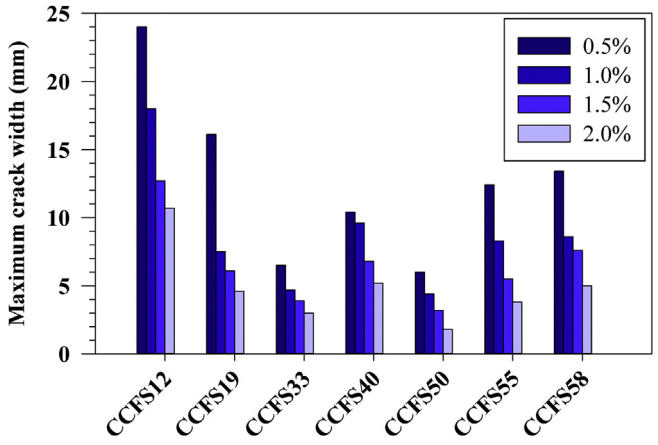

Fig. 13. Effect of fiber type on the maximum crack width (MCW) at different fiber contents.

For all CCFS samples, the tensile strength of the CCFS after the first crack increased with increasing fiber content; hence, the beam was able to carry some residual load. It was also observed that the MCWs decreased with increasing fiber content due to the bridging effect of the embedded fibers. An example of the crack pattern observed in CCFS12 is presented in Fig. 12b. Single failure planes with large MCWs on the CCFS beam were clearly observed for all fiber contents, similar to the crack pattern of the CCS. Due to the existence of fiber reinforcement, CCFS12 was able to carry some residual load but at a lower total amount than the P_1, representing softening-deflection behavior with poor flexural performance. Unlike CCFS33 and CCFS50 at all fiber contents (Fig. 12c), the MCWs were significantly smaller than those for CCFS12, and multiple cracks propagated around the main crack; these observations imply that the steel fibers effectively bridged the crack after the macrocrack had formed and redistributed the stress to the cement-sand matrix through the fiber-matrix interface. The redistributed stress built up and leading to the formation of microcracks without sudden failure. Consequently, the cement-sand matrix carried a higher residual load than P_1, representing a hardening-deflection response with high flexural performance. In the same way, the crack patterns of CCFS with other fiber types exhibited softening- and hardening-deflection responses that were found to be similar to those shown in Fig. 12b and c, respectively. However, the MCWs can be distinguished at the same fiber content due to the different fiber types, as illustrated in Fig. 13. The Fig. summarizes the MCW obtained by the precise measurement of all CCFS specimens with fiber contents of 0.5–2.0%. As expected, the MCWs decreased with increasing fiber content and reduction in the MCWs mainly depended on the fiber type and fiber content, as explained above. CCFS50 provided minimum values of MCW that ranged between 3 and 7 mm, while CCFS12 gave maximum values of MCW between 11 and 24 mm. In addition, other fibers provided MCWs from 5 to 16 mm, 4–13 mm and 6–14 mm for CCFS19, CCFS55 and CCFS58, respectively. It should be noted that the crack widths in CCFS can be effectively reduced by the insertion of steel fibers by as much as 10 times the MCW of CCS. However, CCFS12 only reduces the cracks by as much as 2.7 times the MCW of CCS.

4. Interaction mechanism of fiber-matrix interface by microstructure observation

The effect of fiber type on the crack patterns and crack widths of CCFS beams, as shown in Fig. 12a–c, is present in the form of macro-scale crack behavior, which can be directly observed with the naked eye. However, microstructural observation is required to investigate micro-scale interaction mechanisms between the interface of the cement-sand matrix and the fiber surface micro-scale behavior. This

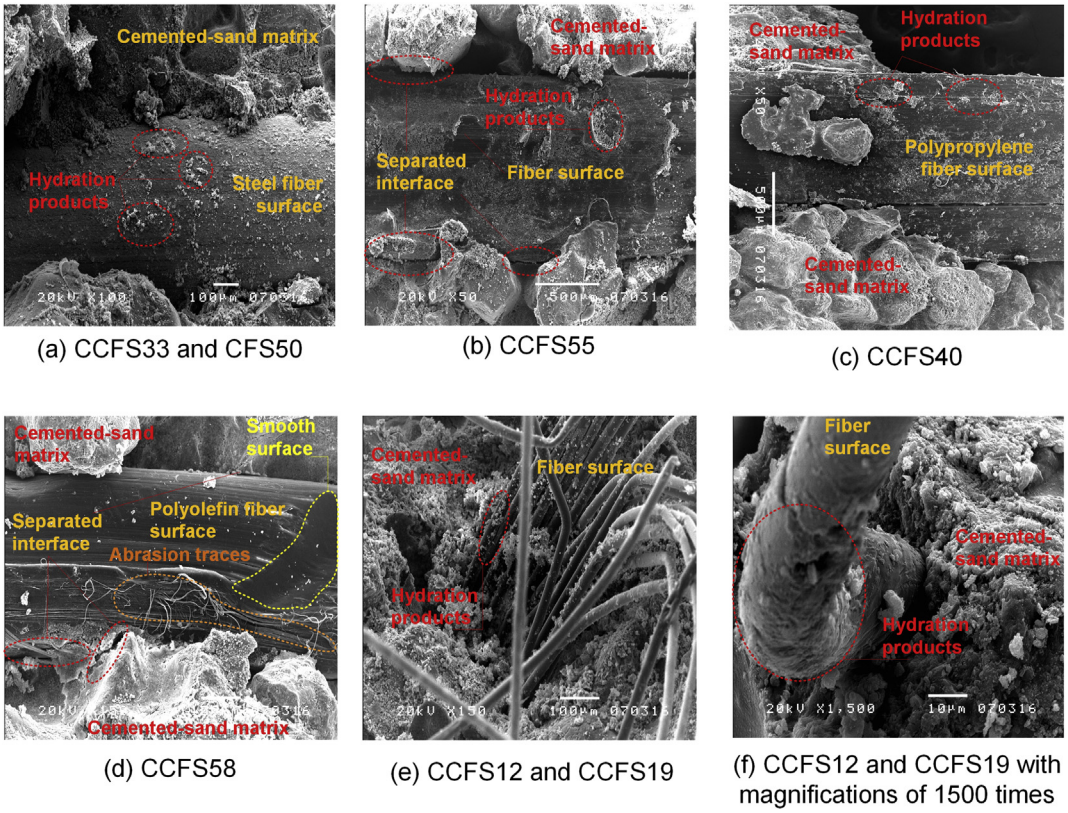

Fig. 14. SEM images of the fiber surface on reinforced stabilized sand.

mechanism is complex and is influenced by the embedded fiber length, fiber surface roughness, shape, etc. (Tang et al., 2010; Hejazi et al., 2012; Hannawi et al., 2016; Simoes et al., 2017). Therefore, the interpretation of the comparative flexural performances presented in previous sections based on a micromechanical approach is interesting and reasonable to support the macro-scale test data. In this study, SEM observation was used to characterize the comparative interfacial bond nature for each fiber type. Prior to the flexural test, the matrix and fiber are initially bonded with each other throughout the entire fiber length by chemical or physical adhesion, e.g., the embedded fiber length is initially equal to the fiber length. After the test beam cracks, the induced shear stress around the interface begins to exceed the interfacial bond strength, resulting in the sliding of fibers along the interfacial zone and, consequently, decreases the embedded fiber length relative to the initial state of the sample. As the crack widths of the test beam continue to enlarge according to the increase of the applied force, the bond force decreases due to a decrease in the embedded fiber length. The fibers pull out of the matrix as the shear force within the fiber exceeds the bond force along the embedded fiber length. The interfacial bonding for a given matrix depends mainly on the shape and length of the fiber. Several researchers have noted that fiber sliding resistance is strongly dependent on the fiber surface roughness (Tang et al., 2010; Hejazi et al., 2012; Hannawi et al., 2016; Simoes et al., 2017). Therefore, the main contributor to performance is the fiber shape and length.

Fig. 14 shows SEM images of the microstructure of the fiber surfaces, cement-sand matrix, hydration products and various interfaces. The fiber surface is attached by hydration products that contribute to the bond strength between the fiber and matrix. After the test beam cracked, all fiber types used to reinforce the CCFSs were pulled out without rupture of the fiber materials, which implies that the tensile strength of the fiber was an insignificant design parameter for CCFS due to the low strength of the matrix in comparison to concrete. In the cases of CCFS33 and CCFS50 (Fig. 14a), the surface of the steel fibers was more hydrophilic and the fiber/matrix interfacial zone was more compact in comparison with that of the other synthetic fibers (Hannawi et al., 2016). Therefore, the cement-sand matrix around the steel fibers was able to properly hydrate and fill a significant fraction of the space between the fiber and the matrix, resulting in no observed gap between the phases or separation of the interfaces. Moreover, it can be seen that the hydration product almost fully covers the surface area of the steel fibers, which results in a high bond strength at the interface and reduced sliding in the interfacial zone. This causes CCFS33 and CCFS50 to provide the deflection-hardening response with a small amount of fiber content (0.5%) and the highest peak strength based on the first peak and post peak loads when compared with the CCFS with other fibers, as described in the previous sections.

In contrast to the samples with embedded steel fibers, a non-compact fiber/matrix interfacial zone was clearly observed in the SEM images for the synthetic and hydrophobic polyolefin and polypropylene fibers (Hannawi et al., 2016), as shown in Fig. 14b–f. Thus, partially separated interfacial zones were observed because the hydrophobic synthetic fiber was able to (a) most significantly, restrict the water needed for cement hydration from entering the structure of the cement-sand specimens during the curing period and, less significantly, (b) draw more air bubbles into the interfacial transition zone. This led to both the lower peak strength and the lower degree of hardening-deflection response and MCW. Thus, greater fractions of synthetic fibers than steel fibers were required to develop the bond strength necessary to obtain a hardening-deflection response.

The nature of the interfacial bonds of the macro polypropylene fibers in CCFS55 and CCFS40 were similar, as shown in Fig. 14b and c, respectively. However, CCFS55 required a smaller fiber content than CCFS40 to obtain a hardening-deflection response because its fiber geometry afforded different interfacial bonding properties. This result implies that the crimped-shaped fibers in CCFS55 provided better interfacial bonding properties than the fibers in CCFS40, which were smooth, flat and wide. Even though the polyolefin fiber (CCFS58) had the greatest fiber length among all of the fibers used in this study,

nonetheless it also required the greatest fiber content to achieve a hardening-deflection response, indicating poor interfacial fiber geometry of the fiber due to its twisted shape. This is demonstrated by the SEM image in Fig. 14d, which reveals that no obvious hydration products were detected on the polyolefin fiber surface. In addition, the rough surfaces of the polyolefin fiber experienced abrasion damage and became smooth due to compaction during specimen preparation, which led to a loss of the beneficial features of the interfacial surface.

For distributed, discrete micro polypropylene fibers in CCFS12 and CCFS19 acted as a three-dimensional network (Fig. 14e), promoting bonding with the cement-sand matrix. As shown in the magnified SEM image in Fig. 14f, the fiber surfaces were well covered by hydration products, leading to high interfacial bonding. As a result, CCFS19 exhibited the deflection-hardening behavior at a 1% fiber content. However, due to insufficient fiber length, CCFS12 was unable to establish hardening behavior at any fiber content.

5. Concept of overall performance of CCFS

To decide which fiber type is best for use in CCFS, the concept of overall performance must be introduced, to provide a general idea regarding the comparative performance of fiber types. The overall performance of CCFS is divided into eight sub design performances, as presented in previous sections; these include (1) peak strength (f_P), (2) peak strength ratio (PSR), (3) residual strength ratio at a deflection of $L/150$ (RSR_{150}), (4) ductility index (DI), (5) toughness at a deflection of $L/150$ (T_{150}), (6) equivalent flexural strength ratio ($R_{T,150}$) and (7) maximum crack width (MCW). The concept used for the determination of overall performance of a CCFS is described as follows:

a) Calculate the average sub performance value for each fiber type, as tabulated in Table 4, which is defined as

$$\text{Average sub performance value} = \frac{\text{Sum of performance values}}{\text{Number of fiber conents}} \times 100 \quad (4)$$

b) Calculate the comparative score of the sub performance for each fiber type based on a full score of 100 as shown in Table 5, which is defined as

$$\text{Comparative score} = \frac{\text{Average sub performance value}}{\text{best average sub performance value}} \times 100 \quad (5)$$

For example, the values of sub performance f_P for each fiber type CCFS50, CCFS33, CCFS19, CCFS55, CCFS40, CCFS58 and CCFS12 were 0.79, 0.66, 0.55, 0.52, 0.44, 0.49 and 0.41 MPa, respectively. It must be noted that CCFS50 provided the best value of sub performance in terms of the highest value of f_p of 0.79 MPa. Consequently, the comparative scores of this sub performance for each fiber type were 100, 84, 69, 66, 55, 63 and 52 for CCFS50, CCFS33, CCFS19, CCFS55, CCFS40, CCFS58 and CCFS12, respectively.

Table 4
Average sub performance values for each fiber type.

Fiber type	Sub performance of CCFS						
	f_P (kPa)	PSR	RSR_{150}	DI	T_{150} (N-m)	$R_{T,150}$ (%)	MCW (mm)
12 mm polypropylene	0.41	1.00	0.36	1.00	1.24	47	16.35
19 mm polypropylene	0.55	1.61	1.50	49.11	3.36	143	8.58
33 mm steel	0.66	1.43	1.22	15.71	4.31	130	4.53
40 mm polypropylene	0.44	1.14	0.95	19.11	2.25	90	8.00
50 mm steel	0.79	1.45	1.27	21.61	5.32	133	3.85
55 mm polypropylene	0.52	1.34	1.20	28.94	3.17	117	7.50
58 mm polyolefin	0.49	1.07	0.72	4.85	2.72	86	8.65

c) Calculate the percentage of overall performance, as shown in Table 6, which is defined as:

$$\text{Percentage of overall performance} = \frac{\text{Sum of score of sub performance}}{\text{Sum of full score of sub performance}} \times 100\% \quad (6)$$

The overall performance rating was divided into seven levels: (1) excellent, (2) very good, (3) good, (4) fairly good, (5) fair, (6) poor and (7) very poor. Because there was no standard to define these levels, the common concept of significance in geotechnical engineering was adopted (Jamsawang et al., 2015b), as listed in Table 7. Table 6 shows the ranks of all fiber types based on the overall performance of CCFS (%). It can be observed that only the 50 mm steel fiber provides excellent overall performance, whereas both the 19 mm polypropylene and 33 mm steel fibers give very good performance. In addition, the 55 mm polypropylene fiber achieved good performance, whereas fair performances were achieved with the 40 mm polypropylene and 58 mm polyolefin fibers. As expected, only the 12 mm polypropylene gives very poor performance. Moreover, some applications may require a specific sub performance rather than an overall performance. Table 5 can help a designer to select the optimal fiber type for a specific application.

6. Discussion

The results of flexural tests, SEM observations and the concept of overall performance of CCFS, as presented in Sections 3, 4 and 5, respectively, are comprehensively discussed in this section. Due to high stiffness, high interfacial bond with a hooked end and sufficient length, the 55 mm steel fiber yielded the highest score in almost all sub performance categories except the DI, resulting in excellence in overall flexural performance. Even though 19 mm polypropylene fiber had a low stiffness and short fiber length, it provided the highest sub performance scores in terms of DI, RSR_{150}, RTD_{150}, PSR and $PCSR_{150}$, which led to very good overall performance due to its large number of fibers at a given fiber content, which is one advantage associated with this kind of fiber. However, both fiber length and fiber shape contribute to the interfacial bond strength of CCFSs. Thus, the 33 mm steel and 12 mm polypropylene fibers provided lower overall performance relative to similar fiber shapes with longer fiber lengths. Specifically, the 12 mm polypropylene fiber with the shortest fiber length yielded the worst of all scores of sub performances, with very poor overall flexural performance and is therefore not recommended for use in CCFS materials. Because the 55 mm polypropylene fiber with its crimped-shape geometry and appropriate length gave high sub performance scores, good overall performance was also obtained. Both the 40 mm polypropylene fiber with its flat and wide geometry and the 58 mm polyolefin fiber with its twisted geometry gave low to medium sub performance scores because they required a large amount of fiber content (2%) to achieve a hardening response, which resulted in fair overall flexural performance.

7. Conclusions

This research was performed as a comparative study of the effect of fiber type on the flexural performance of compacted cement-fiber-sand (CCFS), according to ASTM C1609/C1609M (2010). Seven fiber types were studied: micro 12 mm polypropylene, micro 19 mm polypropylene, 33 mm steel, 50 mm steel, macro 40 mm polypropylene, macro 55 mm polypropylene and macro 58 mm polyolefin fibers. The fiber contents were 0.5–2% by volume, and the cement content was fixed at 5% by dry weight. The crack pattern was investigated, and the interaction mechanism of the fiber-matrix interface was observed by SEM. Based on the experimental results, the following conclusions are drawn:

Table 5
Comparative score of the sub performance for each fiber type based on a full score of 100 points.

Fiber type	Sub performance of CCFS						
	f_P (point)	PSR (point)	RSR_{150} (point)	DI (point)	T_{150} (point)	$R_{T,150}$ (point)	MCW (point)
12 mm polypropylene	52	62	24	2	23	24	24
19 mm polypropylene	69	100	100	100	63	100	45
33 mm steel	84	89	81	32	81	81	85
40 mm polypropylene	55	71	63	39	42	63	48
50 mm steel	100	90	85	44	100	85	100
55 mm polypropylene	67	83	80	59	60	80	51
58 mm polyolefin	63	67	48	10	51	48	45

Table 6
Rank of the effectiveness of each fiber used in this study based on an overall performance rating.

Rank	Fiber type	Average percentage of overall performance	Overall performance rating
1	50 mm steel	90	Excellent
2	19 mm polypropylene	82	Very good
3	33 mm steel	78	good
4	55 mm polypropylene	69	Fairly good
5	40 mm polypropylene	54	Fair
6	58 mm polyolefin	49	Poor
7	12 mm polypropylene	31	Very poor

Table 7
Overall performance rating based on the range of average percentages of overall performance.

Average percentage of overall performance	Overall performance rating
90–100	Excellent
80–89	Very good
70–79	good
60–69	Fairly good
50–59	Fair
40–49	Poor
< 39	Very poor

1. Fiber type affects the behavior in which CCFSs respond to loading. Steel fibers exhibit a hardening response independent of fiber content, whereas relatively shorter micro polypropylene fibers exhibit a fiber-content-independent softening response. The rest of the fiber types show either a softening or hardening response depending on the fiber content. From the cost point of view, steel fiber is recommended in terms of attaining a hardening response at the lowest fiber content of 0.5%.
2. Based on microstructural investigations, steel fiber provides full-contact interfacial surface area due to its hydrophilic surface and high degree of denseness at the interface. In addition, the many hydration products associated with steel fiber can serve as sources of bond strength; because these products fully cover the interfacial surface area of the steel fiber, they result in a high interfacial bond strength. This strength phenomenon contributes to steel fibers showing a deflection-hardening response with the smallest fiber content relative to synthetic fibers. In contrast, the synthetic fibers studied here are hydrophobic materials with a non-compact interfacial zone that results in only a partial-contact interfacial surface. These require greater fiber content to create sufficient bond strength for obtaining a hardening-deflection response.
3. The concept of comparative overall performance is introduced to select and rank reasonably suitable fiber types for use as CCFSs for pavement materials. This approach is chosen because it takes into account the main sub flexural performance categories. Due to having the highest score in almost all performance types, the 55 mm steel fiber has the only rating of excellent in overall flexural performance. The 19 mm polypropylene and 33 mm steel fibers provide the highest scores in some sub performance types, resulting in ratings of very good and good in overall flexural performance, respectively.
4. For a pavement with reasonably good performance, the rest of the fiber types, including 12 mm polypropylene, 40 mm polypropylene, 55 mm polypropylene and 58 mm polyolefin fibers, are not recommended because their overall performance ratings are less than good.
5. A steel fiber is appropriate for use in a CCFS requiring peak strength, toughness and crack reduction, whereas long micro polypropylene is appropriate for CCFS requiring ductility and residual strength. For the same material type, a greater fiber length provides better performance due to the increased interfacial surface area; however, in the case of differential lengths, the fiber surface type dominates over length due to the difference in the nature of the interfacial bond.
6. The micro 19 mm polypropylene fiber is nearly the shortest fiber length studied here but still provides very good overall performance due to the good interfacial bond achieved at the fiber surface, which is well covered with hydration products. In addition, a higher bond strength is obtained due to the large number of fibers at a given fiber content. However, the micro 12 mm polypropylene fiber has an insufficient fiber length, which results in the worst overall performance. Although the 58 mm polyolefin fiber has the longest fiber, it provides poor overall performance due to poor interfacial fiber geometry as a result of the twisted shape of the fiber structure, which prevents coverage by hydration products.

Acknowledgments

This research was supported by the Thailand Research Fund (TRF) and King Mongkut's University of Technology North Bangkok (KMUTNB) under a TRF Grant for New Researcher Contract No. TRG5880161. The authors also extend their appreciation to the TRF and King Mongkut's University of Technology Thonburi (KMUTT) for granting financial support through the TRF Basic Research Contract No. BRG6080011.

References

Al-Aghbari, M.Y., Mohamedzein, Y.E.A., Taha, R., 2009. Stabilization of desert sands using cement and cement kiln dust. In: Proceedings of the Institution of Civil Engineering, Ground Improvement, vol. 16. pp. 145–151.
Anggraini, V., Asadi, A., Syamsir, A., Huat, B.B.K., 2017. Three point bending flexural strength of cement treated tropical marine soil reinforced by lime treated natural fiber. Measurement 111, 158–166.
Anggraini, V., Asadi, A., Farzadnia, N., Jahangirian, H., Huat, B.B.K., 2016. Effects of coir fibres modified with Ca(OH)2 and Mg(OH)2 nanoparticles on mechanical properties

of lime-treated marine clay. Geosynth. Int. 23 (3), 206–218.
ASTM C1018-9, 1997. Standard Test Method for Flexural Toughness and First Crack Strength of Fiber Reinforced Concrete (Using Beam with Third Point Loading). ASTM Standards, United States.
ASTM C1609/C1609M, 2010. Standard Test Method for Flexural Performance of Fiberreinforced Concrete (Using Beam with Third-Point Loading). ASTM Standards, United States.
ASTM D1635-00, 2000. Standard Test Method for Flexural Strength of Soil-cement Using Simple Beam with Third Point Loading. D1635–00. ASTM Standards, United States.
Ates, A., 2016. Mechanical properties of sandy soils reinforced with cement and randomly distributed glass fibers (GRC). Composites Part B 96, 295–304.
Ayeldeen, M., Kitazume, M., 2017. Using fiber and liquid polymer to improve the behaviour of cement stabilized soft clay. Geotext. Geomembranes 45, 592–602.
Chen, M., Shen, S.L., Arulrajah, A., Wu, H.N., Hou, D.W., Xu, Y.S., 2015. Laboratory evaluation on the effectiveness of polypropylene fibers on the strength of fiber reinforced and cement-stabilized Shanghai soft clay. Geotext. Geomembranes 43 (6), 515–523.
Cho, K., Cho, J.R., Chin, W.J., Kim, B.S., 2006. Bond-Slip model for coarse sand coated interface between FRP and concrete from optimization technique. Comput. Struct. 84 (7), 439–449.
Consoli, N.C., Zortea, F., Souza, M., Festugato, L., 2011a. Studies on the dosage of fiber-reinforced cemented soils. J. Mater. Civ. Eng. 23 (12), 1624–1632.
Consoli, N.C., Moraes, R.R., Festugato, L., 2011b. Split tensile strength of monofilament polypropylene fiber-reinforced cemented sandy soils. Geosynth. Int. 18 (2), 57–62.
Consoli, N.C., Corte, M.B., Festugato, L., 2012. Key parameters for tensile and compressive strength of fiber-reinforced soil-lime mixtures. Geosynth. Int. 19 (5), 409–414.
Consoli, N.C., Moraes, R.R., Festugato, L., 2013. Parameters controlling tensile and compressive strength of fiber-reinforced cemented soil. J. Mater. Civ. Eng. 25 (10), 1568–1573.
Correia, A.S.A., Oliveira, P.J.V., Custodio, D.G., 2015. Effect of polypropylene fibres on the compressive and tensile strength of a soft soil artificially stabilised with binders. Geotext. Geomembranes 43, 97–106.
Disfani, M.M., Arulrajah, A., Haghihi, H., Mohammadinia, A., Horpibulsuk, S., 2014. Flexural beam fatigue strength evaluation of crushed brick as a supplementary material in cement stabilized recycled concrete aggregates. Construct. Build. Mater. 68, 667–676.
Estabragh, A.R., Namdar, P., Javadi, A.A., 2012. Behavior of cement-stabilized clay reinforced with nylon fiber. Geosynth. Int. 19 (1), 85–92.
Festugato, L., Menger, E., Benezra, F., Kipper, E.A., Consoli, N.C., 2017. Fibre-reinforced cemented soils compressive and tensile strength assessment as a function of filament length. Geotext. Geomembranes 45, 77–82.
Festugato, L., Silva, A.P.d., Diambra, A., Consoli, N.C., Ibraim, E., 2018. Modelling tensile/compressive strength ratio of fibre reinforced cemented soils. Geotext. Geomembranes 46, 55–165.
Güllü, H., Fedakar, H.I., 2016. Use of factorial experimental approach and effect size on the CBR testing results for the usable dosages of wastewater sludge ash with coarse-grained material. Eur. J. Environ. Civ. En. http://dx.doi.org/10.1080/19648189.2016.1179678.
Hannawi, K., Bian, H., Prince-Agbodjan, W., Raghavan, B., 2016. Effect of different types of fibers on the microstructure and the mechanical behavior of ultra-high performance fiber-reinforced concretes. Composites Part B 86, 214–220.
Hejazi, S.M., Sheikhzadeh, M., Abtahi, S.M., Zadhoush, A., 2012. A simple review of soil reinforcement by using natural and synthetic fibers. Construct. Build. Mater. 30, 100–116.
Horpibulsuk, S., Phetchuay, C., Chinkulkijniwat, A., Cholaphatsorn, A., 2013. Strength development in silty clay stabilized with calcium carbide residue and fly ash. Soils Found. 53 (4), 477–486.
Jamsawang, P., Voottipruex, P., Horpibulsuk, S., 2015a. Flexural strength characteristics of compacted cement-polypropylene fiber. J. Mater. Civ. Eng. 27 (9) 04014243.
Jamsawang, P., Voottipruex, P., Jongpradist, P., Bergado, D.T., 2015b. Parameters affecting the lateral movements of compound deep cement mixing walls by numerical simulations and parametric analyses. Acta Geotechnica 10, 797–812.
Jiang, N.J., Du, Y.J., Liu, S.Y., Wei, M.L., Horpibulsuk, S., Arulrajah, A., 2016. Multi-scale laboratory evaluation of the physical, mechanical, and microstructural properties of soft highway subgrade soil stabilized with calcium carbide residue. Can. Geotech. J. 53, 373–383.
Kumar, A., Gupta, D., 2016. Behavior of cement-stabilized fiber-reinforced pond ash, rice husk ash–soil mixtures. Geotext. Geomembranes 44, 466–474.
Kim, B., Kim, Y., 2017. Strength characteristics of cemented sand–bentonite mixtures with fiber and metakaolin additions. Mar. Georesour. Geotechnol. 53 (3), 414–425.
Kim, D.J., Park, S.H., Ryu, G.S., Koh, K.T., 2011. Comparative flexural behavior of hybrid ultra high performance fiber reinforced concrete with different macro fibers. Construct. Build. Mater. 25, 4144–4155.
Ma, B., Si, W., Li, N., Wang, H.N., Liu, R.W., Adhikari, S., 2014. Loading capacity strengthening to cement-stabilised crushed gravel using reinforced wire mesh. Road. Mater. Pavement 15 (3), 733–745.
Mohammadinia, A., Arulrajah, A., Sanjayan, J., Disfani, M., Bo, M., Darmawan, S., 2015. Laboratory evaluation of the use of cement-treated construction and demolition materials in pavement base and subbase applications. J. Mater. Civ. Eng. 27 (6) 04014186.
Nematollahi, B., Sanjayan, J., Shaikh, F.U.A., 2014. Comparative deflection hardening behavior of short fiber reinforced geopolymer composites. Construct. Build. Mater. 70, 54–64.
Olgun, M., 2013. Effects of polypropylene fiber inclusion on the strength and volume change characteristics of cement-fly ash stabilized clay soil. Geosynth. Int. 20 (4), 263–275.
Oliveira, P.J.V., Correia, A.A.S., Teles, J.M.N.P.C., Custódio, D.G., 2016. Effect of fibre type on the compressive and tensile strength of a soft soil chemically stabilised. Geosynth. Int. 23 (3), 171–182.
Onyejekwe, S., Ghataora, G., 2014. Effect of fiber inclusions on flexural strength of soils treated with nontraditional additives. J. Mater. Civ. Eng. 26 (8) 04014039.
Plé, O., Manicacci, A., Gourc, J.P., Camp, S., 2012. Flexural behaviour of a clay layer: experimental and numerical study. Can. Geotech. J. 49 485–393.
Phummiphan, I., Horpibulsuk, S., Sukmak, P., Chinkulkijniwat, A., Arulrajah, A., Shen, S.L., 2016. Stabilisation of marginal lateritic soil using high calcium fly ash-based geopolymer. Road. Mater. Pavement 17 (4). https://doi.org/10.1080/14680629.2015.1132632.
Sarir, P., Shen, S.L., Arulrajah, A., Horpibulsuk, S., 2016. Concrete wedge and coarse sand coating shear connection system in GFRP concrete composite deck. Constr. Build. 114, 650–655.
Simoes, T., Octavio, C., Valença, J., Costa, H., Dias-da-Costa, D., Júlio, E., 2017. Influence of concrete strength and steel fibre geometry on the fibre/matrix interface. Composites Part B 122, 56–164.
Sukontasukkul, P., Pomchiengpin, W., 2010. Post-crack (or post-peak) flexural response and toughness of fiber reinforced concrete after exposure to high temperature. Construct. Build. Mater. 24 (10), 1967–1974.
Sukontasukkul, P., Jamsawang, P., 2012. Use of steel and polypropylene fibers to improve flexural performance of deep soil–cement column. Construct. Build. Mater. 29, 201–205.
Tang, C.S., Shi, B., Zhao, L.Z., 2010. Interfacial shear strength of fiber reinforced soil. Geotext. Geomembranes 28, 54–62.
Viswanadham, B.V.S., Jha, B.K., Pawar, S.N., 2010. Influence of geofibers on the flexural behavior of compacted soil beams. Geosynth. Int. 17 (2), 86–99.
Yi, X.W., Ma, G.W., Fourie, A., 2015. Compressive behaviour of fibre-reinforced cemented paste backfill. Geotext. Geomembranes 43, 207–215.

Computers and Geotechnics 97 (2018) 27–41

Contents lists available at ScienceDirect

Computers and Geotechnics

journal homepage: www.elsevier.com/locate/compgeo

Research Paper

Dependence of ultimate bearing capacity and failure behavior of T-shaped deep cement mixing piles on enlarged cap shape and pile strength

Chana Phutthananon[a], Pornkasem Jongpradist[a,*], Phatharaphong Yensri[a], Pitthaya Jamsawang[b]

[a] Department of Civil Engineering, Faculty of Engineering, King Mongkut's University of Technology Thonburi, Thailand
[b] Department of Civil Engineering, King Mongkut's University of Technology North Bangkok, Thailand

ARTICLE INFO

Keywords:
Bearing capacity
Failure pattern
Shape factor
Finite element analysis
Small-scale physical model test
T-shaped deep cement mixing pile

ABSTRACT

A numerical investigation of the ultimate pile capacity (Q_{ult}) and failure behavior of T-shape deep cement mixing (TDM) piles is conducted under equivalent volume. Physical model tests are conducted to verify the numerical findings. The results reveal that both the shape of the enlarged pile cap and pile strength play key roles. Sensitivity analyses indicate that the effects of cap shape and pile strength on the complex load carrying behavior of TDM piles are attributable to changes in failure mode, which depend on the mobilized skin friction and bearing of both the cap and pile body.

1. Introduction

Soft ground improvement with deep cement mixing (DCM) piles is a soil stabilization technique that has been used to enhance the performance of on-ground and underground facilities, such as road embankments (e.g., [1–9]), drainage canals (e.g., [10,11]) and deep excavations (e.g., [12–14]). Since the first introduction of DCM piles in Sweden and Japan in the mid-1970s, this technique has been widely used in several countries where the soft ground layer is particularly thick [15]. The primary objectives of DCM piles include improving bearing capacity, minimizing lateral movement, reducing total and differential settlement, and increasing slope stability, as confirmed by many construction cases (e.g., [3,5,9]). Past experience also suggests that using DCM piles to improve soft ground areas reduces construction time and costs.

Generally, DCM piles are formed with the same cross-sectional area throughout their length (hereafter called a conventional DCM pile, see Fig. 1a) to transfer the applied load from the top part of the pile through the surrounding soil to the soil layer below the pile tip. Under an external load in the vertical direction, such as the foundation of a road or structure, the mobilized stress becomes largest at the pile head and then gradually decreases with depth. Thus, the highest compressive stress occurs at the top part of the pile, resulting in a failure pattern that is often dominated by pile head failure if the strength of the DCM pile is insufficient. This failure pattern has been confirmed by field test results in [16], in which more than half of tested conventional DCM piles failed due to pile head failure. When the pile head failure pattern is unfavorable, the cement content has been increased to enhance the strength of the conventional DCM pile. However, this is often an expensive strategy because the deeper pile does not require high strength. Moreover, many researchers (e.g., [17–19]) have revealed that the higher cement content does not economically improve the strength of cement-admixed clay. To solve the above-mentioned problem, new innovations of DCM pile techniques have been introduced, including stiffened and T-shaped DCM piles. A stiffened DCM (SDCM) pile is a composite DCM pile consisting of a DCM socket and stiffened core to reinforce the pile at shallow depths (or pile head) as shown in Fig. 1b. The T-shaped DCM (TDM) pile was first proposed in China [20,21]. The notable feature of TDM piles is that the diameter of the pile at shallow depth (surface pile diameter) is larger than that at greater depth (pile body diameter), resulting in a cross-sectional view of the TDM pile that resembles the letter "T" (see Fig. 1c).

A number of studies have investigated the efficacy of SDCM piles and their mechanical behavior, including full-scale field tests (e.g., [7,8]), numerical analyses (e.g., [7,8,22]) and physical model tests (e.g., [22]). The studies revealed that SDCM piles can resist higher loads than conventional DCM piles of the same size. Failure at the pile head under axial loading could also be mitigated. Based on these studies, the understanding of the impact of a stiffened core in associated with the strength of the DCM socket on ultimate pile capacity and failure behavior has been developed and continually updated. By contrast, studies on the efficacy and key influencing factors of the behavior of TDM piles are rather limited, probably because this innovation is still relatively new. Based on the results from full-scale field tests and small-

* Corresponding author at: Civil Engineering Department, Faculty of Engineering, King Mongkot's University of Technology Thonburi, 126 Pracha Uthit, Bang Mod, Thung Khru, Bangkok 10140, Thailand.
E-mail address: Pornkasem.jon@kmutt.ac.th (P. Jongpradist).

https://doi.org/10.1016/j.compgeo.2017.12.013
Received 15 November 2017; Received in revised form 15 December 2017; Accepted 26 December 2017

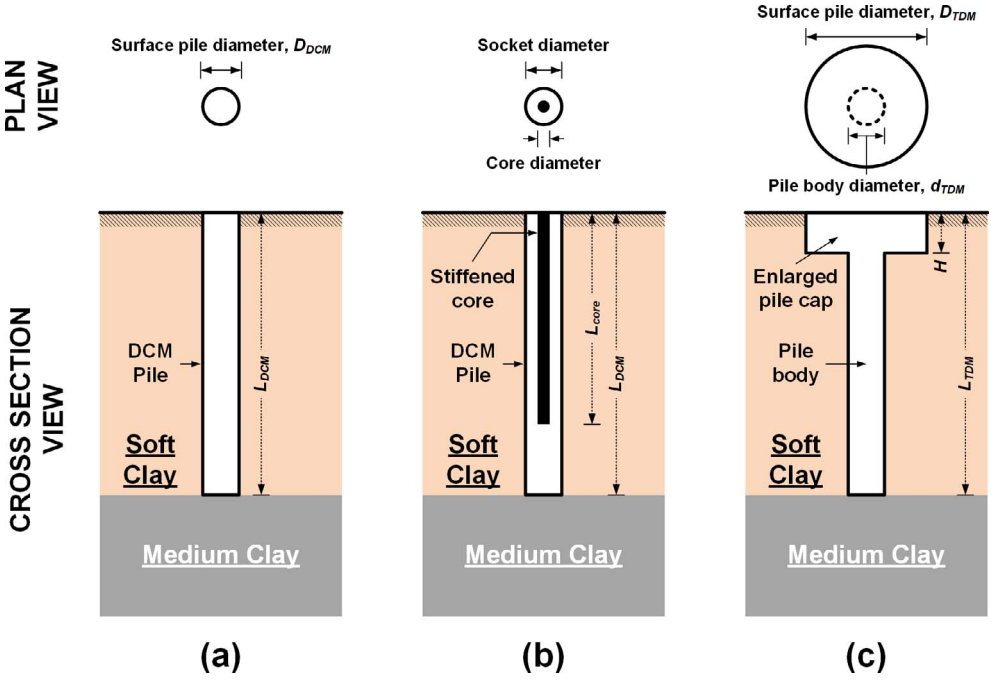

Fig. 1. Schematic of DCM piles: (a) conventional DCM pile; (b) SDCM pile and (c) TDM pile.

scale physical model tests [23,24], enlarging the pile cap (from a DCM pile to a TDM pile), the bearing capacity can be increased, and settlement can be reduced. Physical model tests also revealed that, for a TDM pile, failure occurs at the pile body immediately below the enlarged pile cap. This failure mode implies an association with the bearing capacity of the TDM pile. Under the embankment loading condition as the foundation in physical model tests [25], the enlarged pile cap of a TDM pile provided a higher pile efficacy (defined as the ratio of load carrying at the pile to the entire applied load on the embankment) than a conventional DCM pile. Moreover, TDM piles are more effective in reducing differential settlement between the surrounding soil and the pile. All of these studies indicate the superior performance of TDM piles over conventional DCM piles with the same pile body and strength. However, each of these previous studies focused on an increase of either the diameter or length of enlarged pile cap without consideration on the pile volume. Enlarging the pile cap increases construction costs due to the additional volume of improvement by cement. Consequently, the evaluation of the performance and effectiveness of a TDM pile should be compared with those of a conventional DCM pile on an equal volume basis. Based on the mechanism established in previous studies, it is possible to reduce the size of the pile body while introducing an enlarged pile cap. Moreover, it is assumed that the size of the enlarged pile cap will have an effect on the complex load transfer mechanism of the TDM pile, which, in turn, affects the bearing capacity and failure behavior.

The goal of this work is to study the effect of the size of the enlarged pile cap and pile strength on the behavior of TDM piles in terms of ultimate bearing capacity and failure pattern under controlled pile volume. Numerical analyses of the selected cases of piles under axial loading are preliminarily performed. The total volumes of piles with various shapes and strengths are controlled. A parameter “shape factor” is introduced based on the condition of the control pile volume to assist the interpretation of the results. Small-scale physical model tests under conditions of shape factor equivalent to those in the preliminary investigation are conducted to validate the findings. Finally, a numerical sensitivity study of TDM piles is performed by varying the dimensions of the enlarged pile cap and the strength of the pile with a single value of pile volume to observe changes in ultimate bearing capacity and failure pattern. The complex interaction between the shape of the enlarged pile cap and the strength of the pile is revealed and discussed. Note that deformation behavior is not discussed in the present work.

2. Case history and numerical modelling

This paper offers a series of two-Dimensional (2D) finite element analyses to investigate the ultimate bearing capacity and failure pattern of DCM and TDM piles under axial compression load. First, the numerical method and parameters used were validated by comparing the simulated results with the field pile load test data [26] in term of load-settlement curve at the head of DCM pile. Then, they were adopted to analyze the ultimate bearing capacity and failure pattern of DCM and TDM piles in the sections of preliminary investigation and sensitivity study.

2.1. Case history

Over the past 10 years, TDM piles have been proposed and constructed to support highway embankments in China [20,21]. Because this technology is relatively new, its application and study have not yet spread to other countries. As a result, information on field TDM pile load tests is scarce. In this study, a case study of a previous full scale axial load test of a conventional DCM pile [26] was chosen. The test site was located at the campus of Asian Institute of Technology (AIT) in the Lower Central Plain of Thailand. The field data were used to verify the analysis method of the study. The subsoil profile and some engineering properties of the test site are summarized in Fig. 2. The soil profile at this site comprises a 1.5-m-thick weathered crust underlain by soft clay with a thickness of approximately 5.0–6.5 m. The undrained shear strength obtained from field vane tests of the soft clay was 16–17 kPa. A medium clay with an undrained shear strength greater than 30 kPa was found below the soft clay. The groundwater level was approximately 1.5 m below the ground surface. The conventional DCM pile was constructed in situ by the wet jet mixing method with a cement content of 150 kg/m^3 of soil and a jet pressure of 22 MPa. The length and surface pile diameter of the tested DCM pile were 7.0 m and 0.6 m, respectively. The average value of unconfined compressive strength was approximately 900 kPa. The top of the DCM pile was situated 1.0 m below the ground surface.

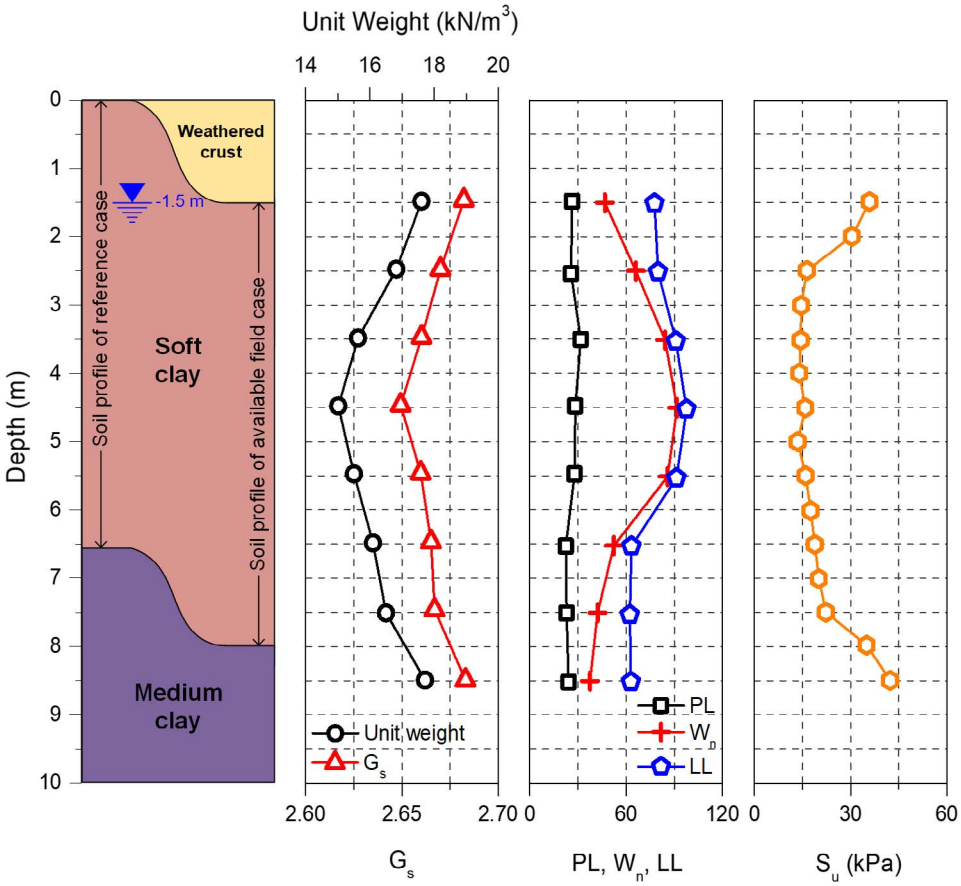

Fig. 2. Subsoil profile of case history and reference case.

2.2. Numerical modelling

2.2.1. Finite element mesh and boundary conditions

A series of 2D finite element (FE) simulations were performed to investigate the mechanical behavior of the conventional DCM and TDM piles under axial compression loading, including the ultimate bearing capacity (Q_{ult}) and failure pattern. The continuum FE software PLAXIS 2D was used. Fig. 3 shows an example of the FE mesh used in the axisymmetric analysis, which consisted of a 25.0-m-deep and 10.0-m-wide domain. The boundary condition for the FE mesh was that both side boundaries were prevented from moving in the horizontal direction, whereas the bottom boundary was prevented from moving in both the horizontal and vertical directions. These conditions were used in all pile load test simulations. The conventional DCM pile, TDM pile and soils were modelled using fifteen-node hybrid triangle elements. For the initial distribution of horizontal and vertical stresses, the soil unit weight and the coefficient of earth pressure were used to calculate the initial soil stress state. The initial pore water pressure was assumed to be hydrostatic. The simulation was divided into five main steps: (i) generation of the stress field and hydrostatic pore water pressure, (ii) excavation of a 1-m-deep pit from the ground surface, (iii) installation of conventional DCM or TDM piles, (iv) installation of a rigid steel plate at the pile top with the same diameter to accommodate the distribution of stresses evenly, and (v) applying an axial load on top of pile the in 10-kN increments until failure occurred. The Q_{ult} values of the DCM and TDM piles were determined from the load-settlement curve using the classic slope tangent method in double logarithmic scale following De Beer [27]. The settlement of the pile was measured at the center of the pile head surface. The weathered crust layer was replaced by a soft clay layer in all preliminary and sensitivity analysis cases to avoid complex interactions between the crust and the enlarged pile cap. Due to the limited depth of the testing box in the physical model tests (see details in section 4), the thickness of the soft clay layer was also decreased from 8.0 m in the available field case to 6.6 m in the numerical investigation to maintain a scaling factor of 13 for the purposes of comparison. Consequently, the length of the piles in the preliminary investigation (section 3) and sensitivity analyses (section 5) was 5.6 m.

2.2.2. Constitutive model and model parameters

In this study, a Mohr-Coulomb (MC) model and a Hardening Soil (HS) model [28] coded in PLAXIS program were applied to the FE analysis. The effective stress analysis under undrained behavior was conducted to simulate the quick pile load tests in the field. The undrained function of material type, namely Undrained, was specified in PLAXIS program in which the effective stress parameters for both soil modulus and shear strength were assigned.

The behavior of the DCM and TDM piles was modelled by the MC model, whereas the HS model was applied to model the behavior of the soft clay, medium clay and stiff clay. For the rigid steel plate, a linear elastic (LE) model was used. The properties of the materials in the numerical analyses are listed in Table 1. The values of the parameters considered in this study are all effective values. For the soil parameters (HS model) of Bangkok subsoil, the parameter sets were adopted from the work of Rukdeechuai et al. [29]. The HS model parameters were mainly calibrated from the triaxial and oedometer testing results of soil samples taken from the Asian Institute of Technology (AIT) together with the field measurement conducted by Prust et al. [30]. These parameter sets have been used to analyze various geotechnical works in Bangkok subsoil (e.g., [29,31,32]). Note that the elastic moduli of the DCM and TDM piles were determined from the simple correlation $E_{SCP} = 113q_u$, where E_{SCP} is the modulus of elasticity in terms of secant ($50\% of q_u$) and q_u is the unconfined compressive strength of the soil-cement pile. This correlation falls within the range of $20q_u$–$360q_u$ for cement-treated clays reported by Voottipruex et al. [8] and Jamsawang

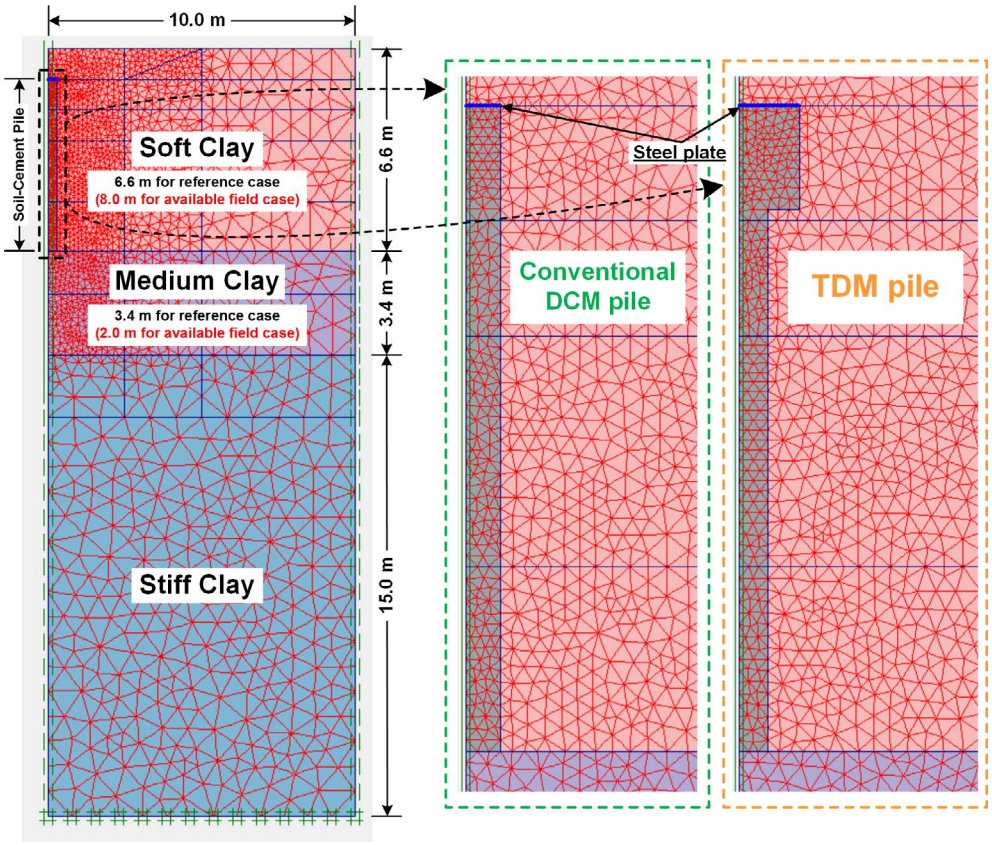

Fig. 3. Geometry, finite element mesh and boundary conditions of the considered problem.

et al. [33] and closes to those used in several previous publications (e.g., [3,34,35]). After converting to effective parameter, the correlation becomes $E'_{SCP} = 100q_u$, which corresponds to previous work of Wonglert and Jongpradist [22].

2.2.3. Verification with field measurement

To verify the analysis method used in this work, the analysis results were compared with the measurement data for a full-scale conventional DCM pile load test [26]. The axial load-settlement curves for the computed and measured results are compared in Fig. 4. The load-settlement curve of the conventional DCM pile from the FE model matches well with the field test results. Therefore, the analysis method and sets of parameters used were considered appropriate for further numerical investigation.

3. Preliminary investigation

In the preliminary investigation, 2D FE axis-symmetry analysis was conducted to examine the impact of key influencing parameters on the Q_{ult} and failure behavior of the conventional DCM and TDM piles. The

Table 1
Materials models, and parameters used in this study.

	Unit	Weathered crust	Soft clay	Medium clay	Stiff clay	DCM pile[a]	Rigid steel plate
Model		MCM	HSM	HSM	HSM	MCM	LE
Material behavior		D	U	U	U	U	Elastic modulus = 10^{12} kPa and Poisson's ratio = 0
Elastic modulus, E'	kPa	5000	–	–	–	90,000	
Secant stiffness, E_{50}^{ref}	kPa	–	5000	20,000	60,000	–	
Tangential stiffness, E_{oed}^{ref}	kPa	–	5000	20,000	60,000	–	
Unloading and reloading stiffness, E_{ur}^{ref}	kPa	–	15,000	100,000	180,000	–	
Poisson's ratio for unloading–reloading, ν_{ur}	kPa	0.25 (=ν')	0.20	0.20	0.20	0.33 (=ν')	
Power of the stress level dependency of the stiffness, m	(–)	–	1	1	1	–	
Coefficient of earth pressure at rest (NC state), K_0^{NC}	(–)	0.600	0.625	0.625	0.625	0.577	
Unit weight, γ	(kN/m^3)	17	15	15	18	15	
Effective cohesion, c'	(kPa)	8	6	10	18	423	
Effective friction angle, ϕ'	(degree)	22	22	22	22	25	
Angle of dilatancy, ψ	(–)	0	0	0	0	0	
Failure ratio, R_f	(–)	–	0.9	0.9	0.9	–	
Over consolidation ratio, OCR	(–)	–	1.1	2.0	2.5	–	
Reference stress, p^{ref}	(kPa)	–	100	65	95	–	

[a] Case history, Material behavior; D = drained, U = undrained.

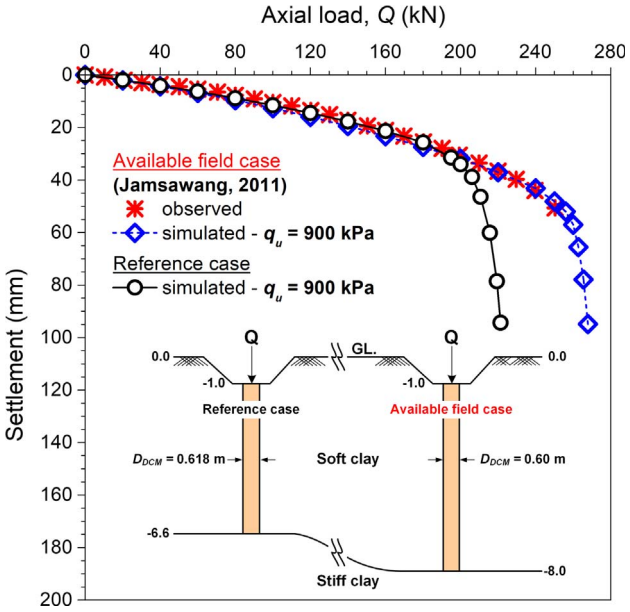

Fig. 4. Comparisons of observed (available field case) and computed (available field and reference cases) axial compression load-settlement curves of conventional DCM piles.

key parameters studied were the surface pile diameter of the conventional DCM piles (D_{DCM}) and TDM piles (D_{TDM}) and the strength (q_u) of the piles. The pile lengths, L_{DCM} and L_{TDM}, and pile body diameter (d_{TDM}) were fixed at 5.6 m and 0.5 m, respectively, throughout the study. The thickness of the enlarged pile cap (H) was varied following D_{TDM} under the condition of pile volume control.

3.1. Effect of surface diameter and strength of the conventional DCM pile on the load-settlement curve compared to the reference case

To provide information for comparison with the TDM piles (in the next subsection), analyses with various values of D_{DCM} and q_u were performed. The three values of D_{DCM} were 0.50 m, 0.618 m (reference case), and 0.70 m. The load-settlement curves are shown in Fig. 5. The results imply that Q_{ult} increases as D_{DCM} increases at the same pile

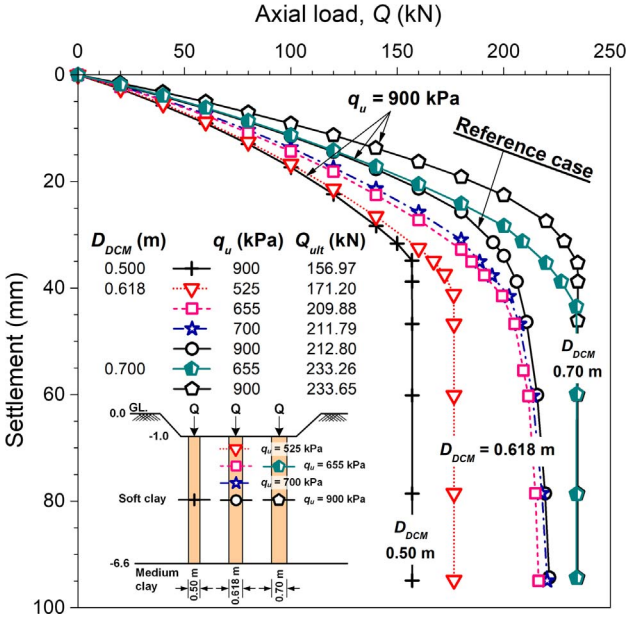

Fig. 5. Effects of pile diameter and strength on the load-settlement curves of conventional DCM piles.

strength, as expected. Moreover, at the same load level, an increase in D_{DCM} significantly leads to decreasing settlement. This effect is caused by the side resistance along the shaft of the pile and tip resistance from the soil below the pile tip. The pile with a higher value of D_{DCM} possesses a larger area of the pile shaft and cross-sectional area of the pile tip, with higher ultimate bearing capacities. To investigate the failure patterns of these piles, the occurrence of plastic points (Mohr-Coulomb points, MCPs in the PLAXIS program) is observed from the simulation results at the applied load of Q_{ult}, as depicted in Fig. 6. MCPs of the DCM piles (D_{DCM} = 0.50,0.618, and 0.70m with q_u of 900 kPa) were found only in the surrounding soil, indicating a soil failure pattern (see Fig. 6a, e and g). These results clearly indicate that the surface pile diameter of the conventional DCM pile plays an important role in Q_{ult} and settlement.

The results of further investigations of the effect of q_u on Q_{ult} are presented in Fig. 5. Piles with D_{DCM} of 0.618 m and varying q_u, including 900 kPa (reference case), 700 kPa, 655 kPa and 525 kPa, were chosen for investigation. The modulus of elasticity was also adjusted to correspond to the correlation described in Section 2.2.2. The Q_{ult} of the conventional DCM pile increased considerably (171.20–209.88 kN) as q_u increased from 525 kPa to 655 kPa. For the case of q_u = 525 kPa, MCPs occurred at the top part of the pile and propagated to the surrounding soil on the periphery of the pile until a depth of 2.5 m below ground surface was reached (see Fig. 6b). Thereafter, the failure pattern was dominated by pile head failure. As q_u increased to 655 kPa, MCPs also propagated in the surrounding soil throughout the pile length (see Fig. 6c), eventually leading to pile head failure (many MCPs at the top part) together with a soil failure pattern. The number of MCPs at the top part of the pile for the case of q_u = 655 kPa was less than for a pile strength of 525 kPa. As q_u increased from 655 kPa to 700 kPa, Q_{ult} slightly increased to approximately 1.91 kN with the same failure pattern as in the case of q_u = 700 kPa. A larger number of MCPs mostly appeared at the soil below the pile tip (see Fig. 6d). Up to a q_u of 900 kPa, Q_{ult} exhibited insignificant development. Additionally, the failure pattern changed to perfect soil failure, with no MCPs occurring in the pile (see Fig. 6e). These results indicate that the q_u of 700 kPa is the optimum value of pile strength to produce the highest Q_{ult}. However, for the same load level, increasing the q_u over the optimum value reduces pile settlement (see Fig. 5). Therefore, it can be concluded that, for the case of q_u less than the optimum value, Q_{ult} is primarily dependent on q_u. By contrast, when q_u is larger than optimum value, Q_{ult} does not significantly develop. Nevertheless, using q_u higher than the optimum value can reduce pile settlement. Moreover, q_u is also a major parameter influencing the failure pattern of the conventional DCM pile. This conclusion was confirmed by the results for the conventional DCM pile, with D_{DCM} = 0.70 m at q_u of 655 and 900 kPa (see Fig. 5). In both piles, the failure pattern was governed by soil failure (see Fig. 6f and g). Moreover, the optimum value of pile strength is related to the surface diameter of the DCM pile and the soil condition.

3.2. Effect of an enlarged pile cap dimension and strength of the TDM pile on the load-settlement curve compared to the conventional DCM pile under controlled volume

The effects of the transformation to a TDM pile and of the enlarged pile cap dimension on the load-settlement curves are numerically investigated in this section. TDM piles with a volume equivalent to that of the conventional DCM pile with a diameter of 0.618 m and a length of 5.6 m was considered. The pile body diameter of 0.5 m was fixed while the enlarged cap size (surface diameter, D_{TDM} and thickness, H) was varied within the same pile volume. Two values of q_u of the pile (525 and 655 kPa) are considered. D_{TDM} values of 0.73, 0.988, 1.17 and 1.32 m with corresponding H values of 2.62, 1.04, 0.65 and 0.50 m, respectively, are considered in the analyses. The simulated load-settlement curves are illustrated in Fig. 7. The values of calculated Q_{ult} are also reported in the figure. For piles with q_u of 525 kPa (Fig. 7a), the

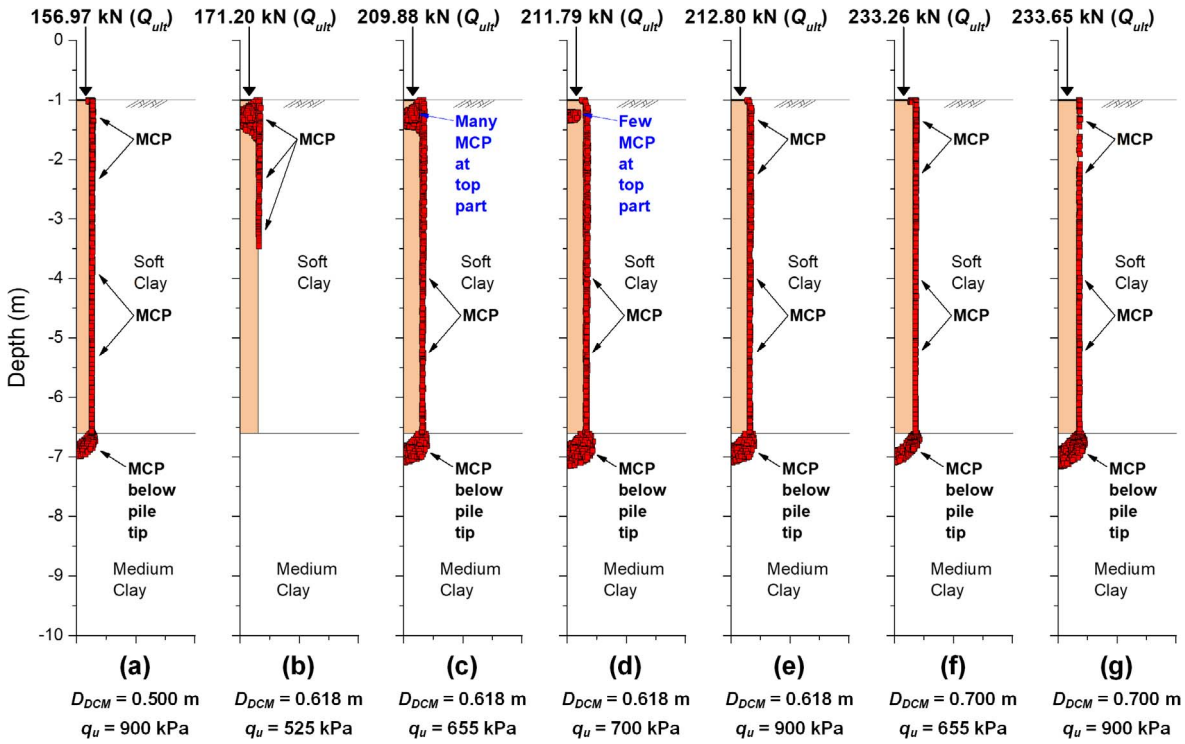

Fig. 6. Failure patterns of conventional DCM piles with various pile diameters and strengths.

results clearly indicate that the change in the pile shape from conventional DCM (D_{DCM} = 0.618 m) to TDM (D_{TDM} up to 1.32 m) leads to an increase in Q_{ult} and reduction of pile settlement at the same load level. Note that Q_{ult} decreases with increasing D_{TDM} from 0.73 to 0.988 m before increasing again when D_{TDM} is 1.17 m. However, Q_{ult} is still greater for D_{TDM} = 0.988 m than for D_{DCM} = 0.618 m.

A dissimilar result was observed for the piles with a q_u of 655 kPa, as shown in Fig. 7b. The values of Q_{ult} slightly decreased as the pile shape changed from conventional DCM to TDM with D_{TDM} = 0.730 and 0.988 m. As D_{TDM} increased to 1.17 m, Q_{ult} increased. Additional insights can be obtained by comparing the results for a pair of selected cases, as shown in Fig. 7c. Q_{ult} of the case for the TDM pile with D_{TDM} of 1.17 m and q_u of 655 kPa is nearly identical to that for the DCM pile of 0.618 m (same pile volume) and q_u of 900 kPa (upper subfigure). These results indicate the potential to reduce the pile strength (i.e., the cement content) while enlarging the pile cap to achieve the same pile capacity. In the lower subfigure, at the same pile strength (655 kPa in this case), Q_{ult} of the TDM pile with D_{TDM} of 1.32 m is almost identical to that of the 0.700-m-diameter DCM pile (larger pile volume). This result indicates the potential to reduce the pile volume while enlarging the pile cap to achieve the same pile capacity. These results confirm the benefits of using TDM piles to reduce construction costs.

The above observations imply that the change from a conventional DCM pile to a TDM pile can offer benefits by reducing either the pile volume or strength for a target pile capacity. However, the effectiveness of the change from a conventional DCM pile to a TDM pile depends on the design of an appropriate shape. A better understanding of the load carrying behavior of TDM piles is necessary. Moreover, both the shape of the pile cap and q_u play important roles in this load carrying behavior. To accommodate the representation of the results regarding the enlargement of pile cap shape, an empirical "shape factor (α_s)" taking the geometry of the TDM pile into account, is hereafter used. Based on the fact that, with continually enlarging the pile cap, the surface diameter and skin area of the TDM piles become larger and smaller, respectively, compared to those of the DCM pile at the same volume. The ratio of bearing area of TDM pile to DCM pile over the ratio of shaft area of TDM pile to DCM pile as shown in Eq. (1) is thus appropriate.

$$\alpha_s = \frac{D_{TDM}^2/D_{DCM}^2}{[(D_{TDM}-d_{TDM})H + d_{TDM}L_{TDM}]/D_{DCM}L_{DCM}} \quad (1)$$

Under a controlled volume and constant pile body diameter, a larger value of α_s indicates a larger but thinner pile cap. The value of α_s for a conventional DCM pile is equal to 1.0. Note that the α_s in the present form is for a controlled volume and constant pile body diameter, further development may be necessary if it will be applied for other conditions. The Q_{ult} values from Fig. 7a and b were plotted against α_s, as shown in Fig. 8, confirming the significant effects of both the shape of the enlarged pile cap and q_u on pile capacity. The transformation to a TDM pile with a small (but thick) cap can either increase or decrease Q_{ult} compared to the originally considered DCM depending on the pile strength.

The failure patterns of the piles were further investigated to obtain insights on the load carrying behavior in association with the failure behavior. The developed MCPs at the applied load of Q_{ult} of piles with q_u of 525 and 655 kPa are illustrated in Fig. 9a–d and e–h, respectively. At q_u of 525 kPa, MCPs occur in the soil surrounding the pile for the entire length (see Fig. 9a), indicating a change in the failure pattern from pile head failure for the DCM pile (see Fig. 6b) to soil failure for the TDM pile with small cap diameter. For the other three TDM piles with larger but thinner pile caps, MCPs occurred at the pile body immediately beneath the enlarged pile cap, indicating "pile body failure" (see Fig. 9b–d). This failure pattern corresponds to that observed in field tests by Yi et al. [24]. As q_u increases to 655 kPa, the conventional DCM pile failed due to pile head failure simultaneous with soil failure (see Fig. 6c). Transformation to TDM piles resulted in a mode of soil failure in which MCPs occurred in the surrounding soil (see Fig. 9e–h). Moreover, the results for these TDM piles indicated that only a few MCPs occurred at the pile body, immediately below the enlarged pile cap. These results indicate that the failure pattern of conventional DCM piles and TDM piles depends greatly on cap shape and pile strength.

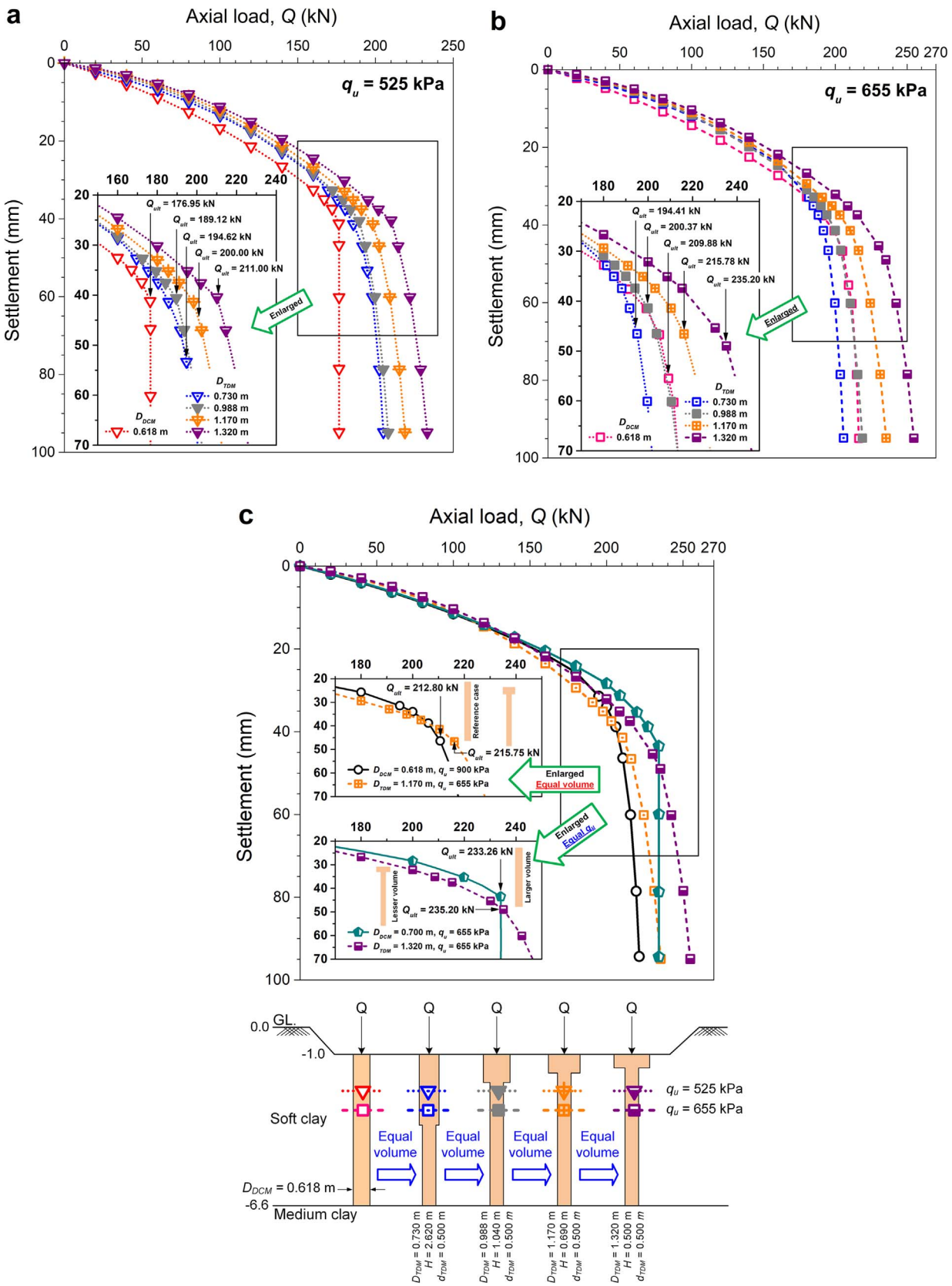

Fig. 7. Effect of an enlarged pile cap dimension of TDM piles with various strengths: (a) q_u = 525 kPa and (b) q_u = 655 kPa. (c) Comparisons of the effectiveness of conventional DCM and TDM piles with equivalent volume and strength.

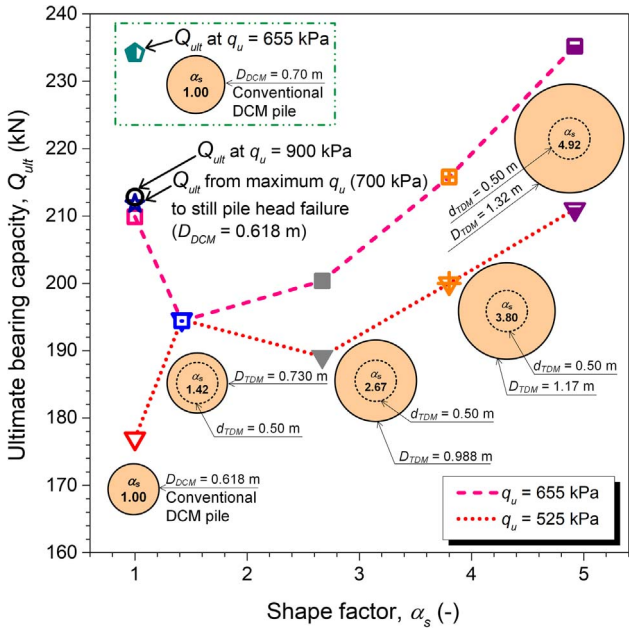

Fig. 8. Changes in ultimate bearing capacity due to the transformation of a DCM pile to a TDM pile under the controlled volume condition.

4. Physical model test

To verify the results of the preliminary investigation analysis with respect to changing Q_{ult} under different α_s, a series of small-scale physical model tests were conducted under equivalent pile volume. Three values of α_s from the preliminary investigation (1.00, 2.67 and 3.80) were selected to construct the model piles in the laboratory. These model piles were tested under vertical loading. A scaling factor of 13 was chosen for this small-scale physical model to reduce the dimensions of the prototype piles. The tests included a ground model and four models of soil-cement piles, as shown in Fig. 10. Two conventional DCM piles with different sizes and volumes and two TDM piles with different pile cap sizes but the same volume were prepared under the same target pile strength. The models of the conventional DCM piles had D_{DCM} = 38 mm and L_{DCM} of 430 mm for the P1 pile (equivalent to the 0.5-m @5.6-m-long DCM pile of the prototype) and D_{DCM} = 47 mm for the P2 pile (equivalent to the 0.6-m @5.6-m-long DCM pile of the prototype). The models of the TDM piles (P3, α_s = 2.72; P4, α_s = 3.88 piles) had the same volume and length as the P2 pile. The dimensions of the enlarged pile cap for the P3 pile were as follows: surface pile diameter of 76 mm; thickness of the enlarged cap of 80 mm; pile body diameter of 38 mm. A larger surface pile diameter of 90 mm and a thinner enlarged cap of 53 mm were used for the P4 pile. The ground model in this study included consolidated remolded soft clay and artificial medium clay. The soft clay was prepared by consolidating remolded soft Bangkok clay, which was mixed with water to achieve a total remolded water content of 100%, to attain the target water content of 70%. The artificial medium clay was prepared from a mixture of the remolded clay slurry and Ordinary Portland Cement type I at a cement content (defined as the ratio of the weight of cement to the weight of dry soil) of 5%. Before installation of the ground model, the inner sides of the rigid test box (1000 × 400 × 1800 mm, deep × wide × long, see Fig. 10) were smeared with grease to minimize the effect of friction. Then, the box was filled with the mixture of medium clay and cured for 7 days. Subsequently, the remolded clay slurry was poured on the artificial medium clay layer and consolidated with an applied surcharge load (5.2 kN/m^2) for 60 days. After completion of the consolidation process, the models of the soil-cement piles were constructed by using PVC tubes as the pile casing to create a hole for the cement-admixed clay paste. The remolded clay slurry was mixed

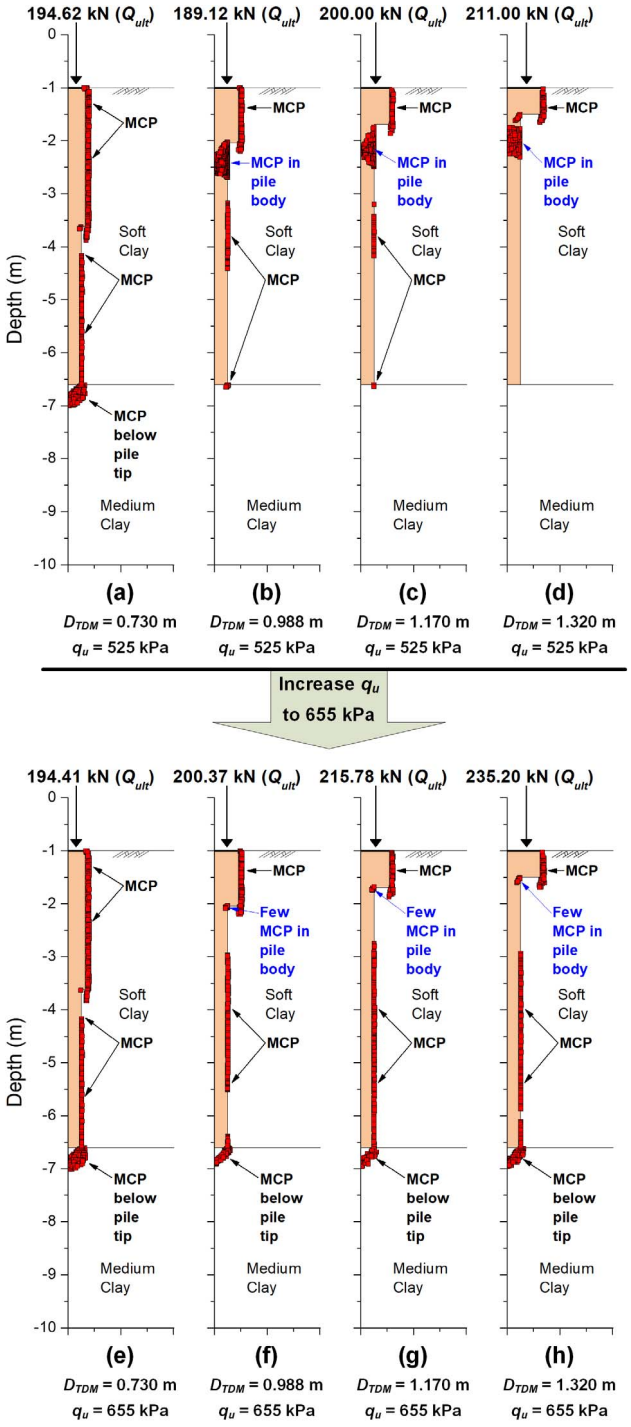

Fig. 9. Failure patterns of conventional DCM and TDM piles under controlled volume with strengths of 525 kPa and 655 kPa.

with a 35% content of Ordinary Portland Cement type I. The target unconfined compressive strength (q_u) of all of the soil-cement piles was 760 kPa. To ensure the target q_u of the soil-cement piles, on-site samples were collected and tested to confirm the strength with a curing time of 28 days. The method for the pile load test was the quick loading test in accordance with "ASTM-D1143". All tests were performed at an incremental axial compression load of 15 N (under the stress control condition) in each loading stage (every 5 min) with an axial penetration load rate of 5 N/min until failure. A pneumatic control system and a computer were used to regulate the pressure in four air cylinders, followed by transfer to a piston rod to press the modelled footing on the

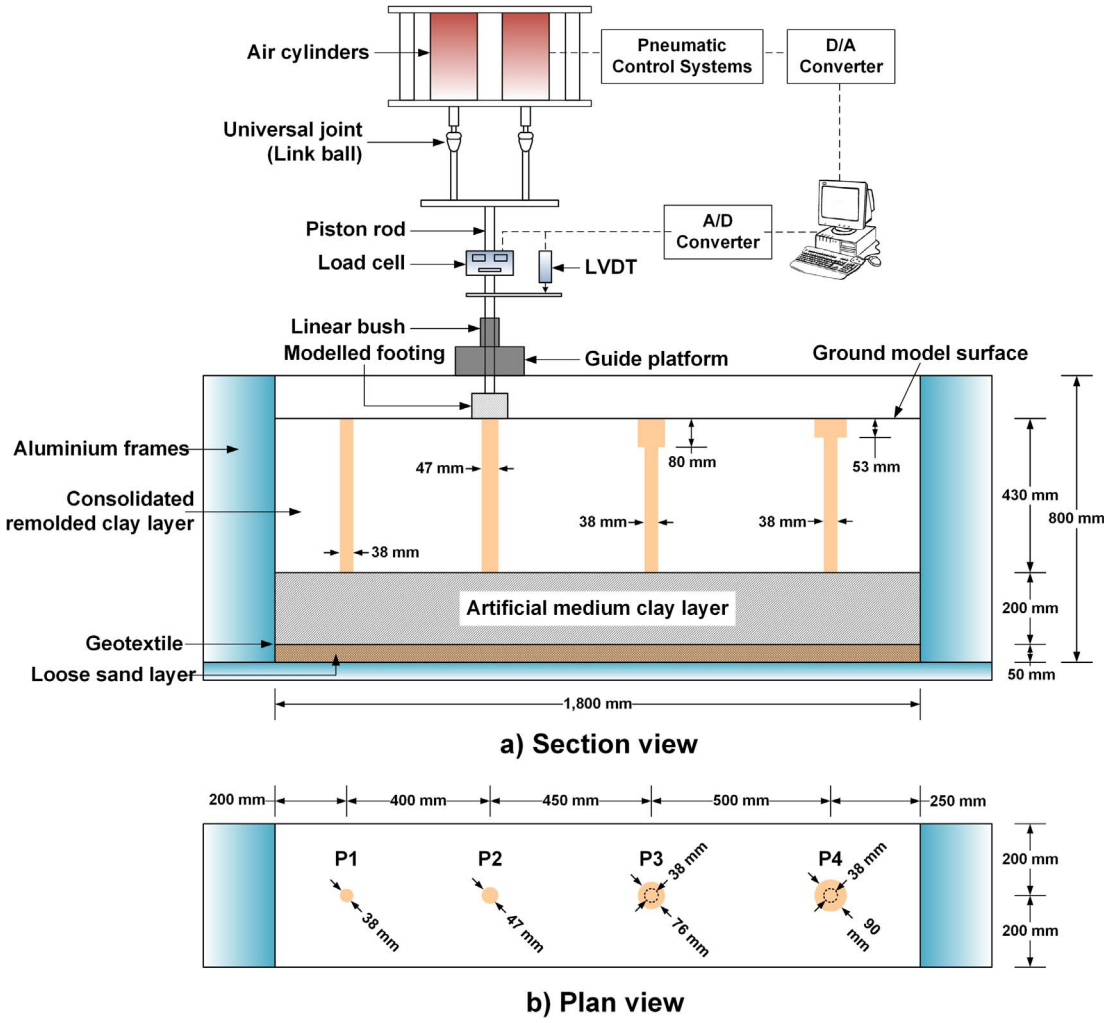

Fig. 10. Soil-cement piles and equipment configuration of the small-scale physical model tests.

pile surface. The value of the axial load was measured and recorded automatically by a load cell and the computer together with a data logger system. A Linear Variable Differential Transformer (LVDT) was used to measure the settlement of the soil-cement pile situated at the piston rod. The details of the equipment configuration are shown in Fig. 10.

After the loading test, the soil around the piles was meticulously excavated to observe the failure of the piles, as illustrated in Fig. 11. The head of the P2 pile (conventional DCM pile) was completely broken (see Fig. 11a). For the P3 pile (TDM pile), small cracks were observed approximately 60 mm below the enlarged pile cap (see Fig. 11b). A crack was observed at the pile body immediately below the enlarged pile cap for the P4 pile (TDM pile) (see Fig. 11c).

The load-settlement curves of the conventional DCM (P1-P2) and TDM (P3-P4) model piles from the laboratory loading tests are presented in Fig. 12. Q_{ult} of the P1 and P2 piles was 0.225 kN and 0.675 kN,

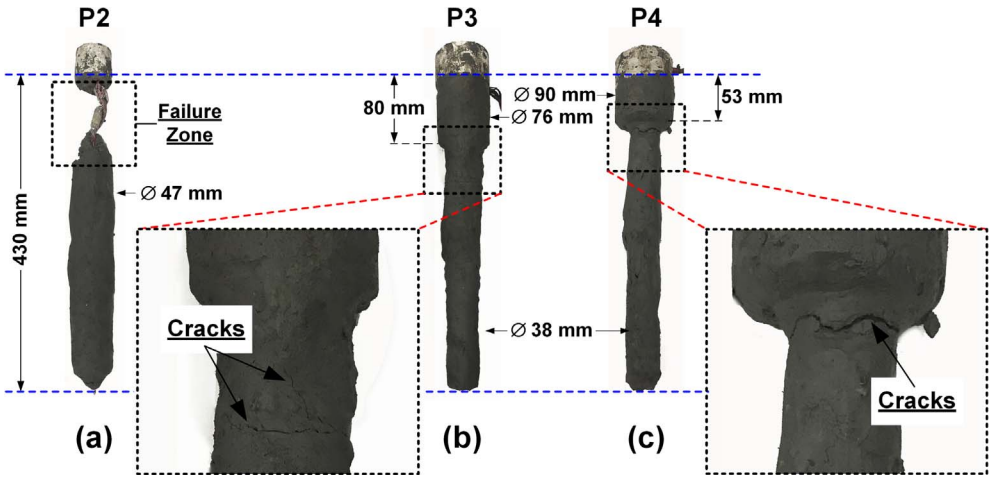

Fig. 11. Photographs showing the failure patterns of conventional DCM and TDM piles after testing.

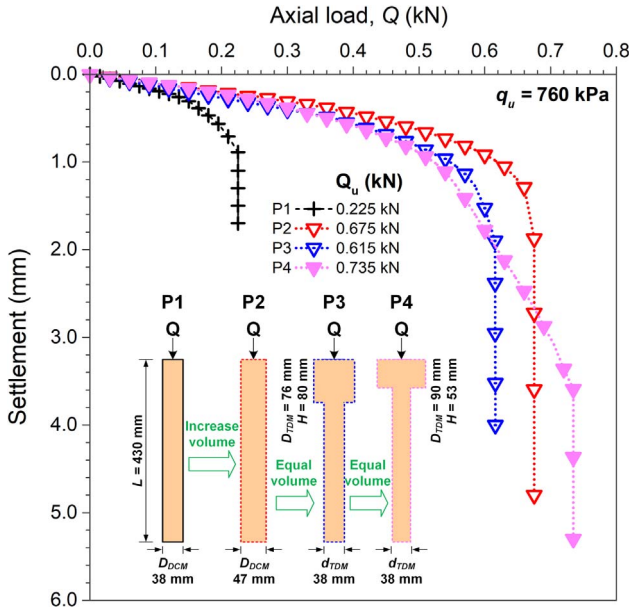

Fig. 12. Load-settlement curves of conventional DCM and TDM piles from the physical model tests.

respectively. Q_{ult} of the P2 pile was 3 times higher than that of the P1 pile because the P2 pile had a larger surface pile diameter, resulting in larger tip and side resistances. Additionally, the curve of the P2 pile shows smaller settlements than that of the P1 pile at the same load level. These observations are consistent with the results of the preliminary investigation in section 3.1. For the DCM and TDM piles with the same pile volume, the curves of the P2, P3 and P4 piles were nearly identical when the axial load was less than 0.3 kN. Once the axial load exceeded 0.3 kN, the curve of the P4 TDM pile indicated larger settlements than those of the other two piles. However, the P4 pile can sustain a larger maximum load, and the P3 TDM pile exhibited a smaller pile capacity than the P2 DCM pile. The results of the small-scale physical model tests are in good qualitative conformity with the results of the preliminary investigation in section 3.2. Enlarging the pile cap does not always guarantee an increase in the pile ultimate capacity. Q_{ult} is strongly influenced by the shape of the enlarged pile cap. Thus, the FE model provides confidence for the further investigations of the behavior of TDM piles in the next section. Not all properties can be maintained between the physical model tests and the numerical investigation in the previous section. However, these differences are unlikely to affect the qualitative conclusions obtained from the physical model tests and the numerical analyses.

5. Sensitivity study

To comprehensively investigate the effect of an enlarged pile cap shape of a TDM pile and pile strength on Q_{ult} and the failure pattern, numerical sensitivity analyses were performed. The pile volume in all cases was equal to the conventional DCM pile, with D_{DCM} = 0.618 m and L_{DCM} = 5.6 m. The pile with a q_u of 700 kPa (optimum value) was set as the baseline case to compare the effectiveness for Q_{ult}. The preliminary investigation indicated that the behavior of TDM piles is strongly influenced by the interaction between (1) the shape of the enlarged pile cap, which can be represented by the shape factor (α_s), and (2) the strength of the soil–cement pile (q_u). To analyze the influence of the shape of the cap, thirteen values (cases No. 2–14) of D_{TDM} and H were considered in ranges of 0.68–1.50 m and 0.37–3.49 m, respectively. d and L_{TDM} were maintained constant of 0.5 m and 5.6 m, respectively. Fig. 13 shows a schematic of the shapes of the DCM and TDM piles in this parametric study. q_u ranged from 320 to 700 kPa. All cases investigated are summarized in Table 2. The strength ratio (α_p) was used to denote the strength of the soil–cement pile in each case compared to the baseline case or optimum pile strength (700 kPa in this study) which provides the highest ultimate bearing capacity (depends on size of DCM pile) as described in ection 3.1. The α_p can be expressed in Eq. (2).

$$\alpha_p = \frac{q_u \text{ in each case}}{q_u \text{ of baseline case}} \tag{2}$$

(1) Failure patterns

The objective of a DCM pile is to transfer the applied load from the shallow depth to deeper strata that are stiffer than the top layer. When the pile possesses low strength (small values of α_p), the DCM pile fails due to pile head failure as depicted in Fig. 14a. When the conventional DCM pile is transformed to a TDM pile under controlled volume at small α_s (i.e., 1.221), the failure pattern of the TDM pile is the same as that of the DCM pile. However, the zone of MCPs between the surrounding soil and TDM pile extends to a deeper level than for the DCM pile, as shown in Fig. 14b. This difference implies that the load can be transferred to greater depth, and thus larger Q_{ult} can be obtained. When α_s is 1.418 (larger pile cap), a higher load can be transferred to a deeper level. In addition to the MCPs at the pile head and between the surrounding soil and pile, the concentration of MCPs at the pile body immediately beneath the cap can be observed, as illustrated in Fig. 14c. As α_s increases to 2.051 as shown in Fig. 14d, MCPs occur only in the pile body immediately beneath the cap and in the soil surrounding the cap, indicating that failure is dominated by pile body failure. In this case, Q_{ult} is lower than the case with α_s of 1.481 because the part of the abruptly smaller cross section from the cap to the pile body is located at insufficient depth. As a result, the stress suddenly increases at the connection between the cap and the pile body. These results again confirm that a proper design of the shape of the TDM pile is necessary. As α_s increases further to 4.029 and 6.425, as illustrated in Fig. 14e and f, respectively, larger Q_{ult} can be obtained. In both cases, failure is governed by pile body failure.

The failure patterns of the DCM and TDM piles represented by the occurrence of MCPs for piles with q_u of 595 kPa (α_p = 0.85) and various shapes (α_s values) are illustrated in Fig. 15. For the case of α_s = 1.00 (DCM pile), the MCPs were concentrated mainly at the top part of the pile and in the soil surrounding the top part of pile (see Fig. 15a). A pile head failure mode was observed. By comparison with Fig. 14a, the MCPs in the soil surrounding the pile in this case extend to greater depth. When α_s is increased to 1.221, the MCPs are not found within the pile but occur in soil surrounding along the pile shaft and below the pile tip (see Fig. 15b). The failure mode of this case is soil failure. Note that the Q_{ult} is nearly identical to that of the case with α_s = 1.00. Similar results are observed for the cases of α_s = 1.418 and 2.051 (see Fig. 15c and d). However, a few MCPs can also be observed at the pile body just beneath the cap. As α_s increases to 2.865, the MCPs mainly occur in the pile body immediately beneath the cap together and partly in the surrounding soil (see Fig. 15d), exhibiting a pile body-soil failure pattern. For α_s values up to 4.029 and 6.425 (see Fig. 15f–g), similar development of MCPs and failure patterns can be observed. However, the MCPs in the surrounding soil and the pile tip decrease or even vanish.

Fig. 16 shows the failure patterns of piles with high strength (α_p = 1.00) and various values of α_s. Since the pile strength in this case is the optimum value, the DCM pile fails by pile head failure together with soil failure as shown in Fig. 16a. When α_s increases to 1.221 (becoming a TDM pile), as shown in Fig. 16b, soil failure continues to occur. However, Q_{ult} becomes smaller than that of the DCM pile. This decrease is probably due to the decrease in the shaft and tip area of the lower part of pile, which are situated in stiffer and stronger soil. The larger upper part (enlarged cap) is too small to sufficiently absorb the applied

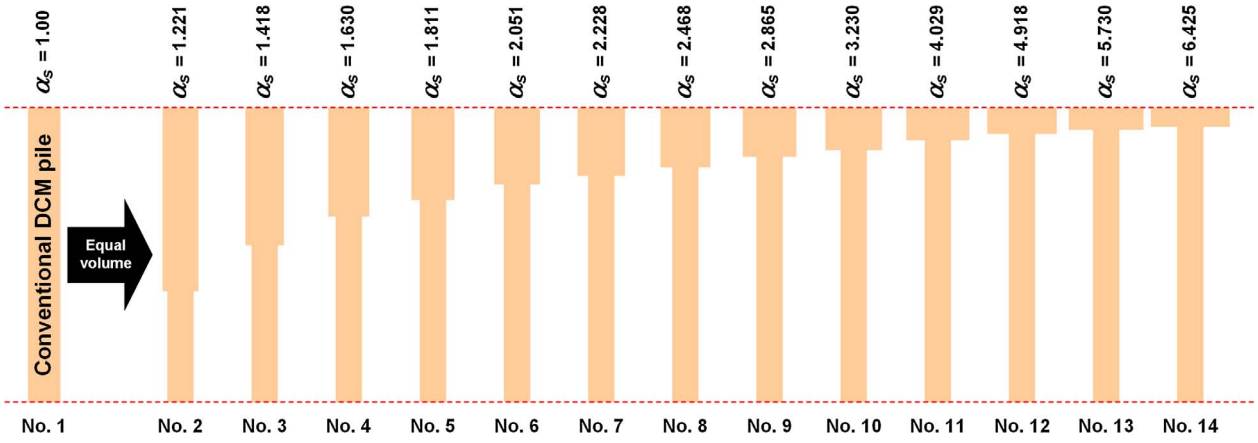

Fig. 13. Schematic of soil-cement piles with varying α_s in the sensitivity analysis.

Table 2
Case investigated in the sensitivity study.

No.	Surface pile diameter (m) D_{DCM} or D_{TDM}	Thick of enlarged pile cap (m) H	Pile body Diameter (m) d_{TDM}	Length of pile (m) L_{DCM} or L_{TDM}	Shape improvement ratio (–) α_s	Pile volume (m^3)	Unconfined compressive strength (kPa) q_u	Strength improvement ratio (–) α_p
1[a]	0.618	–	–	5.600	1.000	1.682	320, 427, 525, 560, 595, 630, 700	0.45, 0.61, 0.75, 0.80, 0.85, 0.90, 1.00
2	0.680	3.490	0.500	5.600	1.221	1.682		
3	0.730	2.620	0.500	5.600	1.418	1.682		
4	0.780	2.070	0.500	5.600	1.630	1.682		
5	0.820	1.760	0.500	5.600	1.811	1.682		
6	0.870	1.460	0.500	5.600	2.051	1.682		
7	0.905	1.300	0.500	5.600	2.228	1.682		
8	0.950	1.140	0.500	5.600	2.468	1.682		
9	1.020	0.940	0.500	5.600	2.865	1.682		
10	1.080	0.810	0.500	5.600	3.230	1.682		
11	1.200	0.620	0.500	5.600	4.029	1.682		
12	1.320	0.500	0.500	5.600	4.918	1.682		
13	1.420	0.420	0.500	5.600	5.730	1.682		
14	1.500	0.370	0.500	5.600	6.425	1.682		

[a] Baseline case (conventional DCM pile, q_u = 700 kPa).

force before transfer to greater depths. This behavior type (soil failure pattern and Q_{ult} less than that of the DCM pile) can be observed with increasing α_s up to 2.051. This pattern indicates that inferior performance would be obtained from transforming a DCM pile to a TDM pile with a size in this range. With greater α_s (4.029 and 6.425), the failure pattern continues to be governed by soil failure, but Q_{ult} becomes larger than that of the DCM pile.

Based on these observations, it was concluded that DCM and TDM piles under the same pile volume can fail in three possible failure patterns, including pile head failure, pile body failure and soil failure. These patterns depend not only on α_s but also on pile strength. The change in the failure pattern (from one TDM shape to another) also affects the change in pile capacity.

(2) Effects of the shape factor (α_s) and strength ratio (α_p) on the ultimate bearing capacity (Q_{ult})

The influence of α_s and α_p on the Q_{ult} of TDM piles is discussed in terms of the ultimate bearing capacity intensity ratio (α_Q), which is defined as

$$\alpha_Q = \frac{Q_{ult} \text{ of conventional DCM or TDM piles}}{Q_{ult} \text{ of baseline case}} \quad (3)$$

Fig. 17 shows the relationship between α_s and α_Q for the various analyzed cases of α_p. The seven symbols in the figure represent seven different failure patterns of the piles as shown in the upper subfigure. Seven lines supersede the seven different α_p of the soil-cement pile, including 0.45, 0.61, 0.75, 0.80, 0.85, 0.90 and 1.00. Each line represents the computed results from cases with various dimension following Fig. 13. For the data set with α_p of 0.45 and 0.61, α_Q increases considerably (from α_s = 1.00 for the conventional DCM pile with a pile head failure pattern) with increasing α_s until reaching values of 1.630 and 1.418, respectively. At these points (star symbol), the top part of the enlarged pile cap and the pile body immediately below the enlarged pile cap fail simultaneously (pile head-body failure pattern). When α_s increases (larger cap dimension), α_Q gradually decreases until α_s reaches 2.468. Beyond that, α_Q continues to increase again, and the failure pattern is governed by pile body failure. Moreover, based on the results for α_p = 0.45, after the reduction of α_Q in the range of 1.630–2.468, α_Q returns to the previous peak value (0.788 at α_s of 1.630) when α_s is equal to 4.3. The failure pattern changes from pile head-body failure to pile body failure. This phenomenon is similar to the results for the case with α_p = 0.61; after decreasing, α_Q increases and approaches the previous peak value at α_s of 4.45. However, for these two pile strengths, α_Q is larger for all TDM pile shapes (all α_s values) than that of the DCM pile of the same strength, indicating the advantage of transforming a DCM pile to a TDM pile. Moreover, for the largest cap considered in this study (α_s of 6.425), the TDM pile with low strength (α_p of 0.61) offers the same pile capacity as the DCM in the baseline case (higher strength).

For the data set with α_p of 0.75 and 0.80, the failure pattern changes from pile head failure (for α_s = 1.00) to soil failure with α_s increasing in the range of 1.221–2.468 with a slight increase in α_Q. When α_s exceeds 2.468, the failure is dominated by pile body failure with gradually

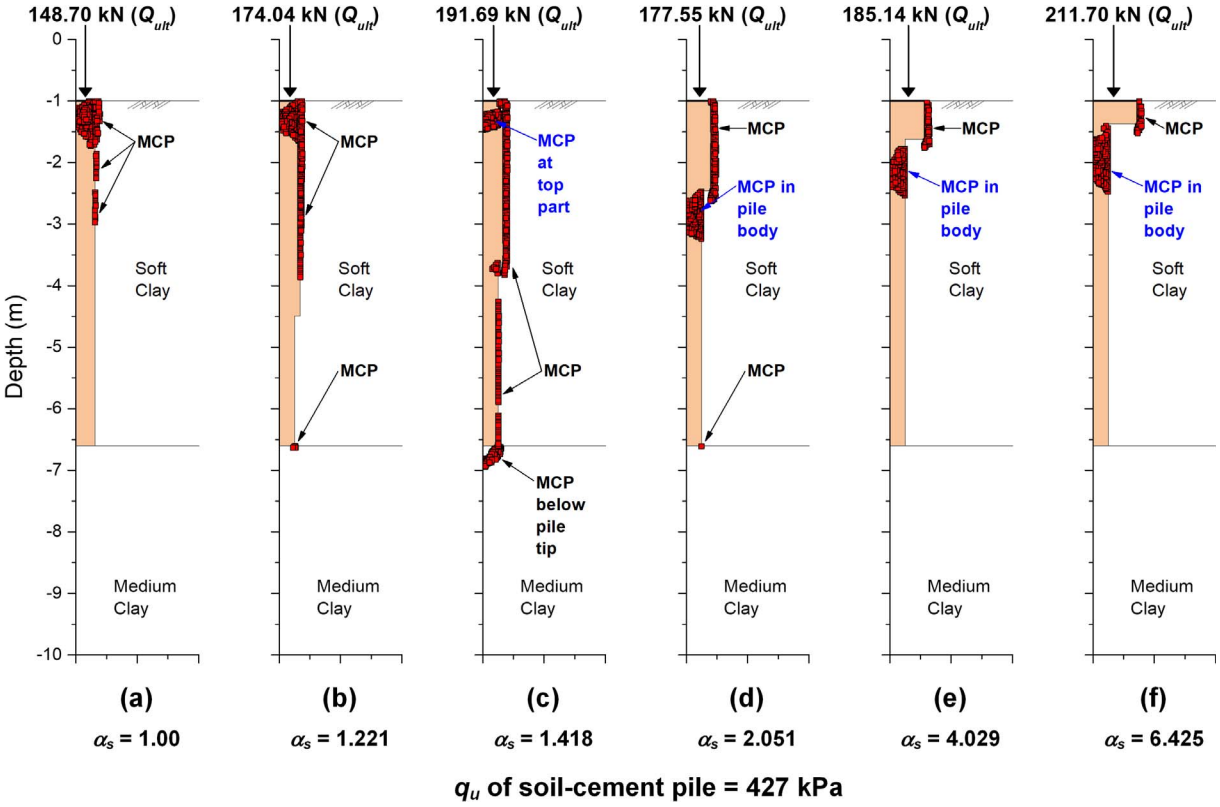

Fig. 14. Mohr-Coulomb points of conventional DCM and TDM piles having q_u of 427 kPa (α_p = 0.61) at failure load with constant pile volume and varying α_s.

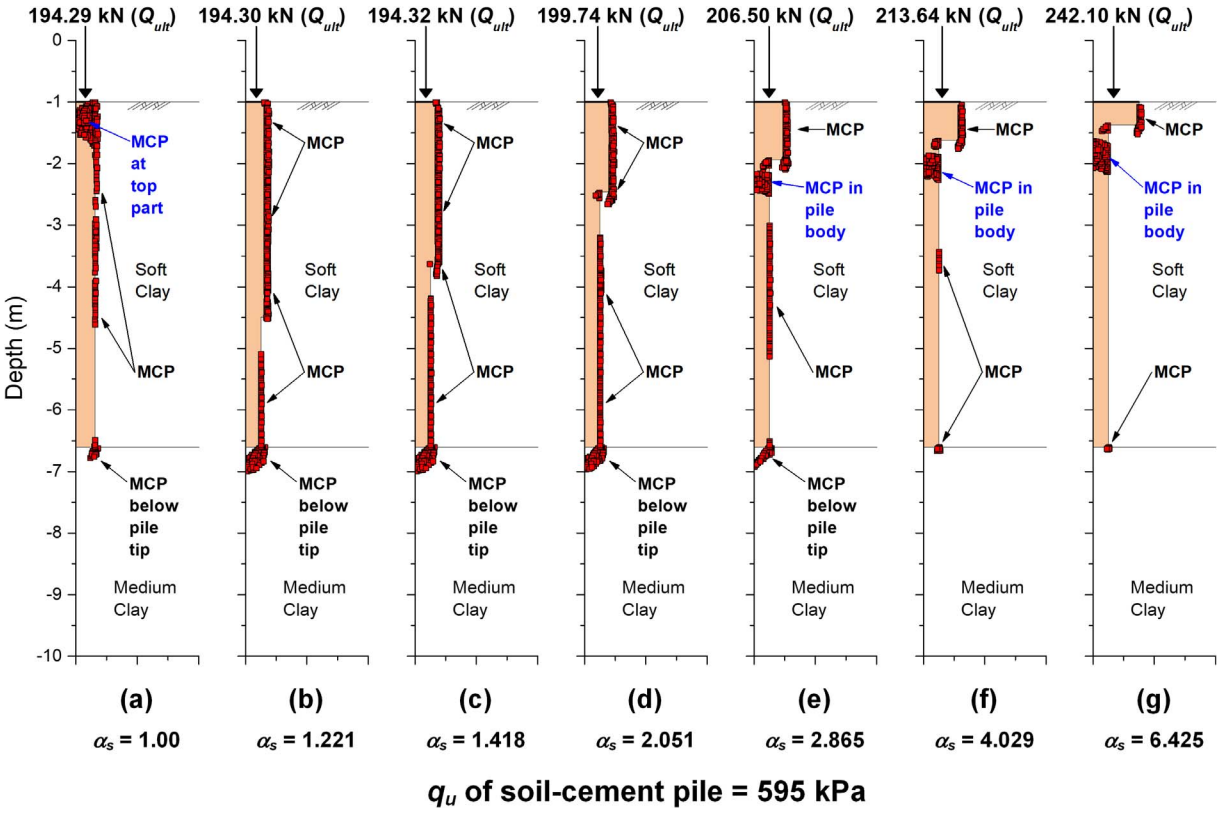

Fig. 15. Mohr-Coulomb points of conventional DCM and TDM piles having q_u of 595 kPa (α_p = 0.85) at failure load with constant pile volume and varying α_s.

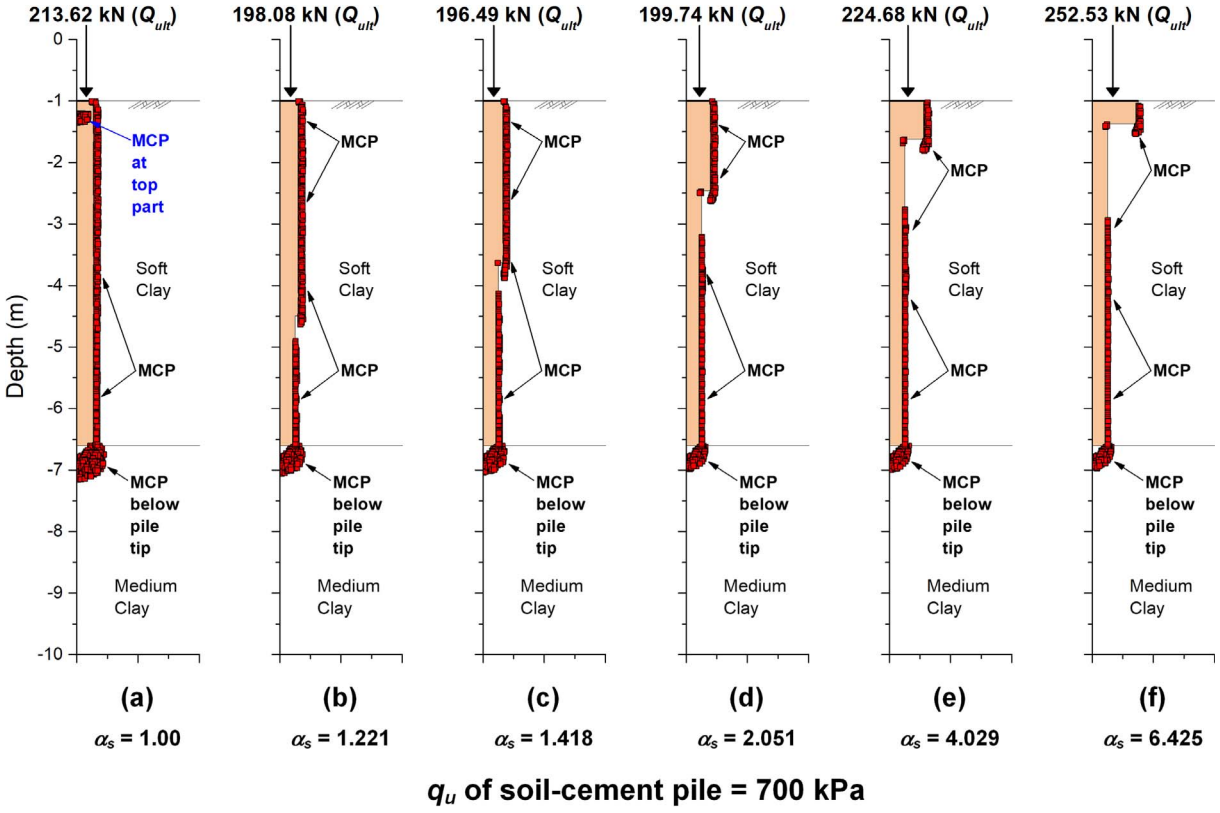

Fig. 16. Mohr-Coulomb points of conventional DCM and TDM piles having q_u of 700 kPa (α_p = 1.00) at failure load with constant pile volume and varying α_s.

increasing α_Q. For all TDM pile shapes with this range of α_p, α_Q is also larger than that of the conventional DCM pile with the same strength. For piles with α_p of 0.85, α_Q continues increasing with increasing α_s. The failure pattern consequently changes from pile head failure (for the DCM pile) to soil failure, pile body-soil failure and pile body failure with increasing α_s.

At higher values of α_p (0.90 and 1.00), α_Q decreases when the DCM pile is transformed to a TDM pile with the α_s in the range of 1.00 to 2.865. The pile head failure of the DCM pile also changes to soil failure for the TDM piles. Thus, transforming a DCM pile to a TDM pile does not always guarantee superior performance. When α_s increases beyond 3.0, the benefit of transforming a DCM pile to a TDM pile is evident. The soil failure mode is maintained with an enlarged pile cap for this case.

From the above-described results, it is concluded that both cap shape and pile strength play important roles in both the TDM pile capacity and the failure pattern. Under constant volume, transforming the DCM pile to a TDM pile does not guarantee superior performance unless both factors are taken into consideration. To ensure that the transformation to a TDM pile will be effective regardless of pile strength, the shape corresponding to an α_s of greater than 3.0 is recommended. For a small enlarged pile cap (α_s less than 3.0), pile strength corresponding to a maximum α_Q of 0.85 is suggested. It is also possible to achieve pile capacity equivalent to the DCM pile at optimal strength by transformation to a TDM pile with lower strength. This finding is very interesting for the use of TDM piles to reduce construction costs.

(3) Mobilization of side and tip resistances at the ultimate bearing capacity (Q_{ult})

The load sharing between the side and tip resistances of the piles at Q_{ult} is further investigated to obtain a better understanding of how Q_{ult} and probably the failure pattern change with the shape factor (α_s). Under a given applied load, the pile-supported load is carried partly by the side resistance at the perimeter surface of the enlarged pile cap and pile body (Q_{sc} and Q_{sp}) and partly by the tip resistance below the enlarged pile cap (Q_{bc}) and below the pile body (Q_{bp}). Fig. 18 presents the mobilized side and tip resistances of the conventional DCM and TDM piles with various shapes with α_p of 0.61 (representing low-strength piles). For the DCM pile (α_s = 1.00), the entire load-carrying ability comes from the side resistance between the pile and the surrounding soil. This is due to the low strength of the pile. Failure occurs at the pile head before the load is transferred to the pile tip. By transforming to a TDM pile (α_s larger than 1.00), the load is shared by all four components. Thus, the applied load can be transferred to the tip, resulting in an increase in Q_{ult}. For the TDM pile with α_s of 1.221 and a thick but small cap, the major contribution is the side resistance of the cap (Q_{sc}). With increasing α_s or a larger but thinner cap, the contribution from Q_{sc} decreases with compensation by cap bearing (Q_{bc}). However, the contribution from the cap (Q_{sc} + Q_{bc}) increases. For TDM piles with α_s of 1.418, which offers the peak Q_{ult}, failure occurs at both the head and pile body simultaneously, and Q_{sp} drastically increases.

For TDM piles with α_s greater than 1.630, in which failure is governed by pile body failure, the increase in Q_{ult} comes directly from the contribution from the cap. Q_{sp} is virtually constant at approximately 80 kN for α_s greater than 2.051. This corresponds to the available maximum compressive load of the pile body ($q_u \times A_{d,TDM}$ = 427 × π·0.5^2/4 = 83.84 kN). The benefit of enlarging the pile cap is thus due to the drastic increase in Q_{bc} compared to the decrease in Q_{sc}. The performance of the low-strength TDM piles is limited by the ability to sustain the load at the pile body.

Fig. 19 shows the mobilized resistances of DCM and TDM piles of various shapes and α_p of 1.00 (refer to the high-strength pile). As shown in the figure, for α_s = 1.00 (conventional DCM pile), the pile fails by pile head failure together with soil failure. Q_{ult} is contributed by the ultimate side and tip resistances. For the cases of α_s > 1.00 (TDM piles), Q_{bp} becomes smaller than that of the DCM pile due to the smaller pile body, resulting in smaller Q_{ult} when the DCM pile is transformed to a TDM pile

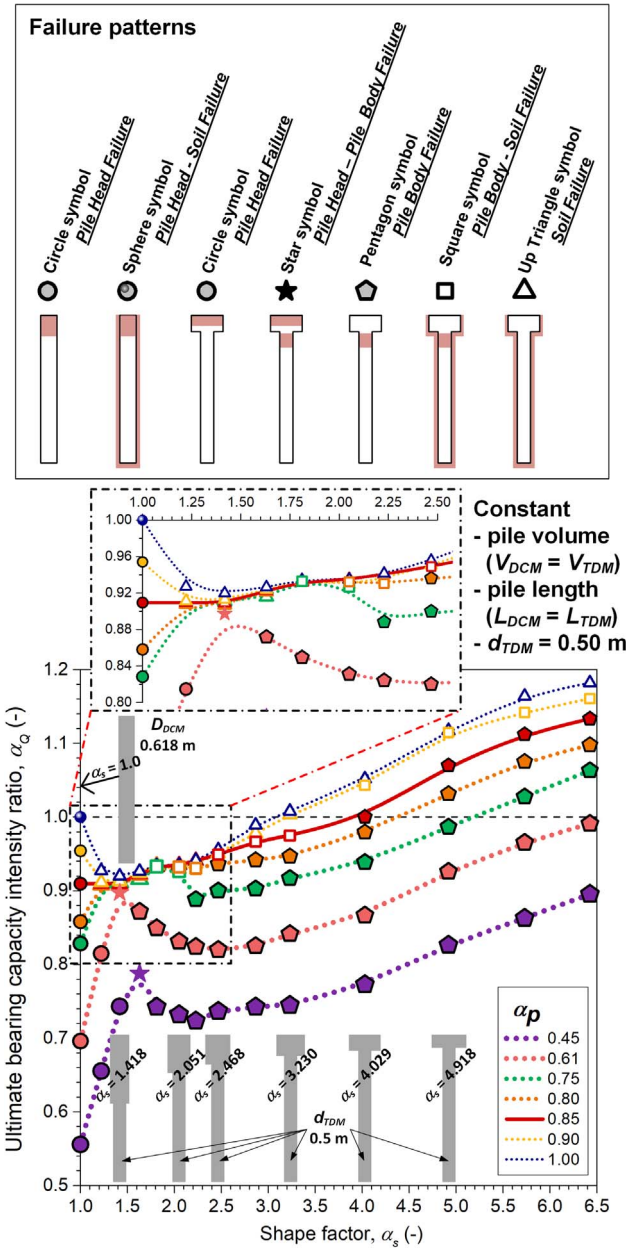

Fig. 17. α_s versus ultimate bearing capacity intensity of piles with various strengths and associated failure patterns.

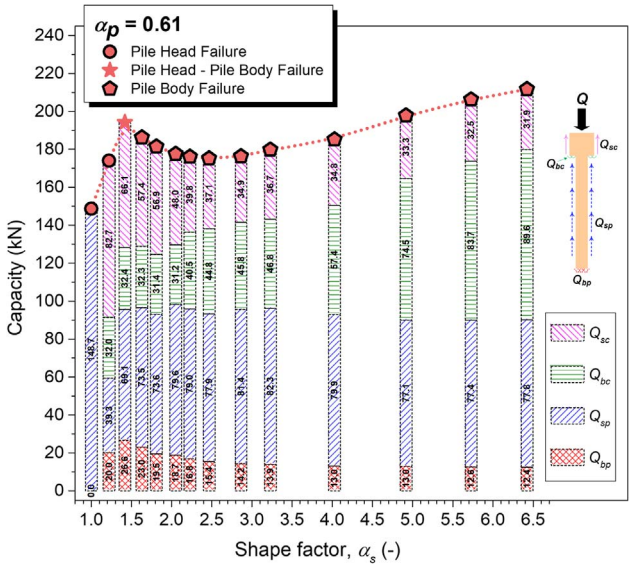

Fig. 18. Mobilized shaft and tip resistances of piles with various shapes at α_p of 0.61.

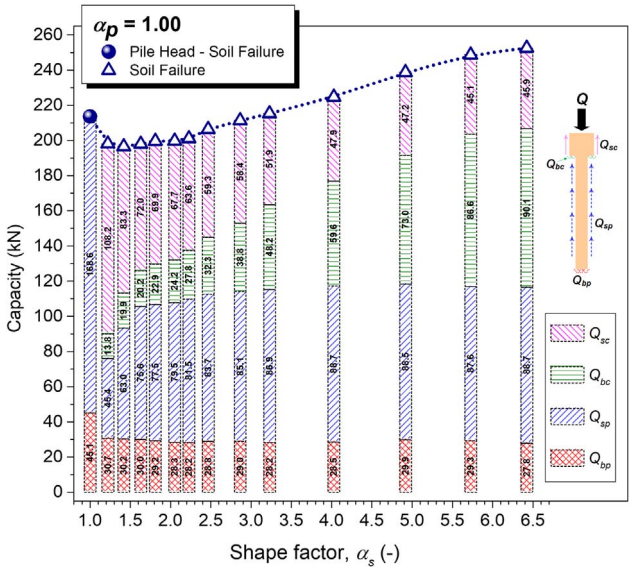

Fig. 19. Mobilized shaft and tip resistances of piles with various shapes at α_p of 1.00.

with a small cap dimension. Q_{bp} remains practically unchanged at 30.0 kN with increasing α_s, implying that this value is the ultimate value the soil at the tip can offer for this size of pile body. By contrast, Q_{sp} continually increases as the length of the pile body increases. Based on back calculation, it can be determined that Q_{sp} is the available maximum pile body skin friction provided by the surrounding soil. It is also observed in the figure that Q_{ult} of the TDM pile is principally affected by Q_{sc} and Q_{bc}.

6. Conclusion

A series of 2D-FE simulations of pile load tests on DCM and TDM piles extended from a reference case were conducted to investigate their load carrying and failure behaviors under controlled pile volume and length. The main focus was effect of the interaction between the shape of the enlarged pile cap and pile strength on those behaviors. A parameter, the shape factor (α_s), is introduced to represent the shape and size of the pile cap. Scaled-down model tests on conventional DCM and TDM piles in the laboratory verified the findings from the preliminary simulation. Additional sensitivity analyses further clarified the effects of the complex interaction of the shape of the enlarged pile cap and pile strength on the pile behaviors. The results are as follows:

(1) Under the same pile volume, enlarging the pile cap does not guarantee an increase in pile ultimate capacity. In addition, the pile strength in relation to the optimum DCM pile strength (α_p) plays an important role in the change in pile capacity.
(2) For relatively high pile strength (α_p > 0.85), enlarging the pile cap by a small degree (α_s < 1.75) leads to a decrease in the pile ultimate capacity followed by an increasing trend. By contrast, a rapid increase in the pile ultimate capacity is obtained when the pile cap is enlarged to a small degree at medium-high pile strength (α_p < 0.85). Beyond an α_s of 1.75, the pile ultimate capacity decreases in a narrow range (1.75 < α_s < 2.50) before continuously increasing.
(3) To guarantee the effectiveness of enlarging the pile cap, an α_s of not less than 3.00 is recommended.
(4) The effects of cap shape and pile strength on the failure pattern and

bearing capacity of TDM piles are attributed to changes in load transfer mechanism, which in turn depend on the mobilized skin friction and bearing by both the cap and the pile body.

(5) By enlarging the pile cap with an appropriate shape factor, the pile strength can be decreased to achieve the same or even greater ultimate pile capacity.

Acknowledgments

The authors would like to express their gratitude for financial support from King Mongkut's University of Technology Thonburi (KMUTT) and the Thailand Research Fund (TRF) through The Petchra Pra Jom Klao PhD scholarship under contract Grant No. 32/2558 and TRF Basic Research Grant No. BRG6080011. The support from the Faculty of Engineering, King Mongkut's University of Technology North Bangkok (KMUTNB) under contract No. ENG-60-20 is also acknowledged.

References

[1] Bergado DT, Ruenkrairergsa T, Taesiri Y, Balasubramaniam AS. Deep soil mixing used to reduce embankment settlement. Gr Improv 1999;3:145–62. http://dx.doi.org/10.1680/grim.1999.3.4.145.

[2] Chai JC, Shrestha S, Hino T, Ding WQ, Kamo Y, Carter J. 2D and 3D analyses of an embankment on clay improved by soil-cement columns. Comput Geotech 2015;68:28–37. http://dx.doi.org/10.1016/j.compgeo.2015.03.014.

[3] Jamsawang P, Yoobanpot N, Thanasisathit N, Voottipruex P, Jongpradist P. Three-dimensional numerical analysis of a DCM column-supported highway embankment. Comput Geotech 2016;72:42–56. http://dx.doi.org/10.1016/j.compgeo.2015.11.006.

[4] Lai YP, Bergado DT, Lorenzo GA, Duangchan T. Full-scale reinforced embankment on deep jet mixing improved ground. Gr Improv 2006;10:153–64. http://dx.doi.org/10.1680/grim.2006.10.4.153.

[5] Venda Oliveira PJ, Pinheiro JLP, Correia AAS. Numerical analysis of an embankment built on soft soil reinforced with deep mixing columns: parametric study. Comput Geotech 2011;38:566–76. http://dx.doi.org/10.1016/j.compgeo.2011.03.005.

[6] Venda Oliveira PJ, Correia AAS, Lemos LJL. Numerical prediction of the creep behaviour of an unstabilised and a chemically stabilised soft soil. Comput Geotech 2017;87:20–31. http://dx.doi.org/10.1016/j.compgeo.2017.02.006.

[7] Voottipruex P, Suksawat T, Bergado DT, Jamsawang P. Numerical simulations and parametric study of SDCM and DCM piles under full scale axial and lateral loads. Comput Geotech 2011;38:318–29. http://dx.doi.org/10.1016/j.compgeo.2010.11.006.

[8] Voottipruex P, Bergado DT, Suksawat T, Jamsawang P, Cheang W. Behavior and simulation of deep cement mixing (DCM) and Stiffened Deep Cement Mixing (SDCM) Piles Under Full Scale Loading. Soils Found 2011;51:307–20. http://dx.doi.org/10.3208/sandf.51.307.

[9] Yapage NNS, Liyanapathirana DS, Kelly RB, Poulos HG, Leo CJ. Numerical modeling of an embankment over soft ground improved with deep cement mixed columns: case history. J Geotech Geoenviron Eng 2014;140:4014062. http://dx.doi.org/10.1061/(ASCE)GT.1943-5606.0001165.

[10] Jamsawang P, Voottipruex P, Boathong P, Mairaing W, Horpibulsuk S. Three-dimensional numerical investigation on lateral movement and factor of safety of slopes stabilized with deep cement mixing column rows. Eng Geol 2015;188:159–67. http://dx.doi.org/10.1016/j.enggeo.2015.01.017.

[11] Jamsawang P, Boathong P, Mairaing W, Jongpradist P. Undrained creep failure of a drainage canal slope stabilized with deep cement mixing columns. Landslides 2016;13:939–55. http://dx.doi.org/10.1007/s10346-015-0651-9.

[12] Larsson S, Malm R, Charbit B, Ansell A. Finite element modelling of laterally loaded lime-cement columns using a damage plasticity model. Comput Geotech 2012;44:48–57. http://dx.doi.org/10.1016/j.compgeo.2012.03.004.

[13] Ignat R, Baker S, Larsson S, Liedberg S. Two- and three-dimensional analyses of excavation support with rows of dry deep mixing columns. Comput Geotech 2015;66:16–30. http://dx.doi.org/10.1016/j.compgeo.2015.01.011.

[14] Jamsawang P, Jamnam S, Jongpradist P, Tanseng P, Horpibulsuk S. Numerical analysis of lateral movements and strut forces in deep cement mixing walls with top-down construction in soft clay. Comput Geotech 2017;88:174–81. http://dx.doi.org/10.1016/j.compgeo.2017.03.018.

[15] CDIT (Coastal Development Institute of Technology). The Deep Mixing Method: Principle, Design and Construction. A.A. Balkema, The Netherlands; 2002.

[16] Petchgate K, Jongpradist P, Panmanajareonphol S. Field pile load test of soil-cement column in soft clay. Proc Int Symp 2003 Soil/gr Improv Geosynth Waste Contain Eros Control Appl 2003;2003:175–84.

[17] Uddin K, Balasubramaniam AS, Bergado DT. Engineering behavior of cement-treated Bangkok soft clay. Geotech Eng 1997;28:89–119.

[18] Lorenzo GA, Bergado DT, Soralump S. New and economical mixing method of cement- admixed clay for DMM Application. Geotech Test J 2006;29:54–63. http://dx.doi.org/10.1520/GTJ12129.

[19] Jongpradist P, Youwai S, Jaturapitakkul C. Effective void ratio for assessing the mechanical properties of cement-clay admixtures at high water content. J Geotech Geoenviron Eng 2011;137:621–7. http://dx.doi.org/10.1061/(ASCE)GT.1943-5606.0000462.

[20] Chen L, Liu SY. Consolidation calculation of soft ground improved by T-shape deep mixing columns. GeoCongress 2008 Geosustainability Geohazard Mitigation, March 9, 2008 - March 12, 2008; 2008. p. 620–7. http://dx.doi.org/10.1061/40971(310)77.

[21] Yi YL, Liu SY. Bearing behavior of single T-shaped cement-soil deep mixing column. Proc Int Symp Lowl Technol 2008:261–5.

[22] Wonglert A, Jongpradist P. Impact of reinforced core on performance and failure behavior of stiffened deep cement mixing piles. Comput Geotech 2015;69:93–104. http://dx.doi.org/10.1016/j.compgeo.2015.05.003.

[23] Liu SY, Du YJ, Yi YL, Puppala AJ. Field investigations on performance of T-shaped deep mixed soil cement column-supported embankments over soft ground. J Geotech Geoenviron Eng 2012;138:718–27. http://dx.doi.org/10.1061/(ASCE)GT.1943-5606.0000625.

[24] Yi YL, Liu SY, Puppala AJ, Xi PS. Vertical bearing capacity behaviour of single T-shaped soil–cement column in soft ground: laboratory modelling, field test, and calculation. Acta Geotech 2017:1–12. http://dx.doi.org/10.1007/s11440-017-0555-z.

[25] Yi YL, Liu SY, Puppala AJ. Laboratory modelling of T-shaped soil–cement column for soft ground treatment under embankment. Géotechnique 2016;66:85–9. http://dx.doi.org/10.1680/jgeot.15.P.019.

[26] Jamsawang P, Bergado DT, Voottipruex P. Field behaviour of stiffened deep cement mixing piles. Proc Inst Civ Eng - Gr Improv 2011;164:33–49. http://dx.doi.org/10.1680/grim.900027.

[27] De Beer EE. Proefondervindlijke bijdrage tot de studie van het grensdraag vermogen van zand onder funderingen op staal. Tijdshift Der Openbar Verken van Belgie; 1967.

[28] Schanz T, Vermeer A, Bonnier P. The hardening soil model: formulation and verification. Beyond 2000 Comput Geotech 10 Years PLAXIS. In: Int proc int symp beyond 2000 comput geotech Amsterdam Netherlands 1820 March 1999; 1999, 281.

[29] Rukdeechuai T, Jongpradist P, Wonglert A, Kaewsri T. Influence of soil models on numerical simulation of geotechnical works in Bangkok subsoil. EIT Res Dev J 2009;20:17–28.

[30] Prust RE, Davies J, Hu S. Part 6: tunnels and underground structures: pressuremeter investigation for mass rapid transit in Bangkok, Thailand. Transp Res Rec J Transp Res Board 2005;1928:207–17. http://dx.doi.org/10.3141/1928-22.

[31] Jongpradist P, Kaewsri T, Sawatparnich A, Suwansawat S, Youwai S, Kongkitkul W, et al. Development of tunneling influence zones for adjacent pile foundations by numerical analyses. Tunn Undergr Sp Technol 2013;34:96–109. http://dx.doi.org/10.1016/j.tust.2012.11.005.

[32] Lueprasert P, Jongpradist P, Jongpradist P, Suwansawat S. Numerical investigation of tunnel deformation due to adjacent loaded pile and pile-soil-tunnel interaction. Tunn Undergr Sp Technol 2017;70:166–81. http://dx.doi.org/10.1016/j.tust.2017.08.006.

[33] Jamsawang P, Voottipruex P, Jongpradist P, Bergado DT. Parameters affecting the lateral movements of compound deep cement mixing walls by numerical simulations and parametric analyses. Acta Geotech 2015;10:797–812. http://dx.doi.org/10.1007/s11440-015-0417-5.

[34] Jongpradist P, Jumlongrach N, Youwai S, Chucheepsakul S. Influence of fly ash on unconfined compressive strength of cement-admixed clay at high water content. J Mater Civ Eng 2010;22:49–58. http://dx.doi.org/10.1061/(ASCE)0899-1561(2010) 22:1(49).

[35] Shen SL, Wang ZF, Horpibulsuk S, Kim YH. Jet grouting with a newly developed technology: The Twin-Jet method. Eng Geol 2013;152:87–95. http://dx.doi.org/10.1016/j.enggeo.2012.10.018.

Applied Clay Science 148 (2017) 83–94

Contents lists available at ScienceDirect

Applied Clay Science

journal homepage: www.elsevier.com/locate/clay

Research paper

Laboratory investigations on the swelling behavior of composite expansive clays stabilized with shallow and deep clay-cement mixing methods

Pitthaya Jamsawang[a,*], Nuttapong Nuansrithong[b], Panich Voottipruex[c], Smith Songpiriyakij[d], Pornkasem Jongpradist[e]

[a] Soil Engineering Research Center, Department of Civil Engineering, King Mongkut's University of Technology North Bangkok, Thailand
[b] Italian-Thai Development Public Company Limited, Thailand
[c] Department of Teacher Training in Civil Engineering, King Mongkut's University of Technology North Bangkok, Thailand
[d] Construction and Building Materials Research Center, King Mongkut's University of Technology North Bangkok, Thailand
[e] Department of Civil Engineering, Faculty of Engineering, King Mongkut's University of Technology Thonburi, Bangkok, Thailand

ARTICLE INFO

Keywords:
Deep mixing
Expansive clay
Shallow mixing
Clay stabilization
Swelling

ABSTRACT

Expansive clays are considered as problematic due to their high swelling potential. Shallow and deep clay-cement mixing can be used in the creation of the composite materials to improve the swelling behavior of such clays. This research aims to observe the swelling characteristics of expansive clays stabilized by shallow and deep cement mixing methods using composite free swelling tests in the laboratory. Bentonite-kaolin mixtures were used as base clays to create high, medium and low degrees of swelling potentials of the expansive clays. The results show that improvements in the volume ratio (V_r), which is a combination of the thickness ratio (T_r) and improvement area ratio (a_r), affect the overall swelling behavior of the composite expansive clays. This study proposes correlations between the maximum swelling potentials, swelling rate and secondary swelling rate versus V_r. The microstructure and mineralogy of unstabilized and stabilized specimens were analyzed by X-ray diffractometry and scanning electron microscopy. The results show that the maximum swelling potentials of the composite clays are a function of the reflection intensities of calcium silicate hydrate and montmorillonite after stabilization.

1. Introduction

Expansive clays contain clay minerals that exhibit high volume changes upon wetting, which creates problems worldwide for civil engineering projects constructed on such clays in many parts of the world and in arid and semi-arid regions in particular (Khemissa and Mahamedi, 2014). Many researchers have reported problems and damages related to construction on expansive clays in different countries (Tang et al., 2009; Yilmaz and Civelekoglu, 2009; Ozer et al., 2012; Voottipruex and Jamsawang, 2014). The expansive clays exhibit high plasticity, high compressibility, high swelling potential, reduced strength, and reduced durability (e.g. reduced ability of soil to retain its strength, impermeability, and dimensional stability over prolonged period of service under the designed conditions. Thus, they are low-quality materials for construction and present difficulties.

Clay stabilization methods have been successfully used to solve the problems associated with expansive clays. These methods consist of the addition of chemicals, soil replacement, compaction and moisture control, surcharge loading, rewetting and thermal methods (Yong and Ouhadi, 2007). Numerous authors have proposed clay-cement mixing as an effective stabilization method to mitigate the problems associated with expansive clays. Clay-cement mixing is based on the cementitious bonds between the calcium silicate and aluminate hydration products of cement and the clay particles. The action of cement reduces both interlayer and intermicellar swelling (Van der Kerkhof, 2001). The basic strategy of cement stabilization is to reduce the liquid limit, plasticity index, permeability, deformation, and potential volume change and to increase the shrinkage limit, strength, and durability.

In situ clay-cement mixing is divided into shallow and deep mixing methods. Both methods create composite foundation clays with improved properties relative to the in situ clays. These methods have been used for many diverse applications, including foundations, retaining structures, liquefaction mitigation water control, and pollution control. The most common improvement goals are increased strength, reduced deformation and decreased permeability for the composite ground (Topolnicki, 2004). The shallow clay-cement mixing method refers to shallow applications of clay-cement, such as levee roads, bike paths, river revetments, and pond linings. The entire clay mass is mixed with

* Corresponding author.
E-mail address: pitthaya.j@eng.kmutnb.ac.th (P. Jamsawang).

http://dx.doi.org/10.1016/j.clay.2017.08.013
Received 12 March 2017; Received in revised form 10 August 2017; Accepted 12 August 2017

cement in a shallow manner, which creates thickness of the stabilized clay layer overlain by the unstabilized clay layer. Road reclaimers or pugmills are the most common equipment used for mixing. They have been effectively used to stabilize soft clays, saving time in comparison to other ground improvement techniques, such as preloading (Bergado et al., 1996). Stabilizing the upper 3 to 5 m is an optimum foundation improvement technique (Saadeldin and Siddiqua, 2013), but this stabilization is not effective for clays that extend to considerable depths. Hence, the deep cement mixing method is more suitable for stabilizing clays of considerable depth. This method has been widely used in Sweden and Finland to strengthen soft clays, such as silt and clay. The increase in strength obtained using this method was reported to be as high as 30 times. The practical deep mixing method is a process involving the installation of columns of improved ground formed by mixing cement with the existing ground via mechanical dry mixing, wet mixing or grouting (Lorenzo and Bergado, 2004; Shen et al., 2008, 2013a,b; Arulrajah et al., 2009; Jongpradist et al., 2010; Jamsawang et al., 2011, 2015, 2016a,b; Chai et al., 2015; Wonglert and Jongpradist, 2015). The deep cement mixing columns are typically installed through soft clay layers to transfer the loads from upper structures to deep and firm strata (Han et al., 2007; Okyay and Dias, 2010; Liu et al., 2012, 2015; Chai et al., 2015). Square grid patterns are typically applied for settlement reduction purposes with improvement area ratios of 0.1 to 0.5 (Kitazume and Terashi, 2013; Topolnicki, 2013). The majority of research on shallow and deep cement mixing methods is related to the improvement of soft clay properties. However, limited studies on the improved properties of expansive clays stabilized with two mixing methods have been conducted.

This study investigates the free swelling behavior of composite expansive clays stabilized with shallow and deep clay-cement mixing methods based on laboratory tests. The effects of the thickness and cross-sectional area of the expansive clays stabilized by shallow and deep mixing methods, respectively, on the properties of the expansive clays were investigated. Microstructural analyses, including X-ray diffraction (XRD) and scanning electron microscopy (SEM), were performed on unstabilized and stabilized expansive clays. The reaction products and microstructure changes resulting from the hydration process obtained from XRD and SEM analysis, respectively, were used to describe and evaluate the swelling potentials of the composite clays. The correlations between swelling potentials and the thickness and cross-sectional area of stabilized expansive clays were determined to evaluate appropriate mixing methods and the thickness or cross-sectional area of stabilized expansive clays for use in practical work.

2. Experimental programs

2.1. Preparation of expansive clays

The representative expensive clays used in this study were mixtures of sodium bentonite and kaolin in powder form (Horpibulsuk et al., 2011). The bentonite and kaolin represent high- and low-swelling clays, respectively. The bentonite:kaolin (B:K) mixtures were divided into three proportions, 25:75, 15:85 and 2:98, to obtain three different degrees of swelling potentials (Latifi et al., 2015). Geotechnical index properties of all clay mixtures were used for clay classification and evaluation of swelling properties, and they were determined by the ASTM Standard Test Methods. The lists of geotechnical index properties were for the particle size distribution, specific gravity of clay solids, liquid and plastic limits, and plasticity index. The clay samples were classified according to the Unified Clay Classification System. Activity is defined as the ratio of the plasticity index to the clay content, which is used to classify the swelling potential of the expansive clay. Three classes of clays were defined according to activity: inactive for activities less than 0.75; normal for activities between 0.75 and 1.25; and active for activities greater than 1.25. Finally, the standard Proctor test was performed to obtain the maximum dry unit weight and optimum moisture content for all mixtures. The geotechnical index properties of all clay mixtures are provided in Table 1.

Table 1
Summary of the measured geotechnical index properties of clay mixtures used in this study.

Properties	ASTM standard test method	Percent by weight (%B:%K)				
		(100:0)	(25:75)	(15:85)	(2:98)	(0:100)
Silt content (%)	D 422-63	25	66	78	79	80
Clay content (%)	D 422-63	75	34	22	21	20
Specific gravity	D 854-10	2.76	2.65	2.65	2.64	2.62
Liquid limit (%)	D 4318-10	367	104	69	35	27
Plastic limit (%)	D 4318-10	39	21	27	24	26
Plastic index (%)	D 4318-10	328	83	42	11	1
Clay classification	D 2487-10	CH	CH	CH	ML	ML
Activity	D 422-63, D 4318-10	4.37	2.44	1.91	0.55	0.05
$\gamma_{d(max)}$ (kN/m^3)	D 698-12	–	15.4	16.0	16.5	–
OMC (%)	D 698-12	–	20.4	19.6	16.9	–

XRD analysis was conducted to evaluate clay minerals of unstabilized raw expansive clays. For a better characterization of clay minerals in the raw clay samples, the XRD analysis was performed in normal, glycoled (Mosser-Ruck et al., 2005) and calcined forms (Gapak et al., 2017). In the glycoled form, the raw clay samples were solvated in ethylene glycole liquid at a room temperature; in the calcined form the samples were heated to 600 °C in muffle furnace and then cooled at the room temperature before carrying out the XRD to determine change in the d-value of clay minerals. The results of XRD analysis were presented in Fig. 1a, b and c for unstabilized raw expansive clays with high, medium and low degrees of swelling potentials, respectively. The d-value and corresponding mineral were presented against the reflection intensities. The XRD data of the studied expansive clays showed the presence of montmorillonite with multiple reflections. Other important minerals such as kaolinite, illite, and quartz were present in all the expansive clays as presented in Fig. 1a–c. The XRD data in glycoled and calcined forms improved the phase identification with the presence of sharp and clear reflections for montmorillonite. After glycolated, d-value was left shift and increased. For heating process, the montmorillonite reflection decreased and right shift. The d-value for illite was constant after ethylene glycole solvated and heated at 600 °C. However, the reflections corresponding to kaolinite were absent in the calcined form, which was also reported by Gapak et al. (2017) and Yoobanpot et al. (2017) as the heating to 600 °C causes kaolinite to lose its crystalline character.

The results show that montmorillonite, which is known as the most active clay mineral, was the major clay mineral. The chemical compositions of clay mixtures obtained from the X-ray fluorescence (XRF) are presented in Table 2. The clay mixtures mainly consisted of silicon oxide (SiO_2), representing 58.49, 59.16 and 61.27% of the clay for the proportions of 25:75, 15:85 and 2:98, respectively. The SiO_2 increased with increasing kaolin contents. Alternately, the ferric oxide (Fe_2O_3) represented 5.14, 3.45 and 1.45% of the clay and the sodium oxide (Na_2O) represented 2.29, 2.15 and 1.86% of the clay for the proportions of 25:75, 15:85 and 2:98, respectively. The Fe_2O_3 and Na_2O decreased with an increasing amount of kaolin, as expected.

2.2. Conventional free swelling test

The conventional free swelling test was performed in accordance with ASTM D 4546-14, 2014 to determine the swelling potentials of unstabilized and stabilized expansive clays and to evaluate the optimum cement content for the cost effectiveness of the stabilized clays. Ordinary Portland cement type 1 was used as a stabilizer. The properties and classifications of cement are presented in Table 3. The mixing ratios of the cement in this study were 1, 3 and 5% by weight of dry

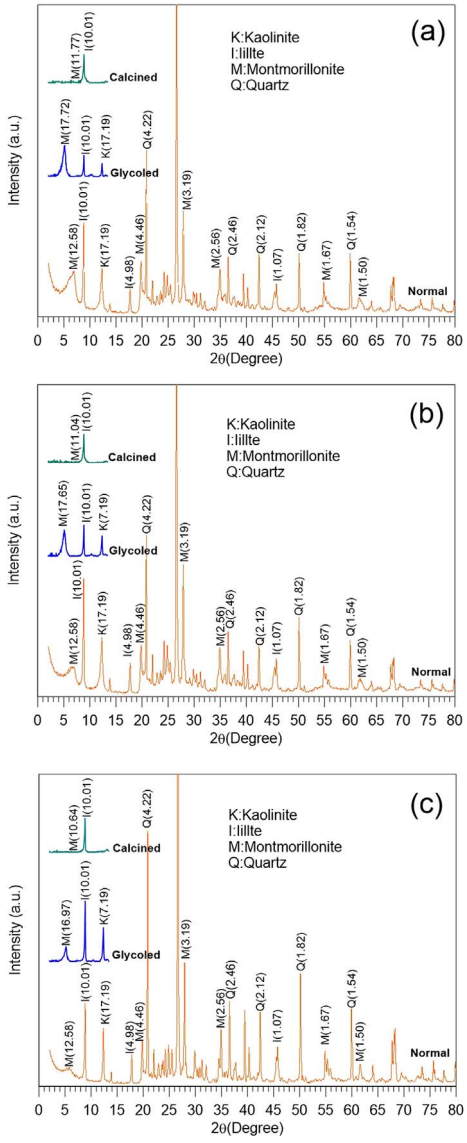

Fig. 1. Clay mineral identification by XRD for unstabilized raw expansive clays with (a) high, (b) medium and (c) low degrees of swelling potentials in normal, glycolated and calcined forms.

Table 2
Summary of the chemical compositions of materials.

Composition	Percent by weight (%B:%K)				
	(100:0)	(25:75)	(15:85)	(2:98)	(0:100)
SiO_2	47.6	58.49	59.16	61.27	61.04
Al_2O_3	15.29	28.71	29.86	30.08	31.55
Fe_2O_3	25.00	5.14	3.45	1.45	0.93
Na_2O	3.56	2.29	2.15	1.86	1.89
K_2O	0.29	3.00	3.32	3.40	3.85
MgO	2.00	0.64	0.54	0.53	0.23
CaO	2.75	0.67	0.47	0.27	0.31
SO_3	0.10	0.05	0.03	0.02	0.01
Others	3.41	1.01	1.02	1.12	0.37

clay. The specimen preparation of both unstabilized and stabilized clays was controlled by the maximum dry unit weight and optimum moisture content of each mixture from the standard Proctor test. Each specimen was pressed carefully in a standard fixed-ring consolidometer made from stainless steel with an inside diameter of 50 mm and a height of 19 mm and was wrapped with plastic film to prevent the loss of moisture. The specimens were cured for 28 days in a humidity room. After the curing period was completed, clay specimens were placed in between two porous stones with a loading plate resting on the upper porous stone in the consolidation cell, and the cell was filled with water. All specimens were inundated under a seating pressure of 1 kPa. The swelling of the clay specimens was periodically recorded by a displacement transducer until the swelling was constant. Swelling is defined as the ratio of the amount of swelling to the original thickness of the sample expressed as a percentage.

Table 3
Summary of the chemical composition of cement used in this study.

Composition	Content (%)
CaO(Lime)	62.81
SiO_2	21.20
Al_2O_3(Alumina)	4.95
Fe_2O_3(Iron)	2.82
MgO (Magesia)	4.00
Na_2O and K_2O (Alkali)	0.30
SO_3(Sulfuric anhydrite)	2.63
Specific gravity	3.15
Loss of ignition (%)	1.23
Classification	Ordinary Portland cement Type1-Grade 53

2.3. Composite free swelling tests

The composite free swelling tests were performed to investigate the swelling behavior of composite materials consisting of shallow and deep cement mixing stabilized and unstabilized expansive clays. The details of the laboratory model are shown in Fig. 2a and b. The unstabilized clay mixtures were prepared in accordance with the conventional free swelling test, whereas the stabilized clays were mixed with cement at the optimum content for each clay mixture obtained from the conventional free swelling test. The thickness of shallow cement mixing and the cross-sectional area of deep cement mixing are deemed to be the major influencing factors of the swelling behavior of the composite expansive clays. A cylindrical PVC mold with an inner diameter of 300 mm and a height of 380 mm was used to contain the composite clays. The valves were installed at the base of the mold to serve as a drainage system. The size of the composite material was 300 mm in diameter and 120 mm in height, which is about 6 times the size of the sample used for the conventional free swelling test. The composite clays were inserted between two 50-mm-thick sand layers. The sand layers were compacted at the maximum dry unit weight and optimum moisture content to avoid undesirable settlements when the composite clays were compacted. The functions of the sand layers are to provide drainage and reduce excess pore water pressure during the test, similar to the porous stone in the conventional free swelling test. Non-woven geotextiles with a density of 150 g/m^2 were also inserted between the compacted sand layers and composite clay to prevent the migration and mingling of materials. The sand layers and composite clays were statically compacted in the mole using a hydraulic jack with a reaction frame to prevent damage to the PVC mold. Their unit weights and optimum moisture contents were controlled at the same values obtained from the standard compaction tests.

2.3.1. Sample preparation for shallow stabilization

The effect of the thickness of shallow stabilized expansive clay ($T_{stabilized}$) on the swelling behavior of the composite clays was investigated by varying the improvement thickness ratio (T_r), the values of which were 0 (unstabilized), 0.2, 0.4, 0.6, 0.8 and 1.0 (fully stabilized). T_r is defined as the ratio of $T_{stabilized}$ to the original thickness of the unstabilized expansive clay ($T_{unstabilized}$). After the compacted sand layer was placed on the bottom of the mold and covered with a geotextile sheet, the unstabilized clay was statically compacted in

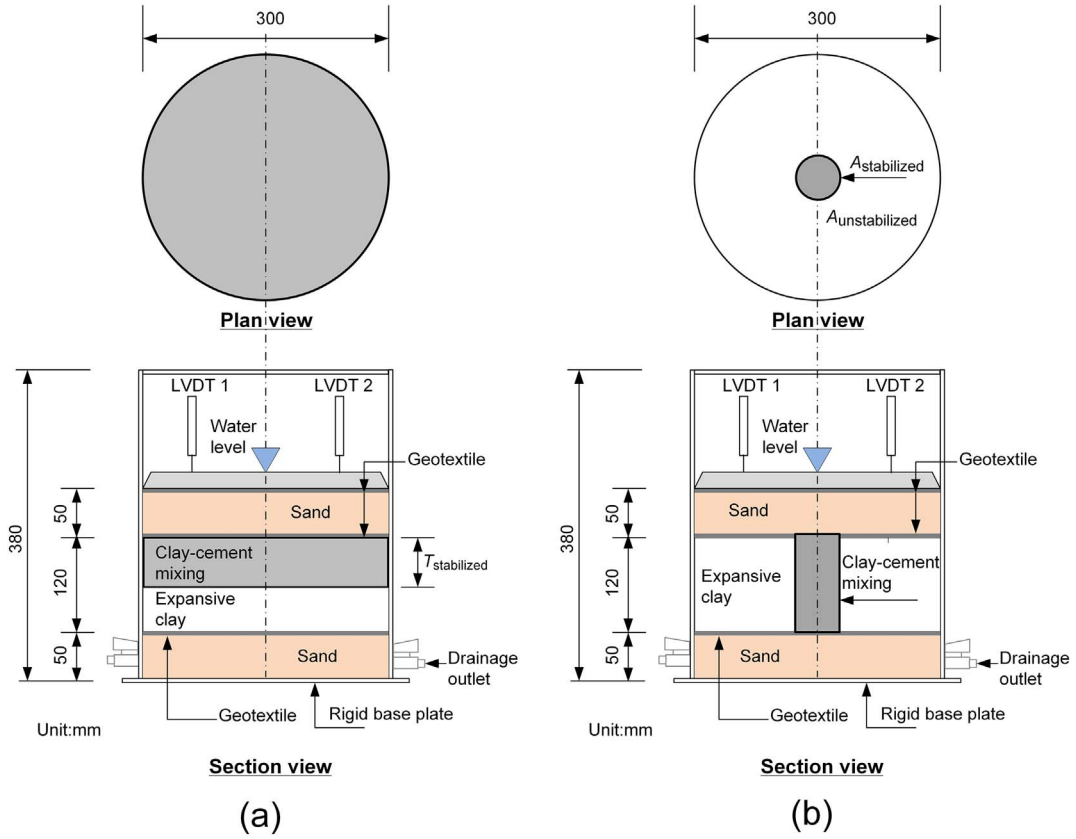

Fig. 2. Schematic diagram of composite free swelling tests for: (a) shallow; (b) deep mixing methods.

accordance with T_r. To prepare the stabilized clay layer, some unstabilized clay was mixed with cement, at which point the optimum content was obtained from conventional free swelling tests. The remaining thickness of 120 mm was stabilized expansive clay, which was statically compacted and covered with a geotextile sheet. Finally, the compacted layer was placed on top of the mold.

2.3.2. Sample preparation for deep stabilization

Improvement area ratios (a_r) of 0, 0.017, 0.068, 0.230, 0.320 and 1.0 were considered to investigate the effect of the cross-sectional area of deep stabilized expansive clay ($A_{stabilized}$) on the swelling behavior. a_r is defined as the ratio of $A_{stabilized}$ to the original cross-sectional area of unstabilized expansive clay ($A_{unstabilized}$). The unstabilized expansive clay was statically compacted to an original thickness of 120 mm in the mold. A thin steel tube (shoe cutter) with an inner diameter corresponding to the value of a_r was pushed into the sample by a hydraulic jack, creating a hole at the center of the unstabilized sample. The unstabilized clay from the tube was collected and mixed with cement, where the optimum content was obtained from conventional free swelling tests, to prepare the cement-admixed expansive clay. The hole was filled by cement-admixed expansive clay, which was statically compacted in four layers, forming a compacted deep cement mixing stabilization at the center of the unstabilized sample. Then, the geotextile sheet and compacted sand was placed on top of the composite clay. The entire set-up, including the mold for both shallow and deep stabilization, was wrapped in a plastic sheet to prevent moisture loss and cured for a period of 28 days.

2.3.3. Testing procedure

After the curing time, the sample was placed in a basin and filled with water. The sample was inundated under a seating pressure of 1 kPa. The 12-kg rigid steel plate was placed on top of the composite clay sample to generate a seating pressure of 1 kPa and to ensure equal strain. The vertical displacements used to calculate the swelling of the composite clay were recorded by two displacement transducers. Water was pumped through the bottom sand layer to ensure that the entire clay sample was soaked. The inflow rate of water was equal to the outflow to prevent excess pore water pressure. The swelling of clay specimens was periodically recorded by a displacement transducer until the swelling was constant.

2.4. Microstructural analysis

2.4.1. Sample preparation for XRD

The reaction products and change in chemical composition from cement mixed with expansive clay were investigated by XRD analysis. In addition, the correlation between the maximum swelling potential of composite clays and quantitative reaction products was also determined. The clay sample was taken after the composite free swelling test was completed. The clay sample was dried in a desiccator over silica gel for 24 h, and the dry clay sample was divided into small fragments. Then, the clay sample fragments were gently crumbled by hand grinding in agate mortar to create a powder material and then sieving it finer than 20 μm.

2.4.2. Sample preparation for SEM

There has been increasing interest in clay microstructure research in recent years. Certain micro-parameters, such as the porosity and clay particle orientation degree, can be extracted from an image of the clay microstructure. This method can be used in clay stabilization studies to visualize the physiognomy features and observe the formation of new cementitious products. To evaluate the interaction between clay samples and cement particles in improved clay, the clay sample and improved clay were subjected to image analysis. Images of samples were magnified 3500 to 5000 times once the swelling of the samples specimens became constant after the free swelling testing in the laboratory

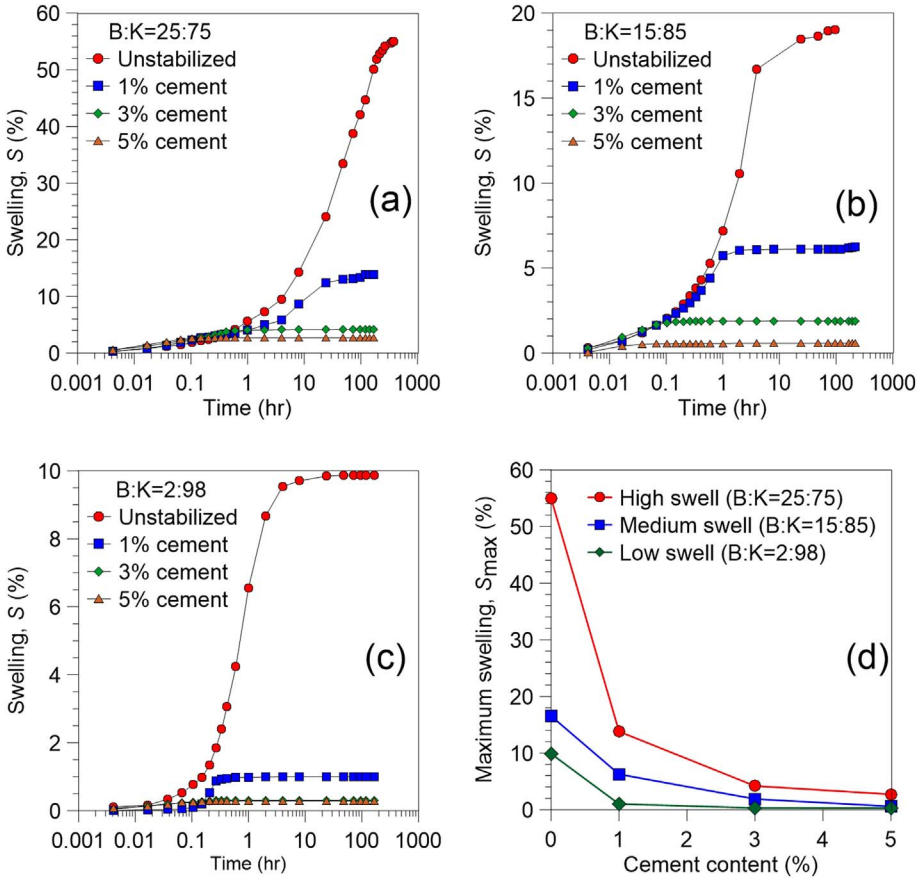

Fig. 3. Swelling versus time curves for unstabilized and stabilized expansive clays with: (a) high; (b) medium; (c) low degrees of swelling potentials and (d) the effect of cement content on S_{max} from conventional free swelling tests.

to evaluate the correlation between the swelling behavior and orientation. After blending the clay sample and cement under dry conditions and mixing them with the required amount of water to achieve the optimum moisture content, the sample was used for analysis; each sample had dimensions of approximately 10 × 10 × 10 mm and was air-dried in a desiccator.

3. Test results and discussion

3.1. Conventional free swelling test

3.1.1. Swelling versus time curve

Fig. 3a to c presents the log of time and swelling (S) for the unstabilized and stabilized expansive clays with cement contents of 1, 3, and 5% at degrees of swelling that are high, medium and low, respectively. For all of the mixtures, the swelling initially increases slowly with log time, then increases more rapidly, and finally reaches an asymptotic value; this behavior corresponds to the three habitual swelling stages (Azam and Wilson, 2006): (1) initial low swelling because of low unsaturated hydraulic conductivity; (2) intermediate primary swelling due to an established wetting front; and (3) secondary low swelling owing to near-saturation conditions. The time required for the completion of each swelling stage and the entire swelling process generally increased with increasing bentonite content in the mixture (Azam, 2007; Azam et al., 2013). Near-equilibrium (e.g., the time required to reach an asymptotic level, t_{asy}) was reached in approximately 240 to 8 h for unstabilized expansive clays. A longer amount of time was required to reach near-equilibrium when the plasticity index was higher. The values of maximum swelling (S_{max}) were found to be 55, 19.5, and 9.9% for mixture proportions of 25:75, 15:85 and 2:98, respectively, which are classified as high, medium and low swelling potentials in this study.

The amounts of S and t_{asy} for stabilized clays were less than those for unstabilized expansive clays. The S_{max} values for the expansive clay with high swelling potential were 13.8, 4.2, and 2.7% for cement contents of 1, 3 and 5%, respectively; for medium swelling potential, they were 10, 1.9, and 0.6%; and for low swelling potential, they were 1, 0.3 and 0.28%, which depends on amount of bentonite (Al-Rawas and Goosen, 2006). The time to reach near-equilibrium was only approximately 24 to 0.1 h. Cokca (2001) found that S_{max} was reduced from 30 to 10%, mainly due to the initial time-dependent pozzolanic effect. This gel gradually crystallizes to form an interlocking structure. The interaction between clay minerals and cement is the replacement of sodium with calcium in montmorillonite. This decreases the electrochemical forces of repulsion between them (Abu Seif, 2015).

3.1.2. Effects of the cement content on S_{max}

The effects of the cement content on the S_{max} of the stabilized expansive clays with low, medium and high swelling potentials are presented in Fig. 3d. The S_{max} for expansive clays with medium and high swelling potentials decreased rapidly as the cement contents increased from 0 to 1%, then slightly decreased as the cement content increased to 3% and finally remained approximately constant for cement contents higher than 3%. However, for low-swelling expansive clays, S_{max} stabilized when the cement content exceeded 1%. Therefore, the optimum cement contents were 3 and 1% for medium and high swelling and low-swelling expansive clays, respectively. The S_{max} for unstabilized clays were 55, 19.5 and 9.9%, whereas the S_{max} for stabilized clays at the optimum cements were 4.2, 1.9 and 0.5%, which correspond to improvement ratios of 13, 10 and 19 for high-, medium- and low-swelling expansive clays, respectively. The improvement ratio is defined as S_{max} for stabilized clay divided by S_{max} for unstabilized clay.

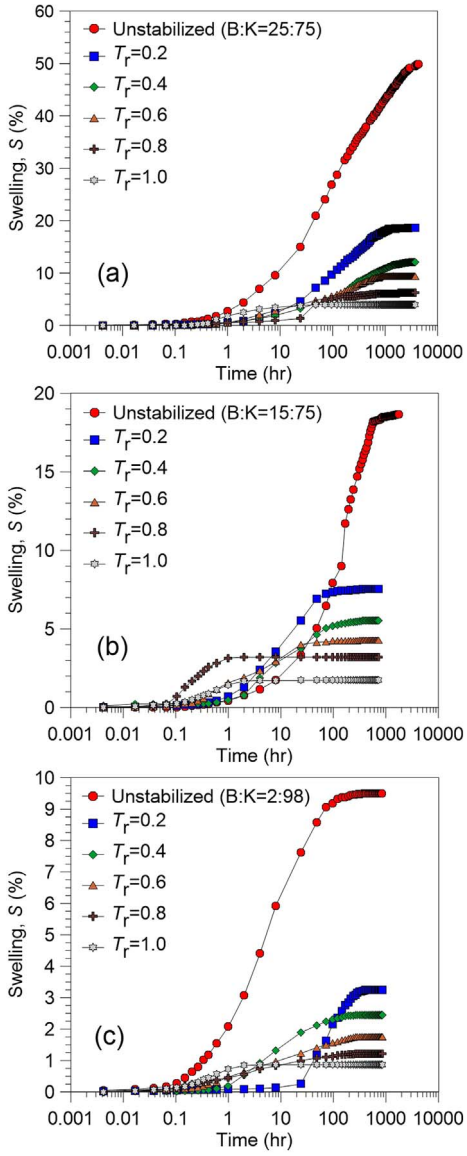

Fig. 4. Swelling versus time curves for unstabilized and stabilized expansive clays with: (a) high; (b) medium; (c) low degrees of swelling potentials from composite free swelling tests for the shallow mixing method.

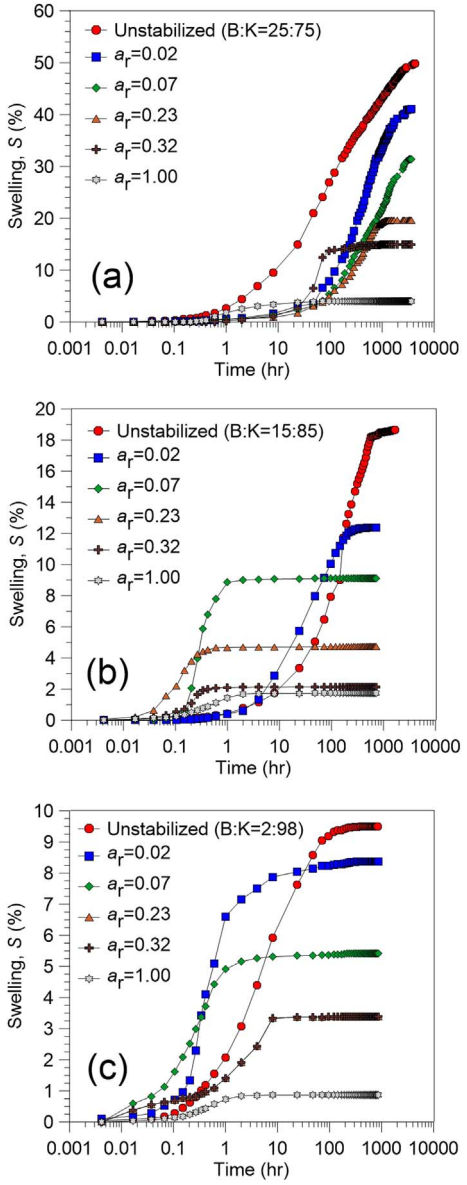

Fig. 5. Swelling versus time curves for unstabilized and stabilized expansive clays with: (a) high; (b) medium; (c) low degrees of swelling potentials from composite free swelling tests for the deep mixing method.

3.2. Composite free swelling test

3.2.1. Swelling versus time curve

Fig. 4a, b and c shows the relationships between the log of time and swelling potential for the composite expansive clays (S_{com}) with shallow cement mixing at high, medium and low degrees of swelling, respectively. Considering the unstabilized clays, the shapes of swelling curves for composite free swelling tests are similar to those for the conventional free swelling test, but the elapsed time to the end of each swelling stage is different because of the different size of the specimens. The observed erratic development of swelling is likely due to the movement of water and ions to the expansive clay clusters (Agus and Schanz, 2008). The hickness of the composite clay sample was higher, which causes the movement of water to clay particles to be slower. The time required to reach an asymptotic value varied considerably. Swelling was nearly complete within 190, 35 and 7 days for the high, medium and low swelling potentials, respectively. Maximum swelling potentials for the unstabilized expansive clays ($S_{max,unstabilized}$) of 49.8, 18.7 and 9.5% were observed for clays with high, medium and low degrees of swelling, respectively. $S_{max,unstabilized}$ was slightly different from S_{max} from the conventional free swelling test because the non-uniform distribution of bentonite during compaction causes uneven permeation throughout the clay.

Fig. 5a to c shows the swelling behavior of stabilized expansive clays by deep stabilization for high, medium and low degrees of swelling, respectively. The curve shapes are similar to those of unstabilized expansive clays. The amount of maximum swelling potential for the composite expansive clays ($S_{max,com}$) decreased with increasing T_r and a_r, as expected, due to the decrease in volumetric unstabilized expansive clays throughout the cross-sectional area and thickness, respectively. $S_{max,com}$ and the corresponding improvement ratio for all degrees of swelling potentials of the expansive clays stabilized with shallow and deep mixing methods are provided in Table 4. It can be seen from Figs. 4 and 5 that t_{asy} decreased with increasing T_r and a_r. The deep mixing method yields lower t_{asy} values than the shallow mixing method. The swelling curves intersected, which implies that t_{asy} was less than that for shallow mixing. The cracks of the unstabilized clay surrounding the clay-cement column occurred due to the effect of construction with deep cement mixing. The water can easily flow

Table 4
Summary of the measured $S_{max,com}$ from composite free swelling tests.

Degree of swell potential	Shallow cement mixing			Deep cement mixing		
	T_r	Measured $S_{max,com}$	Improvement ratio	a_r	Measured $S_{max,com}$	Improvement ratio
High	0.0	49.8	1.0	0.000	49.8	1.0
	0.2	18.7	2.7	0.017	41.1	1.2
	0.4	12.1	4.1	0.068	31.4	1.6
	0.6	9.4	5.3	0.230	19.6	2.5
	0.8	6.3	7.9	0.320	15.0	3.3
	1.0	4.0	12.5	1.000	4.0	12.5
Medium	0.0	18.7	1.0	0.000	18.7	1.0
	0.2	7.5	2.5	0.017	12.4	1.5
	0.4	5.5	3.4	0.068	9.1	2.1
	0.6	4.3	4.3	0.230	4.7	4.0
	0.8	3.2	5.8	0.320	2.6	7.2
	1.0	1.7	11.0	1.000	1.7	11.0
Low	0.0	9.5	1.0	0.000	9.5	1.0
	0.2	3.3	2.9	0.017	8.4	1.1
	0.4	2.5	3.8	0.068	5.4	1.8
	0.6	1.8	5.3	0.230	3.4	2.8
	0.8	1.2	7.9	0.320	2.3	4.1
	1.0	0.9	10.6	1.000	0.9	10.6

through the crack, which accelerates the swelling time (Horpibulsuk et al., 2012).

3.2.2. Effect of T_r and a_r on $S_{max,com}$

Fig. 6a and b shows the relationship between $S_{max,com}$ and both T_r and a_r for the expansive clays stabilized by shallow and deep mixing methods, respectively. $S_{max,com}$ and the corresponding improvement ratio for all degrees of swelling potentials of the expansive clays stabilized with shallow and deep mixing methods are provided in Table 4. The amount of $S_{max,com}$ decreased with increasing T_r and a_r due to the decrease in volumetric unstabilized expansive clays throughout the cross-sectional area and thickness, respectively. In addition, T_r has a direct impact on the value of $S_{max,com}$. In addition, the upper stabilized clay layer is relatively non-swelled compared to the lower unstabilized layer. The upper stabilized clay layer acts as an overburden pressure on the lower expansive clay layer. It affects the decrease of $S_{max,com}$ with the increase in surcharge pressure, thus reducing the value of $S_{max,com}$ (Al-Rawas and Goosen, 2006).

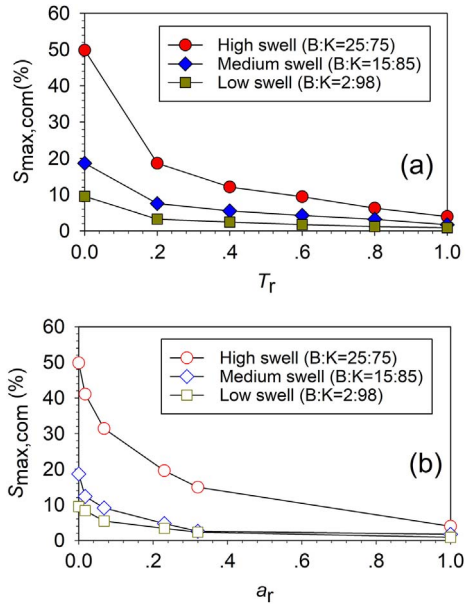

Fig. 6. Effects of (a) T_a and (b) a_r on $S_{max,com}$.

Moreover, the inner stabilized clay is relatively non-swelled compared to the outer unstabilized clay. Thus, the friction between the interface may reduce $S_{max,com}$. A larger a_r results in a smaller amount of friction at the interface, resulting in a reduction in $S_{max,com}$. $S_{max,com}$ is significantly reduced at a T_r of 0.2 and a_r of 0.23 for all degrees of swelling, with $S_{max,com}$ reduced by more than 50%. Thus, a T_r of 0.2 and a_r of 0.23 are suggested as optimal values for civil engineering practice.

$S_{max,com}$ can be normalized by $S_{max,unstabilized}$ for each degree of swelling potential. From Fig. 7a and b, the relationships between $S_{max,com}/S_{max,unstabilized}$ and both T_r and a_r can be expressed as a function of an exponential linear combination in Eqs. (1) and (2), respectively, as follows:

$$\frac{S_{max,com}}{S_{max,unstabilized}} = 0.373 + 0.627e^{11.9T_r} - 0.287T_r, \quad R^2 = 0.9956 \tag{1}$$

$$\frac{S_{max,com}}{S_{max,unstabilized}} = 0.342 + 0.635e^{-15a_r} - 0.259a_r, \quad R^2 = 0.9608 \tag{2}$$

Fig. 7a and b illustrates that T_r and a_r can be combined as an improvement volume ratio, V_r, which is defined as the ratio of the stabilized clay volume to the stabilized clay volume. Thus, Eqs. (1) and (2) can be combined as Eq. (3), which is the relationship of $S_{max,com}/S_{max,unstabilized}$, and V_r is expressed as a function of the exponential linear combination (Fig. 7c) in Eqs. (1) and (2), respectively, as follows:

$$\frac{S_{max,com}}{S_{max,unstabilized}} = 0.357 + 0.653e^{-38V_r} - 0.267V_r, \quad R^2 = 0.9771 \tag{3}$$

The equivalent properties of the composite ground stabilized with the deep mixing method can be estimated based on the area-weighted average values of $S_{max,unstabilized}$ and unstabilized and stabilized grounds (Topolnicki, 2004). This concept is also applied in this study to evaluate $S_{max,com}$ based on the volume-weighted average values of $S_{max,unstabilized}$ and $S_{max,stabilized}$. Thus, $S_{max,com}$ under shallow and deep stabilization can be estimated based on V_r as expressed in Eq. (4).

$$S_{max,com} = S_{max,stabilized} \times V_r + S_{max,unstabilized} \times (1 - V_r) \tag{4}$$

The relationship between the measured and predicted values of $S_{max,com}$, which was calculated by Eq. (4); and the measured $S_{max,com}$ was 1.27 times the predicted $S_{max,com}$, with $R^2 = 0.7616$. The data predicted by the linear relationship in Eq. (4) do not correspond well with the measurement data. Many factors, including cracks in the surrounding clays due to the deep mixing method, the overburden pressure from the upper stabilized clay layer due to the shallow mixing method

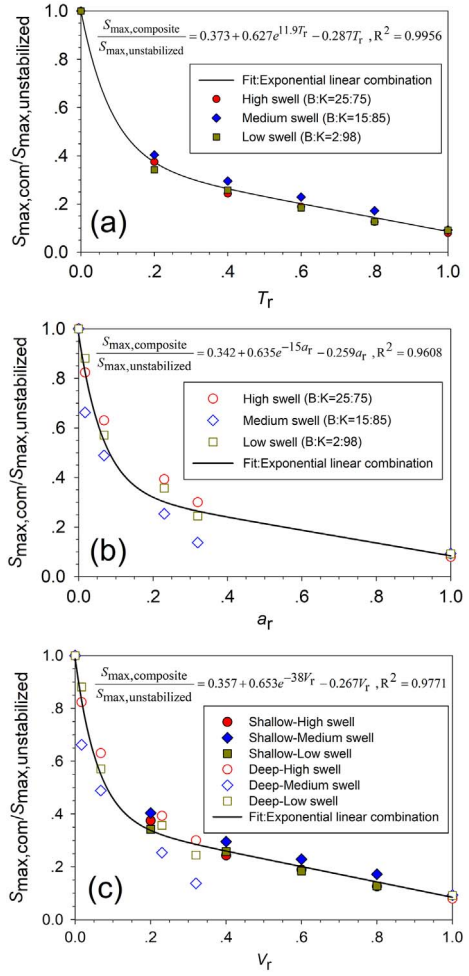

Fig. 7. Relationships between $S_{max,com}/S_{max,unstabilized}$ and (a) T_a, (b) a_r and (c) V_r.

and/or non-uniformity of the clay mixtures, may affect this mismatch. Therefore, the non-linear relationship was proposed to better predict $S_{max,com}$, as expressed in Eq. (5).

$$S_{max,com} = S_{max,stabilized} \times V_r + S_{max,unstabilized} \times (1 - V_r^{0.3}) \quad (5)$$

The measured $S_{max,com}$ is 1.02 times the $S_{max,com}$ predicted using Eq. (5), with $R^2 = 0.9879$. The degree of overestimation was reduced from Eq. (4) by reducing $S_{max,com}$ in the last term of Eq. (5), which is a non-linear power function.

3.2.3. Effect of V_r on the swelling rate

Dakshinamurthy (1978) proposed a hyperbolic equation to predict the swelling of expansive clays as given in Eq. (6):

$$\frac{t}{S} = a + bt \quad (6)$$

In this study, the relationship between $t/S_{max,com}$ and time for composite clays can be plotted. The constants a and b are defined by the straight line. b is the slope of the swelling path. Moreover, the rate of swelling can be determined by the value of the slope, b, which indicates the flow of the swelling path. Therefore, b is defined as the swelling rate coefficient. A steeper slope is a sign that the rate of swelling is smaller. The effects of V_r on the swelling rate coefficient of the composite expansive clays (b_{com}) are presented in Fig. 8a. The swelling rate coefficients for the unstabilized expansive clays ($b_{unstabilized}$) were 0.02, 0.04 and 0.09 for high, medium and low expansive clays. b_{com} increased with increasing V_r due to the greatly reduced time and swelling caused by a decrease in the volume of unstabilized expansive clays. b_{com} can be

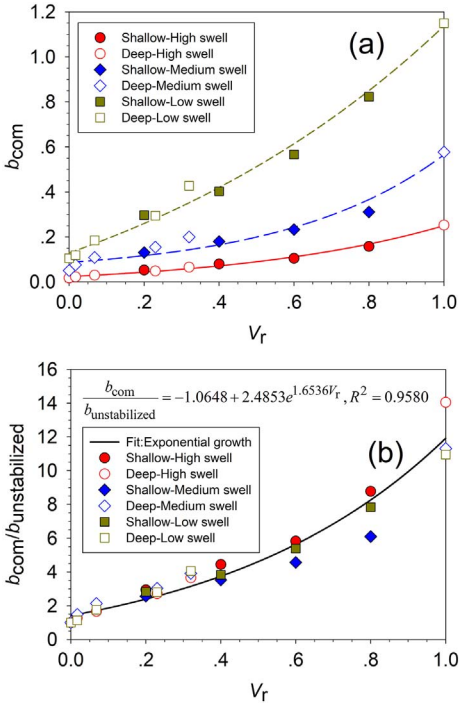

Fig. 8. (a) Effects of V_r on b_{com} and (b) relationships between $b_{com}/b_{unstabilized}$ and V_r.

normalized by $b_{unstabilized}$ for each degree of swelling potentials. Fig. 8b illustrates that the relationships of $b_{com}/b_{unstabilized}$ and V_r can be expressed as an exponential growth function, as shown in Eq. (7).

$$\frac{b_{com}}{b_{unstabilized}} = -1.0648 + 2.4853e^{1.6536V_r}, \quad R^2 = 0.9580 \quad (7)$$

The relationship between the measured $S_{max,com}$ and the $S_{max,com}$ predicted from $1/b_{com}$ show that the measured $S_{max,com}$ is 0.93 times the predicted $S_{max,com}$, with $R^2 = 0.9987$. The correlation in this study exhibits a unique linear curve corresponding to the relationship presented by Sridharan and Gurtug (2004) and Voottipruex and Jamsawang (2014), who proposed that the measured S_{max} is 0.98 times the predicted S_{max} for unstabilized and stabilized expansive clays obtained from conventional free swelling tests. It ought to be more because the predicted swelling is the asymptotic value of the time versus percent swelling plot. The asymptotic value obtained is greater than the value obtained from the experimental results taken up to a finite time. Theoretically, it takes an infinite amount of time to attain the asymptotic value.

3.2.4. Effect of V_r on the secondary swelling rate

The low swelling rate during the initial stage is attributed to the low unsaturated hydraulic conductivity of the samples. Once water mobility was initiated, the high water adsorptive forces on the clay particle surfaces were readily wetted, thereby resulting in a high rate of primary swelling. The gradual reduction in the swelling rate during the primary and secondary swelling is attributed to the increasing sample saturation due to water migration (Shahid, 2006). The secondary swelling rate is similar to the rate of secondary compression. Due to the stabilizing expansive clays in a composite free swelling, it is complex to calculate the change in the void ratio of the unstabilized and stabilized clays. Thus, the change in swelling (ΔS) was used to calculate the secondary swelling rate as follows:

$$R_\alpha = \frac{\Delta S}{\log \frac{t_2}{t_1}} \quad (8)$$

where R_α is the secondary swelling rate and t_1 and t_2 are the time periods. Fig. 9a presents the relationship between V_r and the secondary

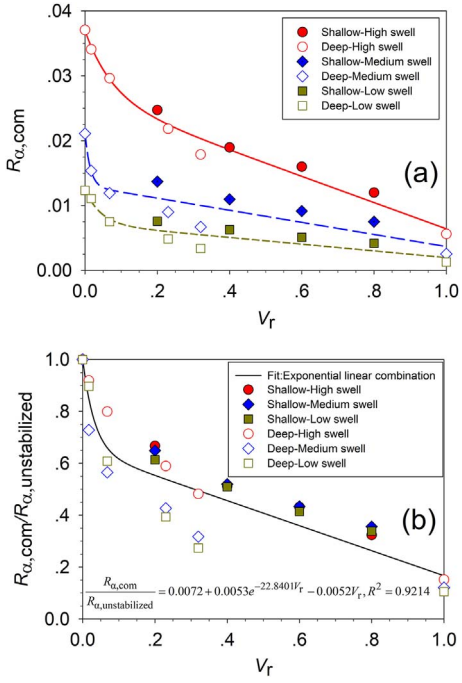

Fig. 9. (a) Effects of V_r on $R_{\alpha,com}$ and (b) relationships between $R_{\alpha,com}/R_{\alpha,unstabilized}$ and V_r.

swelling rate of the composite clays ($R_{\alpha,com}$). The secondary swelling rates of unstabilized clays ($R_{\alpha,unstabilized}$) were 0.038, 0.024 and 0.018 for high-, medium- and low-swelling clays. In this study, $R_{\alpha,com}$ decreased with increasing V_r, and $R_{\alpha,com}$ for the shallow and deep mixing methods decreased from 0.022 to 0.0003 and 0.032 to 0.0003, respectively, due to the increased T_r and a_r, affecting the reduction in volumetric expansive clays. Sridharan and Gurtug (2004) reported that $R_{\alpha,unstabilized}$ is approximately zero for non-swelling kaolin. $R_{\alpha,unstabilized}$ is 0.008 for a less-plastic clay and 0.08 for highly plastic montmorillonite clay. $R_{\alpha,unstabilized}$ for high-, medium- and low-swelling expansive clays is within the range of that for highly plastic montmorillonite clay. Composite clays with V_r values of 0.9, 0.6 and 0.07 can be classified as non-swelling for high, medium and low degrees of swelling potentials, respectively. $R_{\alpha,com}$ can be normalized by $R_{\alpha,unstabilized}$ for each degree of swelling potentials. From Fig. 9b, the relationships of $R_{\alpha,com}/R_{\alpha,unstabilized}$ and V_r can be expressed as an exponential linear combination function as follows:

$$\frac{R_{\alpha,com}}{R_{\alpha,unstabilized}} = 0.0072 + 0.0053e^{-22.8401V_r} - 0.0052V_r, \quad R^2 = 0.9214 \tag{9}$$

3.3. Microstructural analysis

3.3.1. X-ray diffraction

Fig. 10a, b and c shows the XRD profiles for the unstabilized and stabilized expansive clays for high, medium and low degrees of swelling potentials, respectively. The XRD profiles provide a qualitative indication of mineralogy, and the comparison of the intensity of the reflection heights with those for a reference powder can provide a quantitative guide. The dominant clay minerals present in the unstabilized and stabilized clays were montmorillonite, illite and kaolinite, respectively. Although there were noticeable changes in the XRD results of the stabilized clays compared to the unstabilized clays, the intensity of the reflections for montmorillonite decreased because of the additive effect and its weathering action on the clay minerals (Latifi et al., 2015). The interaction between clay minerals in expansive clays with cement is likely to involve the replacement of sodium (Na) with calcium (Ca) in montmorillonite. Some dissolution of montmorillonite may incur an increase in quartz and possible reduction in montmorillonite as a result of stabilization with cement, which apparently reduces the concentration of montmorillonite and reduces its potential for swelling (Mutaz and Dafalla, 2014).

Ouhadi and Yong (2008) noted that the formation of ettringite is a result of the formation of calcium silicate hydrate (CSH), which is a new pozzolanic compound in cement-stabilized expansive clays. The CSH is known as a cementing agent due to its bonding nature and how its action in expansive clays generates strongly bonded particles, which improves the clay strength and reduces the swelling tendency (Khemissa and Mahamedi, 2014). The laboratory test results indicated the S_{max} of expansive clays decreased with increasing cement content. The effectiveness of cement stabilization causes external and internal changes in the structure of clay minerals. The external changes indicate the formation of the CSH. CHS is a gel material, which cements the clay particles and proceeds to coat and bind clay lumps in the clay and block off the clay pore (Abu Seif, 2015). This gel gradually crystallizes to form an interlocking structure. This leads to minimization of the initial surface area of clay mineral particles and reduction of the swell susceptibility of the expansive clays. Reference reflections in montmorillonite and CSH are used to conduct a simple quantitative analysis regarding the reduction in montmorillonite and the formation of the CSH in expansive clays, as shown in Tables 5 and 6, respectively. In this study, the montmorillonite reflection intensities for unstabilized and stabilized clays are referred to as $M_{unstabilized}$ and $M_{stabilized}$, respectively. In addition, the CSH reflection intensities at the reference points are referred to as $CSH_{unstabilized}$ and $CSH_{stabilized}$ for unstabilized and stabilized clays, respectively. The increases in the reference reflections due to the addition of cement in comparison with the unstabilized are shown in Table 6. The values of the improvement ratio based on reflection intensity are higher for a lower degree of swelling potential, e.g., lower amount of montmorillonite.

In the same manner, the reflection intensities of montmorillonite and CSH for composite expansive clays by shallow and deep stabilizations can be calculated by considering V_r using Eq. (4). To account for effects of $M_{stabilized}$ and $CSH_{stabilized}$ on $S_{max,com}$, the relationship between $S_{max,com}$ and the corresponding M_{com} and CSH_{com} can be expressed as in Fig. 10d. $S_{max,com}$ is a rational function of the ratio CSH_{com}/M_{com} and can be expressed as shown in Eq. (10).

$$S_{max,com} = \left(0.556\frac{CSH_{com}}{M_{com}} - 0.1229\right)^{-1}, \quad R^2 = 0.9486 \tag{10}$$

3.3.2. SEM

Latifi et al. (2015) proposed that bentonite has a microstructure of dispersed undulating filmy particles, whereas kaolin exhibits an arranged book-like microstructure. Fig. 11a, b and c shows the microstructure of unstabilized expansive clays before inundation. Montmorillonite clay particles were found in high swelling clays, with randomly oriented-flaky montmorillonite clay particles forming multi-particle aggregates (Ito and Azam, 2010) and concentrated clusters. Such a composition results in impervious clays; the swelling rate of the clays is low in the initial swelling state, and the free swelling tests take a relatively long amount of time. Furthermore, the random particle orientation suggests that swelling deformations can be experienced in all directions, as opposed to the vertical direction used for measurement in the free swelling test. When the proportion of bentonite clay decreases, the amount of montmorillonite clay particles decreases (see Fig. 11b and c). The continuous pores of the clay particles have more space between layers, and the particles are larger because the proportion of kaolin is higher, resulting in a higher permeability and reduced swelling time. Because the low-swelling clay has the lowest amount of bentonite, the clay structure was an arranged book-like microstructure, with a flaky plate-like structure (due to flaky-shaped aluminum oxides) inserted in between. This structure corresponds to the results of the free

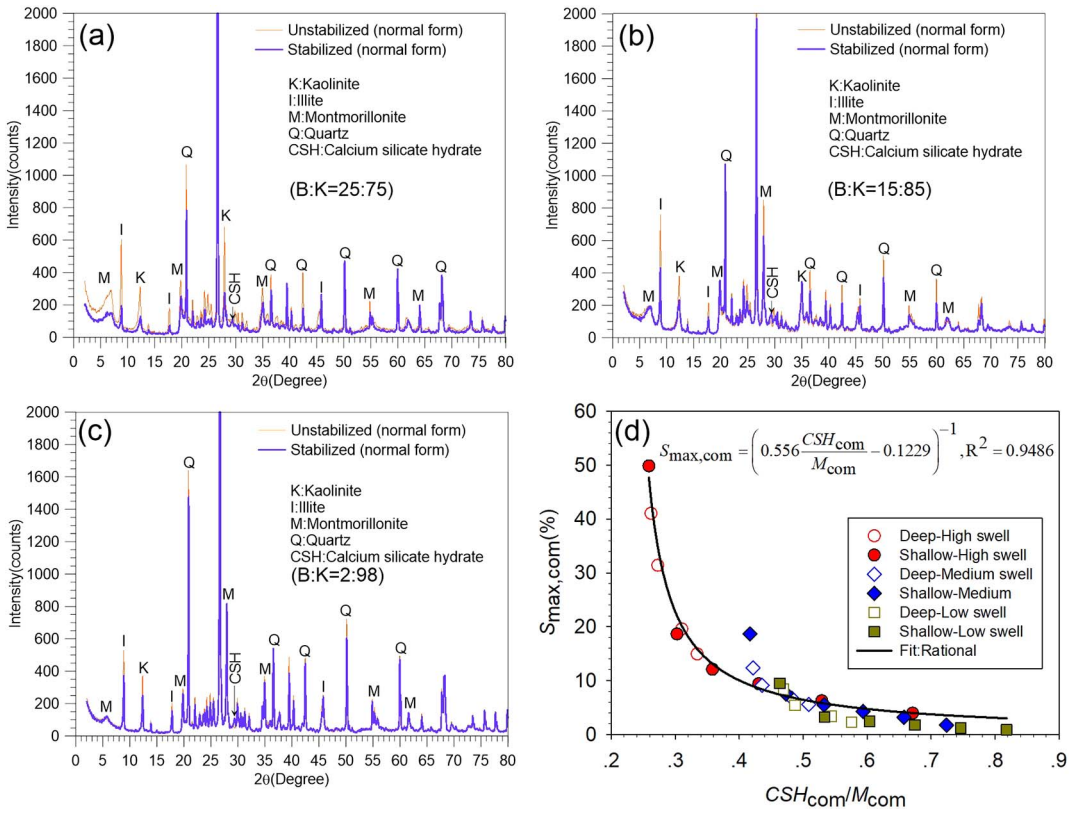

Fig. 10. X-ray diffraction patterns of unstabilized and stabilized raw expansive clays with: (a) high; (b) medium; (c) low degrees of swelling potentials and (d) relationships between $S_{max,com}$ and CSH_{com}/M_{com}.

Table 5
Effect of cement stabilization on the reflection montmorillonite intensities.

Degree of swell potential	$M_{unstabilized}$	$M_{stabilized}$
High	313 (2θ = 6.92°)	149 (2θ = 6.82°)
Medium	192 (2θ = 6.40°)	174 (2θ = 6.42°)
Low	123 (2θ = 6.92°)	121 (2θ = 6.82°)

Table 6
Effect of cement stabilization on the reflection CSH intensities.

Degree of swell potential	$CSH_{unstabilized}$	$CSH_{stabilized}$	Improvement ratio based on peak intensity
	Reference peak at 2θ = 29.46°	Reference peak at 2θ = 29.46°	
High	81	100	1.24
Medium	80	126	1.58
Low	57	99	1.74

swelling test, in which the low-swelling clay has high swelling potential in the initial stage because of the small amount of montmorillonite clay particles and large pore size distribution.

Fig. 11d to f presents the changes in the microstructures of unstabilized expansive clays under full saturation conditions for high, medium, and low swelling potentials. The volume of the clay increased because of the larger voids, which are occupied by water, between the clay particles, resulting in the development of free swelling, as shown in Figs. 4 and 5. The high swelling expansion had the largest void (Fig. 11d) due to the repulsive forces between particles resulting from the high cation exchange capacity due to the large amount of montmorillonite clay particles. The pore size distributions of the microstructures were smaller for the medium and low bentonite contents due to expansive clays, the swelling potentials decreased because CSH was developed from the hydration the lower specific surface area of the mixtures, leading to a lower cation exchange capacity.

When cement was added to unstabilized reaction, the CSH forms ettringite crystals, which are inserted between clay particles and bonded to each other to form a larger cluster. This reduces the pore size since it is occupied by new crystal product (Horpibulsuk et al., 2010), as shown in Fig. 11g to i. Ettringite crystal formation and growth are the main phenomena of the swelling potential of cement-stabilized clays (Aldaood et al., 2014). Ettringite crystals are generally formed in the clay voids during the initial reactions. This formation is expected to occur within a few days to several weeks (Kota et al., 1996]. These crystals will then start to accumulate with the combined reactions between clay and cement. When the existing pore void space of the clay samples cannot accommodate more ettringite crystals, the clay samples will start to swell. Decrease in swelling potential can be attributed to the hydration reactions of ettringite minerals formed inside the clay matrix (Puppala et al., 2005). The amounts of ettringite formation were largest in low-swelling clays and smallest in high-swelling clays, which corresponds to the improvement ratio being based on the reflection intensity of CSH, as shown in Table 6. The concept of a composite material can be adapted to interpret the results of microstructure analysis. The $S_{max,com}$ from the composite free swelling tests in Section 3.3.2 decreased with increasing V_r due to the decrease in the average pore size and pore size distributions of composite materials and the increase in the average proportion of ettringite in the composite materials.

4. Conclusions

In this study, composite free swelling tests were conducted to investigate the effects of increases in thickness, area and volume ratios on the swelling potential, swelling rate and secondary swelling rate. XRD and SEM analyses were performed on unstabilized and stabilized

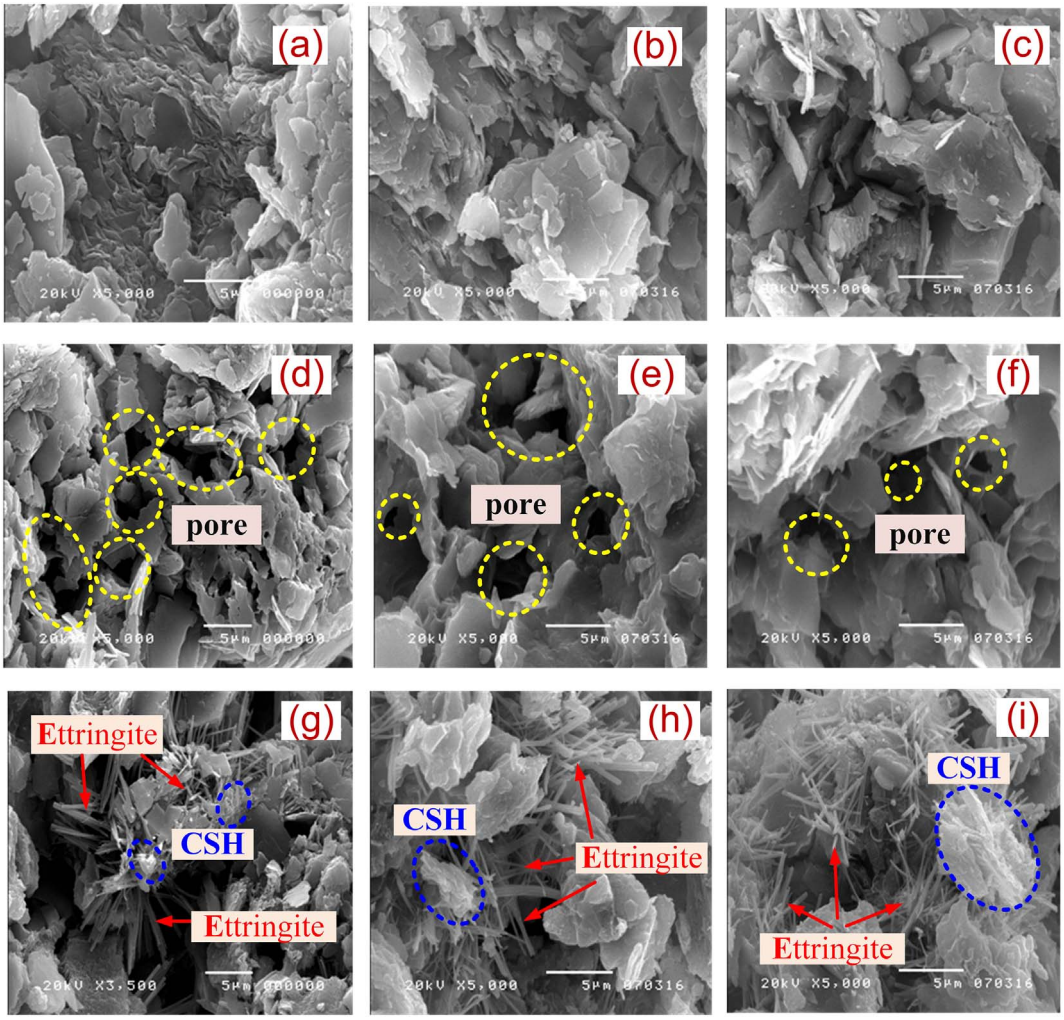

Fig. 11. SEM analysis results for: (a) high, (b) medium and (c) low swelling potentials for unstabilized expansive clay before inundation; (d) high, (e) medium and (f) low swelling potentials for unstabilized expansive clay after complete swelling; and (g) high, (h) medium and (i) low swelling potentials for stabilized expansive clay after complete swelling

expansive clays to study the changes in the minerals and microstructures and to link the microstructural data to the macrostructural data. The results show that the maximum swelling potentials of the composite clays are a function of the reflection intensities of CSH and montmorillonite after stabilization. The following conclusions were drawn from the results of this study:

- $S_{max,com}$ for expansive clays stabilized by the shallow and deep cement mixing methods decreased with increasing T_r and a_r, which can be combined as V_r, because the volume of unstabilized clays was replaced by volumetric cement-stabilized clays.
- A T_r of 0.2 and a_r of 0.23 are suggested as the optimal values for expansive clay stabilization when using the shallow and deep cement mixing methods, respectively, for civil engineering practice based on an improvement ratio higher than 2.
- The time required to reach an asymptotic level, t_{asy}, decreased with increases in T_r and a_r. The t_{asy} for deep mixing was smaller than that for shallow mixing due to cracks in the unstabilized clay surrounding clay-cement column, which occurred due to the effect of construction with deep cement mixing. The water can easily flow through the crack, which accelerates the swelling time.
- The prediction of $S_{max,com}$ using a linear relationship based on the weighted average between $S_{max,unstabilized}$ and $S_{max,stabilized}$ is not accurate, which may be an effect of the non-uniformity of clay mixtures and installation of clay-cement mixing. Thus, a non-linear relationship is more appropriate for predicting $S_{max,com}$.
- Based on XRD analysis, $S_{max,unstabilized}$ decreased due to the decrease and increase in the intensity of $M_{stabilized}$ and $CSH_{stabilized}$, respectively, after stabilization with cement. To link the microstructure results with properties of the composite material, $S_{max,com}$ decreased with increasing $\boldsymbol{V}_r$ due to the smaller M_{com} and larger CSH_{com}, which can be expressed as a rational function of the ratio CSH_{com}/M_{com}.
- Ettringite crystal formation affects the swelling potential of cement-stabilized clays due to the reduced pore sizes and increased bonding between clay particles. The degree of ettringite formation depends on the improvement ratio of CSH. $S_{max,com}$ decreased with increasing V_r due to the decrease in the average pore sizes and pore size distributions of composite materials and increase in the average proportion of ettringite of the composite materials.

Notation

a_r	improvement area ratio
$A_{stabilized}$	cross-sectional area of deep stabilized expansive clay
$A_{unstabilized}$	cross-sectional area of unstabilized expansive clay
b	slope of the swelling path
b_{com}	swelling rate coefficient of composite expansive clay
$b_{stabilized}$	swelling rate coefficients for stabilized expansive clay
$b_{unstabilized}$	swelling rate coefficients for unstabilized expansive clay
CSH	calcium silicate hydrate
$CSH_{stabilized}$	CSH reflection intensities for stabilized clay
$CSH_{unstabilized}$	CSH reflection intensities for unstabilized clay

$M_{stabilized}$ montmorillonite reflection intensities for stabilized clay
$M_{unstabilized}$ montmorillonite reflection intensities for unstabilized clay
ΔS change in swelling
R_{α} secondary swelling rate
$R_{\alpha,com}$ secondary swelling rate of composite expansive clay
$R_{\alpha,unstabilized}$ secondary swelling rate of unstabilized clay
S swelling potential
S_{com} swelling potential for composite expansive clay
SEM scanning electron microscopy
S_{max} maximum swelling potential
$S_{max,com}$ maximum swelling potential for composite expansive clay
$S_{max,stabilized}$ maximum swelling potentials for stabilized expansive clay
$S_{max,unstabilized}$ maximum swelling potentials for unstabilized expansive clay
t time
t_{asy} time required to reach an asymptotic level
T_r improvement thickness ratio
$T_{stabilized}$ thickness of shallow stabilized expansive clay
$T_{unstabilized}$ thickness of the unstabilized expansive clay
V_r improvement volume ratio
XRD X-ray diffraction
XRF X-ray fluorescence

Acknowledgements

This research was funded by King Mongkut's University of Technology North Bangkok under Contract no. KMUTNB-60-ART-006. The authors also extend their appreciation to Thailand Research Fund (TRF) and King Mongkut's University of Technology Thonburi under Basic Research Grant No. BRG6080011.

References

Abu Seif, E.S., 2015. Efficiency of quicklime in reducing the swelling potential of pulverized expansive shale Northern Jeddah, Saudi Arabia. Bull. Eng. Geol. Environ. 74, 637–650.
Agus, S.S., Schanz, T., 2008. A method for predicting swelling pressure of compacted bentonites. Acta Geotech. 3, 125–137.
Aldaood, A., Bouasker, M., Al-Mukhtar, M., 2014. Geotechnical properties of lime-treated gypseous soils. Appl. Clay Sci. 88-89, 39–48.
Al-Rawas, A.A., Goosen, M.F.A. (Eds.), 2006. Expensive Soils: Recent Advances in Characterization and Treatment. Taylor and Francis, London.
Arulrajah, A., Abdullah, A., Bo, M.W., Bouazza, A., 2009. Ground improvement techniques for railway embankments. Proc. Inst. Civil Eng. Ground Improve. 162 (1), 3–14.
ASTM D 4546-14, 2014. Standard Test Methods for One-Dimensional Swell or Collapse of Soils. ASTM International, West Conshohocken, PA, USA.
Azam, S., 2007. Study on the geological and engineering aspects of anhydrite/gypsum transition in the Arabian Gulf coastal deposits. Bull. Eng. Geol. Environ. 66 (2), 177–185.
Azam, S., Wilson, G.W., 2006. Volume change behavior of a fissured expansive clay containing anhydrous calcium sulfate. In: Proceedings of the Fourth International Conference on Unsaturated Soils. ASCE Press, pp. 906–915.
Azam, S., Shah, I., Raghunandan, M.E., Ito, M., 2013. Study on swelling properties of an expansive soil deposit in Saskatchewan, Canada. Bull. Eng. Geol. Environ. 72, 25–35.
Bergado, D.T., Anderson, L.R., Miura, N., Balasubramaniam, A.S., 1996. Soft Ground Improvement in Lowland and Other Environments. ASCE Press, New York.
Chai, J.C., Shrestha, S., Hino, T., Ding, W.Q., Kamo, Y., Cater, J., 2015. 2D and 3D analyses of an embankment on clay improved by soil–cement columns. Comput. Geotech. 68, 28–37.
Cokca, E., 2001. Use of class C-fly ashes for the stabilization of an expansive soils. Geotech. Geoenviron. Eng. 127 (7), 568–573.
Dakshinamurthy, V., 1978. A new method to predict swelling using hyperbola equation. J. South East Asian Society of Soil Eng. – Geotech. Eng. 9 (1), 29–38.
Gapak, Y., Das, G., Yerramshetty, U., Bharat, T.V., 2017. Laboratory determination of volumetric shrinkage behavior of bentonites: a critical appraisal. Appl. Clay Sci. 135, 554–566.
Han, J., Oztoprak, S., Parsons, R.L., Huang, J., 2007. Numerical analysis of foundation columns to support widening of embankments. Comput. Geotech. 34 (6), 435–448.
Horpibulsuk, S., Rachan, R., Chinkulkijniwat, A., Raksachon, Y., 2010. Analysis of strength development in cement-stabilized silty clay from microstructural considerations. Constr. Build. Mater. 24, 2011–2021.
Horpibulsuk, S., Yangsukkaseam, N., Chinkulkijniwat, A., Du, Y.N., 2011. Compressibility and permeability of Bangkok clay compared with kaolinite and bentonite. Appl. Clay Sci. 52 (1–2), 150–159.
Horpibulsuk, S., Chinkulkijniwat, A., Cholphatsorn, A., Suebsuk, J., Liu, M.D., 2012. Consolidation behavior of soil cement column improved ground. Comput. Geotech. 43, 37–50.
Ito, M., Azam, S., 2010. Determination of swelling and shrinkage properties of undisturbed expansive soils. Geotech. Geol. Eng. 28, 413–422.
Jamsawang, P., Bergado, D.T., Voottipruex, P., 2011. Field behavior of stiffened deep cement mixing piles. Proc. Inst. Civil Eng. Ground Improve. 164 (1), 33–49.
Jamsawang, P., Voottipruex, P., Boathong, P., Mairaing, W., Horpibulsuk, S., 2015. Three-dimensional numerical investigation on lateral movement and factor of safety of slopes stabilized with deep cement mixing column rows. Eng. Geol. 188, 159–167.
Jamsawang, P., Boathong, P., Mairaing, W., Jongpradist, P., 2016a. Undrained creep failure of a drainage canal slope stabilized with deep cement mixing columns. Landslides 13, 939–955.
Jamsawang, P., Yoobanpot, N., Thanasisathit, N., Voottipruex, P., Jongpradist, P., 2016b. Three-dimensional numerical analysis of a DCM column-supported highway embankment. Comput. Geotech. 72, 42–56.
Jongpradist, P., Jumlongrach, N., Youwai, S., Chucheepsakul, S., 2010. Strength characteristics of fly ash-cement admixed clay at high water content. J. Mater. Civ. Eng. 22 (1), 49–58.
Khemissa, M., Mahamedi, A., 2014. Cement and lime mixture stabilization of an expansive overconsolidated clay. Appl. Clay Sci. 95, 104–110.
Kitazume, M., Terashi, M., 2013. The Deep Mixing Method. Taylor & Francis Group, London.
Kota, P.B.S., Hazlett, D., Perrin, L., 1996. Sulfate-bearing soils: problems with calcium based stabilizers. Transp. Res. Rec. 1546, 62–69.
Latifi, N., Rashid, A.S.A., Siddiqua, S., Horpibulsuk, S., 2015. Micro-structural analysis of strength development in low-and high swelling clays stabilized with magnesium chloride solution-a green soil stabilizer. Appl. Clay Sci. 118, 195–206.
Liu, S.Y., Du, Y.J., Yi, Y.L., Puppala, A.J., 2012. Field investigations on performance of T-shaped deep mixed soil cement column-supported embankments over soft ground. Geotech. Geoenviron. Eng. 138 (6), 718–727.
Liu, K., Kong, G., Chu, J., Ding, X., 2015. Grouted gravel column-supported highway embankment over soft clay: case study. Can. Geotech. J. 52 (11), 1725–1733.
Lorenzo, G.A., Bergado, D.T., 2004. Fundamental parameters of cement-admixed clay – new approach. Geotech. Geoenviron. Eng. 130 (10), 1042–1050.
Mosser-Ruck, G., Devineau, K., Charpentier, D., Carhelineau, M., 2005. Effects of ethylene glycol saturation protocals on XRD patterns: a critical review and discussion. Clay Clay Miner. 53 (6), 631–638.
Mutaz, E., Dafalla, M.A., 2014. Chemical analysis and X-ray diffraction assessment of stabilized expansive soils. Bull. Eng. Geol. Environ. 73, 1063–1072.
Okyay, U.S., Dias, D., 2010. Use of lime and cement treated soils as pile supported load transfer platform. Eng. Geol. 114, 34–44.
Ouhadi, V.R., Yong, R.N., 2008. Ettringite formation and behavior in clayey soils. Appl. Clay Sci. 42, 258–265.
Ozer, M., Ulusay, R., Isik, N.S., 2012. Evaluation of damage to light structures erected on a fill material rich in expansive soil. Bull. Eng. Geol. Environ. 71 (1), 21–36.
Puppala, A.J., Intharasombat, N., Vempati, R.K., 2005. Experimental studies on ettringite induced heaving in soils. Geotech. Geoenviron. Eng. 131 (4), 325–333.
Saadeldin, R., Siddiqua, S., 2013. Geotechnical characterization of a clay-cement mix. Bull. Eng. Geol. Environ. 72, 601–608.
Shahid, A., 2006. Large-scale odometer for assessing swelling and consolidation behavior of Al-Qatif lay. In: Al-Rawas, A.A., Goosen, M.F.A. (Eds.), Expansive Soils Recent Advances in Characterization and Treatment. Taylor and Francis, London, pp. 85–100.
Shen, S.L., Han, J., Du, Y.J., 2008. Deep mixing induced property changes in surrounding sensitive marine clays. Geotech. Geoenviron. Eng. 134 (6), 845–854.
Shen, S.L., Wang, Z.F., Horpibulsuk, S., Kim, Y.H., 2013a. Jet grouting with a newly developed technology: the twin-jet method. Eng. Geol. 152 (1), 87–95.
Shen, S.L., Wang, Z.F., Sun, W.J., Wang, L.B., Horpibulsuk, S., 2013b. A field trial of horizontal jet grouting using the composite-pipe method in soft deposit of Shanghai. Tunn. Undergr. Space Technol. 35, 142–151.
Sridharan, A., Gurtug, Y., 2004. Swelling behavior of compacted fine-grained soils. Eng. Geol. 72 (1–2), 9–18.
Tang, A.M., Cui, Y.J., Trinh, V.N., Szerman, Y., Marchadier, G., 2009. Analysis of the railway heave induced by soil swelling at a site in southern France. Eng. Geol. 106, 68–77.
Topolnicki, M., 2004. In situ soil mixing. In: Moseley, M.P., Kirsch, K. (Eds.), Ground Improvement. 2004. Spon Press, New York, USA, pp. 331–423.
Topolnicki, M., 2013. In situ soil mixing. In: Kirsch, K., Bell, A. (Eds.), Ground Improvement. CRC Press Taylor & Francis Group, London, UK, pp. 377–378.
Van der Kerkhof, E., 2001. Small scale recycling of plastic soils for trench fills using lime or cement treatment. In: 1st International Symposium on Subgrade Stabilization and In situ Pavement Recycling Using Cement, Vol. 1, pp. 531–540. IECA, Salamanca, Spain.
Voottipruex, P., Jamsawang, P., 2014. Characteristics of expansive soils improved with cement and fly ash in Northern Thailand. Geomech. Eng. J. 6 (5), 437–453.
Wonglert, A., Jongpradist, P., 2015. Impact of reinforced core on performance and failure behavior of stiffened deep cement mixing piles. Comput. Geotech. 69, 93–104.
Yilmaz, I., Civelekoglu, I., 2009. Gypsum: an additive for stabilization of swelling clay soils. Appl. Clay Sci. 44, 166–172.
Yong, R.N., Ouhadi, V.R., 2007. Experimental study on instability of bases on natural and lime/cement-stabilized clayey soils. Appl. Clay Sci. 35, 238–249.
Yoobanpot, N., Jamsawang, P., Horpibulsuk, S., 2017. Strength behavior and microstructural characteristics of soft clay stabilized with cement kiln dust and fly ash residue. Appl. Clay Sci. 141, 146–156.